TTI: 0-6982

Texas A&M Transportation Institute

Utilization of UHPC Bridge Superstructures in Texas—Volume 1: UHPC Mixture Development and Material-Level Experiments

Technical Report 0-6982-R1-Vol1

Cooperative Research Program

TEXAS A&M TRANSPORTATION INSTITUTE
COLLEGE STATION, TEXAS

sponsored by the
Federal Highway Administration and the
Texas Department of Transportation
https://tti.tamu.edu/documents/0-6982-R1-Vol1.pdf

Technical Report Documentation Page

1. Report No.	2. Government Accession No.	3. Recipient's Catalog No.
FHWA/TX-23/0-6982-R1-Vol1		

4. Title and Subtitle	5. Report Date
UTILIZATION OF UHPC BRIDGE SUPERSTRUCTURES IN TEXAS—VOLUME 1: UHPC MIXTURE DEVELOPMENT AND MATERIAL-LEVEL EXPERIMENTS	Published: October 2023
	6. Performing Organization Code

7. Author(s)	8. Performing Organization Report No.
Mary Beth D. Hueste, Anol Mukhopadhyay, Stefan Hurlebaus, John Mander, Hyeonki Hong, Amreen Fatima, Tevfik Terzioglu, and Arash Rockey	Report 0-6982-R1-Vol1

9. Performing Organization Name and Address	10. Work Unit No. (TRAIS)
Texas A&M Transportation Institute The Texas A&M University System College Station, Texas 77843-3135	11. Contract or Grant No. Project 0-6982

12. Sponsoring Agency Name and Address	13. Type of Report and Period Covered
Texas Department of Transportation Research and Technology Implementation Office 125 E. 11th Street Austin, Texas 78701-2483	Technical Report: September 2018–August 2022
	14. Sponsoring Agency Code

15. Supplementary Notes

Project sponsored by the Texas Department of Transportation and the Federal Highway Administration.
Project Title: Utilization of UHPC Bridge Superstructures in Texas
URL: https://tti.tamu.edu/documents/0-6982-R1-Vol1.pdf

16. Abstract

The use of ultra-high performance concrete (UHPC) in Texas bridges has the potential to add substantial improvements to bridge construction. Advanced material properties and superior durability of UHPC can result in significant design and construction benefits. Within this context, this project evaluated the application of UHPC for precast, pretensioned bridge girders. The project scope included a detailed review and synthesis of the relevant literature, analytical feasibility study, development of nonproprietary UHPC mixture designs using locally available materials, material-level experiments for selected UHPC mixtures, fabrication of precast, pretensioned UHPC bridge girder specimens at a precast plant in Texas, full-scale experiments to understand UHPC girder behavior, nondestructive evaluation (NDE) of UHPC girders, fiber distribution and orientation analysis, and development of UHPC production and design guidelines and design examples. Nonproprietary UHPC mixtures were successfully developed to achieve high early strength (14 ksi within 24 hours) for precast applications with desirable outcomes in terms of material properties and durability. Large volume production and girder fabrication were successfully carried out at a precast plant. This Volume 1 research report documents the state-of-the-practice and state-of-the-art for UHPC research conducted domestically and internationally, the development process for eight nonproprietary UHPC mixtures, optimization of a selected UHPC mixture with materials commonly used in precast plants in Texas, and development of a practical mixing procedure for large volume production in precast plant environments. In addition, this volume details the investigation of fresh, hardened, and durability properties of lab-made and plant-made nonproprietary UHPC. Finally, the fabrication of three UHPC girder specimens is documented, along with the NDE of the girders and analysis of cored samples, to assess fiber distribution and orientation and voids by employing X-ray, infrared, and conventional image analysis techniques.

17. Key Words	18. Distribution Statement
Ultra-High-Performance Concrete, UHPC, Mixture Design, Mixing Procedure, Fresh Properties, Hardened Properties, Durability, Service Life Prediction, Precast Plant Production, Girder Fabrication, Nondestructive Evaluation, Fiber Distribution, Fiber Orientation	No restrictions. This document is available to the public through NTIS: National Technical Information Service Alexandria, Virginia https://www.ntis.gov

19. Security Classif. (of this report)	20. Security Classif. (of this page)	21. No. of Pages	22. Price
Unclassified	Unclassified	570	

Form DOT F 1700.7 (8-72)Reproduction of completed page authorized

UTILIZATION OF UHPC BRIDGE SUPERSTRUCTURES IN TEXAS—VOLUME 1: UHPC MIXTURE DEVELOPMENT AND MATERIAL-LEVEL EXPERIMENTS

by

Mary Beth D. Hueste, Ph.D., P.E.
Research Engineer
Texas A&M Transportation Institute

Hyeonki Hong
Graduate Assistant Researcher
Texas A&M Transportation Institute

Anol Mukhopadhyay, Ph.D.
Research Scientist
Texas A&M Transportation Institute

Amreen Fatima
Graduate Assistant Researcher
Texas A&M Transportation Institute

Stefan Hurlebaus, Ph.D.
Research Scientist
Texas A&M Transportation Institute

Tevfik Terzioglu, Ph.D.
Post-Doctoral Research Associate
Texas A&M Transportation Institute

John Mander, Ph.D.
Research Engineer
Texas A&M Transportation Institute

and

Arash Rockey, Ph.D.
Post-Doctoral Research Associate
Texas A&M Transportation Institute

Report 0-6982-R1-Vol1
Project 0-6982
Project Title: Utilization of UHPC Bridge Superstructures in Texas

Sponsored by the
Texas Department of Transportation
and the
Federal Highway Administration

Published: October 2023

TEXAS A&M TRANSPORTATION INSTITUTE
College Station, Texas 77843-3135

DISCLAIMER

This research was sponsored by the Texas Department of Transportation (TxDOT) and the Federal Highway Administration (FHWA). The contents of this report reflect the views of the authors, who are responsible for the facts and the accuracy of the data presented herein. The contents do not necessarily reflect the official view or policies of FHWA or TxDOT. This report does not constitute a standard, specification, or regulation.

This report is not intended for construction, bidding, or permit purposes. The researcher in charge of the project was Mary Beth D. Hueste. The United States Government and the State of Texas do not endorse products or manufacturers. Trade or manufacturers' names appear herein solely because they are considered essential to the object of this report.

ACKNOWLEDGMENTS

This project was conducted at Texas A&M University and was supported by TxDOT and FHWA through the Texas A&M Transportation Institute as part of Project 0-6982, Utilization of UHPC Bridge Superstructures in Texas.

The authors are grateful to the individuals who were involved with this project and provided invaluable assistance, including Tom Schwerdt (TxDOT, project manager), Robert Owens (TxDOT, project director), and the TxDOT Project Monitoring Committee: Ahmed Al-Basha, Biniam Aregawi, Rachel Cano, Geetha Chandar, Chad Dabbs, Jamie Farris, Igor Kafando, Andy Naranjo, Joe Roche, Prapti Sharma, and Jason Tucker.

Co-authors Hyeonki Hong and Amreen Fatima were the principal Ph.D. students on the project, and this work comprised a major part of their doctoral research.

The authors also wish to acknowledge the students involved in the early stages of the project, particularly master's students Brittni Cooper and Jay Shah, and undergraduate students Chase Ottmers and Victoria Prado.

In addition, the following students contributed to this project by helping with the laboratory work and precast plant production process: Stephin Joseph Anna, Victor Balangero, William (Jake) Irr, Mikhail Lanier, Matthew Leffler, Isabel Mlo, Anirutthan Narayanan, Samir Palepu, Jay Parmar, Pushkar Shivechchhu, Nikhil Ganesh Tandel, Xincheng Ethan Wang, Seunghyun Yoon, and Zhen Zhang.

Assistance from the Center for Infrastructure Renewal staff is gratefully acknowledged, including Kai-wei (Victor) Liu, Rick Canatella, Tony Barbosa, Charles Droddy, Kirk Martin, and Dr. Peter Keating (director of the High-Bay Structural & Materials Testing Laboratory).

The TTI staff who supported the project are gratefully acknowledged, especially Madalyn Salcido, who provided overall administrative and business support for the project.

The research team is grateful to Heldenfels Enterprises Inc., San Marcos, Texas, who supported this project by working with the research team to conduct a trial batch of the developed UHPC mixture and fabricated the UHPC girder specimens at its precast plant.

TABLE OF CONTENTS

Page

LIST OF FIGURES

Page

LIST OF TABLES

Page

LIST OF ACRONYMS

A&A	Andreasen and Andersen model
AASHTO	American Association of State Highway and Transportation Officials
ACCT	Accelerated concrete cylinder test
ACI	American Concrete Institute
ASR	Alkali-silica reaction
ASTM	American Society of Testing and Materials
BSG	Bulk specific gravity
C_2S	Dicalcium silicate
C_3A	Tricalcium aluminate
C_3S	Tricalcium silicate
CC	Conventional concrete
CMOD	Crack mouth opening displacement
CoV	Coefficient of variation
CSA	Canadian Standards Association
CT	Computed tomography
DEF	Delayed ettringite formation
DOT	Department of transportation
DR	Distribution ratio
FHWA	Federal Highway Administration
FRC	Fiber-reinforced concrete
GGBFS	Ground-granulated blast furnace slag
GPR	Ground penetrating radar
HPC	High performance concrete
HPFRCC	High performance fiber-reinforced cement concrete
HRWR	High-range water reducer
HRWR/c	HRWR-to-cement
HRWR/cm	HRWR-to-cementitious material
HSC	High strength concrete
JSCE	Japan Society of Civil Engineers
LRFD	Load and Resistance Factor Design
LSCT	Linear strain conversion transducer
LVDT	Linear variable displacement transducer
MOE	Modulus of elasticity
NIST	National Institute of Standards and Technology
NSC	Normal strength concrete
PCI	Precast/Prestressed Concrete Institute
PSR	Pore solution resistivity
RCPT	Rapid chloride ion penetration test
RDM	Relative dynamic modulus of elasticity
RH	Relative humidity
RPC	Reactive powder concrete
RSRH	Rapid set rapid hardening
SCC	Self-consolidating concrete
SCM	Supplemental cementitious materials

SFRC	Steel fiber-reinforced concrete
SIFCON	Slurry infiltrated fiber concrete
SiO_2	Silicon dioxide
TxDOT	Texas Department of Transportation
UHPC	Ultra-high performance concrete
UHP-FRC	Ultra-high performance fiber-reinforced concrete
UPV	Ultrasonic pulse velocity
w/*b*	Water-to-binder
w/*c*	Water-to-cement
w/*cm*	Water-to-cementitious material

1 INTRODUCTION

1.1 BACKGROUND AND SIGNIFICANCE

The advanced properties of ultra-high-performance concrete (UHPC) make it attractive for applications in the bridge industry. Generally, UHPC is defined as concrete that has minimum compressive strength of 22 ksi with specified durability, toughness, and tensile ductility from fibers (ACI 239R-18 2018). Due to the presence of fibers, the ductility and energy absorption of UHPC is typically 300 times greater than that of high-performance concrete (HPC) (Wang et al. 2015). The development of UHPC began in the early 1990s and has evolved into its current form over the last 30 years (Naaman and Wille 2012). In its early applications, it was also referred to as reactive powder concrete (RPC) and was first studied by Richard and Cheyrezy (1995). They achieved ultra-high compressive strength from 29–116 ksi while also improving the ductility by two orders of magnitude. Their design was later optimized in the late 1990s at the Lafarge Research Center in collaboration with the Bouygues group and Rhodia to develop the first marketed UHPC—Ductal® (Resplendino 2011).

The high strength, enhanced ductility and energy absorption, and superior durability of UHPC leads to longer service structure life with reduced maintenance. In order to take advantage of the beneficial properties of UHPC in larger volume applications, such as precast, pretensioned bridge girders, more cost-effective nonproprietary UHPC mixtures have been studied and developed in recent years (Berry et al. 2017; El-Tawil et al. 2018; Joe et al. 2017; Khayat and Valipour 2018; Mendonca et al. 2020; Weldon et al. 2010). Nonetheless, a need remains to further develop and assess nonproprietary UHPC mixtures for application to bridge girders and to better understand their performance in terms of fresh and hardened properties, durability and longer-term properties, and the structural behavior of UHPC members.

1.2 OBJECTIVES AND SCOPE

The use of UHPC in Texas bridges has the potential to produce substantial improvements to bridge construction by reducing the number of girders and/or weight of the superstructure, increasing span length, minimizing the use of conventional reinforcing bars, developing new structural systems, and enhancing durability and service life. However, several challenges have slowed the application of UHPC in the precast industry, such as the high cost of available proprietary UHPC

mixtures in the market, slower production due to longer curing times, additional precast facility requirements for heat or steam curing and material storage, and limited structural design guidance. The aim of this research is to address these concerns and to support the application of UHPC in the precast industry, with a specific focus on precast, pretensioned bridge girders in Texas.

There are three main objectives of this research:

1. Conduct an analytical feasibility study to identify the material properties that a nonproprietary UHPC mixture design should incorporate to deliver the optimal design benefits.
2. Develop a nonproprietary concrete mixture design to meet the needs identified in Objective 1.
3. Conduct experiments (full-scale and material-level) to study long-term mechanical properties to eliminate or minimize the use of ordinary reinforcing bars in UHPC applications.

This Volume 1 report documents the following aspects of the research project:

- Review of the literature related to mixture proportions and properties of UHPC.
- Development of nonproprietary UHPC mixtures for use in Texas precast, pretensioned bridge girders that achieve target properties identified from the analytical feasibility study.
- Production of a trial batch for a selected UHPC mixture at a precast plant.
- Fabrication of three precast, pretensioned UHPC bridge girder specimens at a precast plant.
- Material-level experiments—including fresh properties, short-term and long-term hardened properties, durability, microstructure, and fiber orientation and distribution.

The Volume 2 report describes the analytical feasibility study and full-scale UHPC girder testing in detail. The Volume 3 report includes guidelines for production of UHPC, design guidelines for precast, pretensioned UHPC bridge girders, and UHPC girder design examples.

1.3 RESEARCH PLAN

The findings of this research study support implementation of precast, pretensioned UHPC bridge girders in Texas. The following tasks were conducted to achieve the goals of this research project systematically:

- Task 1. Project Management and Research Coordination
- Task 2. Review State-of-the-Art and State-of-the-Practice
- Task 3. Conduct Analytical Feasibility Study
- Task 4. Develop Nonproprietary UHPC Mixture Design
- Task 5. Material-Level Experiments for Selected Mixes
- Task 6. Full-Scale Experiments
- Task 7. Develop Design Guidelines and Examples

1.4 REPORT OUTLINE

This Volume 1 report includes nine chapters that describe the findings from Tasks 2–6.

Chapter 1 describes the background and significance, objectives and scope, and research plan of this study and outlines the Volume 1 report.

Chapter 2 summarizes a review of the state-of-the-practice and state-of-the-art on UHPC. This chapter focuses on the UHPC mixture design, along with mixing, fresh and hardened properties, durability, and applications of UHPC. The literature review documents domestic and international research published in journals, conferences, and reports. Based on the findings from a thorough literature review, possible issues and areas of improvement were identified for the development of the UHPC mixture design, material-level experiments, and full-scale experiments.

Chapter 3 presents the test procedures and methods for the material-level experiments used in this research. The testing for fresh properties includes flow spread, time of set, and unit weight. The test methods for hardened properties are documented for compressive strength, direct and indirect tensile strength, modulus of elasticity (MOE), creep, and shrinkage. The test methods for durability are described and include rapid chloride ion penetration, bulk resistivity, surface resistivity, freeze-thaw resistance, scaling resistance, abrasion resistance, and alkali-silica reaction (ASR).

Chapter 4 presents the development process for the nonproprietary UHPC mixture designs. Understanding the fundamental mechanism for proportioning constituent materials is essential to achieve the target properties identified from the analytical feasibility study. The mixing procedure was studied and developed for the best mixing efficiency. A total of eight UHPC mixtures were developed with Type I/II and Type III cement. Based on the key properties, material cost, and service life prediction, a UHPC mixture was selected for further study and precast plant application. In addition, the optimum fiber volume that satisfied structural performance and cost was studied and determined.

Chapter 5 shows the optimization of the selected mixture for precast plant applications and further study. The selected UHPC mixture was optimized with the materials used at the selected precast plant in Texas, including cement, wet sand, and a high-range water reducer (HRWR). The proportions of the selected mixture were updated accordingly. The mixing procedure was also updated to accommodate wet sand conditions with considerations of the additional time for a large volume of steel fibers. A 2 cyd trial batch of UHPC was produced at the precast plant. The companion specimens for investigation of the properties of plant-made UHPC were cast at the plant and evaluated at the lab. This chapter describes the lessons learned from the trial batch at the plant and offers a comparison of the properties between lab-made and plant-made UHPC.

Chapter 6 presents the fabrication process of the three UHPC girder specimens, including two Tx34 girders (50 ft long) and one Tx54 girder (70 ft long). Key observations while mixing and casting the girders are described. The companion small-scale specimens of the girders were investigated both at the plant and the lab for fresh and hardened properties and durability. The properties are compared with previous lab-made and plant-made UHPC. Long-term hardened properties such as creep and shrinkage were also studied. Updated prediction models for creep and shrinkage of the developed UHPC mixture were proposed for use in prestress loss estimation.

Chapter 7 presents the results of the nondestructive evaluation of the girders. The girders were investigated by employing infrared thermography, ground penetrating radar (GPR), ultrasonic tomography, and ultrasonic pulse velocity (UPV). Infrared thermography and GPR were used to detect subsurface defects. Ultrasonic tomography detected discontinuities of UHPC, such as fiber distribution. UPV was employed to evaluate the strength of the UHPC girder specimens and

identify fiber distribution and orientation that can be determined whether the UPV is uniform or not.

Chapter 8 describes fiber distribution and orientation in the UHPC girder specimens. The samples were collected by coring the three girder specimens at locations along the girder length and by evaluating different locations over the girder height. The surface images of the cored samples were carefully documented. The cored samples were evaluated by both X-ray computed tomography scan and image analysis techniques.

Chapter 9 provides a summary of key findings from each of the tasks documented in this Volume 1 report.

2 LITERATURE REVIEW

2.1 INTRODUCTION

UHPC is a new generation of concrete technology for developing more ambitious structures with enhanced performance and aesthetics. This section briefly summarizes the history of UHPC development and its definition in the literature.

The origin of UHPC dates to the 1970s; it emerged from research initiatives aimed at increasing the compressive strength of concrete by the variation of the cementitious composite properties, curing and treatment methods, and other related criteria. Unlike the compressive strengths of normal strength concrete (NSC) of around 3 to 6 ksi (MacGregor et al. 1997), UHPC attains strengths up to 25 to 30 ksi. Rossi (2000) stated that the endeavors to achieve high compressive strength in concrete began as early as the 1930s. Naaman and Wille (2012) noted that the process of generating such composites commenced in the early 1970s with the goal of increasing the compressive strength by altering different parameters, such as the composition of the cementitious matrix, and adding fiber content that interacts with the cementitious matrix and the cumulative composite material.

Yudenfreund et al. (1972) found that limiting the water-to-cement ratio between 0.2 and 0.3 results in the strength of the paste being as high as 33 ksi. Roy et al. (1972) showed that the use of high pressure and hot pressing can further enhance the strength of cement pastes up to 74 ksi. Several predecessors to UHPC that were instrumental in directing the scientific and cement manufacturing industry to develop UHPC are as follows:

- Micro-defect-free paste composite with a polymer (Alford and Birchall 1985)
- DENSIT® (Bache 1981)
- Densified small particles (Hjorth et al. 1983)
- High-strength concrete (HSC) (Ahmad and Shah 1985)
- HPC (Aitcin 1993)
- Slurry infiltrated fiber concrete (SIFCON) (Lankard 1984; Naaman and Homrich 1989)
- Compact reinforced concrete (Bache 1987)

- High-performance fiber-reinforced cement concrete (HPFRCC) (Reinhardt and Naaman 1992)
- Engineered cementitious composites (Li and Wu 1992)

Both SIFCON and engineered cementitious composites (having a compressive strength less than 10 ksi each) are mentioned due to their high uniaxial tensile strength, although they did not possess a compact or dense matrix (Rossi 2000).

2.1.1 Development of UHPC Class Material

The rapid advancement in the achievement of exceedingly high compressive strengths motivated the development of a material with superior performance above that of NSC, HSC, and HPC. Table 2.1 summarizes typical material characteristics of NSC, HSC, and HPC. Subsequent sections of this chapter discuss these properties. de Larrard and Sedran (1994) developed an ultra-high-performance cementitious material by increasing the packing density of the material. The authors developed two models for the prediction of packing density of the particle mix by using Mooney's suspension viscosity model. The main objective was optimizing the parameters during the mix-design process such that the material has optimal ranges of consistency of the fluid, the essential ingredients, and heat treatments of reasonable extents. Therefore, the developed mixes were investigated for optimal performance using the solid suspension model and relevant experimental tests. The research led to the production of a fluid mortar with a compressive strength of 34 ksi.

Table 2.1. Comparison of NSC, HPC, and UHPC (adapted from Ahlborn et al. 2008b).

Mixture Composition Parameter	**NSC**	**HPC**	**UHPC**
Maximum Aggregate Size, in.	0.75–1.00	0.38–0.50	0.016–0.024
Water to cement (w/c) Ratio	0.40–0.70	0.24–0.35	0.140–0.270
Mechanical Performance Parameter			
Compression Strength, ksi	3.0–6.0	6.0–14.0	25.0–33.0
Split Cylinder Tensile Strength, ksi	0.36–0.45	0.50–0.90	1.00–3.50
Poisson's Ratio	0.11–0.21	0.13–0.16	0.19–0.24
Creep Coefficient, C_u	2.35	1.6–1.9	0.2–0.8
Porosity, Percent	20–25	10–15	2–6
Fracture Energy, k-in/in^2	0.00057–0.00086	–	0.057–0.228
Young's Modulus, ksi	2000–6000	4500–8000	8000–9000
Modulus of Rupture 1st Crack, ksi	0.4–0.6	0.8 to 1.2	2.4–3.2
Flexure Strength—Ultimate, ksi	–	–	3.0–9.0
Shrinkage	–	Post Cure 40 to 80 × 10^{-5}	Post Cure < 1 × 10^{-5}, No autogenous shrinkage after cure
Coefficient of Thermal Expansion, per °F	4.1–7.3 × 10^{-6}	–	7.5–8.6 × 10^{-6}
Durability Performance Parameter			
Freeze/Thaw Resistance	10 percent Durable	90 percent Durable	100 percent Durable
Chloride Penetration, Coulombs Passing	> 2000	500 to 2000	< 100
Air Permeability (k) at 24 hrs and 40°C, in^2	4.65 × 10^{-14}	0	0
Water Absorption at 225 hrs, lb/in^2	4 × 10^{-3}	5 × 10^{-4}	7.1 × 10^{-5}
Chloride Ion Diffusion Coefficient (by steady state diffusion), in^2/s	1.55×10^{-9}	7.75 × 10^{-10}	3.1 × 10^{-11}
Penetration of Carbon / Sulfates	-	-	3.1 × 10^{-11}
Scaling Resistance, lb/ft^2	Mass Removal > 0.205	Mass Removal 0.016	Mass Removal 0.002

–: not available

Richard and Cheyrezy (1995) developed an ultra-high-strength concrete called RPC with enhanced ductility by altering the composition and handling of the mix. It was reported that RPC could find a huge market for the prestressed structures. The authors found that the incorporation of steel aggregate resulted in a compressive strength as high as 117 ksi. The authors concluded that improved mechanical performance is achieved by excluding coarse aggregate and using an optimal granular mixture that makes the cementitious matrix dense and homogenous. The density is further improved by subjecting the fresh concrete to a confining pressure to remove excess water. Induced microcracks due to confining pressure did not lead to any hinderance in the development of additional compressive strength. The RPC showed higher ductility due to the addition of small-size steel fibers (5.9 × 10^{-3} in. diameter and 0.5 in. long) at a 2.0–2.5 percent by volume ratio.

The optimization of their design at Lafarge Research Centre (in partnership with Bouygues and Rhodia) led to the development of Ductal®, patented and launched by Lafarge in 2001 (Resplendino and Toulemonde 2013a). Moreover, the Laboratoire Central des Ponts et Chaussées (LCPC, France) developed the multi-scale fiber-reinforced concrete known as CEMTEC® (Rossi 2000). CARDIFRC® in the United Kingdom (Alaee and Karihaloo 2003) and CERACEM® in Switzerland (Maeder et al. 2004) are also worth mentioning in the discussion of commercial production of UHPC.

The brand-name UHPC products are very expensive compared to conventional concrete (CC), and that motivates most contractors to opt for nonproprietary UHPC. In response to this concern, (Wille et al. 2011) later conducted research to develop UHPC that can develop a compressive strength of up to 29 ksi using locally available materials in the United States without the use of expensive treatment processes involving heat curing and compaction. Many other research initiatives, such as those conducted by the Iowa (Aaleti et al. 2013), Virginia (Ozyildirim 2011), Michigan (Ahlborn et al. 2008; El-Tawil et al. 2016), New York (Royce 2016), Montana (Berry et al. 2017), New Mexico (Weldon et al. 2010), and Colorado Departments of Transportation (Kim 2018), also serve as a good resource for the development of UHPC. Both international and national scientific communities have participated in such investigations.

Several countries around the world have started using UHPC in various construction applications such as bridges, building, and retrofitting. Canada, South Korea, Germany, France, Switzerland, Australia, Japan, and the United States have used UHPC based on the objective of implementing challenging design aspirations. The French Standardization Association was first in the world to publish design codes for UHPC (NF-P-18-451 2018; NF-P-18-470 2016; NF-P-18-710 2016) based on the recommendations of the French Association of Civil Engineers (AFGC 2013). Other nations are constantly developing a streamlined version of the design and testing of UHPC members. The leading organizations are the Swiss Institute of Engineers and Architects (Swiss Society of Engineers and Architects 2013), Standards Australia, Canadian Standards Association (CSA, Canada), German Committee on Structural Concrete, Spanish Association of Concrete No. 1 (ACHE Spain), and Japan Society of Civil Engineers (JSCE 2006). In the United States, the American Society of Testing and Materials (ASTM) has prepared the modifications that should be applied for the testing of UHPC. Chapter 3 describes the material testing procedures. The Volume

2 report discusses the design requirements and recommendations given by various major structural design codes and guides. Many state departments of transportation (DOTs) in the United States have also followed suit, along with the Federal Highway Administration (FHWA), in developing bridge structures from UHPC. Section 2.6 discusses some pioneering and significant UHPC applications in the United States and other countries.

2.1.2 Definitions of UHPC

There is an abundance of work that was undertaken at the same time in this field that resulted in the emergence of different variants of a superior cementitious material being overlapped with the common ultimate target of increased compressive strength and enhanced durability.

The American Concrete Institute (ACI) Committee 239 on UHPC guidance (ACI 239R-18 2018) provided a definition of UHPC as follows:

> Ultra-High-Performance Concrete (UHPC) is a concrete that has a minimum specified compressive strength of 22,000 psi (150 MPa) with specified durability, tensile ductility and toughness requirements; fibers are generally included to achieve specified requirements.

The Precast/Prestressed Concrete Institute (PCI) developed a definition of PCI-UHPC with the following minimum properties (eConstruct 2020):

- Flow spread: 8 to 11 inches
- Compressive strength: >10 ksi at prestress release and >18 ksi at service
- Flexural strength: 1.5 ksi for first crack and 2.0 ksi for peak strength
- Resistance to chloride ion penetration: <500 Coulombs at 28 days

Another definition that may be considered a milestone in the process of distinguishing UHPC from its forerunner composites is stated by Russell et al. (2013) in Project Report FHWA-HRT-13-060, as follows:

> UHPC is cementitious-based composite materials with discontinuous fiber reinforcement, compressive strengths above 22 ksi, pre-and post-cracking tensile

> strengths above 0.70 ksi, and enhanced durability via their discontinuous pore structure (Graybeal 2011).

The French Association of Civil Engineers (AFGC 2013) defined UHPC as follows:

> Ultra High Performance Fiber-Reinforced Concrete are materials with a cement matrix and a characteristic compressive strength of more than 150 MPa (22 ksi) and a maximum of 250 MPa (36 ksi).

Naaman and Wille (2012) proposed the following definitions for the class of composite materials that may be categorized as UHPC and ultra-high-performance fiber-reinforced concrete (UHP-FRC).

- Ultra-high-performance concrete (UHPC) is a hydraulic cement-based concrete with a compressive strength at least equal to 22 ksi.
- Ultra-high-performance fiber reinforced concrete (UHPFRC) is a UHPC with fibers added in order to significantly improve a particular mechanical property (or properties), or to qualify the concrete by attributes such as the minimum water to binder ratio, minimum cement content, minimum packing density or minimum level of durability performance.

These definitions help set the standards that need to be met while developing UHPC mixtures.

Resplendino and Toulemonde (2013a) revealed further distinct features of UHPFRC that set it apart from high-performance and very high-performance concrete, such as the presence of fibers for making the structure more ductile and the potential to dispense with the requirement of "passive reinforcement." This feature suggests that only "the main passive or active reinforcement bars" suffice to resist the external actions that are in excess of those actions resisted by the fiber reinforcement.

UHPC is generally defined as a cementitious material with steel fibers, a compressive strength of 22 ksi or higher, a direct tensile strength above 1.0 ksi, and a reduced capillary porosity due to high binder content. These criteria also agree with the definitions provided above by Naaman and

Wille (2012), Russell et al. (2013), AFGC (2013), and the latest ACI 239R-18 (2018); thus, researchers and related guidelines are approaching a consensus on the characteristic definitions of UHPC.

2.2 MIXTURE DESIGN OF UHPC

2.2.1 General

A significant amount of research has been conducted on the development and application of UHPC in the United States and around the world. Most of the conducted research focuses on two main areas. The first area is the development of nonproprietary mixture designs with locally available materials to reduce the material cost without compromising hardened properties, including compressive strength, tensile strength, and durability. The second area is the use of UHPC in structural applications. This section focuses on the review and synthesis of UHPC mixture designs. The following subsection describes principles of UHPC mixture design to achieve advanced mechanical properties. The next section presents typical UHPC constituent materials that have been studied. The last two sections compile literature related to mixture methods and optimizing the material proportions to develop cost-effective UHPC mixtures.

2.2.2 Principles of Mixture Design

Berry et al. (2017) listed the basic principles of UHPC to achieve the advanced properties as the following:

- High particle packing density
- Low water to cement (w/c) ratio
- Pozzolanic reactions and filler effect of supplemental cementitious materials (SCM)
- Optimized particle dispersion during mixing by using a high-range water reducer
- High-quality aggregates and cements
- Crack bridging effect from steel fibers

The authors noted that the most important principle for UHPC mix design is the high particle packing density because it can significantly reduce the porosity of UHPC.

Wille and Boisvert-Cotulio (2015) conducted a research study investigating the material efficiency in UHPC mixture design and suggested that an increase in particle packing density is one of the key parameters to achieve appropriate fresh and hardened properties and durability. Based on a review of literature related to UHPC mixture design, particle packing density is one of the key parameters that affects the rheological behavior (de Larrard and Sedran 1994; Li and Kwan 2014; Richard and Cheyrezy 1995; Russell et al. 2013; Wille and Boisvert-Cotulio 2015; Zdeb 2013). The effect of the particle packing density on the UHPC performance can be summarized as follows:

- Increase in the particle packing density improves rheological behavior, mechanical performance, and durability of UHPC.
- High particle packing density reduces the volume of water-filled voids. As a result, less water is trapped in voids and the remaining water coats cementitious particles. More water covering the surface of the particles reduces the viscosity of the paste and therefore, the rheological behavior of the paste is improved. It means that the flowability of the paste can be improved while maintaining the *w*/*c* ratio or that the flowability can be maintained while reducing the *w*/*c* ratio.
- In addition, because a low *w*/*c* ratio contributes to limit the amount of unreacted water in the mix, the formation of capillary pores is decreased. Thus, low porosity of the paste can be obtained by the achievement of high particle packing density. The low porosity improves the durability performance of UHPC.

Wille et al. (2011) demonstrated that a table test in accordance with ASTM C230 (2008) for identifying spread values of fresh concrete can be used to evaluate particle packing density of the paste because the rheological behavior and the mechanical performance of the paste are strongly correlated.

To achieve high particle packing density, particle size distribution has to be optimized. Optimization of particle size distribution for spacing packing was introduced by Richard and Cheyrezy (1995) while developing RPC. The authors noted that maintaining the diameter ratio of fine aggregate-to-cement particles at a minimum of 13 gives the optimum spacing packing that allows high compressive strength, mechanical homogeneity, and high density. Thus, optimization

of particle size distribution of material constituents for UHPC is one of the key parameters to obtain the desired particle packing density.

Wille et al. (2011) provided the basic material constituents and their recommended ratios for UHPC to improve packing density as:

- Cement
- Pozzolanic reactive material such as silica fume with a particle size ratio of 0.05 to 0.20 to that of cement
- A fine material as filler such as SCMs, ground quartz, and glass powder with a range of particle size between that of cement and silica fume
- Fine aggregate with maximum particle size of 0.05 in.
- HRWR to optimize particle dispersion and avoid agglomeration during mixing

2.2.3 UHPC Constituent Materials

A typical mixture proportion of UHPC is comprised of binder (cement and pozzolanic reactive materials), filler (inert fine materials such as ground quartz), aggregate, HRWR, and steel fibers. Table 2.2 shows the mixture proportions of a commercial UHPC product. Binder and filler materials account for approximately 40 percent and 10 percent by weight, respectively (Graybeal 2006b).

Table 2.2. Typical Mixture Proportions of Commercial UHPC (Graybeal 2006b).

Material	Amount (lb/yd^3)	Proportion by Cement Weight	Percentage by Total Weight
Portland cement	1200	1.00	28.5
Silica fume	390	0.33	9.3
Ground quartz	355	0.30	8.4
Fine sand	1720	1.43	40.8
Superplasticizer	51.8	0.04	1.2
Accelerator	50.5	0.04	1.2
Water	184	0.15	4.4
Steel fibers	263	0.22	6.2

2.2.3.1 Binder

To achieve advanced hardened properties and durability, a large amount of binder materials is necessary for UHPC. The proportion of binder accounts for 38 percent by total weight of the

mixture shown in Table 2.2. Sakai et al. (2008) reported that the desired chemical composition in the cement is a high percentage of tricalcium silicate (C_3S) and dicalcium silicate (C_2S) due to its contribution for strength development. In addition to the proportion of C_3S and C_2S, a low percentage of tricalcium aluminate (C_3A), which is normally less than 8 percent, is suggested (Wille and Boisvert-Cotulio 2015). The rapid hydration of C_3A and the large surface area of the particles increase water demand and viscosity and thus lead to a high *w*/*c* ratio. The authors did not recommend use of Type III Portland cement because its C_3A content is usually higher than 8 percent.

Silica fume accounts for 9.3 percent by total weight of the mixture shown in Table 2.2. Alkaysi and El-Tawil (2016) suggested that the ratio of silica fume-to-cement by weight can be adjusted within a range from 0.1 to 0.3. The authors also noted that silica fume contributes to improved compressive strength and durability due to its pozzolanic reaction and fine particle size. In addition, silica fume creates a filler effect because it fills the voids in UHPC paste due to its fine particle size (Magureanu et al. 2012). However, according to de Larrard and Sedran (1994), the amount of the silica fume that substitutes for the cement should be optimized. They reported that overdosage of silica fume may decrease mechanical properties of concrete because the silica fume remaining after filling voids in the paste can lead to repulsion of the cement particles. Meng et al. (2016) conducted an experimental study with 26 mixtures that consist of binary and ternary pastes created by a combination of cement, silica fume, fly ash, and granulated blast furnace slag. The mixture that achieved the highest early strength is the binary paste that had the lowest content of silica fume among binary and ternary pastes that include silica fume (95 percent cement with 5 percent silica fume).

2.2.3.2 Filler

The filler consists of inert material with fine particles that are smaller than cement particles and larger than silica fume. Its fine particle size plays an important role in filling voids between sand, unhydrated cement particles, and the hydration products. The filler contributes to a reduction of porosity and permeability and an increase in compressive strength. Therefore, the particle size distribution of filler materials should be between the particle sizes of cement and of silica fume to make a dense paste (Alsalman et al. 2017). Typically, fly ash, silica powder, ground quartz,

metakaolin, and rice husk ash are used as fillers in the UHPC matrix. Generally, filler materials in the total mixture correspond to 10 to 30 percent of the cement weight (Alkaysi and El-Tawil 2016; Wille et al. 2011). Ground quartz as a filler material accounts for 8.4 percent by total weight of the mix, which corresponds to 30 percent of the cement weight (Table 2.2). In addition to particle size, the particle shape of filler materials affects the rheological behavior of the UHPC paste. Wille and Boisvert-Cotulio (2013) reported that fly ash is the most efficient filler material due to its low cost, rounded shape of particles, and appropriate particle size in comparison to silica powder, metakaolin, ground-granulated blast furnace slag (GGBFS), and limestone power.

2.2.3.3 High-Range Water Reducer

An HRWR is indispensable for a UHPC mix to achieve low *w*/*c* ratio while maintaining appropriate workability. However, a large dosage of HRWR may delay the setting time of UHPC; however, the delay can be avoided by using an accelerator admixture to increase the hydration reaction by dispersing the cement particles in the water to decrease the setting time. Lafarge, which developed a commercial UHPC, Ductal®, suggests an accelerator dosage of 50 lb/yd^3 for UHPC to mitigate the delay of setting time due to the large dosage of HRWR (Russell et al. 2013).

2.2.3.4 Aggregate

Richard and Cheyrezy (1995) indicated that the homogeneity of concrete can be enhanced by eliminating coarse aggregate. The authors reported that replacing coarse aggregate (0.8 in. maximum size) with fine aggregate (0.015 in. maximum size) improves mechanical properties and reduces porosity due to high particle packing density. Wille and Boisvert-Cotulio (2015) reported that aggregate in UHPC can be optimized by maximum size, particle size distribution, and aggregate-to-cement ratio. Maximum size and particle size distribution of aggregate are related to particle packing density; thus, these factors affect workability, strength, and durability like filler materials (Wille and Boisvert-Cotulio 2015). Park et al. (2008) investigated an optimum aggregate-to-cement ratio, and the authors suggested 1.1 to achieve the highest compressive strength. Li and Kwan (2011) indicated that the required volume of the paste should be more than the volume of voids between fine aggregate particles, and thus a high aggregate-to-cement ratio may be not enough to fill the voids. Wille and Boisvert-Cotulio (2015) reported that using an aggregate-to-cement ratio from 1.0 to 2.0 is helpful to develop cost-effective UHPC because the

cost of fine aggregate is relatively cheaper than cement, and the aggregate does not significantly decrease workability and strength. Kim (2018) noted that the shape of silica sand particles is spherical, and its particle size is relatively constant in comparison to natural sand, which allows better rheological characteristics in the UHPC matrix.

2.2.3.5 Steel Fibers

Steel fibers enhance ductility and provide additional tensile strength for UHPC. The various fiber characteristics, such as fiber length, shape, volume of fiber content, aspect ratio, orientation, and distribution, affect the tensile behavior and strength of UHPC members. Even though an increase in steel fiber content increases tensile strength, a practical limit of around 2 to 3 percent by volume is recommended to have consistent fiber distribution and good workability. In addition, the high cost of steel fibers also requires optimizing the amount of steel fiber (Yoo et al. 2013).

Wille et al. (2011) and Pyo et al. (2015) conducted tests to identify the effect of fiber volume by testing 1.0 to 2.5 percent fiber content with straight, hooked-end, and twisted fiber shapes. The authors found that an increase in fiber volume improved the tensile strength and strain capacity regardless of the steel fiber shape. However, in the case of hooked-end steel fibers, even though the fiber volume was increased from 1.5 to 2.5 percent, the tensile strain held constant at about 0.46 percent.

2.2.4 Mixture Design Methods and Procedures

2.2.4.1 Mixture Design Methods

Two methodologies have been primarily employed for UHPC mix design. The first approach is to reduce porosity in the UHPC paste by decreasing the water-to cementitious material ratio with high temperature or pressure curing (Richard and Cheyrezy 1995). However, Wille et al. (2011) reported that this approach results in a high amount of entrapped air due to the reduced water-to-cementitious material (*w*/*cm*) ratio. In addition, Meng et al. (2016) pointed out that high temperature/pressure curing is not appropriate for cast-in-place UHPC. The second approach is to increase particle packing density (de Larrard and Sedran 1994). Li and Kwan (2014) adopted a modified Andreasen and Andersen model to reduce porosity of the UHPC mix by increasing

particle packing density. Generally, this second approach has been employed by researchers to develop UHPC mixture designs that avoid temperature/pressure curing.

2.2.4.2 Mixture Design Procedures

Two commonly used procedures to develop UHPC mixture designs have been identified in the literature. The first approach uses a multiphase method that separately develops the paste (cement + silica fume + filler + HRWR + water), the cementitious matrix (paste + aggregate), and the cementitious composite (matrix + steel fiber) (Wille and Boisvert-Cotulio 2015; Wille et al. 2011). Research conducted by FHWA and the Michigan Department of Transportation developed the UHPC mixture design using a multiphase approach. In Phase I, researchers focused on the development and optimization of the paste. In Phase II, the cementitious matrix was optimized with the aggregate. In Phase III, the cementitious composite was developed and optimized with steel fiber. Wille and Boisvert-Cotulio (2015) reported that the development of the UHPC paste is the most important step because the paste binds other constituents such as aggregate and steel fiber. In addition, the particle packing density of the paste determines its rheological behavior, compressive strength, and permeability. Particle size distribution of the aggregate also affects the particle packing density of the matrix and therefore its workability and strength. The steel fiber content is optimized to achieve sufficient tensile capacity and ductility. Meng et al. (2016) proposed another multiphase approach for developing the paste, the matrix, and the composite in six steps:

1. Optimize binder combinations for paste.
2. Determine preliminarily the ratio of water to binder (*w*/*b*).
3. Determine the sand combination.
4. Assess the binder to sand volume ratio.
5. Optimize the fiber volume.
6. Adjust the *w*/*b* and/or HRWR and evaluate UHPC properties.

The second approach is based on selected values for ratios of constituents. Berry et al. (2017) employed the absolute volume method with specific values for water-to-cement ratio; SCM-to-cement ratio (SCM includes silica fume and fly ash, and the SCM-to-cement ratio is fixed at a value of 0.5); HRWR to cement ratio; aggregate-to-cement ratio; and silica fume-to-fly ash ratio.

This method has the advantage of being free from considering the several different specific gravities of the constituent materials.

2.2.4.3 Nonproprietary UHPC Mixture Proportions by Other Researchers

Wille and Boisvert-Cotulio (2013) conducted research to develop nonproprietary UHPC mixtures with locally available materials. The authors developed four mixture designs using fine aggregates available in several areas covering northeastern, midwestern, northwestern United States, and all area of United States (Table 2.3). The target workability and required compressive strength were 11 to 13.5 in., measured by ASTM C230 (2008), and 20 ksi, respectively (Wille and Boisvert-Cotulio 2013). The authors also recommended the following ratios of constituent materials:

- Cement: silica fume: filler materials = 1.0 : 0.25 : 0.25 by weight
- *w*/*c* ratio = 0.2 to 0.3 by weight
- Aggregate-to-cement ratio = 1.0 to 2.0 by weight
- Steel fiber volume fraction = 1.0 to 2.0 percent by volume

Table 2.3. Nonproprietary UHPC Mixture Proportions (Wille and Boisvert-Cotulio 2013).

Material	Northeast (Basalt)	Upper Midwest (Limestone)	Northwest (Volcanic Rock)	United States (Quartz)
White Cement	1	1	1	1
Silica Fume	0.25	0.25	0.25	0.25
Fly Ash	0.24	0.24	0.24	0.24
HRWR	0.04	0.04	0.04	0.04
Fine Aggregate, (particle size: 0.003–0.05 in.)	1.50	1.50	1.50	1.50
Water-to-Cement Ratio	0.23	0.24	0.23	0.23
Spread Value, in.	11.4	10.4	11.3	12.4
Average Compressive Strength at 28 Days, ksi	26.9	24.1	23.5	29.0
Cost, $/yd^3	494	472	496	652
Cost, $/yd^3 with 1.5% of Steel Fiber	966	944	968	1124

2.2.5 Optimization to Develop Cost-Effective UHPC

2.2.5.1 Cost Proportion of Constituents

The cost of commercial proprietary UHPC with a 2 percent steel fiber volume fraction is about \$2000/yd^3 (Ahlborn et al. 2008). Wille and Boisvert-Cotulio (2013) developed a low cost UHPC mix with locally available materials at a cost of approximately \$750/yd^3. The authors provided the cost proportion of each material (Table 2.4), and the steel fibers accounted for nearly 63 percent of the total cost. Therefore, the optimization of steel fiber content is the most critical parameter in developing a cost-effective UHPC mixture.

Table 2.4. Cost of Material per Volume of Mixture (Wille and Boisvert-Cotulio 2013).

Material	Cost (\$/yd^3)	Percentage
Portland cement II/V	73.66	9.8
Silica fume	82.57	11.0
Fine aggregate	12.82	1.7
Fly ash	7.54	1.0
HRWR	103.60	13.8
Steel fibers (1.5%)	472.39	62.8
Total	752.58	100.0

2.2.5.2 Steel Fiber

Wille et al. (2012) conducted research to identify the tensile performance of UHPC with different fiber shapes and fiber volume fractions as low as 1 percent. Based on direct tension tests, the authors found that deformed fibers of 1.5 percent by volume result in a peak tensile strength of 1.9 ksi and 0.6 percent tensile strain due to the mechanical bonding effect of deformed steel fibers. This peak tensile strength is 60 percent higher than UHPC with the same volume fraction of straight steel fibers. This result indicates that UHPC with a low steel fiber content can be optimized using deformed fibers to achieve sufficient tensile performance for most applications. Alkaysi and El-Tawil (2016) investigated the effect of fiber volume fractions of straight and smooth steel fibers for six performance parameters: compressive strength, post-cracking strength, average number of cracks, strain capacity, energy absorption capacity, and fiber tensile stress. Prior to their study, most researchers did not study the performance of UHPC with a low fiber volume fraction (0.5 to 1.5 percent). One notable finding was that 1 percent of steel fiber content provides 1.25 ksi of peak

post-cracking tensile strength with 0.13 percent of peak tensile strain, whereas 0.5 percent of steel fiber content provides 0.84 ksi of peak post-cracking tensile strength with 0.07 percent of peak tensile strain (Alkaysi and El-Tawil 2016). In addition to the tensile performance parameters, the other performance parameters with 1 percent of steel fiber content are a compressive strength of 24.8 ksi, an average of 5.5 cracks, an energy absorption capacity of 0.63 kJ/ft^3, and a fiber tensile stress of 138.7 ksi (Alkaysi and El-Tawil 2016).

2.2.5.3 Proportion of Cement, Silica Fume, and Supplementary Cementitious Materials

Wille (2008), Wille et al. (2011), and Wille et al. (2012) investigated the optimum proportion of cement, silica fume, and silica powder to obtain improved spread values and compressive strength. Wille (2008) first recommended the proportion of 1 : 0.18 : 0.53 and continued to optimize this ratio by evaluating the spread value for workability and the compressive strength with varying proportions. Wille et al. (2011) reported that the proportion of 1 : 0.25 : 0.2 showed the best result, with a 12.9 in. spread value and 26.7 ksi compressive strength. Wille et al. (2012) continued to investigate the optimum proportion without silica powder and concluded that 1 : 0.25 : 0 (without silica powder) is the most efficient proportion because the effect of silica powder on fresh and hardened properties of the paste was very minor and its cost was relatively high. Alkaysi and El-Tawil (2016) investigated the various proportions of cement, silica fume, and silica powder needed to achieve high tensile strength and low cost. The authors started their investigation with a proportion of 1 : 0.25 : 0.25 and then increased the amount of silica fume from 0.25 to 0.35 and decreased the proportion of silica powder from 0.25 to 0. They also concluded the effect of silica powder on tensile capacity is not significant; thus, the proportion of 1 : 0.25 : 0 for cement: silica fume: silica powder was recommended.

Weldon et al. (2010) developed a nonproprietary UHPC mix and optimized the amount of silica fume and fly ash by evaluating compressive strength gain and workability. The authors first selected the ratio of *w*/*cm* as 0.14 and then conducted tests with various proportions of fly ash by replacing percentages of silica fume—from 12.5 to 100 percent—with fly ash. The authors concluded that 37.5 and 50 percent replacement of silica fume with fly ash are the optimum ratios.

2.2.5.4 Aggregates

Two approaches have been identified in the literature related to optimization of aggregate content. The first approach is to improve particle packing density by limiting the maximum particle size of fine aggregate. Wille and Boisvert-Cotulio (2015) reported that a 0.047 in. maximum particle size for fine aggregate is more appropriate than a 0.37 in. limit because the latter does not have significant cost benefit and also gives a lower particle packing density. Weldon et al. (2010) used fine aggregate having 0.187 in. maximum particle size to achieve a target compressive strength of 21 ksi. Although the authors achieved a higher compressive strength than 21 ksi with a smaller fine aggregate particle size, their target compressive strength of 21 ksi was reached using a 0.187 in. maximum particle size. The authors noted that obtaining smaller particle size may increase the cost of fine aggregate due to an increase in labor cost.

The second approach to optimizing aggregate content is to replace fine aggregate with coarse aggregate to reduce the cost of UHPC. Ma et al. (2004) reported that the addition of crushed basalt coarse aggregate with 0.2 in. maximum particle size in a UHPC mix can have better rheological behavior and decrease mixing time without a significant difference in compressive strength (21.7 to 24 ksi at ambient temperature for 28 days). Collepardi et al. (1997) also reported that substitution of fine aggregate (0.006 to 0.016 in.) for coarse aggregate (0.31 in. maximum size) does not influence the compressive strength. On the other hand, coarse aggregate decreased the autogenous shrinkage by approximately 40 percent. However, Orgass and Klug (2004) reported that coarse aggregate decreases the tensile and flexural capacity of the UHPC due to the low bond strength between the steel fibers and the resulting matrix.

2.3 MIXING AND FRESH PROPERTIES

2.3.1 General

The quality and performance of UHPC varies depending on mixing, placement, and curing methods, even when the mixtures are the same. Mixing procedure, casting practice, and test methods to measure fresh properties of UHPC are unlike that of normal concrete due to different constituents and the behavior of fresh concrete. Many research studies have been conducted on these topics, and several implementations of UHPC structures have provided lessons learned from experiences during the last 2 decades. This section focuses on the conducted research and current

practices for mixing, fresh properties, placing, and curing. The following subsection describes the development of mixing procedures in the laboratory and optimization of the procedures for implementation in the batch plant. The next subsection focuses on the fresh properties, such as workability and set time. The third subsection compiles the literature related to placement of UHPC, specifically the effects of placement on fiber orientation and dispersion. The last subsection briefly introduces curing methods to improve mechanical properties.

2.3.2 Mixing

Graybeal (2011) reported that high mixing energy is required to obtain homogeneity of UHPC because of the large content of fine materials included in a UHPC mix; thus, the mixing time of UHPC is usually extended in comparison to that of NSC. To achieve an acceptable consistency of the paste without a long mixing time, the use of a high-energy mixer can be effective (Sbia et al. 2017).

2.3.2.1 Mixing Procedure in Laboratory

Haber et al. (2018) reported the following common steps in the mixing procedures of the commercial UHPC products that are provided by the proprietary UHPC companies:

1. Short time mixing for dry constituents such as cement, silica fume, SCMs, and aggregate provides homogeneous distribution of fine materials before adding liquid materials such as HRWR or water.
2. All liquid materials should be added slowly into the mixer during mixing for a better distribution.
3. After adding the liquid constituents, sufficient mixing time is required to allow all mixed materials to become a fluid-like matrix.
4. After achieving appropriate consistency of the matrix, fibers must be added slowly while continuing mixing to ensure uniform distribution of the fibers.

Other researchers who developed nonproprietary UHPC mixtures have also developed and verified a similar mixing procedure to that of proprietary UHPC. Alkaysi and El-Tawil (2016) used a large Hobart food-type mixer that provided adequate mixing energy. In their laboratory, they first added dry powders, including silica fume and two silica sands, into the mixer and then mixed for about

5 minutes at 136 rpm. The second step was to add silica powder and cement into the mixer and mix for an additional 5 minutes at 136 rpm. The third step was to add water and the HRWR gradually and mix for 2 minutes at 136 rpm, then for 5 minutes at 281 rpm, or until obtaining a homogeneous mixture. Fourth, the authors added the steel fibers into the mixer and mixed at 136 rpm until the uniform distribution of the fiber was ensured. Kim (2018) also reported similar steps for the mixing procedure as the ones mentioned above. However, the difference between both procedures is that Kim (2018) added water plus 40 percent of the HRWR amount first and mixed for 2 minutes; the remaining HRWR was added into the mixer later.

2.3.2.2 Mixing Procedure in Batch Plant

Mixing procedures must be optimized for mixing the UHPC at the batch plant because laboratory mixing practices cannot be directly applied. To investigate this transition from the laboratory to the batch plant, Giesler et al. (2016) conducted five mixing experiments: first, the UHPC was mixed in the laboratory using a similar mixing procedure presented in Section 2.3.2.1; the two trial batches were conducted in the precast plant with a small batch volume of around 3.0 ft^3 using a small drum-style mixer; the last two trial batches used the batch plant facilities, which had a batch volume of approximately 1.0 yd^3. The authors found that the addition of fine aggregate at the dry mixing step caused agglomerate formation between silica fume and the wet fine aggregate. To solve this problem, the authors modified the mixing procedure:

1. Dry mixing (cement, silica fume, and fly ash) was conducted and mixed for 1 minute.
2. Fine aggregate and half of the water were added and mixed for 9 minutes.
3. The remaining water with the HRWR was added and mixed for 10 minutes.
4. Steel fibers were added and mixed for 5 minutes.

The total mixing time was 25 minutes in the batch plant compared to 40 minutes in the laboratory because the drum-style mixer used in the lab had a low mixing energy compared to the batch plant facilities. The authors concluded that UHPC can be mixed by using current facilities in a batch plant.

2.3.3 Fresh Properties

2.3.3.1 Workability

Workability is a key property to achieve desired flowability and also an indicator of the particle packing density, as discussed in Section 2.2.2. Wille et al. (2011) evaluated the appropriateness of using workability of fresh UHPC as an implicit parameter for evaluating particle packing density. The authors indicated the cause-and-effect relationship between workability and particle packing density as follows:

1. High particle packing density reduces voids in the paste.
2. The amount of water trapped in voids is decreased.
3. More water can cover the surface of cementitious particles.
4. Thus, the viscosity of the paste decreases; thus, rheological behavior is improved.
5. Finally, improved rheological behavior implies achieving a high particle packing density along with high compressive strength.

In other words, due to the low *w*/*c* ratio of UHPC, suitable workability cannot be obtained without achieving high particle packing density. Wille et al. (2011) conducted the flow table test according to ASTM C230 (2014), *Standard Specification for Flow Table for Use in Tests of Hydraulic Cement*, to measure the spread values of 38 different mixtures, which indicate the level of workability.

As reported by Russell et al. (2013), ASTM C1437 (2015), *Standard Test Method for Flow of Hydraulic Cement Mortar*, is the most commonly used test method to measure workability. Scheffler and Schmidt (2012) indicated that ASTM C143 (2012), *Standard Test Method for Slump of Hydraulic-Cement Concrete*, may be appropriate for non-self-consolidating UHPC, such as pavement white-topping.

In 2017, ASTM published the standard test methods for UHPC, ASTM C1856 (2017), *Standard Practice for Fabricating and Testing Specimens of Ultra-High-Performance Concrete*, which consists of modified ASTM test methods. Because most UHPC mixtures exhibit rheological behaviors similar to self-consolidating concrete (SCC), ASTM C1856 (2017) adapted modified

ASTM C1437 (2015) for measurements of workability. According to ASTM C1437 (2015), the test procedure is as follows:

1. Immediately after mixing, cast UHPC into the cone-shaped mold on the flow table.
2. Lift the mold carefully and allow UHPC to flow.
3. After the flow stops, measure the average diameter of UHPC, which is the static flow.
4. Drop the table 20 times and then measure the average diameter, which is the dynamic flow.

However, tamping the UHPC in the mold and dropping the table are not allowed in accordance with ASTM C1856 (2017). Wille and Boisvert-Cotulio (2015) indicated that the target range of spread value from the flow table test is 11.0 to 13.4 in. dynamic flow. Ozyildirim (2011) used a minimum 9.0 in. dynamic flow value for Ductal®. AFGC (2013), which is the second edition of the initial worldwide design guidelines for UHPC, provides two test methods for workability of UHPC: (1) a slump test conforming to EN 12350-2 (2011), *Testing Fresh Concrete Part 2: Slump Test*, or (2) a flow test on a vibrating table in accordance with EN 12350-5 (2011), *Testing Fresh Concrete Part 5: Flow Table Test*.

2.3.3.2 Set Time

Russell et al. (2013) observed that the setting time of UHPC is relatively longer than NSC. Yoo and Banthia (2016) reported that the setting time of UHPC is affected by the amount and type of cementitious materials, amount of HRWR, and presence of an accelerating admixture. Zhang et al. (2012) used UPV measurement to identify the factors that affect the setting of UHPC and reported the following observations:

- High curing temperature accelerates the hydration reaction.
- Increase in silica fume promotes the hydration reaction.
- The hydration process is retarded by adding fly ash and slag.
- The addition of steel fibers causes delay of the microstructure formation.

Graybeal (2006b) conducted tests for initial and final setting times according to the American Association of State Highway and Transportation Officials (AASHTO) AASHTO T 197 (2015), *Standard Method of Test for Time of Setting of Concrete Mixtures by Penetration Resistance*, and

reported that the results ranged between 70 minutes to 15 hours for initial set and 5 to 20 hours for the corresponding final set. Haber et al. (2018) also measured the setting times of five commercial UHPC products according to ASTM C403 (2016), *Standard Test Method for Time of Setting of Concrete Mixtures by Penetration Resistance*. The authors reported that the initial setting times were between 4.3 to over 9 hours, and final setting times were between 7 to under 24 hours. However, Yoo and Banthia (2016) indicated that measuring the setting times precisely is difficult due to rapid condensation of the surface caused by low *w*/*c* ratio and high fine particle content, and thus ASTM C403 (2016) tends to overestimate the setting time of UHPC. Therefore, ASTM C1856 (2017) recommends ASTM C191 (2018), *Test Methods for Time of Setting of Hydraulic Cement by Vicat Needle*, as a test method for time of setting.

2.3.4 Steel Fiber Content in Fresh UHPC

Steel fiber content in fresh UHPC is measured for the purpose of quality assurance/quality control. Even though there is no standard test method for UHPC, the two test methods for fiber reinforced concrete (FRC) are (1) the wash-out test method—introduced by JSCE-SF7 (1984), *Method of Tests for Fiber Content of Steel Fiber Reinforced Concrete*, and published by Japanese Society of Civil Engineers; and (2) the magnetic probing test method—introduced by SFRC Consortium (2014), *Design Guideline for Structural Applications of Steel Fibre Reinforced Concrete*, and published by Danish Technological Institute.

2.3.4.1 Wash-out Test Methods

JSCE-SF7 (1984) provides the required apparatus and procedure for the wash-out test method. The minimum capacity of the metal cylinder container is 1.6 gallon. The diameter of the container is required to be equal to the depth. The weighing accuracy is 0.35 oz for concrete and 0.035 oz for steel fibers. The procedure to measure steel fiber content can be summarized in five steps:

1. Fresh concrete is sampled for at least two containers.
2. The fresh concrete in the containers is washed by water.
3. During the washing process, the steel fibers are collected without loss (using a magnet is recommended).

4. The collected steel fibers are dried, and their weight is measured.
5. The steel fiber content by volume is calculated using Equation (2.1):

$$V_f = \frac{W_f}{V\rho_f} \times 100 \quad (2.1)$$

where:

V_f = Steel fiber content, percent

W_f = Weight of steel fibers in a container, lb

V = Volume of a container, in^3

ρ_f = Unit weight of steel fibers, lb/in^3

The average value of the two measurements is the steel fiber content.

SFRC Consortium (2014) measures the ratio of the weight of steel fibers to the volume of fresh concrete. The required apparatus to sample fresh concrete according to the SFRC Consortium (2014) is three buckets having sizes between 2.64 and 3.96 gallons. For weighing the steel fibers, the accuracy of measurement is 0.035 oz. The procedure of the SFRC Consortium (2014) is the same as the JSCE-SF7 (1984) procedure for Steps (1) to (4), except that SFRC Consortium (2014) requires three measurements. The steel fiber content is calculated using Equations (2.2) and (2.3), and the average value of three measurements is the steel fiber content:

$$V_{fc,i} = \frac{M_{fc,i}}{\rho_{fc,i}} \quad (2.2)$$

$$m_{f,i} = \frac{M_{f,i}}{V_{fc,i}} \quad (2.3)$$

where:

$V_{fc,i}$ = Volume of fresh concrete of one sample, in^3

$M_{fc,i}$ = Weight of fresh concrete of one sample, lb

$\rho_{fc,i}$ = Fresh concrete density, lb/in^3

$m_{f,i}$ = Steel fiber content, lb/in^3

$M_{f,i}$ = Weight of steel fibers in one sample, lb

2.3.4.2 Magnetic Test Methods

The magnetic test method uses electromagnetic induction with a probe and measuring apparatus. JSCE-SF7 (1984) requires a probe that has coils and a circular hole into which the specimen (ϕ 3.94 × 7.87 in.) can be inserted. The required accuracy for weighing operations is the same as the wash-out test method (0.35 oz for concrete and 0.035 oz for steel fibers). The container should be made of nonmagnetic material with an inner size of ϕ 3.94 × 7.87 in. The test procedure can be summarized as follows:

1. Six specimens are sampled from fresh concrete.
2. The specimen is inserted into the probe.
3. Steel fiber content is determined by the measuring apparatus.
4. The reading in terms of electric current is calibrated by the calibration curve to determine steel fiber content.
5. The mean of six measurements is taken to determine the average steel fiber content.

JSCE-SF7 (1984) recommends confirming the result from the magnetic method with the results from the wash-out method.

SFRC Consortium (2014) also provides magnetic test methods to determine steel fiber content. The required apparatus is a cubical plastic container with internal length of 5.9 in. and an induction measurement device with a cubical double-inductor sensor. The test method calls for at least three specimens. The procedure is as follows:

1. The induced voltage of the empty sensor V_{empty} is measured.
2. The cubical plastic container is filled with fresh concrete.
3. The double-inductor sensor is placed on the container and the induced voltage is measured for three directions.
4. The average of three readings is taken.
5. By using Equation (2.4), the voltage difference V_{diff} between the average of the three readings and the induced voltage of the empty sensor V_{empty} is calculated.
6. The steel fiber content is determined using a calibration curve.
7. The average of three steel fiber contents is taken.

$$V_{diff} = \frac{V_x + V_y + V_z}{3} - V_{empty} \quad (2.4)$$

where:

V_{diff} = Induced no-load voltage with the empty sensor, mV

V_x = Measured voltage for x-direction, mV

V_y = Measured voltage for y-direction, mV

V_z = Measured voltage for z-direction, mV

V_{empty} = Induced voltage of the empty sensor, mV

2.3.5 Placement

Graybeal (2011) reported that the dwell time of UHPC before starting the hydration reaction of cementitious materials is generally longer than normal concrete; thus, self-desiccation of the UHPC should be prohibited during dwell time. Graybeal also suggested that the internal vibration is not allowed because it may cause settling of steel fibers, but the external vibration may be helpful to release entrapped air.

Ferrara (2012) reported that appropriate placement methods should be considered to ensure preferred fiber orientation and dispersion because the alignment of fibers influences tensile capacity of UHPC elements. Boulekbache et al. (2010) studied the rotation of fibers by two types of placement locations and flow directions to identify the effects of fiber orientation and dispersion. The authors reported that the fibers are forced by the fluid, and thus the fibers tend to align perpendicularly to the flow direction in a case of radial flow. However, when UHPC is placed from end to end, fibers align parallel to the flow direction.

Yang et al. (2010) investigated the effects of fiber orientation by two different placement methods. The first method allows UHPC to flow from the one end of the forms to the other end. The second method is to place UHPC at the center so that it flows in both directions. The authors reported that the first method resulted in a 15 percent higher tensile capacity because the flow of UHPC aligns the direction of fibers along the beam length at midspan region. Wille and Parra-Montesinos (2012) studied the effects of the casting speed on the flexural behavior of UHPC. The authors concluded that an increase in the casting speed improves flexural performance because the fast speed leads to better fiber alignment.

Ozyildirim (2011) and Giesler et al. (2016) recommended casting practices for UHPC. Ozyildirim (2011) reported that the mix was transferred from the mixer to the prestressing bed by ready-mix concrete trucks, and it took about 20 to 25 minutes. Giesler et al. (2016) indicated that casting within 20 minutes is recommended to guarantee acceptable workability. The authors also reported that the standard auger-fed delivery vehicles currently used in the batch plants can be used for the delivery of the UHPC and suggested external vibration only to achieve suitable consolidation and to avoid the settlement of steel fibers by internal vibration.

2.3.6 Curing

Due to the low water content, mitigating loss of internal water by sealing the system or maintaining a high humidity environment is critical during the curing of UHPC. Most commonly used curing methods for UHPC are steam curing and heat curing. Graybeal (2006b) suggested that steam-curing methods could increase the mechanical properties and decrease creep and shrinkage of UHPC. Another curing strategy is to use post-set heat curing, and Heinz and Ludwig (2004) and Schachinger et al. (2008) achieved UHPC with much higher compressive strengths under heat curing than that achieved under normal temperature curing. Section 2.4 discusses the effects of various curing methods on mechanical properties in more detail. Although steam- and heat-curing methods improve the mechanical properties of UHPC, these methods are not practical for large members at precast plants or for cast-in-place UHPC (Graybeal and Stone 2012). Therefore, Wille et al. (2011) and Berry et al. (2017) developed their nonproprietary UHPC mixtures without any special curing treatment and achieved 22 ksi and 20 ksi of compressive strength at 28 days, respectively.

2.4 HARDENED PROPERTIES

2.4.1 General

The hardened material properties of UHPC are of particular importance when assessing the viability of the composite material for its utilization for large-scale structures. Several studies have identified the mechanical properties of the many variants of UHPC in the United States and around the world. An overview of the investigations and findings is provided in this section. Mechanical properties such as compressive strength, tensile strength, flexural behavior, MOE, shrinkage, creep, and ductility are some of the key areas discussed in this section.

2.4.2 Behavior under Compression

One of the most significant characteristics of UHPC is its high compressive strength, which makes UHPC a material with the potential to revolutionize construction practices and turn highly ambitious projects into a reality. Compressive strengths ranging from 20 to 30 ksi were recorded for UHPC with and without fibers (Russell et al. 2013). The densely packed matrix of fine, cementitious material is largely responsible for the high strength (Richard and Cheyrezy 1995).

2.4.2.1 State-of-the-Art

Because compressive strength is most commonly measured due to its significance for concrete in general, investigations have been undertaken to identify the specimen geometry that captures the compression behavior of UHPC accurately. The limiting factors that control are the need for testing machines with high load-carrying capacity and expensive equipment for cylinder end grinding (Graybeal and Davis 2008; Kusumawardaningsih et al. 2015). Schmidt and Fröhlich (2010) reported that the measured compressive strength is much lower for UHPC than CC in the presence of an uneven surface of the specimen when it is loaded. Graybeal and Davis (2008) tested several samples and concluded that the compressive strength may be tested using cylinders of 3 or 4 in. in diameter and cubes with a 4 in. side length. In the case that limiting factors prevail, the use of 2.78 in. cubes with a factor of 0.96 is recommended to convert the strength to an equivalent 3 in. diameter cylinder strength.

Another factor that impacts the compressive strength is the curing conditions. Figure 2.1 presents the variation of compressive strength with the density of approximately 1000 concrete cylinders subjected to different curing regimes (Graybeal 2006b). The samples were made from the brand-named UHPC premix with water, HRWR (Glenium 3000NS), accelerator (Rheocrete CNI), and steel fibers of 0.5 in. length and 0.008 in. diameter at 2 percent by volume concentration. It is clear that thermal treatment increases the compressive strength of the material. Graybeal (2006b) also stated influencing factors on the compressive strength include the environment in which the samples are exposed prior to the steam treatment, and the conditions of the steam curing—such as temperature, relative humidity (RH), and duration of the curing treatment.

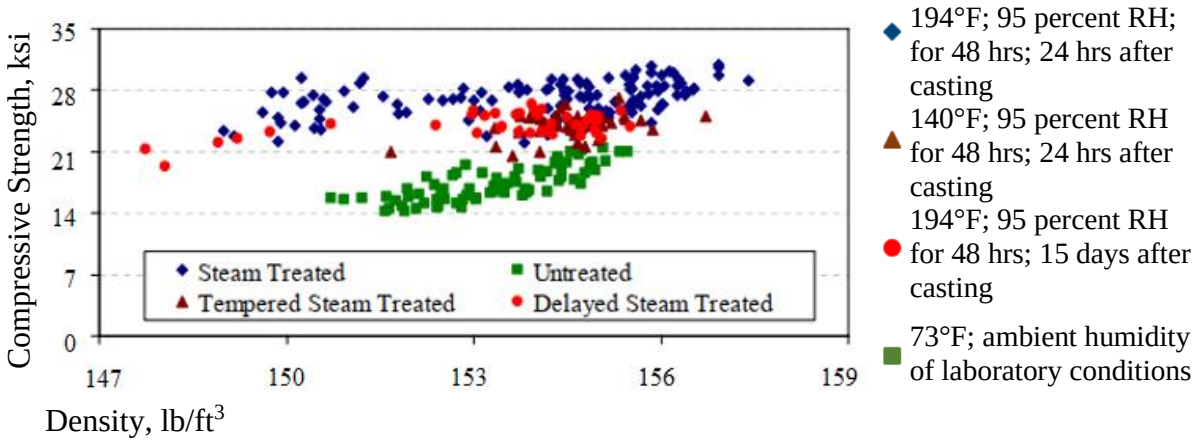

Figure 2.1. Compressive Strength Variation with Density under Different Curing Conditions (adapted from Graybeal 2006a).

Graybeal (2006c) developed an expression for the compressive strength gain for the untreated curing regime for any time t, after a duration of 0.9 days, as shown:

$$f'_{ct} = f'_c \left[1 - exp\left(-\left(\frac{t-0.9}{3}\right)^{0.6}\right)\right] \tag{2.5}$$

where:

f'_{ct} = Compressive strength of UHPC at age t days, ksi

f'_c = Compressive strength of UHPC at 28 days, ksi

t = Time after casting, days

Graybeal and Stone (2012) developed an expression for the compressive strength at time t days after the start of the mixing process, with parameter a (in days) and exponent b depending on the curing temperature for field-cast connection purposes, as:

$$f'_{c,t} = f'_{c,28d} \left[1 - exp\left(-\left(\frac{t-t_{start}}{a}\right)^{b}\right)\right] \tag{2.6}$$

$$t_{start} = \frac{0.47}{\sqrt{T}} \tag{2.7}$$

where:

$f'_{c,t}$ = Compressive strength of UHPC at age t days after the initiation of mix, ksi

$f'_{c,28d}$ = Compressive strength of UHPC at 28 days, ksi

t_{start} = Time of strength-gain initiation, days

T = Temperature at which curing takes place, Fahrenheit

Table 2.5 gives the parameters a and b. Equation (2.6) is consistent with the findings of a similar study.

Table 2.5. Parameters a and b (adapted from Graybeal and Stone 2012).

Curing Temperature	$f'_{c,28d}$ (ksi)	a (days)	b
105°F	24.5	0.25	0.25
73°F	24	1.0	0.30
50°F	22.5	4.0	0.50

Roy et al. (1972) considered elevated temperature (428°F) and high pressure (7.3 ksi) techniques for the development of compressive strengths as high as 74 ksi. Heinz and Ludwig (2004) evaluated the expansion and crack formation due to the delayed ettringite formation (DEF) in UHPC subjected to thermal treatment. In this process, they tested sulfate-resistant cement composites with the composition shown in Table 2.6. Heinz and Ludwig (2004)concluded that UHPC does not have a severe threat from DEF. Figure 2.2 presents the 1-day and 28-day strengths of the mix considered. Heat treatment increases the strength gain. The heat treatment is applied in five different regimes at one of two stages of heating at temperatures ranging from 149°F to 356°F, followed by a cooling period ranging from 39 minutes to 2.5 hours. The thermal treatment accelerates the rate of hydration that in turn improves the compressive strength of UHPC (Collepardi et al. 1997; Müller et al. 2008).

Table 2.6. Composition of CEM I 425 R-HS and CEM III/B 425 NW/HS (adapted from Heinz and Ludwig 2004).

Duracrete Products – Schwenk	SO_3	C_3A	SO_3/Al_2O_3	Na_2O_2	GGBFS	Silica Fume (sf)	Water
	Percent Weight	Percent Weight	Mol. Ratio	Percent Weight	Percent Weight	sf/cement	*w/c*
CEM I 425 R-HS	2.7	1.9	0.93	0.73	–	0.25	0.22
CEM III/B 425 NW/HS	3.5	–	–	0.69	69	0.12	0.22

Note:
1. Quartz (grain size < 0.02 in.) may be added.
2. Superplasticizer on polycarboxylate based ether may be added to adjust the consistency.
3. GGBFS: Ground-granulated blast-furnace slag
4. SO_3: Sulfur trioxide
5. C_3A: Tricalcium aluminate
6. Al_2O_3: Aluminum Oxide
7. Na_2O_2: Sodium peroxide
8. –: Not available

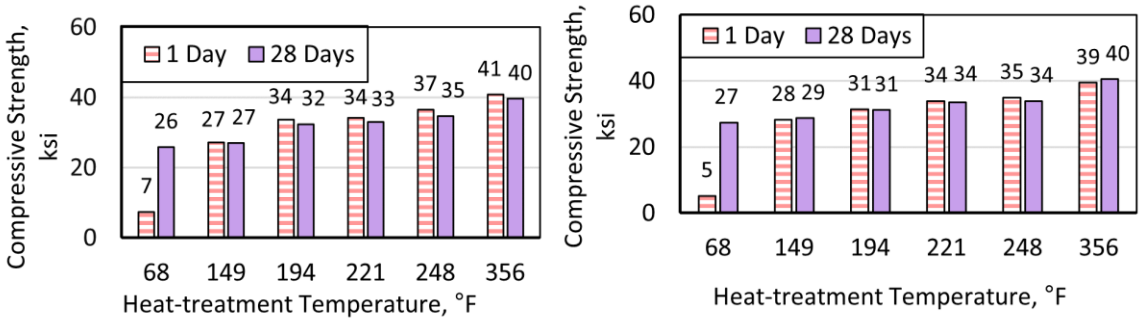

(a) Compressive strength of UHPC with CEM I 42,5 R-HS

(b) Compressive strength of UHPC with CEM III/B 42,5 NW/HS

Figure 2.2. Effect of Thermal Treatment on Compressive Strength (adapted from Heinz and Ludwig 2004).

Table 2.7 summarizes a research study by Garas et al. (2012) by giving the compressive test results that highlight the influence of different thermal treatment on the properties of UHPC.

Table 2.7. 7-Day Results of Compressive Strength (adapted from Garas et al. 2012).

Sample	Test	7-Day Compressive Strength (ksi) at		
		73°F	140°F	194°F
3×6 in. cylinders	ASTM C39	16.9	21.4	24.6
Mix Constituent				**lb/ft^3**
UPHC premix				137
Water				6.80
High-range water reducing admixture				1.94
Steel fibers				9.74

Note: High-strength steel fibers are 0.5 in. long with 0.008 in. diameter; 97 to 140 ksi tensile strength Bekaert's Dramix ultra-high-strength steel fibers.

Wille et al. (2011) focused on developing a mix to optimize flowability, packing density, and compressive strength by controlling the parameters other than heat and pressure treatments, such as the binder ratio, water to cementitious material ratio, and HRWR. Silica fume is also known to improve the strength of the UHPC due to the inherent pozzolanic reactions (Abbas et al. 2016; Ma and Schneider 2002; Richard and Cheyrezy 1995; Wille et al. 2011). Moreover, it is recommended to minimize the *w*/*b* ratio for high strength of the material (de Larrard and Sedran 1994; Richard and Cheyrezy 1995; Wen-yu et al. 2004), but it may not be the sole governing factor (Wille et al. 2011). The use of superplasticizers and elimination of coarse aggregates to avoid the deterioration at the interfacial transition zone are additional measures that enhance strength. Denarié et al. (2005) developed UHPC for the Sustainable and Advanced Materials for Road Infrastructure project that applied UHPFRC in the rehabilitation of bridge structures. The authors reported a 28-day compressive strength of up to 26 ksi at ambient curing conditions. Park et al. (2015) evaluated the early-age strength of UHPC when it is subjected to different curing conditions. The authors recommended that a state of total dryness must be avoided due to the low water-binder ratio of the K-UHPC developed by the Korea Institute of Civil Engineering and Building Technology. That mix, when cured at 140°F, attained a compressive strength of 22 ksi (Park et al. 2015).

As demonstrated in the existing literature, the compressive strength of UHPC depends on several factors, such as particle packing density and thermal/pressure treatment. An optimal combination is one that may use the impact of each factor to attain the desired requirements of strength within practicable methods. Graybeal (2006b) also mentioned that the fiber-reinforced UHPC does not

show the usual brittle and explosive failure (associated with UHPC) under compression due to the confining effect of the fiber reinforcement.

El-Helou et al. (2022) developed a constitutive curve for predicting the behavior of UHPC in compression. The bilinear model comprises a linear elastic branch sloping at the MOE of the UHPC and a perfectly plastic curve indicating the reduced compressive strength to account for the nonlinearity of the actual stress strain curve. Figure 2.3 shows the idealized compressive design model proposed.

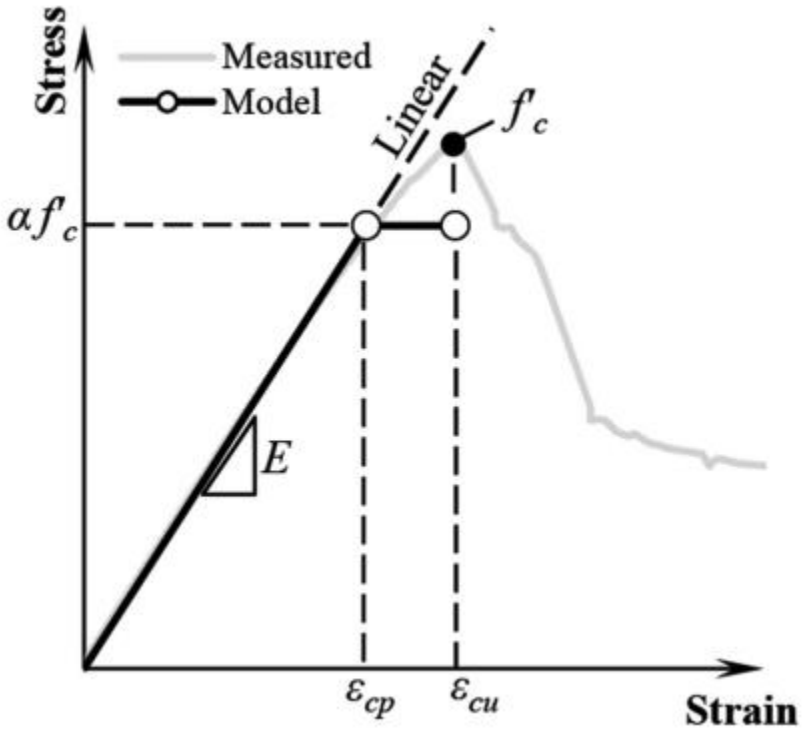

Figure 2.3. Compressive Stress-Strain Model (El-Helou et al. 2022).

2.4.2.2 State-of-the-Practice

This section briefly discusses the information reported by different standards, codes, and recommendations on UHPC on the subject of compressive strength of concrete.

2.4.2.2.1 ASTM Standard Tests

Compressive strength tests may be conducted per ASTM standard tests such as ASTM C39 (2020), *Standard Test Method for Compressive Strength of Cylindrical Concrete Specimens*, and ASTM

C109 (2016), *Standard Test Method for Compressive Strength of Hydraulic Cement Mortars (Using 2-in. or [50-mm] Cube Specimens)*, with modification for UHPC as specified by ASTM C1856 (2017). Among several changes, such as the loading rate of the specimen and prohibiting the use of tamping rods and vibrators for the preparation of the specimens, the major modification for UHPC is the size of specimens used. Several recommendations for the temperature, humidity, and duration of treatment applied for metallic and nonmetallic fibers are presented in detail for the thermal treatments that may be applied to UHPC samples under testing. The diameter of the specimens is restricted to 3 in., the length is 6 in., and the stress rate applied is 145 ± 7 psi/s.

2.4.2.2.2 Texas Department of Transportation Standard Test

TxDOT (2008), *Compressive Strength of Cylindrical Concrete Specimens Archives,* may also be used to test the compressive strength of UHPC.

2.4.2.2.3 AFGC (2013)

Compressive behavior is predominantly elastic over a wide range of strain until it reaches a peak characteristic strength f_{ck}, after which the stress continues to decrease. AFGC (2013) suggests the use of approximately 2 percent fiber content by volume such that "non-brittleness" is ensured. AFGC (2013) also describes the procedure to be undertaken to establish the constitutive law in compression. A minimum of six specimens taken from three samples during the placement, such that at least two specimens are from each mix, are required to be tested under compression strength tests. These tests assess the suitability of the concrete to meet the tolerance limits of the design tests. The concrete specimens being tested are produced from the nominal mix design developed from the standard mixing, handling, transporting, and placing procedures documented in the recommendations.

2.4.2.2.4 JSCE (2008)

JSCE (2008) suggested that the compressive stress-strain relation for UHPFRC may be derived from the reliable past data of a suitable test at the ultimate state. The data may be fit to an existing model to obtain the stress-strain relationship by following the procedure listed in the Japanese guidelines. JSCE (2008) recommended the use of JIS A 1108, "*Method of Test for Compressive Strength of Concrete*," for compressive testing of the UHPFRC.

2.4.2.2.5 ACI 544.4R-18 (2018)

ACI 544.4R-18 (2018) reported that the presence of steel fibers affects the compressive strength only slightly—from approximately 0 to 23 percent—when up to 2 percent of steel fibers are added by volume as prescribed in Williamson (1974).

2.4.2.2.6 ACI 363R-10 (2010)

ACI 363R-10 (2010) reported that the compressive strength of HSC depends on the parameters associated with the test, such as the size of the specimen, the boundary conditions, and the strain rate. The report also stated that HSC cylinders of dimensions 4 × 8 in. have been shown to give higher compressive strengths than 6 × 12 in. specimens.

2.4.2.2.7 FHWA (2022)

FHWA (2022) recommends the use of ASTM C39 (2020) and ASTM C1856 (2017). The strain observed at the experimental compressive strength is recommended to be used for the compressive design strain that, in the absence of laboratory data, is specified to be 0.0035. A reduction factor less than 0.85 is specified to account for the nonlinearity of the stress-strain response in compression (El-Helou et al. 2022).

2.4.3 Modulus of Elasticity and Poisson's Ratio

MOE is calculated from the stress-strain curve that captures the compressive behavior of UHPC and is an important parameter in general for quantifying the stiffness of materials and structural members. Gu et al. (2015) observed that due to the dense structure of UHPC, the MOE of UHPC is higher than the MOE of NSC and HSC despite the use of the same aggregate for all types of concrete. The Poisson's ratio gives a measure of the relative lateral strain as a fraction of the strain in the direction of loading under the action of uniaxial loading (Zia et al. 1997). This ratio is an important property needed to calculate the shear modulus of the material and to study the behavior of the material under loading.

2.4.3.1 State-of-the-Art

Russell et al. (2013) documented that the Poisson's ratio for UHPC determined by several researchers ranges from 0.18 to 0.21. Cheyrezy (1999) and Graybeal (2007) reported that the compressive stress-strain curve for UHPC grows as a linear elastic function up to 80 to 90 percent of the maximum compressive stress whereas the linear-elastic behavior is up to 30 percent of the ultimate compressive strength of NSC.

Several empirical models have been proposed for the computation of MOE of UHPC as a function of concrete compressive strength. Ma et al. (2004) developed an expression to represent the experimental results for the samples having an absence of coarse aggregate, as shown in Equation (2.8). Further, the authors reported that the experimental results show the MOE to be around 6962 ksi without any coarse aggregate, while those samples with basalt split had a modulus of 8412 ksi, and samples with a bauxite split had a modulus of 10,153 ksi.

$$E_c = 525{,}000\left(\frac{f_c'}{10}\right)^{\frac{1}{3}} \text{ (psi)} \tag{2.8}$$

where:

f_c' = Compressive strength of concrete, psi

In a later study, Graybeal and Stone (2012) conducted testing to study field-cast connection material and found that the MOE is more dependent on the compressive strength than on the temperature of the curing environment. The authors proposed a model to compute the MOE E_c of UHPC, as follows:

$$E_c = 49000\sqrt{f_c'} \text{ (psi)} \tag{2.9}$$

where:

f_c' = Compressive strength of UHPC, psi

Additionally, in a recent FHWA report, Haber et al. (2018) developed the best-fit model for expressing MOE of UHPC as a function of its compressive strength.

$$E_c = 45220\sqrt{f_c'} \text{ (psi)} \tag{2.10}$$

where:

f_c' = Compressive strength of concrete, psi

Richard and Cheyrezy (1994), Graybeal (2006b), Graybeal (2007), and Abbas et al. (2016) noted that MOE is dependent on effects of heat treatment. Experimental test results by Garas et al. (2012) that are tabulated in Table 2.8 show how the thermal conditions during the curing regimes influence the MOE.

Table 2.8. 7-Day Results for MOE (adapted from Garas et al. 2012) .

Description	Sample	Test	7-Day MOE, ksi at		
			73°F	140°F	194°F
E_c (Compression)	4 × 8 in. cylinder	ASTM C469	6510	7376	6953
E_t (Tension)	2 × 2 in. dog bone	N/A	8241	8420	8336
Mix Constituent			**lb/ft³**		
UHPC premix			137		
Water			6.80		
HRWR admixture			1.94		
Steel fibers			9.74		

Notes:
1. High-strength steel fibers are 0.5 in. long and 0.008 in. diameter; 97 to 140 ksi tensile strength.
2. N/A: Not applicable

2.4.3.2 State-of-the-Practice

This section discusses the standard testing methods and the recommendations on the study of the MOE and Poisson's ratio of concrete.

2.4.3.2.1 ASTM Standard Tests

The MOE and Poisson's ratio can be measured through ASTM C469 (2014), *Standard Test Method for Static Modulus of Elasticity and Poisson's Ratio of Concrete in Compression* (Tadros and Morcous 2009). ASTM C1856 (2017) provides the modifications that should be implemented to the standard tests for CC for use in testing UHPC. The major modification, in addition to the preparation of the specimens, is that the extensometers that are specified are linear variable differential transducers (LVDTs) or any other sensors for the precise readings of the displacements. The loading rate applied to the specimen should be 145 ± 7 psi/s.

2.4.3.2.2 AFGC (2013)

A direct formula may not be applicable to find the MOE of UHPC from the compressive strength of concrete. However, the *French Institute of Science and Technology for Transport, Development and Networks*' three-sphere model of homogenization theory (Le Roy 1995) may be used to find the elastic modulus (AFGC 2013). The French code also suggests that the Poisson's ratio may be assumed to be 0.2 if no data are available.

2.4.3.2.3 JSCE (2008)

JIS A 1149 (2017)—*Method of Test for Static Modulus of Elasticity of Concrete*—is suggested for finding the MOE of HPFRCC, which is approximately one-half to two-thirds times that of ordinary concrete. The Poisson's ratio is suggested to be approximately 0.226 by the JSCE (2008).

2.4.3.2.4 ACI 544.1R-96 (2002)

ACI 544.1R-96 reports that the MOE and the Poisson's ratio of steel FRC having a fiber volume of less than 2 percent is close to that of similar unreinforced concrete, which is defined by ACI Committee 318 (2019) in Section 19.2.2.1 as the MOE of normal weight concrete. ACI 318-19 notes that this expression, given below, is more accurate for a concrete compressive strength not greater than 8000 psi:

$$E_c = 57{,}000\sqrt{f_c'} \text{ (in psi)} \tag{2.11}$$

where:

f_c' = Compressive strength of concrete, psi

2.4.3.2.5 ACI 363R-10 (2010)

A different equation is recommended for HSC based on the work done by Carrasquillo et al. (1981). This report also encourages the verification of the results by a field batch trial or other tests.

$$E_c = 40{,}000\sqrt{f_c'} + 1.0 \times 10^6 \text{ (in psi)} \quad (2.12)$$

where:

f_c' = Compressive strength of HSC, psi

2.4.3.2.6 AASHTO LRFD Specifications (2020)

The following expression is recommended for finding the MOE of normal weight concrete with design compressive strengths up to 15.0 ksi based upon the research of Greene and Graybeal (2013), as follows:

$$E_c = 120{,}000K_1 w_c^{2.0} f'^{0.33}_c \quad (2.13)$$

where:

E_c = MOE for normal weight concrete, psi

K_1 = Correction factor that depends on the source of aggregate (to be considered 1.0 if no data are available)

w_c = Unit weight of concrete, kips/ft^3

f_c' = Compressive strength of concrete, ksi

2.4.3.2.7 CEB FIP Model Code 2010 fib (2010)

The following equation is used in the CEB FIP Model Code 2010 fib (2010) to compute the MOE of normal weight concrete:

$$E_{ci} = 76E_{c0}\alpha_E \left(\frac{f_{ck}+\Delta f}{10}\right)^{1/3} \quad (2.14)$$

where:

E_{ci} = MOE at 28 days for ordinary concrete, psi

f_{ck} = Characteristic compressive strength of concrete, psi

Δf = 1160 psi

α_E = Coefficient depending on the aggregate type

Poisson's ratio of CC may be assumed to be 0.20, and it generally falls in the range of 0.14 to 0.26 in.

2.4.3.2.8 CSA S6:19 (2019)

The MOE for any FRC possessing compressive strength of greater than 12 ksi is recommended to be measured per CSA A23.1 of Annex U by the Canadian Highway Bridge Design Code (CSA S6:19 2019).

2.4.3.2.9 FHWA (2022)

In case the MOE cannot be experimentally determined per the provisions of ASTM C1856 (2017) and ASTM C469 (2014), the following equation is proposed for the MOE, or E_c, for UHPC. The parameters are based on experimental research of UHPC specimens with a compressive strength range of 14 to 29 ksi conducted by El-Helou et al. (2022). This equation does not include a density correction parameter because the density of the UHPC specimens does not vary significantly, and the values lie within a range of 144 to 175 lb/ft^3.

$$E_c = 2{,}500 K_1 f'^{0.33}_c \quad (2.15)$$

where:

E_c = MOE for UHPC, ksi

K_1 = MOE correction factor that depends on different types of UHPC with a typical unit weight of 0.155 kcf (to be considered 1.0 if it is not determined by physical test)

f'_c = Compressive strength of UHPC, ksi

2.4.4 Behavior under Tension

One of the key aspects of UHPC that sets it apart from all its counterpart higher strength concrete variants is its improved tensile strength, ductility, and energy absorption capacity due to the presence of fibers. This section discusses the relevant literature on the tensile behavior of UHPC.

2.4.4.1 State-of-the-Art

2.4.4.1.1 Indirect Tension Testing

Garas et al. (2010) attributed the overestimation of the tensile capacity by the indirect tension testing methods to the following underlying assumptions. The modulus of rupture tests, such as

ASTM C78 (2009) and ASTM C293 (2016), *Standard Test Method for Flexural Strength of Concrete (Using Simple Beam with Center-Point Loading)*, overestimate the strength due to (a) the assumption of the linear variation of stress to compute the flexural strength, (b) the invalidation of the linear stress variation due to the shear deformations indicated by the presence of the low span-to-depth ratio of the typical specimens, and (c) because the region resisting the high tensile force in a flexural test is very small. ASTM C469 (2014) overestimates the tensile capacity, according to Garas et al. (2010), due to (a) the assumption that the material is homogenous, (b) neglect of the high compressive stresses that are developed at the extremities of the vertical plane during the computations, and (c) lack of consideration of the lateral restraints arising from the friction between the specimen and the bearing strips. The authors further discourage the use of direct tension testing methods because they are difficult to set up due to stress concentration, induced secondary flexure, and torsion drawbacks.

Russell et al. (2013) reported that standard tests such as ASTM C78 (2009), ASTM C496 (1996) may be used to test the behavior prior to first cracking; however, they discourage using them to capture the strain hardening behavior of UHPFRC since these tests may tend to overestimate the capacity. Graybeal (2006c) proposed modification of ASTM C469 (2014) for computing the split tensile strength. The author recommended the use of more accurate and sophisticated LVDT for recording the strain data instead of the simpler measures originally mentioned in the ASTM standard. Table 2.9 summarizes the results by Russell et al. (2013). Baby et al. (2012) considered using flexural tensile tests for the back or inverse computation of the uniaxial tensile strength.

Table 2.9. First Cracking Tensile Strength, $f_{ct,1}$ (Russell et al. 2013).

Test/Empirical Method	Details	$f_{ct,1}$: Steam-Cured Specimen, ksi	$f_{ct,1}$: Untreated Specimen, ksi
Split Cylinder Test	ASTM C496 (1996)	1.7	1.3
Tensile Strength of Hydraulic Cement Mortar	AASHTO T 132-87 (2009)	1.0 to 1.4	0.9
Direct Tensile Strength	4 × 8 in. cylinders	1.1 to 1.6	0.8 to 1.0
From Measured Compressive Strength, f_c'	Depending on curing method, if any	$7.8\sqrt{f_c'}$ or $8.3\sqrt{f_c'}$	$6.7\sqrt{f_c'}$

2.4.4.1.2 Direct Tension Testing

Garas et al. (2010) developed their own modified test using dog bone specimens after considering many indirect methods, such as the methods of the ASTM C190 (1990), the Todd (1955) direct

tension test method, and direct testing of the notched and unnotched cylinders. The test specimens in Garas et al. (2010) are loaded uniformly, and the dog bone specimens having smaller cross sections can be effectively used instead of the notched specimens. The key observations and the testing specifications from the direct and indirect testing conducted by Garas et al. (2010) are listed in Table 2.10. It is evident from the results that the indirect test method of finding the tensile strength overestimates the tensile capacity of the material.

Table 2.10. 7-Day Results of Tensile Strength (adapted from Garas et al. 2010).

Method	Sample	Method	Test	7-Day Tensile strength, ksi at		
				73°F	140°F	194°F
Splitting Tension	4 × 8 in. cylinders	Splitting Tension	ASTM C469	2.3	2.8	3.2
Direct Tension	2 × 2 in. dog bones	Direct Tension	N/A	1.1	1.4	1.5

Mix Constituent	lb/ft^3
UHPC premix	137
Water	6.80
HRWR admixture	1.94
Steel fibers	9.74

Notes:
1. High-strength steel fibers are 0.5 in. long and 0.008 in. diameter; 97 to 140 ksi tensile strength.
2. Dog bone specimen was 9.25 in. long and a mid-section cross section of 2 × 2 in. for direct tension test.
3. Tensile load applied through 3 × 2 × 1 in. steel plates that were fixed through 1.5 in. embedded bolts (Direct Tension).
4. The longitudinal strains were measured using electrical resistance strain gauges connected in half-bridge configuration (Direct Tension).
5. N/A: Not applicable

Graybeal and Baby (2013) developed a direct tensile testing method that resembles the standard test methods used for metals. The test results of the proposed experiment showed that the two UHPCs (cured in steam and ambient conditions) used for the research took up to 1.3 ksi of load under a strain of 4000 millionths.

AFGC (2013) and JSCE (2006) described methods of conducting uniaxial tensile testing of UHPC through direct and indirect methods. However, there is a dearth of standard testing conditions and associated parameters, such as specimen size and geometry, that can be narrowed down for consistent characterization of the strain-hardening behavior of the UHPFRC. The major challenge in conducting direct tensile testing for studying the tensile behavior is the method of distributing stresses while maintaining a stable load-deflection response (Wille et al. 2014a). The authors also

mentioned that the specimen shape and size play an important role in determining the testing procedure, and they developed tensile testing methods by using the suggestions in AASHTO T 132-87 (2009) and direct tensile strength testing recommendations by Sujivorakul (2002).

These testing methods were aimed at complying with the essential qualities that allow testing of small specimens to save on the quantity of the material, with a focus of using specimens that are convenient for casting, treatment, practical installation (elimination of adhesives), and reduction in the errors arising due to alignment and end rotations. The specimen should ideally have a uniform area to accurately investigate the multiple cracking phenomenon. No reinforcement in the head of the specimens must be required. The testing setup must comprise a simple and efficient system that is easily deployable, with low inertia to allow for high strain rate tests in the future with a reusable measurement recording device. The loading should ideally be uniaxial with minimal bending, and the crack growth should be spread uniformly. It is also recommended that the largest constituent material be limited to 1/5th of the smallest specimen size (0.2 in.). Although the dimensions are well within the size gradient of the fine particles of UHPC mortar, the fibers are usually between 0.5 to 1.2 in., which is greater than the dimension of the specimen (in the range of 0.984 × 0.984 in). This configuration helps in the orientation of the fibers, particularly if the fresh mix is poured in layers. Some of the key findings of this research were that the direct tensile strength depends on the volume of the fiber added in the mix design, and smooth fibers showed higher bond strength. Moreover, this research revealed the results are dependent on the rate of strain and the size of the specimen. The high ductility indicated a huge potential for this material in high strain rate situations that occur during blast and impact loading. Thus, further testing must be undertaken to see the extent to which this material may sustain such loading, especially for moving vehicular structures.

Kusumawardaningsih et al. (2015) tested the axial and bending tensile testing methods for several mixes using notched, cylindrical dog bone specimens for axial tests and prismatic beams for bending tests. The tests on stress-crack opening behavior were conducted in the Official Material Testing Institute for Construction Industry—Amtliche Materialprüfanstalt für das Bauwesen of Kassel University. The steel fibers used in the specimen were 0.354 in. long and 0.004 in. in diameter and added in 2 percent by volume. A series of prismatic specimens were tested using a cross section of 1.57 in. × 1.57 in. The notches were 0.197 in. × 0.197 in. The measured

compressive strength was 26 ksi. The specimens were cured under room temperature. An RBO2000 Tension Testing Machine with a maximum load of 360 kips was used. The load rating was 4×10^{-4} in./sec and was increased by five times after the crack opening exceeded 0.08 in. The mean tensile strength measured was 0.58 ksi (crack opening length of 3×10^{-4} in.) and 0.95 ksi (crack opening length of 2.68×10^{-4} in.) for specimens with and without fibers, respectively.

Pyo et al. (2016) conducted direct tensile strength testing of fiber-reinforced UHPC at high strain rates and developed a testing set up to carry out the various tasks involved in analyzing such behavior. They used a Strain Energy Frame Impact Machine with proposed modifications to capture the full strain hardening and softening loading regimens. The strain gate was attached to the transmitter bar, which captured the stress in the specimen. The signal amplifier VISHAY 2310B was used for signal conditioning and recorded using an oscilloscope. The digital image correlation method was used to record the strain history. The direct tension load was applied at strain rates ranging from 90 to 146/s. It was concluded that the strain capacity increases under impact loading irrespective of the type of fiber used.

Thus, a vast variety of testing methods are available for the evaluation of the tensile behavior of concrete. However, a need exists to develop a standard to characterize the behavior with the same consistency as that of the testing procedures available for other properties, such as compressive strength.

2.4.4.1.3 Tensile Behavior and Stress-Strain Models

Russell et al. (2013) reported that UHPC continues carrying tensile stresses even after first cracking. Graybeal and Baby (2013) proposed an idealized stress-strain response for capturing the strain-hardening behavior of the material in tension, shown in Figure 2.4, where the pre-cracking and post-cracking behavior is represented as a series of elastic phases followed by the multiple crack formation when the stress is higher than the cracking strength of the matrix. The third phase initiates when no further individual cracking is possible and the existing cracks widen. The final phase initiates when the strain limit of the individual cracks is reached, and there is pull-out of the fiber that was threading the crack in the matrix. The authors also mentioned that the strength of the bridging of the crack by the fiber (in case of localization) is greater than the cracking strength (in case of multi-cracking).

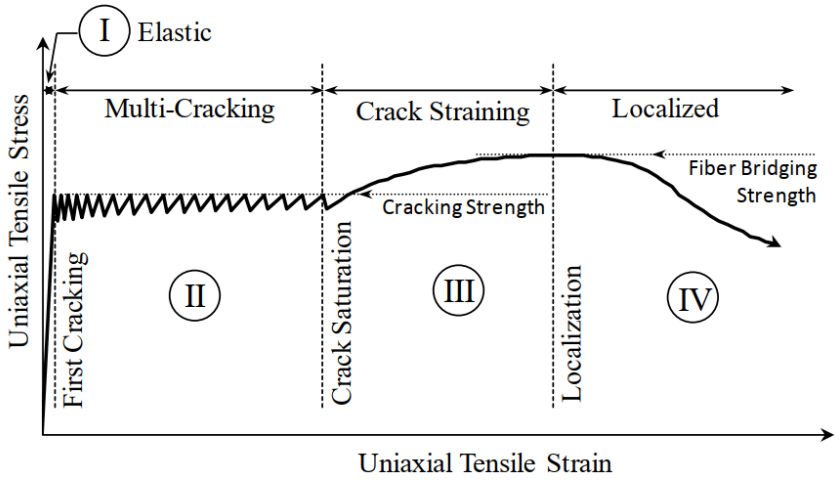

Figure 2.4. Idealized Stress-Strain Curve Developed from Direct Tension Test (Graybeal and Baby 2013).

Wille et al. (2014a) investigated the behavior of UHPC under direct tensile loading based on the definition of the performance levels set forth by Namman and Reinhardt (2003), namely, the deflection softening with low improvement of mechanical properties, the deflection hardening, the tensile strain hardening, and the high energy absorbing level. The energy absorption capacity of the material before the occurrence of tensile softening, g, was experimentally reported by Wille et al. (2014a), as seen in Table 2.11.

Table 2.11. Energy Absorption Capacity Pre-Tension Softening, g (adapted from Wille et al. 2014).

Source	Name	Percentage Volume of Fiber	Energy Absorption Capacity, g (lb-ft/ft^3)
Jungwirth and Muttoni (2004)	Ceracem®	2.5	523
Chanvillard and Rigaud (2003)	Ductal®	2.0	826
Wille et al. (2011)	SIFCON-UHP-FRC	5.5	6354
Wille et al. (2014a)	Research Mix	2–3	1150–1965

Wille et al. (2014a) discussed the strain hardening behavior of UHPFRC using the plot between the tensile stress and the elongation (Figure 2.5). The authors stated the material will be in strain hardening if the tensile strength σ_{pc} is greater than the cracking stress σ_{cc} and explained the mechanism as follows. The initial tensile behavior shapes the first part of strain-based elastic tension. The variable σ_{cc} denotes the imaginary stress at which the ideal linear elastic behavior transitions into the strain-hardening curve modeled based on a best fit of the data. It is computed

using the corresponding strain ε_{cc} and MOE E_{cc}. The second part is based on the energy dissipated per unit volume, $g_{f,A}$, and is related to the multiple cracking. This curve denotes the strain hardening effect. The 99th percentile of the tensile capacity of the material (σ_{pc}) and the corresponding strains (ε_{pc} and ε_{soft}), hardening modulus (E_{hc}), and residual stress (ε_{res}) also influence this part. The third part deals with the crack opening that depends on strain softening, which is largely influenced by the energy dissipated per crack surface area ($G_{f,B}$). The unloading modulus E_{pc} distinguishes between the volume-based strain hardening energy dissipation and the area-based softening phase energy dissipation.

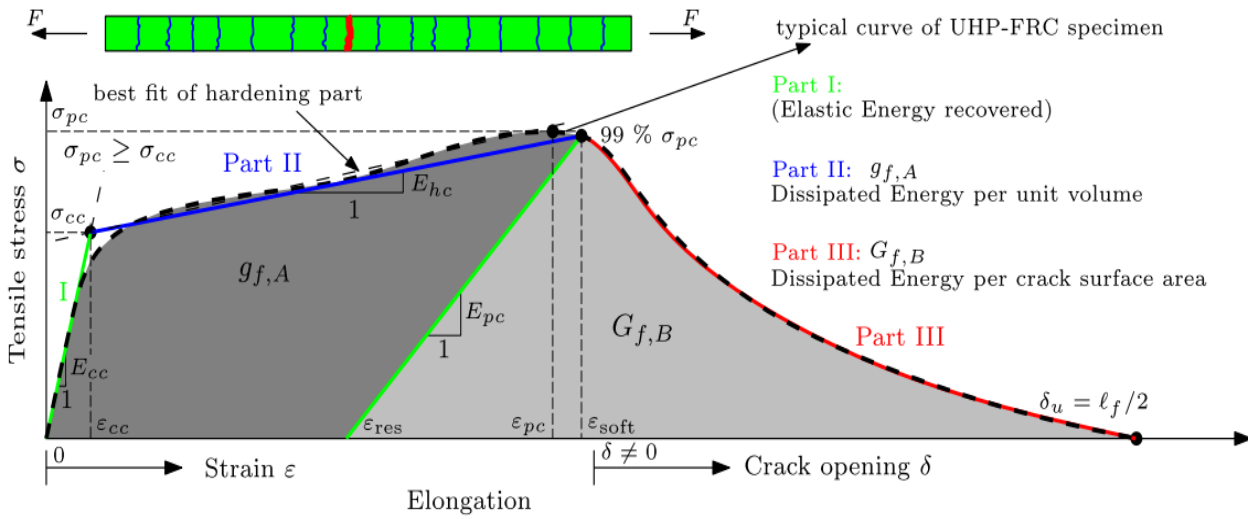

Figure 2.5. Tensile Behavior of UHPFRC under Strain Hardening with Idealized Modeling (Wille et al. 2014a).

El-Helou et al. (2022) conducted several uniaxial tensile strength tests and developed a tensile behavior design model for UHPC (Figure 2.6). The authors recommended the determination of the MOE, the effective strength at cracking, and the stress and strain at localization be achieved using the AASHTO T 397 Draft (AASHTO 2022) proposed standard test. They defined the minimum tensile parameters for the design model as an effective cracking strength greater than 0.73 ksi, which is required to be maintained at least up to a localization strain of 0.0025. These minimum requirements are considered essential for attaining ductile UHPC behavior with the necessary crack control.

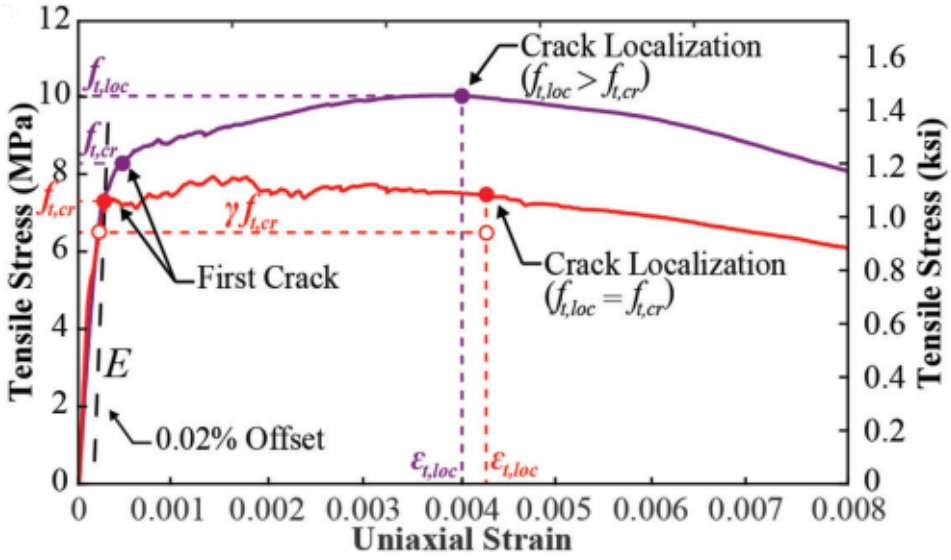

(a) Tensile stress-strain characteristic curves for UHPC test specimens

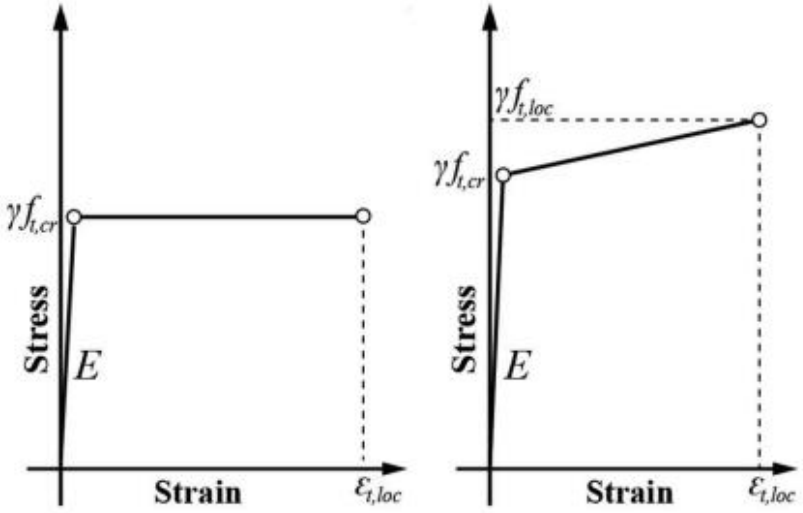

(b) Idealized stress-strain models for UHPC with stress plateau (left) and with a continuous rise in post-cracking stress (right)

Figure 2.6. Tensile Behavior of UHPC under Strain Hardening with Idealized Modeling (El-Helou et al. 2022).

2.4.4.2 State-of-the-Practice

Standard testing methodologies with their respective modifications and recommendations by different guidelines and codes are elaborated on in the following sections.

2.4.4.2.1 ASTM Standard Tests

Standard tests such as ASTM C78 (2009) may be used to test the tensile behavior of UHPC prior to first cracking. However, Russell et al. (2013) discouraged their use for capturing the strain hardening behavior of UHPFRC because those tests may tend to overestimate the capacity. Graybeal (2006a) proposed a modification of ASTM C469 (2014) for determining the split tensile strength of UHPC.

Other indirect methods of testing the tensile strength include ASTM C1018 (1997), *Standard Test Method for Flexural Toughness and First-Crack Strength of Fiber-Reinforced Concrete (Using Beam with Third-Point Loading) (Withdrawn 2006)*; ASTM C1609/C1609M (2012), *Standard Test Method for Flexural Performance of Fiber-Reinforced Concrete (Using Beam With Third-Point Loading)*; and RILEM TC 162-TDF (2002) methods. ASTM C1609/C1609M (2012) is specifically recommended for testing the flexural strength, and the modifications for UHPC are given in ASTM C1856 (2017). The modifications include the dimensions of the prismatic specimen, which depend on the length of the fibers (Table 2.12).

All the standard tests of concrete shall be modified as per the recommendations of ASTM C1856 (2017) for conducting tests on UHPC. ASTM C78 (2009), *Standard Test Method for Flexural Strength of Concrete (Using Simple Beam with Third-Point Loading)*, may also be used for testing the modulus of rupture of the concrete. Russell et al. (2013) used ASTM C1018 (1997) and ASTM C496 (1996), *Standard Test Method for Splitting Tensile Strength of Cylindrical Concrete Specimens*, to test the modulus of rupture of UHPC specimens. They reported the modulus of rupture at first cracking for the prisms ranged from 1.3 to 1.5 ksi. The values varied depending on the curing temperature, and an average of 1.3 ksi was suggested for untreated specimens.

Table 2.12. Beam Specimen Dimensions Based on Fiber for Flexure Testing (adapted from ASTM C1856 (2017)) .

Length of Fiber, l_f (Maximum)	**Cross Section of the Prism (Nominal)**
Less than 0.6 in.	3 × 3 in.
0.6 to 0.8 in.	4 × 4 in.
0.8 to 1.0 in.	6 × 6 in.
Greater than 1.0 in.	8 × 8 in.

2.4.4.2.2 AFGC (2013)

The post-peak resistance beyond the elastic limit is attributed to the presence of fibers in UHPFRC. The linear elastic behavior up to the peak tensile strength is stated to be similar to that of CCs. The effect of fibers in the post-cracking behavior of UHPFRC, particularly in imparting the additional strength of drawing the cracked section together after cracking, has been defined by the constitutive laws under tension in the French code of practice. These laws are characterized by the limit that defines the linear elastic stage by the elastic tensile stress $f_{ct,el}$ and the post-cracking stage using a stress-crack width ($\sigma_t - w$) law or a stress-strain ($\sigma_t - \varepsilon$) law. AFGC (2013) suggests that the orientation of the fibers plays an important role in determining the tensile strength, and the extent of this influence is computed using fiber orientation coefficient K. AFGC (2013) defines the different constitutive laws based on *strain-softening FRC*, *low strain-hardening FRC*, and *high strain-hardening concrete*. AFGC (2013) also recommends the use of a modification factor given by the Model Code (1990) if bending tests are considered. AFGC (2013) further suggests the use of six four-point bending tests or six direct tension tests to determine the value of $f_{ct,el}$ and to obtain the post-cracking ($\sigma_t - \varepsilon$) law. The bending tests and direct tensile tests to assess the elastic limit involve testing a minimum of six unnotched specimens for each mix; to assess the post-cracking constitutive law involves testing a minimum of six notched specimens (also referred to as prisms or diabolos) (Figure 2.7).

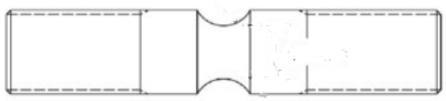

Figure 2.7. Schematic Description of Notched Diabolos (Holmen et al. 2017).

2.4.4.2.3 JSCE (2008)

The use of a testing method of uniaxial direct tensile strength is recommended for the determination of the characteristic value of the ultimate tensile strength f_{tk} and the characteristic value of the ultimate tensile strain ε_{tuk}.

2.4.4.2.4 ACI 544.1R-96 (2002)

This report for FRC noted an increase in direct tensile strength by about 30 to 40 percent with the steel fiber addition of 1.5 percent by volume of the concrete or mortar. ACI 544.4R-18 (2018)

states that fibers impact the flexural properties more significantly than they impact the compressive strength properties. ACI 544.1R-96 (2002) also noted that for the case of steel FRC, there is an approximate 50 to 70 percent improvement in the flexural strength over that of unreinforced concrete.

2.4.4.2.5 ACI 363R-10 (2010)

The modulus of rupture for HSC is reported for moist- and steam-cured conditions, as follows:

$$f_r = 0.71 {f_c'}^{0.79} \text{ (in psi)} \quad (2.16)$$

where:

f_c' = Compressive strength of concrete, psi

2.4.4.2.6 CEB FIP Model Code 2010 fib (2010)

The International Federation for Structural Concrete facilitates the collection and organization of the latest research of the scientific community prior to developing standard code-based provisions in the field of concrete to aid the standardization of norms in design codes for practice. The tensile strength of CC is defined as the uniaxial tensile strength, and equations are provided to compute the tensile strength based on the characteristic compressive strength when experimental testing is not possible. The use of indirect tests such as the split tensile strength and flexural tests is discouraged because the indirect methods may lead to uncertainties in the results. The uniaxial tensile testing may lead to erroneous results if used for standard testing of FRC primarily because the small size of the specimens may orient the fiber, depending on the method of manufacture, thereby causing less fiber to be available in the governing plane. CEB FIP Model Code 2010 fib (2010) recommended the use of bending tests that provide the load-deflection behavior to derive the stress-crack width relations. A three-point bending test, as shown in Figure 2.8(a), is recommended to be conducted, as per EN 14651, using notched beam specimens. The residual flexural tensile strength is defined using the applied force versus deformation plot, as shown in Figure 2.8(b). The residual flexural tensile strength is calculated using Equation (2.17). Crack mouth opening displacement (CMOD) is used to express the deformation obtained. CEB FIP Model Code 2010 fib (2010) recommended the use of RILEM CPC 7 (1975)—the direct tension of concrete specimens test—if no test procedure is specified.

$$f_{R,j} = \frac{0.22 F_j l}{b h_{sp}^2} \quad (2.17)$$

where:

$f_{R,j}$ = Residual flexural tensile strength corresponding to CMOD = $CMOD_j$, psi

F_j = Load that corresponds to CMOD = $CMOD_j$, kips

l = Span length, in.

b = Width of specimen, in.

h_{sp}^2 = Height measured between the tip of the notch and the specimen top, in. (5 in.)

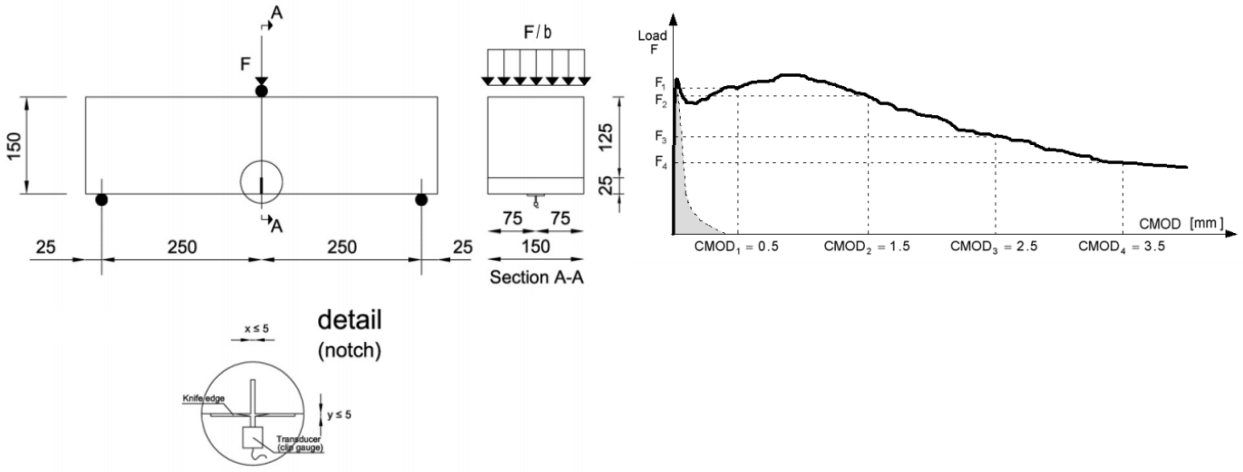

(a) Set-up of test recommended by EN 14651 (dimensions in mm)

(b) Typical load F-CMOD curve for plain concrete and FRC

Figure 2.8. Behavior in Tension (CEB FIP Model Code 2010 fib 2010).

2.4.4.2.7 CSA S6:19 (2019)

The Canadian Highway Bridge Design Code (CSA S6:19 2019) classifies FRC with compressive strengths greater than 17.4 ksi as tension-hardening UHPC or tension-softening UHPC based on an increase or decrease in tensile strength, respectively; post-cracking; and until a specified deformation occurs when subjected to uniaxial tension, as per CSA A.23.1 Annex U. The tensile strength is determined using a four-point flexure prism test, and the properties are studied using inverse analysis. The code also proposes the use of a fiber efficiency factor to account for the orientation and dispersion of the fibers with respect to the tensile stresses in a structure. This factor is less than or equal to 1.

2.4.4.2.8 AASHTO T 397 Draft (AASHTO 2022)

The FHWA (2022) proposed that the AASHTO T 397 Draft (AASHTO 2022), *Standard Method of Test for Uniaxial Tensile Response of Ultra-High Performance Concrete*, be the designated test for determining the behavior in tension for strain hardening UHPC and also for strain softening UHPC, with slight modifications to the analysis sections. The standard proposes the testing of prismatic specimens of UHPC loaded in tension uniaxially. The parameters that characterize the tensile behavior that can be determined by the standard include the stress-strain response, the elastic tensile strength, effective cracking strength and strain at that strength, MOE, and tensile strain limit.

2.4.4.2.9 FHWA (2022)

In the draft AASHTO design specifications for UHPC, the experimental tensile parameters are determined for the design models using the AASHTO T 397 Draft (AASHTO 2022). Bilinear idealized stress-strain models are prescribed for UHPC. One type is applicable when the post-cracking stress continues to be equal to or greater than the effective cracking stress from the effective cracking to localization strain range. The other type is applicable when the stress after cracking continuously increases from post-cracking to localization strain range, with the peak being equal to or greater than 1.2 times the effective cracking stress. These recommendations are being drafted based on the research conducted by El-Helou et al. (2022).

2.4.5 Thermal Properties

UHPC is known for its superior performance, which facilitates the application of UHPC for structures that are subjected to severe conditions, such as nuclear reactors and power plants. It is important to understand how the material will perform under the action of high temperatures. Russell et al. (2013) provided values for the coefficient of thermal expansion of UHPC based on the work done by several researchers, and they range between 5.6×10^{-6} to 8.6×10^{-6} per °F.

2.4.5.1 AFGC (2013)

AFGC (2013) suggested a coefficient of thermal expansion value of 6.1×10^{-6} per °F if no data are available.

2.4.5.2 JSCE (2008)

JSCE (2008) reported the thermal conductivity of HPFRCC as 0.268 Btu/(h ft °F) and the specific heat as 3.44×10^{-4} Btu/(lb °F).

2.4.5.3 FHWA (2022)

It is recommended that the coefficient of thermal expansion be experimentally determined based on AASHTO T 336 (2019), *Standard Method of Test for Coefficient of Thermal Expansion of Hydraulic Cement Concrete*. The standard specifies the value of 7.0×10^{-6} per °F if the laboratory test data are not available. Mohebbi and Graybeal (2022) observed that the coefficient of thermal expansion is similar to that of CC composed of siliceous aggregates.

2.4.6 Creep and Shrinkage

Time-dependent deformations such as creep and shrinkage are important parameters to be considered for concrete structures, particularly in the case of long-span bridges. Creep occurs due to prolonged application of load (Mindess et al. 1981). Water content alterations and long-term chemical reactions lead to volumetric deformations or shrinkage in concrete structures that may be detrimental to the structures. Such time-dependent deformation may lead to severe cracks and alignment problems in the structure.

2.4.6.1 State-of-the-Art

Russell et al. (2013) conducted creep testing using four different curing regimes, as recommended by ASTM 512 (2015): steam, tempered steam, delayed steam treatment, and air treatment. For samples that followed the steam and tempered steam regimes, the samples were loaded at 4 days of age for creep testing after the casting, while for the samples subjected to delayed steam- and air-treated curing, the loading occurred at 21 days and 28 days after casting, respectively. The creep coefficient computed after 1 year varied from 0.29 to 0.78, and the specific creep was in the range of 0.04 to 0.15 millionth/psi; it was controlled by the age at which the specimen was loaded and the curing method. The creep was approximately 0.15 times less than that of CC.

Garas et al. (2012) conducted a detailed year-long study on the creep behavior of UHPC in both tension and compression using a commercial brand-named product—Ductal®. The specimens were subjected to three different curing regimes that were designed as follows:

Regime 1 met the requirements of the premix manufacturer such that the specimens were cured at 194°F for 48 hours at 100 percent RH.
Regime 2 simulated conditions that may be attained in the casting plant in the United States while meeting the requirements of the manufacturer in the longer duration. The temperature was 140°F from the age of 48 hours to 72 hours at 100 percent RH for steam curing.
Regime 3 simulated ambient curing conditions that provided the closest representation to the in-situ conditions with no thermal treatment at 73°F.

Table 2.13 summarizes the results of the experimental testing by Garas et al. (2012). The experiments were conducted at a 40 percent stress to strength ratio at the time of loading, and this loading was maintained for 1 year of testing. The fibers used are 0.5 in. long, 0.008 in. diameter, and 2 percent by volume. The specific tensile creep was deduced by the authors by computing the ratio of the adjusted tensile creep strain and the stress that was initially applied. The results show that the heat treatment mitigated the creep effect of the UHPC.

Table 2.13. 1-Year Results for Creep and Shrinkage (adapted from Garas et al. 2012) .

Description	Specific tensile creep at 1 year, με/ksi		Free shrinkage strains at 1 year, με	
	Compression	Tension	Compression	Tension
Sample	6 × 12 in. (after modification)	3 × 3 × 19 in. prism	6 × 12 in. (after modification)	3 × 3 × 19 in. prism
Test	ASTM 512 (2015)	Modified (Bissonnette and Pigeon 1995)	ASTM C157 (2008)	Modified (Bissonnette and Pigeon 1995)
73°F	59.8	1216	238	296
140°F	28.5	443	83	105
194°F	22.6	372	65	82

Notes:

1. High-strength steel fibers are 0.5 in. long and 0.008 in. diameter; 97 to 140 ksi tensile strength Bekaert's.
2. Tensile creep testing set-up allows a load-carrying capacity of up to 15,000 lb. Three 3 × 3 × 9 in. specimens could be tested in the set-up and loaded at 40 percent of measured direct tension strength at the end of 7 days at 73°F±2°F and 50±3 percent RH.
3. Compressive creep was determined using ASTM 512 (2015) with modified specimens of 4 × 15 in. to account for the high strengths of UHPC.
4. For free shrinkage in compression, one cylinder sample of 4 × 15 in. was used.
5. For free shrinkage in tension, three free shrinkage prisms of 3 × 3 × 9 in. were used.

ASTM C157 (2008), *Standard Test Method for Length Change of Hardened Hydraulic-Cement Mortar and Concrete*, was used by Russell et al. (2013) to conduct the drying shrinkage test in compression. The authors reported the range of the total shrinkage—drying and autogenous combined—to be up to 900 millionths strain.

Mohebbi and Graybeal (2022) and Mohebbi et al. (2022) conducted extensive experimental tests to develop creep and shrinkage data and to propose methods of predicting the creep coefficient and shrinkage strain for a UHPC product of a given compressive strength, age, and maturity at the time of loading. Mohebbi et al. (2022) evaluated the data-driven prestress loss model in comparison to the performance of seven full-scale UHPC pretensioned girders. The authors observed that the existing AASHTO models tend to underestimate the ultimate creep coefficient and the shrinkage strain, while the European predictions are more reasonable in predicting the trends observed experimentally for the UHPC products tested. Mohebbi and Graybeal (2022) also studied compressive creep, unrestrained shrinkage, and thermal expansion coefficients under the influence of different compressive strengths, age, and maturity when loading while varying the humidity conditions. The ultimate creep coefficient was reported to be in the range of 0.68 to 0.17 when the specimens were loaded at matured age, which is less than that found in CC. The shrinkage

of the tested materials was observed to be higher than that of CC. The shrinkage values were reported over a wide range—from 300 to 1300 microstrain measured at 300 days past demolding (50 percent humidity). The authors reported that the drying shrinkage was lower than CC at 50 percent humidity conditions, with autogenous shrinkage being accountable for 80 percent of the total shrinkage.

Mohebbi et al. (2022) studied creep and shrinkage of UHPC to update parameters of the predictive models in the AASHTO Load and Resistance Factored Design (LRFD) Bridge Design Specifications 9th edition (AASHTO (2020). The effects of compressive strength, loading age and maturity, and humidity were studied. The effects of other parameters such as size, shape, and time-development response in the predictive models were described by Mohebbi and Graybeal (2022) for prestress loss prediction. Table 2.14 describes the proposed equations and parameters.

Table 2.14. Creep and Shrinkage Predictive Models.

Parameter	AASHTO Equations Section 5.4.2.3, AASHTO (2020)	Proposed Equation for UHPC by Mohebbi and Graybeal (2022)
Shrinkage Strain	$0.48 \times 10^{-3} k_s k_{hs} k_f k_{td}$	$0.6 \times 10^{-3} k_s k_{hs} k_f k_{td} k_4$
Creep Coefficient	$1.9 k_s k_{hc} k_f k_L k_{td}$	$1.2 k_s k_{hc} k_f k_L k_{td} k_3$
Humidity for Shrinkage, k_{hs}	$2 - 0.014H$	$1.5 - 0.01H$
Humidity for Creep, k_{hc}	$1.56 - 0.008H$	$1.12 - 0.0024H$
Compressive Strength, k_f	$\frac{5}{(1 + f'_{ci})}$	$\frac{18}{(1.5 f'_{ci} - 3)}$
Size, k_s	$1.45 - 0.13\frac{V}{S} > 1$	1
Time-development, k_{td}	$\frac{t}{(61 - 4f'_{ci} + t)}$	$\frac{t}{(\frac{300}{f'_{ci} + 30} + 0.8t^{0.98})}$
Loading age, k_L	$t_i^{-0.118}$	1 for $t_i < 7$ $(t_i - 6)^{-0.15} \geq 0.5$ for $t_i \geq 7$

Notes:
- H = Humidity, %
- V = Volume, in^3
- S = Surface area, in^2
- t = Time, day
- t_i = Age of concrete at time of loading application, day
- f'_{ci} = Compressive strength at release, ksi
- k_3 = UHPC material correction factors for creep, assumed to be 1.0 without the physical test. By the creep test, according to ASTM 512 (2015), it is determined to be the ratio of the measured ultimate creep coefficient to the predicted value.
- k_4 = UHPC material correction factors for shrinkage, assumed to be 1.0 without the physical test. By the shrinkage test, according to ASTM C157 (2017), it is determined to be the ratio of the measured total shrinkage strain to the predicted value.

2.4.6.2 State-of-the-Practice

This section discusses the standard test methods and recommendations for creep and shrinkage assessment of UHPC.

2.4.6.2.1 ASTM Standard Tests

ASTM 512 (2015), *Standard Test Method for Creep of Concrete in Compression*, can be used for the assessment of creep in compression on 4 in. diameter cylinders. The specifications suggest that the loading should be done in the stages of 2, 7, 28, and 90 days, and 1 year if the complete creep behavior of the concrete is to be studied. As per ASTM C39 (2016), it is recommended the compressive strength be determined immediately before the loading of the creep specimens. It is recommended the specimens be loaded at an intensity of less than 40 percent of the compressive strength measured at the age of loading. The strain readings are to be taken immediately before and after the loading, 2 to 6 hours after loading, and then daily for 1 week, followed by weekly recordings for a month, and then monthly recordings for a year. The total strain per unit stress due to the loading is calculated as per the equation specified in the standard, and it is to be reported in psi^{-1}.

ASTM C1856 (2017) specifies the modifications that need to be incorporated to use ASTM 512 (2015) for UHPC. The dimensions of the creep specimens are specified to be a minimum of 3 in. diameter and 6 in. length. Additional requirements for grinding the ends and other preparation guidelines are specified in ASTM C1856 (2017).

ASTM C157 (2017), *Standard Test Method for Length Change of Hardened Hydraulic-Cement Mortar and Concrete*, is used for the shrinkage measurement. Specimens should be cured for 28 days in the moist room in 73°F at 95 percent RH. After readings at the age of 28 days, the specimens are stored in the drying room at 73°F and 50 percent RH. Readings are taken at 4, 7, 14, and 28 days and 8, 16, 32, and 64 weeks after curing. The specimen size is modified to a 3 × 3 × 11.25 in. prism, according to ASTM C1856 (2017).

2.4.6.2.2 AFGC (2013)

AFGC (2013) recommendations suggest a value of 550 μin./in. may be considered for endogenous shrinkage in the absence of any heat treatment, and a value of 150 μin./in. may be considered for drying shrinkage in 70 percent RH conditions (outdoors) if no data are available for the long-term properties of UHPFRC. These recommendations also suggest the use of 0.8 as the long-term creep for the condition of absence of heat treatment if no data are available.

2.4.6.2.3 JSCE (2008)

JSCE (2008) reported that the shrinkage of UHPFRC should be evaluated using the JIS A 1129 *Methods of Measurement for Length Change of Mortar and Concrete*. The use of expansive additives and other shrinkage reducing agents are recommended for reducing the drying shrinkage to the same levels as that of ordinary concrete. The Japanese guidelines suggest determining the tensile creep of UHPFRC by using the existing data or experimental evidence. The compressive creep strain, for a compressive strength at work, is determined as follows:

$$\varepsilon'_{cc} = \varphi \sigma'_{cp} / E_{ct} \tag{2.18}$$

where:

ε'_{cc} = Compressive strain for corresponding compressive strength

σ'_{cp} = Compressive strength

φ = Creep coefficient

E_{ct} = MOE at the age of the application of loading

2.4.6.2.4 ACI 209R-92 (1997)

The ACI 209R-92 (1997) expressions for finding the creep coefficient and shrinkage, respectively, after 1 to 3 days of steam curing are given as follows:

$$\nu_t = \frac{t^{0.60}}{10 + t^{0.60}} \nu_u \tag{2.19}$$

where:

ν_t = Creep coefficient of CC for 7 days of loading for moist-cured concrete and for 1 to 3 days of steam-cured concrete

ν_u = Specific creep for the local aggregates and conditions

t = Time after loading, days

$$(\epsilon_{sh})_t = \frac{1}{55+t}(\epsilon_{sh})_u \quad (2.20)$$

where:

$(\epsilon_{sh})_t$ = Shrinkage after 1 to 3 days for steam-cured concrete

$(\epsilon_{sh})_u$ = Specific shrinkage based on the local aggregates and conditions

t = Time after the period of initial wet curing, days

2.4.6.2.5 ACI 544.1R-96 (2002)

ACI 544.1R-96 (2002) reported that creep and shrinkage properties are not significantly influenced by the presence of fibers in FRC with less than 1 percent of steel fibers by volume. ACI 544.4R-18 (2018) stated that crack control may be observed in plastic and drying shrinkage phenomena due to fibers.

2.4.6.2.6 AASHTO (2020)

Because creep and shrinkage are largely time dependent properties, the AASHTO LRFD Bridge Design Specifications 9th edition (AASHTO 2020) stated that a need exists for conducting physical tests to determine the behavior under these effects and that any code expression can be reliable only up to a 50 percent confidence. The expressions of creep and shrinkage are based on the recommendations by the ACI 209R-92 (1997).

2.4.6.2.7 CEB FIP Model Code 2010 fib (2010)

The CEB FIP Model Code 2010 fib (2010) gives expressions for creep and shrinkage that are valid for strengths of concrete of up to 19 ksi. The expression for the creep strain at time $t > t_0$ for a constant stress applied at time t_0 is represented as follows:

$$\varepsilon_{cc}(t, t_0) = \frac{\sigma_c(t_0)}{E_{ci}} \varphi(t, t_0) \quad (2.21)$$

where:

$\varepsilon_{cc}(t, t_0)$ = Creep strain at time $t > t_0$

$\sigma_c(t_0)$ = Constant stress applied at time, t_0, ksi

$\varphi(t, t_0)$ = Creep coefficient

E_{ci} = MOE at 28 days

This expression is valid for creep under tension. CEB FIP Model Code 2010 fib (2010) also reported that the total shrinkage of normal weight high-strength structural concrete after drying for 50 years ranges between -0.51×10^3 for 50 percent RH to -0.32×10^3 for 80 percent RH.

2.4.6.2.8 CSA S6:19 (2019)

The Canadian Highway Bridge Design Code (CSA S6:19 2019) recommended that the creep strain and shrinkage strain for FRC with compressive strength in excess of 12 ksi be determined based on laboratory tests as per CSA A23.1, Annex U.

2.4.6.2.9 FHWA (2022)

Based on the research conducted by Mohebbi and Graybeal (2022) and Mohebbi et al. (2022), the draft specifications for the AASHTO LRFD Bridge Design Specifications recommends equations for creep coefficient and shrinkage strain. These equations are provided for use when creep and shrinkage data for the UHPC product being used are not available. These empirical equations may not be effective in predicting the effects of creep and shrinkage for UHPC materials with different compositions due to potential deviation in behavior with different mixtures and products.

2.4.7 Impact of Fibers on the Hardened Properties

Many researchers have investigated the impact of fibers on the hardened properties of UHPC. Behloul et al. (1996) achieved a tensile strength of 1.13 ksi using straight steel fibers of 0.5 in. with a 0.006 in. diameter at a volume of 2.5 percent. However, Grünewald and Walraven (2001), Martinie et al. (2010), Boulekbache et al. (2010), and Wee et al. (2006) noted that the use of fibers severely impacts workability, flowability, and the resulting hardened properties of UHPC, in addition to making it uneconomical. ACI 544.4R-18 (2018) classified fibers with a diameter less

than 0.012 in. as microfibers and fibers with a diameter greater that 0.012 in. as macrofibers. The mechanical behavior is considered to be improved by fibers due to the interlocking of the material, particularly at crack locations. Orgass and Klug (2004) further recommended the use of short fibers because the grain size of UHPC is better fitted to the spatial orientation of these fibers. As a result, the concrete's compressive and tensile strength improved due to better uncracked concrete behavior. The authors also suggested that there may be higher durability due to the accumulation of water at the surface of fibers such as polypropylene, and therefore shrinkage cracks are avoided by preventing the evaporation of water from the surface. Hertel et al. (2002) mentioned that polypropylene fibers melt at approximately 320°F, which creates a channel for the steam arising from water that has not been used for the hydration of concrete. This channel reduces the pressure and stress that may lead to explosive flaking. This phenomenon, coupled with the high impermeability of UHPC, makes it feasible for fire resistance purposes.

Orgass and Klug (2004) studied the effect of fibers for improving the post-cracking behavior of UHPC. They evaluated the impact of different fiber types and the grain sizes (ranging from the 0.03 in. grain size typically used in RPC to the 0.2 in. grain size commonly used in UHPC). Orgass and Klug (2004) concluded that steel fibers result in the improvement of ductility by reducing an explosive failure generally expected from UHPC. The steel fibers increase the fracture energy and consequently the ductility, along with an enhanced mechanical behavior. Passuello et al. (2009) stated that synthetic fibers can help with the problems of drying shrinkage and cracking of concrete. Orgass and Klug (2004) observed that polypropylene fibers decrease the microscopic crack growth under application of high load, improve the resistance to fire, and reduce the premature shrinkage phenomenon. They also mentioned that glass fibers help in lowering the internal stresses arising in young concrete.

Meng and Khayat (2018) and Chen et al. (2017) discouraged the use of polyvinyl alcohol (PVA), glass, and carbon fibers due to the high water demand for achieving sufficient workability. The problem of balling of fibers can be remedied by the use of an equal mix of hooked steel fibers and thin fibers at 1.5 percent volume by weight (Chen et al. 2017). Figure 2.9 shows different kinds of fibers that were considered by Meng and Khayat (2018). Orgass and Klug (2004) recommended a blend of steel fibers of different sizes for the improvement of ductility and the fracture toughness of the material because the fibers join the microcracks developed and therefore dissipate the tensile

energy that is released upon crack formation. The authors suggested the use of short plain fibers with a uniform distribution in the UHPC matrix. Rossi (2001) explained the mechanism of crack interaction by the fibers under tensile loading with the graphical representation shown in Figure 2.10.

(a) Straight steel fibers *(b) Hooked-end steel fibers* *(c) PVA fibers*

Figure 2.9. Different Types of Fibers Considered for Hybrid Blend (Meng and Khayat 2018).

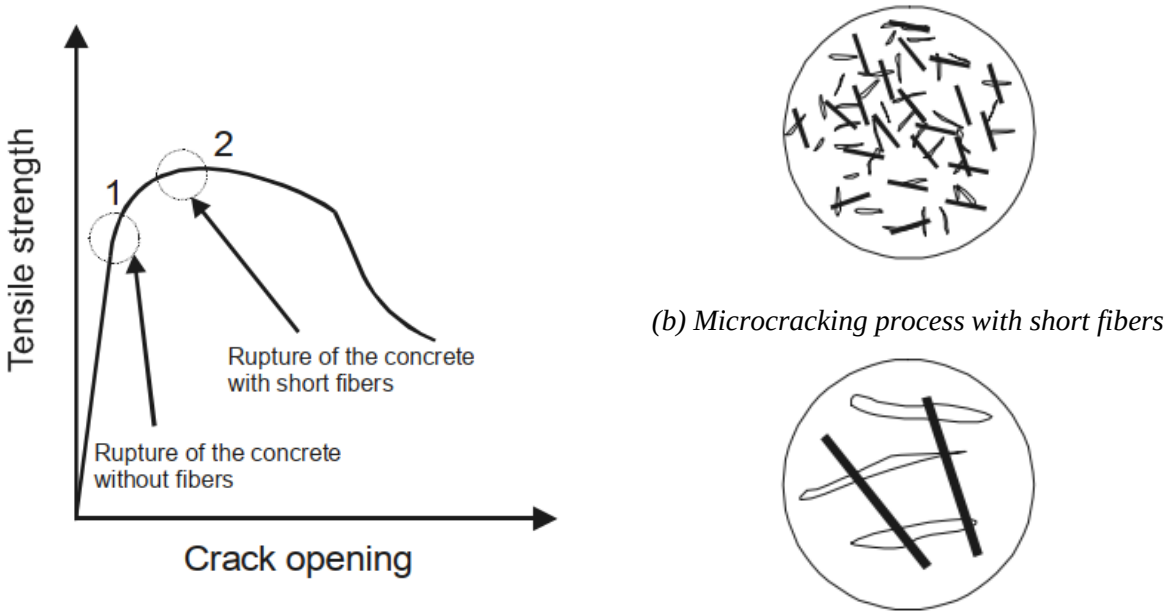

(a) Tensile behavior of UHPFRC *(b) Microcracking process with short fibers* *(c) Macrocracking process with long fibers*

Figure 2.10. Stages of Tensile Cracking of UHPFRC (adapted from Rossi 2001).

Benson and Karihaloo (2005), Lawler et al. (2005), Wille et al. (2011), Park et al. (2012), Yoo et al. (2013), Kwon et al. (2014), Yoo and Banthia (2016), Kang et al. (2016) and Hannawi et al.

(2016) have conducted research to ascertain the influence of fibers on the mechanical behavior and the microcracking and macrocracking mechanism of UHPFRC. Table 2.15 summarizes the different types of fibers used by the researchers and their findings of the tensile strength. It may be concluded from the observations of different research studies that an increase occurs in the tensile strength due to the use of a hybrid fiber combination. However, this increase may not be significant enough to compensate for the drawback of decreased workability on account of the synthetic fibers.

The orientation of the fibers, dependent on the direction of the flow of the mix during the casting of the specimen, also influences the flexural capacity of the prism (Graybeal 2006b). When tested under the three-point bending flexure test, the flexural strength recorded at the peak load of the specimen—with fiber alignment perpendicular to the principal flexure-tensile loading—was more than three times lower than with a parallel fiber alignment, while the compressive strength and the MOE tested using cubes remained largely unaffected by the preferential alignment of fibers (Stiel et al. 2004).

Wille et al. (2011) and Kwon et al. (2014) summarized the results from the tests conducted on the commercial products and test mixes prepared by researchers for the assessment of the influence of the steel fibers on the mechanical behavior (Table 2.16). The longer fibers add to the tensile strength of the specimens; however, the lower workability may pose a greater problem in comparison to the relatively smaller percentage increase in the tensile strength when compared to the 0.5 in. fibers that are 0.008 in. diameter.

These studies show how the fibers play an important role in controlling the mechanical behavior of UHPC. When designing a mix proportion, these effects need to be kept under consideration to see if enhancement in the property of the UHPC due to the addition of fibers warrants the higher cost and reduction of workability of the mix.

Table 2.15. Tensile Strength Results with Different Fiber Combinations.

Source	Fiber			Volume Percent	Specimen		Tensile Strength (ksi)
	Type	Length (in.)	Diameter (in.)		Length (in.)	Area (in^2)	
Behloul et al. (1996)	Straight steel fiber	0.5	0.006	2.5	18	11	1.1
Benson and Karihaloo (2005)	Straight steel fiber	0.5	-	6	20	5	2.0
Wille et al. (2011)	Deformed fibers + Micro straight steel	1.2	0.015	1	7	2	1.9
		0.5	0.008	1.5			
Park et al. (2012)	Deformed steel fiber + Straight steel fiber	1.2	0.015	1	9	8	2.2
		0.5	0.008	1.5			
Kwon et al. (2014)	Straight steel fiber + Hooked steel fiber	0.2	0.006	1	3	0.9	2.9
		1.2	0.015	2			
Kang et al. (2016)	Steel fiber (SF1) + Steel fiber (SF2)	0.8	0.008	1	13	4	2.07 ± 0.3
		0.6	0.008	0.5			
	SF1+SF2 + Basalt	0.8, 0.6	0.008	0.67+0.33	13	4	2.14 ± 0.2
		0.5	0.0005	0.5			
	SF1+SF2 + PVA	0.8, 0.6	0.008	0.67+0.33	13	4	1.72 ± 0.2
		0.5	0.002	0.5			
	SF1+SF2 + Polyethane (PE)	0.8, 0.6	0.008	0.67+0.33	13	4	2.35 ± 0.12
		0.7	0.004	0.5			

- : Not available

Table 2.16. Influence of Steel Fibers on Mechanical Behavior (adapted from Wille et al. 2011 and Kwon et al. 2014).

Source	Name	Type	Fiber			Tensile Strength (ksi)	Compressive Strength (ksi)
			Length (in.)	Diameter (in.)	Volume Percent		
Jungwirth and Muttoni (2004)	Ceracem®	Straight	0.8	0.012	2.5	1.4	27.7
Chanvillard and Rigaud (2003)	Ductal®	Straight	0.5	0.008	2.0	2.2	29.0
Behloul et al. (1996)	RPC	Straight	0.5	0.010	2.4	1.1	33.4
Bornemann et al. (2001)	M1Q	Straight	0.2	0.006	2.5	1.3	21.8
Sujivorakul (2002)	HPFRC	Straight	1.2	0.012	2.0	1.7	12.2
Wuest and Brühwiler (2008)	UHPFRC1	Straight	0.4	0.008	6.0	1.4	21.8
Wuest and Brühwiler (2008)	UHPFRC2	Straight	0.5	0.006	4.0	1.8	21.8
Wille et al. (2011)	S-UHP-FRCC	Hooked	0.5	0.008	2.5	2.1	29.0
Wille et al. (2011)	H-UHP-FRCC	Twisted	1.5	0.012	2.0	2.0	29.0
Wille et al. (2011)	T-UHP-FRCC	Mono	1.2	0.012	2.0	2.2	29.0
Rossi (1997)	MSCC	Hybrid	1.0	0.012	2.0	2.2	28.0
			0.2	0.010	5.0		
Benson and Karihaloo (2005)	CARDIFRC®	Hybrid	0.5	0.006	5.0	2.0	26.8
			0.2	0.006	1.0		
Boulay et al. (2004)	CEMTEC®	Hybrid	3 Fiber Types	3 Fiber Types	Total 11	2.9	31.9

2.5 DURABILITY

2.5.1 General

UHPC shows better durability performance than NSC and HSC. The pore structure is engineered such that the material exhibits highly durable characteristics that facilitate the use of UHPC to extend the life of structures, for repair purposes, and for structures that are continually exposed to harsh environmental conditions that NSC and HSC may not be able to withstand successfully. Moreover, improved durability cuts the maintenance and repair costs by increasing the longevity

of the structures. This section reviews and synthesizes the literature related to the durability performance of UHPC and identifies the factors affecting durability of UHPC.

2.5.2 Permeability

The permeability of concrete is a key characteristic that is defined as the ability to resist penetration of water and other chemical agents into the concrete structure. Such inflow of deteriorating agents causes damage to the material and impacts the pore structure and microstructure. Crack formation that arises from such an interaction of the material with its surrounding environment can have detrimental consequences for load bearing structures. The pore structure and the permeability of the material provides significant insight when assessing the durability properties under different environments.

Permeability is one of the most significant aspects of durability of the material. Several research studies have focused on the determination of the permeability of UHPC to various substances because the crack formation, pore structure, and other physical and chemical deterioration of the material are influenced by the infiltration of harmful substances. The following sections present an overview of the general practices and investigations that are relevant to the permeability of UHPC.

2.5.2.1 State-of-the-Practice

2.5.2.1.1 ASTM Standard Tests

ASTM C1202 (2017), *Standard Test Method for Electrical Indication of Concrete's Ability to Resist Chloride Ion Penetration*, may be used for studying the permeability of UHPC after exercising the modifications given by ASTM C1856 (2017). However, ASTM C1856 (2017) states that ASTM C1202 (2017) is not applicable to those specimens that contain metallic fibers.

ASTM C1760 (2021), *Standard Test Method for Bulk Electrical Conductivity of Hardened Concrete*, is a test method to determine conductivity of specimens by quantifying a passed electrical charge through the specimens. The conductivity depends on pore solution resistivity (PSR), pore sizes, and connectivity of pores of the concrete (Spragg et al. 2016). The resistivity of the specimen is the reciprocal of the conductivity. Bulk resistivity measurements with proper

consideration to PSR is a measure of permeability that can effectively be correlated with the durability performance of UHPC.

2.5.2.1.2 AASHTO Standard Tests

AASHTO T358 (2017), *Standard Method of Test for Surface Resistivity Indication of Concrete's Ability to Resist Chloride Ion Penetration*, is a test method similar to the bulk resistivity test that measures the conductivity of concrete specimens. The difference between ASTM C1760 (2021) and AASHTO T358 (2017) is the measuring direction. The measuring direction of surface resistivity is on the side surface of specimens, whereas the direction of bulk resistivity is from top to bottom.

2.5.2.1.3 AFGC (2013)

Recommendations suggest the use of Grandeurs Associées à la Durabilité des Bétons *Determination of Effective and Apparent Chloride Ion Coefficients in Concrete by Steady State and Transient Migrations Tests* method developed by Hornain (2007) and adopted from the Nordtest Build Standard 492. AFGC (2013) further noted that the coefficient of chloride diffusion of UHPC assessed after testing for 5 years was 2.15×10^{-13} ft^2/s (Tanaka et al. 2010). The water porosity of UHPC has been found to be much lower (1.5 to 5 percent) than that of HPC (10 to 13 percent) and NSC (14 to 20 percent), as measured using the *Determination of Apparent Density and Water Voids* method (Hornain 2007). The permeability of UHPC to oxygen is found to be much lower ($<1.08 \times 10^{-18}$ ft^2) than that of HPC (1.08×10^{-16} ft^2) and NSC (1.08×10^{-15} ft^2).

2.5.2.2 State-of-the-Art

Several researchers, such as Roux et al. (1996), Graybeal (2006b), Ahlborn et al. (2008), Scheydt and Muller (2012), Thomas et al. (2012), and Alkaysi (2016), have conducted tests to investigate the permeability of UHPC. Graybeal (2006b) conducted permeability tests using ASTM C1202 (2017) for specimens subjected to four different curing regimes, and Table 2.17 summarizes the results. The cylindrical specimens used in these tests were 3 in. long and 4 in. diameter. The author also conducted tests in accordance with AASHTO T 259 (2002), *Standard Method of Test for Resistance of Concrete to Chloride Ion Penetration*, and AASHTO T 260 (2009), *Standard Method of Test for Sampling and Testing for Chloride Ion in Concrete and Concrete Raw*

Materials, with the same curing regimes. Figure 2.11 presents the results of the chloride ion content after ponding in 3 percent sodium chloride solution for 90 days on the concrete surface. The results indicate that a very small penetration of chloride ion occurred in the samples.

Table 2.17. Test Results of Rapid Chloride Ion Penetrability Based on ASTM C1202 (1997) (adapted from Graybeal 2006a).

Curing Regime	Details of Curing Regime	Chloride Ion Permeability
Steam Treated	194°F; 95 percent RH; for 48 hours; 24 hours after casting	Negligible at 28 days
Tempered Steam Treated	140°F; 95 percent RH for 48 hours; 24 hours after casting	Negligible at 28 days
		Negligible at 56 days
Delayed Steam Treated	194°F; 95 percent RH for 48 hours; 15 days after casting	Negligible at 56 days
Untreated	73°F; ambient humidity of laboratory conditions	Very Low at 28 days
		Negligible at 56 days

Note: The value of <100 coulombs is indicative of negligible chloride ion penetrability

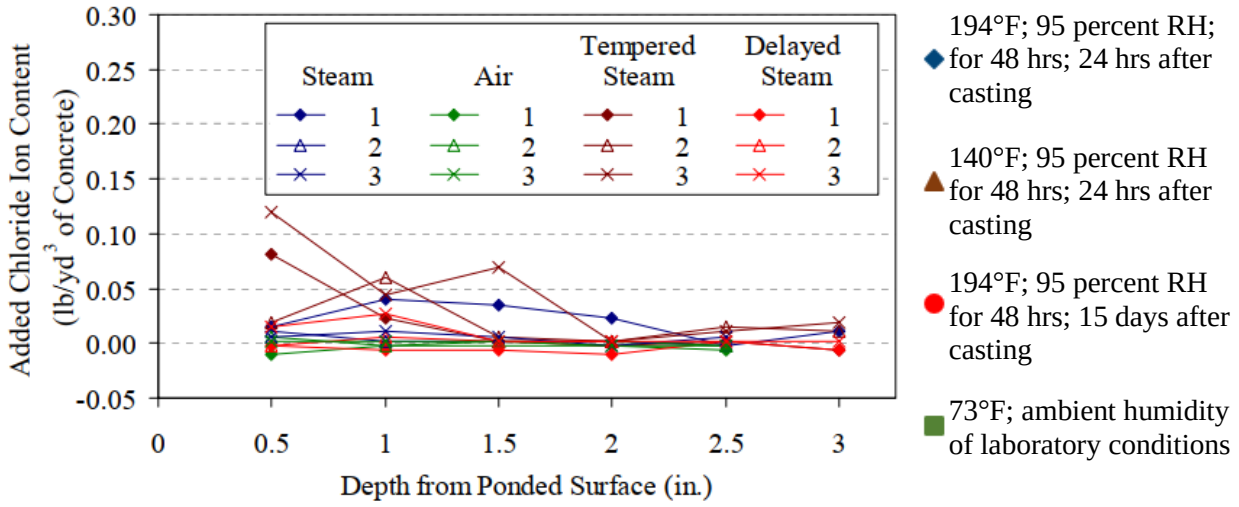

Figure 2.11. Results of Content of Chloride Ion after Ponding for 90 Days (adapted from Graybeal 2006a).

reported that the coefficient of permeability of UHPC for water is only 0.0005, which is much less than that of NSC (approximately 0.0015). Cheyrezy et al. (1995) employed mercury porosimetry, thermogravimetric analysis, and x-ray diffraction to study how the optimization of the granulometry and thermal treatment can influence the durability of the RPC. The authors reported less than 9 percent porosity in volume and a pore diameter ranging between 1.48×10^{-7} in. to 0.004 in. The porosity was also lowered by the application of pressure leading to the

removal of the entrapped air and excess water trapped in the matrix (Bonneau et al. 1997; Richard and Cheyrezy 1995; Roux et al. 1996).

Yazıcı et al. (2008) used scanning electron microscope technology to conclude that the high material cost of RPC due to high cement and silica fume content can be lowered by replacing some of the cement with fly ash or ground granulated blast-furnace slag (GGBFS) without much loss in the superior performance of the material. Yazıcı et al. (2008) concluded that the increase of silica fume content by approximately 10 percent by weight of cement showed an improved performance in terms of freeze-thaw resistance and chloride ion penetration resistance in SCC.

Alkaysi et al. (2016) and Alkaysi (2016) studied the impact of individual components of the UHPC mix on the durability. The authors investigated the effect of silica powder content and cement type. There was very low chloride ion penetration and high resistance to freeze-thaw. The authors concluded that the superior durability is largely due to the high density of the UHPC matrix. The authors also concluded that samples of mix with Portland Type I and GGBFS cement were the least permeable. The samples with white cement performed better that those of Portland Type V cements but were inferior to those samples made from Portland Type I and GGBFS cements. The authors reported that the best performance in terms of durability was with specimens containing 0 percent silica powder content, followed by specimens with 15 percent silica powder content; lower durability was observed for specimens with 25 percent silica powder. Therefore, in light of the comparatively high cost of the silica powder, the authors recommended that silica powder be completely avoided to improve the economy of the mix.

Ahlborn et al. (2008) conducted rapid chloride permeability tests for air-cured and thermal treated samples, and the results were less than 100 coulombs. Table 2.18 presents the values for the coefficient of chloride diffusion as a measure of chloride ion penetration compiled by various researchers and summarized by Russell et al. (2013) and Abbas et al. (2016). Roux et al. (1996) reported that the chloride diffusion coefficient of HPC is approximately 6×10^{-12} ft^2/s and of NSC is nearly 1.08×10^{-11} ft^2/s, both of which are much higher than UHPC's 2.15×10^{-13} ft^2/s.

Table 2.18. Coefficient of Chloride Diffusion.

Source	Condition	Coefficient of Chloride Diffusion, ft^2/s
Thomas et al. (2012)	At 28 days	1.40×10^{-12}
Piérard et al. (2012)	Non-steady state	2.15×10^{-12}
Scheydt and Muller (2012)	63 days	1.40×10^{-12}

Note: Steady state is when the rate of the total number of atoms passing a unit cross-sectional area perpendicular to a given direction is constant, while it is not constant for a non-steady state.

Vernet (2004) and Wang et al. (2014) stated that the oxygen permeability of UHPC (less than 1×10^{-18} ft^2) is much less than that of HPC and NSC. Andrade et al. (1996) reported no signs of penetration due to carbon dioxide after an exposure of 2 years. Moreover, Schmidt and Fehling (2005) also reported a relatively low carbonation depth of 0.06 in. after an exposure of 3 years, which is much less than HPC and NSC. Piérard et al. (2012) reported that after 1 year of exposure to 1 percent atmospheric carbon dioxide, the carbonation depth ranged from 0.006 in. to 0.008 in.

2.5.3 Porosity

As mentioned in the previous section, understanding the pore structure is very important when examining and assessing the durability of UHPC. Several research studies were undertaken to engineer the properties of UHPC such that the porosity and the pore radius distribution are minimized by opting for a dense mixture design and by using thermal treatments (Heinz and Ludwig 2004; Herold and Müller 2004). The UHPC mix design should consider physical durability against abrasion, freezing and thawing, precipitation, and chemical durability against ASR, sulphate, and chloride attacks (Mindess et al. 1981). Heinz and Ludwig (2004) studied the impact of heat treatment on the porosity of UHPC for the mixture proportions summarized in Table 2.19, and the results are plotted in Figure 2.12.

Table 2.19. Composition of CEM I 425 R-HS (adapted from Heinz and Ludwig 2004).

Duracrete products—Schwenk	SO_3	SC_3A	SO_3/Al_2O_3	Na_2O_e	GGBFS	Silica Fume (sf)	Water
	Percent Weight	Percent Weight	Mol. Ratio	Percent Weight	Percent Weight	sf/cement	*w*/*c*
CEM I 425 R-HS	2.7	1.9	0.93	0.73	–	0.25	0.22

Notes:
1. Quartz (grain size < 0.02 in.) may be added.
2. Superplasticizer on polycarboxylate-ether may be added to adjust the consistency.
3. GGBFS: Ground-granulated blast-furnace slag
4. - : Not available

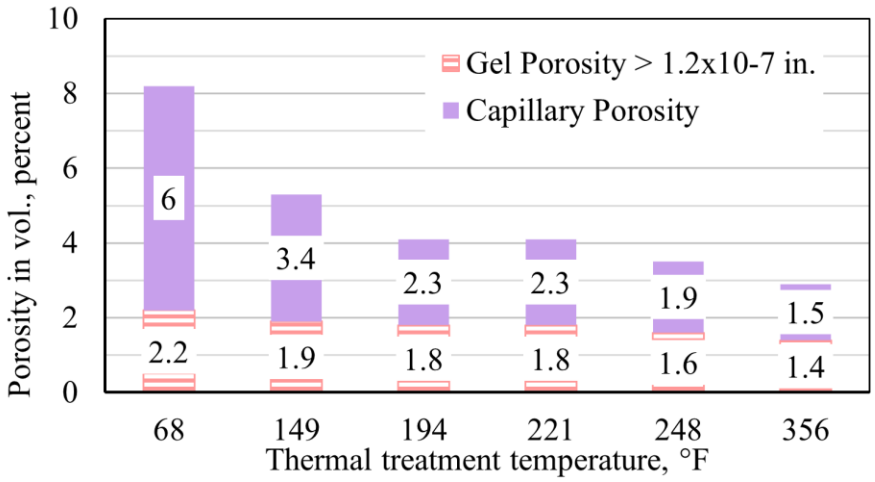

Figure 2.12. Effect of Thermal Treatment on Porosity Capillary and Gel Porosity of UHPC with CEM I 42,5 R-HS (adapted from Heinz and Ludwig 2004).

Table 2.20 summarizes several research studies that investigated the influence of the water/binder ratio and the curing process on the total porosity of the structure. Herold and Müller (2004) and Cwirzen (2007) showed that a decrease in the total porosity occurs when the specimens are subjected to heat treatment. Scheydt and Muller (2012) reported a similar effect of temperature on porosity and showed that specimens with steel fibers have more total porosity than specimens without the steel fibers for the same curing conditions.

Table 2.20. Effect of Water/Binder Ratio and Curing Process on Porosity (adapted from Abbas et al. 2006).

Source	Steel Fiber Content, *L* (in.) / *D* (in.)	*w/b*	Curing Regime	Total Porosity (percent)
Herold and Müller (2004)	2.5 percent by volume, 0.31 / 0.007	0.16	68°F and 93% RH	10.5
			194°F for 2 days	6.4
Cwirzen (2007)	None	0.17	Storage at 95% RH	5.8
			194°F for 4 days	1.1
Scheydt and Muller (2012)	12 lb/ft^3, 0.31 / 0.007	0.21	Water cured at 82.4°F	8.9
			194°F for 3 days	5.4
	None		Water cured at 82.4°F	10.9

Notes: *L* = Length of fiber (in.), *D* = Diameter of fiber (in.)

2.5.4 Freeze-Thaw Resistance

Freezing and thawing of concrete can be detrimental to the structure due to the mechanism of water expansion that leads to the development of internal stresses in the pores of the concrete. If the stresses are high enough, they may cause tensile rupture of concrete. Therefore, it is important to

study the freeze-thaw resistance of UHPC to assess its usage and application in cold climatic conditions.

2.5.4.1 State-of-the-Art

Jeroen et al. (2015) attributed the resistance of UHPC to freeze-thaw cycles to the dense matrix of the material. Yazıcı et al. (2008) concluded that a silica fume content of 10 percent by volume not only increased the compressive strength but also showed better performance in terms of resistance to freeze-thaw cycles. Bonneau et al. (2000) and Graybeal (2006b) reported that the low permeability and porosity of UHPC may be responsible for the better performance of UHPC when subjected to freeze-thaw cycles. Piérard et al. (2012) reported that no degradation was observed for UHPC samples having 20.3 to 23.2 ksi compressive strength after being subjected to 112 freeze-thaw cycles. Liu et al. (2009) and Shaheen and Shrive (2006) also reported that the change in length and weight of the tested UHPC specimens was insignificant after being subjected to 300 freeze-thaw cycles.

Graybeal (2006b) suggested that the resistance to freeze-thaw damage may be gauged by examining the air-void system. Graybeal (2006b) conducted tests to evaluate the effect of various parameters of the air-void system, such as voids of 2.0 to 7.6 in., specific surface of 250 to 405 in^2/in^3, and a spacing factor of 0.009 to 0.027 in. Acker and Behloul (2004) conducted tests on the commercially available UHPC mix and subjected the specimens to 400 cycles of freeze-thaw condition. The authors did not observe any deterioration of the samples.

2.5.4.2 State-of-the-Practice

2.5.4.2.1 ASTM Standard Tests

With suitable modifications from ASTM C1856 (2017), ASTM C666 (2015), *Standard Test Method for Resistance to Rapid Freezing and Thawing*, Procedure A can be used to test the freezing and thawing resistance of UHPC. The modification states that the test should be continued until the specimens are subjected to a minimum of 300 cycles or until the time the relative dynamic MOE falls to 90 percent of the initial modulus, depending on whichever limit occurs first.

2.5.4.2.2 AFGC (2013)

The AFGC (2013) described the study conducted by the University of Delft to assess the freeze-thaw resistance of UHPC specimens with reinforced steel fibers, without any fibers, and with synthetic fibers. The specimens were subjected to 56 cycles of freezing and thawing (+32°F to −32°F). The results indicate that UHPC resists freeze-thaw conditions well. The performance was consistently good despite the absence of fibers in the specimen. The performance of UHPC was observed to be better than that of CC. AFGC (2013) attributed the improved performance of UHPC to the low *w*/*c* that eliminates the presence of residual water, along with low water penetration and superior mechanical strength.

2.5.4.2.3 JSCE (2008)

The recommendations suggested that the freeze-thaw resistance can be verified on the basis of the JSCE (2007), *Standard Specifications for Concrete Structures—Materials and Construction.* JSCE (2008) stated that the reinforcing fibers may serve to bridge the cracks that are developed as a result of exposure to freezing and thawing. The Japanese standard also reported a negligible change in mass and the relative dynamic elastic modulus.

2.5.5 Resistance to Scaling

Graybeal (2006b) conducted tests on UHPC samples to study the resistance to scaling when subjected to deicing chemicals using ASTM C672 (2012), *Standard Test Method for Scaling Resistance of Concrete Surfaces Exposed to Deicing Chemicals.* The author conducted the tests using samples subjected to steam curing, tempered treatment, and air curing regimes. Graybeal (2006b) reported no signs of scaling after inspection of the ponded surface and that curing regimes did not influence the outcomes, although observable roughness existed in the texture after the tests were conducted. During testing, the joints of the slab specimens that were not sealed fully were exposed to extremely aggressive environmental conditions. However, despite the 70 plus 145 cycles of freezing and thawing in these conditions, very little damage occurred on the exposed surfaces. It was also observed that the fiber corrosion did not appear to infiltrate the slab, and no observable scaling, chipping, and/or spalling of the surface was found. Cwirzen et al. (2008) reported that heat treatment showed an increased scaling of the surface. The authors also reported

that steel fibers reduced the internal deterioration but increase the scaling damage on the surface of samples.

2.5.6 Resistance to Abrasion

The behavior of UHPC when subjected to abrasion is an important aspect to consider when developing a better understanding of the wearing and tearing mechanism of the material, especially when it is to be used for bridge superstructure applications.

2.5.6.1 ASTM Standard Tests

The abrasion resistance of concrete can be tested using ASTM C944 (2012), *Standard Test Method for Abrasion Resistance of Concrete or Mortar Surfaces by the Rotating-Cutter Method*. ASTM C1856 (2017) recommended that for UHPC the load should be doubled to 44 ± 0.4 lbf. Graybeal (2006b) conducted the test, as per ASTM C944 (2012), on UHPC cylinders of 6 in. diameter and 3 in. deep. Figure 2.13 shows the results of the test. Graybeal (2006b) reported that the air-cured specimens are susceptible to abrasion, while the steam-cured specimens indicate good resistance to abrasion. Liu et al. (2009) attributed the superior abrasion performance of UHPC to the less connected network between the pores.

2.5.6.1.1 AFGC (2013)

The recommendations described UHPFRC as a “structural and protective” component due to its performance when the material was tested for abrasion resistance. The French standard compared the high mechanical strength of UHPFRC to that of the wearing surfaces employed in concrete.

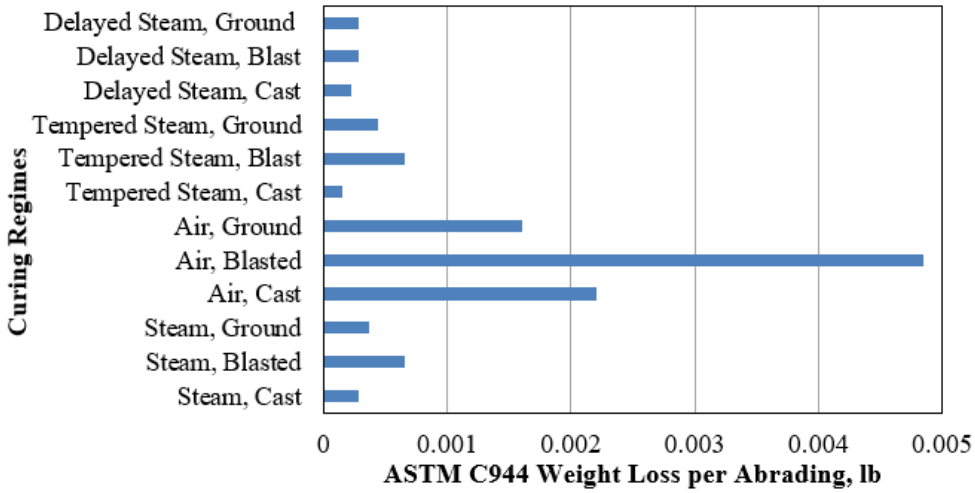

Figure 2.13. Results of Abrasion Resistance Test (Graybeal 2006a).

2.5.7 Resistance to Alkali-Silica Reactivity and Delayed Ettringite Formation

An ASR takes place due to the interaction of the alkaline cement paste with the amorphous reactive silica. This reaction causes the expansion of the aggregate by forming a viscous gel around it. This expansion leads to cracking and may lead to severe damage, including collapse of the structure in some cases. Due to the composition of UHPC, which is predominantly cementitious with silica fume, it is essential to check the vulnerability of UHPC to ASR.

2.5.7.1 ASTM Standard Tests

As demonstrated by Graybeal (2006b), with certain modifications, ASTM C1260 (2014), *Standard Test Method for Potential Alkali Reactivity of Aggregates (Mortar-Bar Method)*, can be used to quickly examine the resistance of UHPC to alkali-silica reactivity. Graybeal (2006b) also observed, based on the test results, very little expansion, most likely attributable to the high impermeability of UHPC that prevents the availability of free water that is essential for ASR to occur.

Möser et al. (2008) conducted research on the same subject and reported a maximum expansion of 0.02 percent due to ASR for pre-damaged and undamaged specimens of UHPC when tested after 600 days, which is less than half the threshold limit (0.04 percent). Haber et al. (2018) stated that UHPC is known as resistant to ASR, and the risk of DEF was not associated with UHPC. Heinz

and Ludwig (2004) evaluated the effect of heat treatment on DEF in UHPC and found that at a temperature of about 194°F, there was no damage due to DEF despite trace amounts of anhydrite.

2.5.7.2 AFGC (2013)

AFGC (2013) suggested both the compactness and dense matrix of UHPC is due to silica fumes, and the low permeability of UHPC to water may prevent the risk of DEF.

2.5.7.3 JSCE (2008)

JSCE (2008) noted that HPFRC structures are not likely to be damaged by alkali-aggregate reactions and recommended the use of the JSCE (2007) Section 6.4.7, *Verification for Resistance to Alkali Aggregate Reactions.*

2.5.8 Resilience under the Action of High Temperatures or Fire

The behavior of UHPC when it is exposed to high temperature may be of particular interest for applications such as nuclear reactor plant construction due to its enhanced mechanical behavior, especially long-term creep behavior.

2.5.8.1 State-of-the-Art

Pimienta et al. (2012) documented that the concrete is susceptible to spalling and damage under the action of elevated temperatures because of thermal expansion, change in its thermal characteristics, and mechanical strength. The authors compared the thermal behavior with the decay curves of Eurocode 2 (2004) for NSC and HPC. This comparison employed ISO 834-11 (2014), *Fire Resistance Tests,* thermal curves, and the *Increased Hydrocarbon (HC_{inc})* temperature curve. It was reported that the use of polypropylene fibers minimizes the spalling under high temperature. The authors also stated that the behavior of concrete under fire needs to be assessed thoroughly because it may lead to the collapse of integral structural members if exposed to elevated temperature.

Way and Wille (2012) attribute the relative susceptibility of UHPC structures under fire to the low porosity of the material, which leads to the entrapment of the vapor pressure. Aarup (2004), however, stated that the performance of UHPC when examined 1 week after the testing for fire

exposure was better than that of ordinary concrete. This behavior may be due to the high silica fume present in the mix and the extremely low content of calcium hydroxide, as reported by the authors.

Heinz et al. (2004) conducted thermal testing of 3.9 in. diameter cylinders and 4.7 by 9.4 in. columns. The 1-day-old specimens were subjected to 194°F after 1 day, and the thermal curves of DIN 4102-2 (1977), *Fire Behaviour of Building Materials and Building Components; Building Components; Definitions, Requirements and Tests*, of the German standard were used. The combination of 3.05 percent of steel fibers and 0.6 percent of polypropylene fibers (both by volume) is an optimal mix to minimize damage when exposure to fire is anticipated.

Behloul et al. (2002) studied a commercially available UHPC mix specifically tailored for fire resistance called Ductal-AF®. The dense microstructure of UHPC prevents the steam from escaping, thereby creating high pressure within the lattice of concrete. This results in spalling and damage. This problem was addressed by providing an optimum volume of synthetic fibers that would melt at elevated temperatures, therefore creating escape vents for the water vapor. The specimens designed using this principle were tested under ISO, and high fire resistance was observed.

2.5.8.2 State-of-the-Practice

2.5.8.2.1 AFGC (2013)

The recommendations suggested that most UHPFRC mixes that contain polypropylene fibers have resistance against spalling. Annex 15 is devoted to discussion of experimental testing on the exposure of UHPC to high temperatures and its impact on the thermal and mechanical properties. AFGC (2013) reported a decrease in the mechanical performance of the material similar to HPC. Table 2.21 summarizes the reduction in mechanical strength of UHPC when exposed to high temperatures. The code also suggested that the thermal diffusivity of UHPFRC and UHPC is similar to that obtained from Eurocode 2 (2004) and DTU—*Prediction Method for Calculating the Fire Behavior of Concrete Structures* (Kruppa 1988).

Table 2.21. Reduction in Strength due to Exposure to High Temperature (as per AFGC 2013).

Property	Percentage Drop in Mechanical Performance (Percent)	Temperature (°F)
Compressive Strength	10 to 50	1112
	80	1470
Tensile Strength	40	302
	55	1382
Post-Cracking Tensile Strength	50 to 80	1112

2.5.8.2.2 JSCE (2008)

JSCE (2008) indicated that the resistance of HPFRC is comparable to that of ordinary concrete because its major component is mortar—excluding the fibers. JSCE (2008) also suggested that the quick reduction in strength due to the melting of the fibers is also a cause of concern. Japanese guidelines recommend the use of the *Verification for Fire Resistance* in the *Standard Specifications for Concrete Structures—"Materials and Construction"* (JSCE 2007).

2.5.9 Durability Performance under Marine Exposure

UHPC is reported to show high durability when exposed to tidal conditions (20 ft), freeze-thaw cycles (100 cycles per year), and when immersed in sodium sulphate solution (500 days) (Piérard et al. 2012; Thomas et al. 2012). Thomas et al. (2012) reported that upon visual inspection conducted after 20 years, the prismatic specimens tested at the United States Army Corps of Engineers Long-Term Marine Exposure Station in Maine at Treat Island were found to be intact with sharp corners. Piérard et al. (2012) reported that despite the immersion in sodium sulphate solution, there was negligible deterioration to the prismatic specimens.

Voo et al. (2014) documented the experience of designing a UHPC jetty and its performance under the marine exposure. UHPC structures showed much better performance in terms of durability when subjected to marine exposure based on several chloride ion penetration experiments and as per the calculation based on the 2nd Fick's Law of Diffusion. The authors also advised that prestressing the structural members to avoid any cracking under service load conditions yields better durability.

2.6 APPLICATIONS OF UHPC

2.6.1 General

The application of UHPC around the world has led to some impressive concrete structures built in the 21st century. The first application of UHPC in the world was the Sherbrooke Footbridge in Canada. Known as the world's first RPC structure (Blais and Couture 1999), this bridge set the standard for initial UHPC applications around the world. After this project, several companies and research institutions developed more creative solutions that would incorporate UHPC as a strong, durable, and efficient material. The leading companies and the UHPC solutions they provide are Lafarge's Ductal® in North America and Europe, Eiffage and Sika's BSI/CERACEM® in Europe, and Dura Technology's Dura® in Malaysia. The following sections provide some examples of the broad variety of applications of UHPC both in bridges and other architectural projects.

2.6.2 UHPC Applications in Pedestrian Bridges

There have been several applications of UHPC for the construction of innovative pedestrian bridges. Table 2.22 summarizes the major footbridge applications discussed in this section.

Table 2.22. List of Pedestrian UHPC Bridge Applications.

Name of the Bridge	Place	Year	Span Length (ft)	Source
Sherbrooke Footbridge	Canada	1997	198	Blais and Couture (1999)
Seonyu Footbridge	Seoul, South Korea	2002	394	Rebentrost et al. (2008)
Sakata-Mirai Footbridge	Japan	2002	164	Rebentrost et al. (2008)
Akakura Onsen Yukemuri	Japan	2004	120	Tanaka et al. (2011)
Keio University Pedestrian Bridge	Japan	2005	37	Rebentrost et al. (2008)
Papatoetoe Pedestrian Bridge	New Zealand	2005	120	Resplendino and Toulemonde (2011)
Penrose Station Footbridge	New Zealand	2006	266	Rebentrost et al. (2008)
Hikita Footbridge	Japan	2007	574	Rebentrost et al. (2008)
Mikaneike Footbridge	Japan	2007	869	Musha et al. (2007)
Gaertnerplatzbridge	Germany	2007	426	Schmidt (2012)
Papakura Station Footbridge	New Zealand	2007	174	Rebentrost et al. (2008)
Glenmore/Legsby Pedestrian Bridge	Canada	2007	221	Perry and Seibert (2008)
Passerelle de Anges Footbridge	France	2009	198	Resplendino and Toutlemonde (2013b)

Figure 2.14 shows the first structure built using UHPC, the Sherbrooke Footbridge in Canada. The precast prestressed pedestrian bridge was completed in 1997 and consists of a lattice structure with six 33 ft precast segments that make up a total span of 198 ft. The bridge has a width of 11 ft, a 1.2 in. thick slab, and a total depth of 10 ft. To support the deck, a series of diagonal UHPC members enclosed in stainless steel tubes make up a truss system throughout the span of the bridge. At the bottom of the bridge are two beams with longitudinal prestressing that act as the base of the structure. This bridge was the first one to push the boundaries of a structure, with an unprecedented compressive strength of 29 ksi and no conventional steel reinforcement in its diagonal members (Blais and Couture 1999).

Figure 2.14. Sherbrooke Footbridge, Canada (Russell et al. 2013).

After the first UHPC structure was constructed, several studies were conducted to develop different beam shapes that would have the same mechanical properties but a better overall performance. This led to the design of a pie-shaped cross section. Figure 2.15 shows the first bridge that implemented this design, the Seonyu footbridge in Seoul, South Korea, also known as the Peace Footbridge. This bridge has a 394 ft long arch made up of six curved post-tensioned segments (Behloul and Lee 2003). It is a single-span bridge with an arch structure supporting its 1.2 in. thick RPC deck. The pi-shaped sections are 0.2 ft deep, the top flange is a ribbed slab with transverse reinforcement, and the webs are 6.3 in. (160 mm) thick. Besides having the mechanical

properties of UHPC, this design had the characteristic of only using half of the materials that a CC bridge would have required (Voo et al. 2014).

Figure 2.15. Seonyu Footbridge, Seoul, South Korea (Planete-tp 2008).

Japan also initiated the use of UHPC for bridges quite early in the era of this new class of bridges that aimed at greater structural capacity with intrinsic architecture. Figure 2.16 presents some of the UHPC footbridges in Japan. The Sakata-Mirai Footbridge (Figure 2.16(a)), built in October 2002 was the first bridge in Japan that used UHPC by Ductal® (Tanaka et al. 2010). This 164 ft long footbridge led to the shaping up of the *Guidelines for the Design and Construction of Ultra High Strength Fiber Reinforced Concrete—Draft* by the JSCE (2008).

Another footbridge that used UHPC is the 120 ft long Akakura Onsen Yukemuri Bridge (Figure 2.16(b)), completed in 2004 with a span-to-girder depth ratio of 40 (Tanaka et al. 2011). UHPFRC was cast in-situ into the Perfobond strips (PBS) that were employed to connect the top slab with the U-shaped girders.

Another pedestrian bridge in Japan that was completed in 2005 is the Keio University Pedestrian Bridge (Figure 2.16(c)) (Tanaka et al. 2011). This bridge is 37 ft long and consists of a slab of 9 in. thickness. The UHPFRC compressive strength recorded was 11 ksi.

The Hikita Footbridge (Figure 2.16(d)), completed in 2007, is another noteworthy bridge because it is one of the longest through-girder bridges to be composed of UHPFRC. This bridge is 212 ft long and 7 ft wide.

The Mikaneike Footbridge (Figure 2.16(e)), which was completed in 2017, is 266 ft long, 11 ft wide and has a span-to-girder depth ratio of 40. It has two 129 ft long continuous prestressed

concrete box girders. These girders were two of the first prestressed concrete girders cast using UHPFRC.

(a) Sakata-Mirai Footbridge

(b) Akakura Onsen Yukemuri Pedestrian Bridge

(c) Keio University Footbridge

(d) Hikita Footbridge

(e) Mikaneike Footbridge

Figure 2.16. UHPC Footbridges in Japan (Tanaka et al. 2011).

Schmidt (2012) described the first large-scale footbridge in Germany, the Gaertnerplatzbridge in Kassel. The structure is composed of a slender steel truss that supports the longitudinal girders and deck slabs of UHPC (Figure 2.17). Rebentrost et al. (2008) lists many of the footbridges made from Ductal® developed in New Zealand, most of them a result of the station redevelopment by the Auckland Regional Transport Network Ltd. The Papatoetoe Pedestrian Bridge used UHPC to reduce the weight of the structure and improved the earthquake survival chances; its slender sections also reduced the cost. The footbridge is 574 ft long, with 10 simply supported spans, each 66 ft in length. Figure 2.18 presents a span composed of UHPC being lifted for placement. Additional examples of such footbridges in Auckland, New Zealand, include one with a span length of 869 ft at Penrose Station and one at the Papakura Station that was completed in 2007.

Figure 2.17. Gaertnerplatzbridge in Kassel, Germany (Schmidt 2012).

Figure 2.18. Lifting of UHPC Spans with the Railing of Papatoetoe Footbridge, New Zealand (Rebentrost et al. 2008).

Figure 2.19(a) presents another footbridge application completed in Calgary, Canada, called the Glenmore/Legsby Pedestrian Bridge (Russell et al. 2013). This single-span 12 ft wide pedestrian bridge uses a 174 ft long Ductal® T-beam that is cantilevered over the UHPC abutments that are 328 ft apart. The beam is 3.6 ft deep and includes 42 post-tensioned strands of 0.6 in. diameter. One of the advantages to using UHPC on this project is more resistance to chlorine, which proves to be an advantage given the amount of salt used in the roads during the winter in Canada.

Figure 2.19(b) presents the Passerelle de Anges Footbridge in France, another bridge that pushed boundaries in 2008. This single-span 230 ft bridge is made up of two parallel bone-shaped beams that act as guard rail and a 1.2 in. thick slab. One of the most impressive characteristics of this bridge is its span-to-depth ratio of 38 (Toutlemonde and Resplendino 2011), with a total span of 221 ft and a beam height of 5.9 ft. The bridge is made up of 15 precast Ductal® segments assembled by prestressing tendons. The high 26 ksi compressive strength of the concrete provides a reduced weight but the lightness of the bridge requires dampers to control the vibration due to wind.

(a) Glenmore/Legsby Pedestrian Bridge, Calgary (Alberta), Canada (Russell et al. 2013)

(b) Passerelle de Anges Footbridge, France (Resplendino and Toutlemonde 2013b)

Figure 2.19. UHPC Pedestrian Bridge Applications in Canada and France.

2.6.3 UHPC Applications in Highway Bridges

2.6.3.1 Overview

Government transportation and highway departments around the world have studied the performance of UHPC to gauge the effectiveness of its higher load demand in public road bridge design. Table 2.23 lists the highway bridge applications.

Table 2.23. List of Highway UHPC Bridge Applications.

Name of the Bridge	Place	Year	Span Length (ft)	Source
Shepherds Creek Road Bridge	Canada	2005	49	Rebentrost et al. (2008)
n°34 Overpass (PS34)	A51 motorway, France	2005	156	Resplendino (2008)
Horikoshi C-Ramp Bridge	Kita Kyushu Junction, Japan	2005	54	Resplendino (2008)
Bridge of St. Pierre La Cour	France	2005	62	Resplendino (2008)
Pinel Bridge	France	2007	89	de Matteis et al. (2008)
Jakway Park Bridge	Buchanan County, Iowa	2008	115	Keierleber et al. (2010)
Route 21 Bridge Canandaigua Outlet	New York	2009	87.42	Shutt (2009)
Batu 6 Bridge	Malaysia	2015	328	Voo et al. (2014)
Kampung Baharu-Kampung Teluk Bridge	Malaysia	2017	138 (10 spans)	Voo et al. (2017)

Table 2.24. Other Bridge Applications of UHPC.

Name of the Bridge	Place	Details	Year	Maximum Span Length (ft)	Source
Franklin Avenue Bridge	Minnesota	Rehabilitation	2016	400	Graybeal (2017)
Chillon Viaducts	Switzerland	Overlays	2014	341	Brühwiler et al. (2015)

2.6.3.2 Shepherds Creek Road Bridge

Figure 2.20 presents the Shepherds Creek Road Bridge in New South Wales, Australia, that was built in 2005 using Ductal®. Rebentrost et al. (2008) documented the details of the bridge. The bridge is 49 ft long with a 16-degree skew. The Road Traffic Authority tested the bridge at the beginning and end of a 1-year period, after which the bridge was approved for use.

Figure 2.20. Shepherds Creek Road Bridge, Australia (Rebentrost et al. 2008).

2.6.3.3 n°34 Overpass (PS34)

The n°34 Overpass (PS34) on the A51 motorway in France was developed using Benton Composite Vicat (BCV®) by Campenon Bernard Regions (Vinci group) in 2005. Resplendino (2008) reported that the use of UHPFRC led to an economic material consumption because only 2825 cyd of UHPFRC was required as opposed to 4234 cyd of CC.

2.6.3.4 Horikoshi C-ramp Bridge

The Horikoshi C-ramp Bridge at the Kita Kyushu Junction, Japan, is 54 ft long (Tanaka et al. 2011) and was completed in 2005. This bridge is noteworthy because of the reduction of weight by about 30 percent when compared to a conventional design.

2.6.3.5 Bridge of St. Pierre La Cour

Another example of the application of UHPFRC in highway bridges is that of the Bridge of St. Pierre La Cour, France. Resplendino (2008) reported that this 62 ft long, 43 ft wide bridge is made of Ductal®. Investigations resulting from this application indicate high durability of the structure.

2.6.3.6 Pinel Bridge

Figure 2.21 shows one of the most innovative bridges constructed in the past 2 decades—the Pinel Bridge in France. It was built in 2007 using 17 prestressed UHPC inverted T-beams having a compressive strength of 24 ksi and an NSC deck slab. This shallow single-span bridge has a total length of 89 ft, a width of 46 ft, and a depth of 24 in. (Ngo 2016; Thibaux 2008). One of the most impressive characteristics about this bridge is that the span-to-depth ratio is 43.5, while most bridges have a ratio ranging from 20 to 30.

Figure 2.21. Pinel Bridge, France (Thibaux 2008).

2.6.3.7 Jakway Park Bridge

The first UHPC pi-girder bridge built in the United States was the Jakway Park Bridge in Buchanan County, Iowa, completed in 2008 and shown in Figure 2.22(a). The 25 ft wide bridge has three 51 ft long girders made of Ductal® UHPC with a 21.5 ksi compressive strength (Keierleber 2008). The girders are connected by longitudinal joints that consist of a shear key with dowel bars. Figure 2.22(b) shows the cross section of the girder, which is 2.46 ft deep and can contain a maximum of 16 prestressing strands. This pi-girder was developed by the FHWA and MIT to optimize the UHPC mix and take advantage of having the full depth deck as part of the girder unit. The UHPC pi-girder bridge does not require a supplemental reinforced concrete deck and can span up to 98 ft (Graybeal 2009).

(a) Elevation view

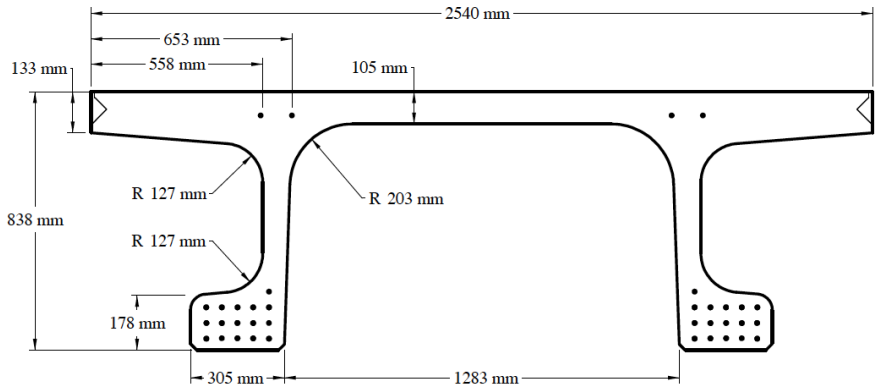

(b) Pi-girder cross-sectional view

Figure 2.22. Jakway Park Bridge, Iowa (Graybeal 2009).

2.6.3.8 Batu 6 Bridge

One of the longest-spanning UHPC bridges was built in 2013 in Malaysia. Figure 2.23(a) shows the single-lane Batu 6 Bridge, which is 328 ft long and consists of a single-span post-tensioned segmental box unit made of UHPC. At the time of construction, this was the longest single-span road bridge in which the structure is only composed of UHPC (Voo et al. 2014). The bridge consists of 40 segments, with 36 standard intermediate box segments and four anchorage segments containing post-tensioning anchorages. The geometric properties of the cross section are given in Figure 2.23(b). The Batu 6 bridge was designed and constructed without any shear reinforcement in the webs due to the high compressive and tensile strength of UHPC. The downward deflection at 28 days was only 0.24 in. at the midspan, and the 28-day compressive strength was 23.5 ksi (Voo et al. 2014).

(a) Side elevation

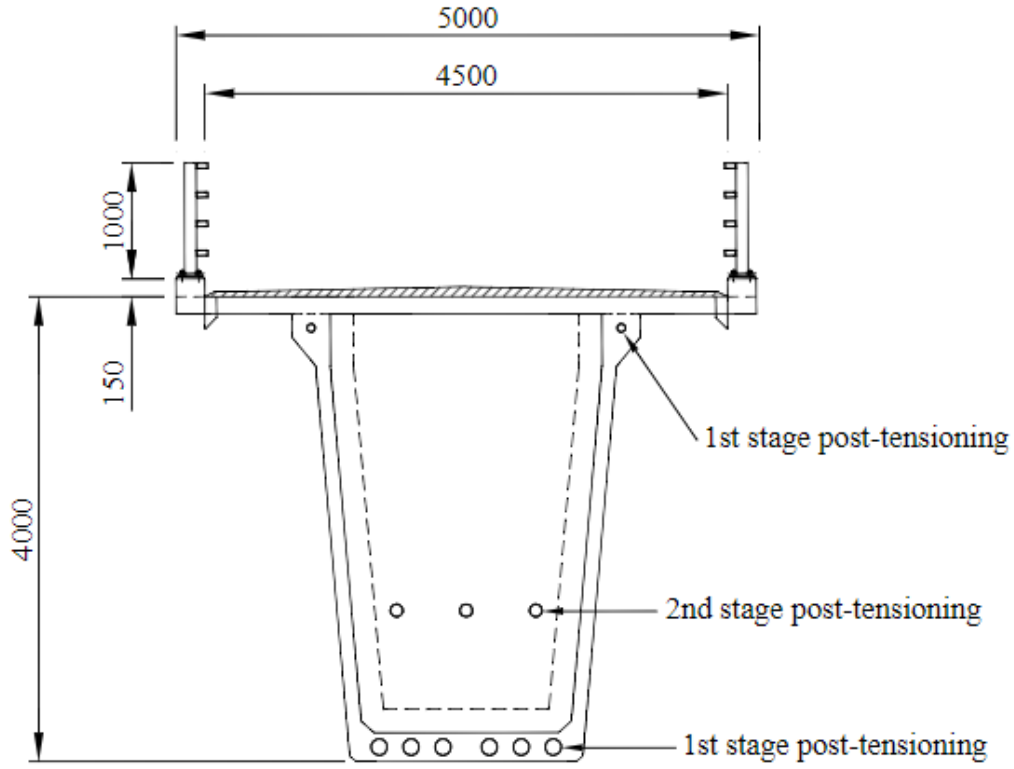

(b) Cross-sectional view of Batu 6 box girder

Figure 2.23. Batu 6 Bridge, Malaysia (Voo et al. 2014).

2.6.3.9 Kampung Baharu-Kampung Teluk Bridge

Figure 2.24(a) shows the world's longest (as of 2017) UHPC precast-prestressed segmental bridge. Found in Malaysia, the 1378 ft long Kampung Baharu-Kampung Teluk Bridge has 10 138 ft long spans. Each span has two segmental U-girders with six precast segments that are post-tensioned on site. The 28-day compressive strength of the girder concrete was 22 ksi (Voo et al. 2017). The cross-sectional details of the bridge are provided in Figure 2.24(b). No shear reinforcement was used in the 4.9 in. thick webs. The only shear reinforcement was included in the anchorage zones and in the connections with the slab.

(a) Side elevation

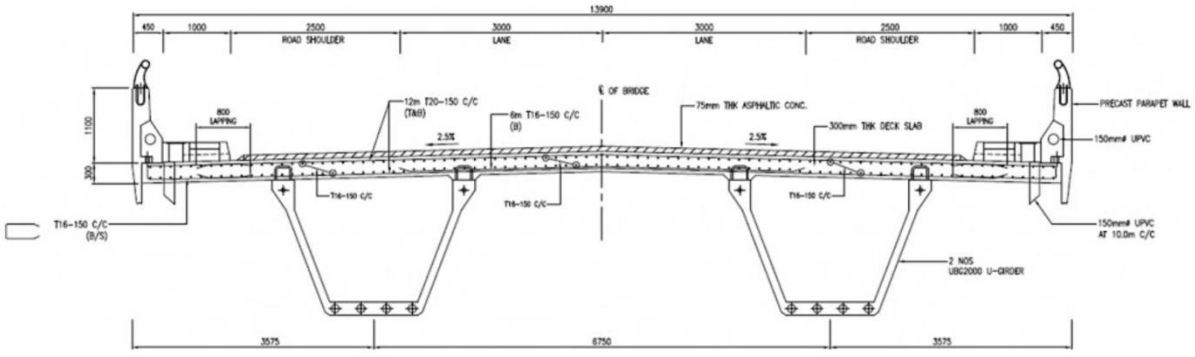

(b) Cross-sectional view of girders

Figure 2.24. Kampung Baharu-Kampung Teluk Bridge, Malaysia (Voo et al. 2017).

2.6.4 Additional UHPC Bridge Applications

Another way to use UHPC in bridge design is to use NSC girders but integrate UHPC as a closure pour material. An example of this design is the State Route 31 Bridge over Canandaigua Outlet, in Lyons, New York. This single-span bridge was completed in 2009 and consists of eight prestressed deck bulb tee girders that are 85 ft long each. Figure 2.25 shows the connection between the girders—a diamond-shaped, female-female shear key 6 in. wide and an epoxy-coated rebar to provide greater strength. The material was mixed on-site in a mortar mixer provided by Ductal® and was then poured into the joints. The compressive strength was 20 ksi after 28 days. This technique has been implemented in several other projects in New York state because it increases the strength of the bridge by providing a better bond development length.

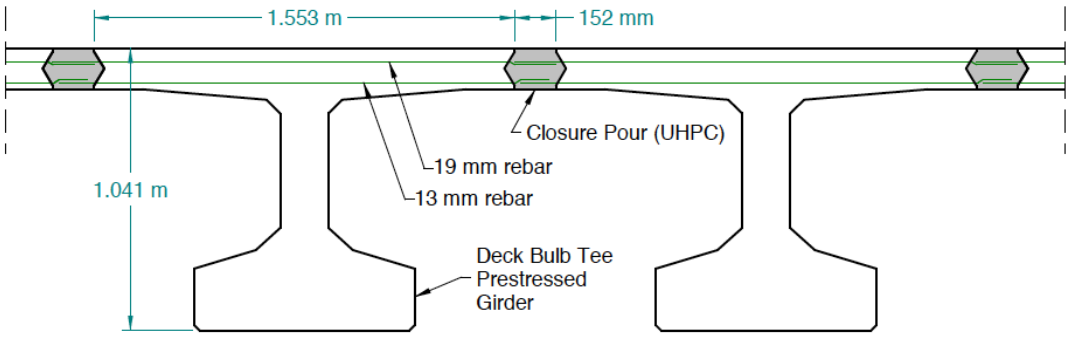

Figure 2.25. Cross-Sectional View of State Route 31 Bridge, Lyons, New York (Graybeal 2009).

Another application of UHPC in roadway bridges includes using anchor plates for retaining walls, retrofitting bridge piers for higher shock and abrasion resistance, and rehabilitating bridge decks or expansion joints that have deteriorated over time. An example of one such bridge rehabilitation that has been done is the Franklin Avenue Bridge in Minneapolis, Minnesota. The project consisted of re-decking the bridge with prefabricated elements and joining them with UHPC in the field. Other practices include replacing leaking joints with a field-cast UHPC link that provides a strong seal in the joint (Graybeal 2017).

The use of UHPFRC overlays for the strengthening of the Chillon Viaducts' deck slabs is another important application of UHPFRC. Figure 2.26 shows the elevation of the Chillon Viaducts. Brühwiler et al. (2015) reported that this structure of extremely historic significance in Switzerland

(total length of 6956 ft) was under severe distress due to alkali-aggregate reaction (AAR). To prevent the deterioration of the compressive strength of the concrete, the structure was rehabilitated using UHPFRC overlays in areas of severe exposure to de-icing salts, marine environment, and high impact loading.

Figure 2.26. Chillon Viaduct, Switzerland (Brühwiler et al. 2015).

2.6.5 Additional Applications of UHPC

The characteristics of UHPC provide such high structural performance that the material has been used for many attractive structural applications besides bridges. These include building elements, façade elements, canopies, and other innovative structures. Some of the architectural applications include the Kyoto Clock Tower in Japan, the Millau Viaduct toll gates in France, the canopies of the Shawnessy LRT Station in Canada, and the RATP Bus Center's textured wall panels in France. Figure 2.27 presents some of the striking applications of UHPC. Stoeux et al. (2011) commented that the perforated panels may even qualify to be a lattice designed to structurally influence the building due to the high mechanical strength of the material used, such as the UHPFRC, especially when the voids are more than 50 percent. One such example of this concept is the Hypergreen Tower's perforated panels.

Two of the most recent applications include the roof of the Enrico Navarra Gallery and the building envelope of the Jean Bouin Stadium. The roof of the gallery consists of an ultra-thin structure that behaves like a cantilever over 26 ft. It provides an alternative to having a metallic frame or a heavy, classical concrete-reinforced roof while still providing a strong element with minimal deflection. Last, the reconstruction of the Jean Bouin Stadium included a building envelope entirely made of UHPC (Toutlemonde and Resplendino 2011). This innovative solution provides bearing support, protection for the audience against rain, and a great aesthetic appeal to the structure.

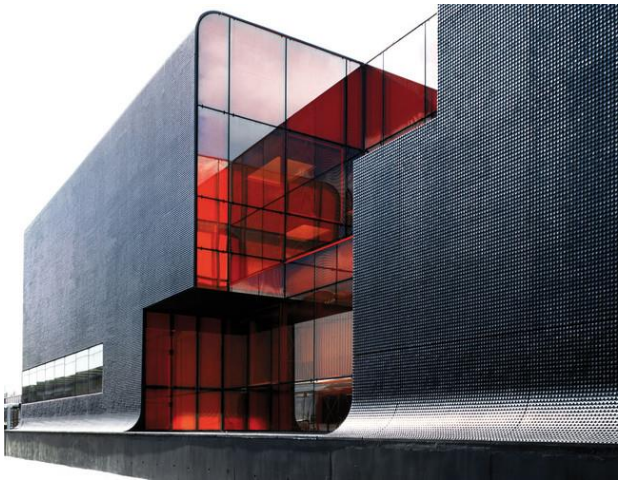

(a) RATP Bus Center, France (Batoz and Behloul 2011)

(b) Perforated Panels of Hypergreen Tower (Stoeux et al. 2011)

(c) Enrico Navarra Gallery Roof, France (LafargeHolcim 2016)

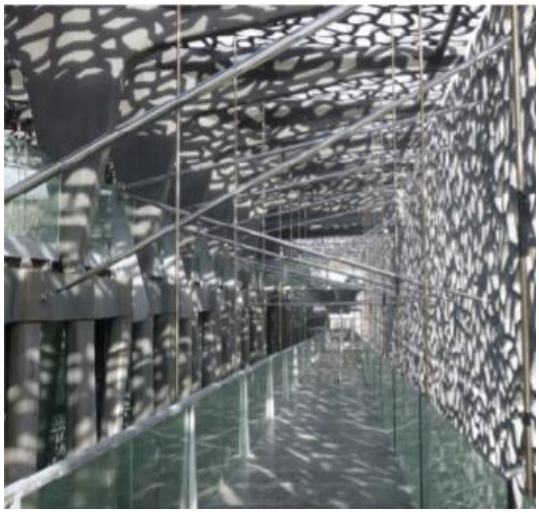

(d) Jean Bouin Stadium, France (Resplendino and Toutlemonde 2013b)

Figure 2.27. Architectural UHPC Applications.

2.7 SUMMARY

UHPC is an advanced concrete with superior mechanical and durability properties. ACI 239R-18 (2018) defined UHPC as a concrete having a minimum compressive strength of 22 ksi with specified durability and tensile ductility and toughness. PCI defined PCI-UHPC with the following minimum properties: 8–11 in. flow spread, compressive strength greater than 10 ksi at prestress release and 18 ksi at service, flexure strength with 1.5 ksi for first crack, and 2.0 ksi for peak

strength (eConstruct 2020). The key principles of a UHPC mixture are high packing density, low *w*/*c*, a filler effect of SCMs, and a crack bridging effect by steel fibers (Berry et al. 2017; Richard and Cheyrezy 1995; Russell et al. 2013; Wille and Boisvert-Cotulio 2015). The constituent materials of UHPC are cement and silica fume as a binder, SCMs and sand as a filler, HRWR, and steel fibers (Russell et al. 2013).

Many researchers have studied the hardened properties of UHPC. According to Graybeal (2006b), the compressive strength of UHPC achieves 14–21 ksi without heat treatment and 21–32 ksi with heat treatment. Gu et al. (2015) noted that the MOE of UHPC is higher than NSC due to the dense matrix of UHPC. The MOE of proprietary UHPC was reported to range from 8000–9000 ksi (Ahlborn et al. 2008). The post-cracking tensile strength of proprietary UHPC ranges from 0.73–1.8 ksi (El-Helou et al. 2022; Riding et al. 2019). The peak flexure strength of UHPC ranges from 2.4–3.6 ksi (eConstruct 2020), which includes nonproprietary UHPC. The range of the creep coefficient for proprietary UHPC is 0.70–1.17 and 1.37–2.47 when loading at 40 and 65 percent of the test age compressive strength, respectively (Haber et al. 2018). The total shrinkage range of proprietary UHPC is 600–1200 microstrain. However, researchers reported that shrinkage of UHPC is negligible after steam curing (Acker and Behloul 2004).

Several research studies show high durability of UHPC due to high packing density. The highly dense microstructure increases the service life span of the UHPC structures due to increased durability. Many researchers have focused on determining the permeability and porosity of UHPC to various substances because the crack formation, pore structure, and other physical and chemical deteriorations of the material are influenced by the infiltration of harmful substances (Alkaysi 2016; Thomas et al. 2012). In addition, UHPC has high resistance to freeze-thaw, scaling, and abrasion. Test results showed that there was no degradation of UHPC from freeze-thaw, scaling, and abrasion (Cwirzen et al. 2008; Graybeal 2006b; Jeroen et al. 2015).

Since the first UHPC pedestrian bridge (Sherbrooke Footbridge, built in 1997) was built in Canada, many countries have built UHPC bridges. The first UHPC bridge built in the United States was the Jakway Park Bridge in Buchanan County, Iowa, completed in 2008. The pi-shaped girders were made of Ductal® UHPC with a 21.5 ksi compressive strength. Recently, UHPC is being more commonly used for overlays (Haber et al. 2017; Khayat and Valipour 2014), bridge girders

(eConstruct 2020; Ozyildirim 2011; Tadros and Morcous 2009; Weldon et al. 2010), and rehabilitation of bridges (El-Tawil et al. 2018; Foden and McDonagh 2016).

3 TEST METHODS

3.1 INTRODUCTION

This chapter describes test methods to evaluate fresh and hardened properties and durability of UHPC. The UHPC mixtures developed in this project were evaluated by the test methods discussed in this chapter. The tests for fresh properties discussed in Section 3.2 include the flow table test (ASTM C1437 2015), time of set (ASTM C191 2018), and density (unit weight) and air content (ASTM C138 2015). Hardened properties were evaluated by compressive strength (ASTM C39 2016), MOE and Poisson's ratio (ASTM C469 2014), uniaxial tensile strength (AASHTO T 397 Draft AASHTO 2022), modulus of rupture (ASTM C1609 2019), shrinkage (ASTM C157 2017), and creep in compression (ASTM C512 2015) in Section 3.3. The test methods for durability discussed in Section 3.4 are rapid chloride ion penetration (ASTM C1202 2017), bulk resistivity (ASTM C1760 2021), surface resistivity(AASHTO T 358 2017), freeze-thaw resistance (ASTM C666 2015), scaling resistance (ASTM C672 2012), abrasion resistance (ASTM C944 2012), and ASR (Mukhopadhyay et al. 2019). ASTM test methods are modified for UHPC applications according to ASTM C1856 (2017), *Standard Practice for Fabricating and Testing Specimens of Ultra-High-Performance Concrete*, and these adjustments are described for each test.

3.2 TEST METHODS FOR FRESH PROPERTIES

This section describes the test methods for fresh properties. Fresh properties are a significant indicator for the quality of UHPC mixtures. This section describes testing procedures and the modifications of the testing methods used for NSC.

3.2.1 Flow Table Test

The standardized test method for workability of UHPC is the flow table test, which measures a spread value in accordance with ASTM C1437 (2015), *Standard Test Method for Flow of Hydraulic Cement Mortar*, and modifications for UHPC by ASTM C1856 (2017). The modifications provided in ASTM C1856 (2017) are that the static diameter is measured without dropping the table, and tamping is not allowed. Figure 3.1 shows the flow table test apparatus and a static flow spread.

(a) Apparatus

(b) Static flow spread

Figure 3.1. Flow Table Test by Modified ASTM C1437 (2015).

The apparatus must follow ASTM C230 (2014). The testing procedure is described as follows:

1. Fill the mold in a single layer with the fresh UHPC.
2. Do not tamp the UHPC and do not drop the table.
3. After lifting the mold, wait 2 minutes ± 5 seconds.
4. Measure the diameters of the UHPC along the lines of maximum and minimum diameters.
5. Average of the two diameters is the spread value.

3.2.2 Test for Time of Set

Time of set is measured in accordance with ASTM C191 (2018), *Test Methods for Time of Setting of Hydraulic Cement by Vicat Needle*, and modifications for UHPC by ASTM C1856 (2017). ASTM C1856 (2017) does not allow consolidation of UHPC in a conical ring. The initial set time is the time elapsed after the addition of water to the cement during the mixing operation until the needle penetrates the UHPC sample a distance of 25 mm (1 in.). The time elapsed until no indentation mark can be seen is the final set time. Figure 3.2 shows the test set-up for the setting time with the apparatus as per ASTM C191 (2018). The testing procedure is as follows:

1. Prepare mix materials at 73°F ± 6°F and mixing water at 73°F ± 4°F.
2. Fill the conical ring without tamping.

3. Place the specimen in the moist room for 30 minutes after casting.
4. Fix the needle on the top surface of the UHPC and release the needle quickly.
5. Allow the needle to settle for 30 seconds and take the reading.
6. Repeat Steps 4 and 5 every 15 minutes (10 minutes for Type III cement).
7. Determine initial and final setting times as per the definition.
8. Initial setting time is calculated using Equation (3.1).

$$T_i = \left(\left(\frac{(H-E)}{(C-D)} \right) \times (C - 25) \right) + E \tag{3.1}$$

where:

E = Time in minutes of last penetration greater than 25 mm (1 in.)

H = Time in minutes of first penetration less than 25 mm (1 in.)

C = Penetration reading at time E

D = Penetration reading at time H

T_i = Initial setting time, minutes

Figure 3.2. Time of Setting in Accordance with Modified ASTM C191 (2018).

3.2.3 Test for Density and Air Content

Density and air content is measured in accordance with ASTM C138 (2015), *Standard Test Method for Density (Unit Weight), Yield, and Air Content (Gravimetric) of Concrete*, and modifications for UHPC by ASTM C1856 (2017). The apparatus includes a scale with 0.1 lb accuracy, a cylindrical container, strike-off plate, and mallet. For UHPC, tamping using a tamping rod is not applied. The testing procedure steps are as follows:

1. Prepare mix materials.
2. Weigh the cylindrical container.
3. Fill the cylindrical container.
4. Do not use vibrating or tamping (modification for UHPC application).
5. Strike off the top surface.
6. Clean all excess concrete from the exterior of the cylinder.
7. Weigh the concrete in the container.

8. Calculate density using Equation (3.2).
9. Calculate air (gravimetric) using Equation (3.3).

$$D = \frac{(M_c - M_m)}{V} \tag{3.2}$$

$$A = \frac{(T - D)}{T} \times 100 \tag{3.3}$$

where:

M_m = Weight of an empty cylindrical container, lb

M_c = Weight of a concrete filled cylindrical container, lb

D = Measured density, lb/ft^3

V = Volume of a cylindrical container, ft^3

A = Gravimetric air content, percent

T = Theoretical density, lb/ft^3

3.3 TEST METHODS FOR HARDENED PROPERTIES

This section describes the test methods for hardened properties, including short-term and long-term properties. The short-term hardened properties include compressive strength, uniaxial tensile strength, MOE, Poisson's ratio, and modulus of rupture. The long-term hardened properties are creep and shrinkage.

3.3.1 Compression Test

The compression test for UHPC must comply with ASTM C39 (2016), *Standard Test Method for Compressive Strength of Cylindrical Concrete Specimens*, and modifications for UHPC by ASTM C1856 (2017). ASTM C1856 (2017) recommends a 3 in. diameter and 6 in. height cylinder with a 145 psi/s loading rate for compression strength testing of UHPC. ASTM C1856 (2017) recommends end preparation of a UHPC cylinder for perpendicularity of less than 0.5 degrees. Even though 4 in. cubes are not standardized specimens for compression testing of UHPC, cube specimens have also been used for compression testing at the precast plant due to unavailability of an end grinder. Graybeal and Davis (2008) reported that the compression test results from cube specimens are interchangeable with the cylinder specimens. In addition, capping compounds and neoprene pads are not allowed because capping compounds or pads increase the measured

compressive strength due to a confinement effect (Pistilli and Willems 1993). Therefore, both ends of a specimen are ground before testing (Figure 3.3).

(a) End grinder *(b) End ground cylinders* *(c) Compression test*

Figure 3.3. Compression Test in Accordance with Modified ASTM C39 (2016).

Immediately after casting the UHPC samples, the specimens are covered by a plastic cap and cured in a humidity room with RH 95 percent at 68°F for the first 24 hours and demolded at 24 hours ± 30 minutes. After demolding, samples are placed in the same curing room before testing. Prior to compression testing, the cylinders are end ground. Even though there is no standardized grinding method for cylinders, all specimens were ground following the steps below:

1. Grind both top and bottom surfaces for 225 seconds each.
2. If unground surface remains after grinding, grind for an additional 225 seconds.
3. Clean the ground and side surfaces.
4. After completing cylinder grinding, check flatness.
5. Wipe water from the surfaces of cylinders.

3.3.2 Modulus of Elasticity and Poisson's Ratio Test

The MOE of UHPC in compression is measured as per ASTM C469 (2014), *Standard Test Method for Static Modulus of Elasticity and Poisson's Ratio of Concrete in Compression*, with modifications for UHPC prescribed in ASTM C1856 (2017). The test for UHPC is conducted using 3 × 6 in. cylinders with ends ground flat in a cylinder end grinder. In addition, ASTM C1856 (2017) recommends the use of accurate strain measuring sensors such as LVDTs for higher accuracy and a load rate of 145 psi/s. Figure 3.4 shows the compressometer-extensometer with linear strain conversion transducers (LSCTs). The specimens are loaded at up to 40 percent of the peak compressive strength measured prior to the MOE test. The test is conducted in three cycles, and the MOE is computed as the ratio of the difference of stresses and difference of strains measured at the stage of 40 percent of the peak compressive strength load and when 50 με is attained longitudinally.

The Poisson's ratio is calculated based on the transverse strain measured from the LSCT at the mid-height of the cylinder and is taken as the ratio of the difference of the transverse strains and longitudinal strains occurring when 40 percent of the peak load is applied and when 50 με is attained longitudinally.

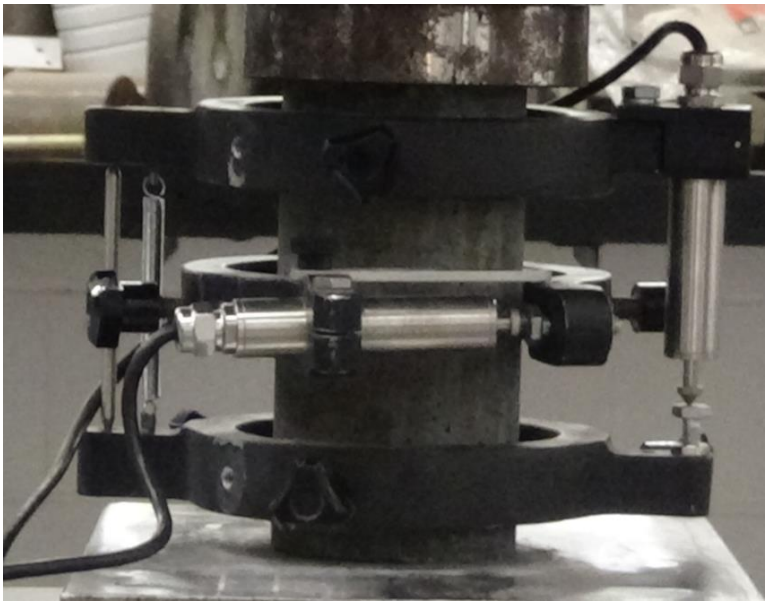

Figure 3.4. Test Setup for MOE of UHPC.

Prior to testing, the cylinders are ground following the same steps as mentioned in Section 3.3.1. The test procedure can be summarized in the following steps:

1. Grind both top and bottom cylinder surfaces to get a flat surface on each end.
2. Mount the compressometer-extensometer with two LSCTs on the specimen at mid-height and set the LSCTs to zero.
3. Load the specimen in compression for three cycles at a rate of 145 ± 7 psi/s up to 40 percent of the peak compressive strength of the companion specimens.
4. Use the second and third cycle to compute the average MOE and Poisson's ratio under compression based on Equations (3.4) and (3.5).

$$E = \frac{(S_2 - S_1)}{(\varepsilon_2 - 0.000050)} \tag{3.4}$$

where:

E = MOE computed to the nearest 50 ksi, ksi

S_2 = Stress at 40 percent ultimate load, ksi

S_1 = Stress when the longitudinal strain ε_1 = 0.000050 is attained, ksi

ε_2 = Longitudinal strain when stress is S_2

$$\mu = \frac{(\varepsilon_{t2} - \varepsilon_{t1})}{(\varepsilon_2 - 0.000050)} \tag{3.5}$$

where:

ε_{t2} = Strain measured at stress S_2 at mid-height of the specimen in the transverse direction

ε_{t1} = Strain measured at stress S_1 at mid-height of the specimen in the transverse direction

3.3.3 Direct Uniaxial Tension Test

At the time of the material-level testing phase of this research project, the uniaxial tensile strength of UHPC was measured using the direct tension test with 2 × 2 × 17 in. prisms recommended by Graybeal and Baby (2019). The test procedure is consistent with the most recent draft procedure submitted by FHWA to AASHTO for standardization of the direct tension test for UHPC—

AASHTO T 397 Draft (AASHTO 2022), *Standard Method of Test for Uniaxial Tensile Response of Ultra-High Performance Concrete.*

The specimens should be cast using high-density polyethylene molds with the UHPC poured from one end until the prism mold is completely full. The prisms are tapped to remove the entrapped air. The top surface is finished with a screed and covered with a plastic sheet to prevent moisture loss. Four aluminum grip plates are attached with epoxy to the top and bottom of the specimen to prevent crushing of the specimen where it will be gripped during the test. The aluminum plates are 6.25 in. long, 2 in. wide, and 0.19 in. thick. The plates gradually taper over a length of 2 in. from one end to ensure gradual transfer of force during the test (Figure 3.5**)**. The specimens should be cured at 95 percent RH at 68°F, as per ASTM C511 (2019).

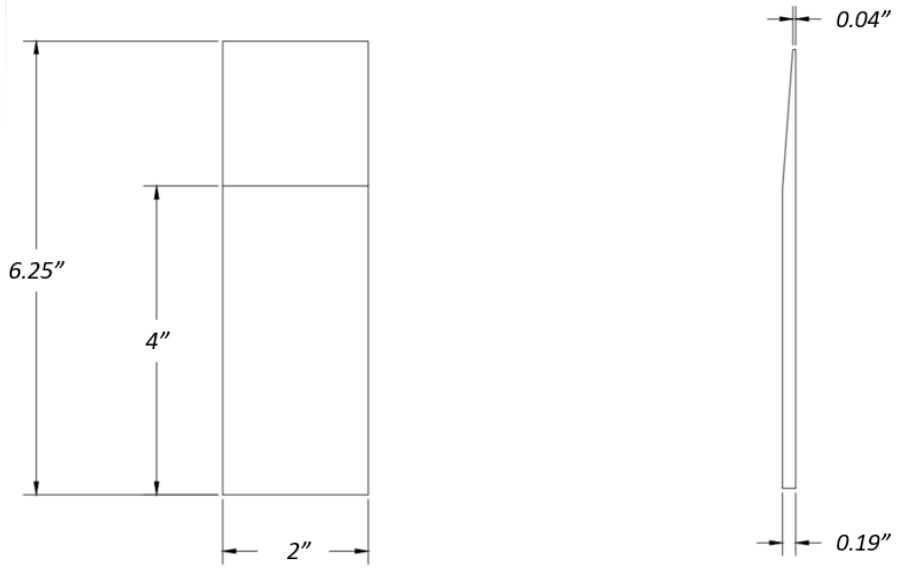

(a) Plan view *(b) Elevation view*

Figure 3.5. Grip Plates for Uniaxial Tension Test.

Figure 3.6(a) shows the uniaxial tensile test setup in the laboratory. Based on the stress-strain response and the type of cracking that occurs, the specimen is recommended to be categorized into one of three major categories, including strain hardening, strain softening, and least resistance to post-cracking. Depending on the observation of distress in the specimens and the location of the cracks, as shown in Figure 3.6(b), the specimens are further classified.

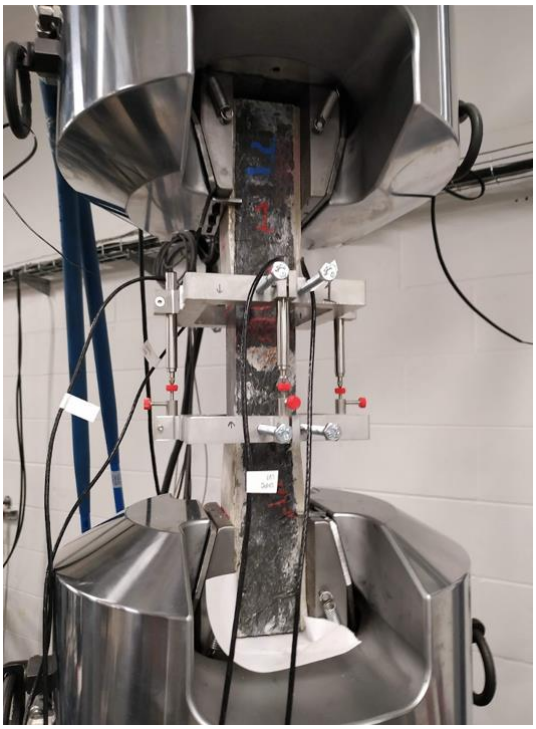

(a) Uniaxial Tensile Test Setup

(b) Tested specimens with crack at the grips, within the gage length, and at bottom mounting screw

Figure 3.6. Uniaxial Tensile Strength Test for UHPC.

The direct tension testing procedure is as follows:

1. Prepare the specimens by gluing the specimen on opposite ends formed by the mold at top and bottom.
2. Mount the extensometer with four LVDTs connected to the data acquisition system.
3. Place the specimen within the grips at the top, then the bottom, and hold in place using the prescribed lateral pressure of 40.4 kips in force control.
4. After adjusting the LVDTs to zero, switch the load to displacement control.
5. Apply a compressive force at a rate of −0.00010 in./s in displacement control until a 4-kip compressive load is applied to the specimen.
6. The tensile load is applied at the same rate in the opposite direction until 25,000 με is attained longitudinally (read from the average of four LVDTs) or strain localization is observed.
7. At that stage, the displacement rate is increased by 10 times.

8. The test is terminated at an average displacement of 0.2 in. or when strain localization occurs.
9. Find the forces corresponding to (a) the first crack stress when the first crack is observed, which is determined as the intersection of the line with a slope matching the MOE of the elastic part of the stress-strain curve and passing through 0.02 percent strain (at zero stress) and the stress-strain curve, (b) the peak stress observed at maximum stress, and (c) the crack localization stress and strain when the stress begins to drop with an increase in strain.
10. The stress is computed by dividing the force by the specimen cross-sectional area.

Figure 3.7 illustrates the first cracking strength, the peak strength, and the 0.02 percent offset line used to determine the first cracking stress per AASHTO T 397 (AASHTO 2022) and FHWA (2022). In addition, the recommended PCI (eConstruct 2020) limit of 0.004 strain and 0.75 ksi stress for a typical uniaxial tensile stress-strain plot is shown.

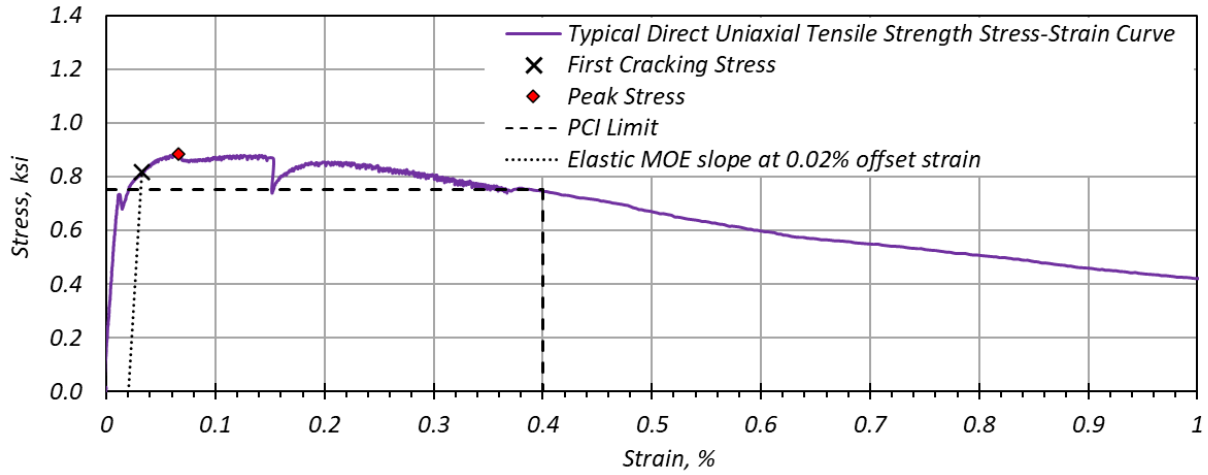

Figure 3.7. Typical Uniaxial Tensile Strength Stress-Strain Curve.

3.3.4 Inferred Tension Bending Test

Flexural testing, which is used for indirect tension testing, follows the procedure outlined in ASTM C1609 (2019), *Standard Test Method for Flexural Performance of Fiber-Reinforced Concrete (Using Beam With Third-Point Loading)*, with the modifications for UHPC listed in ASTM C1856 (2017). The standard recommends the use of specimen size based on fiber length. For the 0.5 in. fibers used in this research study, the recommended specimen size is 4 × 4 × 14 in. prism. The following steps describe the test procedure.

1. Prepare the specimen by marking the location of the supports at 6 in. from the center and the location of the load points at 2 in. from the center along the span.
2. Glue tabs to serve as LVDT end stoppers.
3. Mount the deflection measurement frame on the specimen and adjust the LVDTs to read zero.
4. Load the prism in a four-point bending set-up at a strain-controlled net rate increase of deflection at midspan of 0.002 in./s up to a midspan deflection of 0.013 in., after which the deflection should be increased in increments of 0.002 in./s up to 0.008 in./s.
5. The test is terminated at a midspan deflection of 0.08 in.
6. The peak stress is determined using Equation (3.6).

$$f = \frac{PL}{bd^2} \tag{3.6}$$

where:

P = Load at the desired stage of loading, kips

L = Length of the span of the specimen, 12 in.

b = Measured width of the specimen

d = Measured depth of the specimen

7. The toughness T_{150}^{D} is determined as the area under the load deflection curve up to a deflection equal to the span length divided by 150, 0.08 in. deflection, reported in lb-in.

8. The equivalent flexural strength ratio $R_{T,150}^{D}$, reported as a percentage, is defined by ASTM C1609 (2019) as follows, using the first peak strength and toughness determined for the specimen.

$$R_{T,150}^{D} = \frac{150\, T_{150}^{D}}{f_1 bd^2}\, 100\% \tag{3.7}$$

where:

T_{150}^{D} = Area under the load deflection curve up to $L/150$ deflection, lb-in.

f_1 = First peak cracking strength, ksi

b = Measured width of the specimen, in.

d = Measured depth of the specimen, in.

Figure 3.8 shows the test setup with the flexure specimen with the crack within the middle third of the span.

Figure 3.8. Inferred Tension Test Setup.

3.3.5 Creep Test

Creep testing is conducted in accordance with ASTM C512 (2015), *Standard Test Method for Creep of Concrete in Compression*, with modifications for UHPC per ASTM C1856 (2017). ASTM C1856 (2017) recommends 3 in. × 6 in. cylinders for creep in compression. A total of eight cylinders are used for the creep test: two cylinders for creep in compression, two cylinders for associated shrinkage, two halves of one cylinder as a loading distribution block at each end, and three cylinders for a companion compression test. The end surfaces of the cylinders for creep and the loading distribution cylinder blocks are ground as discussed in Section 3.3.1. Two different target loading levels (maximum $0.4f_c'$ and $0.65f_c'$) in which f_c' is the measured average

compressive strength at time of loading the creep frame are considered, whereas ASTM C512 (2015) recommends $0.4f_c'$. The value of $0.65f_c'$ was selected as an additional parameter to be representative of the prestressing transfer at early age (Haber et al. 2018). Thus, the $0.65f_c'$ loading was applied to the creep cylinders at the age of 10 days, while the $0.4f_c'$ was loaded to the creep cylinders at the age of 28 days. The cylinders were prepared at the precast plant while casting the precast, pretensioned UHPC bridge girder specimens. After transporting the cylinders, they were demolded and stored in the 50 percent RH moisture room at 68°F. The strains of the creep and shrinkage cylinders are recorded using a data acquisition system every 5 minutes for the first month and then read every 20 minutes.

Figure 3.9. Loading a Creep Frame.

3.3.6 Shrinkage Test

Shrinkage testing is conducted in accordance with ASTM C157 (2017), *Standard Test Method for Length Change of Hardened Hydraulic-Cement Mortar and Concrete*, with modifications for UHPC by ASTM C1856 (2017). Two test groups are prepared with three specimens for each group. One group is for autogenous shrinkage and the other is for total shrinkage. *Total shrinkage* is defined as the sum of the drying shrinkage and autogenous shrinkage. For autogenous shrinkage, three 3 × 3 × 11.25 in. prisms are sealed with aluminum foil to prevent water evaporation from the specimens, while the other three specimens for total shrinkage are not sealed (Figure 3.10). All the specimens are cured in the curing room at 68°F with a RH of 95 percent for the first 24 hours and then demolded at 24 hours ± 30 minutes. Immediately after the demolding, zero readings are recorded, and then the specimens are stored in the curing room at 68°F with RH 50 percent. Length change measurements of the specimens are taken every 2 days for the first week and then once a week for the first month and then once a month for later ages. All the specimens have 1.5 percent fiber volume. Equation (3.8) shows the expression for calculating length change:

$$\Delta L_x = \frac{CRD - initial\ CRD}{G} \times 100 \tag{3.8}$$

where:

ΔL_x = Length change of specimen at any age, percent

CRD = Difference between the comparator reading of the specimen and the reference bar at any age

G = The gage length, 10 in.

(a) Length Comparator with a Prism

(b) Total Shrinkage and Autogenous Shrinkage Specimens

Figure 3.10. Shrinkage Test Device and Specimens.

3.4 TEST METHODS FOR DURABILITY

Durability of UHPC mixtures is evaluated by the testing of rapid chloride ion penetration, bulk and surface resistivities, ASR, freeze-thaw resistance, scaling resistance, and abrasion resistance tests. Lab-cast test specimens without steel fibers are used for measuring true bulk and surface resistivities, rapid chloride ion penetration, and ASR to avoid interference due to steel fibers. The specimens cast at the plant are used for freeze-thaw resistance, scaling resistance, and abrasion resistance tests.

3.4.1 Rapid Chloride Ion Penetration

The rapid chloride ion penetration test (RCPT) is conducted to investigate the resistance of the developed UHPC mixtures to chloride ion penetration in accordance with ASTM C1202 (2017), *Standard Test Method for Electrical Indication of Concrete's Ability to Resist Chloride Ion Penetration*. The test measures a passing electrical charge through a specimen. Two specimens of 2 in. thickness and 4 in. diameter are made by cutting a cylinder specimen used for the bulk and surface resistivity tests at the age of 56 days of the specimens (Figure 3.11). The side surface of the specimens is coated with epoxy and then allowed to dry for 24 hours. The coated specimens are air-vacuumed for 3 hours. After air-vacuuming, the specimens are submerged in water for 18 hours. The top and bottom end surfaces are exposed to sodium hydroxide and sodium chloride, respectively. A 60 V direct current passes through the specimens for 6 hours. Figure 3.11 shows the cut specimens and RCPT test setup. After the 6-hour test, the charge passed is measured. The measured charge is classified according to ASTM C1202 (2017) (Table 3.1).

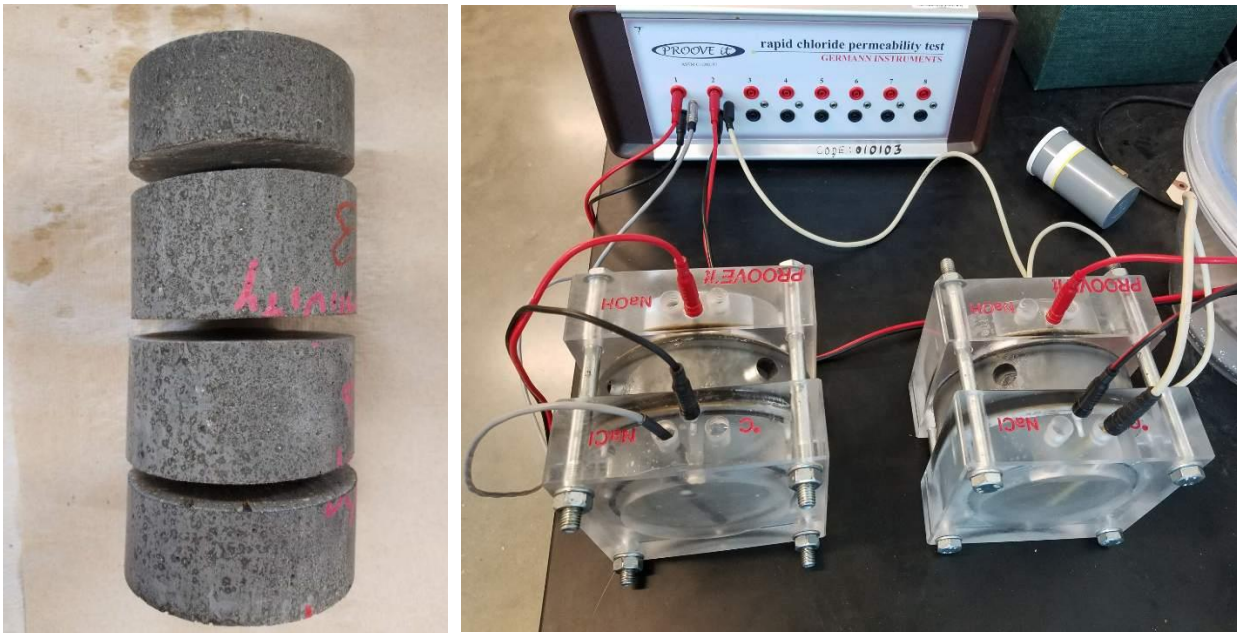

(a) Cut specimens *(b) Test setup*

Figure 3.11. Specimen Preparation and Test Setup for RCPT.

Table 3.1. RCPT and Surface Resistivity Classification (adapted from ASTM C1202 (2017) and AASHTO T 358 (2017)).

Chloride Ion Penetration	Electrical Charge, coulombs	Surface Resistivity, kΩ-cm
High	> 4000	< 12
Moderate	2000–4000	12–21
Low	1000–2000	21–37
Very Low	100–1000	37–254
Negligible	< 100	> 254

3.4.2 Bulk and Surface Resistivity

The bulk resistivity test measures the conductivity of concrete specimens in accordance with ASTM C1760 (2021), *Standard Test Method for Bulk Electrical Conductivity of Hardened Concrete*. Conductivity is quantified by passing an electrical charge through the specimens (Figure 3.12). The conductivity depends on PSR, pore sizes, and connectivity of pores of the concrete (Spragg et al. 2016). The resistivity of the specimen is the reciprocal of the conductivity. Bulk resistivity measurement with proper consideration to PSR is a measure of concrete transport properties (i.e., permeability), which can effectively be correlated with the durability performance of UHPC. Three 4 × 8 in. cylinder specimens without steel fibers are cast for resistivity testing and cured in a room at 68°F and 95 percent RH as per ASTM C192 (2016). The bulk resistivity readings are taken at 7, 14, 21, 28, and 56 days.

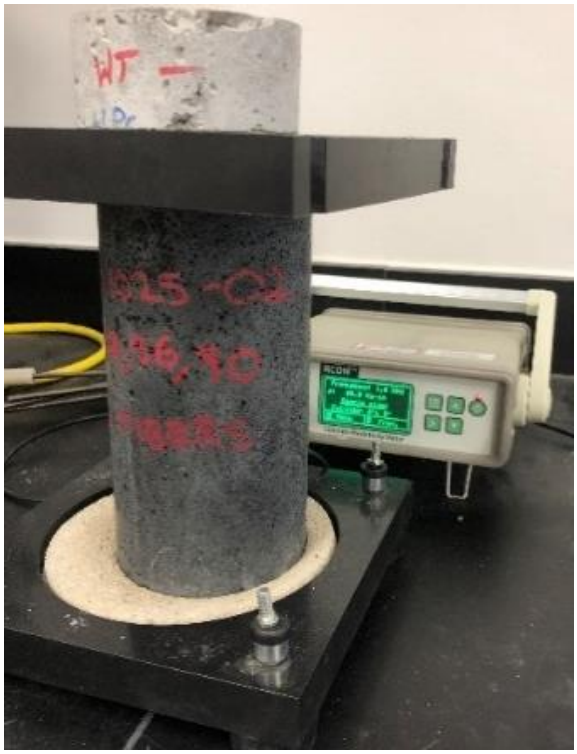

(a) Bulk Resistivity Testing

(b) Surface Resistivity Testing

Figure 3.12. Bulk and Surface Resistivity Testing Equipment and Specimens.

The surface resistivity test also measures conductivity like the bulk resistivity in accordance with AASHTO T 358 (2017). However, the measuring direction is on the side surface of specimens (Figure 3.12). The same specimens for the bulk resistivity test are used for the surface resistivity test. The surface resistivity readings were taken at 7, 14, 21, 28, and 56 days, which are the same ages used for the bulk resistivity test.

3.4.3 Freeze-Thaw Resistance

The freeze-thaw resistance test is used to determine the resistance of the UHPC mixture in the laboratory in accordance with ASTM C666 (2015), *Standard Test Method for Resistance of Concrete to Rapid Freezing and Thawing*, with modifications for UHPC by ASTM C1856 (2017). Three 3 × 3 × 11.25 in. prisms are stored in 68°F with 95 percent RH for 14 days. A total of 300 freeze-thaw cycles are applied with a 4-hour duration for each cycle, which consists of a freezing environment at 0°F for 3 hours and thawing environment at 40°F for 1 hour. Prior to the test, the fundamental transverse frequency and weight are measured as per ASTM C215 (2019), *Standard Test Method for Fundamental Transverse, Longitudinal, and Torsional Resonant*

Frequencies of Concrete Specimens. Readings of fundamental transverse frequency and mass are performed every 30 cycles (Figure 3.13).

Figure 3.13. Fundamental Transverse Frequency Test Setup.

ASTM C666 (2015) recommends repeating the test for 300 cycles or until its relative dynamic modulus of elasticity (RDM) reaches 60 percent of the initial modulus, whichever is achieved first. For UHPC, ASTM C1856 (2017) recommends testing to at least 300 cycles or to when RDM reaches 90 percent of the initial modulus, whichever is achieved first. The equation for the calculation of RDM is shown in Equation (3.9) as per ASTM C666 (2015):

$$P_c = (n_1^2/n^2) \times 100 \quad (3.9)$$

where:

P_c = RDM, after c cycles of freezing and thawing, percent

n = Fundamental transverse frequency at 0 cycles of freezing and thawing, Hz

n_1 = Fundamental transverse frequency at specific cycles of freezing and thawing, Hz

The freeze-thaw resistance of concrete is evaluated by a decrease in RDM, mass loss, and visually observed defects in a concrete specimen.

3.4.4 Scaling Resistance

The scaling resistance test is conducted to evaluate scaling resistance of the developed UHPC mixture qualitatively in accordance with ASTM C672 (2012), *Standard Test Method for Scaling Resistance of Concrete Surfaces Exposed to Deicing Chemicals*. The surface of the concrete is exposed to a deicing chemical—calcium chloride solution—in a freezing-thawing environment. The specimen has an 81 in^2 top surface area with a 1 in. high dike around the perimeter of the top surface. Two specimens are exposed to a total of 50 freezing and thawing cycles. Each cycle consists of exposure to a freezing temperature (0°F) for 18 hours and a thawing temperature (68°F) for 6 hours. The calcium chloride solution is replaced at the end of every five cycles. The specimens are evaluated visually according to the rating criteria outlined in ASTM C672 (2012) and shown in Table 3.2.

Table 3.2. Visual Rating Criteria (adapted from ASTM C672 [2012]).

Rating	Condition of Surface
0	No scaling
1	Very slight scaling (1/8 in. depth, no coarse aggregate visible)
2	Slight to moderate scaling
3	Moderate scaling (some coarse aggregate visible)
4	Moderate to severe scaling
5	Severe scaling (coarse aggregate visible over entire surface)

3.4.5 Abrasion Resistance

The surface abrasion resistance of the developed UHPC mixture is evaluated using rotating cutters in accordance with ASTM C944 (2012), *Standard Test Method for Abrasion Resistance of Concrete or Mortar Surfaces by the Rotating-Cutter Method*, with modifications for UHPC based on ASTM C1856 (2017). Three 4 × 8 in. cylinders are cured in a room at 68°F and 95 percent RH for 28 days. The top and bottom surfaces from a 4 × 8 in. cylinder are prepared by cutting the cylinder specimens to the 4 in. height of the specimen. The modification from ASTM C944 (2012) for UHPC is to double the applied loading from the 44 lb used per ASTM C1856 (2017), thus giving a load of 88-lb. The size of the cutter is modified to 2.375 in. diameter, even though 1.5 in. diameter is recommended by ASTM C944 (2012), because the device in the lab cannot

accommodate 1.5 in. diameter cutters. Note that the increase in the diameter will likely provide a more severe abrasion to the concrete surface. Figure 3.14 shows the test setup.

Figure 3.14. Abrasion Resistance Test Setup.

The six surfaces of the specimens, including the top and bottom surfaces of three specimens, are abraded for 2 minutes each, and then debris on the surface is cleaned by blowing with air. This 2-minute abrasion is repeated five times for a total of 10 minutes for each surface. Mass loss is measured at the end of each 2-minute abrasion period.

3.4.6 Alkali-Silica Reaction

The ASR of the developed UHPC mixture is evaluated by the accelerated concrete cylinder test (ACCT) method in accordance with AASHTO TP142 (2021) developed by Mukhopadhyay et al. (2019) with modifications for UHPC applications. The ACCT for NSC is initiated using a sample at the age of 7 days, whereas ACCT for UHPC begins at the age of 1 day. Three 3 × 6 in. cylinders (two cylinders using reactive aggregate and a cylinder using the sand used for the UHPC mixture) are cured in a room at 68°F and 95 percent RH for the first 24 hours. The specimens are demolded at the age of 24 hours. Immediately after demolding, the specimens are placed in containers filled

with the pore solution. The containers, which are equipped with an LVDT, are stored in an oven at 140°F (Figure 3.15). The LVDT measures the length change of the cylinder.

Figure 3.15. ACCT Test Setup.

ASTM C1260 (2014), *Standard Test Method for Potential Alkali Reactivity of Aggregates (Mortar-Bar Method)*, is also conducted to identify the reactivity of the sand used in the specimens. Two 1 × 1 × 11.25 in. prisms are prepared by mixing Type I/II cement and sand, which are then mixed with 0.47 *w*/*c*. The weight ratio of sand to cement is 2.25. The specimens are cured for the first 24 hours in the moisture room at 68°F and 95 percent RH and are demolded at the age of 24 hours. Immediately after demolding, an initial reference reading is recorded. The specimens are placed in the 73°F water container. The water container is placed in the oven at 176°F for 24 hours. After 24 hours, the surfaces of the specimens are dried using a towel, and a zero reading is recorded (Figure 3.16). The specimens are placed in a container with a 1N NaOH solution. The container with the NaOH solution is placed in the oven at 176°F for 14 days and three intermediate readings

are taken. Table 3.3 shows the interpretation of the test results as per the appendix in ASTM C1260 (2014).

Figure 3.16. Length Change Measurement of ASTM C1260 (2014).

Table 3.3. Relationship between Expansion and Alkali Reactivity of Aggregates (adapted from Appendix of ASTM C1260 [2014].

Expansion, percent	Alkali Reactivity of Aggregates
<0.10	Innocuous aggregates
Between 0.10 and 0.20	Containing both innocuous and deleterious aggregates
>0.20	Potentially deleterious aggregates

4 NONPROPRIETARY UHPC MIXTURE DESIGN

4.1 INTRODUCTION

Properly proportioning UHPC is critical to the successful implementation of this product. This chapter documents Task 4, which includes the methodology and findings for the development of nonproprietary UHPC mixtures. The developed UHPC mixtures are designed to meet the requirements identified in the Task 3 analytical feasibility design study, discussed in Chapter 3 of Volume 2 of this report. The required release and 28-day compressive strengths identified in Task 3, along with appropriate workability, are key target properties considered for mixture development. The theoretical background and the mechanism of UHPC in terms of strength gain and water demand to achieve the target workability and strength have been reviewed. Section 4.2 discusses several key factors affecting the required properties and proportioning methods to develop successful UHPC mixtures.

Locally available materials were selected to develop nonproprietary UHPC mixtures for the Texas precast bridge girders' applications. Information on locally available materials was collected and documented as part of the Task 2 questionnaire. Appendix A contains the results of the questionnaire. In addition, preferences of the respondents (precasters, material suppliers, ready-mix suppliers, and Texas Department of Transportation (TxDOT)) for type of cement, curing method, and time to prestress release were considered. The major findings from the questionnaire are the following:

- The precasters prefer to use currently used materials due to limited material storage facilities such as silos.
- Steam curing is not preferred due to its high cost and because steam curing is not currently needed in the precast industry in Texas.
- According to precasters, prestressing release time within 24 hours is preferred, and it can be extended with additional cost if necessary.

The other aspects identified for material selection are cost-effectiveness, availability, and sustainability. Several materials were used for preliminary testing to identify the most favorable materials in terms of cost-effectiveness, sustainability, and practicality. Section 4.3 discusses characteristics of these constituent materials.

The mixing procedure for UHPC is an important aspect because it affects fresh and hardened properties. Mixing procedures for proprietary and nonproprietary UHPCs developed by several other research studies have common steps. The optimized mixing procedure developed in Task 4 maintains these common steps while incorporating specific modifications as needed. These modifications are adopted to increase the effectiveness of the HRWR in achieving the desired quality of fresh UHPC within an appropriate mixing time. In addition, the mixing procedure is further optimized to accommodate precast plant material conditions, such as wet sand and large volume production, for precast plant application.

The selected material tests to evaluate the preliminary UHPC mixtures include the compression test, flow table test, and setting time test. The existing ASTM standard test methods that are modified for UHPC application in accordance with ASTM C1856 (2017) were used for the preliminary tests and are summarized in Chapter 3. Based on the test results, mixtures were screened or modified to achieve the target properties:

- A sufficient spread value (9–11 in.)
- 1-day compressive strength of 10–14 ksi without any special curing treatment
- 28-day compressive strength of 18–20 ksi without any special curing treatment
- 4–8 hours for initial set and 7–10 hours for final set

The sequence of development of the candidate UHPC mixtures presented in Section 4.5 provides a good understanding of the approaches to UHPC mixture design development. The criteria for specific compressive strength requirements (1 day) and cost-effectiveness were applied to develop these candidate mixtures. A total of eight mixtures were developed, each with their own compressive strength ranges. The mixture design methods and significant factors that affect target properties are explained. Section 4.5 includes the test results of the developed mixtures. Promising mixtures were selected for further study of properties and durability in Section 4.6. Section 4.7 discusses the optimum steel fiber volume study with respect to cost and required properties.

4.2 MECHANISM OF FRESH AND HARDENED PROPERTY DEVELOPMENT

An appropriate balance between high packing density, low water content, and adequate workability is essential for the desired fresh, hardened, and durability properties of UHPC. Even

though packing density can be improved by increasing the fineness of cementitious materials, excessive fineness requires more water, thereby decreasing early strength gain and durability due to increased water content (Soliman and Tagnit-Hamou 2017). Likewise, low water content is favorable for durability and early strength gain, but it increases HRWR demand, which can cause retardation of cement hydration (Arora et al. 2018). As a result, an excessively lowered water content for early strength gain can instead lead to delayed strength gain. Therefore, well-balanced material proportions, along with the optimum water, HRWR content and type, and packing density, are the key factors to develop a successful UHPC mixture for precast, pretensioned bridge girder application. This section focuses on understanding the mechanisms of fresh and hardened properties for development of UHPC mixtures, which facilitate the effective design of UHPC mixtures with desired properties. The section describes the workability of UHPC as a self-consolidating class of concrete; presents governing factors affecting strength development at early and later ages; and discusses particle size distribution and packing density at the paste level and matrix level.

4.2.1 Workability

This section discusses three main factors that impact the workability of UHPC: HRWR, cementitious materials, and sand. Each subsection below explains how the factor influences workability and what characteristics of the factor should be considered.

4.2.1.1 High-Range Water Reducer

One of the important fundamental principles of UHPC is high packing density. An increase in solids concentration for high packing density increases viscosity and yield strength due to the flocculation of the cementitious materials (Yahia et al. 2016). Thus, a paste with high solid concentration and a low *w*/*c* like UHPC has a high viscosity and a high yield stress of cement suspensions due to a high attractive force, which reduces the workability substantially. This workability issue can be resolved by HRWR. A polycarboxylate-based HRWR disperses particles by both electrostatic and steric repulsion using its long side chain length (Gelardi and Flatt 2016). Side chains of HRWR hinder flocculation of particles by the steric repulsion. As a result, physically separated particles by HRWR provide enough workability and extended slump life (Gelardi and Flatt 2016; Tue et al. 2008). In addition, recently developed HRWRs in the market

include a viscosity modifying agent (Sika 2018). As a result, it improves workability while placing fresh concrete. Another aspect is the adsorption speed of HRWR that depends on the charged level of HRWR. Highly charged HRWR can be adsorbed quickly by cement particles. Thus, it reduces the mixing time of UHPC to achieve consistency of the paste and setting time. The effect of the charged level of HRWR on setting time is described in Section 4.2.2.1 in detail.

One of the developed pastes in this study achieved the target spread value with 0.15 *w*/*c* by increasing the dosage of HRWR, even though the high dose of HRWR caused retardation. Generally, a 0.18–0.19 *w*/*cm* ratio with an adequate HRWR-to-cementitious material ratio (*HRWR*/*cm*) has provided the desired flow spread value (9–10.5 in.) without retardation of hydration.

4.2.1.2 Cementitious Materials

In addition to *w*/*c* and HRWR, mineral admixtures such as fly ash and silica fume may influence the rheology of UHPC positively or negatively depending on particle size distribution, fineness, and morphology (Yahia et al. 2016). Replacing a portion of cement with fly ash improves rheology because it reduces both yield stress and viscosity (Tattersall and Banfill 1983). A small volume of silica fume (between 5–15 percent by cement weight) can improve the rheology of the mix by filling voids between cement particles. Consequently, the water previously trapped between cement particles is released to contribute to the workability of the mix. However, a large proportion of silica fume (larger than approximately 15 percent) diminishes the spread of UHPC due to an increase in water demand. Furthermore, a loosening effect occurs when the volume of silica fume exceeds the volume of gaps between cement particles (Figure 4.1). Small silica fume particles push larger cement particles away from each other, thus creating more voids for water to fill, which leads to reduction in workability (Hermann et al. 2016).

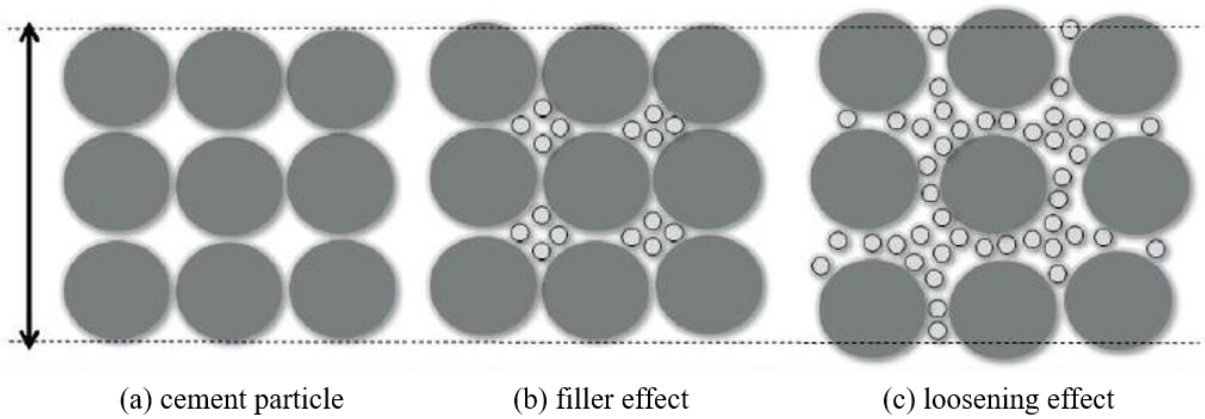

Figure 4.1. Effects of Silica Fume Proportion (Hermann et al. 2016).

4.2.1.3 Sand

Two characteristics of sand influence the rheology of UHPC: shape and gradation of sand. Angular shapes of sand contain more surface area than rounded shapes, which causes higher internal friction, thereby negatively affecting the rheology (Yahia et al. 2016). The gradation of sand affects the packing density and the required volume of a paste for optimum workability. The paste covers sand particles and fills interparticle voids. The thickness of a paste, which covers sand particles, is directly related to rheology. More thickness provides a higher spread value (Yahia et al. 2016). Because well-graded sand has low interparticle voids, more paste can be available to cover sand particles. Therefore, well-graded and rounded sands improve flowability.

4.2.2 Strength Development

For pretensioned bridge girders, both early age (e.g., 1 day) and later age (e.g., 28 days) strengths are important factors. Rapid strength gain at an early age (e.g., within 1 day) is necessary for economical production of pretensioned girders. High early strength can reduce the curing time in a casting bed for releasing prestress strands; therefore, a precaster can produce a girder with a shorter production period, thus providing cost benefits. In addition, sufficient strength development prior to prestress transfer minimizes creep and shrinkage. Furthermore, high strength at later ages is a decisive design parameter for service and strength limit states. Therefore, significant factors affecting strength development are discussed below. First, the theoretical background of how the *w*/*c*, flow, and air voids influence strength development are described.

Then, favorable proportioning methods of cementitious materials to achieve required early and later age strength are explained.

4.2.2.1 Water Demand versus Early Age Strength Improvement

Understanding how *w*/*c* affects the hydration of cement and strength development is key for understanding the true impact of *w*/*c* in a dense system such as UHPC. The surface of the cement particles begins to form hydrates (e.g., calcium-silicate-hydrate gel) immediately after contacting water. Calcium-silicate-hydrate gel acts as a glue. The hydrated surface grows gradually and is connected with the surface of adjacent cement particles and other particles such as silica fume, fly ash, and fillers (Richardson 2004). The connected hydrates and particles of cementitious materials form a solid network (Barcelo et al. 2001). When the distance between cement particles is short, the hydrates are connected to the adjacent particles with the small amount of hydration at the surface of the cement. Previous research studies (Bentz and Aitcin 2008; Granju and Grandet 1989; Richardson 2004) have shown that *w*/*c* is a governing factor for the average distance between cement particles, and a low *w*/*c* leads to close distance between cement particles. Therefore, a low *w*/*c* accelerates strength development due to the proximity of cement particles.

Water demand can be reduced by adjusting the fineness of cementitious materials to achieve a low *w*/*c*. Since Type III cements are in general finer than Type I/II cements, the water demand for UHPC mixes using Type III cement can be slightly higher. However, adequate use of HRWR and a slight increase in water content can provide adequate workability (i.e., spread value) for UHPC mixtures using Type III cement. Silica fume is one of the most commonly used ingredients for making UHPC. In general, the higher the silica fume content, the higher the water demand. Meng et al. (2016) showed that a 5 percent volume replacement of silica fume in the paste was found to be effective to increase early strength (twice that of the control mix) without increasing the water demand. However, silica fume replacement greater than 5 percent resulted in an increase of water demand with a slight decrease of 1-day compressive strength (Meng et al. 2016). Although an increase of silica fume content increases water demand with slight decrease of early strength, it provides a beneficial effect of improvement in later age strength and in durability. Therefore, an effective balance between *w*/*c*, HRWR dosage, and silica fume content needs to be established to

ensure both early and later age strengths and durability. Section 4.2.2.3 presents a more detailed discussion on the effect of the silica fume on the later age compressive strength.

The use of HRWR, especially a polycarboxylate-based superplasticizer, provides a solution for addressing the workability issue of concrete mixes with a low *w*/*c*. HRWR has superior capacity to disperse fine particles. As a result, water is not trapped by cementitious materials; additionally, water contacts evenly dispersed cement particles by the dispersion effect of HRWR (Nkinamubanzi et al. 2016). Thus, *w*/*c* can be reduced to lower than 0.2 while still providing sufficient flowability. As a result, cement particles can form a solid network within a very short time due to the proximity of the cement particles. Although the core of the cement particle remains unreacted due to the lack of water for full hydration, this unreacted core acts as a rigid inclusion that is fully connected to hydrates. As a result, the unreacted core also contributes to strength (Aïtcin 2016), so *w*/*c* is the primary factor for short-term strength gain.

The use of an adequate amount of HRWR was found to be a requirement to ensure sufficient flowability of UHPC mixtures because *w*/*c* is very low. However, an overdose of HRWR tends to retard the hydration reaction of the cement and thus decreases early strength gain (Arora et al. 2018). In addition, the selection of HRWR is important for early strength gain. Schmidt et al. (2011) reported that high-charged polycarboxylate HRWR is more efficiently and quickly adsorbed to cementitious particles than low-charged polycarboxylate HRWR. As a result, a high-charged polycarboxylate HRWR has a shorter setting time than that of a low-charged polycarboxylate HRWR, even though it has a shorter slump life. Consequently, the use of a high-charged polycarboxylate HRWR improves early strength gain. Therefore, ensuring an appropriate balance between *w*/*c* and HRWR dosage, as well as the selection of an HRWR, are vital for achieving high early strength.

The findings mentioned in the previous paragraphs were demonstrated by the paste development study described in Section 4.5.2.1.1. The 1-day compressive strength increased with a decrease in *w*/*c* while keeping all other proportions, such as cementitious materials and HRWR, the same. This result provided a key principle to develop the UHPC mixtures: minimize the amount of water by maximizing the amount of HRWR up to the quantity that does not cause retardation but still achieves the target flowability.

4.2.2.2 Flow and Air Voids

Sufficient flowability of fresh UHPC is a crucial property. The flowability is measured according to ASTM C1437 (2015), *Standard Test Method for Flow of Hydraulic Cement Mortar*, modified for UHPC by ASTM C1856 (2017). A spread value is an indicator for not only flowability, but also packing density and voids (Wille et al. 2011). El-Tawil et al. (2018) showed that an optimum spread provides an effective reduction of air void volume in UHPC, which is related to an increase in compressive strength. Although high fluid behavior of fresh UHPC is preferred, excessive flowability results in the segregation of constituent materials, especially steel fibers. Thus, many researchers have suggested a feasible range for the spread value, several of which are summarized in Table 4.1

Table 4.1 Recommended Flow Spread Value Ranges.

Description	El-Tawil et al. (2018)	Berry et al. (2017)	Wille and Boisvert-Cotulio (2013)
Flow Spread Value, in.	7–12	11–13	10–12

Based on experimental observations in this study, an ideal spread value range was identified as between 9–11 in. for the developed UHPC mixtures, which is described in detail in Section 4.5. A spread value greater than 11 in. caused segregation of the steel fibers, while a spread value lower than 9 in. resulted in low flowability and an inability to place fresh UHPC appropriately, which might cause more voids.

4.2.2.3 Approaches for Later Age Strength Improvement

To satisfy long-term strength and durability requirements, an adequate amount of silica fume in the mixture is an important aspect. The silica fume reacts with calcium hydroxide (called portlandite or lime) and produces secondary calcium-silicate-hydrate, which fills micro pores (Mindess et al. 2003). Silica fume also facilitates faster cement hydration through the nucleation effect and fills relatively larger pores (filler effect). The combined effect of the nucleation effect, the filler effect, and a reduction in micro-pores creates a denser microstructure, which causes improvement in hardened properties and durability. Earlier, it was mentioned that the higher the silica fume content, the higher the water demand. Therefore, it is important to find an appropriate balance between the positive effect of improving the microstructure through a secondary reaction

and the negative effect of an increase in water demand. Kang et al. (2017) showed that half of silica fume was reacted when a 0.16 silica fume proportion by cement weight is used. This research result gives insight on the appropriate proportion of silica fume for the secondary reaction. Increasing silica fume up to an approximate 0.08 proportion by cement weight might improve strength and durability by the secondary reaction.

Even though fly ash is a pozzolanic reactive material, it is classified as a filler material in UHPC. Fly ash normally begins reacting after 56–91 days and requires calcium hydroxide and free water for the reaction (ACI 232.3R-14 2014; Aïtcin 2016); however, due to the low water content of UHPC, free water might not be available when the fly ash begins reacting. Thus, it is classified as a filler material. Substitution of fly ash for some portion of cement increases the *w*/*c* when water content is the same, which means an increase in the average distance of cement particles by diluting the cement (Aïtcin 2016). As a result, the substitution decreases early strength gain because the initial strength comes from the cement (ACI 232.3R-14 2014). However, replacing some portion of sand with fly ash can increase both early and later age strength unless the substituted portion is not excessive because fine fly ash particles improve packing density. Therefore, after developing a binder combination of cement and silica fume first, finding an appropriate proportion of filler materials such as sand and fly ash is a good approach to develop UHPC because it satisfies both short-term and long-term strength goals.

The optimum proportion of cementitious materials for early and later strengths is described in this section. A low *w*/*c* with an optimum amount of HRWR (which does not cause retardation of hydration) is the basis for evaluating the proportion of paste, as mentioned in Section 4.2.2.1. The test results in this project showed that a paste composed of 5 percent silica fume and 95 percent cement by volume has a higher 1-day compressive strength (14.4 ksi) than other paste proportions (8 percent, 9 percent, 14 percent, and 17 percent silica fume in a paste). Furthermore, replacing 5 and 10 percent cement by volume with fly ash reduced water demand even though the 1-day compressive strength was decreased. However, substituting fly ash for 7.5 percent sand volume instead of cement increased both 1-day compressive strength and the spread value. The experimental results are consistent with the findings of other researchers in the literature. Section 4.5 discusses test results and mixture development methods in detail.

4.2.3 Particle Size Distribution and Packing Density

This section explains the evaluation methods of packing density. Depending on particle size, the evaluation method is different. The packing density of large particles like sands is evaluated directly using particle size distribution, whereas the packing density of fine particles—such as cement, silica fume, and fly ash—is evaluated indirectly with strength and a spread value. Therefore, the following two subsections discuss the packing density of sands and paste. Then, in the last subsection, the packing density at the matrix level is described.

4.2.3.1 Sand

A popular method to evaluate particle size distribution of sand is the modified Andreasen and Andersen model (A&A). This method was modified by Brouwers and Radix (2005) to find an ideal particle size distribution for SCC. Because the rheology characteristics of UHPC are close to SCC, many researchers have applied this method to UHPC. The equation for the modified A&A curve is provided in Equation (4.1):

$$P(D) = \frac{D^q - D_{min}^q}{D_{max}^q - D_{min}^q} \tag{4.1}$$

where:

P(D)	=	Passing percentage
D	=	Particle size
D_{min}	=	Minimum particle size
D_{max}	=	Maximum particle size
q	=	Distribution modulus

Andreasen (1930) introduced $q = 0.37$ for conventional NSC. However, Hunger (2010) showed that $q = 0.37$ is not appropriate for concrete containing a large amount of fine powders and suggested $q < 0.25$ for UHPC. Meng et al. (2016) and El-Tawil et al. (2018) have used $q = 0.23$ and $q = 0.22$, respectively.

In addition to the value of the q parameter, the minimum particle size, D_{min}, should be considered carefully. The A&A curve does not reflect the electrostatic force between fine particles such as

silica fume and cement but only considers gravitational force (Soliman and Tagnit-Hamou 2017). Therefore, minimum particle size should be in the range governed by the gravitational force. El-Tawil et al. (2018), Wille and Boisvert-Cotulio (2015), and Berry et al. (2017) have used 1.0 µm, 50 µm, and 75 µm as the minimum particle size, respectively.

In this study, $D_{min} = 75\ \mu m$ (the minimum grain size of sand) was used to evaluate particle size distribution of sand because gradation of fine particles such as cement and silica fume cannot be evaluated adequately due to electrostatic force between fine particles. For the distribution modulus, $q = 0.22$ was used. The particle packing density of fine particles was evaluated indirectly through spread and strength values.

4.2.3.2 Paste

The high packing density of a paste is beneficial for workability because highly compacted solid materials can reduce the volume of voids in a paste, which decreases the amount of entrapped water in voids; therefore, more water is available to cover cementitious particles. However, excessive solid concentration in the paste can have an adverse effect on rheology because of high viscosity and friction. Furthermore, the reduced rheology may decrease strength due to large voids in the hardened UHPC (Soliman and Tagnit-Hamou 2017). Therefore, if a UHPC mixture satisfies both high solid concentration and a sufficient spread value simultaneously, it indirectly indicates that the mixture is coming close to optimum high packing density. Based on this approach, Wille and Boisvert-Cotulio (2015) considered a spread value and a 28-day compressive strength an indicator of high packing density. Wille and Boisvert-Cotulio (2015) evaluated combinations of several cementitious materials with this approach.

Based on trial batches in this project, the 1-day compressive strength should also be considered an indicator for evaluating packing density of the paste because early strength is significantly affected by the distance of highly compacted cement grains. Therefore, three test results, which are (1) the spread value, (2) the 1-day compressive strength, and (3) the 28-day compressive strengths, were used in this study as the important indicators of packing density.

4.2.3.3 Excess Paste Approach

The two previous subsections discussed particle size distribution and packing density of a paste and sand. This subsection deals with the combination of a paste and sand. The required volume of a paste can be divided into two parts in regards to rheology: the first part is to fill voids between sand particles, and the second part is to cover sand particles to lubricate them (Figure 4.2) (Yahia et al. 2016).

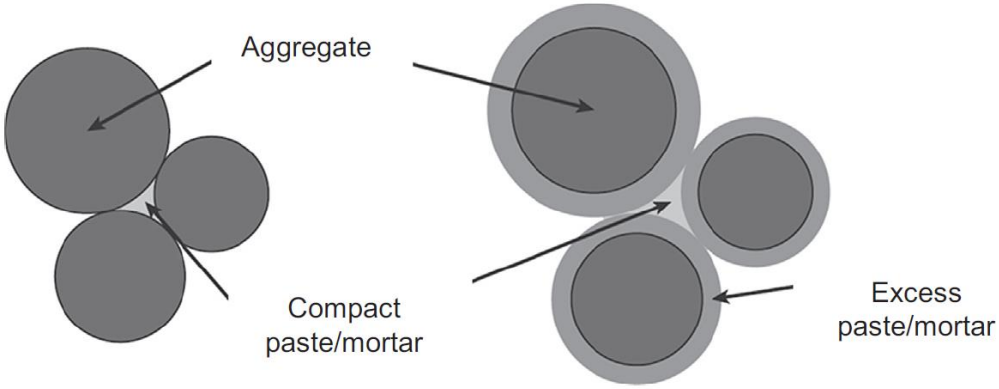

Figure 4.2 Excess Paste Approach (Oh et al. 1999).

A certain volume of a paste fills the voids first, and this volume significantly depends on the particle size distribution and the packing density of sand. After filling the voids, the excess paste covers sand particles. This excess paste provides the lubrication effect. The workability increases with the thickness of the excess paste. To achieve sufficient workability, the thickness of excess paste should be ensured. The ratio of a paste to sand by volume can be evaluated by the flow table test, according to ASTM C1437 (2015). The volume of a paste can be reduced by minimizing voids, which can be achieved by using well-graded sand having a rounded particle shape. Thus, well-graded sand reduces paste content while achieving required properties. Consequently, good particle size distribution with high packing density of both sand and paste are beneficial to develop cost-effective UHPC with advanced properties.

Experiments to identify an optimum ratio of a paste to sand by volume (V_p/V_s) were performed to develop UHPC mixtures in this project. The experimental results showed that the spread value decreased when the V_p/V_s is lower than 0.9. Conversely, the amount of cement was high when

V_p/V_s was greater than 1.0. Therefore, the optimum range of V_p/V_s was found to be between 0.9 and 1.0 based on mechanical properties and the cost-effectiveness of UHPC.

4.3 MATERIALS

This section discusses material selection for the development of UHPC. Three factors are considered for the material selection. The first factor is the recommended characteristics—such as chemical composition and particle size distribution—for achieving advanced properties of a UHPC mix based on literature. Second, local availability and preferences of precasters are considered in accordance with the results of a questionnaire that was conducted as part of this project. The last aspect is the benefit in terms of cost-effective and sustainable UHPC mixtures. Based on these three aspects, the materials for preliminary development of UHPC are selected.

4.3.1 Cement

Many researchers have studied optimum characteristics of cement for UHPC. One generally accepted cement characteristic is low C_3A with low Blaine fineness for minimizing water demand. Sakai et al. (2008) showed that the rapid hydration of C_3A leads to an increase in water demand and viscosity. Thus, they suggested using cement with less than 8 percent C_3A content. Wille and Boisvert-Cotulio (2015) investigated the performance of 12 different cements, including Portland Cement (PC) Type I/II, Type II, Type III, Type II/V, White PC Type I, and oil well cement. These cements were evaluated based on their spread value according to ASTM C230 (2014) and on their 28-day compressive strength. Although oil well cement had a good spread value due to extremely low C_3A (less than 1.0 percent), its compressive strength was not higher than other cements. PC Type II/V has the optimum C_3A content (4 percent), but there is limited availability in the eastern United States. Although the C_3A contents of PC Type I/II and Type III are 7 percent and 8–9 percent, respectively, the cost is cheaper than others, and it is widely used in the United States. The performance of White PC Type I was superior, with moderate C_3A content and a high content of C_3S and C_2S that are beneficial for strength development. However, its high cost ($250 per ton) is an obstacle for a cost-effective UHPC compared to the cost range of other cements ($90–$130 per ton) (Wille and Boisvert-Cotulio 2015). Several state DOTs and FHWA have studied an appropriate type of cement for UHPC, which is given in Table 4.2. DOTs and FHWA, while

considering local availability and cost, have selected a type of cement with low C_3A and low Blaine fineness.

Table 4.2. Type of Cement Used in DOT and FHWA Studies.

Agency	Author	Cement Type
Michigan DOT	El-Tawil et al. (2018)	PC Type I
Montana DOT	Berry et al. (2017)	PC Type I/II
New Mexico DOT	Weldon et al. (2010)	PC Type I/II
Colorado DOT	Kim (2018)	PC Type III
Missouri DOT	Khayat and Valipour (2018)	PC Type III
FHWA	Wille and Boisvert-Cotulio (2013)	White PC Type I or PC Type II/V

Another aspect to consider for early strength gain for prestressing is high C_3S content. Contradictory findings exists in the literature on more than 50 percent C_3S content. Wille and Boisvert-Cotulio (2015) indicated that high C_3S content (62–74 percent) of White PC Type I is preferred for strength development, whereas Coppola et al. (1996) and Aïtcin (1998) found that the best cement properties for RPC is a maximum 5 percent C_3A and maximum 50 percent C_3S with low Blaine surface area. The experimental tests in this project showed that high C_3S content increases water demand but also increases 1-day compressive strength. Thus, high C_3S content is preferred for UHPC for precast, pretensioned bridge girders.

The responses to the questionnaire from precasters, material suppliers, ready-mix suppliers, and the Material Division of TxDOT reveal a preference for conventionally used cement such as Type III cement due to concerns about availability, storage area and condition, and soundness of concrete product when other cement types are used.

Based on the findings of other research studies and the responses to the questionnaire, two favorable cement types (Type I/II and Type III) for short-term strength have been studied in this project as part of Task 4. The low water demand of Type I/II is beneficial for early strength gain because the short distance between cement particles with low *w*/*c* helps to form a solid network quickly. On the other hand, Type III cement has a higher water demand and HRWR demand than Type I/II cement, but its hydration speed is faster due to finer particle size and higher C_3S content. Thus, Type III cement also can achieve high early strength. To study and compare these two favorable effects for early strength gain, two different Type I/II cements and one Type III cement were used for preliminary development of UHPC mixtures. After preliminary development of

nonproprietary UHPC mixtures, two additional Type III cements were studied. Particle size distribution analysis of the considered cements was conducted with a HORIBA Laser Scattering Particle Size Distribution Analyzer LA-960. Table 4.3 and Figure 4.3 show the results.

Table 4.3. Particle Size of Considered Cements.

Particle Distribution	Cement Type		
	C-1: PC Type I/II	C-2: PC Type I/II	C-3: PC Type III
10%	2.0 µm	1.8 µm	1.4 µm
Median	4.2 µm	3.6 µm	2.8 µm
90%	7.2 µm	6.3 µm	4.7 µm

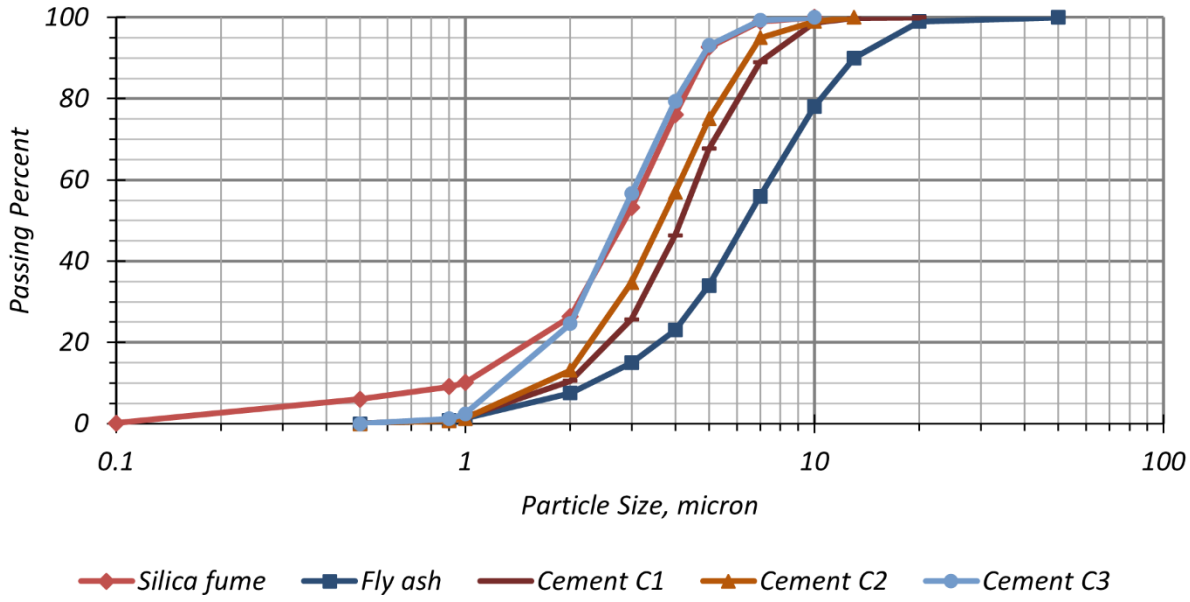

Figure 4.3. Particle Size Distribution of Cementitious Materials.

Table 4.4 presents X-ray diffraction test results for the two different Type I/II cements and the Type III cement used in the UHPC mixtures. The X-ray diffraction results indicate relatively high C_3S content in C-2 cement. Even though trial batches with C-2 reduced the spread value due to this high C_3S content, it was beneficial for early strength gain when compared to C-1 cement because C_3S reacts immediately and significantly contributes to the 1-day strength, but C_2S reacts slowly and contributes to the 28-day strength (Aïtcin 2016). For 28-day compressive strength, UHPC mixes using C-1 and C-2 may have similar 28-day compressive strengths because of the same C_2S plus C_3S value. However, it was difficult to make a direct comparison of compressive strength values of UHPC mixes using C-1 and C-2 because the strength of the mix with C-1

(19.6 ksi) was obtained from cylinders with a capping compound and neoprene pads, whereas the strength of the mix with C-2 (17.6 ksi) was obtained from cylinders with a ground surface at the ends.

Table 4.4. X-Ray Diffraction Test Results.

Description	C-1	C-2	C-3
Type	Type I/II	Type I/II	Type III
C_2S, %	16	8	16
C_3S, %	57	65	55
C_3A, %	4	2	11
C_4AF, %	13	11	6
$C_2S + C_3S$, %	73	73	71

Note: C-3 data are based on the mill certification from the cement company.

4.3.2 Silica Fume

Silica fume is a byproduct of silicon, ferrosilicon, or zirconium (Shi et al. 2015). During the producing process in the furnace, SiO contacts oxygen and is transformed into silicon dioxide (SiO_2,) which has a very fine spherical shape (Aïtcin 2016). Because of its high fineness, it is also called micro silica. The color of silica fume is whitish when a heat recovery system is in the furnace because high temperature (approximately 1500°F) burns all carbon traces. However, if a heat recovery system is not in the furnace, the color is gray due to low temperature (approximately 400°F). Carbon and iron contents also affect its color. El-Tawil et al. (2018) suggested that low carbon content is preferred to reduce water demand. ASTM C1240 (2015), *Standard Specification for Silica Fume Used in Cementitious Mixtures*, requires SiO_2 content of the silica fume to be more than 85 percent.

The proportion of silica fume in UHPC depends on a target *w*/*c*. Even though a high content of silica fume in UHPC improves durability and long-term strength, it increases water demand and decreases short-term strength (Van and Ludwig 2012). Therefore, the optimum proportion of silica fume should be based on targeted early and later age strengths with appropriate durability, as discussed in Sections 4.2.2.1 and 4.2.2.3. The material producer list for silica fume (TxDOT 2019) lists five silica fume suppliers that are pre-qualified in accordance with DMS-4630 (TxDOT 2016). One of these qualified silica fume suppliers was used to acquire silica fume, which has a median particle size of 2.9 micron, for the development of UHPC mixtures in Task 4. The particle size

distribution analysis showed that 10 percent of the silica fume particles are smaller than 1.0 micron, and 90 percent of the silica fume particles are smaller than 4.9 microns (Figure 4.3).

4.3.3 Fly Ash

Fly ash is the byproduct of the burning process of pulverized coal in power plants. Burnt impurities in the coal form a spherical shape to minimize their surface area when they are cooled down. Because fly ash is quenched rapidly within a short duration, the cooling time is not sufficient for fly ash to crystallize; thus, it transforms into a vitreous state and reacts with lime that results from hydration of cement as a pozzolanic material (Aïtcin 2016). Even though it is classified as a pozzolan, fly ash has a certain degree of cementitious properties. ASTM C618 (2019), *Standard Specification for Coal Fly Ash and Raw or Calcined Natural Pozzolan for Use in Concrete*, classifies fly ash into Class F and Class C. Class F fly ash has only pozzolanic properties with a very small amount of lime, while Class C fly ash has both pozzolanic properties and some cementitious properties with approximately 10 percent lime (Aïtcin 2016). In the United States, both Class C and Class F fly ashes are used widely, and based on the responses to the questionnaire, both are available in Texas. As a byproduct, partial replacement of cement with fly ash can reduce the carbon footprint; thus, the use of fly ash contributes to the sustainability of UHPC (Malhotra and Mehta 2012).

Numerous previous studies have shown that the use of fly ash in UHPC improves fresh and hardened properties and durability. Fly ash decreases both viscosity and yield stress in concrete by the ball-bearing effect, which increases workability (Mindess et al. 2003; Tattersall and Banfill 1983). For NSC, fly ash helps to increase long-term strength, while it influences negatively on early strength gain because it tends to retard C_3A hydration (Dhir et al. 1988). In the UHPC system, however, this same result may not be true because the appropriate proportion of fly ash can improve both early and later strength by increasing particle packing density, as mentioned in Section 4.2.2.3. One of the important benefits of fly ash is that it can reduce the shrinkage of UHPC and improve durability. As a filler, unreacted fly ash fills voids; thus, it restrains shrinkage and improves durability (Arezoumandi et al. 2014).

Moreover, the use of fly ash has a cost advantage. Wille and Boisvert-Cotulio (2015) showed that the cost of fly ash is less expensive than other SCMs such as silica powder, metakaolin, GGBFS,

and limestone powder. Based on its relatively low price, availability in Texas, and durability, Class F fly ash was selected for preliminary development of nonproprietary UHPC mixtures in Task 4. The fly ash used for development of preliminary UHPC mixes was sourced from one of the suppliers that is prequalified in accordance with DMS-4610 (TxDOT 2009). Figure 4.3 shows the results of particle size distribution analysis for fly ash used in this project. In summary, 10 percent of the fly ash particles are smaller than 2.3 micron, 90 percent of the particles are smaller than 12.7 micron, and the median particle size is 6.8 micron.

4.3.4 High-Range Water Reducer

A polycarboxylate-based superplasticizer was developed in the mid-1980s. This superplasticizer, also known as an HRWR, consist of three components, which are a backbone, grafted side chains, and carboxylic groups for adsorption. Its main characteristic that differs from other superplasticizers is the grafted side chains that provide steric repulsion (Mardani-Aghabaglou et al. 2013). Ran et al. (2009) studied the dispersion effect of the side chain length. The results showed that a polymer having long side chains disperses particles more efficiently than a polymer with short side chains.

The amount of an HRWR to fully cover cement surface is called saturation dosage (Nkinamubanzi and Aïtcin 2004). Even though less than the saturation dosage of an HRWR can have an appropriate spread from the flow table test, its spread value will sharply decrease over time. Thus, the optimum dose of an HRWR should be at least the saturation dosage to have a good slump life of 1–2 hours, and it should be less than the excessive dose in order not to cause retardation of cement hydration. However, it is difficult to know the saturation dosage of an HRWR without testing trial batches because different HRWR products have specific side chain lengths, and the performance of the HRWR depends on the combination of the HRWR and cement. In addition, the negative charge amount of carboxylic groups is also different between different products, which determines adsorption speed and affects turnover time (Hirschi and Wombacher 2008; Nkinamubanzi et al. 2016). Turnover is considered to occur when the paste reaches a good consistency. Therefore, trial batches to find an optimum dosage of an HRWR are necessary.

Two HRWRs were selected based on the TxDOT material producer list for chemical admixtures for concrete, DMS-4640 (TxDOT 2008; TxDOT 2019). As mentioned above, these two HRWRs have very different efficiencies; thus, each was used at different dosages in the UHPC mixes.

4.3.5 Sand

The source, maximum size, and gradation should be considered when selecting an appropriate sand. Most proprietary UHPCs use quartz sand (Wille et al. 2011). Quartz sand (also called silica sand) has a relatively small particle size with a spherical shape. From a quality control and quality assurance point of view, the use of quartz sand is beneficial for UHPC because it has very low impurities and a high SiO_2 content, normally higher than 95 percent (Kim 2018). However, quartz sand has a high cost in comparison to natural sand, which is more widely used in the concrete industry. Therefore, many researchers have studied the effect of natural sand on fresh and hardened properties of UHPC. Meng et al. (2016) studied the combination of Missouri river sand and masonry sand. Berry et al. (2017) studied masonry sand because this type of sand is standardized, according to ASTM C144 (2018), *Standard Specification for Aggregate for Masonry Mortar*, with appropriate particle size distribution. This standardization means that the use of masonry sand does not require extra time and effort for additional sieving work. Wille and Boisvert-Cotulio (2013) and Weldon et al. (2010) also used natural sand in nonproprietary UHPC mixes to reduce the cost.

The effect of using the maximum particle size of sand has been studied by many researchers. Collepardi et al. (1997) showed that substitution of coarse sand (maximum 0.3 in.) for fine sand (0.006–0.16 in.) does not affect the compressive strength significantly. However, it reduced flexural strength due to the lower bond strength between the steel fibers and the matrix (Collepardi et al. 1997). Wille and Boisvert-Cotulio (2013) compared properties of mixtures with sands having maximum particle sizes of 0.047 in. and 0.37 in., respectively. The mixtures with coarser sand have slightly lower spread values and 28-day compressive strengths. Weldon et al. (2010) also studied UHPC mixtures with a maximum sand size of 0.05 in. (#16 sieve) and 0.19 in. (#4 sieve) and found that the compressive strength decreased with an increase in the maximum sand size.

Based on material availability for sustainable and cost-effective UHPC, two river sands and one masonry sand were selected for developing the preliminary UHPC mixes in Task 4. Before using the sands in mixing, all sands were washed, oven-dried, and sieved to have a maximum particle

size of 0.05 in. The gradation of sand is critical for improved packing density. As discussed in Section 4.2.3.1., the A&A curve (Figure 4.4) was employed for optimum sand gradation. A minimum particle size of $D_{min} = 75\ \mu m$ (Sieve #200) and a distribution modulus $q = 0.22$ were adopted for developing the A&A curve. By sieving, the particle size distribution of all three sand types was adjusted to be between #16–#200 sieve (1180–75 µm, 0.047–0.003 in.). The particle size distribution of Sand-3 (Masonry) is coarser than the A&A curve throughout the entire sieve range. The particle size distributions of two river sands are closer to the A&A curve than masonry sand. However, all three sand types have a shortfall of fine particles within the range of 75–130 µm.

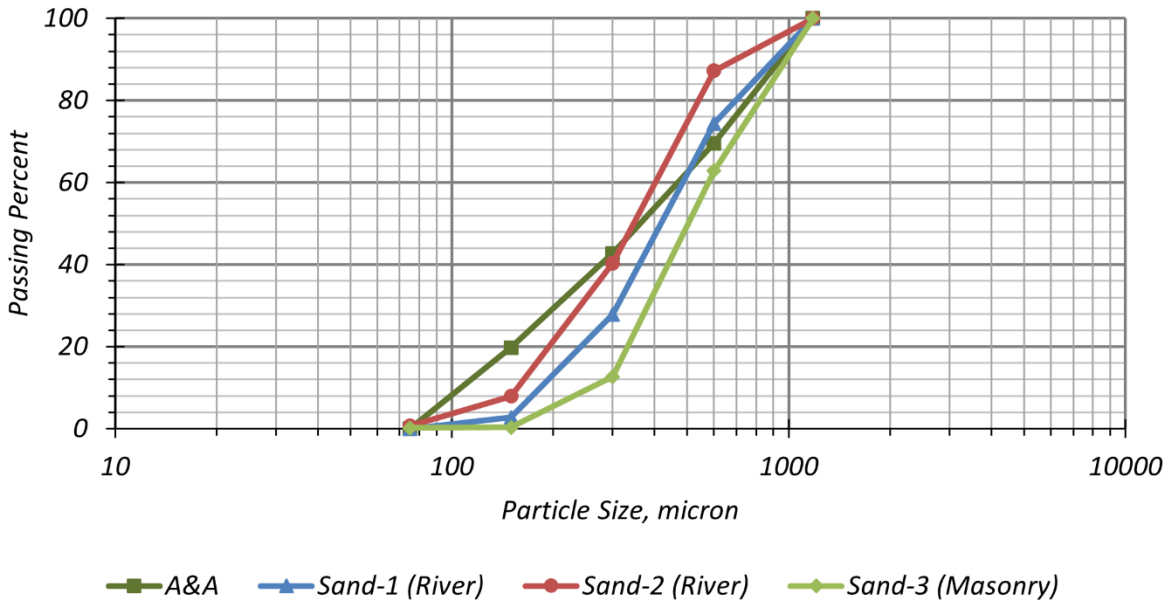

Figure 4.4. Particle Size Distribution of Considered Sands.

In addition to particle size distribution, particle geometries of these three sand types were identified using a microscope (Figure 4.5). The particle shapes of the three sands are subangular and/or rounded. Even though the shape of some particles is not ideal, like quartz sand, mixtures with these sands had acceptable workability and packing density. Despite their irregular particle shapes, these natural sands are acceptable to use for a UHPC mixture based on workability and packing density criteria, while they also provide an economic solution due to local availability.

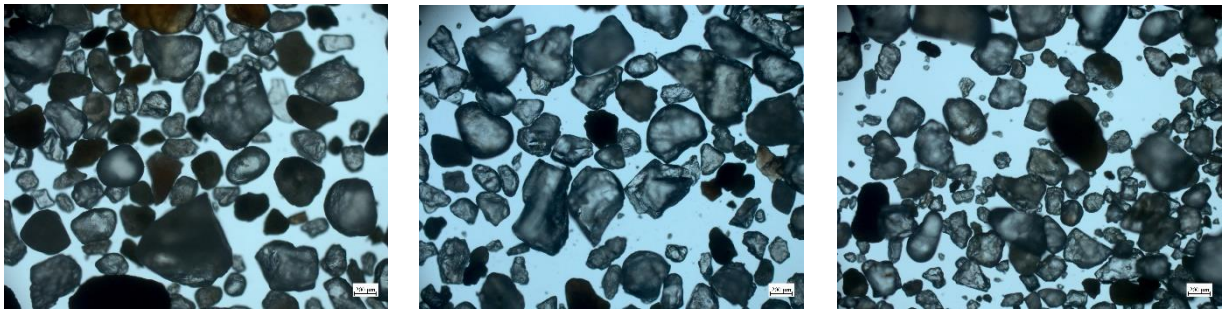

(a) Sand-1 *(b) Sand-2* *(c) Sand-3*

Figure 4.5. The Shape of Sand Particles.

4.3.6 Steel Fiber

The volume fraction of steel fibers for preliminary mixture development was selected based on the cost and impact on fresh and hardened properties of UHPC. Most proprietary UHPC mixes use a steel fiber volume of at least 2 percent. Haber et al. (2018) studied the performance of six commercial UHPC mixtures and found that the steel fiber volume fraction ranges from 2 percent to 4.5 percent. El-Tawil et al. (2018) and Wille and Boisvert-Cotulio (2013) reported that the cost of steel fiber with 1.5 percent by volume fraction accounts for 70.4 percent and 62.8 percent of the total mix cost, respectively. This cost analysis demonstrated that reducing the steel fiber volume is vital to developing an economical UHPC mixture. Therefore, numerous researchers have made an effort to reduce the steel fiber volume fraction in UHPC mixtures. Alkaysi and El-Tawil (2016) studied mechanical properties of UHPC with 0.5 percent, 1.0 percent, and 1.5 percent volume of steel fibers instead of 2.0 percent or more. Although compressive strength at 28 days, post-cracking tensile strength, and strain capacity increase as the volume of steel fibers increases, they concluded that 1.0 percent or 1.5 percent volume of steel fibers can reduce crack localization effectively under dead load and working conditions (Alkaysi and El-Tawil 2016).

Wille et al. (2011) studied the impact of the steel fibers on the workability of UHPC. They formulated a parameter called *fiber factor* to evaluate the effect of steel fibers on the workability of UHPC. The fiber factor is the product of the volume fraction and the aspect ratio of steel fiber, as shown in Equation (4.2). The aspect ratio of the steel fiber is length divided by diameter of the steel fiber.

$$\chi_f = V_f \times \frac{l_f}{d_f} \quad (4.2)$$

where:

χ_f = Fiber factor

V_f = Volume of steel fiber

l_f = Length of steel fiber

d_f = Diameter of steel fiber

Wille et al. (2011) suggested a maximum limit of the fiber factor at approximately 2.0. A fiber factor lower than 2.0 was found to not have a significant effect on the workability of UHPC.

The most commonly used fiber type for UHPC is straight steel fibers with a length of 0.5 in. and diameter of 0.008 in. Therefore, this type of short straight steel fiber with a 1.5 percent volume fraction was used in this project to develop the preliminary UHPC mixtures. Because the corresponding fiber factor is 0.975, workability may not be affected significantly by the steel fibers. The volume of steel fibers was selected based on the developed UHPC mixture performance, especially with respect to tensile and flexural behavior. Section 4.7 discusses the experimental study to evaluate the steel fiber volume.

4.4 MIXING PROCEDURE

The consistency of fresh UHPC is crucial for achieving ideal fresh and hardened properties. As such, the primary role of mixing is to achieve good homogeneity of UHPC without agglomerates. Excessively extended mixing time compared to NSC may reduce the workable time to place the UHPC. Therefore, the mixing procedure should be optimized to obtain the desired homogeneity of UHPC within an appropriate mixing time. Generally, common mixing steps of proprietary and nonproprietary UHPC are composed of three parts: (1) mixing dry powder, (2) adding and mixing liquids such as water and admixtures, and (3) adding and mixing steel fibers (Haber et al. 2018). Especially in the second part, various UHPC mixing procedures use unique methods for adding superplasticizer and water to maximize the dispersion effect. Mixing time, which is the required time to achieve a fluid-like paste with good homogeneity, depends on the power of a mixer, the adsorption speed of the superplasticizer, and the amount of fine particles (Mazanec and Schießl 2008). This section summarizes common mixing procedures used for proprietary and

nonproprietary UHPC mixtures and presents an optimized mixing procedure used for this study to develop preliminary UHPC mixtures in Task 4.

4.4.1 Mixing Procedures Used for Proprietary UHPC Mixes

The common mixing sequence for proprietary UHPCs gives insight on key steps for achieving consistency in the mix. Haber et al. (2018) studied six commercial UHPCs. Generally, those UHPCs perform dry mixing for a maximum of 2 minutes and then add and mix water and an HRWR slowly for 1–2 minutes. After adding liquids, additional mixing time varies from 6–8 minutes. During this additional mixing, the matrix generally achieves desired consistency. Next, steel fibers are introduced over 2–3 minutes. Mixing is then continued for an additional 1–5.5 minutes. The total mixing time with a maximum 4 ft^3 volume ranges between 12.5–17 minutes in the lab. Even though mixing time varies, all mixing procedures have three main steps in common, which are dry mixing, the slow addition of water and an HRWR, and the addition of steel fibers after achieving homogeneity of the matrix. Note that the dry mixing time of proprietary UHPC is relatively shorter than nonproprietary UHPC because its fine materials are already blended and packaged in the bag. In cases of nonproprietary UHPC, dry mixing generally last about 3–5 minutes. Mixing procedures of many nonproprietary UHPC mixtures keep the key steps mentioned above along with some additional considerations to improve mixing quality.

4.4.2 Mixing Procedures Used for Nonproprietary UHPC Mixes

The common first step of the mixing procedure for nonproprietary UHPCs is dry mixing of all solid materials. One exception noted in a study by de Larrard and Sedran (1994) suggested dry mixing all solid materials except cement. El-Tawil et al. (2018) modified the dry mixing step by splitting sand addition to reduce the power demand of the mixer. The next step is the addition of water and an HRWR, which varies between different nonproprietary mixes.

Tue et al. (2008) conducted an experiment to find the most efficient time interval between water and an HRWR addition. They classified HRWR addition methods into three categories: the direct addition, the stepwise addition, and the delayed addition. For the direct addition, all the HRWR is added at once with water. In the stepwise addition, some of the HRWR is added first with water, and the remaining HRWR is added with or without water after a specific time. In the delayed

addition, the HRWR is added a specific time after adding water. Tue et al. (2008) investigated the efficiency of these three HRWR addition methods. Immediately after cement particles contact water, the surface of the cement particles is hydrated. Although the backbone of a polycarboxylate-based superplasticizer is adsorbed onto the hydrated surface and is soon buried by hydrates, its long side chains still can disperse particles by steric repulsion (Figure 4.6). However, this dispersion effect may diminish gradually as hydrates grow, and finally it will lose the dispersion effect when the thickness of hydrates is larger than side chain length. The authors concluded that the stepwise and the delayed additions are more efficient ways for slump flow and slump life. The results indicated that the slump flow increases as the time between the first addition of all water and the partial HRWR and the second addition of HRWR increases up to 2 minutes.

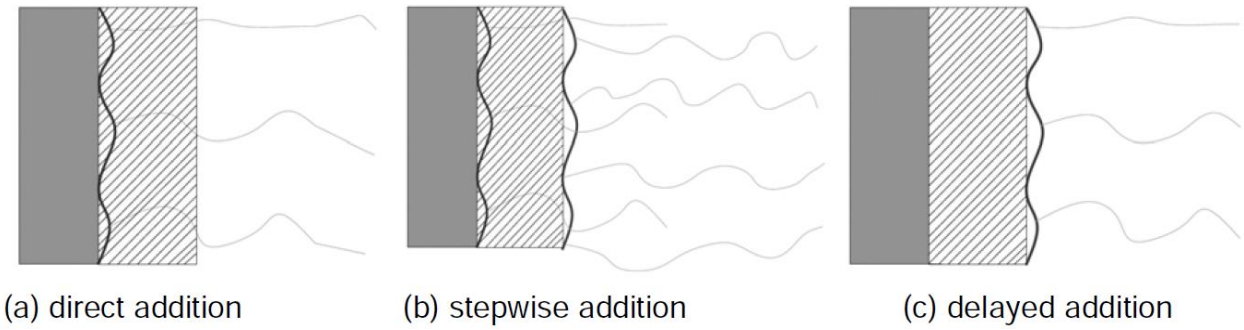

Figure 4.6. Three HRWR Addition Methods (Tue et al. 2008).

The method of water addition is categorized into split or all at once. Generally, an HRWR is blended with some water for better initial physical dispersion of the HRWR at the laboratory. However, there is a limitation to the use of blending an HRWR with water prior to adding them to a mixer at a precast plant because an automated material addition system in a precast plant generally has separate hoses for water and the HRWR.

Mazanec and Schießl (2008) studied the required power of a mixer during mixing. They indicated that the power demand is sharply increased when water is added, and the power demand is very quickly decreased after reaching a peak power demand because the consistency of the mixture increases as mixing continues and the HRWR increases the flowability. It was concluded that the required capacity of a mixer can be decreased by reducing peak power demand after the water addition.

El-Tawil et al. (2018) introduced the split sand addition to mitigate the peak power demand of a mixer by adding half of the sand after a certain time. Initially, their original mixing protocol developed in their laboratory did not include the split sand addition. However, the quality of fresh UHPC mixed in the field was not adequate due to the insufficient power capacity of the mixer. Therefore, the mixing protocol was revised based on their field experience and the research results of de Larrard and Sedran (1994). In the final version of their mixing procedure, half of the sand is added after turnover. The later added sands also help to break apart agglomerates (El-Tawil et al. 2018).

4.4.3 Mixing Procedure in the Laboratory

Based on the findings of other researchers from the literature and trial mixes developed as part of this research study, a mixing procedure for laboratory mixing was developed to maximize mixing efficiency by fully using the dispersion effect of a superplasticizer and by reducing the power demand of the mixer. The effectiveness of a superplasticizer can be achieved by controlling the quantity and time interval of adding water and the superplasticizer. The power demand of the mixer can be reduced by adjusting the sand addition step. This mixing procedure was used for preliminary UHPC mixture development, and the mixing sequences are described as follows:

1. Dry mixing (cement, silica fume, fly ash, and half of sand) for 5 minutes
2. Slow addition of 80 percent of the water and mixing for 2 minutes
3. Slow addition of the HRWR and the remaining water blend and mixing for 4 minutes
4. Slow addition of the remaining sand and mixing for 5 minutes
5. Slow addition of steel fibers and mixing for additional 5 minutes

A 1.9 ft^3 planetary high shear mixer, Sicoma MP75 Lab Mixer, was used in the laboratory for this project. Less than 70 percent of the volume capacity was used for developing UHPC mixtures to ensure a sufficient power supply for mixing.

4.5 DEVELOPMENT OF UHPC MIXTURES

The constituent materials of RPC, the first developed UHPC, were proportioned by cement weight—unlike CC, which is designed with the volumetric proportioning method recommended by ACI 211.1-91 (1991), *Standard Practice for Selecting Proportions for Normal, Heavyweight,*

and Mass Concrete (Richard and Cheyrezy 1995). After developing RPC, several researchers have used the proportioning method by cement weight to find an optimum ratio of constituent materials (Alkaysi and El-Tawil 2016; Alsalman et al. 2017; Berry et al. 2017; El-Tawil et al. 2018; Kim 2018; Wille et al. 2011), but some researchers have developed UHPC mixtures with the proportioning method by volume (Arora et al. 2018; Khayat and Valipour 2018; Meng et al. 2016; Soliman and Tagnit-Hamou 2017). In Task 4, both methods were used for development of UHPC mixtures: Mix-1 and Mix-2 were developed with the proportioning method by cement weight; Mix-3 and Mix-4 were developed with the volumetric design method. Each developed mixture was designed to have a specific target range of early compressive strength. The developed UHPC mixtures were evaluated by three properties, which are flow spread, time of set, and compressive strength for initial screening. Testing methods for UHPC are modified by ASTM C1856 (2017). Chapter 3 discusses the testing procedures and the modifications from testing methods for NSC. Table 4.5 shows the mixture designs and achieved ranges of properties for the four developed UHPC mixtures with Type I/II cement. After developing the mixtures with Type I/II cement, a companion set of mixtures using Type III was developed. Appropriate modifications of water and HRWR contents due to the higher water demand of Type III cement were applied for the mixtures with Type III cement to maintain the desired workability.

Table 4.5. Summary of Developed UHPC Mixtures with Type I/II Cement.

Description	**Mix-1a**	**Mix-2a**	**Mix-3a**	**Mix-4a**
Cement	1445	1238	1579	1528
Silica fume	217	186	63	115
Fly ash	72	310	121	159
Sand	1671	1662	1715	1647
Water	329	312	320	320
HRWR	27	24	26	27
Steel fiber, %	1.5	1.5	1.5	1.5
Spread, in.	8.4–9.7	9.5–10.8	10.4–11.9	11.0–11.1
$f'_{c\,1-d}$, ksi	10.5–11.6	9.1–10.2	13.1–14.0	13.2–13.6
f'_c, ksi	16.1–17.6	16.1–18.2	17.9–21.0	19.9
Initial set	5h 45m	6h 00m	6h 30m	6h 00m
Final set	8h 30m	9h 30m	9h 30m	9h 20m

Notes:
1. Unit is lb/yd^3 unless otherwise noted.
2. 0.5 in. long, 0.008 in. diameter straight steel fibers are used.

The following subsections discuss the development history of each mixture and test results. A comparative study was then conducted to evaluate the differences between Type I/II and Type III cements in achieving target properties for precast prestressed UHPC girder applications. The developed mixtures are named Mix-1a, Mix-1b, Mix-2a, Mix-2b, Mix-3a, Mix-3b, Mix-4a, and Mix-4b. The letters "a" and "b" denote Type I/II cement and Type III cement, respectively.

4.5.1 Proportioning Method by Cement Weight

The weight proportion method was used to find the optimum proportions of constituents for Mix-1a and Mix-2a.

4.5.1.1 Development of Mix-1

4.5.1.1.1 Proportioning Mix-1 with Type I/II Cement

The first step to develop a UHPC mixture based on the weight proportion method is to determine the amount of cement because cement content was found to be the governing factor for achieving high early strength (Arora et al. 2018). The design guideline for field-cast UHPC connections published by FHWA recommended a compressive strength of $0.65\,f_c'$ prior to introducing sustained loads to minimize creep, which is approximately 14 ksi when the design compressive strength is $f_c' = 22$ ksi as per the definition of UHPC (Graybeal 2019). In addition to strength, the current practice is to demold a precast concrete member from a casting bed within 16 hours. The results of the questionnaire from this project indicated that two Texas precasters prefer to release prestressing within 24 hours, while another would consider extending the prestressing release time to more than 24 hours. By considering the above requirements, the initial target compressive strength was determined to be 14 ksi at 1 day without heat treatment. However, based on previous research to develop nonproprietary UHPC mixtures for DOT applications (summarized in Table 4.6), obtaining a 1-day compressive strength greater than 10 ksi without any heat treatment or use of an accelerator agent has rarely been achieved.

Table 4.6. UHPC Mixtures Developed by Other State DOTs.

Sponsor	New Mexico	Montana	Colorado	Michigan	Missouri
Reference	Weldon et al. (2010)	Berry et al. (2017)	Kim (2018)	El-Tawil et al. (2018)	Khayat and Valipour (2018)
Cement (Type)	1264 (I/II)	1300 (I/II)	1517 (III)	650 (I)	1117 (III)
Silica fume	158	273	280	327	71
Fly ash	158	364	0	0	619
GGBFS	0	0	0	650	0
Silica powder	0	0	512	0	0
Sand	1900	1820	1582	1975	1704
HRWR	71	59	35	39	20
Water	221	312	334	286	288
Steel fiber, %	1.5	1.5	2.0	1.5	1.5
$f'_{c,1-d}$, ksi	9.0	N/A	N/A	N/A	9.4
$f'_{c,28-d}$, ksi	21.0	19.2	21.5	21.5	18.0

Notes:
1. Unit is lb/yd^3 unless otherwise noted.
2. All strength data are not heat-treated.
3. GGBFS: Ground-granulated blast-furnace slag.

As mentioned in Section 4.2.2.1, the use of a low *w*/*c* and maintaining an optimum fineness of the cementitious materials are important to achieve early strength. The use of a relatively higher cement content along with maintaining a lower *w*/*c* and lower silica fume content (discussed in Section 4.2.2.1) was found to be effective to achieve high early strength. For example, the use of 1428 lb/yd^3 Type I cement with a total binder content of 1700 lb/yd^3 (95 percent cement and 5 percent silica fume) was found to be adequate to maintain both early (e.g., 1-day compressive strength of 10.6 ksi) and later strength requirements (Alsalman et al. 2017). Based on this study, a cement content of 1500 lb/yd^3 was considered as an initial base cement content for this project, which was subsequently optimized through a detailed evaluation.

The most commonly used proportion of silica fume is 0.25 or more by cement weight (Ahlborn et al. 2008; El-Tawil et al. 2018; Richard and Cheyrezy 1995; Sbia et al. 2017; Soliman and Tagnit-Hamou 2017; Wille et al. 2011). In order to consume all available portlandite through pozzolanic reaction, a silica fume proportion ≥ 0.25 is needed for a cement paste with *w*/*c* ≥ 0.42 (Richard and Cheyrezy 1995). Since the UHPC system uses a low *w*/*c* (generally provides 50 percent hydration corresponding to consumption of half of 0.25 silica fume through pozzolanic reaction), it is unlikely that all silica fume of the 0.25 proportion will be consumed by pozzolanic reaction. However, the unreacted silica fume portion contributes dense packing through a filler effect.

Therefore, the combined effects of pozzolanic reaction and filler effects ensure the maximum benefit of using a 0.25 silica fume proportion in UHPC. Because a 0.25 silica fume proportion is on the relatively higher side, it generally causes a reduction of early strength due to its high water demand, as discussed in Section 4.2.2.1. Alsalman et al. (2017) reported that an increase in silica fume proportion greater than 0.1 did not notably increase the 28-day compressive strength, whereas an increase in silica fume proportion up to 0.1 significantly improved the 28-day compressive strength. Therefore, determining an optimum silica fume content is needed to obtain optimum pozzolanic and filler effects and achieve desired levels of both 1- and 28-day compressive strengths. Lowering the silica fume proportion (e.g., below 0.25) gives an additional benefit of lowering the shrinkage. An increase in autogenous shrinkage due to the use of a larger proportion of silica fume was reported in the literature (Karim et al. 2019). In addition, even though a large amount of silica fume such as a 0.25 proportion can be reacted by heat treatment, a UHPC mixture without heat treatment may use a limited amount of silica fume as a pozzolanic reaction (Kang et al. 2017). As a result, a silica fume proportion of 0.15 was adopted as a base proportion for developing Mix-1.

Replacement of cement with fly ash is a widely used approach to develop cost-effective, eco-friendly, and sustainable UHPC that contributes to long-term compressive strength and durability. However, lower early strength due to slower hydration is a common limitation of fly ash addition (Alsalman et al. 2017; Amen 2011). To avoid lower strength gain at early ages, a 0.05 fly ash proportion by cement weight was selected as an initial trial. However, different fly ash replacement levels (more than 0.05) were investigated in the development of subsequent mixes (i.e., Mix-2, Mix-3, and Mix-4) to explore the benefits of reducing viscosity and improving packing density, as explained in Section 4.2.1.2. Packing density improved when sand was replaced by the selected level of fly ash replacement while developing Mix-3.

The recommended sand proportion (sand/cement by weight) range from other studies is between 1.1 and 1.4 (Park et al. 2008; Richard and Cheyrezy 1995; Wille et al. 2011). Through trial batches, an appropriate sand proportion was determined to be 1.2, whereas more than a 1.2 sand proportion decreased workability. A 1.5 percent steel fiber volume fraction was used for all developed mixtures. Section 4.7 discusses the impact of steel fiber content to tensile strength that was investigated as part of Task 5.

The values of *w*/*c* and a ratio of HRWR to cement (*HRWR*/*c*) were optimized through trial batches. Initially two different HRWR products (HRWR-1 and HRWR-2) were used to explore their performance. The water reduction performance and adsorption speed of HRWR-1 were not sufficient for UHPC; thus, HRWR-2 was used to develop all mixtures. The optimization of *w*/*c* and *HRWR*/*c* proportions was conducted using the following steps:

1. A base *w*/*c* that was expected to provide the targeted spread value (9–11 in.) was selected, or a *w*/*c* was selected based on information from literature related to development of nonproprietary UHPC mixes.
2. Several *HRWR*/*c* were explored to find an optimum *HRWR*/*c* meeting the target spread range between 9–11 in. through trial and error.
3. The *w*/*c* and *HRWR*/*c* were evaluated based on the spread value and 1-day compressive strength.
4. The 28-day compression strength test was conducted for mixes having acceptable spread value and 1-day compressive strength.

Table 4.7 shows the results of the initial trial batches for this parametric study. The compressive strength values were obtained using neoprene caps at both ends of the cylinder specimens (prior to having a cylinder end grinder in the laboratory). B7 was tested to check repeatability and obtain 28-day compressive strength.

Table 4.7. Example of Optimization Procedure for *w*/*c* and *HRWR*/*c*.

Batch No.	*w*/*c*	*HRWR*/*c*	Spread, in.	$f'_{c\,1-d}$, ksi	f'_c, ksi
B1	0.21	0.030	> 10[1]	3.5[2]	N/A
B2	0.21	0.020	> 10[1]	3.0[2]	N/A
B3	0.21	0.015	6.8	> 7.4[3]	N/A
B4	0.22	0.015	6.2	> 7.4[3]	N/A
B5	0.22	0.017	> 10[1]	7	N/A
B6	0.22	0.016	8.8	10.4	N/A
B7	0.22	0.016	9.7	9.8	19.6

Notes:
1. The diameter of a flow table as per ASTM C230 (2014) is 10 in.
2. These results show the retardation of hydration due to overdose of HRWR.
3. Compressive strength more than 7.4 ksi could not be captured due to a capacity limit of the test device.
4. Compression specimens are 3 × 6 in. cylinders tested with neoprene pads.

Table 4.8 shows the design of the first version of Mix-1a with C-1 cement. Even though this initial mixture achieved the target spread and acceptable 1-day compressive strength, the total volume was not accurately proportioned for 1 cyd because the first version of Mix-1a was designed based on the material proportions by cement weight recommended from other researchers, as mentioned above. Therefore, the weight of constituent materials was corrected using the bulk specific gravity (BSG) of materials while keeping the proportions of materials the same. Table 4.9 shows the BSG values for constituent materials. In addition, C-2 cement was more effective for achieving high early strength in comparison to C-1 cement due to a higher C_3S content (Table 4.4). Because C_3S immediately reacts with water upon contact, the water demand of C-2 cement is somewhat higher than C-1 cement. Therefore, water and HRWR contents were increased to satisfy the target workability. As a result, the second version of Mix-1a with Cement C-2 has a higher 1-day compressive strength (Table 4.8).

Another improved variation of Mix-1a was developed based on the observations from a larger volume batch. An increase in batch volume tends to decrease the spread value and compressive strength. It was anticipated that the inadequate mixer power, insufficient robustness of the mixture due to the low *w*/*c*, and inadequate thickness of paste covering sand particles were the main reasons for this reduction in spread value and compressive strength. Even though the simplest way to resolve this issue is to increase water content, increasing *w*/*c* can retard strength gain. Therefore, the ratio of paste-to-sand by volume, (V_p/V_s), was increased. Paste includes cement, silica fume, fly ash, water, and HRWR in this ratio calculation. The value of V_p/V_s for the first and second versions of Mix-1a was 0.900, and the ratio of the third version of Mix-1a was increased to 0.936. After this adjustment, the mixture design for the third version of Mix-1a is shown in Table 4.8.

Table 4.8. Development History of Mix-1a with C-1 and C-2.

Description	First version with C-1		Second version with C-2		Third version with C-2	
	Proportion	lb/yd^3	Proportion	lb/yd^3	Proportion	lb/yd^3
Cement	1	1500	1	1422	1	1445
Silica fume	0.15	225	0.15	213	0.15	217
Fly ash	0.05	75	0.05	71	0.05	72
Sand	1.20	1800	1.20	1710	1.16	1671
Water	0.220	330	0.228	324	0.228	329
HRWR	0.016	24	0.019	26	0.019	27
Steel fiber	1.5%	200	1.5%	200	1.5%	200
V_p/V_s	0.900		0.900		0.936	
Spread, in.	9.7		8.8		9.6	
$f'_{c\,1-d}$	9.8 ksi		11.1 ksi		11.6 ksi	

Table 4.9. BSG of Materials Used in UHPC Mixtures.

Cement	Silica fume	Fly ash	Sand	Water	HRWR
3.14	2.2	2.3	2.65	1	1.08

Note: BSG of sand is oven-dried condition.

Several trial batches were repeated to check repeatability and the range of test results for Mix-1a (third version with C-2) (Table 4.10). The ranges of spread values and 1-day compressive strengths are 8.4–9.6 in. and 10.7–11.6 ksi, respectively.

Table 4.10. Trial Batch Results of Mix-1a to Check Repeatability.

Batch No.	Spread, in.	$f'_{c\,1-d}$, ksi	f'_c, ksi	Volume, ft^3
B1	8.4	10.7	N/A	0.56
B2	8.8	11.4	N/A	0.56
B3	9.6	11.6	16.1	0.51
B4	8.6	11.4	17.6	0.40

4.5.1.1.2 Mix-1 with Type III Cement

Type III cement (C-3) was employed to determine the benefit of early strength gain. While keeping the same proportions of silica fume, fly ash, and sand by cement weight, water and HRWR contents were optimized to achieve the desired spread value (achieved 9.9–10.6 in.). The mixture designs of Mix-1a and Mix-1b are compared in Table 4.11 together with their corresponding spread values and setting times. Figure 4.7 shows compressive strength development over time for Mix-1a and Mix-1b. The test specimens were 3 × 6 in. cylinders with end preparation accomplished by using the grinder.

Table 4.11. Mixture Design of Mix-1a and Mix-1b.

Description	Mix-1a (Type I/II)		Mix-1b (Type III)	
	Proportion	lb/yd^3	Proportion	lb/yd^3
Cement	1	1445	1	1397
Silica fume	0.15	217	0.15	210
Fly ash	0.05	72	0.05	70
Sand	1.16	1671	1.16	1615
Water	0.228	329	0.258	360
HRWR	0.019	27	0.026	37
Steel fiber	1.5%	200	1.5%	200
Spread, in.	8.6		10.6	
Initial setting time	5h 45m		4h 40m	
Final setting time	8h 30m		9h 00m	

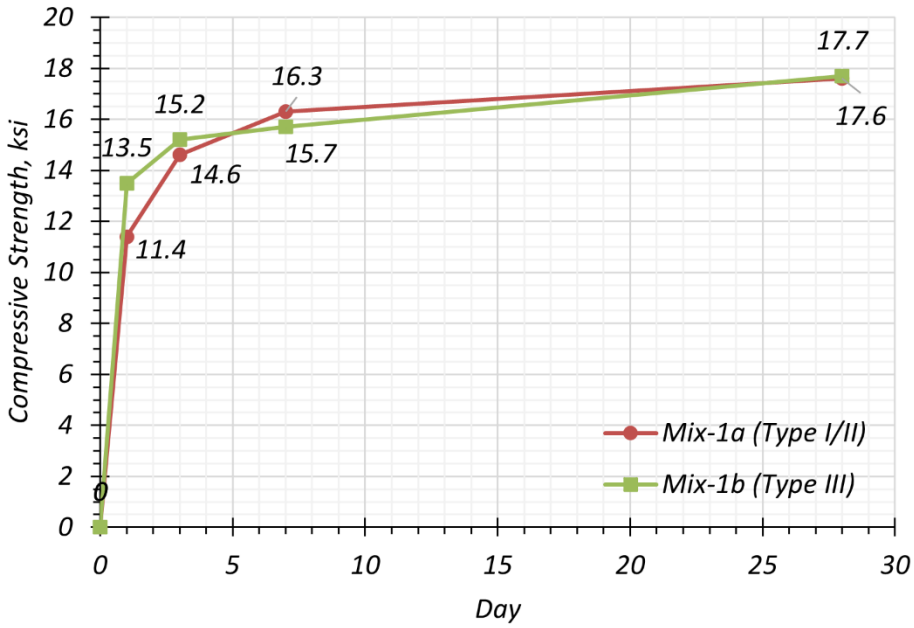

Figure 4.7. Compression Test Results for Mix-1a and Mix-1b.

Setting time results of both Mix-1a and Mix-1b are in the appropriate range based on results provided for proprietary UHPCs by Haber et al. (2018), which are 4.3–8 hours for initial set and 7–10.1 hours for final set. The 1-day compressive strength of Mix-1a, 11.4 ksi, satisfies $f'_{c,1-d} \geq 0.65\, f'_c$, which is the recommended strength prior to applying sustained loads to minimize creep. In the case of Mix-1b, although it achieved a higher 1-day compressive strength of 13.5 ksi due to high reactivity as a result of combined effects of high fineness and C_3S content, the 28-day compressive strengths of both mixtures are similar. A relatively lower rate of strength gain from 1

day to 28 days for Mix-1b can be attributed to two reasons. First, the 55 percent C_3S content of Cement C-3 (Type III cement) is actually lower than the 65 percent C_3S content for Cement C-2 (Type I/II cement) (Table 4.4). This result is unexpected, although the fineness of Type III cement is typically higher than for Type I/II cement. It seems the lower C_3S content in the Type III cement resulted in a lower rate of strength gain for Mix-1b as compared to Mix-1a. The second reason is the liquid volumes (water + HRWR) of Mix-1a and Mix-1b are 21.0 percent and 23.4 percent, respectively. Thus, Mix-1b may have a higher porosity than Mix-1a. Although the higher spread value of Mix-1b is favorable to reduce air voids, the higher liquid volume seems to cancel this favorable effect. Mix-1b also satisfied $f'_{c,1-d} \geq 0.65\, f'_c$.

Another UHPC mix (Mix-2) was developed by manipulating Mix-1 based on the experience gained on workability and strength development while developing Mix-1. The cement content of Mix-1a and Mix-1b is relatively high compared to other published mixtures from DOT studies (Table 4.6). Other DOTs may have provided less emphasis on high early strength gain because their studies were not related to developing mixes for precast, pretensioned girder applications. However, UHPC with a lower cement content may be a good option for reducing the cost. Mix-2 was designed to study the possibility of reducing the cement content while still achieving satisfactory strength (i.e., 12–14 ksi compressive strength at 1 day). The details for Mix-2 development are provided below.

4.5.1.2 Development of Mix-2

4.5.1.2.1 Proportioning Mix-2 with Type I/II Cement

Mix-2a was developed by replacing a portion of the cement in Mix-1a with fly ash while maintaining a similar total weight of cementitious materials of the first version of Mix-1a, which is 1800 lb/yd^3. As a result, the fly ash proportion was increased from 0.05 to 0.25, whereas the amount of cement was decreased from 1500 lb/yd^3 to 1300 lb/yd^3. The proportion of silica fume was maintained to provide sufficient particle packing density and a pozzolanic reaction. The amount of sand was also kept at a similar level as Mix-1a. The *w*/*c* and *HRWR*/*c* were optimized to achieve the target workability using the same procedure as Mix-1a. The second version of Mix-2a was tuned due to the change of cement from C-1 to C-2 with a volume correction using BSG. The third version of Mix-2a was adjusted to increase V_p/V_s from 0.940 to 0.978 to increase the

thickness of paste covering the sand particles. Table 4.12 lists the material proportions for all three versions of Mix-2a. The repeatability of the final version (third version) of Mix 2a was investigated as summarized in Table 4.13.

Table 4.12. Development History of Mix-2a with C-1 and C-2.

Description	First version with C-1		Second version with C-2		Third version with C-2	
	Proportion	lb/yd^3	Proportion	lb/yd^3	Proportion	lb/yd^3
Cement	1	1300	1	1219	1	1238
Silica fume	0.15	195	0.15	183	0.15	186
Fly ash	0.25	325	0.25	305	0.25	310
Sand	1.40	1820	1.40	1702	1.34	1662
Water	0.235	306	0.252	307	0.252	312
HRWR	0.016	21	0.020	24	0.020	24
Steel fiber	1.5%	200	1.5%	200	1.5%	200
Spread, in.	9.8		9.8		9.5	
V_p/V_s	0.940		0.940		0.978	
$f'_{c\,1-d}$	9.0 ksi		10.3 ksi		10.2 ksi	

Table 4.13. Trial Batch Results of Mix-2a to Check Repeatability.

Batch No.	Spread, in.	$f'_{c\,1-d}$, ksi	f'_c, ksi	Volume, ft^3
B1	9.5	10.2	16.1	0.51
B2	9.8	10.1	17.0	0.40

4.5.1.2.2 Mix-2 with Type III Cement

Mix-2b with Cement C-3 (Type III cement) was developed using the same procedure as Mix-1b. The mixture designs of Mix-2a and Mix-2b are provided in Table 4.14 together with their corresponding spread values and setting times. Figure 4.8 shows compressive strength development over time for Mix-2a and Mix-2b. The ratio $f'_{c,1-d}/f'_c$ of Mix-2a and Mix-2b are 0.59 and 0.66, respectively. Mix-2a may need more time to achieve 0.65 f'_c for release of prestressing. Setting time results of Mix-2a and Mix-2b also are similar with Mix-1a and Mix-1b, which are in the acceptable range in comparison with proprietary UHPCs. Compressive strength results of Mix-2a and Mix-2b are relatively lower than Mix-1a and Mix-1b due to lower cement content. If heat curing is available (a more common practice in other states), Mix-2, with a relatively lower cement content, can provide the target high early strength. The explanations for relatively lower rate of strength gain from 1 day to 28 days that were provided for Mix-1a and Mix-1b earlier are also applicable for Mix-2a and Mix-2b.

Table 4.14. Mixture Design of Mix-2a and Mix-2b.

Description	Mix-2a (Type I/II)		Mix-2b (Type III)	
	Proportion	lb/yd^3	Proportion	lb/yd^3
Cement	1	1238	1	1206
Silica fume	0.15	186	0.15	181
Fly ash	0.25	310	0.25	302
Sand	1.34	1662	1.34	1619
Water	0.252	312	0.280	338
HRWR	0.020	24	0.027	32
Steel fiber	1.5%	200	1.5%	200
Spread, in.	9.8		8.1	
Initial setting time	6h 00m		5h 15m	
Final setting time	9h 30m		9h 30m	

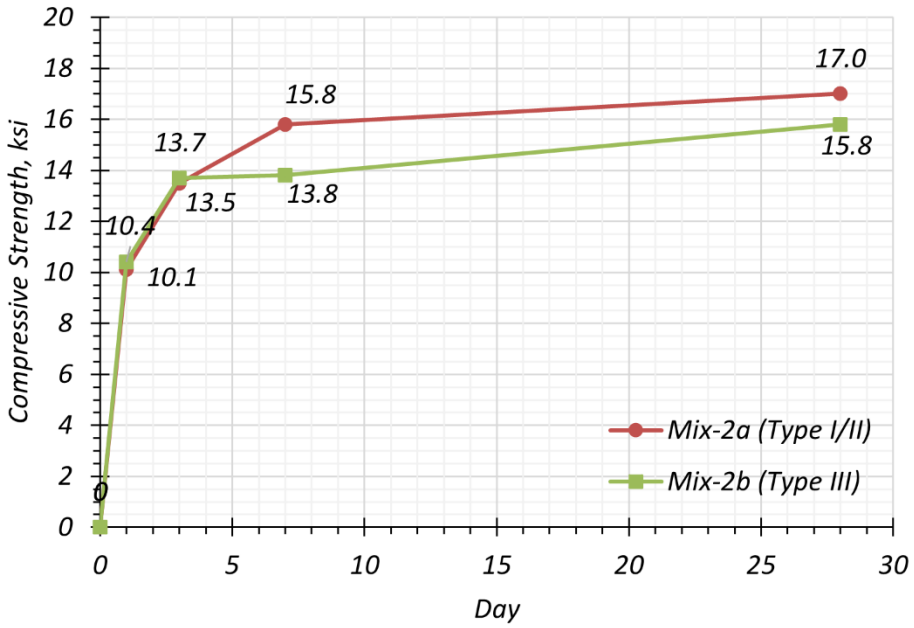

Figure 4.8. Compression Test Results for Mix-2a and Mix-2b.

4.5.2 Proportioning Method by Volume

Proportioning materials by cement weight is a convenient way to find appropriate proportions as a parametric study. However, this method cannot capture the effect from the change of volume fraction of each material. For example, if the silica fume proportion is increased from 0.1 to 0.2 while keeping cement and SCM contents constant, it reduces the volume fraction of sand in the mix. Therefore, it is difficult to understand whether the higher silica fume proportion or the higher volumetric paste to sand ratio affects the results. The proportioning method by volume is a good

approach to investigate the optimum volume fraction of constituents. Meng et al. (2016) proposed a systematic procedure for this method as follows:

1. Select cementitious materials.
2. Select initial *w*/*cm*.
3. Find optimum paste-to-sand ratio.
4. Determine volume of steel fiber.
5. Optimize water content and HRWR content based on test results.

Mix-3 and Mix-4 were developed following this procedure with appropriate modifications and an additional paste proportion study. The main objective of Mix-3 was to achieve high early strength, up to 14 ksi, without application of any heat treatment. The following subsections discuss the development history of Mix-3.

4.5.2.1 Development of Mix-3

4.5.2.1.1 Parametric Study for Paste Proportioning

Prior to developing Mix-3, a parametric study was conducted to identify ideal material proportions of the paste for early strength gain. As discussed in Section 4.2.2.1, one key factor to achieve high early strength is to minimize water content. Even though water demand of silica fume is high due to its high fineness, a certain amount of silica fume increases early strength since it improves packing density. Therefore, the first step of the paste proportioning study was to find an optimum silica fume proportion. Meng et al. (2016) studied four pastes composed of cement and silica fume with the same water content (Table 4.15). Even though the HRWR demand and 28-day compressive strength of the four cases are not significantly different, a certain amount of silica fume content was found to be beneficial for 1-day compressive strength. The 1-day compressive strength increased with an increase in silica fume volume fraction up to 5 percent, but more than 5 percent silica fume volume (5 to 11 percent) did not provide additional strength gain. Conversely, a slight reduction in 1-day compressive strength (13.9 to 12.9 ksi) was noticed. This result is due to filling or loosening effects of silica fume depending on its proportion, as discussed in Section 4.2.1.2. Hermann et al. (2016) showed that appropriate silica fume content improves packing density due to filler effect. In addition, SCM can accelerate the early hydration reaction by

providing an additional place for nucleation of early CSH (Thomas et al. 2012). Thus, it can contribute to early strength gain. However, an overdose of silica fume can push cement particles away from each other, thereby causing larger volumes between cement particles. Based on these results, the paste proportion study for developing Mix-3 began with 5 percent silica fume volume fraction in a paste.

Table 4.15. Effect of Silica Fume Volume Fraction on Paste Compressive Strength (Meng et al. 2016).

Case No.	Cement, %	Silica fume, %	*HRWR*/*cm*	$f'_{c\,1-d}$, ksi	f'_c, ksi
Case 1	100	0	0.76	6.6	20.3
Case 2	95	5	0.74	13.9	20.0
Case 3	92	8	0.77	13.5	19.7
Case 4	89	11	0.76	12.9	19.2

The next step was to find an appropriate portion of replacement of cement with fly ash. Even though high cement content is helpful for early strength gain, adding fly ash into a paste improves workability by reducing viscosity. As a result, *w*/*c* can be decreased, which is beneficial for high early strength. In addition, substituting fly ash for cement also reduces shrinkage because of low capillary pores as a result of low *w*/*cm*. Table 4.16 shows a total of four proportion cases studied. The *w*/*cm* and *HRWR*/*cm* were optimized through trial batches with the following procedure:

1. The initial *w*/*cm* and *HRWR*/*cm* were used.
2. The *HRWR*/*cm* was increased to achieve a 14.5 in. spread value.
3. After achieving a 14.5 in. spread, the *w*/*cm* was decreased.
4. Steps 1–3 were repeated until a reduction in strength due to retardation of hydration as a result of HRWR overdose was detected.

The water and HRWR proportions that achieved the highest 1-day compressive strength were selected as the optimum values. A target maximum spread value of 14.5 in. was considered to investigate the possibility of decreasing V_p/V_s because lowering the V_p/V_s is desired to reduce cement content, but it may decrease workability. A high spread value of a paste may allow more reduction of V_p/V_s while achieving the target workability of UHPC. Another finding from the paste proportion study is that retardation due to the HRWR overdose is not only due to the amount of HRWR but also due to the HRWR to water ratio (*HRWR*/*w*). The maximum limit of *HRWR*/*w* that

does not cause retardation is approximately 0.079 (Figure 4.9). This optimum *HRWR*/*w* value may be applicable only for this specific combination of C-2 cement and HRWR-2. The use of high fineness cement showed different optimum values.

Table 4.16. Paste Proportion Study Results.

Case No.	C	SF	FA	*w/cm*	*HRWR/cm*	*HRWR/w*	Spread, in.	$f'_{c\,1-d}$, ksi
Case 1	95	5	0	0.200	0.013	0.065	15.3	11.4
	95	5	0	0.180	0.012	0.067	13.3	11.4
	95	5	0	0.180	0.013	0.072	14.4	13.5
	95	5	0	0.180	0.014	0.078	13.3	14.4
	95	5	0	0.170	0.015	0.088	12.9	13.7
	95	5	0	0.170	0.016	0.094	13.4	13.0
Case 2	90	5	5	0.180	0.013	0.072	13.1	12.6
	90	5	5	0.180	0.014	0.078	13.3	9.8
Case 3	85	5	10	0.180	0.012	0.067	13.5	9.7
	85	5	10	0.180	0.013	0.072	14.2	9.7
	85	5	10	0.180	0.014	0.078	14.4	11.8
	85	5	10	0.170	0.013	0.076	13.4	12.6
	85	5	10	0.170	0.014	0.082	13.5	12.3
	85	5	10	0.170	0.015	0.088	14.4	10.3
	85	5	10	0.165	0.013	0.079	14.3	13.6
	85	5	10	0.165	0.014	0.085	13.8	11.4
	85	5	10	0.165	0.015	0.091	13.6	9.7
Case 4	80	5	15	0.160	0.013	0.081	13.3	11.1
	80	5	15	0.160	0.014	0.088	12.8	9.2

Notes: C: C-1 cement, SF: silica fume, FA: fly ash, w: water, cm: cementitious materials

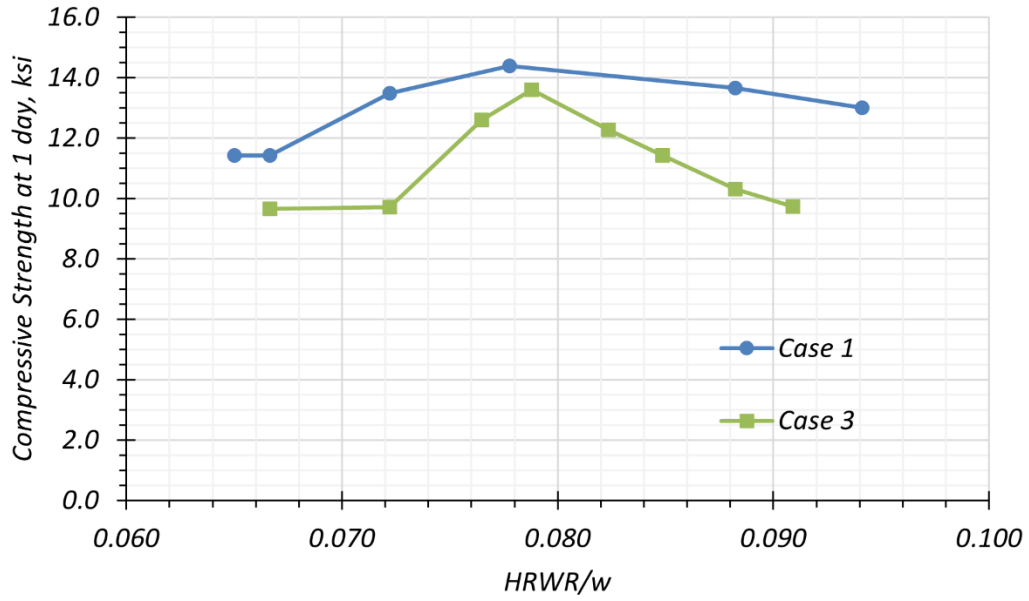

Figure 4.9. Retardation Effect of *HRWR/w*.

4.5.2.1.2 Ratio of Paste Volume to Sand Volume

Two paste proportions that provided high 1-day compressive strength are the following: (1) Case 1 (95 C 5 SF 0 FA) with 0.180 *w*/*cm* and 0.014 *HRWR*/*cm*; and (2) Case 3 (85 C 5 SF 10 FA) with 0.165 *w*/*cm* and 0.013 *HRWR*/*cm* (where C corresponds to cement, SF corresponds to silica fume, and FA corresponds to fly ash). These two pastes were further studied for an optimum ratio of paste to sand by volume, V_p/V_s. Case 1 (95 C 5 SF 0 FA) was tested with 0.90, 0.85, and 0.80 V_p/V_s (Table 4.17). The results show that 0.9 V_p/V_s gives the highest compressive strength. After changing the cement type from C-1 to C-2, this UHPC mixture achieved a 1-day compressive strength of 14.3 ksi. However, Case 3 (85 C 5 SF 10 FA), with 0.9 V_p/V_s, did not achieve a 1-day compressive strength greater than 11 ksi, possibly due to the lower amount of cement. Trial batches of the Case 3 paste with 0.9 V_p/V_s and *w*/*cm* less than 0.170 had a turnover time of more than 23 minutes. The turnover time of other mixtures was around 15–18 minutes. To reduce the turnover time, the amount of water was increased. Even though a turnover time of 19 minutes was achieved with 0.170 *w*/*cm*, its 1-day compressive strength was not close to the target strength of 14 ksi. Finally, Case 1 (95 C 5 SF 0 FA) with 0.180 *w*/*cm*, 0.014 *HRWR*/*cm*, and 0.9 V_p/V_s was selected for the next optimization step.

Table 4.17. V_p/V_s Study Results.

Case No.	C	SF	FA	*w/cm*	*HRWR/cm*	V_p/V_s	Spread, in.	$f'_{c\ 1-d}$, ksi
Case 1	95	5	0	0.180	0.0140	0.90	10.9	12.9
	95	5	0	0.180	0.0140	0.85	11.3	10.8
	95	5	0	0.180	0.0140	0.80	11.1	10.7
	95	5	0	0.180	0.0140	0.90	9.3[1]	14.3[1]
Case 3	85	5	10	0.165	0.0130	0.90	10.3	10.3
	85	5	10	0.167	0.0130	0.90	11.9	10.6
	85	5	10	0.168	0.0130	0.90	10.1	10.8
	85	5	10	0.170	0.0130	0.90	10.4	10.7

Notes:
1. C-2 cement was used. All other batches used C-1 cement.
2. C: cement, SF: silica fume, FA: fly ash, w: water, cm: cementitious material

Although the selected mixture (95 C 5 SF 0 FA) with 0.9 V_p/V_s achieved more than the target 1-day compressive strength of 14 ksi, it contains 1726 lb/yd^3 cement (Table 4.18). Because this cement content was relatively high compared to UHPC mixtures developed by other DOTs, an alternative approach was introduced to reduce cement content while maintaining the high early strength. The alternative approach considered fly ash as a filler material rather than a binder material. Even though traditionally fly ash is classified as a binder material having a pozzolanic reaction, it is most likely not the case in a UHPC mix design. For a pozzolanic reaction, a pozzolan material should combine with water and lime (Mindess et al. 2003); then, fly ash starts reacting after 56 days (Aïtcin 2016). At this later age, there is no water available and lime rarely remains in a UHPC for a reaction to fly ash because water is consumed by cement and silica fume at a very early age, and most of the remaining lime is consumed by silica fume. Therefore, fly ash can be reclassified as a filler when designing UHPC mixes.

In this new classification, binder materials are cement and silica fume, and filler materials are sand and fly ash. Replacing binder with filler, such as replacing cement with fly ash, may lower strength gain. However, replacing a filler with another filler, such as replacing sand with fly ash, can improve both packing density and workability without compromising strength gain significantly. The first step is to decrease V_p/V_s from 0.9 to 0.7 to reduce cement content. As a result, the cement content could be reduced from 1726 lb/yd^3 to 1546 lb/yd^3, as shown for B1 and B2 in Table 4.18. However, the reduction of V_p/V_s decreased the spread value from 9.3 in. to 6.3 in., which is not an

acceptable spread value. Even though *w*/*cm* and *HRWR*/*cm* were increased to 0.191 and 0.015 to achieve the target workability, respectively, the spread value and 1-day compressive strength were 7.5 in. and 12.2 ksi, respectively, as shown for Batch B4 in Table 4.18. Because the main goal of this mixture is to achieve high early compressive strength, the water content was not increased. Instead, 7.5 percent volume of sand was replaced with fly ash while keeping all other material contents the same to improve workability based on the mechanism discussed in Sections 4.2.1.2 and 4.2.3.3. This approach was taken because early compressive strength is not affected by the paste-to-sand ratio, V_p/V_s, but by the binder-to-filler ratio, V_b/V_f. As a result, a 10.4 in. spread value and a 13.8 ksi 1-day compressive strength were achieved, as shown for Batch B5 in Table 4.18. The substitution of fly ash for 7.5 percent sand volume gave a paste proportion composed of 85 percent cement, 5 percent silica fume, and 10 percent fly ash.

The repeatability of Mix-3a for larger quantities was investigated by increasing the total volume from 0.20 ft^3 to 0.95 ft^3, as shown for Batches B5 and B6 in Table 4.18. The spread value for the large volume mix decreased to 8.6 in. Frohlich and Schmidt (2012) reported that many factors influence repeatability and reproducibility of UHPC mixes, including the power of a mixer, mixing time, water temperature, and water-binder ratio. They showed that increasing the water-to-binder ratio improves repeatability but decreases strength and durability. Therefore, the paste portion was increased to improve repeatability. The value of V_b/V_f was increased from 0.70 to 0.76, which is the same as a V_p/V_s of 0.9. Finally, Mix-3a was developed as shown for Batch B7 in Table 4.18. Then, a limited number of trial batches were investigated to understand the effect of total volume on the consistency and mechanical properties. A low spread value and low 1-day compressive strength were observed for Batch B8. It showed that other factors such as water temperature influence the quality of a mixture. This effect was studied further for larger batch volumes.

Table 4.18. Alternative Approach to Develop Mix-3a.

Batch No.	C, lb/yd^3	SF, lb/yd^3	FA, lb/yd^3	*w*/*cm*, lb/yd^3	*HRWR*/ *cm*, lb/yd^3	V_b/V_f	Spread, in.	$f'_{c\,1-d}$, ksi	Volume, ft^3
B1	95 (1726)	5 (69)	0 (0)	0.180 (323)	0.014 (26.9)	0.90	9.3	14.3	0.20
B2	95 (1546)	5 (62)	0 (0)	0.180 (289)	0.014 (23.3)	0.70	6.3	13.7	0.20
B3	95 (1541)	5 (62)	0 (0)	0.183 (293)	0.015 (24.0)	0.70	7.3	-	0.10
B4	95 (1528)	5 (61)	0 (0)	0.191 (304)	0.015 (28.4)	0.70	7.5	12.2	0.20
B5	85 (1528)	5 (61)	10 (127)	0.177 (304)	0.014 (28.4)	0.70	10.4	13.8	0.20
B6	85 (1528)	5 (61)	10 (127)	0.177 (304)	0.014 (28.4)	0.70	8.6	12.6	0.95
B7	86 (1578)	5 (63)	9 (121)	0.182 (320)	0.015 (26.4)	0.76	11.6	13.1	0.20
B8	86 (1578)	5 (63)	9 (121)	0.182 (320)	0.015 (26.4)	0.76	10.6	11.7	0.51
B9	86 (1578)	5 (63)	9 (121)	0.182 (320)	0.015 (26.4)	0.76	11.9	14.0	0.40

Notes:
1. The number in parentheses is the material weight per volume in the mixture design.
2. V_b: the volume of binders, which are cement and silica fume.
3. V_f: the volume of fillers, which are sand and fly ash.
4. C: cement, SF: silica fume, FA: fly ash, *w*: water, *cm*: cementitious material
5. - : Not available

4.5.2.1.3 Mix-3 with Type III Cement

Mix-3b with C-3 (Type III cement) was developed by optimizing water and the HRWR in Mix-3a for workability. The mixture designs of Mix-3a and Mix-3b are given in Table 4.19, along with the spread and set values. Mix-3a with Cement C-2 achieved a 1-day compressive strength of 11.7–14.0 ksi. However, the range of the spread value was 10.6–11.9 in. Even though an increase in the spread value up to 11 in. improves mechanical properties by reducing air voids, a spread value greater than 11 in. can cause segregation of the steel fibers. To assess the volume effect and potential segregation of steel fibers, a mix with larger volume was further studied.

Table 4.19. Mixture Design of Mix-3a and Mix-3b.

Description	Mix-3a (Type I/II)		Mix-3b (Type III)	
	Proportion	Weight, lb/yd^3	Proportion	Weight, lb/yd^3
Cement	1	1578	1	1529
Silica fume	0.04	63	0.04	61
Fly ash	0.08	121	0.08	117
Sand	1.09	1713	1.09	1660
Water	0.203	320	0.229	350
HRWR	0.017	26	0.023	36
Steel fiber	1.5%	200	1.5%	200
Spread, in.	10.6–11.9		10.1	
Initial setting time	6h 30m		6h 00m	
Final setting time	9h 30m		10h 00m	

Note: Cement C-2 for Mix-3a and Cement C-3 for Mix-3b

Figure 4.10 provides the compressive strength gain plots of Mix-3a and Mix-3b. Mix-3a with Cement C-2 achieved a target 1-day compressive strength of 14 ksi and a slightly lower 28-day compressive strength than the target value of 20 ksi. Mix-3b achieved a 1-day compressive strength of 13.6 ksi, which is slightly lower than the target value, and the 28-day compressive strength is also lower than the target value. The reason for the slightly lower compressive strength at 28 days of Mix-3b might be a relatively low packing density due to a higher liquid volume and the low C_3S content of Cement C-3 (Type III cement)—like Mix-1b. The 55 percent C_3S content of Cement C-3 (Type III cement) is lower than the 65 percent C_3S content for Cement C-2 (Type I/II cement) (Table 4.4). Additionally, the liquid volumes (water + HRWR) of Mix-3a and Mix-3b are 20.4 percent and 22.7 percent, respectively. Thus, Mix-3b may have a higher porosity than Mix-3a. Mix-3a and Mix-3b satisfied the target $f'_{c,1-d} \geq 0.65\, f'_c$, with $f'_{c,1-d}/f'_c$ of 0.67 and 0.75 for Mix-3a and Mix-3b, respectively.

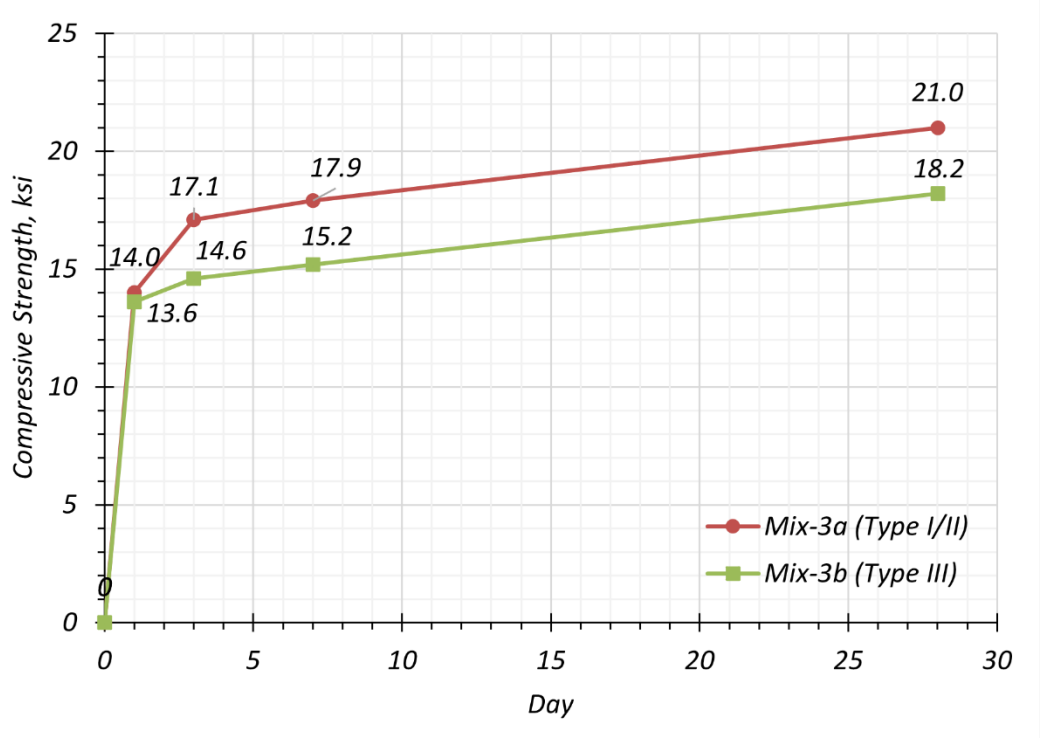

Figure 4.10. Compression Test Results for Mix-3a and Mix-3b.

4.5.2.1.4 Low Silica Fume Content Impact on Resistivity

Mix-3a exhibited the desired properties for key fresh and hardened properties for initial screening. As part of the next screening, shrinkage and resistivity were also tested. Section 3.3.5, 3.4.1, and 3.4.2 discuss the test methods of shrinkage and bulk and surface resistivities, respectively. The low silica fume content of Mix-3a helps to reduce shrinkage while increasing the compressive strength. The shrinkage result of Mix-3a (520 με) was lower than Mix-1a (700 με) and Mix-2a (630 με) (Table 4.29). Section 5.6.2.7 describes the shrinkage results of the developed mixtures in detail.

Figure 4.11 shows bulk resistivity measurements and the silica fume proportions for three mixes. Based on the resistivity measurements, Mix-3a is also categorized as *Very Low* in terms of permeability although Mix-3a showed relatively lower resistivity values than Mix-1a and Mix-2a. Note that the higher the resistivity, the lower the permeability. The main reason for obtaining relatively lower resistivity results for Mix-3a may be related to the low silica fume content of this mix. The resistivity test results of Mix-1a and Mix-2a, which have 0.15 silica fume proportion by cement weight, were 101–104 kΩ-cm; whereas Mix-3a, which has 0.04 silica fume proportion by cement weight, was 58 kΩ-cm. However, the surface resistivity results for permeability of all three

mixtures are in the *Very Low* category as per ASTM C1202 (2017) and AASHTO T358 (2017). Table 3.1 shows the classification. Thus, all three mixes have acceptable durability.

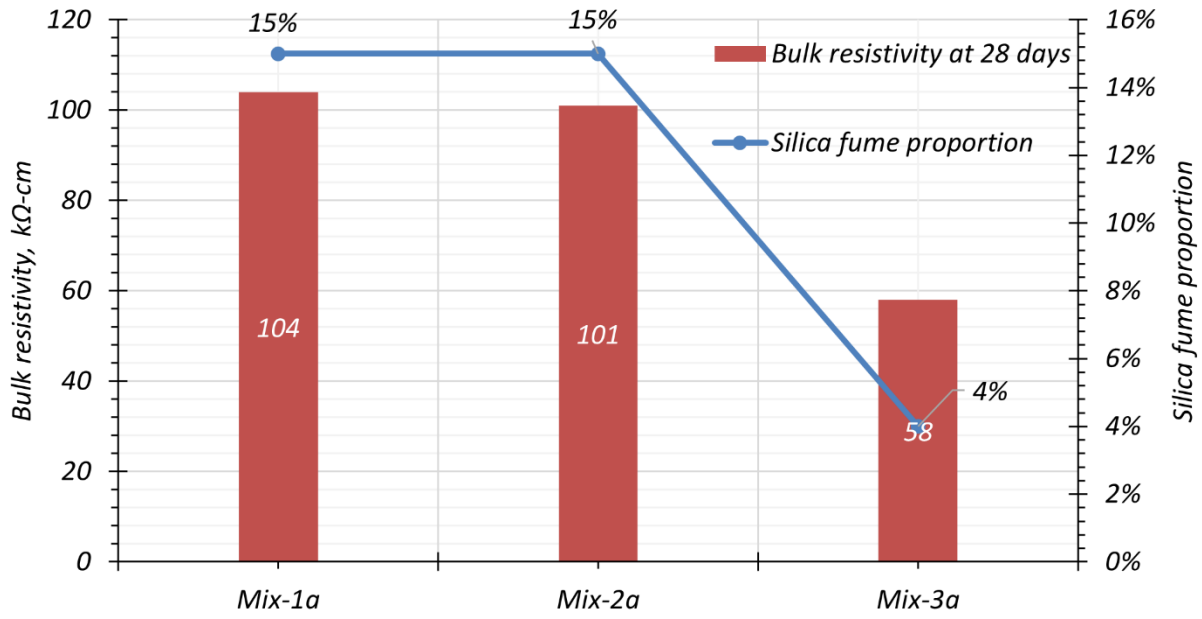

Figure 4.11. Relationship between Resistivity and Silica Fume Content.

4.5.2.2 Development of Mix-4

4.5.2.2.1 Proportioning Mix-4 with Type I/II Cement

Mix-3a achieved a 1-day compressive strength ranging from 13–14 ksi. Resistivity testing is an effective way to measure permeability and transport properties. Even though the resistivity of Mix-3a was classified in the *Very Low* category for permeability, the resistivity was relatively low compared to Mix-1a and Mix-2a. The low content of silica fume of Mix-3 may be responsible for the relatively low resistivity value. Mix-4 was designed to improve the resistivity by increasing silica fume content. The main purpose for developing Mix-4a was to increase the resistivity values of Mix-3a (i.e., more than 58 kΩ-cm) without compromising high early strength.

An optimum amount of silica fume is necessary to improve the resistivity and later age strength without diminishing early strength gain because a large proportion of silica fume can decrease early strength due to high water demand. As explained in Section 4.2.2.1, half of the silica fume proportion reacts with portlandite when a 0.16 silica fume proportion by cement weight is contained in a mixture (Kang et al. 2017). Based on this result, a 0.08 silica fume proportion was

used for Mix-4a, which is 10 percent volume fraction in a paste. Fly ash content was also increased to compensate for the increased water demand due to the higher silica fume content. Table 4.20 shows the two fly ash proportions that were investigated. A 0.17 fly ash proportion decreased early strength gain. This result might be due to the retardation of setting time by fly ash, as explained in Section 4.3.3. Therefore, the fly ash proportion was decreased from 0.17 to 0.10 for Batch B2, and this mixture achieved a 1-day compressive strength of 13.6 ksi.

Table 4.20. Two Fly Ash Proportions for Development of Mix-4a.

Batch No.	C	SF	FA	Spread, in.	$f'_{c\,1-d}$, ksi	Volume, ft^3
B1	1	0.08	0.17	11.3	11.7	0.2
B2	1	0.08	0.10	11.0	13.6	0.2

Notes: C: cement, SF: silica fume, FA: fly ash

The repeatability of Mix-4a was investigated, and Table 4.21 shows the results for Batch B2 and Batch B3 when having the same proportions. Both the spread values and 1-day compressive strengths from the two batches are acceptable.

Table 4.21. Repeatability Check of Mix-4a.

Batch No.	Spread, in.	$f'_{c\,1-d}$, ksi	f'_c, ksi	Volume, ft^3
B2	11.0	13.6	N/A	0.2
B3	11.1	13.2	19.9	0.4

4.5.2.2.2 Mix-4 with Type III Cement

Mix-4b was developed by optimizing water and the HRWR while keeping other material proportions the same. Table 4.22 summarizes the mixture designs of Mix-4a and Mix-4b.

Table 4.22. Mixture Design of Mix-4a and Mix-4b.

Description	Mix-4a (Type I/II)		Mix-4b (Type III)	
	Proportion	Weight, lb/yd^3	Proportion	Weight, lb/yd^3
Cement	1	1528	1	1487
Silica fume	0.08	115	0.08	112
Fly ash	0.10	159	0.10	155
Sand	1.08	1647	1.08	1603
Water	0.210	320	0.231	344
HRWR	0.018	27	0.025	38
Steel fiber	1.5%	200	1.5%	200
Spread, in.	11.1		8.9	
Initial setting time	6h 00m		4h 30m	
Final setting time	9h 30m		8h 30m	

Figure 4.12 shows test results for Mix-4a and Mix-4b. Initial and final setting time results of both Mix-4a and Mix-4b are in the acceptable range in comparison with proprietary UHPCs. Mix-4a showed acceptable 1-day and 28-day compressive strengths, whereas Mix-4b did not achieve the target 1-day and 28-day compressive strengths. Both mixes satisfied $f'_{c,1-d} \geq 0.65\, f'_c$, with $f'_{c,1-d}/f'_c$ of 0.66 and 0.78 for Mix-4a and Mix-4b, respectively.

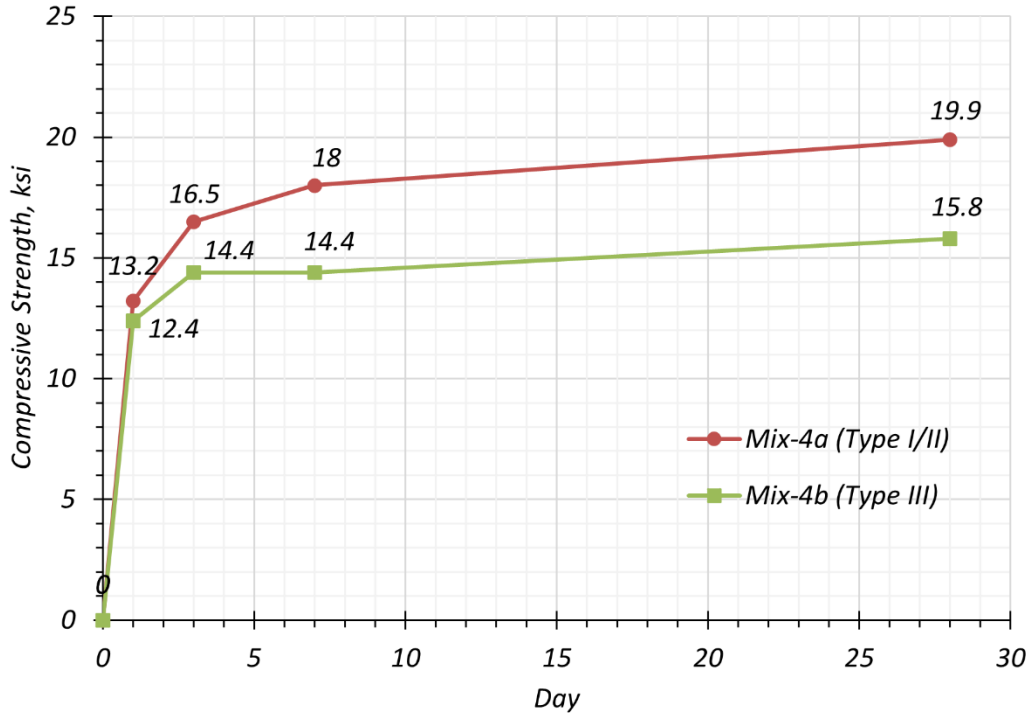

Figure 4.12. Compression Test Results for Mix-4a and Mix-4b.

4.5.3 Summary of Developed Mixtures

Additional testing was conducted on the same day for the same numbered mixtures, such as Mix-1a and Mix-1b, to minimize differences in ambient environmental conditions such as water temperatures and materials for an appropriate comparison of the companion mixtures for the two cement types. Table 4.23 provides the mixture designs of all eight mixtures. Setting time, spread value, and compressive strength at 1, 3, 7, and 28 days were measured during the test program. Figure 4.13 shows the initial and final setting times, and Figure 4.14 shows the compressive strength development over time. Figure 4.15 shows a comparative bar chart of strength gain rates for all investigated mixtures.

Table 4.23. Mixture Designs of Developed Mixtures.

Description	Mix-1a	Mix-1b	Mix-2a	Mix-2b	Mix-3a	Mix-3b	Mix-4a	Mix-4b
Cement	1445	1397	1238	1206	1579	1529	1528	1487
Silica fume	217	210	186	181	63	61	115	112
Fly ash	72	70	310	302	121	117	159	155
Sand	1671	1615	1662	1619	1715	1660	1647	1603
Water	329	360	312	338	320	350	320	344
HRWR	27	37	24	32	26	36	27	38
Steel fiber	200	200	200	200	200	200	200	200
Spread, in.	8.6	10.6	9.8	8.1	11.9	10.1	11.1	8.9
$f'_{c\,1-d}$, ksi	11.4	13.5	10.1	10.4	14.0	13.6	13.2	12.4
f'_c, ksi	17.6	17.7	17.0	15.8	21.0	18.2	19.9	15.8

Note: All units are lb/yd^3, unless otherwise noted.

Table 4.24. Compressive Strength at Specific Ages.

Mixture	$f'_{c\,1-d}$, ksi	$f'_{c\,3-d}$, ksi	$f'_{c\,7-d}$, ksi	$f'_{c\,28-d}$, ksi
Mix-1a	11.4	14.6	16.3	17.6
Mix-2a	10.1	13.5	15.8	17.0
Mix-3a	14.0	17.1	17.9	21.0
Mix-4a	13.2	16.5	18.0	19.9
Mix-1b	13.5	15.2	15.7	17.7
Mix-2b	10.4	13.7	13.8	15.8
Mix-3b	13.6	14.6	15.2	18.2
Mix-4b	12.4	14.4	14.4	15.8

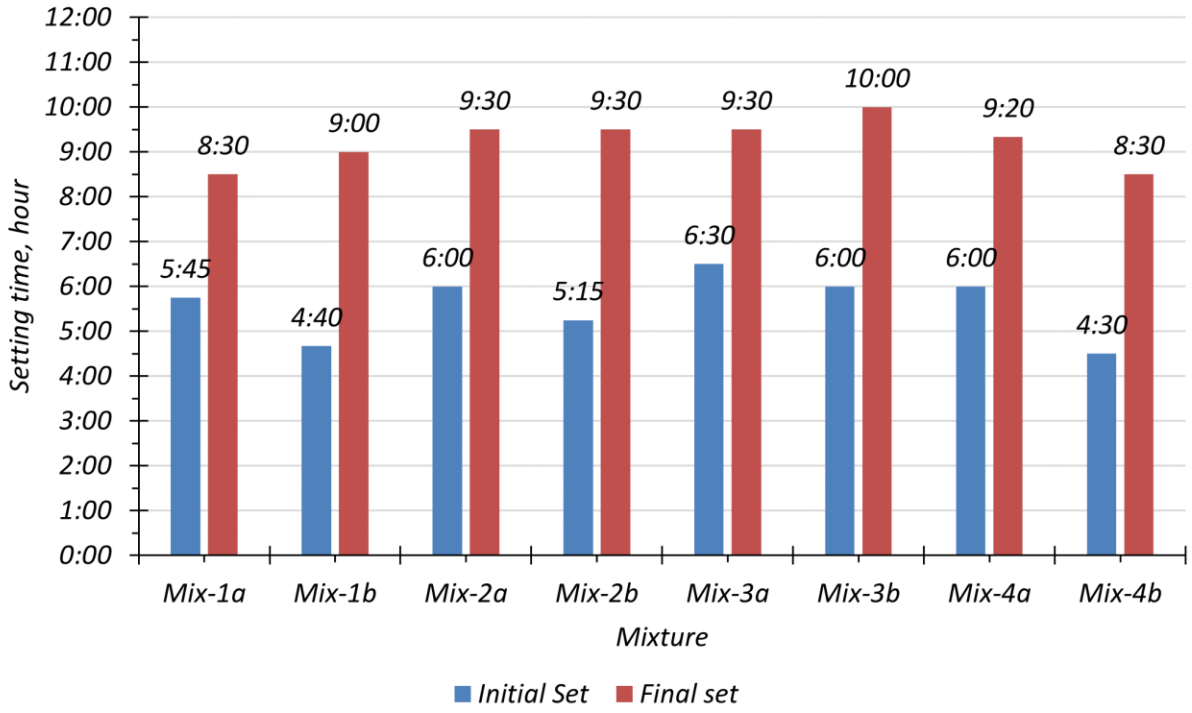

Figure 4.13. Setting Time Results.

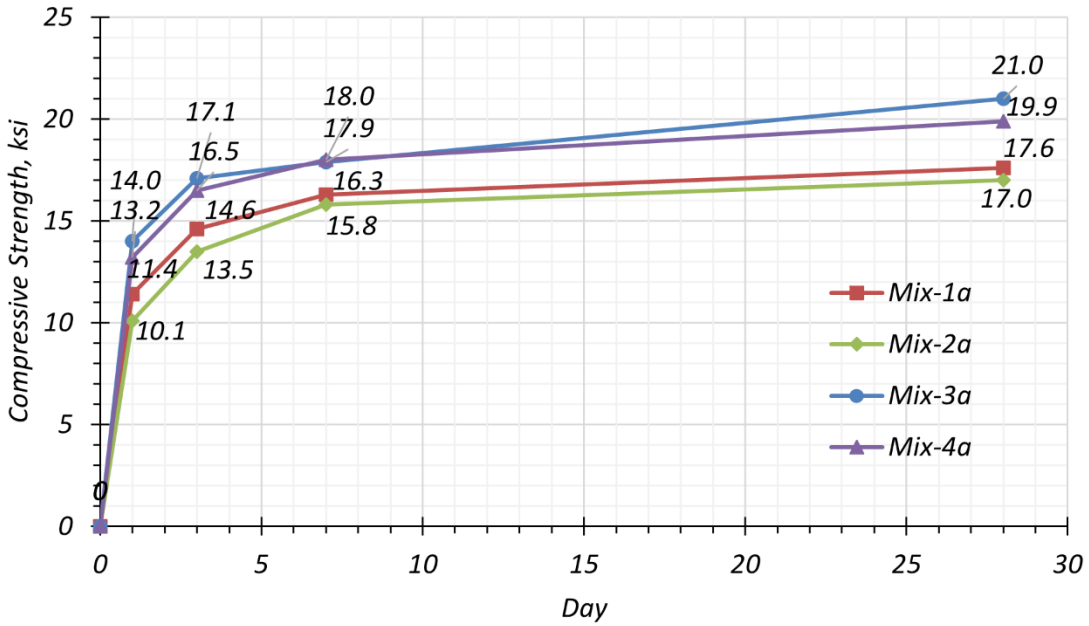

(a) Strength Development Results of Mixtures with Type I/II Cement

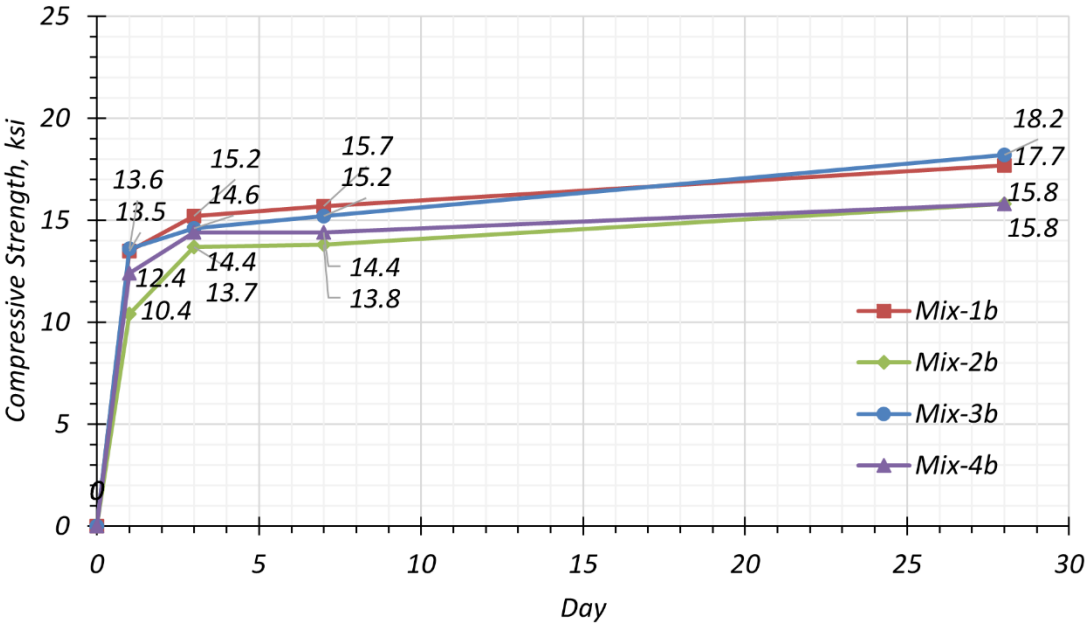

(b) Strength Development Results of Mixtures with Type III Cement

Figure 4.14. Compressive Strength Development Results of All UHPC Mixtures.

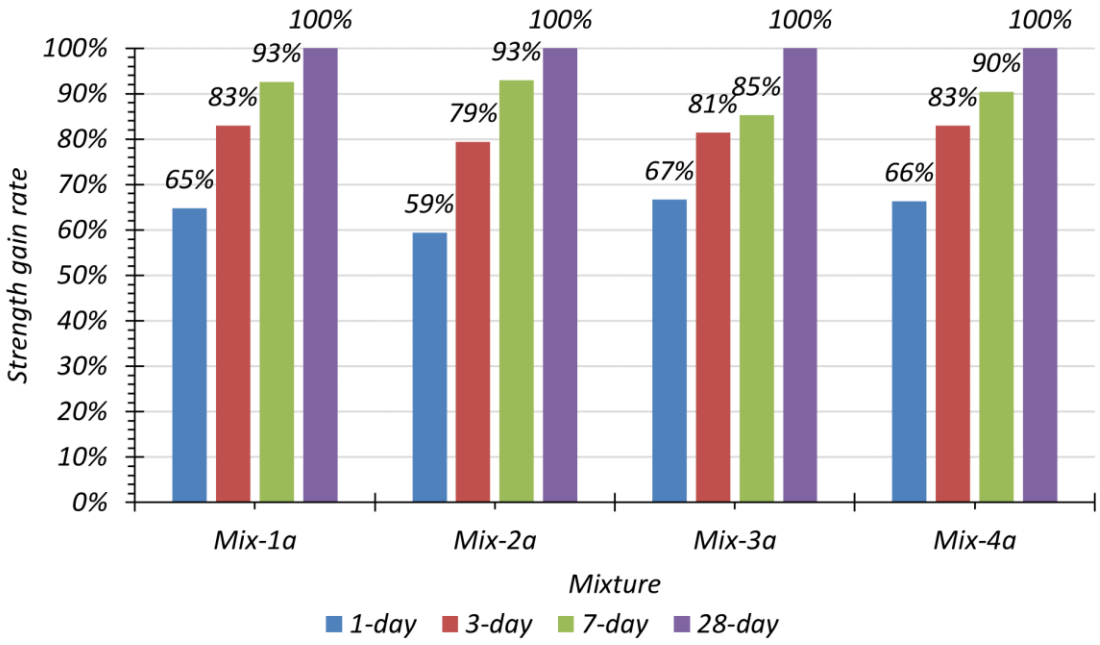

(a) Mixtures with Type I/II Cement

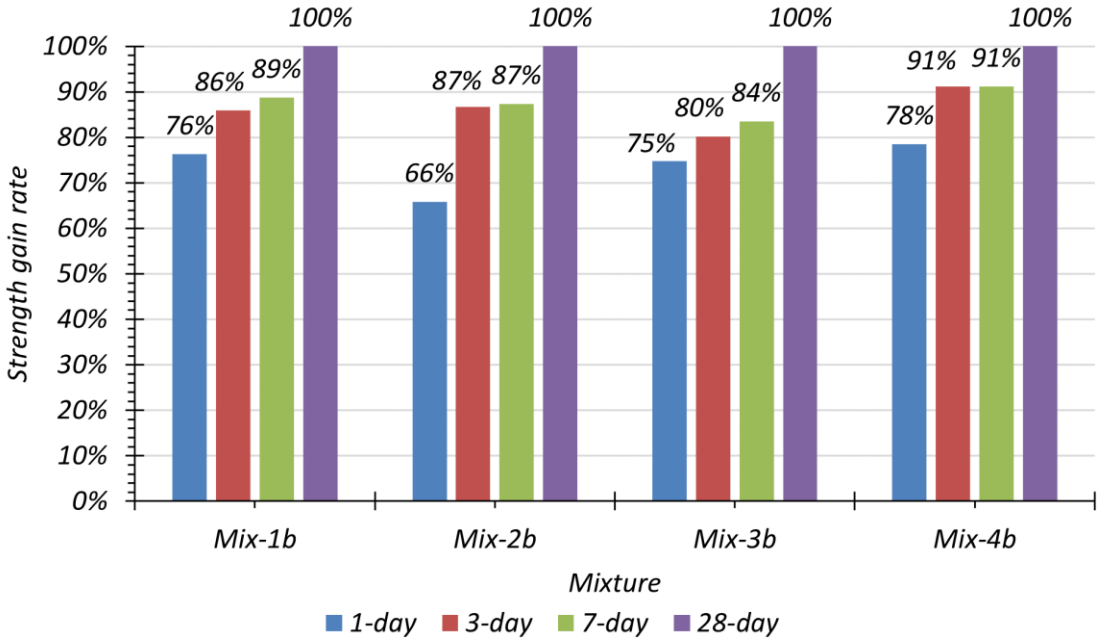

(b) Mixtures with Type III Cement

Figure 4.15. Strength Gain Rate of All Developed Mixtures.

The strength gain rates of the mixtures with Cement C-2 (Type I/II cement) have a similar trend, wherein the majority of the 28-day compressive strength is gained in the first 24 hours and then the rate of strength increase begins to decline. As expected, in the case of mixtures with Cement

C-3 (Type III cement), the strength gain in the first 24 hours is higher than for Cement C-2 (Type I/II cement), while strength gain rates between 1 and 3 days are lower than mixtures with Cement C-2 (Type I/II cement), with the exception of Mix-2b. In addition, the strength development of the four mixtures with Cement C-3 (Type III cement) between 3 to 7 days is very small, while the strength gain rates are higher between 7 to 28 days.

The strength gain results of the four mixtures with C-3 (Type III cement) were further studied to understand the mechanism and differences. The following conclusions were drawn from these observations:

The same mix proportion may not be valid for cements having different fineness and chemical composition. High fineness of C-3 (Type III cement) may cause different packing density and water demand. As a result, the same proportion of a paste may not give the optimum packing density.

- Low C_3S content may cause low strength gain. C-3 (Type III cement) has a 55 percent C_3S content, whereas Cement C-2 (Type I/II cement) has 65 percent C_3S.
- High fineness and high C_3A content increase water demand. C_3A reacts right after contacting water and forms ettringite immediately (Mindess et al. 2003). Cement C-3 (Type III cement) has 11 percent C_3A, whereas Cement C-2 (Type I/II cement) has 2 percent C_3A.
- The particle size of C-3 (Type III cement) is finer than C-2 (Type I/II cement) (Figure 4.3). As a result, increased water content due to higher water demand increases porosity and decreases packing density.

4.5.4 Cost Analysis

Except for fly ash and steel fibers, the material cost of the developed mixtures is estimated based on the unit prices obtained from a precaster in Texas in 2020. The unit price for fly ash is provided from one of the approved suppliers by TxDOT (also in 2020). The unit price for steel fibers is based on the cost of an imported small quantity of steel fibers, including shipping for this project. If steel fibers are manufactured in the United States, the cost of steel fibers will likely be less. Table 4.25 shows the unit prices of materials. The cost of the sand may vary depending on the maximum allowable size of sand particles.

Table 4.25. Unit Price of Materials.

Material	Unit Price
Type I/II Cement/ton	$140
Type III Cement/ton	$160
Silica fume/ton	$860
Fly ash/ton	$94
HRWR/gallon	$12.5
Sand/ton	$20
Steel fibers/ton	$3560

Table 4.26 shows the material cost ($/cyd) of the developed mixtures. The ranges of the total cost without steel fibers and with steel fibers are $197–$273 and $553–$629, respectively. The material cost of proprietary UHPC is more than $2000 per cyd (Tadros 2019). Therefore, the developed mixtures are cost-effective UHPC mixtures compared to proprietary UHPC. The cost comparison with proprietary UHPCs developed by other DOTs and FHWA in Table 4.27 shows the developed mixtures in this study are cost competitive. The cost analysis shows that a mixture with a low silica fume proportion, such as Mix-3a and Mix-4a, leads to a relatively economic UHPC mixture for precast prestressed girder applications. Furthermore, the cost of steel fibers accounts for about 60 percent of the total cost for all the mixtures (Figure 4.16 and Figure 4.17), which suggests that the best way to reduce the cost of a UHPC mixture is to use an optimum steel fiber content. In addition, beyond the cost of the materials, consideration must be given to the cost of implementing steel fiber addition and UHPC production into plant batching operations.

Table 4.26. Material Cost ($/cyd) of Developed Mixtures.

Description	Mix-1a	Mix-1b	Mix-2a	Mix-2b	Mix-3a	Mix-3b	Mix-4a	Mix-4b
Cement	101	112	87	96	110	122	107	119
Silica fume	93	90	80	78	27	26	49	48
Fly ash	3	3	15	14	6	5	7	7
HRWR	38	52	34	45	37	50	38	53
Sand	17	16	17	16	17	17	16	16
Steel fibers	356	356	356	356	356	356	356	356
Total cost without fibers	252	273	232	250	197	221	218	243
Total cost with fibers	608	629	588	606	553	577	574	599

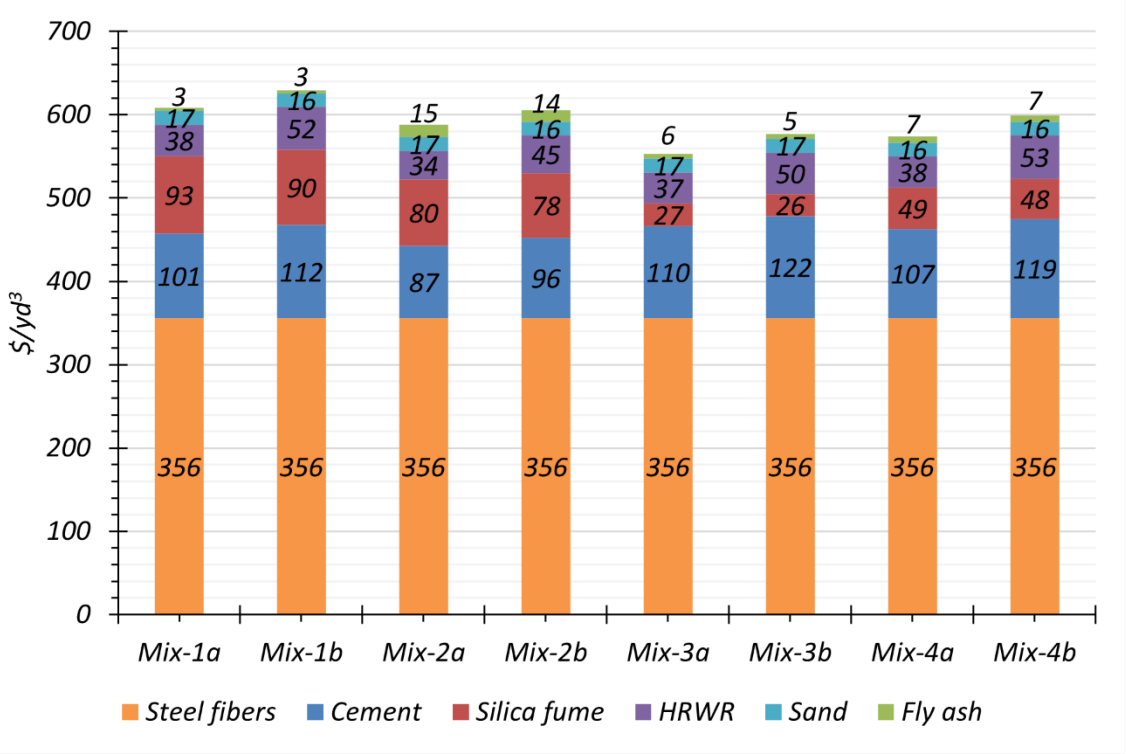

Figure 4.16. Material Cost Comparison of Mixtures.

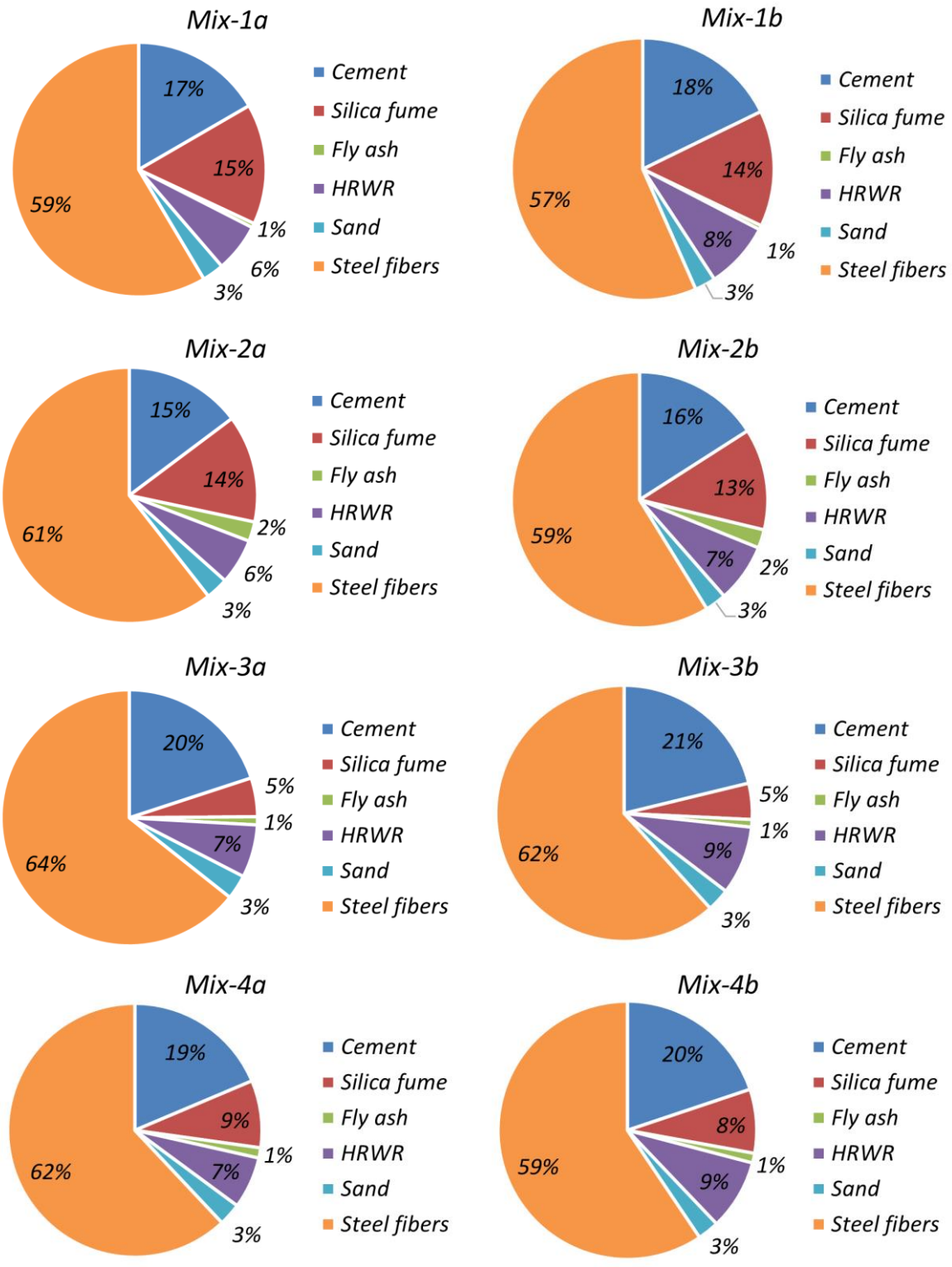

Figure 4.17. Cost Composition of Mixtures.

Table 4.27. Cost Comparison with Other Nonproprietary UHPCs.

Nonproprietary UHPC	Cost, $/cyd	Materials (cement, sand, fiber volume)	Source
TxDOT	$553–629	Type III, Natural, 1.5%	This study
Michigan DOT	$893	Type I, Quartz, 2.0%	El-Tawil et al. (2018)
Montana DOT	$561	Type I/II, Masonry, 2.0%	Berry et al. (2017)
Missouri DOT	$1017	Type III, Natural, 2.0%	Khayat and Valipour (2018)
FHWA	$730	White, Natural sand, 1.5%	Wille and Boisvert-Cotulio (2013)
	$965	White, Natural sand, 1.5%	
	$1122	White, Quartz, 1.5%	

4.6 SELECTION OF DEVELOPED UHPC MIXTURES FOR FURTHER STUDY

Four UHPC mixtures with different proportions were developed, as described in the previous section. Based on preliminary evaluation, including an examination of key fresh and hardened properties, durability, and material cost, two mixtures that ranked first and second among the developed mixtures were selected for further study. In addition, further optimization of the selected mixtures using Type III cements common to the Texas precast industry was considered to facilitate implementation of the developed UHPC mixtures for precast, pretensioned bridge girders in Texas. Note that discussions with precasters indicated that having a separate silo for Type I/II cement is likely not practical at this stage. Simultaneously, preliminary service life prediction has been studied for the developed mixtures to understand the impact of low silica fume content in the selected mixtures. Bulk and surface resistivity results of all mixtures, according to ASTM C1760 (2021) and AASHTO T358 (2017), were in the *Very Low* classification in terms of chloride ion penetration, according to ASTM C1202 (2017). Even though this classification indicates that all mixtures have high durability, limitations to understanding differences in durability among the developed UHPC mixtures based on this classification exist. To evaluate the durability among the developed mixtures in detail, preliminary service life prediction was studied. A mixture among the two top ranked mixtures was selected for plant production based on the results of the preliminary service life prediction and performance evaluation in Section 4.6.3.

4.6.1 Comparison of Developed Mixtures with Type I/II Cement

As discussed in Section 4.5.3, four UHPC mixtures were developed to achieve the target properties, which were as follows:

- A sufficient spread value (9–11 in.)
- 1-day compressive strength of 10–14 ksi without any heat treatment
- 28-day compressive strength of 18–20 ksi without any special treatment

Table 4.28 and Table 4.29 show mixture designs and properties evaluated in Section 4.5.3, using Type I/II cement, respectively. Chapter 3 discusses the test methods. In addition to the first screening, the following preliminary testing was also conducted, which is summarized herein:

- Shrinkage in accordance with ASTM C157 (2017), *Standard Test Method for Length Change of Hardened Hydraulic-Cement Mortar and Concrete*, with modifications by ASTM C1856 (2017)
- Bulk resistivity in accordance with ASTM C1760 (2021), *Standard Test Method for Bulk Electrical Conductivity of Hardened Concrete*
- Surface resistivity in accordance with AASHTO T 358 (2017), *Standard Method of Test for Surface Resistivity Indication of Concrete's Ability to Resist Chloride Ion Penetration*
- RCPT in accordance with ASTM C1202 (2017), *Standard Test Method for Electrical Indication of Concrete's Ability to Resist Chloride Ion Penetration*, with modifications by ASTM C1856 (2017)
- Abrasion resistance in accordance with ASTM C944 (2012), *Standard Test Method for Abrasion Resistance of Concrete or Mortar Surfaces by the Rotating-Cutter Method*, with modifications by ASTM C1856 (2017)

The volume of steel fibers are 1.5 percent in all mixtures. Mix-1a was the first developed mixture, which has 15 percent silica fume content by cement weight to enhance durability. Mix-2a was developed to reduce cement content while keeping the same silica fume proportion. However, both mixtures did not achieve the desired high early compressive strength without heat treatment due to the silica fume content. As a result, Mix-3a was developed to achieve a higher early strength by reducing the silica fume proportion to 4 percent. Even though Mix-3a achieved the desired high early strength, its durability was expected to be lower than Mix-1a and Mix-2a. To increase the durability relative to Mix-3a and maintain a high early strength gain, Mix-4a was developed with 8 percent silica fume content.

Table 4.28. Mixture Designs of the Developed Mixtures with Type I/II Cement.

Description	Mix-1a		Mix-2a		Mix-3a		Mix-4a	
	Weight, lb/yd^3	Proportion	Weight, lb/yd^3	Proportion	Weight, lb/yd^3	Proportion	Weight, lb/yd^3	Proportion
Cement	1445	1.00	1238	1.00	1579	1.00	1528	1.00
Silica fume	217	0.15	186	0.15	63	0.04	115	0.08
Fly ash	72	0.05	310	0.25	121	0.08	159	0.10
Sand	1671	1.16	1662	1.34	1715	1.09	1647	1.08
Water	329	0.23	312	0.25	320	0.20	320	0.21
HRWR	27	0.019	24	0.019	26	0.016	27	0.018
Steel fiber	200	1.5%	200	1.5%	200	1.5%	200	1.5%

Table 4.29. Evaluation of Developed Mixtures with Type I/II Cement in Task 4.

Description	Mix-1a	Mix-2a	Mix-3a	Mix-4a
Spread, in.	8.6	9.8	11.9	11.1
$f'_{c\,1-d}$, ksi	11.4	10.1	14.0	13.2
f'_c, ksi	17.6	17.0	21.0	19.9
Total/Autogenous Shrinkage[1], με	−700 / −580	−630 / −510	−520 / −330	−620 / −520
Bulk/Surface Resistivity[2], kΩ-cm	Very Low[4] 207 / 211	Very Low[4] 208 / 214	Very Low[4] 105 / 101	Very Low[4, 6] 202/195
RCPT, Coulombs	Negligible 70.0	Negligible 74.2	-	-
Abrasion[3], Mass Loss, oz	0.053	0.047	0.041	N/A
Cost, $/yd^3	608	588	553	574
Selection for Further Study	No	No	Yes	Yes

Notes:
1. Shrinkage was measured at 28 days of age.
2. Surface and Bulk resistivity were measured at 56 days of age.
3. Formed surface was used for average mass loss per 2 minutes for abrasion test.
4. Surface resistivity classification can be correlated to chloride ion penetration categories from ASTM C1202 (2017) according to AASHTO T 358 (2017).
5. - : Not available
6. Resistivity values are for Mix-4 with Type III cement
7. Additional information for durability testing for Mix-1a, Mix-2a, and Mix-3a can be found in Cooper (2020).
8. Additional information for shrinkage testing for Mix-1a, Mix-2a, Mix-3a, and Mix-4a can be found in Shah (2021).

The first selected mixture was Mix-3a, which shows the highest 1-day and 28-day compressive strengths, the lowest shrinkage and mass loss for abrasion resistance, *Very Low* resistivity-based chloride penetration category, and the lowest material cost. The *Very Low* rating is based on the surface resistivity classification correlated to chloride ion penetration categories according to ASTM C1202 (2017) and AASHTO T 358 (2017), as shown in Table 3.1. Thus, Mix-3a can be considered to have good durability compared to CC or HPC. However, the impact of the relatively

low resistivity value of Mix-3a compared to Mix-1a and Mix-2a was further investigated through preliminary service life predictions.

The other selected mixture is Mix-4a, which has comparable 1-day and 28-day compressive strengths, a material cost similar to Mix-3a, and better resistivity results than Mix-3a. Even though Mix-4a has slightly lower strength than Mix-3a, it has comparable high resistivity to Mix-1a and Mix-2a. Thus, Mix-4a was selected for further study.

4.6.2 Further Study of Selected Mixtures with Type III Cement

4.6.2.1 Overview

The results of the questionnaire given to Texas precasters showed a concern about the need for an additional storage location, such as a silo, if commonly used cement materials are not adopted in UHPC mixtures. Thus, the selected mixtures, Mix-3 and Mix-4, were further optimized using two common Type III cement products used in Texas precast plants.

4.6.2.2 Mixture Optimization with Type III Cement

4.6.2.2.1 Analysis of Type III Cements Used at Precast Plants

In Section 4.3.1, two Type I/II cements, labeled C-1 and C-2, and one Type III cement, labeled C-3, were investigated. The C-3 cement has relatively low C_3S content (55 percent) and high C_3A content (11 percent). The high C_3A content increased the water demand for a desired flow spread; therefore, it was not favorable to achieve high early strength. In addition, the 55 percent C_3S content is in the low part of the typical range for C_3S in Type III cement. As a result, the developed mixtures with C-3 cement did not obtain the expected benefit of Type III cement with respect to high early strength gain. After reviewing more Type III cements, two commonly used Type III cements by the Texas precast industry, labeled C-4 and C-5, were considered in this study. Table 4.30 and Figure 4.18 show the chemical compositions and particle size distribution of the selected Type III cements, respectively. It was expected that C-5 provides the most favorable cement for UHPC because of its low C_3A content and high C_3S plus C_2S content with high fineness. The combined effect of reduction in water demand due to low C_3A content and high C_3S plus C_2S content and high fineness was expected to ensure high early strength using C-5 (Aïtcin 2016).

Table 4.30. Chemical Composition of Type III Cements.

Cement	C_3S	C_2S	C_3A	Blaine Fineness, m^2/kg
C-3	55%	16%	11%	607
C-4	62%	12%	11%	609
C-5	58%	17%	5%	526

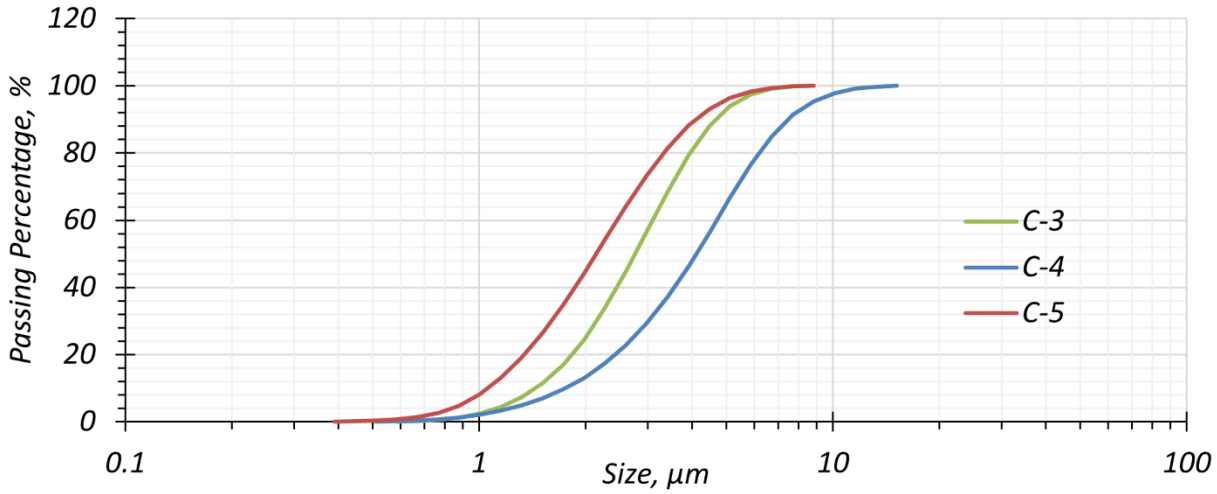

Figure 4.18. Particle Size Distribution of Type III Cements.

To understand the water demand of each Type III cement, the mixture proportions for Mix-3b, with identical water and HRWR contents, were used with the C-3, C-4, and C-5 cements. Table 4.31 shows the mixture proportions for Mix-3b used for the water demand comparison of the three cements. Figure 4.19 shows the flow spread results, which indicate the relative water demand of the three cements. A higher flow spread value indicates a lower water demand. As expected, Mix-3b with C-5 cement had the lowest water demand, with a 12.3 in. flow spread, and the highest 1-day compressive strength (13.7 ksi).

For Mix-3b with C-5 cement, there are two benefits to water content reduction. The first is that it can mitigate the risk of steel fiber segregation. A flow spread value greater than 11 in. tends to cause segregation of steel fibers based on observations during the laboratory study. Thus, the segregation can be avoided by reducing the water content. The second benefit is that a higher 1-day compressive strength can be achieved by reducing water content because lowering the *w/c* reduces the distance between cement particles (Aïtcin 2016). Thus, Mix-3b was optimized with C-5 cement to see the highest achievable 1-day compressive strength with an appropriate spread value.

Table 4.31. Mixture Proportions for Mix-3b.

Description	Proportion	Mix-3b (lb/yd^3)
Cement	1	1529
Silica fume	0.04	61
Fly ash	0.08	117
Sand	1.09	1660
Water	0.229	350
HRWR	0.023	36
Steel fiber	1.5%	200

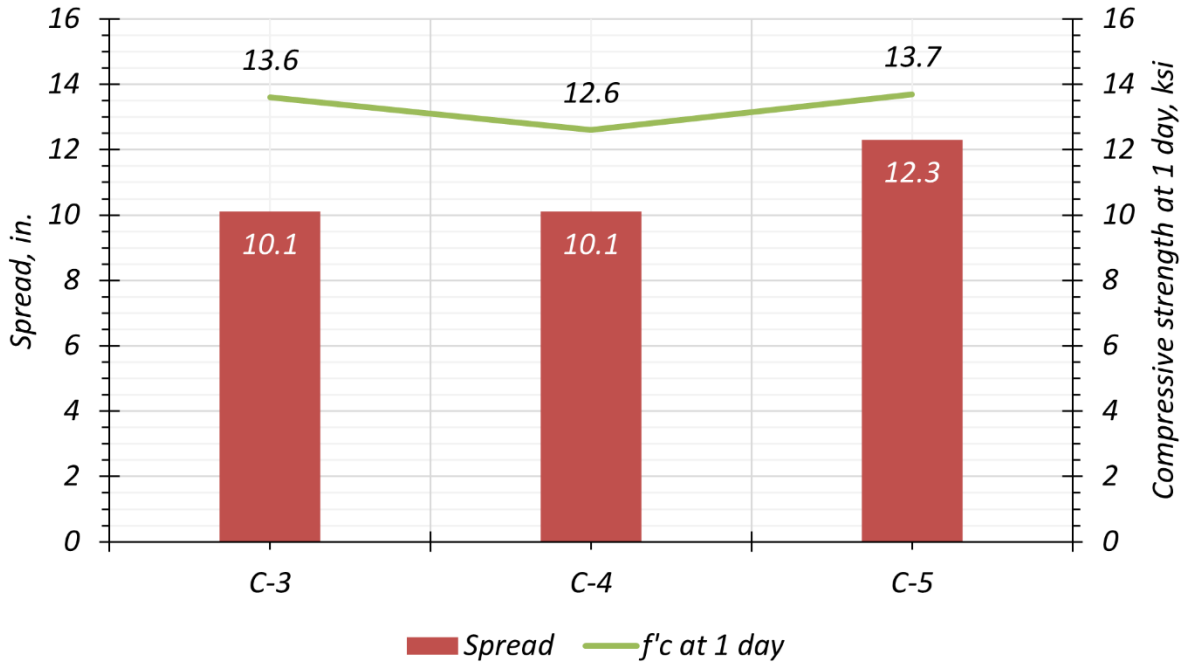

Figure 4.19. Comparison of Flow Spread and 1-Day Compressive Strength for Different Type III Cements and Identical Mixture Proportions.

4.6.2.2.2 Optimization of Mix-3 with the Selected Type III Cement

The optimization of Mix-3b with C-5 cement was performed with three trial batches (Table 4.32). The results in Figure 4.20 show that Trial Batch T3 for Mix-3b with C-5 cement achieved a 16.0 ksi 1-day compressive strength with an 11.1 in. flow spread. Reaching 16 ksi within 24 hours without any special treatment, such as heat or steam curing, shows promising results for application in precast, pretensioned bridge girders. The curing temperature of all specimens was maintained at 68°F.

Table 4.32. Optimization Process for Mix-3b with C-5 Cement.

Description	Trial Batch		
	T1	T2	T3
Cement	1	1	1
Silica fume	0.04	0.04	0.04
Fly ash	0.08	0.08	0.08
Sand	1.09	1.09	1.09
Water	0.229	0.229	0.208
HRWR	0.023	0.021	0.021
Steel fiber	1.5%	1.5%	1.5%
w/cm	0.20	0.20	0.19
HRWR/cm	0.0205	0.0187	0.0187
Flow spread, in.	12.3	12.2	11.1
$f'_{c,1\text{-}d}$, ksi	13.7	15.8	16.0

Note: $f'_{c,1\text{-}d}$: 1-day compressive strength

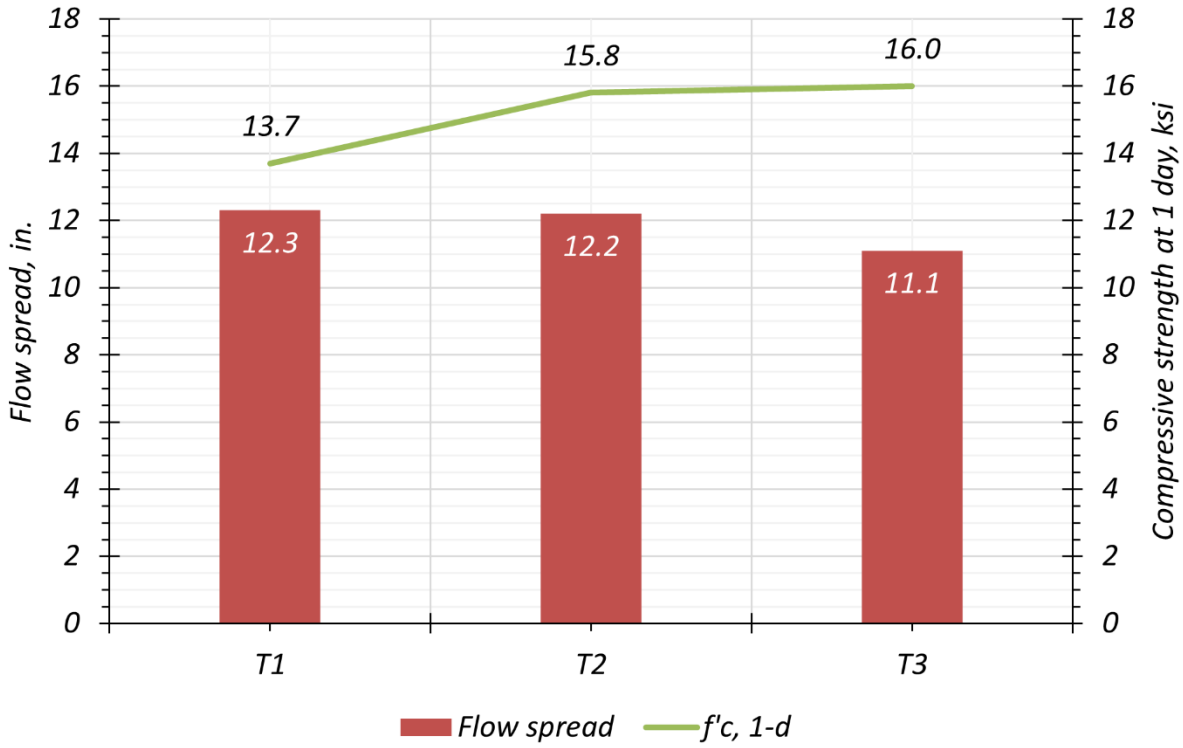

Figure 4.20. Results of Optimization for Mix-3b with C-5 Cement.

4.6.2.2.3 Optimization of Mix-4 with Selected Type III Cement

The other selected mixture, Mix-4b, was optimized with C-5 cement to see the performance comparison with Mix-3b with C-5 cement. Table 4.33 shows the initial mixture design of Mix-4b.

The optimization process was the same as for Mix-3b with C-5 cement. The reduced amount of water and HRWR for the target flow spread can be calculated from the optimization results of Mix-3b with C-5 using the same water reduction proportion by cement weight. Table 4.34 shows the optimization results. The optimized Mix-4b with C-5 achieved 11.0 in. flow spread and 13.1 ksi compressive strength at 1 day.

Table 4.33. Mixture Proportions for Mix-4b.

Description	Proportion	Mix-4b (lb/yd^3)
Cement	1	1487
Silica fume	0.08	112
Fly ash	0.10	155
Sand	1.08	1603
Water	0.231	344
HRWR	0.025	38
Steel fiber	1.5%	200

Table 4.34. Optimization Process for Mix-4b with C-5 Cement.

Description	Trial Batch	
	T1	T2
Cement	1	1
Silica fume	0.08	0.04
Fly ash	0.10	0.08
Sand	1.08	1.08
Water	0.283	0.214
HRWR	0.019	0.022
Steel fiber	1.5%	1.5%
w/*cm*	0.240	0.181
HRWR/*cm*	0.0160	0.0186
Flow spread, in	8.9	11.0
$f'_{c,1\text{-}d}$, ksi	12.4	13.1

Notes $f'_{c,1\text{-}d}$: 1-day compressive strength

4.6.3 Evaluation of Durability by Service Life Prediction

Preliminary service life predictions for the developed UHPC mixtures were also conducted to understand the influence of the silica fume content. While Mix-1a and Mix-2a have 15 percent silica fume proportion by cement weight, Mix-3a was designed to have 4 percent silica fume proportion to achieve high early strength. As a result, Mix-3a achieved the highest 1-day compressive strength but has a lower resistivity due to the lower silica fume content. Even though the resistivity of Mix-3a was lower than other mixtures, it was classified as *Very Low* permeability,

similar to Mix-1a and Mix-2a, based on the classifications given by ASTM C1202 (2017) and AASHTO T 358 (2017), shown in Table 3.1. However, the results from resistivity measurements alone were not definitive in explaining the long-term impact of low silica fume content. Therefore, a preliminary service life prediction was conducted. Details are provided below.

Life-365 is a commercially available service life prediction model (Ehlen 2019). This model is based on Fick's second law equation with an error function solution for service life prediction, as shown in Equation (4.3) (ASTM C1556 2011; Ehlen 2019):

$$C_{x,t} = C_o + (C_s - C_o)\left(1 - erf\left(\frac{x}{2\sqrt{\frac{D_o}{F}t}}\right)\right) \tag{4.3}$$

where:

$C_{x,t}$ = Chloride concentration at depth x, %

C_o = Initial chloride concentration, %

C_s = Surface chloride concentration, %

x = Depth to reinforcement, in.

D_o = Chloride ion self-diffusion coefficient, in^2/s

F = Formation factor

t = Time for exposure limit to be reached, s

The application of Life-365 for UHPC has limitations, such as the lowest *w*/*cm* considered for the model is 0.25, while the developed UHPC mixtures only have a range of *w*/*cm* from 0.178 to 0.190. However, Fick's second law equation with an error function solution can be used to estimate the service life span for UHPC mixtures by computing the formation factor using the bulk resistivity measurement. To understand the process of service life calculation for a UHPC mixture, background information on the formation factor is necessary.

Bulk resistivity, according to ASTM C1760 (2021), is commonly used for CC as an indicator of durability. Even though resistivity results help evaluate durability, the values alone cannot be used for an effective comparison of different concrete mixtures in terms of their durability performance because the resistivity values are largely dependent on the PSR of a concrete mixture. For example,

even if two mixtures have the same bulk resistivity value, the two mixtures may have different durability performances due to different PSR. Recently, many researchers have used the term *formation factor F* to indicate the fundamental transport property of concrete that is defined as an ionic transport rate in concrete (Weiss et al. 2018). The formation factor is defined as the inverse of porosity multiplied by connectivity (Archie 1942) and is a ratio of the bulk resistivity to PSR, as shown in Equation (4.4) (Weiss et al. 2016).

$$F = \frac{\rho}{\rho_o} \cong \frac{1}{\phi \beta} = \frac{D_o}{D} \tag{4.4}$$

where:

ϕ = Porosity

β = Connectivity

ρ = Bulk resistivity, kΩ-cm

ρ_o = PSR, kΩ-cm

D_o = Chloride ion self-diffusion coefficient, in^2/s

D = Diffusion coefficient, in^2/s

As shown in Equation (4.4), the PSR of each mixture is required to obtain the formation factor. The National Institute of Standards and Technology (NIST) model is generally used to estimate PSR (NIST 2017). To estimate PSR, this model requires mix proportions, chemical constituents of cementitious materials, and degree of hydration with an assumption of a 75 percent alkali free factor for sodium and potassium. Using the NIST model (NIST 2017), the PSRs of Mix-1a, Mix-2a, Mix-3a, and Mix-4a were calculated to be 0.0047, 0.0038, 0.0032, and 0.0044 kΩ-cm, respectively (Table 4.35).

Table 4.35. Pore Solution Resistivity Using NIST Model.

Description	Mix-1a	Mix-2a	Mix-3a	Mix-4a
w/*c*	0.23	0.25	0.20	0.21
Water, lb	329	312	320	320
Cement, lb	1445	1238	1579	1528
Silica fume, lb	217	186	63	115
Fly ash, lb	72	310	121	159
Hydration, %	47	47	47	47
σ_{ps} (S/m)	21.29	26.59	31.27	22.74
PSR, kΩ-cm	0.0047	0.0038	0.0032	0.0044

Notes:
1. Degree of hydration is assumed to be 47 percent based on Acker (2004).
2. σ_{ps}: Conductivity
3. S/m: Siemens/meter
4. PSR: Inverse of conductivity
5. Cement composition: 0% SiO_2, 0.2% Na_2O, and 0.64% K_2O from X-ray fluorescence analysis
6. Fly ash composition: 53.9% SiO_2, 0.34% Na_2O, and 0.93% K_2O from X-ray fluorescence analysis
7. Silica fume composition based on NIST (2017): 96% SiO_2 and 0.2% Na_2O and K_2O

However, Tanesi et al. (2019) reported that PSR estimation using the NIST model tends to be overestimated when fly ash is included in a mixture. In addition, measuring the degree of hydration of UHPC is difficult. Thus, an assumption of the degree of hydration is needed. The degree of hydration was assumed to be 0.47 based on the literature (Acker 2004) for the calculation of the PSR of Mix-1a, Mix-2a, Mix-3a, and Mix-4a with the NIST model. Because of the shortcomings noted, it is questionable if the use of the NIST model for PSR estimation for UHPC is appropriate. Note that issues of the NIST model for the PSR estimation of concrete containing fly ash were resolved by Mukhopadhyay et al. (2019), and they developed a new model.

Spragg et al. (2019) has used a 0.005 kΩ-cm PSR value for proprietary UHPC mixtures based on the literature (Bentz 2007; Spragg et al. 2016; Taylor 1997). This value is in the range of the values computed for Mix-1a, Mix-2a, Mix-3a, and Mix-4a with the NIST model. Because of the limitations of applicability of the NIST model to UHPC containing fly ash, for this preliminary service life prediction study, 0.005 kΩ-cm PSR ρ_o for all mixtures was assumed. Even though the estimation method for PSR should be refined to calculate the appropriate value more accurately, the use of 0.005 kΩ-cm PSR value for preliminary service life prediction was used to allow a comparison of mixtures.

Measured bulk resistivity values should be corrected by multiplying the geometry factor, *k*, which is a ratio of the cross-sectional area to the length of a specimen in centimeters, as shown in Equation (4.5). For a 4 × 8 in. cylinder, which is a sample size used for the bulk resistivity test, the geometry factor is 3.989 cm (Spragg et al. 2019).

$$\rho = R \times k \tag{4.5}$$

where:

R = Measured bulk resistivity, kΩ-cm

k = Geometry factor, cm

After calculating the formation factor using Equation (4.4), the predicted service life can be computed using Fick's second law, as shown in Equation (4.3). Table 4.36 and Table 4.37 show the assumed variables used for Fick's second law and the predicted service life of each mixture, respectively. The variables of $C_{x,t}$, C_o, and C_s are based on Life-365 (Ehlen 2019). A value of 0.68 percent for C_s corresponds to an urban highway bridge. The depth to reinforcement x is the reinforcement clear cover thickness taken from the *TxDOT Bridge Design Manual—LRFD* (TxDOT 2023).

Table 4.36. Variable Assumptions for Fick's Second Law.

Variable	Variable Description	Assumption	Source
$C_{x,t}$	Chloride concentration at depth *x* and time *t* that initiates corrosion (%)	0.05	Ehlen (2019)
C_o	Initial chloride concentration (%)	0	Ehlen (2019)
C_s	Surface chloride concentration (%)	0.68	Ehlen (2019)
x	Depth to reinforcement (in.)	1.5	TxDOT (2023)
D_o	Chloride ion self-diffusion coefficient (in^2/s)	3.0×10^{-6}	Spragg et al. (2019)

Table 4.37. Formation Factor and Predicted Service Life of Developed UHPC Mixtures.

Mixture	Silica fume content by volume, %	Measured bulk resistivity at 28 days, kΩ-cm	$\rho = R \times k$, kΩ-cm	Formation factor $F = \rho / \rho_o$	Predicted service life, years
Mix-1a	16.7	105	422	84,487	314
Mix-2a	13.8	106	426	85,285	317
Mix-3a	4.9	58.7	234	46,831	174
Mix-4b	8.6	78.8	314	62,867	233

Notes:
1. Except the cement for Mix-4b, the same materials were used.
2. Mix-4b is considered because Mix-4a resistivity data was not available.

Even though the resistivity results of all developed mixtures are in the category of *Very Low* according to ASTM C1202 (2017), the predicted service life results vary. Figure 4.21 shows the predicted service life as a function of silica fume content by volume for the four mixtures. This plot indicates that the predicted service life is highly dependent on silica fume content up to approximately 14 percent by volume.

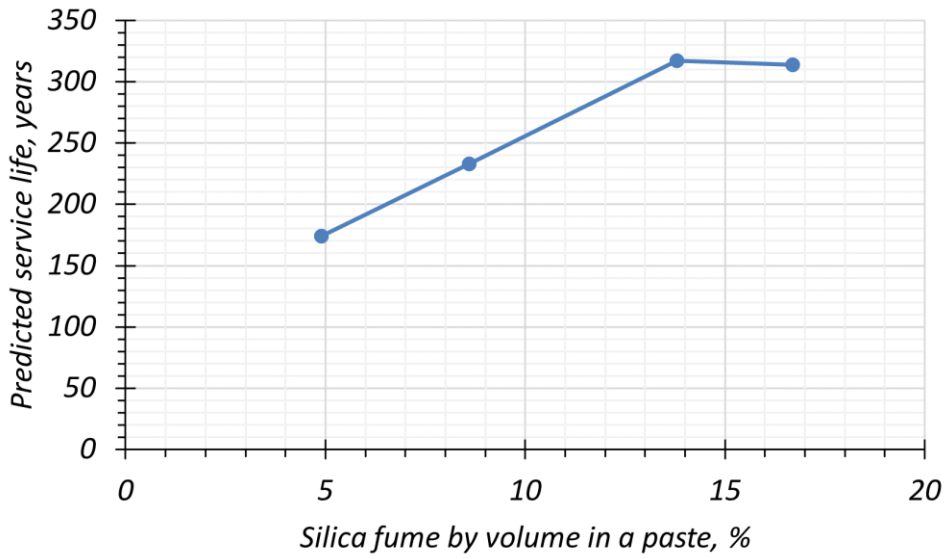

Figure 4.21. Relationship between Silica Fume Content and Predicted Service Life.

4.6.4 Summary

To develop a UHPC mixture with high durability and a long service life, increasing silica fume content may provide a simple solution. However, this approach may cause low early strength. Because achieving high early strength is one of the essential requirements for this project, the low silica fume content of Mix-3a was adopted strategically. For high early strength, low water content is required because it reduces the average distance between cement particles (Aïtcin 2016). When the distance between cement particles is less, the hydrates are connected to the adjacent particles with a smaller amount of hydration at the surface of the cement (Barcelo et al. 2001). However, water demand increases with silica fume content because silica fume is the finest material (Van and Ludwig 2012). Therefore, high early strength gain can be achieved by maintaining a proper balance between silica fume content (the lower the better), cement content, and water content. A good balance was achieved in Mix-3a with respect to early strength gain, and as a result, this mix provided the highest early strength.

However, Mix-3a has the lowest resistivity and thus the lowest service life estimate among the developed mixtures. To improve durability while maintaining high early strength, Mix-4a was designed by increasing the silica fume content. Increasing the silica fume content may reduce workability if the water content is not increased accordingly. However, an increase in water content can lower early strength gain because it causes an increase in the average distance of cementitious particles. Thus, the fly ash content was increased slightly to enhance workability because the spherical shape of fly ash acts as a ball bearing (Mindess et al. 2003). Consequently, Mix-4a achieved comparable workability, 1-day and 28-day compressive strengths, and better durability than Mix-3a while maintaining the same water content. Based on the results of service life prediction, the measured fresh and hardened properties, and cost analysis, Mix-4b was selected for further study in this research program. Mix-4 was used for two 50 ft and one 70 ft long girder fabrication, as well as for a fiber volume optimization study discussed in Section 4.7 and other material-level experiments discussed in Section 5.2.

4.7 FIBER VOLUME OPTIMIZATION STUDY

Fibers are an important component in UHPC because they are responsible for UHPC's tensile strength and significantly higher ductility and energy absorption capacity relative to CC. For the development of the nonproprietary UHPC mixtures in this study, a range of fiber volume was evaluated to choose an optimum percentage of fiber for the selected mixture. The tensile strength of UHPC was considered one of the key parameters for the performance evaluation of specimens with different fiber volumes. Direct tension testing of UHPC was used to evaluate the uniaxial tensile capacity of the selected trial mixes. The following sections discuss the motivation behind the study and the procedure for evaluation. The end of the section discusses the results of the experimental testing and recommendations for the optimized fiber volume.

4.7.1 Background and Motivation

Several investigations have been conducted by researchers to study the impact of different types and volumes of fibers on the properties of UHPC. Steel fibers were selected over synthetic or mineral fibers for this study due to the significant merits reported in literature in terms of the workability and mechanical properties of the mix (Hannawi et al. 2016). Le Hoang and Fehling

(2017) reported that the mix with 0.5 in. fibers performed better under tension testing than mixes with 0.35 in. and 0.8 in. fibers.

For this investigation, commonly used straight steel fibers of 0.5 in. length and 0.008 in. diameter were considered. The volume of fiber content was chosen based on the performance of two primary parameters—the hardened properties (compressive strength and tensile strength) and the economy of the mix. In addition, workability was also considered while finalizing the fiber percentage for the selected UHPC mixture.

4.7.1.1 Hardened properties

Larsen and Thorstensen (2020) presented a detailed literature review that provides an overview of the findings of several experimental investigations undertaken to identify the relationship between steel fibers and hardened properties of UHPC. The authors highlighted that while FRC commonly contains fiber contents varying between 0.25 to 2 percent by volume, commercial mixture proportions of UHPC have fiber contents ranging from 2 to 6 percent by volume. Compressive strength is shown to have negligible (Le Hoang and Fehling 2017; Park et al. 2017) to substantial (El-Tawil et al. 2016; Ibrahim et al. 2017; Wang and Gao 2016; Wu et al. 2016) improvement from increased fiber content due to the delayed formation of microcracks. However, an adverse impact on compressive strength was observed when increasing the fiber volume over 3 percent, which can be attributed to the agglomeration of fibers and the air entrapped in the matrix (Le Hoang and Fehling 2017; Meng et al. 2016).

The peak flexural tensile strength of UHPC was approximately three times higher for fiber volumes of 2 percent compared to volumes of 0.5 percent (Park et al. 2017). Although Meng and Khayat (2018) observed that a higher percentage of fibers, such as 3 percent and above, reduced the flexural tensile strength due to agglomeration of fibers, Abbas et al. (2015) reported that the tensile strength improved with the addition of fiber content up to as high as 6 percent and created only a very slight reduction in flow and workability. Therefore, the impact of steel fiber appears to depend on the rheology and other constituents of the mixture; moreover, its effect on the hardened properties may vary with different mixture proportions. Thus, it is important to investigate the influence of fiber content on the nonproprietary UHPC mixture being developed.

El-Helou et al. (2022) noted that the crack propagation is retarded by the crack bridging property of steel fibers when the cementitious matrix is no longer capable of sustaining cracks. This ability to interlock the structure with the fibers is directly dependent on the number of fibers per unit area of the cracking surface. The authors conducted a series of direct tension tests on specimens with UHPC containing fiber volumes ranging from 2 percent to 4 percent. They observed a 35 percent and 48.4 percent increase in cracking and ultimate tensile strength when increasing the fiber volume from a baseline of 2 percent to 3 and 4 percent by volume, respectively, for one of the products they tested. The authors also reported an increase in tensile and post-cracking capacity of the specimens with a decrease in localization strain as the fiber volume increases.

4.7.1.2 Economy of Mix

It is essential to optimize the fiber content to control the overall economy of the mix because fibers drive up the cost of UHPC significantly. El-Tawil et al. (2016) reported every 1 percent increase in fiber content by volume with locally produced steel fibers increased the cost of the UHPC per cubic yard by $516/cyd. Kim (2018) demonstrated that the 2 percent by volume of steel fibers contributed to 40.3 percent of the total cost of the nonproprietary mixture developed in Colorado for bridge construction. This cost was more than any other constituent of the mix. Therefore, it its evident that the fiber content should be examined for the selected mixture. Cost analysis developed in this study of the trial mixtures with 1.5 percent fiber volume showed that the steel fibers account for approximately 60 percent of the total cost of the mix. Therefore, this study aimed at studying other fiber volumes to evaluate the performance of the mix design with varying fiber contents.

4.7.2 Methodology

The fiber volume was varied to identify the minimum fiber content needed for the selected mix to meet the design requirements. This section discusses the basis of selection of the fiber volumes chosen for the trial mixes, the mix proportions used for the fiber volume study, and the test matrix that was conducted at different ages to assess the performance of the selected mix.

4.7.2.1 Fiber Volume and Mix Compositions

For this research, Mix-4b with C-5 Type III cement was selected for the fiber volume study. Parameters such as compressive strength, post-cracking strength, energy absorption capacity, and

strain capacity were reported by El-Tawil et al. (2016) to be lower for 0.5 percent fiber content than for 1 percent and 1.5 percent. The authors also noted that the crack localization may be eliminated due to strain hardening provided by 1.0 and 1.5 percent fibers, which may not be possible with 0.5 percent fiber content in large-scale structures (with random fiber orientation) under dead loads. Significant improvement in strain hardening is reported with a steel fiber content of 2 percent and above (Arora et al. 2019; Hassan et al. 2012; Wang and Gao 2016). Based on several research studies conducted in the past (Arora et al. 2019; Hassan et al. 2012; Le Hoang and Fehling 2017; Park et al. 2017; Wang and Gao 2016), fiber contents of 1 percent, 1.5 percent, and 2 percent by volume were chosen for evaluation. To account for the change in the fiber volume, the fine aggregate proportion was adjusted. Table 4.38 presents the mix proportions of the variants of Mix-4 in which the adjusted fiber volumes were compensated with modifications to the fine aggregate proportion.

Table 4.38. Mix Proportions by Cement Weight for Different Fiber Contents.

Constituents	Proportions		
	Steel fiber 1.0%	Steel fiber 1.5%	Steel fiber 2.0%
Cement	1.00	1.00	1.00
Silica Fume	0.08	0.08	0.08
Fly ash	0.10	0.10	0.10
HRWR	0.022	0.022	0.022
Fine Aggregate	1.09	1.08	1.06
Water	0.214	0.214	0.214
Steel fibers	0.09	0.13	0.18

4.7.2.2 Test Matrix

The hardened properties of compression and tension were evaluated for this study. The primary objective of the test matrix was to investigate the impact of varying the steel fiber content on compressive strength and tensile strength. Table 4.39 presents the test matrix of the fiber volume study with age of testing. At least three cylinders of 3 × 6 in. were tested under compression at 7 days and 28 days for the three different fiber volumes. A control mix without fibers was used for compressive strength testing. Five prisms of 2 × 2 × 17 in. were tested under uniaxial tension at 7 days and 28 days.

Table 4.39. Test Matrix for Fiber Volume Study.

Test	Age, days	Fiber Percent by Volume	Number of Specimens	Dimension of Specimens, in.
Compressive Strength Test	1	0	6	3 × 6
		1.0	6	3 × 6
		1.5	6	3 × 6
		2.0	6	3 × 6
	7	0	6	3 × 6
		1.0	6	3 × 6
		1.5	6	3 × 6
		2.0	6	3 × 6
	28	0	3	3 × 6
		1.0	6	3 × 6
		1.5	6	3 × 6
		2.0	6	3 × 6
Uniaxial Tension Test	7	1.0	5	2 × 2 × 17
		1.5	5	2 × 2 × 17
		2.0	4	2 × 2 × 17
	28	1.0	5	2 × 2 × 17
		1.5	5	2 × 2 × 17
		2.0	6	2 × 2 × 17

Note: Because two out of four specimens cracked within the gage length for 2 percent fiber at 7 days, one was saved for testing at 28 days due to a lower probability of cracking within the gage length during the direct tension test.

It was decided against uniaxial tension tests at early ages, such as 1 day and 3 days, because the prisms with 1 percent fiber volume were becoming damaged within the grip length or outside the gage length. Graybeal and Baby (2019) and Riding et al. (2019) reported the challenges of conducting the uniaxial tension test due to the cracking of the specimens during gripping. The misalignment of the specimen can cause bending and lead to cracks outside the gage length. As a result, it is impossible for the linear variable displacement transducers (LVDTs) to record any data on the tensile behavior of the specimen. These challenges were faced for almost all the specimens tested under tension at 3 days. Therefore, the ages of 7 days and 28 days were selected those ages offered more reliable data for comparing the tension performance for the various fiber contents.

4.7.3 Test Results

This section presents the results of the compressive strength and tensile strength tests. ASTM C39 (2020), with modifications for UHPC from ASTM C1856 (2017), was followed for compressive strength testing. An MTS load frame and load cell of 500-kip axial capacity was used for the test at a load rate of 145 ± 7 psi/s under force control. Section 4.7.2 discusses further details of the test.

The tensile strength test is based on the uniaxial direct tension test method developed by Graybeal and Baby (2019). In this research, a load frame and load cell of 100-kip axial capacity was used for the test at a displacement rate of 0.00010 in./s in tension before strain localization.

4.7.3.1 Variation of Compressive Strength with Fiber Volume

Figure 4.22 presents the compressive strength gain at 1, 7, and 28 days with the selected percentages of fiber by volume. Table 4.40 lists the compressive strengths of specimens tested for the comparison of the fiber volume. The mix with 1.5 percent fiber by volume showed the highest compressive strength among all the trials. The compressive strength of the control mix without fibers had slightly less compressive strength compared to other mixes, but also had a high early strength gain. The early age compressive strength of the mix with 1 percent fibers was slightly higher than the mix with 2 percent fibers, but both 1 and 2 percent fiber mixes showed very similar compressive strength. The workability of the mix with 2 percent fibers was less than the other mixes. Table 4.41 presents the results of the flow table test.

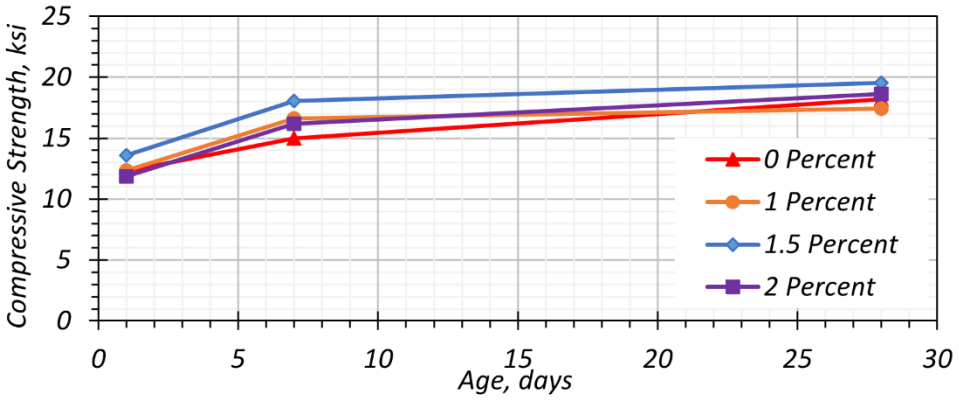

Figure 4.22. Influence of Fiber Content on Average Compressive Strength.

Table 4.40. Compressive Strength for Different Fiber Content.

Age, days	Specimen Number	Compressive Strength, ksi			
		0% Fiber	1% Fiber	1.5% Fiber	2% Fiber
1	1	13.3	11.7	12.1	13.2
	2	-	13.2	13.8	11.5
	3	12.7	-	14.3	12.0
	4	11.6	-	13.5	11.0
	5	-	11.8	14.0	11.4
	6	11.6	12.6	13.8	12.1
	Average	**12.3**	**12.3**	**13.6**	**11.9**
	Std. Dev.	0.75	0.62	0.71	0.68
	CoV	6%	5%	5%	6%
7	1	16.1	15.4	-	15.9
	2	-	16.3	18.1	16.2
	3	13.7	-	-	16.0
	4	-	-	19.0	15.6
	5	-	17.5	-	17.4
	6	15.1	17.3	17.1	15.8
	Average	**15.0**	**16.6**	**18.1**	**16.2**
	Std. Dev.	1.01	0.82	0.79	0.59
	CoV	7%	5%	4%	4%
28	1	17.5	-	20.1	-
	2	18.5	17.0	19.6	19.1
	3	18.5	17.1	-	18.4
	4	-	18.1	19.1	19.5
	5	-	17.6	19.3	-
	6	-	-	-	17.4
	Average	**18.2**	**17.4**	**19.5**	**18.6**
	Std. Dev.	0.50	0.41	0.39	0.77
	CoV	3%	2%	2%	4%

Notes:
1. Some specimens were discarded due to improper grinding of ends, indicated by dashed entries.
2. - : Not available
3. Bold: Average value

4.7.3.2 Variation of Tensile Strength with Fiber Volume

Due to the challenges noted with the uniaxial tensile test, the success rate of the tests was quite low, ranging from one in five to three in six specimens cracking with the gage length. Figure 4.23 illustrates the tensile specimens that cracked within the gage length during the direct tension test at 28 days. The top and bottom frame (extensometer) mark the boundary of the gage length for the LVDTs. The failure of the specimens during gripping or cracking outside the gage length is not a reflection of the performance of the mix or the fiber content. Therefore, the comparison provided

below is based on those specimens that cracked within the gage length such that the data from the LVDTs is a reliable estimation of the tensile behavior of the material.

(a) 1 percent fiber *(b) 1.5 percent fiber* *(c) 2 percent fiber*

Figure 4.23. Specimens after Uniaxial Tensile Strength Test.

Table 4.41 lists the first cracking stress, peak stress, MOE in tension, and the flow for the three different fiber contents at 7 days and 28 days. Those specimens in which the crack occurred within the gage length are indicated by bold face font in Table 4.41. Figure 4.24 and Figure 4.25 present the stress-strain curves for the tested specimens at 7 days and 28 days, respectively, for all three fiber contents. The recommended limit of tensile strength by PCI for quality control purposes based on their idealized tensile stress-strain model, 0.75 ksi at 0.004 strain (eConstruct 2020), is marked with dashed lines. The tensile strength was observed to increase with fiber content.

Figure 4.26 presents the comparison of tensile strength under uniaxial tension at 7 and 28 days for different fiber contents. It was observed that the tensile performance was enhanced with an increase in the fiber volume. Those specimens that had crack formation within the gage length are presented for comparison. The specimens with a crack forming at the extremities of the gage length where the crack may have initiated due to a stress concentration from the mounting screw of the extensometer are not presented in this comparison. At 7 days, the mix with 1 percent fiber showed

a lower post-cracking strength compared to the other two mixes, indicating less bridging of cracks by the fibers.

Table 4.41. Uniaxial Tensile Strength for Different Fiber Content.

Age, days	Speci-men No.	1% Fiber			1.5% Fiber			2% Fiber		
		First Crack Stress, ksi	**Peak Stress, ksi**	**MOE, ksi**	**First Crack Stress, ksi**	**Peak Stress, ksi**	**MOE, ksi**	**First Crack Stress, ksi**	**Peak Stress, ksi**	**MOE, ksi**
7	1	0.82	0.82	6580	1.02	1.04	6561	0.54	1.13	6679
	2	0.39	0.55	6635	**0.85**	**0.87**	**5452**	**0.75**	**1.09**	**4617**
	3	**0.91**	**0.91**	**6453**	1.29	1.29	2260	1.06	1.20	6902
	4	0.35	0.70	6253	0.15	0.92	5216	**1.19**	**1.27**	**6745**
	5	-	-	-	0.27	0.71	4180	-	-	-
	Flow	11 in.			11.2 in.			10.6 in		
28	1	**1.14**	**1.14**	**6761**	**0.77**	**1.08**	**6730**	**0.97**	**1.20**	**6289**
	2	0.84	0.91	6145	0.96	0.96	6353	1.03	1.12	6935
	3	0.52	1.02	6675	0.59	1.10	6536	**0.85**	**1.06**	**3937**
	4	**0.89**	**1.04**	**6807**	0.84	1.09	6890	1.08	1.11	6771
	5	0.72	0.84	5120	0.83	1.10	6698	0.73	1.17	6963
	5*	-	-	-	-	-	-	**0.912**	**1.19**	**6958**
	Flow	10.9 in.			11 in.			10.8 in.		

Note:
1. Specimen 5 of 1 percent fiber by volume was damaged during gripping and could not be tested.
2. Specimen 5* was saved from the 7-day test batch to test at 28 days because sufficient results for comparison were obtained with the two successful 7-day tests.
3. The 7-day and 28-day specimens were cast in different batches; therefore, flow from each batch is presented.
4. Those specimens in which the crack occurred within the gage length are in **bold** font.
5. - : Not available

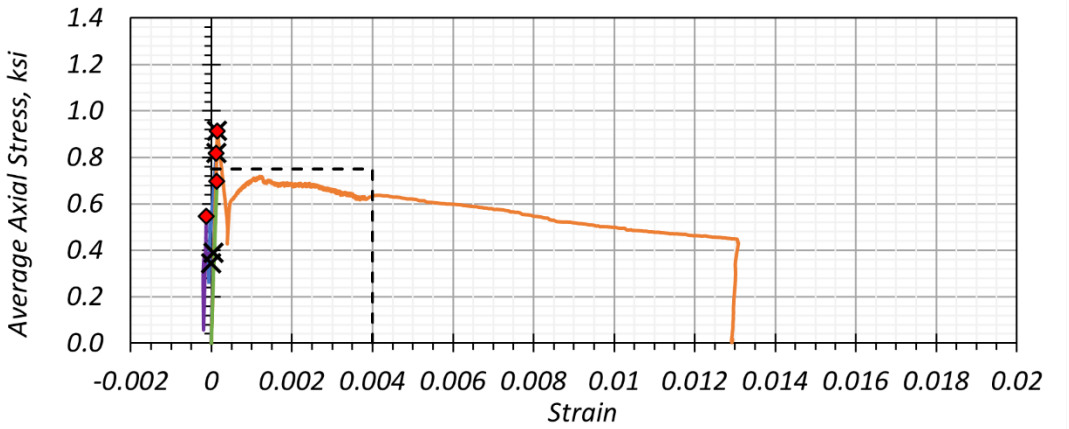

(a) 1% Fiber by Volume

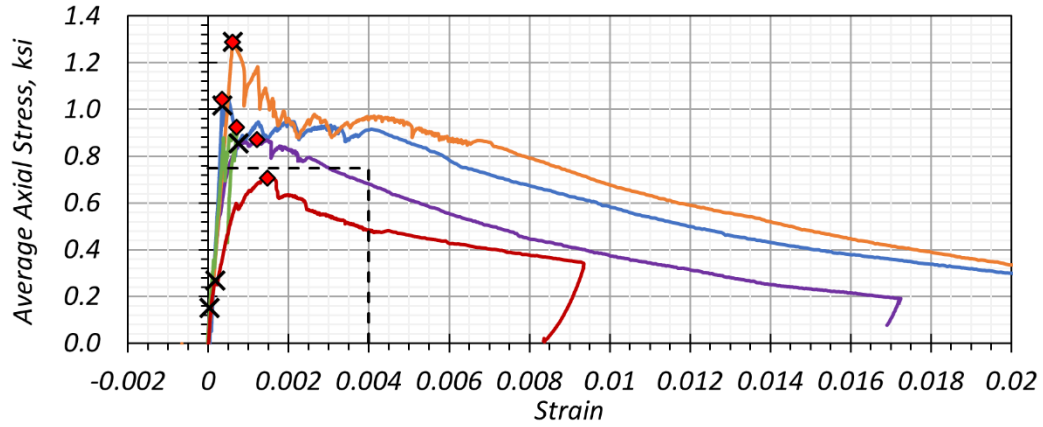

(b) 1.5% Fiber by Volume

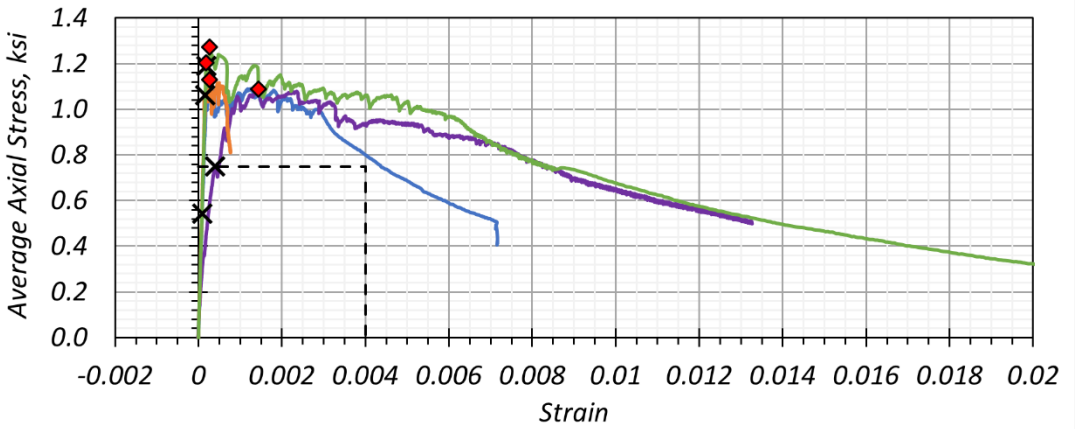

(c) 2% Fiber by Volume

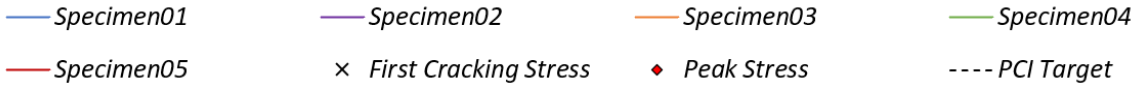

Figure 4.24. Influence of Fiber Content on Tensile Strength at 7 Days.

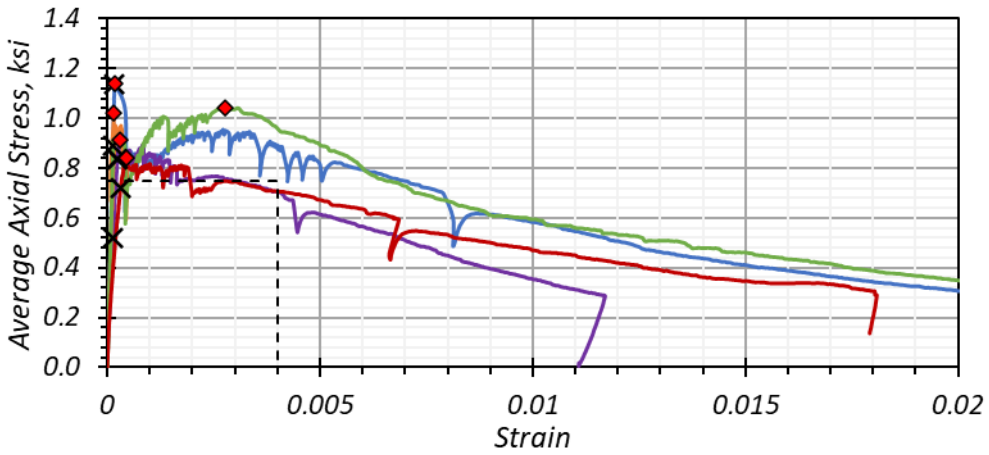

(a) 1% Fiber by Volume

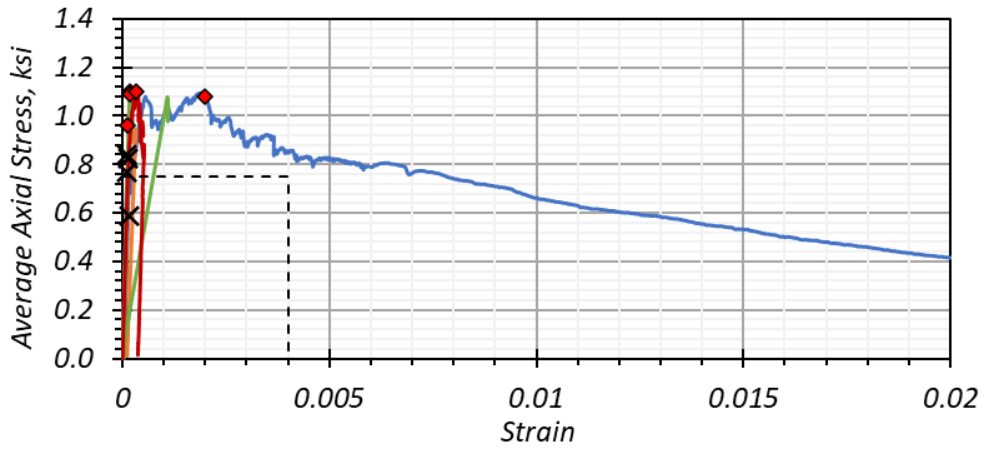

(b) 1.5% Fiber by Volume

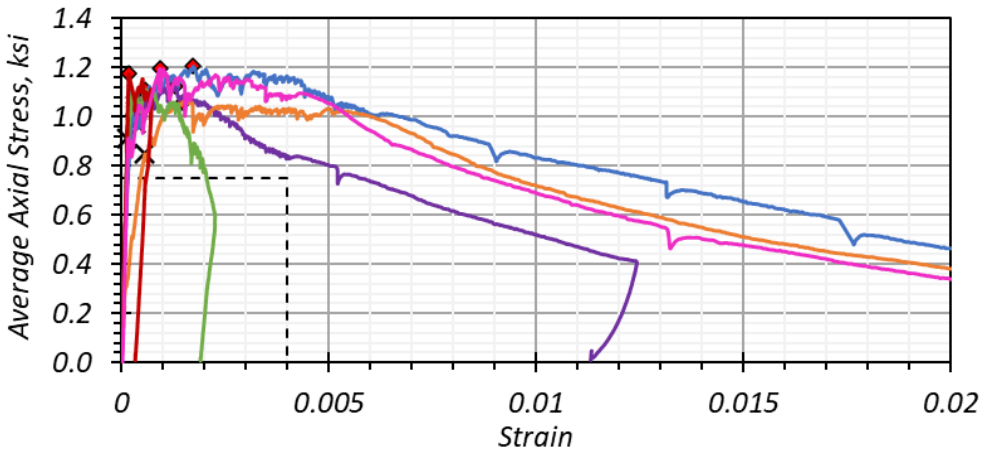

(c) 2% Fiber by Volume

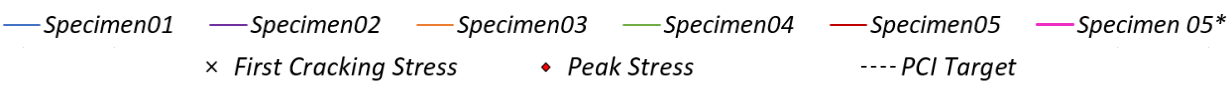

Figure 4.25. Influence of Fiber Content Tensile Strength at 28 Days.

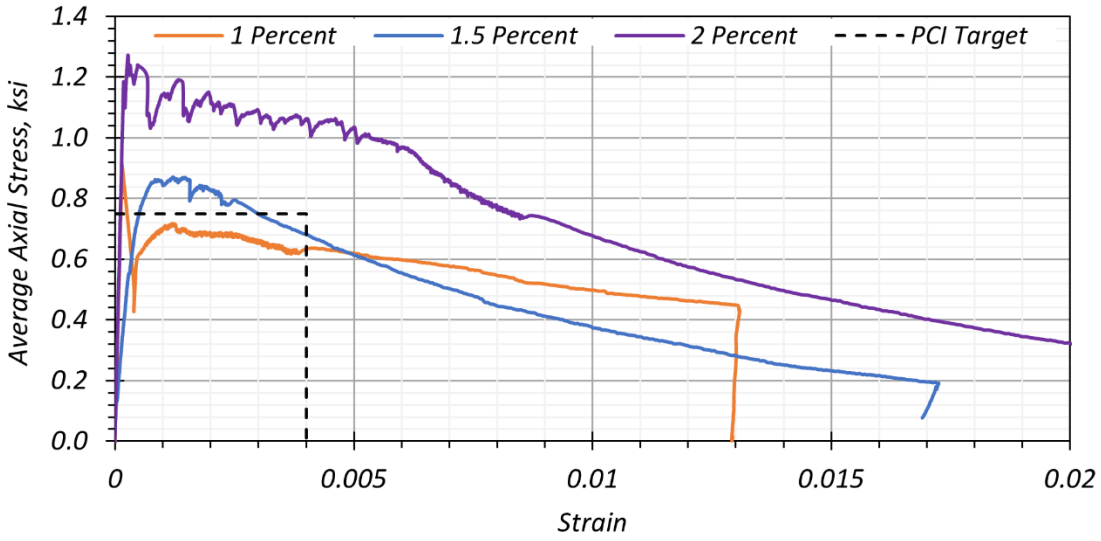

(a) 7 days

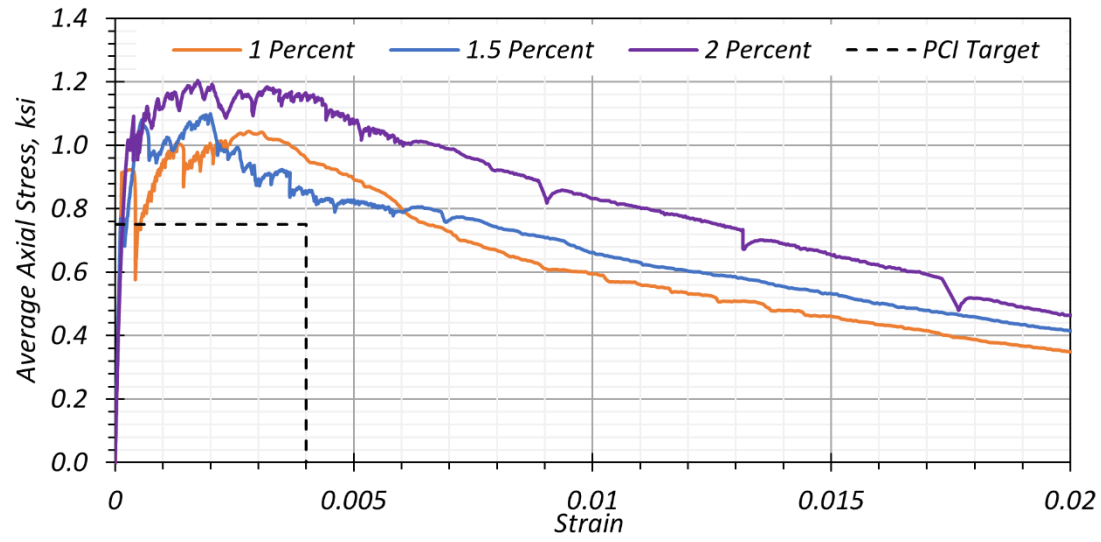

(b) 28 days

Figure 4.26. Comparison of Tensile Stress-Strain Behavior for Different Fiber Volumes and Ages.

4.7.4 Discussion of Results and Recommendations

Figure 4.27 presents a comparison of the average compressive strength at different ages and Table 4.42 tabulates the data presented in the chart. No significant difference in compressive strength exists between the control mix without fibers and the mix with 1 percent fibers. An increase in compressive strength occurs at all three ages for the mix with 1.5 percent fibers by volume. The compressive strength of the mix with 2 percent fibers was found to be lower than the 1.5 percent fiber mix, which may be attributed to the entrapped air and agglomeration of fibers for the higher

volume. Although the flow spread value of the mixtures for all three fiber volumes was within the acceptable range of 9–11 in., during casting of the specimens, the mix with 2 percent fiber volume felt less workable than the mixtures with 1 percent and 1.5 percent fiber volumes. In terms of performance under compressive load, the 1.5 percent fiber mix exhibited the best results among all three fiber contents tested.

Figure 4.28 and Figure 4.29 present a comparison of first cracking strength and peak strength, respectively, of the UHPC mixture under uniaxial tensile loading for different fiber contents. Table 4.43 and Table 4.44 tabulate the data for the same charts. The specimens that cracked within the gage length were selected for this comparison. The first cracking stress is not largely influenced by the fiber volume. The first cracking strength is attributed more to the tensile capacity of the cementitious matrix, whereas the post-cracking strength is more reflective of the capacity of fibers to bridge the cracks (Park et al. 2017; Yoo et al. 2013). The peak tensile strength of the mixes tends to increase with an increase in fiber volume. This effect can be more clearly observed in the 28-day data and is likely due to the bridging of microcracks by the fibers.

Based on the results, the 1.5 percent fiber volume is recommended for the nonproprietary mix developed. Though the peak stress of the mix with 1 percent fiber is higher than the 1.5 percent fiber mix at 7 days, the 1.5 percent mix performed better in the overall tensile performance over a larger strain range. While the 2 percent fiber mix had superior tensile strength, its workability and compressive strength was less than observed for the 1.5 percent mix. Even though 1 percent mix is more economical, the 1.5 percent fiber volume was chosen because of its superior tensile capacity over a larger strain range and because it meets the tensile design target of 0.85 ksi tensile strength at early age and 1 ksi at 28 days. It also meets the target compressive strengths of 14 ksi at 1 day and 20 ksi at 28 days.

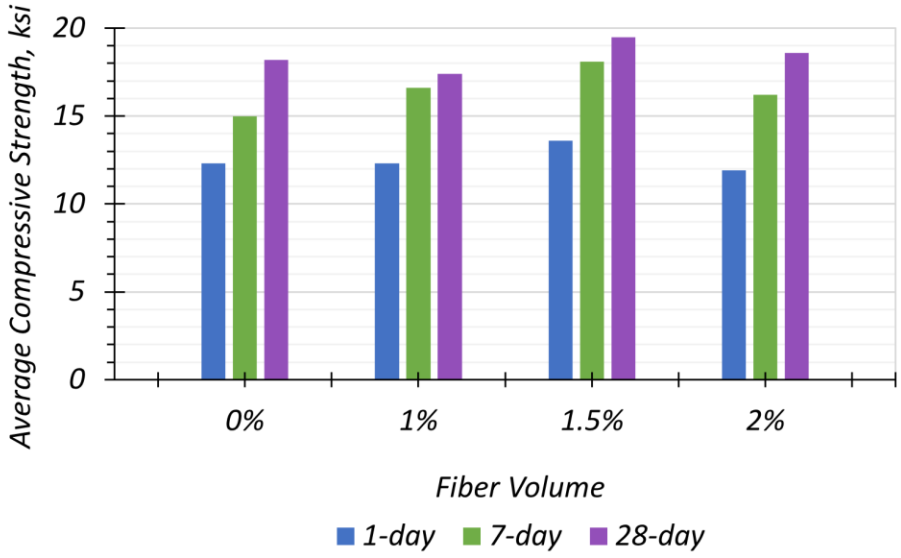

Figure 4.27. Average Compressive Strength Comparison over Different Fiber Volumes and Ages.

Table 4.42. Average Compressive Strength for Different Fiber Volumes and Ages.

Age, days	Average Compressive Strength, ksi			
	0% Fibers	1% Fibers	1.5% Fibers	2% Fibers
1	12.3	12.3	13.6	11.9
7	15.0	16.6	18.1	16.2
28	18.2	17.4	19.5	18.6

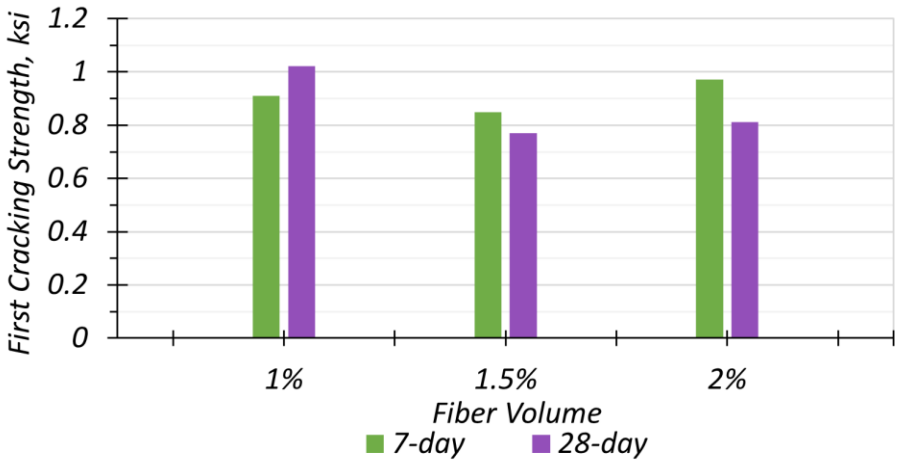

Figure 4.28. First Cracking Strength for Different Fiber Volumes and Ages.

Table 4.43. First Cracking Strength for Different Fiber Volumes and Ages.

Age, days	First Cracking Strength, ksi		
	1% Fibers	1.5% Fibers	2% Fibers
7	0.91	0.85	0.97[1]
28	1.02[1]	0.77	0.81[1]

Note:
1. Average value of the specimens that had the crack within the gage length.

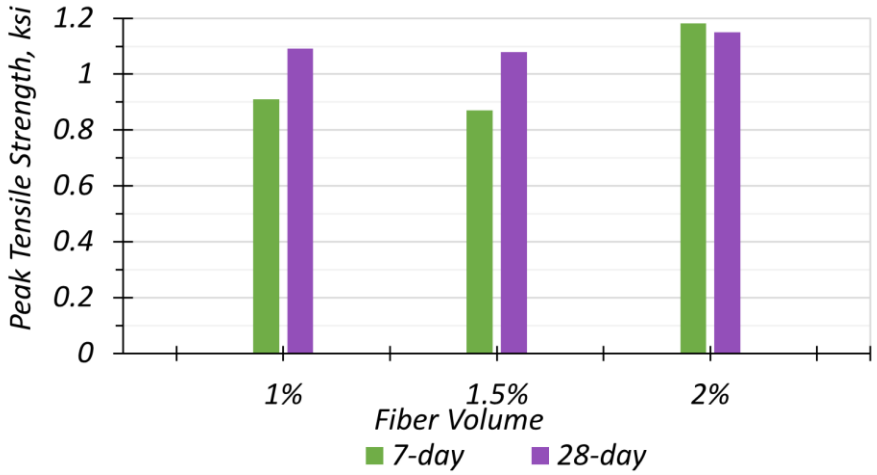

Figure 4.29. Peak Tensile Strength for Different Fiber Volumes and Ages.

Table 4.44. Peak Tensile Strength for Different Fiber Volumes and Ages.

Age, days	Peak Stress, ksi		
	1% Fibers	1.5% Fibers	2% Fibers
7	0.91	0.87	1.18[1]
28	1.09[1]	1.08	1.15[1]

Note:
1. Average value of the specimens that had the crack within the gage length.

4.8 SUMMARY

This chapter discussed the development process of nonproprietary UHPC mixtures from locally available materials to achieve the target properties identified in the analytical feasibility design study. The target properties are:

- A sufficient spread value (9–11 in.)
- 1-day compressive strength of 10–14 ksi without any special treatment
- 28-day compressive strength of 18–20 ksi without any special treatment
- 4–8 hours for initial set and 7–10 hours for final set

To achieve the target properties, the background theories of materials, strength development, particle size distribution, and packing density were discussed. In addition, the characteristics of the materials that were used for development of UHPC were studied. The materials were selected based on the evaluation of both the results of trial batches and the material characterization tests. Based on the background theories and the material characteristics, the first mixture proportion was established. The mixing procedure of proprietary and nonproprietary UHPCs was studied to develop a mixing procedure at the lab. The findings from literature, such as benefits of sand split addition and HRWR split addition, were adopted, and the practice of the common mixing procedure of proprietary UHPCs was maintained.

The four UHPC mixtures were developed using two different proportioning methods, which are (1) proportioning by cement weight, and (2) the volumetric proportioning method. For the first UHPC mixture, Mix-1, the recommended proportions by cement weight from literature were used. The second UHPC mixture, Mix-2, was developed by replacing cement with fly ash. However, the 1-day compressive strength of both mixtures were lower than the target value. Therefore, the third mixture, Mix-3, was developed with the volumetric paste proportioning study. The paste for high early strength and low water demand and low silica fume proportion was considered. As a result, the third mixture achieved the target 1-day and 28-day compressive strengths. The fourth mixture, Mix-4, was developed to improve the durability of the third mixture by increasing silica fume content without compromising the high early strength gain of Mix-3. Mix-4 was evaluated by compressive strength, shrinkage, bulk and surface resistivities, RCPT, abrasion resistance, and cost. As a result, Mix-3 and Mix-4 were selected for further study. The two selected mixtures were optimized with the Type III cement used in the precast plants in Texas. Because both mixtures have comparable compressive strength results and durability category, service life prediction was studied for comparison. Mix-4 showed a longer service life span than Mix-3. Thus, Mix-4 was selected for the additional material-level experiments and girder fabrication.

Based on the recommendations in literature, 0.5 in. long fibers that are 0.008 in. diameter were selected for this project. The selected Mix-4 was considered for a fiber volume optimization study. Several trials were conducted with the Mix-4 while varying the fiber volume from 1 percent, 1.5 percent, to 2 percent. It was observed that the tensile strength increases with an increase in fiber content. The behavior of the test specimens under tension was comparable for 1.5 percent

and 2 percent, although the latter was superior. The compressive strength and workability of the 1.5 percent mix was the best among the three fiber volumes. Based on the overall strength performance, workability, and economy of the mix, a 1.5 percent fiber volume was chosen for this research project as the final fiber volume.

5 OPTIMIZATION OF SELECTED UHPC MIXTURE FOR PRECAST PLANT APPLICATION AND FURTHER STUDY

5.1 INTRODUCTION

Four nonproprietary UHPC mixtures were developed with Type I/II and Type III cements (for a total of eight UHPC mixtures) as part of Task 4, described in Section 4.5. Each mixture has been designed to achieve certain target properties, especially a compressive strength of 14 ksi at release (1-day) and 20 ksi at service (28 days), that were identified in the analytical feasibility design study. In addition to the target compressive strengths, the mixtures have been evaluated for key fresh and hardened properties; selected durability testing—including bulk and surface resistivities, RCPT, and abrasion resistance; and material cost evaluation. The key properties that were measured include the following:

- Flow spread and setting time as fresh properties
- Compressive strength as hardened properties
- Shrinkage, bulk and surface resistivities, rapid chloride penetration, and abrasion resistance as durability properties

Based on the evaluation, two promising UHPC mixtures for application to Texas precast prestressed UHPC bridge girders were selected and further studied in Task 5, including optimization with the Type III cement commonly used in the Texas precast industry. Both UHPC mixtures have acceptable strength with respect to the requirements for release and 28-day compressive strength determined for the analytical feasibility design study. Therefore, durability was a factor considered when selecting a UHPC mixture for further investigation. All the developed UHPC mixtures are classified as *Very Low* chloride ion penetration based on the surface resistivity based classification system class (AASHTO T 358 2017). However, the predicted service life spans of the mixtures are different. As a result of service life prediction, along with fresh and hardened properties and durability, Mix-4 was selected for additional material-level testing and use for precast, pretensioned UHPC girder specimen fabrication at the precast plant. This section documents the methodology and findings for material-level experiments and production of UHPC at a Texas precast plant for the selected nonproprietary UHPC mixture.

The selected mixture was further optimized using the materials (i.e., Type III cement, HRWR, and as-received wet sand) from the selected precast plant in Texas. Since the change in the above parameters (cement, HRWR, and sand) impacted the fresh and hardened properties, adjustments were made in the mixture proportions to achieve the required key fresh and hardened properties. Section 4.7 discusses the optimization of the selected mixture with Type III cement. Section 5.2 describes the plan of material-level testing. Section 5.3 describes the optimization of water, HRWR, and paste volume to maintain desirable properties such as time duration for turnover, flowability, and 1-day and 28-day compressive strengths. Introducing wet sand that was not washed or sieved to the selected mixture required optimization of the mixing procedure. Section 5.4 presents the optimization of the mixing procedure for application at the batch plant. In the trial batch at the precast plant, the longer time required to add steel fibers caused a considerable increase in the mixing time. In addition, the total water content added to the mixer at the precast plant was higher than the target value. Section 5.5 discusses the potential areas of improvement and corrective measures to maintain target water content in the plant-made UHPC mixture and to reduce the time needed for fiber addition.

The required number of specimens were cast using the plant trial batch UHPC mixture to measure the selected fresh, hardened, and durability properties. Section 5.6 presents test results of fresh properties, such as flowability over time, unit weight, air content, temperature, and setting time. Section 5.6 also documents the hardened properties, such as compressive strength, MOE, tensile strength (direct and indirect), and shrinkage. Section 5.6 discusses durability test results. Freeze-thaw resistance, scaling resistance, and abrasion resistance of the plant-made UHPC were studied. Bulk and surface resistivities and rapid chloride ion penetration were tested using specimens made of lab-made UHPC mixtures because these tests require specimens without metallic fibers. In addition, a petrographic examination was conducted using two thin sections made of lab-made UHPC to study microstructure, which was considered an effective supporting tool for better understanding the hardened and durability properties that were measured. Section 5.7 presents a summary of the findings of this chapter.

5.2 OVERALL PLAN OF MATERIAL-LEVEL TESTING

Fresh and hardened properties, durability, microstructure, and fiber distribution and orientation of the selected mixture, Mix-4, were investigated through four stages:

- Stage 1: Mix-4 was first developed in the lab using locally available materials. This stage is the first stage that evaluated Mix-4 and is described in Section 4.7.
- Stage 2: The second stage was conducted to optimize Mix-4 with materials sourced from the selected precast plant before the plant trial batch. For the second stage, the mix was reproduced in the lab using the precast plant materials followed by verification of the relevant fresh and hardened properties.
- Stage 3: The third stage is the evaluation of the specimens produced at the plant with a 2 cyd volume UHPC trial batch. This stage verified applicability of the mixing procedure for large volume production using a 6 cyd capacity twin-shaft mixer. In addition, the properties of the plant-made UHPC specimens were evaluated in comparison to the properties of the lab-made UHPC from the second stage.
- Stage 4: The last stage was the fabrication of three girders. Companion specimens with the girders were prepared at the precast plant and used to evaluate the properties.

Table 5.1 provides the nomenclature that was used to distinguish the different variations of Mix-4 corresponding to different stages of development. The evaluated properties at each stage are described in Table 5.2. Table 5.3 provides the test methods used for evaluation of UHPC properties.

Table 5.1. Nomenclature for the Selected Mixture.

Nomenclature	Description
Mix-4-LM-L	Mix-4—developed in the lab using locally available materials (Type I/II cement [C-2], oven-dried sand, fly ash, silica fume, HRWR-2)
Mix-4-PM-L	Mix-4—verified in the lab using materials from the selected precast plant (Type III cement [C-5], wet sand, HRWR-3)
Mix-4-PM-P	Mix-4—production at the selected precast plant. The lab-verified mix (i.e., Mix-4-PM-L) was adjusted in the plant based on actual sand moisture content on the day of production.

Table 5.2. Material-Level Experiment Plan.

Properties	**Mix-4-LM-L**	**Mix-4-PM-L**	**Mix-4-PM-P (Trial batch)**	**Mix-4-PM-P (Girder Specimens)**
Fresh Properties	• Flow spread • Time of set	• Flow spread • Time of set • Temperature • Density • Working time	• Flow spread • Temperature • Density • Working time	• Flow spread • Temperature • Density
Hardened Properties	• Compression • Direct tension • Shrinkage	• Compression • Direct tension • Shrinkage • MOE	• Compression • Direct tension • MOE • Modulus of rupture	• Compression • Direct tension • MOE • Modulus of rupture • Shrinkage • Creep in compression
Durability	• Rapid chloride ion penetration • Bulk resistivity • Surface resistivity	• Rapid chloride ion penetration • Bulk resistivity • Surface resistivity • ASR	• Freeze-thaw resistance • Scaling resistance • Abrasion resistance	N/A
Microstructure	N/A	Petrographic study	N/A	N/A
Fiber distribution and orientation	N/A	N/A	N/A	• X-ray computed tomography (CT)

N/A: Not applicable

Table 5.3. Test Methods Used for Evaluation of UHPC Properties.

Property	Test Method
Fresh Properties	• Flow spread (ASTM C1437)[1] • Temperature (ASTM C1064) • Time of set (ASTM C191 2018)[1] • Density (ASTM C138) • Working time
Hardened Properties	• Compressive strength (ASTM C39)[1] • Direct tension (AASHTO T 397 Draft) • MOE and Poisson's ratio (ASTM C469)[1] • Modulus of rupture (ASTM C1609)[1] • Shrinkage (ASTM C157) • Creep in compression (ASTM C512)[1]
Durability	• Bulk resistivity (ASTM C1760) • Surface resistivity (AASHTO T 358) • Rapid chloride ion penetration resistance (ASTM C1202)[1] • Freeze-thaw resistance (ASTM C666)[1] • Scaling resistance (ASTM C672) • Abrasion resistance (ASTM C944)[1] • ASR (ACCT method; Mukhopadhyay et al. 2018 and AASHTO TP142)
Microstructure	• Petrographic study (ASTM C856)
Fiber distribution and orientation	• X-ray CT

Note: 1. The modified test methods according to ASTM C1856 (2017).

5.3 OPTIMIZATION OF SELECTED MIXTURE WITH PRECASTER MATERIALS

The research team worked with a Texas precast plant to evaluate the implementation of UHPC. The first step was to determine adjustments needed to optimize the selected mixture, Mix-4, using the same materials used at the plant—including the cement, an HRWR, and sand. The selected mixture was already optimized with the Type III cement used by the precaster, labeled as C-5 in Section 4.6.2. This section focuses on further optimization using the typical HRWR and sand available at the precast plant.

HRWR-2 was used in the lab, whereas the selected precast plant uses HRWR-3. The change of the HRWR product largely influences the dosage of the HRWR and water contents in the mixture design, total mixing time, fresh properties, and early-age-hardened properties due to the change in setting time. This effect is because of the different characteristics of each HRWR product, such as solid content, adsorption speed, and polymer structure—including side chain length (Hirschi and Wombacher 2008; Nkinamubanzi and Aïtcin 2004; Nkinamubanzi et al. 2016). Thus, it was

necessary to further optimize the mixture proportions due to the change in the HRWR to meet the target properties.

The sand used for the development of the UHPC mixtures in the development of the UHPC mixture discussed in Section 4.5 was oven-dried river sand (with 0.05 in. maximum particle size, washed and sieved by #16 sieve at the lab) sourced from a local supplier in Bryan, Texas. The selected mixture (Mix-4) was further optimized using the as-delivered sand taken directly from the precast plant. Precast plants in Texas normally use sand stored on site without additional washing, sieving, or drying.

The mixture optimization using the same materials as the precast plant was an essential step for implementation of UHPC mixtures in the precast industry. The goal was to obtain similar fresh and hardened properties as those achieved for UHPC mixtures developed in the laboratory.

5.3.1 High-Range Water Reducer

Each commercial HRWR product has a specific amount of negative charge and polymer structure. The amount of negative charge and side chain length of a polymer are factors in adsorption speed and dispersion efficiency, respectively. Therefore, these factors influence the turnover time, dosage of the HRWR, setting time, and early strength gain of UHPC (Nkinamubanzi et al. 2016). Turnover is the state in which a paste achieves consistency. In Task 4, two HRWR products (HRWR-1 and HRWR-2) were investigated. After investigating the performance of these two HRWRs, HRWR-2 was selected for the development of mixtures because the water reduction performance of HRWR-1 was not sufficient for UHPC applications. An HRWR used by the precaster involved in this study was obtained, which is labeled HRWR-3. The manufacturer of HRWR-2 and HRWR-3 is the same. In addition, the approximate solid content of both HRWR-2 and HRWR-3 is the same (TxDOT 2019). However, based on the manufacturer's specifications, differences exist between the two HRWRs (Table 5.4).

Table 5.4. Summary of Specifications of HRWR-2 and HRWR-3.

Description	HRWR-2	HRWR-3
Water reduction	Up to 45%	Up to 40%
High plasticity and cohesion	Yes	Yes
High early strength	N/A	Yes
Slump life	60–90 minutes with normal setting time	Extended slump life during warmer months
Main characteristic	Extended slump retention with normal setting time	High early strength

The specifications show that HRWR-2 and HRWR-3 are noted for longer slump life with normal setting time and high early strength, respectively, and have a comparable water reduction efficiency. However, similar performance of HRWRs is not guaranteed for UHPC applications. Generally, the dose of an HRWR for UHPC is much higher than the recommended dosage in specifications, which is commonly provided for SCC. Therefore, trial batches were conducted for the performance comparison of the two HRWRs.

The identical mixture proportions of Mix-4, except for the HRWR product, were used for the trial batches. Table 5.5 presents the mixture designs and the results of the trial batches.

Table 5.5. Mixture Design and Results for HRWR Comparison.

Description	T1 (HRWR-2)	T2 (HRWR-3)	T3 (HRWR-3)
Cement	1516[1]	1516	1513
Silica fume	114	114	113
Fly ash	158	158	157
Sand	1634	1634	1631
Water	324	324	324
HRWR	33.2	33.2+3.3[2]	36.4
Steel fiber	200	200	200
Turnover time,[3] min.	6	18+	5
Total mixing time, min.	23	36	20
Spread at discharge, in.	11.1	10.2[4]	10.9
$f'_{c\,1-d}$, ksi	14.7	12.8	14.3
f'_c, ksi	20.4	19.3	20.8

Notes:
1. All units are lb/yd^3, unless otherwise noted.
2. Additional 10 percent HRWR (3.3 lb/yd^3) was added to achieve turnover.
3. Time duration between addition of the HRWR and turnover of the paste.
4. Spread value after adding an additional 10 percent HRWR.

As shown in Table 5.5, the T1 trial batch for the mixture with HRWR-2 gave an 11.1 in. flow spread at discharge. The required time for the turnover of the paste after adding HRWR-2 was 6 minutes. However, the T2 trial batch for the mixture with HRWR-3 did not achieve turnover

until 18 minutes after adding HRWR-3. After adding an additional 10 percent of HRWR-3, the T2 mixture turned over into a flowable paste, and the flow spread of UHPC at discharge was 10.2 in. This result of T2 shows that HRWR-2 has a higher water reduction effect than HRWR-3, which matches the information from the specifications described in Table 5.4. The total mixing time was 36 minutes for T2, whereas the total mixing time of T1 was 23 minutes. The T3 trial batch was conducted with a 10 percent increased dose of HRWR-3. For the T3 mixture, the proportions of the other materials were kept the same while increasing the HRWR. T3 showed a comparable turnover time, flow spread, 1-day and 28-day compressive strength to T1. The shorter turnover and total mixing time of T3 over T1 were expected due to the high charged level of HRWR-3 that gives a faster adsorption speed and a shorter setting time (Schmidt et al. 2011). As a result, it helps to achieve high early strength as specified in the specification. The reduction of mixing time is beneficial for multiple batches for large volume production at a precast plant because it can reduce the time between placements. Therefore, the risk of a cold joint in a girder between batches is reduced. Therefore, the mixture design of T3 was selected for the next step, which was to optimize the mix with the as-received wet sand.

5.3.2 Sand

For the development of the UHPC mixtures for Task 4, described in Section 4.6, the sands were preprocessed by washing, oven-drying, and sieving with a #16 (0.05 in.) sieve before using the sand for the UHPC batches in the lab. However, the sand was used in an as-received condition from the stockpile in a precast plant, with appropriate adjustments made to the mix proportions based on the measured moisture content. The sand from the precast plant stockpile was a wet sand with #4 maximum particle size (0.2 in.). Figure 5.1 shows a sieve analysis of the sand used in Task 4 for the development of the UHPC mixtures, labeled Sand-2, and the stockpile condition sand from the precaster, labeled Sand-4. The A&A in the plot indicates an ideal gradation of sands for particle packing density (Brouwers and Radix 2005).

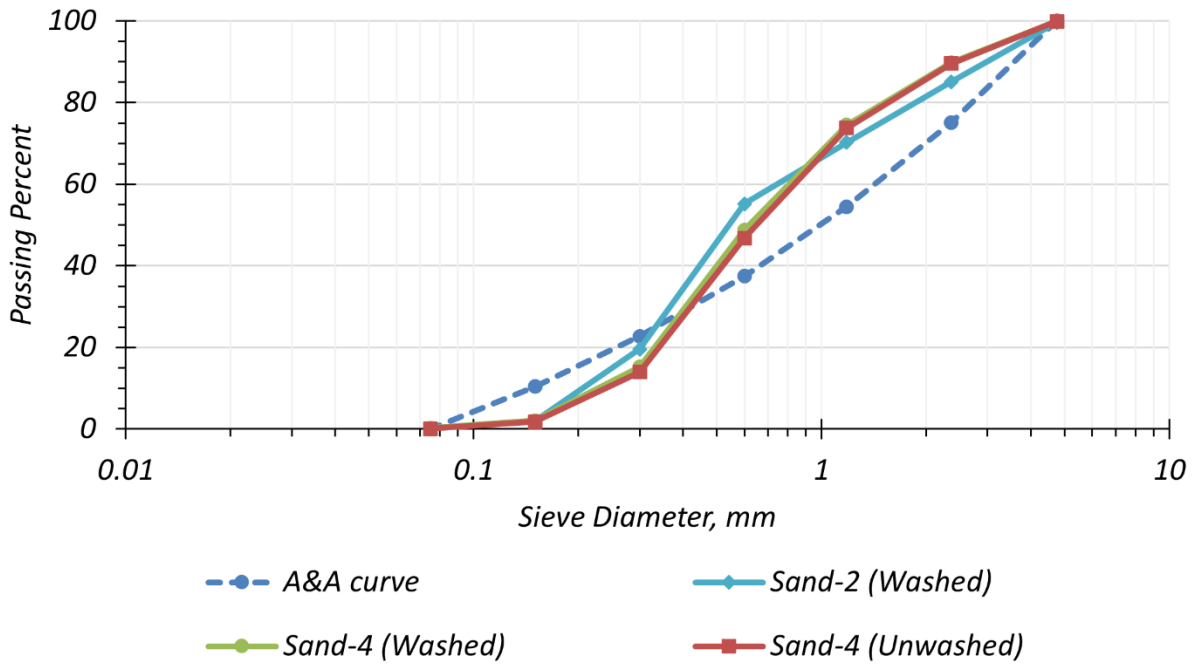

Figure 5.1. Particle Size Distribution of Lab and Stockpile Sands.

Comparison of Sand-4 (Washed) and Sand-4 (Unwashed) in Figure 5.1 shows that the washing process at the lab did not cause significant loss of sand particles. Sand-2 and Sand-4 have similar gradation. Based on the sieve analysis results, changing sand from Sand-2 to Sand-4 was expected to have only a minor impact on the performance of the selected UHPC mixture with regard to the particle packing density.

To investigate effects of several parameters—washing, oven-drying, and maximum particle size of sands—a test matrix was prepared (Table 5.6). The mixture optimized with HRWR-3 was taken as reference for this sand optimization study. Each trial batch, T1 through T4, has a factor that was adjusted relative to the previous trial: the sand source for T1, sieving for T2, washing for T3, and oven-drying for T4.

Table 5.6. Test Matrix for Optimization of Sand.

Description	Trial					CoV
	Reference	T1	T2	T3	T4	
Source	A local supplier	Precaster	Precaster	Precaster	Precaster	N/A
Sieving	#16 (0.05 in.)	#16 (0.05 in.)	#4 (0.2 in.)	#4 (0.2 in.)	#4 (0.2 in.)	N/A
Washing	Yes	Yes	Yes	No	No	N/A
Oven-drying	Yes	Yes	Yes	Yes	No	N/A
Flow spread, in.	10.9	11.1	10.8	11.0	10.6	0.02
$f'_{c\,1-d}$, ksi	14.3	14.6	13.7	13.7	14.3	0.03
f'_c, ksi	20.8	18.9	20.9	18.9	21.1	0.06
Mixing time, min.	23	23	23	23	34	0.20

Notes:
CoV: Coefficient of Variation
N/A: Not applicable

Effects of the factors through the trial batches exhibited a low range of CoV: 0.02 for flow spread, 0.03 for 1-day compressive strength, and 0.06 for 28-day compressive strength. Thus, changing sands from lab conditions to stockpile conditions has a relatively small impact on the flow spread and 1-day and 28-day compressive strengths. However, the use of the stockpile condition sands influenced negatively on the total mixing time, which was increased from 23 to 34 minutes (see the mixing times of T3 and T4 in Table 5.6). To reduce the total mixing time, the optimization of the mixing procedure was needed, as detailed in Section 5.4.

5.3.3 Paste Volume Optimization

The role of the paste volume can be divided into two parts in regard to rheology; the first part is to fill voids between sand particles, and the second part is to cover sand particles to lubricate (Figure 5.2). If the paste volume that covers the sand particles is not sufficient, the desired flowability cannot be achieved. On the other hand, a paste volume that is more than a specific volume giving a desired flowability is unnecessary; that scenario can lead to excessive autogenous shrinkage and will be less cost-effective due to an overdosage of cementitious materials. Therefore, an optimum volume of paste is ideal for fresh and hardened properties and for cost.

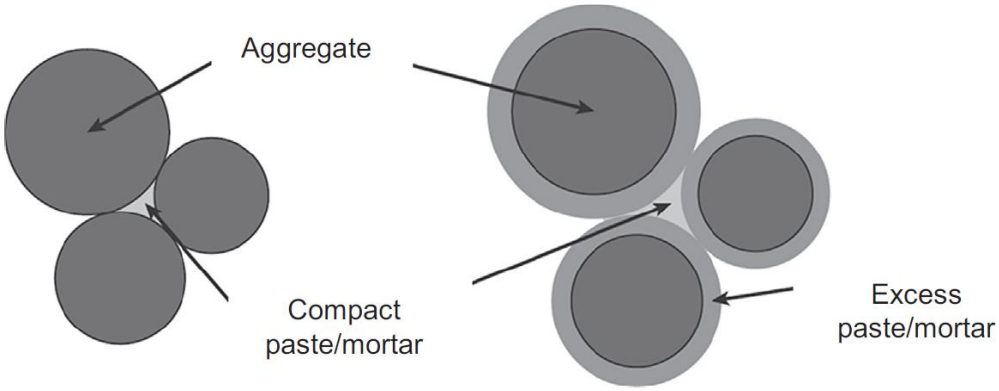

Figure 5.2. Required Paste Volume for Rheology (Oh et al. 1999).

Changing the sand and maximum particle size changes the void volume between the sand particles. Thus, the required filling paste volume changes. For optimization of the paste volume, quantification of the void volume between sand particles was studied first; next, filling and covering paste volumes were computed. Based on the calculation, a paste volume in the mixture was adjusted. Finally, a trial batch was conducted for validation of the paste volume optimization.

For the quantification of the void volume between sand particles, the following test method was considered:

1. Measure the weight of an empty 3 × 6 in. cylinder mold.
2. Fill the cylinder mold fully with oven-dried sand (shake the cylinder mold sufficiently).
3. Measure the weight of the cylinder mold filled with sand.
4. Pour water into the cylinder up to the top.
5. Measure the weight of the cylinder mold.
6. Compute the added water volume percentage in the cylinder mold.

Table 5.7 shows the test results. Sand-2 and Sand-4 are river sand, and Sand-3 is a masonry sand. Sand-3 was included in the test to measure the void volume of a different sand source. The maximum particle size #4 group represents the sands without sieving at the lab, whereas the #16 group is for the sieved sands at the lab. The test results show that the sieved sands using a #16 sieve have a 33–34 percent void volume, whereas the sands without sieving have a 29–30 percent void volume, which indicates that manipulation of sand gradation by eliminating large sand particles might not be favorable for high particle packing density. For Sand-4, the void volumes for maximum particle size #16 and #4 are 33 percent and 30 percent, respectively.

Table 5.7. Quantification of Void Volume between Sand Particles.

Max. Sand Size	Sand	Mold Weight, oz	Mold + Sand Weight, oz	Mold + Sand + Water Weight, oz	Water Weight, oz	Void Volume, %
#4 (0.2 in.)	Sand-2	1.8	44.5	51.6	7.1	29
	Sand-3	1.8	44.8	51.9	7.1	29
	Sand-4	1.8	44.2	51.5	7.3	30
#16 (0.05 in.)	Sand-2	1.8	44.5	49.7	8.3	34
	Sand-3	1.8	42.8	50.8	8.0	33
	Sand-4	1.8	41.6	49.7	8.1	33

The mixture was developed originally with #16 sand. By introducing #4 sand, the paste volume can be reduced because the required filling paste volume of #4 sand (30 percent) is smaller than #16 sand (33 percent). To calculate the filling paste volume of the reference mixture in Table 5.6, the volumes of the paste and the sand were calculated using the BSG of materials (Table 5.8).

Table 5.8. BSG of Materials.

Material	BSG_{od}
Cement	3.14
Silica fume	2.2
Fly ash	2.3
HRWR	1.08
Sand	2.65

Note: BSG_{od}: Bulk specific gravity of material in oven-dried condition.

The paste and sand volumes of the reference mixture are 56.9 percent and 36.5 percent, respectively (Table 5.9). Because the filling paste volume is 33.0 percent of the volume of #16 sand, the filling paste volume is 12.0 percent (36.5 percent × 33.0 percent = 12.0 percent). The covering paste volume can be computed by subtracting the filling paste volume from the paste volume. The covering paste volume, 44.9 percent, is the required amount to have the desired flowability. Therefore, the 44.9 percent covering paste volume should be kept the same when the mixture is optimized with #4 sands. The filling paste volume for the mixture with #4 sands can be calculated using 30.0 percent of the sand volume. A filling paste volume of 11.2 percent and a sand volume of 37.4 percent were calculated (Table 5.9**)**. Figure 5.3 provides the optimized volume fraction.

Table 5.9. Paste Volume Optimization Results.

Description	Mixture with #16 Sands (Reference)	Mixture with #4 Sands
Paste volume[1]	56.9%	56.1%
Filling paste[2]	12.0%	11.2%
Covering paste[3]	44.9%	44.9%
Sand volume	36.5%	37.4%
Steel fiber volume	1.5%	1.5%
Air volume[4]	5.0%	5.0%

Notes:
1. Paste volume: the sum of cement, silica fume, fly ash, HRWR, and water volume.
2. Filling paste volume: 33 percent and 30 percent of sand volume for #16 and #4 sands, respectively.
3. Covering paste volume: paste volume – filling paste volume.
4. 5 percent air volume assumed based on El-Tawil et al. (2018).

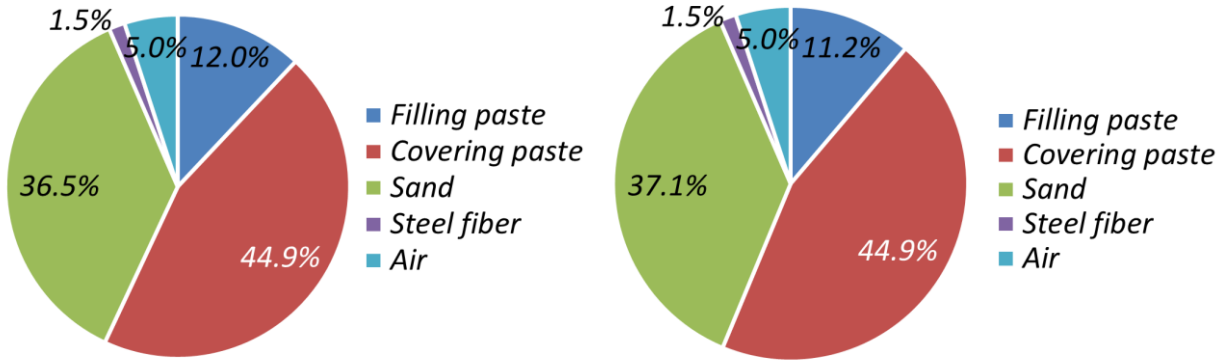

(a) Mixture with #16 sands (b) Mixture with #4 sands

Figure 5.3. Volume Fraction after Optimization of Paste Volume.

To validate the paste volume optimization, a trial batch was conducted with the mixture based on the calculated volume fractions of paste and sand (Table 5.10). Because the calculation of the filling and the covering paste volumes does not consider the effect of the change in the total surface area of the sands that may affect the covering paste volume, the flow spread results are very similar between the reference mixture and the mixture with #4 sand (Table 5.10). In addition, the 1-day and 28-day compressive strengths were comparable between the two mixtures. This result shows that the optimization process based on the calculation of the filling and the covering paste volumes can provide guidance to select an initial volume fraction of paste and sand prior to a trial batch.

Table 5.10. Optimization of the Mixture Design with #4 Sands.

Description	Mixture with #16 Sands (Reference)	Mixture with #4 Sands
Cement	1513	1490
Silica fume	113	112
Fly ash	157	155
Sand	1631	1670
Water	324	319
HRWR	36.4	35.9
Steel fiber	200	200
Flow spread, in.	10.9	10.8
$f'_{c\,1-d}$, ksi	14.3	13.7
f'_c, ksi	20.8	20.9

Air content in the mixture design was assumed to be 5 percent based on El-Tawil et al. (2018) for the whole optimization process in the development of the UHPC mixture in Sections 4.5, 4.6, and this section. In order to finalize the mixture design, air content was measured by the gravimetric method according to ASTM C138 (2015). The results were 2.51 percent and 3.96 percent. For the mixture design, 3.0 percent air content was considered based on the results. The final updated mixture design (Mix-4-PM-L), shown in Table 5.11, is used for the trial batch and girder fabrication at the precast plant.

Table 5.11. Mixture Design Update Based on Air Content Results.

Description	Material Weight, lb/yd^3
Cement	1522
Silica fume	114
Fly ash	158
Sand	1706
Water	326
HRWR	36.6
Steel fiber	200

5.4 MIXING PROCEDURE FOR PRECAST PLANT APPLICATIONS

Minimizing the mixing time while achieving the desired consistency of fresh UHPC is a key factor for successful UHPC production in a precast plant because the total number of batches to fabricate a bridge girder is approximately three to five (or more), and mixing each batch generally takes 20 to 30 minutes (Berry et al. 2017; El-Tawil et al. 2018; Weldon et al. 2010). As a result, casting a bridge girder may require more than 2 to 3 hours. A long cumulative batch time may cause degradation of the quality of fresh UHPC. Therefore, minimizing the mixing time is critical. To develop a method to optimize the mixing procedure at a plant, it is important to first identify the

differences between mixing in the lab and at the plant. This step helps to determine why the mixing time at a plant is longer than at the lab, key factors that increase the mixing time, and how to reduce the mixing time.

5.4.1 Mixing Procedure from Lab to Plant

The range of mixing time of laboratory-mixed UHPC batches is generally 12.5 to 17 minutes for proprietary UHPC and 20 to 26 minutes for nonproprietary UHPC (Berry et al. 2017; El-Tawil et al. 2018; Haber et al. 2018; Weldon et al. 2010). Proprietary UHPC mixtures have a shorter mixing time than nonproprietary UHPC because they do not require the time for dry mixing of cementitious materials. Proprietary UHPCs are supplied as a pre-blended bag of cementitious materials and silica sand (Haber et al. 2018). For nonproprietary UHPC mixtures, many researchers have developed a lab mixing procedure with a total time less than 25 minutes. However, challenges exist in applying lab-based mixing procedures at a precast plant. Lab-based mixing procedures, with relatively small volume batches, do not account for additional time to add materials into the mixer for a large batch volume as is done in a precast environment. In addition, proprietary and nonproprietary UHPCs developed in the lab have generally used oven-dried sands. As discussed in Section 5.3.2, the condition of the sand is an important factor for the mixing time. Therefore, wet sand conditions and longer time for the addition of materials, especially the manual addition of steel fibers, should be considered when optimizing the mixing procedure for precast plant applications.

The PCI has studied the development of UHPC mixtures in a precast plant environment with six precasters (eConstruct 2020). The six precasters disclosed the mixing time of a batch in their precast plant (Table 5.12). As expected, the mixing time of Precaster F, who used oven-dried sands with a small batch volume (0.5 cyd), was shorter than that of the other precasters.

Table 5.12. Mixing Time at Precast Plants (eConstruct 2020).

Precaster	Batch Volume, cyd	Mixer Capacity, cyd	Batch Volume / Mixer Capacity	Mixing Time, min.	Sand Condition	Time Duration of Fiber Addition, min.
A	1.0	3.0	33%	57	Wet	13.5
B	3.0	5.0	60%	47	Wet	19
C	3.2	6.0	53%	28	Wet	9
D	1.5	2.0	75%	44	Wet	16.5
E	2.5	6.0	42%	54	Wet	17
F	0.5	1.0	50%	18	Oven-dried	3

Graybeal (2011) reported that high mixing energy is required to obtain homogeneity of UHPC because of the large content of fine materials included in a UHPC mix. To ensure high mixing energy, the batch volume used by the precasters was approximately 50 percent of their mixer capacity. The mixing time was 28 to 57 minutes, except for Precaster F (Table 5.12). There are two factors for the long mixing times at the precast plant noted above. The first factor is the sand condition. Even though every precaster has their own mixing procedure, all precasters added sands at the beginning of mixing. This step might increase turnover time because wet sand causes agglomerates between cementitious materials and sands. To avoid agglomerates and reduce mixing time, the sand addition step was studied in the lab in this research. Adding the sand after turnover of the paste can reduce the mixing time, which is discussed in Section 5.4.2 in detail.

Another factor is the time required to add steel fibers into the mixer. All precasters added steel fibers manually. No automated system to add steel fibers exists because it is not a common material used in the precast industry. In addition, adding steel fiber directly from a bag caused fiber clumps. Precaster C dumped steel fibers directly from a bag into the mixer. As a result, although the total mixing time was relatively short due to the reduction of the steel fiber addition time, many steel fiber balls and clumps were observed. To resolve this issue, Precasters A, D, E, and F added steel fibers through a screen. Even though the use of a screen mitigated the fiber clump issue, this step extended the mixing time. Thus, with the exception of Precaster F, it took from 13.5 to 19 minutes to add the fibers.

Precaster F used oven-dried sand, while the other plants used wet sand (stockpile condition). In addition, the batch volume of Precaster F was smaller than the others. Thus, they needed to add smaller amount of steel fibers than the other precasters. As a result, the total mixing time for

Precaster F was 18 minutes. However, the use of wet sand and a large volume batch might be unavoidable at a precast plant for UHPC bridge girder production. Therefore, the mixing procedure for a reduced mixing time requires further development for successful UHPC girder production at a precast plant.

5.4.2 Optimization of Mixing Procedure

5.4.2.1 Lab Mixing Procedure

The mixing procedure developed in the laboratory as part of Task 4, discussed in Section 4.4, is summarized as follows and depicted visually in Figure 5.4:

1. Dry mixing (cement, silica fume, fly ash, and half of sand) for 5 minutes
2. Slow addition of 80 percent of the water and mixing for 2 minutes
3. Slow addition of the HRWR and the remaining water blend and mixing for 4 minutes
4. Slow addition of the remaining sand and mixing for 5 minutes
5. Slow addition of steel fibers and mixing for an additional 5 minutes
6. Discharge at 21 minutes

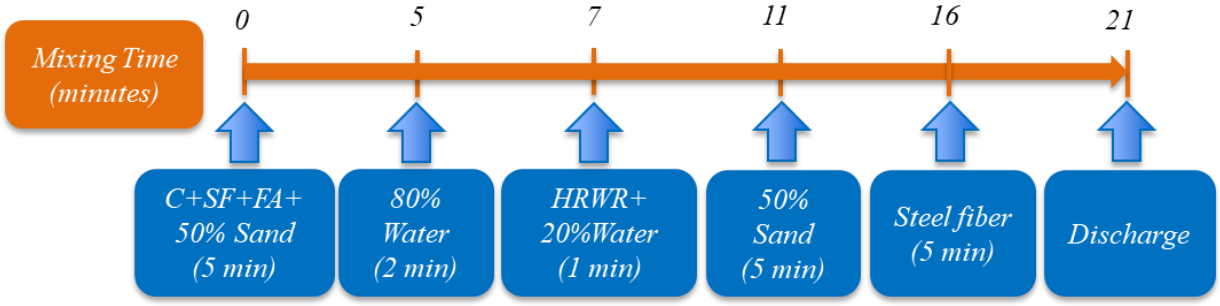

Figure 5.4. Mixing Procedure Developed in the Laboratory.

Although this mixing procedure works well in the laboratory, it should be optimized to accommodate the precast plant environment, such as the power of the twin-shaft mixer used at the selected plant; an automated system for material addition; wet sand; steel fiber addition; and a large batch volume.

5.4.2.2 Timing of Sand Addition

The first step to reduce the total mixing time was to move the sand addition from the first step to after turnover of the paste. This step was done to reduce the mixing time. Even though the total mixing time for Mix-4-LM-L was 21 minutes, as per the mixing procedure shown in Figure 5.4, it was increased to 26 minutes after replacing HRWR-2 (lab) with HRWR-3 (precast plant) due to the relatively slow adsorption speed of HRWR-3. Two trial batches (T2 and T3) were performed to see the effects of varying the sand addition sequence (Table 5.13). Oven-dried sand was used to clearly identify the effects of changing the timing of the sand addition.

Table 5.13. Comparison of Sand Addition Step.

Description	**T1[1] (reference)**	**T2[2]**	**T3[3]**
Dry mixing time, min.	5 minutes with cement + silica fume + fly ash + sand	5 minutes with cement + silica fume + fly ash	3 minutes with cement + silica fume + fly ash
Turnover time[4], min.	14	5	6
Total mixing time, min.	26	20	19
Flow spread, in.	11.1	10.9	10.8
$f'_{c\,1-d}$, ksi	14.6	14.3	13.7

Notes:
1. T1: Batch with sand added at the beginning
2. T2: Batch with sand added after turnover of paste
3. T3: Batch with dry mixing for 3 minutes
4. Time duration from adding HRWR to turnover

The sand was added in the dry mixing step for the T1 batch, while the sand was added after the paste reached turnover in the T2 batch. The turnover time of T2 was 9 minutes shorter than T1 yet achieved similar flow spread and 1-day compressive strength. The results show that adding the sand after turnover can reduce the total mixing time to achieve a target flowability. Therefore, sand addition after paste turnover was selected. A 5-minute dry mixing time was targeted for the case where half of the sand is added at the beginning with the cementitious materials. Adding the sand after paste turnover can also shorten the required dry mixing time by reducing the load for dry mixing. Trial Batch T3 reduced the dry mixing time from 5 minutes to 3 minutes. Its turnover time and flow spread are comparable with Trial Batch T2. Therefore, the dry mixing time for cement, silica fume, and fly ash was selected as 3 minutes. The updated mixing procedure is described as follows and is represented visually in Figure 5.5:

1. Dry mixing (cement, silica fume, and fly ash) for 3 minutes
2. Addition of water and mixing for 2 minutes
3. Slow addition of the HRWR and mixing for 6.5 minutes
4. After turnover of paste, addition of sands and mixing for 2 minutes
5. Addition of steel fibers and mixing for 10 minutes
6. Discharge at 23.5 minutes

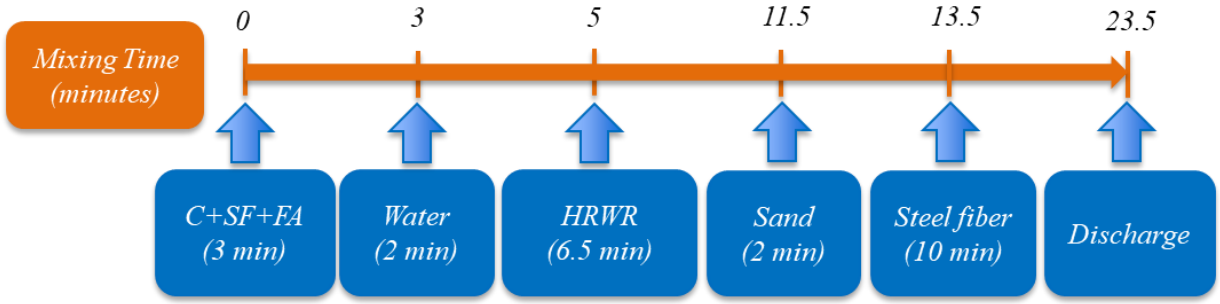

Figure 5.5. Updated Mixing Procedure for Sand Addition after Turnover.

Assuming the same additional time is needed to add steel fibers for a large batch volume in the plant, 10 minutes time is anticipated for adding steel fibers. Materials added by an automated system at a precast plant are cement, fly ash, water, HRWR, and sands. Silica fume and steel fibers were added manually at the selected precast plant for this research project. However, the above mixing procedure can be used with a fully automated system.

5.4.2.3 Wet Sand Addition

The next step in optimizing the mixing procedure was to account for the water content (moisture content status) of the wet sand at the plant. To understand the effects of wet sand on mixing, a trial batch was made following the updated mixing procedure. The moisture content in the sand used for the optimization study was 2.58 percent. The water content was adjusted according to the moisture content in the sand. As a result, the quantity of water to be added in the water addition step was reduced. Before adding the wet sand, turnover of the paste did not occur until after mixing for 20 minutes. The cause was a lack of available water for paste turnover. When oven-dried sand was used, the available water content for the paste during Step 2 and 3 in the mixing procedure was 0.181 *w/cm*. However, the use of wet sand reduced the available water for paste mixing before

adding the sand because the adjusted water content due to the water in the sand was 0.156 *w*/*cm*. Thus, turnover of the paste did not occur due to the insufficient water content for paste mixing.

For the next trial batch, wet sand was added after 11 minutes of mixing regardless of paste turnover, following the above mixing procedure, to see if the available water in the sand could be used quickly for turnover of the UHPC mix. Even though wet sand was added at 11 minutes, the UHPC mixture achieved consistency at 21 minutes. After turnover, steel fibers were added, and the mixing was continued until 31 minutes. The reason the paste turnover was not achieved even after 11 minutes of mixing was a lack of adequate water (0.156 *w*/*cm* at paste mixing stage). To achieve paste turnover before adding wet sand within the expected time (i.e., 11.5 minutes), adding extra water is required. However, if extra water is added during the paste mixing stage before adding wet sand, the final *w*/*cm* of the UHPC will increase (more than 0.181), which can create detrimental effects on strength gain and durability performance. Thus, a split cement addition method was considered to solve this issue.

5.4.2.4 Split Cement Addition

The split cement addition method involves addition of cement in two stages. The addition of the reduced quantity of the total cement (main cement) at the beginning represents the first stage of cement addition. The amount of the main cement is determined depending on the available water during the paste mixing stage. For a 2.58 percent sand moisture content, 13.9 percent of the water remains in the sand, which means that only 86.1 percent of the water is available during the paste mixing stage. Accordingly, 86.1 percent of the cement content, referred to as the main cement, was added in the first stage, and the remaining 13.9 percent cement, referred to as the tail cement, was added in the second stage (i.e., after adding the wet sand). Specific quantities of the main and tail cements depend on the moisture content of the sand. The mixing procedure with the split cement addition method is described as follows; the procedure is depicted visually in Figure 5.6:

1. Dry mixing (main cement, silica fume, and fly ash) for 3 minutes.
2. Addition of the water and mixing for 2 minutes.
3. Slow addition of the HRWR and mixing for 6.5 minutes.
4. After turnover of paste, addition of sands and mixing for 1 minute.
5. Addition of tail cement and mixing for 1.5 minutes.

6. Addition of steel fibers and mixing for 10 minutes.
7. Discharge at 24 minutes.

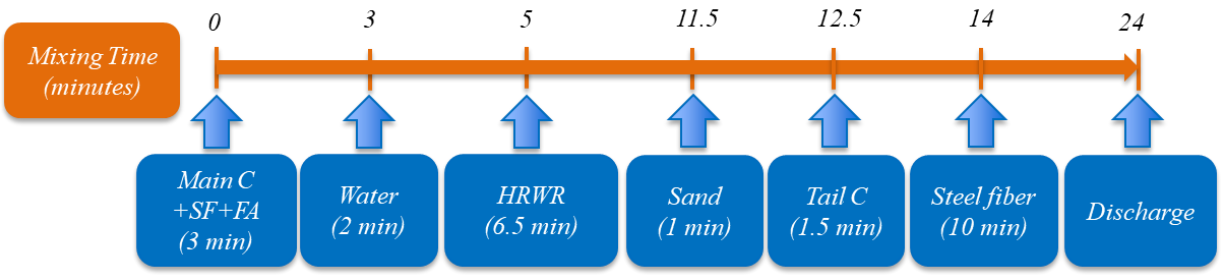

Figure 5.6. Updated Mixing Procedure for Split Cement Addition.

The total mixing time was 24 minutes. The flow spread and the 1-day compressive strength were 10.6 in. and 14.8 ksi, respectively. These results were similar to the results from a batch with oven-dried sand produced in the lab.

5.4.2.5 Tail HRWR Addition

Three to five batches to provide the required volume for girder casting might take 2 or more hours. To maintain workability for 2 hours, the effect of an additional tail HRWR addition was studied. At 3 minutes prior to the end of the mixing, an additional 10 percent quantity of the HRWR is added to improve slump life retention (Figure 5.7). Because an HRWR needs more than 5 minutes to disperse materials based on lab experience, adding an HRWR 3 minutes prior to completing mixing did not cause an excessive flow spread leading to segregation of steel fibers.

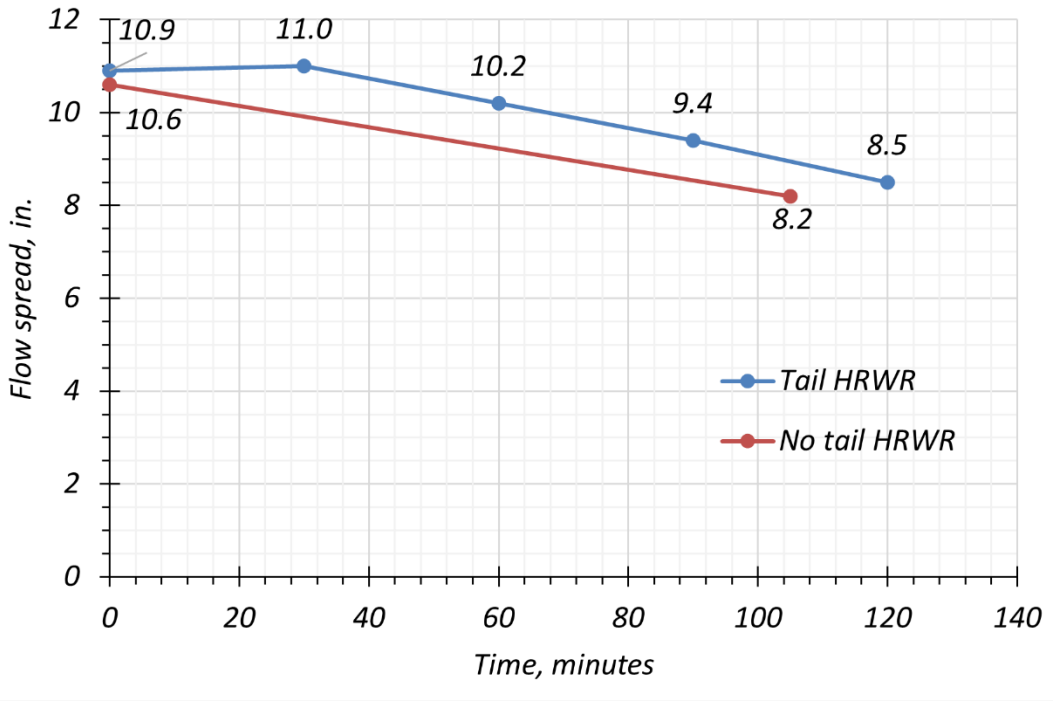

Figure 5.7. Comparison of Working Time.

Finally, the optimized mixing procedure with an optional step of adding a tail HRWR is described as follows; Figure 5.8 depicts the procedure visually:

1. Dry mixing (main cement, silica fume, and fly ash) for 3 minutes.
2. Addition of water and mixing for 2 minutes.
3. Slow addition of the HRWR and mixing for 6.5 minutes.
4. After turnover of the paste, addition of sands and mixing for 1 minute.
5. Addition of tail cement and mixing for 1 minute.
6. Addition of steel fibers and mixing for 7 minutes.
7. Addition of a tail HRWR and mixing for 3 minutes (optional).
8. Take a sample for a flow table test and mixing for 3 minutes.
9. Discharge at 26.5 minutes.

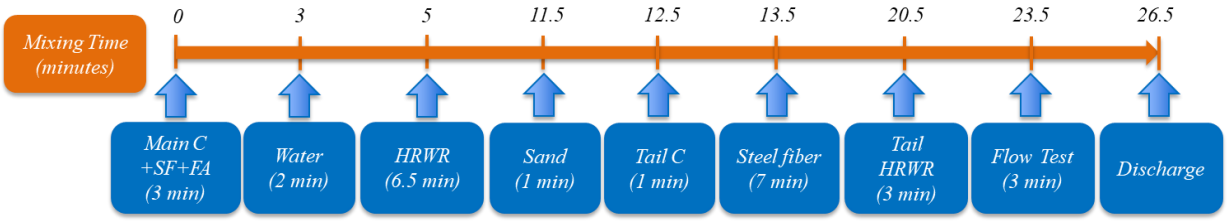

Figure 5.8. Updated Mixing Procedure for Tail HRWR.

The total mixing time is 26.5 minutes. A trial batch with the optimized mixing procedure showed a 10.9 in. flow spread, 14.7 ksi 1-day compressive strength, and 19.4 ksi 28-day compressive strength. For precast plant applications, a flow table test before discharging UHPC is needed to check if the consistency of UHPC is achieved. Section 5.5 discusses the implementation at the plant in detail.

5.5 OBSERVATIONS OF UHPC PRODUCTION AT PRECAST PLANT

A trial batch of the selected UHPC mix with a volume of 2 cyd was conducted at a precast girder fabrication plant located in Texas. The aim of the task was to identify the effects of parameter changes between the lab and plant, such as the power of the mixer, a larger batch volume, outdoor temperature, wind, sand moisture content, and the required time for the addition of materials. The required specimens for testing fresh and hardened properties and durability were cast using the UHPC mix from the trial batch and tested to comprehensively investigate the plant-made UHPC. Additionally, a UHPC block (2.0 ft × 1.6 ft × 6.0 ft) was cast with the remaining UHPC from the batch to study the change of the internal temperature caused by the heat of hydration. In addition, cores were obtained from the block at later ages to evaluate strength development through a comparative assessment between cast cylinders and cores and to study the fiber orientation and distribution. The method of steel fiber addition, effective adjustment of the water quantity, and other relevant aspects were verified through this trial batch. The knowledge gained through the trial batch facilitated refinements to the mixing procedure and mixing time during batching operations for girder specimen fabrication.

5.5.1 UHPC Production at Plant

The trial batch was performed on October 8, 2020. The highest temperature on the day was 87°F. Weather conditions are important factors for UHPC production. Especially, hot weather can

influence workability negatively. El-Tawil et al. (2018) recommended the use of ice in place of 40–50 percent of the water during the hot weather season to keep the temperature of fresh UHPC less than 85°F, which is required to maintain workability. Chilled water was used to maintain the required temperature of fresh UHPC in the trial batch at the precast plant. A twin-shaft mixer with a 6 cyd capacity was used. Table 5.14 shows the conditions for the trial batch.

Table 5.14. Batch Information.

Parameter	Details
Batch Date	October 8, 2020
Weather Conditions	58–87°F, Cloudy
Mixer Type	Twin-Shaft Mixer
Mixer Capacity	6 cyd
Batch Volume	2 cyd (33 percent of the mixer capacity)

The moisture content of sand stored at the precast plant, which is free water on the surface of the sand particles, was measured twice prior to mixing UHPC. The first moisture content measurement was taken at the batch plant using a probe, and the second measurement was taken in the laboratory at the plant. The measured moisture content was 3.60 percent and 4.06 percent from the probe and at the laboratory, respectively. Because this was the first UHPC batch at the plant, a 3.60 percent moisture content was considered conservatively for the adjustment of sand and water quantities. The absorption capacity of the sand was 0.7 percent. Table 5.15 shows mixture designs after considering the sand moisture content. The targeted mixture is the mix design developed at the lab with oven-dried sand, and the adjusted targeted mixture is the mixture with the adjustment according to the moisture content.

Table 5.15. Target and Batched Mixture Design.

Description	Target Mix	Adjusted Target Mix	Batched Mix	Difference
Cement	1522	1522	1510	−0.8%
Silica fume	114	114	114	0
Fly ash	158	158	160	+1.3%
Sand	1706	1770	1720	−2.8%
Water	326	264.2	275.2 + α	+4.2% + α
HRWR	36.6	36.6	36.6	0
Steel fibers	200	200	200	0
w/*cm*	0.181	0.181	0.189	+4.4%

Notes:
1. Unit: lb/yd^3
2. Air content 3 percent considered based on lab test results.
3. Adjustment was made based on 3.6 percent moisture content.

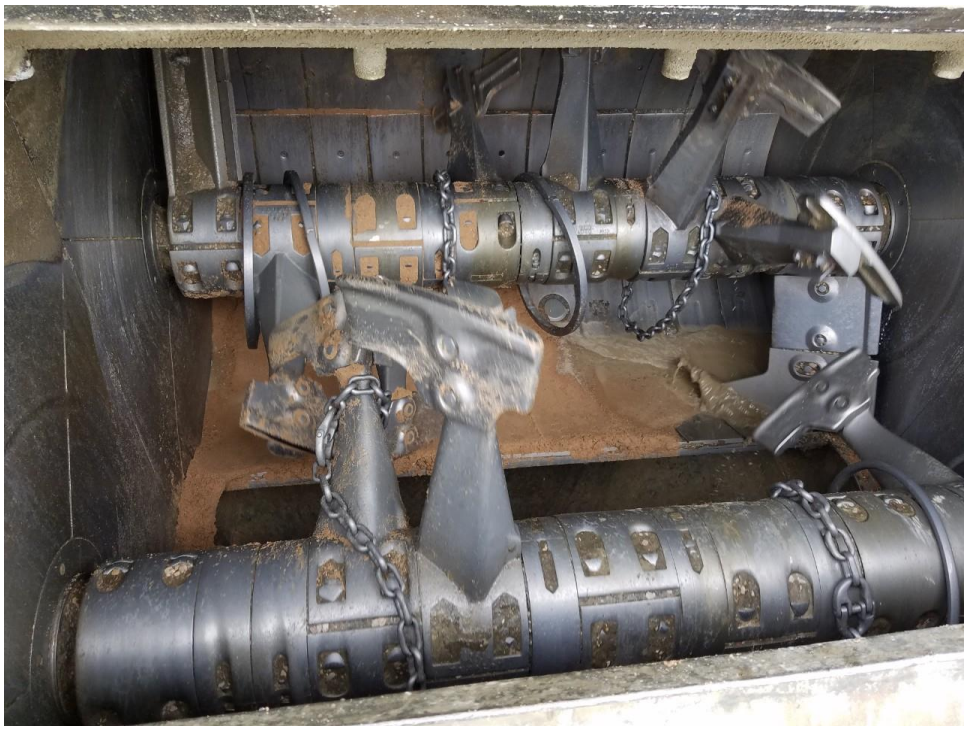

Figure 5.9. Remaining Sand and Water in the Mixer before Mixing.

Mixing was started after adding all dry cementitious materials in the mixer. Table 5.16 shows the mixing sequence and time duration of each step. The power of the mixer was sufficient to achieve a paste turnover within 5 minutes after adding the HRWR. Even though turnover time might be affected by the additional water, reducing the time duration between the addition of the HRWR and sands was promising. The time durations of most of the steps were on schedule as planned. However, similar to silica fume, steel fibers were also added manually while mixing. This step (Step 8) added about 17 minutes to the total mixing time. Steel fibers were added through a screen (23 in. long × 15 in. wide) that was smaller than the mixer opening size (5 ft long × 18 in. wide) to prevent clumps. One person poured steel fibers from a bag onto the screen while two persons shook the screen. Even though this manual method worked well in terms of dispersion of steel fibers, it was a slow process, and adding 400 lb of steel fibers within the targeted duration of 10 minutes was not achieved. Section 5.5.2 discusses a new method to add steel fibers that was considered to ameliorate this practice.

The mixing was paused momentarily at 33 minutes to take a small amount of fresh UHPC for a flow table test. While conducting the flow table test, mixing was continued to ensure the homogeneity of the UHPC. The measured flow spread value was 11.5 in., which was more than

the targeted range (9–11 in.) and possibly caused by the additional water (Table 5.15). Because fresh UHPC achieved sufficient flowability, the mixing was stopped at 36 minutes, and the UHPC was discharged into the Tuckerbuilt concrete transporter to take the UHPC to the sample casting location.

Table 5.16. Planned and Batched Mixing Sequence and Time.

Step	Description	Planned, minute		Batched, minute	
		Step Duration	Elapsed Time	Step Duration	Elapsed Time
0	Add silica fume (M)	1	0	2	0
	Add main cement (A)	1		0.5	
	Add fly ash (A)	1		0.5	
1	Dry mixing	3	3	3	3
2	Add water (A)	1	4	1	4
3	Mixing	1	5	1	5
4	Add HRWR (M)	1	6	1	6
5	Mixing	5.5	11.5	5	11
6	Add sand (A)	1	12.5	1	12
7	Add tail cement (A)	1	13.5	1	13
8	Add steel fiber (M)	10.5	24	17	30
9	Flow test	3	27	3	33
10	Discharge	3	30	3	36

Notes:
1. M: Material addition performed manually.
2. A: Material addition performed by automated system.

The UHPC block and specimens for investigation of the plant-produced UHPC properties were cast (Table 5.17). All specimens were prepared within 30 minutes after the mixing was stopped. The flow spread value was 11.4 in. after 80 minutes. Thus, the flowability of UHPC was retained for sufficient duration, and there were no issues related to the workability of freshly mixed UHPC. The commonly used specimen for measuring compressive strength in the lab is an end-ground 3 × 6 in. cylinder. However, 4 in. cubes were used for the 16-hour compressive strength test at the plant due to the unavailability of a concrete end grinder. Section 5.6.1 discusses the hardened properties of plant-produced UHPC in detail.

Table 5.17. Cast Specimens for Test.

Test	Specimen Type	Dimensions	Number of Specimens
Compressive Strength MOE	Cylinder	3 × 6 in.	56
Abrasion Resistance	Cylinder	4 × 8 in.	4
Compressive Strength at Plant	Cube	4 in.	9
Modulus of Rupture	Prism	4 × 4 × 15 in.	6
Direct Tension Strength	Prism	2 × 2 × 17 in.	20
Freeze-Thaw Resistance	Prism	3 × 3 × 11.25 in.	3
Scaling Resistance	Slab with a dike	Slab: 11× 11 in. × 3 in. thickness Dike: 1 in. wide and 1 in. height	2
Temperature Development Fiber Orientation and Dispersion Compressive Strength	Block	2 × 1.6 × 6 ft	1

5.5.2 Observations from Batch at Plant

5.5.2.1 Steel Fiber Addition

Two issues were reported by eConstruct (2020) related to manual steel fiber addition while mixing. The first issue is agglomeration of fibers. There are two terms to define agglomeration caused by fibers: *fiber balls* and *fiber clumps*. Fiber balls are agglomerated dry powder with fibers, whereas fiber clumps are agglomerated fibers in fully mixed UHPC. Generally, fiber balls occur when steel fibers are added during the dry mixing stage or into a paste that does not achieve a proper viscosity through an effective turnover. Existence of fiber balls increases the total mixing time because it takes time to break the agglomerated balls. To avoid this phenomenon, steel fibers should be added after achieving an effective turnover of UHPC mixture. Fiber clumps occur when steel fibers are added directly from a bag into the mixer. Fiber clumps can be avoided by adding fibers slowly through a screen or a sieve to disperse them physically (eConstruct 2020). For the trial batch, agglomeration issues were avoided by adding steel fibers after achieving paste turnover and by adding steel fibers using a sieve.

The second issue related to steel fiber addition is an extended mixing time due to the manual addition of steel fibers. This issue was the main reason for increased total mixing time. Two aspects need to be considered to reduce the time required for fiber addition: deciding the optimum dimension of the screen and use of a motorized vibrator. For the trial batch, the research team used

a sieve with a 1.5 in. opening. The dimension of the sieve was 23 in. long and 15 in. wide, whereas the opening of the mixer was 60 in. long and 18 in. wide. As a result, the opening area of the mixer could not be fully used. Fabrication of a screen similar to the size of the mixer opening might be helpful to improve the speed of fiber addition. Additionally, by employing a motorized vibrator instead of manually shaking the screen, fibers can be screened through the sieve more efficiently and disperse into the UHPC mix. For girder fabrication at the precast plant, both the size of sieve fit with the size of the mixer opening and a standard concrete vibrator were applied to the fabricated screen. As a result, fiber addition time for 3.1 cyd was reduced to 7.0–9.5 minutes.

5.5.2.2 Water Content

Another concern was the addition of the remaining water (adhered water inside the mixing drum) after cleaning the mixing drum. The mixer was cleaned using sand and water before mixing the UHPC. After cleaning, the sand and water were discharged from the mixer. However, an unknown amount of water remained in the mixer, which was difficult to remove before mixing the UHPC. To prevent extra water from being mixed with the UHPC, only 90 percent of the targeted water should be added at the water addition step (Step 2 in Table 5.16). The addition of the 10 percent tail water should be determined depending on the flowability level of the paste right before adding the sand (Step 6 in Table 5.16). If the paste flowability looks adequate by visual inspection, there is no need to add the tail water, which facilitates avoiding additional water in the mixture.

The small difference in sand moisture content between the probe and laboratory-based measurements can cause a large difference in flowability since maintaining an extremely low *w*/*cm* is a strict requirement for UHPC mixtures. Therefore, determining a reliable value of sand moisture content by a similar method is very important to adjust water and sand quantities to the right level. For the trial batch, the lower value of moisture content from the batch plant was used conservatively to ensure sufficient water quantity for mixing. However, this approach was not an appropriate way to prevent an overdose of water. Therefore, first, a greater moisture content value in the sand should be considered, thus providing a lower quantity of water at Step 2 (see Table 5.16). Then, in case the paste does not achieve the target flowability, additional water should be added as a solution to mitigate the low flow of the UHPC.

5.6 PROPERTIES OF LAB-MADE AND PLANT-MADE UHPC

5.6.1 Fresh Properties

This section discusses fresh properties of the lab-made UHPC (Mix-4-PM-L) and plant-made UHPC (Mix-4-PM-P). Flow spread at discharge and the slump life were studied to identify a workable time for placement. Unit weight and air content were measured to quantify density and entrapped air in the studied UHPC. The core and edge temperature of the UHPC block (2.0 ft × 1.6 ft × 6.0 ft) were measured to understand the effects of heat of hydration in a larger volume sample. The trend of the core temperature increase can be used to verify the measured final setting time in the lab.

5.6.1.1 Flow Spread and Slump Life

The standardized test method for workability of UHPC is the flow table test, which measures a spread value in accordance with ASTM C1437 (2015) and modifications by ASTM C1856 (2017). Section 3.2.1 discusses the test method. Figure 5.10 presents the flow table (ASTM C1437) test results for Mix-4-PM-L and Mix-4-PM-P mixtures. The flow spread values at discharge right after completing mixing were 10.6 in. and 11.5 in. for Mix-4-PM-L and Mix-4-PM-P, respectively. The spread value of Mix-4-PM-P was maintained over time up to 80 minutes, whereas the spread value of Mix-4-PM-L was decreased to 8.2 in. at 105 minutes after discharge. As discussed in Section 5.5.2, the increase in the flow spread value and the extended slump life of Mix-4-PM-P were due to the effect of the additional water in the mixer drum. The purpose of using a tail HRWR in Mix-4-PM-L was to extend the slump life. An extension of slump life (i.e., maintaining workability up to 120 minutes) for the Mix-4-PM-L with the tail HRWR (Figure 5.10) is evident. Flow spread as a function of time was measured at static storage conditions in a bucket without any agitating effect like a mixer truck. Therefore, employing a mixer truck during temporary storage of fresh UHPC at a plant might maintain its slump life better than when measured under static storage conditions (eConstruct 2020).

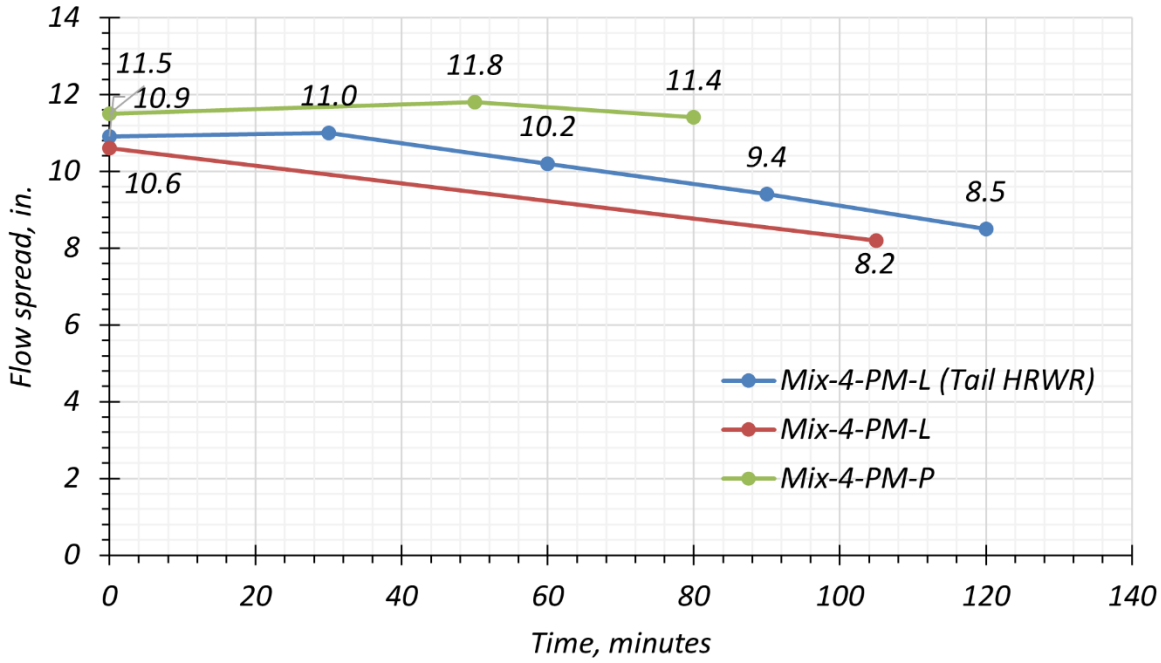

Figure 5.10. Flow Spread Values of Mix-4—Lab and Plant Conditions.

5.6.1.2 Unit Weight and Air Content

Unit weight and air content of the UHPC mixtures were measured in accordance with ASTM C138 (2015). Section 3.2.3 discusses the test method. Table 5.18 shows the test results. Graybeal (2019) reported that the expected unit weight of UHPC is in the range of 144–157 lb/ft^3; therefore, the test results (149.0 lb/ft^3 and 151.3 lb/ft^3) were in the expected range.

Table 5.18. Results of Unit Weight and Air Content.

Test Batch	Unit Weight, lb/ft^3	Air Content, %
Mix-4-PM-L	151.3	2.51
Mix-4-PM-P	149.0	3.96

El-Tawil et al. (2018) reported that the ranges of air content for UHPC are 4.0–4.2 percent and 4.7–5.8 percent with and without steel fibers, respectively. The air contents of both Mix-4-PM-L and Mix-4-PM-P (2.51 and 3.96 percent with steel fibers) are slightly lower than the test results reported by El-Tawil et al. (2018). Therefore, unit weight and air content of the plant trial mix are within the normal range of UHPC. Unit weight and air content might be an indirect indicator for packing density. Based on that perspective, Mix-4-PM has a well-packed matrix.

5.6.1.3 Setting Time

The time of setting for UHPC was measured in accordance with ASTM C191 (2018) and modifications by ASTM C1856 (2017). Section 3.2.2 discusses the test method. Setting time was measured for Mix-4-PM-L and Mix-4-LM-L at the lab. The initial and final setting times of Mix-4-LM-L were 5.5 hours and 8.5 hours, respectively (Table 5.19). The initial and final setting times of Mix-4-PM-L were 5.3 hours and 8.5 hours, respectively. Due to the similar setting times, both mixtures achieved similar 1-day compressive strengths (14.1 and 14.7 ksi).

Table 5.19. Initial and Final Setting Times.

Test Batch	Initial Setting, hour	Final Setting, hour	1-day compressive strength, ksi
Mix-4-PM-L	5.3	8.5	14.1
Mix-4-LM-L	5.5	8.5	14.7

5.6.1.4 Temperature

A UHPC block (2.0 ft × 1.6 f t × 6.0 ft) was cast using the trial batch mix at the precast plant to measure temperature development due to heat of hydration at the core and near the surface of the block. The peak temperature at the core was 214°F at 13 hours after casting (Figure 5.11).

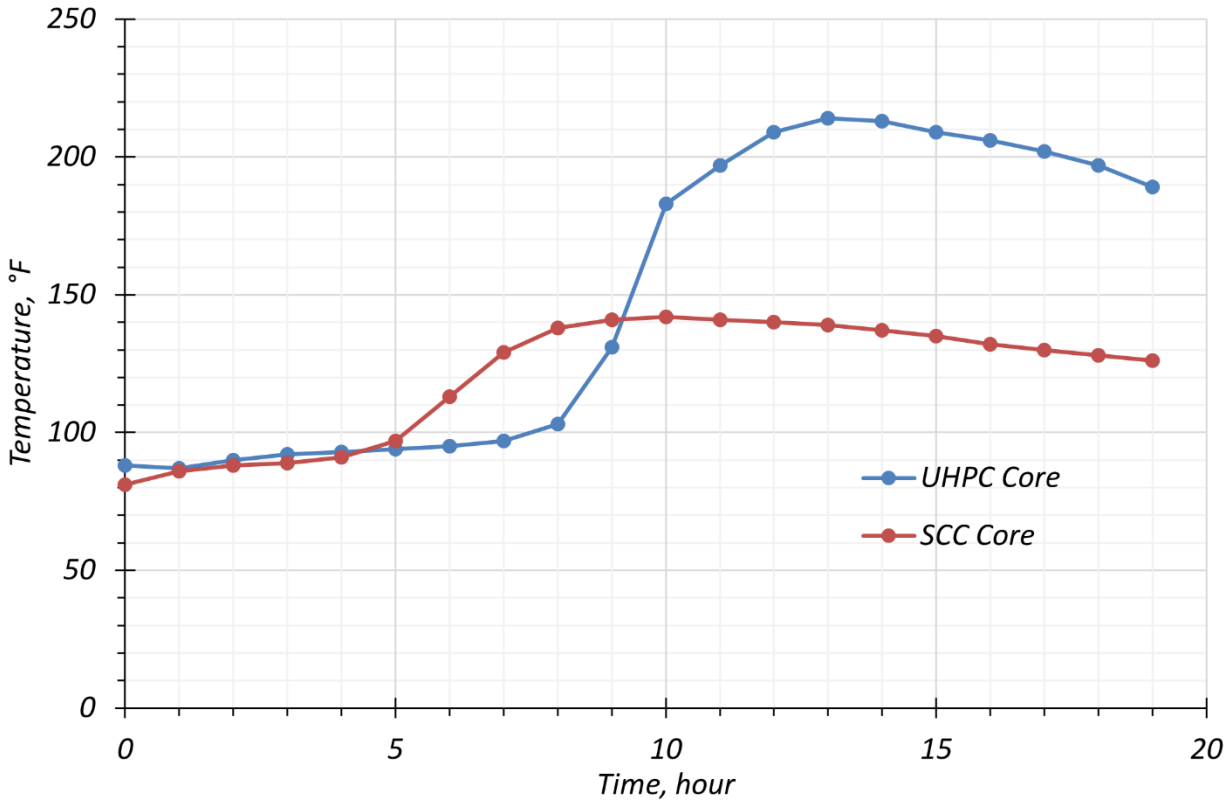

Figure 5.11. Core Temperature Comparison between UHPC and SCC.

The peak temperature of UHPC at the core was 72°F higher than the temperature at the core of a SCC precast girder cast on the same date, which was 142°F. Even though a difference might exist in the distance between the temperature probe and the surface of the SCC girder in comparison to the temperature of the UHPC block, the relatively large heat gain might be mainly due to the higher cement content of UHPC (Table 5.20). The high heat at the core might be beneficial with respect to strength gain of the studied UHPC. The compressive strength of cored samples from the UHPC block was 9.5 percent higher than the corresponding cylinder compressive strength at 61 days. Section 5.6.2.2 discusses this topic in detail.

Table 5.20. Relationship between Gained Heat and Cement Content.

Concrete	Gained Heat, °F	Cement Content, lb/yd^3
UHPC	124	1510
SCC	52	650
UHPC/SCC	2.4	2.3

Note: The initial temperature was 90°F.

The UHPC block had a dormant period approximately 8 hours after placement, while the SCC girder began showing a temperature increase at approximately 5 hours after placement. The dormant period is defined as the period in which very low chemical activity takes place. After the dormant period, a strong reaction of the C_3S begins. As a result, the heat increases significantly (Aïtcin 2016). The factor contributing to the longer dormant period is that the large dosage of the HRWR of the UHPC mixture might retard its final setting (Marchon and Flatt 2016). The heat gain of the UHPC block from approximately 8 hours is well-matched with the test results of the setting time in the lab, which showed an 8.5 hour final setting time.

Figure 5.12 shows the temperatures at the core and at the edge near the surface of the UHPC block. The maximum difference between the two temperatures is 31°F and occurred at 20 hours. If an insulated membrane is used to cover the UHPC block until 40 hours, the heat can be maintained longer. As a result, higher early-age strength gain than the lab test results might be possible because the generated heat can provide a heat curing-like effect. The fluctuation of temperature after 40 hours is due to the air temperature change from night to day.

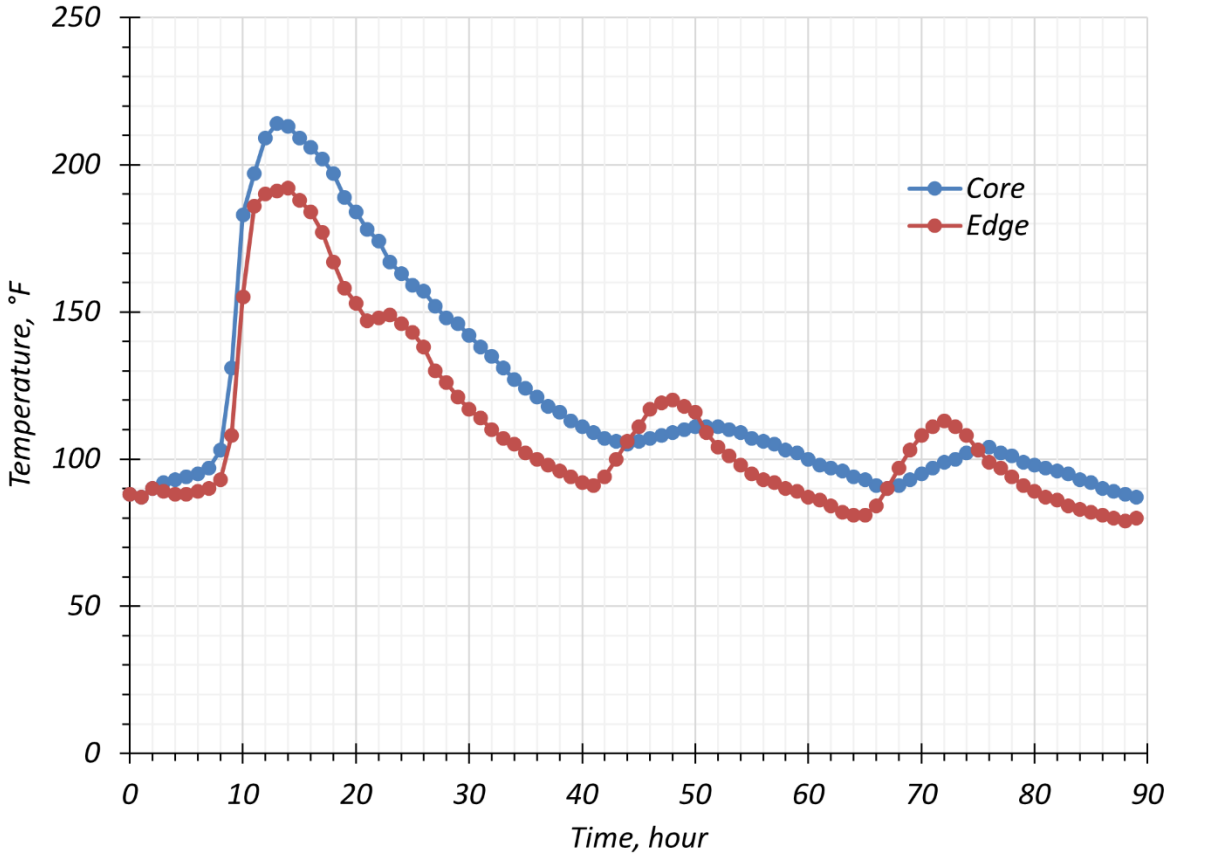

Figure 5.12. Temperature Change at Edge and Core.

5.6.2 Hardened Properties

Mechanical performance of the nonproprietary UHPC mix was evaluated based on several hardened properties, including compressive strength, MOE, tensile strength (direct and indirect), and shrinkage. This section explains the tests conducted to study the hardened properties and the results.

5.6.2.1 Compressive Strength

5.6.2.1.1 Comparison of Lab and Plant Mixes

Compressive strength testing of plant-made UHPC was conducted at the lab in accordance with ASTM C39 (2020) and modifications from ASTM C1856 (2017). The exception is the 16-hour compressive strength test, which was conducted at the plant using 4 × 4 in. cubes with a 145 psi/s loading rate as per ASTM C1856 (2017). Section 3.3.1 discusses the test method. Figure 5.13 and Table 5.21 show compressive strength gain as a function of time.

Table 5.21. Compressive Strength Results.

Mixture	Specimen Number	Compressive Strength, ksi					
		16 hours	1 day	2–4 days	7 days	28 days	56 days
Mix-4-LM-L	S1	9.4	13.0	17.0 (2)[1]	18.9	20.6	-
	S2	9.9	13.2	14.0 (2)[1]	18.1	19.3	-
	S3	9.3	Note 4	15.3 (2)[1]	17.7	21.2	-
	Average	9.5	13.1	15.4 (2)[1]	18.2	20.4	-
	CoV	2.4%	0.7%	7.8%	2.8%	3.9%	-
Mix-4-PM-L	S1	-	13.7	16.8 (3)[1]	18.1	18.4	-
	S2	-	14.4	16.5 (3)[1]	16.7	18.5	-
	S3	-	14.3	15.4 (3)[1]	16.5	19.1	-
	Average	-	14.1	16.2 (3)[1]	17.1	18.7	-
	CoV	-	2.2%	3.7%	3.9%	1.6%	-
Mix-4-PM-P	S1	9.2[2]	13.7	15.7 (4)[1]	16.3	18.2	17.8
	S2	7.7[2]	14.2	16.9 (4)[1]	16.9	17.7	18.3
	S3	8.2[2]	15.1	Note 4	16.5	17.7	18.7
	Average	8.4	14.3	16.3 (4)[1]	16.6	17.9	18.3
	CoV	7.1%	4.2%	3.7%	1.6%	1.3%	2.1%

Notes:
1. Testing age in parentheses (days)
2. Tested with three 4 × 4 in. cubes at the plant.
3. - : Not available
4. The measured value is not included as per the precision recommendations of ASTM C39 (2020). Imperfections in the specimen may have caused the deviation in behavior.

The target strengths at 1 day and 28 days were 14 ksi and 20 ksi, respectively. Mix-4-PM-P achieved 14.3 ksi at 1 day, which is slightly higher than the target strength. Even though the water content exceeded the target value in Mix-4-PM-P during the plant trial, the compressive strength in this mix is higher than for Mix-4-PM-L. The possible reasons include:

- Higher outdoor temperature (> 68°F in the lab) caused some acceleration effect on cement hydration (all the specimens were cured outdoors for the first 16 hours, followed by transporting to the lab).
- The high-power mixer in the plant was more effective in ensuring a homogeneous UHPC mix without any concern related to fiber segregation.

Note that 16–24 hours is the target age for releasing the strands, so sufficient strength for prestressing of plant-made UHPC can be gained within 24 hours. However, the 28-day strength of Mix-4-PM-P was 17.9 ksi, which is lower than the target strength. The lower strength might be due to the additional water and small-scale segregation of materials because these factors influence packing density negatively. The higher outside temperature may have compensated for the lower

packing density for 1-day compressive strength by accelerating the heat of hydration. However, this acceleration effect did not compensate for the lower 28-day compressive strength. As a result, the density might be reduced slightly, as shown in Table 5.18 in Section 5.6.1.2. In addition, some small-scale segregation of the cement, silica fume, and fibers was observed while casting specimens. This segregation may have played a minor role in the reduction of the 28-day compressive strength as well. Although compressive strength at 28 days for Mix-4-PM-P was lower than 20 ksi, a higher strength can be achieved through better control during batching and mixing to maintain the water content closer to the target value, as discussed in Section 5.5.2.

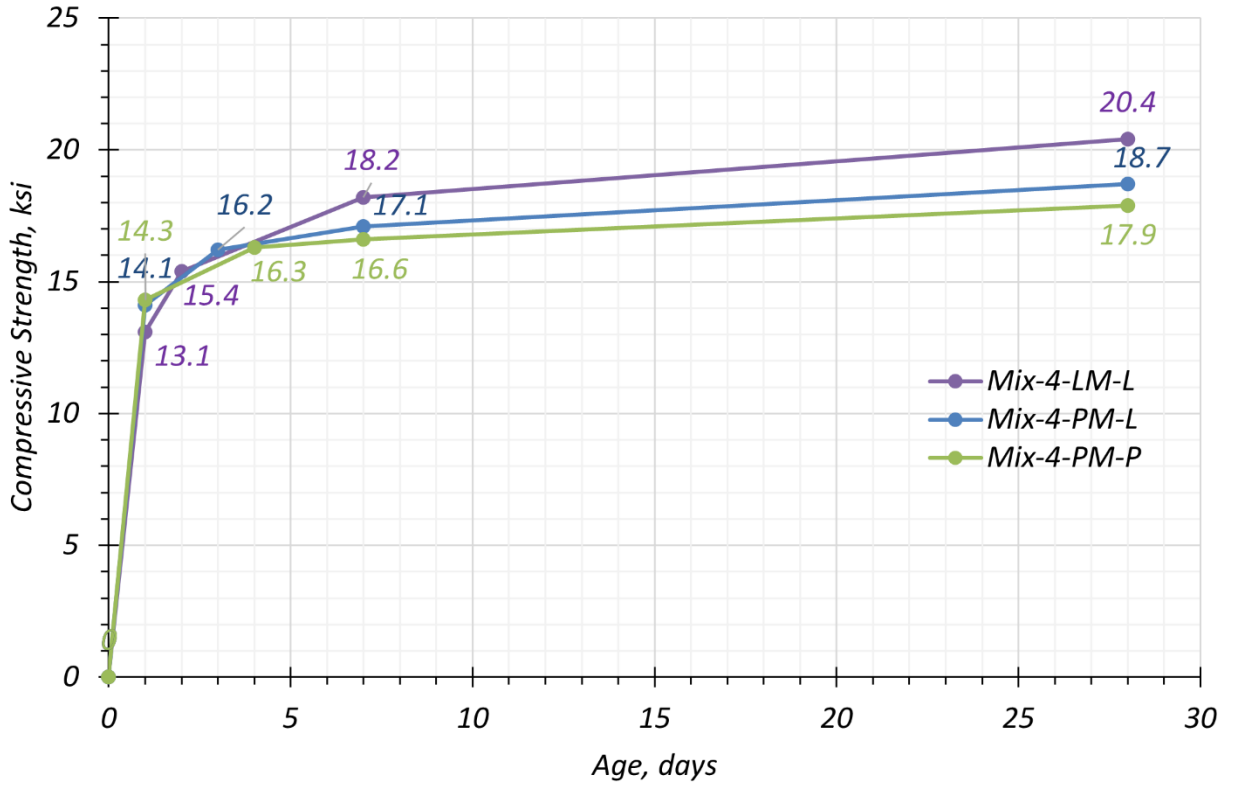

Figure 5.13. Compressive Strength Gain.

5.6.2.2 Comparison of Cast Cylinders and Cored Specimens

Comparison of the compressive strength from 3 × 6 in. cast cylinders and 3 × 6 in. cored specimens from the UHPC block was performed at the age of 61 days. Table 5.22 shows the test results. The compressive strength of the cored specimens is 9.5 percent higher than the cast cylinder. Since the temperature inside the block was higher than the near surface temperature and the tested core specimen was from the center of the block, high temperature might have provided a heat-curing

effect to the cored specimens. Based on the same analogy, it is expected that the strength of a girder made of UHPC should be higher than the strength measured in the lab using cylinders.

Table 5.22. Compressive Strength of Cast Cylinder and Cored Specimen.

Description	Specimen Number	Cast Cylinder	Cored Specimen
Compressive strength at 61 days, ksi	S1	18.1	18.9
	S2	18.6	20.4
	S3	17.0	19.5
	Avg.	17.9	19.6
	CoV	3.7%	3.2%

Note: Cored specimen from the center of the block.

Fiber orientation and distribution were investigated using cored samples. The fractured surfaces of the cored sample showed that fibers were randomly oriented and distributed (Figure 5.14).

(a) Front View *(b) Vertical View*

Figure 5.14. Steel Fiber Distribution and Orientation of Cored Specimen.

5.6.2.3 Modulus of Elasticity

The MOE of UHPC in compression was measured as per ASTM C469 (2014) and modifications for UHPC prescribed in ASTM C1856 (2017). Section 3.3.2 discusses the test method.

Mixes with different materials and batching locations using the same proportions as the selected Mix 4 are distinguished by suffix LM-L, PM-L, and PM-P (Section 5.6.1). Table 5.23 list the results of the MOE of Mix-4-PM-L, Mix-4-PM-L and Mix-4-PM-P specimens at different ages.

Table 5.23. MOE Comparison of Mix-4.

Mixture	Specimen ID	MOE, ksi				
		1 day	3–4 days	7 days	28 days	56 days
Mix-4-LM-L	S1	-[1]	-	-	N/A	-
	S2	-	-	-	6497	-
	S3	-	-	-	6672	-
	Average	-	-	-	6585	-
	CoV	-	-	-	1.3%	-
Mix-4-PM-L	S1	5331	5726 (3)[2]	5965	6327	6237
	S2	5081	5399 (3)[2]	6124	5984	Note 3
	S3	5510	5730 (3)[2]	5701	6125	6657
	Average	5307	5618 (3)[2]	5930	6145	6447
	CoV	3.3%	2.8%	2.9%	2.3%	3.3%
Mix-4-PM-P	S1	5348	5504 (4)[2]	6024	Note 3	Note 3
	S2	5330	5264 (4)[2]	5741	7063	6639
	S3	5588	Note 5	5560	6564	6561
	Average	5422	5384 (4)[2]	5775	6814	6600
	CoV	2.2%	2.2%	3.3%	3.7%	0.59%

Notes:
1. - : Not available
2. Testing age in parentheses
3. The measured value is not included as per the precision recommendations of ASTM C469 (2014). Imperfections in the specimen may have caused the deviation in behavior.

Figure 5.15 presents the MOE values measured for the Mix-4 specimens that were cast from the precaster materials at the laboratory and at the precast plant. Figure 5.15(a) presents the results of the trend of MOE over time. The MOE of Mix-4-PM-L and Mix-4-PM-P are quite similar. Figure 5.15(b) presents the MOE as a function of the compressive strength of specimens tested at the same age as the MOE specimens.

The MOE measured for the batch prepared from precaster materials can be expressed by Equation (5.1):

$$E_c = 1430\sqrt{f_c'} \tag{5.1}$$

where:

E_c = MOE, ksi

f_c' = Compressive strength, ksi

The coefficient is similar to the coefficient of 1460 reported by Haber et al. (2018). The above expression is used for the predicted MOE values shown in Figure 5.15.

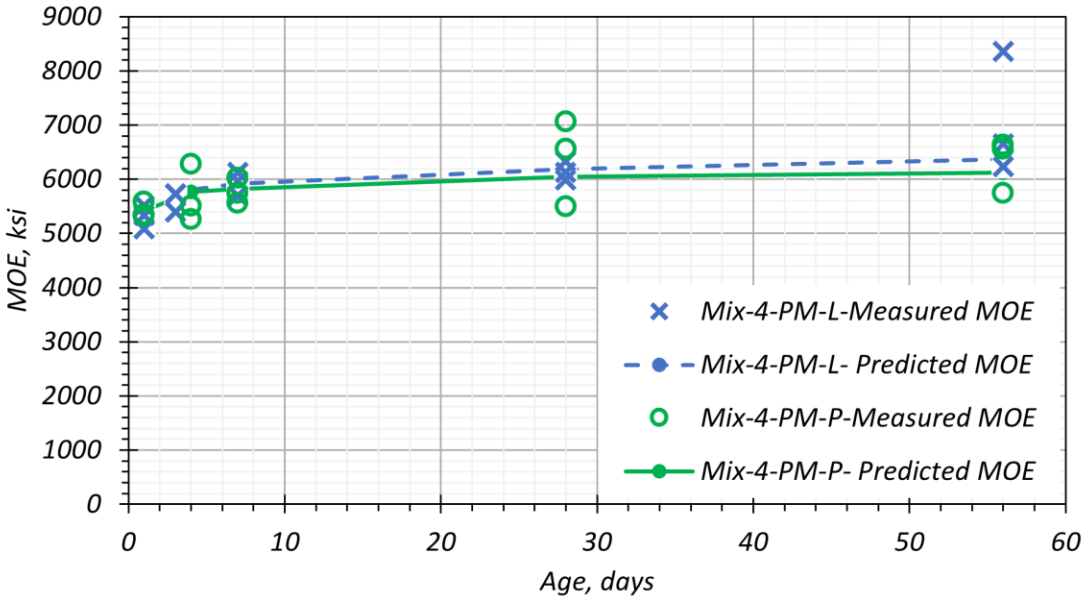

(a) MOE at Different Ages

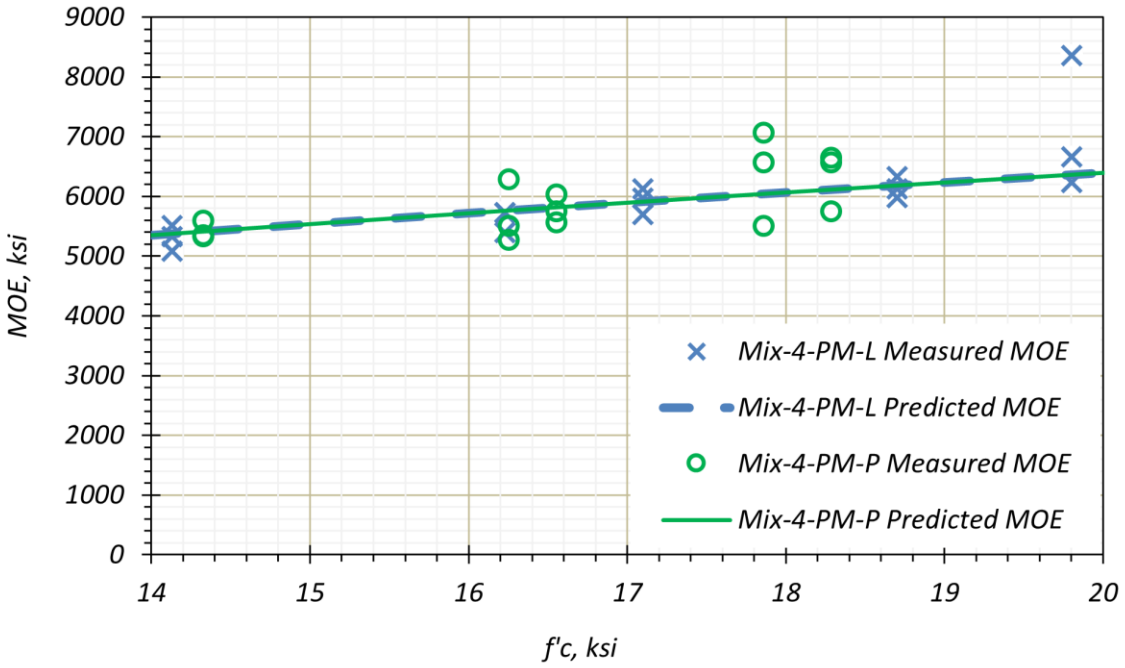

(b) MOE versus Compressive Strength

Figure 5.15. MOE for Mixtures Utilizing Precaster Materials.

The Poisson's ratio of the UHPC mixtures was also measured during the MOE tests. Table 5.24 lists the results of the Poisson's ratio for the same mixtures at different ages. The average Poisson's ratio was comparable for all mixtures, with an average of 0.26 at 28 days of age. This value is

slightly higher than the typical value of Poisson's ratio for UHPC, which ranges from 0.19 to 0.24 as reported in the literature (Ahlborn et al. 2008; Russell et al. 2013).

Table 5.24. Poisson's Ratio Comparison of Mix-4.

Mixture	Specimen ID	Poisson's Ratio				
		1 day	3-4 days	7 days	28 days	56 days
Mix-4-LM-L	S1	-	-	-	N/A	-
	S2	-	-	-	0.25	-
	S3	-	-	-	0.26	-
	Average	-	-	-	0.26	-
	CoV	-	-	-	2.6%	-
Mix-4-PM-L	S1	0.23	0.28 (3)[1]	0.25	0.27	0.27
	S2	0.22	0.20 (3)[1]	0.25	0.24	Note 5
	S3	0.23	0.23 (3)[1]	0.26	0.24	0.25
	Average	0.23	0.24 (3)[1]	0.25	0.25	0.26
	CoV	2.5%	12.9%	2.4%	6.3%	3.8%
Mix-4-PM-P	S1	0.25	0.27 (4)[1]	0.23	Note 5	Note 5
	S2	0.28	0.23 (4)[1]	0.27	0.26	0.26
	S3	0.22	Note 5	0.24	0.28	0.24
	Average	0.25	0.25 (4)[1]	0.25	0.27	0.25
	CoV	9.2%	8.0%	6.1%	3.7%	4.0%

Notes:
1. Testing age in parentheses
2. - : Not available
3. The measured value is not included as per the precision recommendations of ASTM C469 (2014). Imperfections in the specimen may have caused the deviation in behavior.

5.6.2.4 Direct Uniaxial Tension Test

The following sections document the uniaxial tensile strength test conducted in this research program. The tensile behavior of UHPC was studied for a trial mixture proportion and for the selected mixtures batched at the laboratory and at the precast plant. The uniaxial tensile strength of UHPC was measured using the direct tension test recommended by Graybeal and Baby (2019), with 2 × 2 × 17 in. prisms. This method is consistent with the recently drafted AASHTO T 397 Draft (AASHTO 2022), which is discussed in Section 3.3.3. The specimens were cured at 95 percent RH at 68°F, as per ASTM C511 (2019).

The test was conducted using an MTS 20-kip servo-controlled uniaxial tensile testing machine with hydraulic wedge grips. Figure 3.6 presents the uniaxial tensile test set-up with the specimens cracked within the gage length of 4 in. centrally located along the height of the specimen. The fibers bridge the cracks in the concrete, thereby imparting more ductility and tensile strength to

UHPC than to CC. The extensometer frame is adjusted such that the LVDTs measure the strain over a gage length of 4 in. The load protocol begins under force control to grip the specimens with a lateral force of about 40 kips followed by a compressive load at a rate of −0.00010 in./s in displacement control until a 4-kip compressive load is applied. The tensile load is applied at the same rate in the opposite direction until 25,000 με is attained longitudinally (read from the average of four LVDTs), or strain localization is observed. At that stage, the displacement rate is increased by 10 times. The test is terminated at an average displacement of 0.2 in. or when strain localization occurs.

(a) Uniaxial Tensile Test Setup

(b) Specimen after being tested—crack within gage length

(c) Fibers bridging the crack

Figure 5.16. Direct Uniaxial Tension Test.

Conducting the direct uniaxial tension test was challenging because the prisms might crack prematurely during gripping or from bending due to misalignment of the prism as a result of specimen imperfections. This effect leads to crack formation outside the gage length, impeding the LVDTs from capturing the specimen behavior under tensile loading. Those specimens in which the cracks form within the gage length provide more reliable data that represent the tensile behavior of the specimens. Figure 5.17 shows the different locations where cracking occurs with respect to

the gage length. The MOE in tension of the specimens under the tensile load is also computed as the slope of the stress-strain curve between the range of −1 to 0 ksi.

(a) Crack occurring within the gage length

(b) Crack occurring on the gage length

(c) Crack occurring outside the gage length

Figure 5.17. Crack Location with Respect to Gage Length.

5.6.2.5 Initial Investigation Using Mix-1a

Specimens cast in the lab using Mix-1a, which used laboratory materials and Type I/II cement, were tested to study the uniaxial tensile behavior of UHPC. Figure 5.18 presents the test results at 1 day, 3 days, and 14 days.

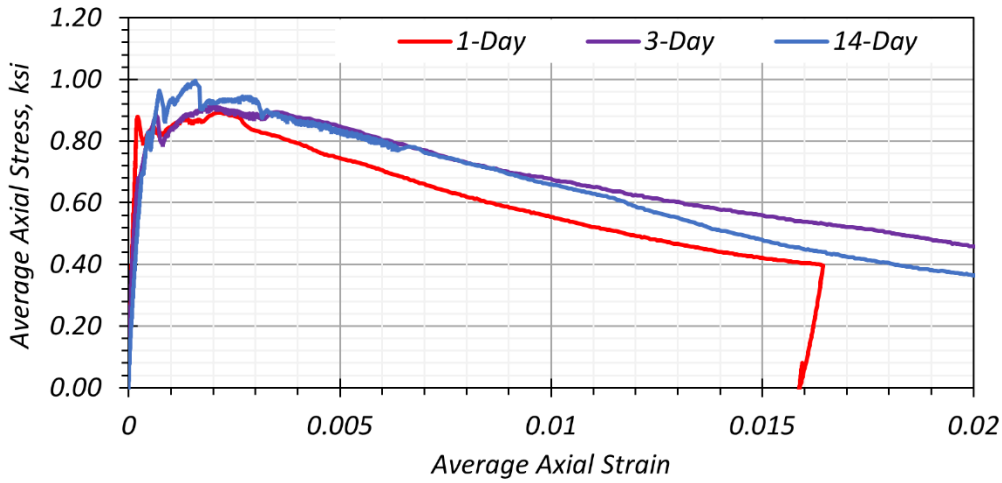

(a) Comparison of Uniaxial Tensile Behavior at Different Ages

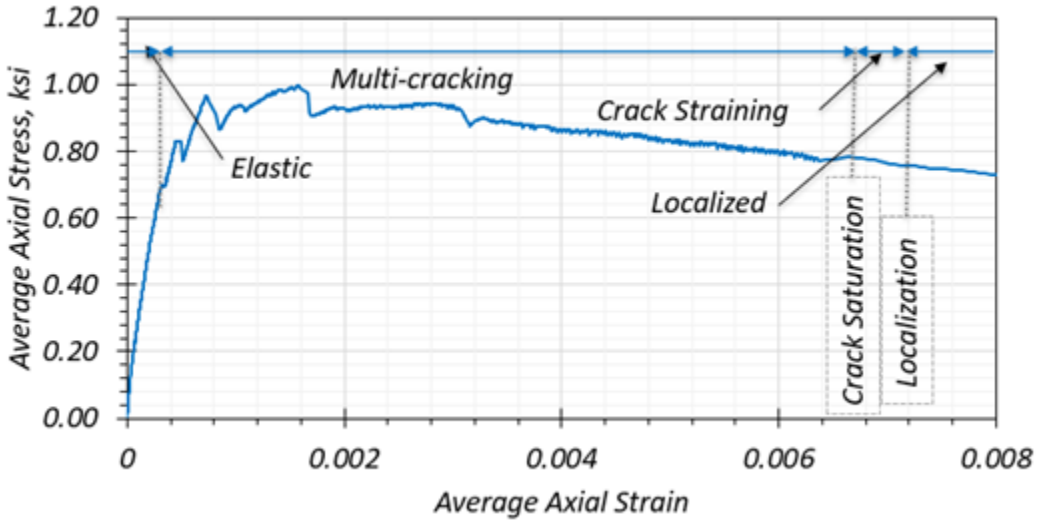

(b) Phases of Stress-Strain Curve in Uniaxial Tension at 14 Days

Figure 5.18. Behavior of Mix-1a under Uniaxial Tension.

Five specimens were tested at each age. Only two out of the five specimens per age tested had crack formations within the gage length. The other specimens were either damaged during gripping or had crack formations outside the gage length. Table 5.25 presents the results of the specimens from Mix-4a that cracked within the gage length. The first distinct crack is computed based on 0.02 percent offset strain (Haber et al. 2018) and based on visual inspection.

Table 5.25. Tensile Strength Comparison of Mix-1a at Different Ages.

Specimen ID	First Cracking Stress		Peak Stress		MOE, ksi	Age, days
	Strain, με	Stress, ksi	Strain, με	Stress, ksi		
01	161	0.880	2291	1.01	5986	1
02	**212**	**0.879**	**212**	**0.88**	**5410**	**1**
02	355	0.931	3131	0.99	6008	3
03	**330**	**0.741**	**1986**	**0.91**	**5697**	**3**
01	**332**	**0.702**	**1573**	**1.00**	**5318**	**14**
02	368	0.882	875	0.90	5247	14

Note: The specimens shown in Figure 5.18(a) are shown in bold font.

5.6.2.5.1 Results for Mix-4

The tensile behavior of the selected mixture (Mix-4b) was tested with two batches. Specimens from Mix-4-PM-L were cast at the laboratory with the precaster materials, and the specimens from Mix-4-PM-P were cast at the precast plant.

5.6.2.5.1.1 Mix-4-PM-L

Out of the 15 specimens cast in the laboratory using a triple batch of Mix-4b with precaster materials, the 10 specimens cast first had the most uniform surface preparation, while the five specimens cast last had the highest imperfections. Those specimens cast last showed more cracking outside of the gage length, possibly due to bending occurring from misalignment. Therefore, the order in which the specimens were cast also impacted the success of the direct uniaxial tension test.

Specimens from the Mix-4-PM-L triple batch were cured at two different curing conditions: 95 percent RH at 68°F and 50 percent RH at 77°F. The former conditions were used by Riding et al. (2019), while the latter conditions were used by Graybeal and Baby (2019). Figure 5.19 presents the stress-strain curves for different specimens that were tested under different curing conditions. Five specimens cast first and five specimens cast last were cured at 95 percent RH, and those specimens cast second were cured at 50 percent RH. This ensured reasonable comparison since the preparation of the first 10 specimens cast was quite similar.

All the specimens cured at 95 percent RH at 68°F are represented by lines with shades of blue, and those specimens at 50 percent RH at 77°F are represented by lines with shades of green. Solid lines denote that the specimens cracked within the gage length, whereas the dashed lines show specimens with cracks occurring at the mounting screw such that the cracks were partially within the gage length and partially outside it. The other specimens—the ones that failed during gripping or the ones whose cracks occurred completely outside the gage length, are not shown here. In this research, no discernable difference was found between the two curing conditions, and the 95 percent RH at 68°F was chosen for all other tension tests. Table 5.26 summarizes the findings of the direct uniaxial tension test conducted on specimens cast in the laboratory from Mix-4-PM-L at 28 days.

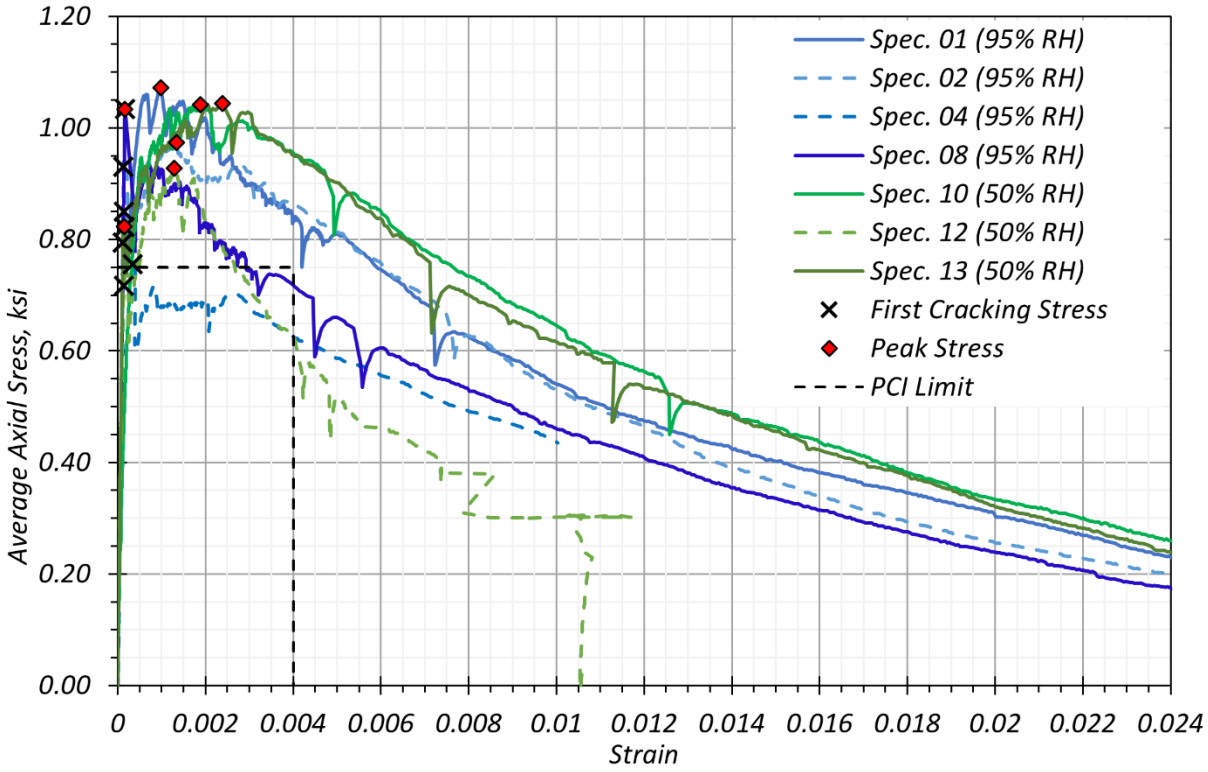

Figure 5.19. Tensile Behavior at Different Curing Conditions for Mix-4-PM-L (28 Days).

Table 5.26. Tensile Strength Results of Mix-4-PM-L at 28 Days.

Specimen ID	Relative Humidity, %	First Cracking Stress		Peak Stress		MOE, ksi
		Strain, με	Stress, ksi	Strain, με	Stress, ksi	
01	95	139	0.85	981	1.07	6648
02	95	132	0.93	1340	0.97	7313
04	95	150	0.82	150	0.82	6309
08	95	163	1.03	160	1.03	6625
10	50	340	0.76	1880	1.04	5599
12	50	147	0.72	1280	0.93	6402
13	50	120	0.79	2390	1.04	6790

5.6.2.5.1.2 Mix-4-PM-P

Out of the 20 direct uniaxial tension test prisms cast at the precast plant from Mix-4-PM-P, 15 were tested on 28 days, of which only five cracked within the gage length such that the displacements could be recorded by the LVDTs. Specimens 01, 11, and 15 cracked within or on the gage length. Specimens 07 and 13 cracked partially within the gage length and partially outside such that the LVDTs at two or more faces remained stationary or compressed without any meaningful data being recorded. The remaining five specimens were tested at 56 days. Table 5.27 summarizes the direct uniaxial tension test results for all the individual specimens that cracked within the gage length for Mix-4-PM-P. Figure 5.20 presents the tensile behavior of the specimens.

Table 5.27. Tensile Strength of Mix-4-PM-P at 28 and 56 Days.

Specimen Number	First Cracking Stress		Peak Stress		MOE, ksi	Age, days
	Strain, με	Stress, ksi	Strain, με	Stress, ksi		
01	**207**	**1.28**	**207**	**1.28**	**6648**	**28 Days**
07	310	0.08	1056	0.73	3728	28 Days
11	8	0.03	132	0.76	5942	28 Days
13	−1	0.01	115	0.40	3279	28 Days
15	9	0.08	118	0.71	5847	28 Days
01	2	0.01	105	0.65	6577	56 Days
02	119	0.78	127	0.81	6373	56 Days
03	**180**	**1.02**	**555**	**1.21**	**6459**	**56 Days**
04	−153	−0.48	164	0.38	4766	56 Days
05	81	0.50	133	0.80	6370	56 Days

Note: The specimens that cracked within the gage length are shown in bold face font.

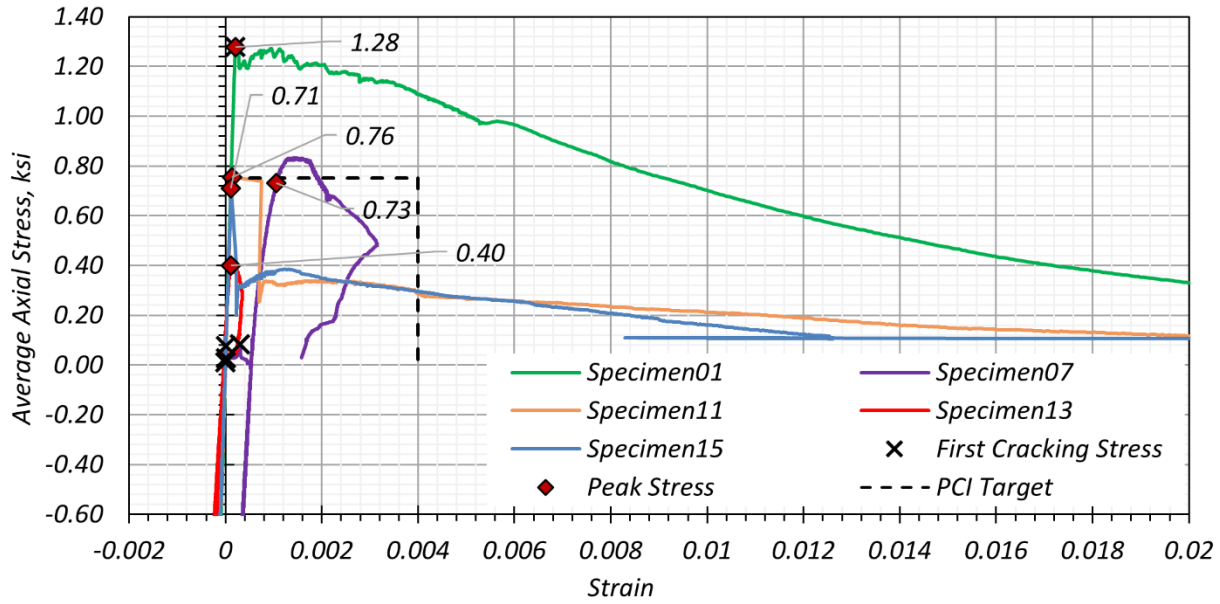

(a) Stress-Strain Curves at 28 days

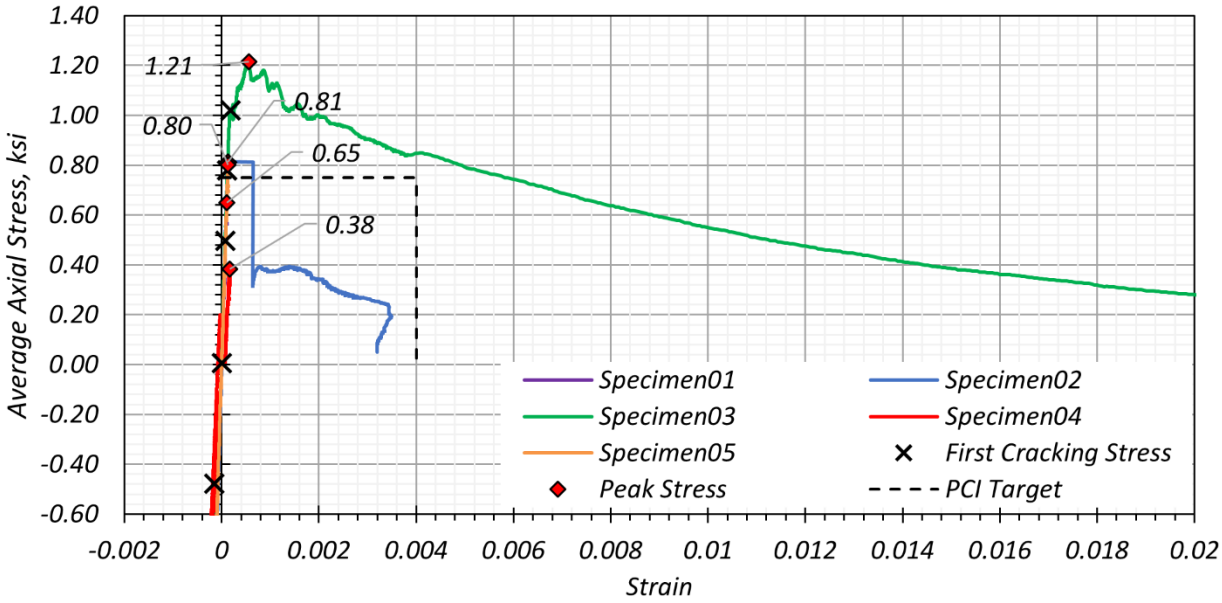

(b) Stress-Strain Curves at 56 days

Figure 5.20. Tensile Strength Results of Mix-4-PM-P.

Figure 5.21 presents the Mix-4-PM-P specimens after the crack formation when subjected to a tensile load at 56 days. Only Specimen 3 had crack formations within the gage length. The low success rate of the specimens prepared at the precast plant are indicative of the imperfections that occurred while casting the specimens in the field due to the platform, which was less level than the one used under laboratory conditions.

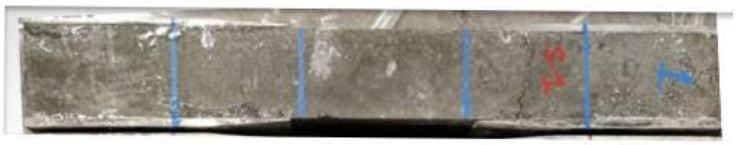

(a) Specimen 01 cracked within grips

(b) Specimen 02 cracked on mounting screw

(c) Specimen 03 cracked within the gage length

(d) Specimen 04 cracked within the grips

(e) Specimen 05 cracked within the grips

Figure 5.21. Mix-4-PM-P Specimens after Direct Uniaxial Tension Test at 56 Days.

5.6.2.5.1.3 Comparison

The tensile behavior of the selected Mix-4-PM-L prepared with laboratory materials was compared to the tensile behavior of Mix-4-PM-L and Mix-4-PM-P, which were prepared from precaster materials at the laboratory and at the precast plant, respectively. Section 4.7 discusses the individual specimen results of Mix-4-LM-L. Figure 5.22 presents the comparison of the tensile behavior of Mix-4 with different material sources and different casting locations under uniaxial tension at 28 days of age. While the performance of all three mixtures is quite similar, Mix-4-PM-P exhibited a higher first cracking and peak strength compared to the other mixtures. Table 5.28 lists the results of the specimens compared for each mixture. Specimens that cracked within the gage length were used for the comparison.

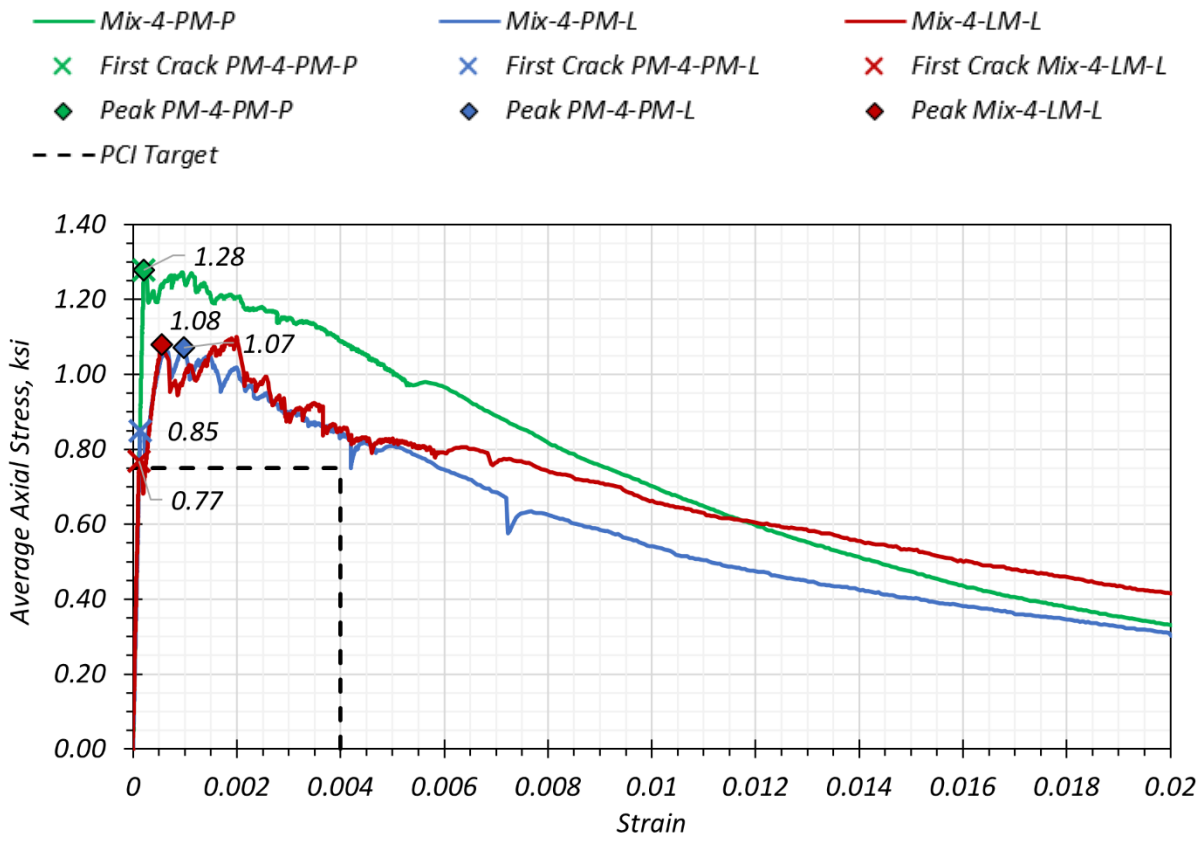

Figure 5.22. Comparison of Tensile Strength at 28 Days for Mix-4.

Table 5.28. Tensile Strength Comparison of Mix-4 at 28 Days.

Properties	Mix-4-LM-L	Mix-4-PM-L	Mix-4-PM-P
MOE (ksi)	6730	6648	6648
First Cracking (ksi)	0.77	0.85	1.28
First Cracking Strain (με)	115	139	207
Peak Strength (ksi)	1.08	1.07	1.28
Peak Crack Strain (με)	556	981	207

5.6.2.6 Inferred Tension Bending Test

This section documents the flexural performance test conducted to indirectly study the tensile behavior of UHPC. The section also describes the modifications to the standard evaluated to counter some of the problems faced during the testing. The results of the flexural strength of the selected mixtures using precaster materials are provided for the specimens cast at the laboratory and at the precast plant. Due to the challenges of conducting the direct uniaxial tension test due to the potential for cracking outside the gage length and the lack of a standardized test method, it may be more practical to indirectly assess the tensile capacity of UHPC. One approach that may be

more practically viable is to conduct an inferred tension bending test and compute the tensile capacity through an inverse analysis (eConstruct 2020; Graybeal and Baby 2019). Flexural testing was conducted as per ASTM C1609 (2019) and the modifications for UHPC listed in ASTM C1856 (2017). Section 3.3.4 discusses the test method. Figure 5.23 illustrates the test set-up for a third-point loading test with the deflection measurement frame fastened around the beam. The two LVDTs on opposite faces of the specimen measure the midspan deflections, which in turn controls the movement of the actuator in the strain-controlled mechanism (Bernard 2009).

Figure 5.23. Inferred Tension Bending Test Setup.

5.6.2.6.1 Results for Mix-4b

Flexure prisms cast from Mix-4b with precaster materials at the lab and at the precast plant were tested and compared. Some segregation of fibers was observed for both the cases, with the fiber settling down at the bottom of the specimen. This result led to a partially brittle failure in the specimen under bending and a resulting sharp load drop. Therefore, the ductility requirement recommended by eConstruct (2020), which is based on the requirement from ACI Committee 318 (2019) for FRC, is slightly greater than the observed flexural strength at midspan deflections of 0.04 in. and 0.08 in. (Figure 5.24). Table 5.29 summarizes the flexural strength parameters for both batches. High first crack strength and high peak strength was observed among all the

specimens. The toughness values for both batches were comparable but the equivalent flexural strength ratio differed due to the difference in the first peak crack strength of the two batches.

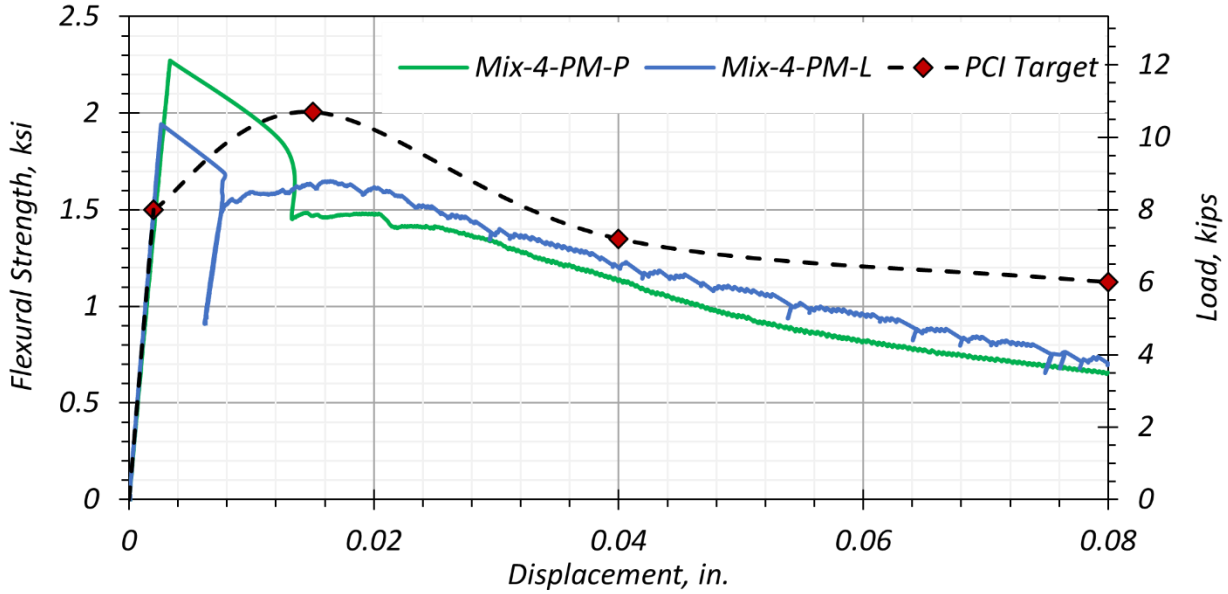

Figure 5.24. Comparison of Flexural Strength of Selected Mix at Precast Plant and Lab.

Table 5.29. Flexural Strength Comparison of Mix-4.

Description	**Mix-4-PM-L**[1]	**Mix-4-PM-P**[2]
First Peak Crack Strength, ksi	1.51	2.17
Deflection at First Crack, in.	0.0026	0.0032
Ultimate Flexural Strength, ksi	1.51	2.17
Deflection at Ultimate Flexural Strength, in.	0.0026	0.0032
Residual *L*/300 as Percentage of First Crack Strength[3,4]	62%	50%
Residual *L*/150 as Percentage of First Crack Strength[5]	37%	38%
Toughness, lb-in.	520	500
Equivalent Flexural Strength Ratio	81.0%	54.0%

Notes:
1. Mix-4-PM-L specimens are tested at 21 days.
2. Mix-4-PM-P specimens are tested at 28 days.
3. *L* is the span length of the prism—in this case 12 in.
4. Residual strength at midspan deflection of *L*/300
5. Residual strength at midspan deflection of *L*/150

5.6.2.6.2 Trials with Displacement Control

Due to the sharp load drop observed during testing of most of the specimens among the six specimens tested at 28 days under load control, the remaining three specimens from the total set of nine specimens, were tested in a displacement-controlled mode at a rate of 0.006 in./s. Though the displacement-controlled mechanism provided some aid in countering the sharp load drop and abrupt stopping of the test before the 0.08 in. midspan displacement was reached, the load-deflection curve was highly unstable. Figure 5.25 shows the results. This behavior exhibited a brittle failure. The settlement of fibers to the bottom of the prism may be indicative of the higher water content in the mix at the precast plant. Table 5.30 summarizes the results of the inferred tension bending test under displacement control.

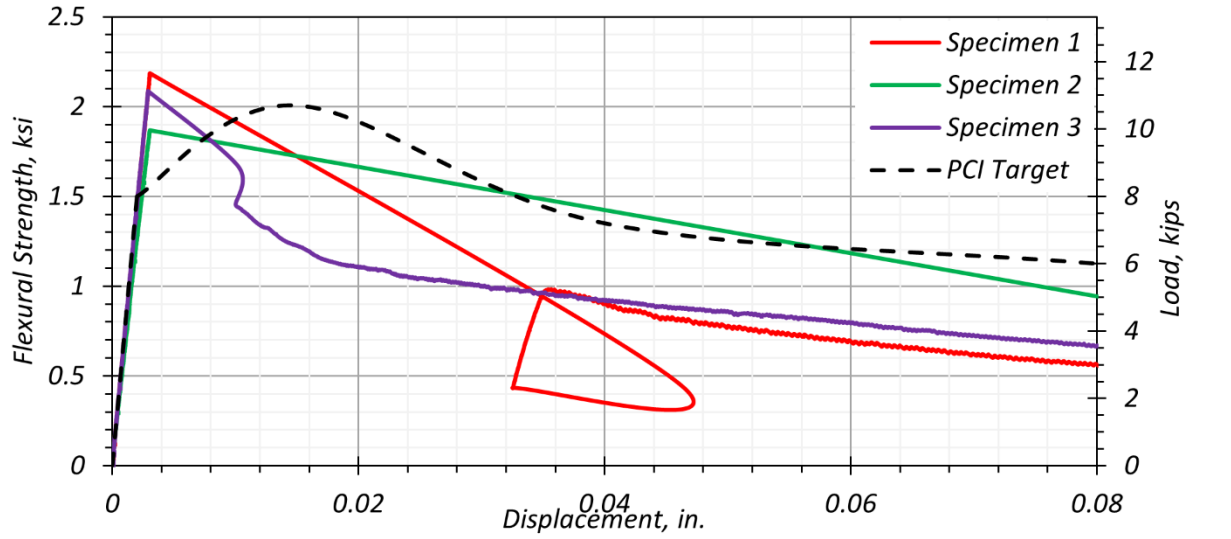

Figure 5.25. Flexural Strength of Mix 4-PM-P at 56 Days under Displacement Control.

Table 5.30. Flexural Strength Comparison of Mix-4 under Displacement Control.

Specimen ID	First Cracking Strength		Ultimate Flexural Strength		Tough-ness	Equiv. Flexural Strength Ratio	L/300 = 0.04 in.	L/150 = 0.08 in.
	Disp., in.	Stress, ksi	Disp., in.	Stress, ksi	lb.-in.	Percent	Stress, ksi	Stress, ksi
1	0.003	2.09	0.003	2.09	470	53.0	0.87	0.55
2	0.003	1.78	0.003	1.78	590	78.0	1.34	0.52
3	0.003	1.99	0.003	1.99	430	50.5	0.88	0.64

Notes: Specimen 2 had an abrupt drop in load. The equivalent flexural strength ratio may be overestimated because of the sudden load drop that is a consequence of the brittleness of the specimen at the given orientation.

5.6.2.6.3 Effect of Fiber Distribution

Only Specimen 3 showed a stable load-deflection curve, which may be attributed to Specimen 3 having a higher fiber content than the other two specimens (Figure 5.26). As per ASTM C1609 (2019), the specimen is to be turned on its side with respect to the position it was cast in (as-cast position) such that the free surface of prism, not bound by the wall of the mold, is not placed in contact with the loads or the support. However, this position leads to the bottom surface that undergoes tension to have differential fiber content between longitudinally parallel sides, with one side having high fiber content (bottom face) and the other end having low fiber content (top face) in the case of fiber segregation in the mix. This results in a brittle failure on one side of the prism, causing a sudden load drop and unstable load-deflection curve, as illustrated in Figure 5.26.

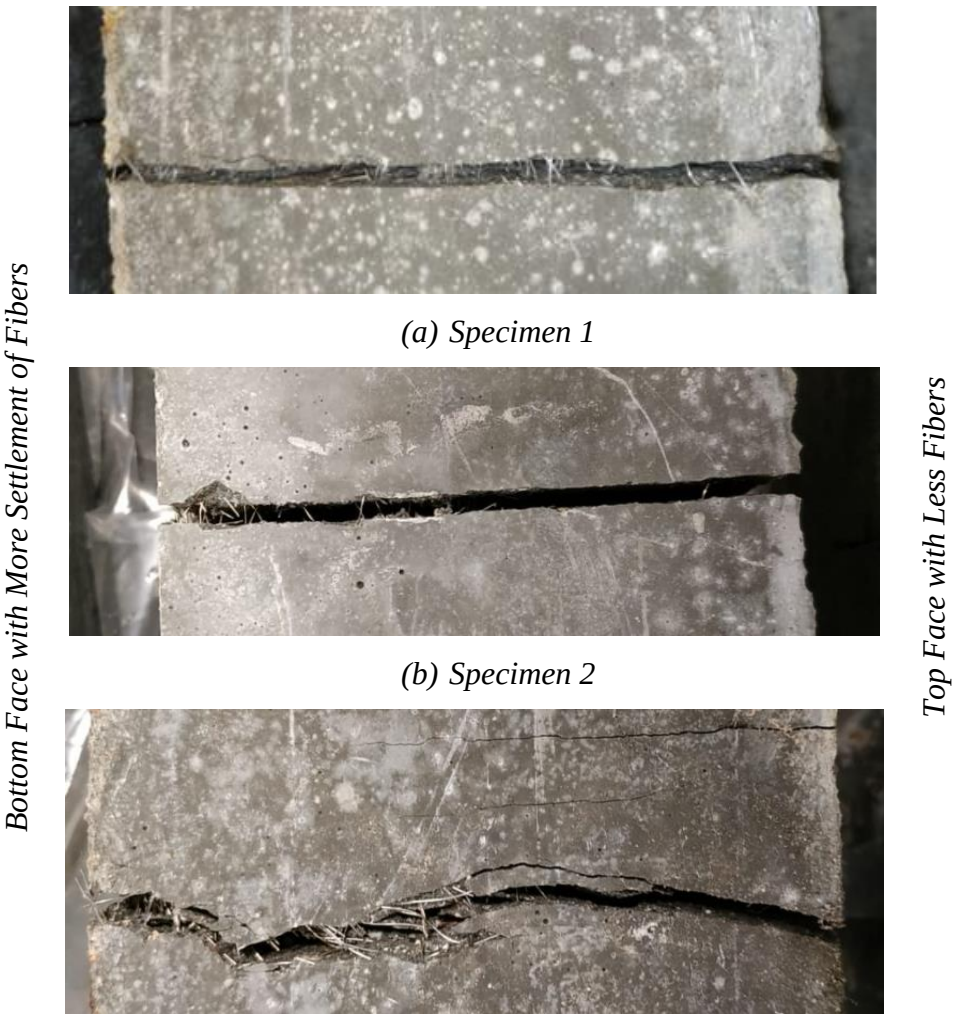

(a) Specimen 1

(b) Specimen 2

(c) Specimen 3

Figure 5.26. Segregation of Fibers at Tensile Face of Prism.

To counter this issue, the Mix-4-PM-L specimens were tested with a different orientation. The specimen was positioned on the supports as the specimen was cast with respect to the mold such that the face with higher fiber concentration was at the tensile face of the beam during the inferred tension bending test. This approach was also tested by Mendonca et al. (2020). Figure 5.27 shows a comparison between the load deflection curves obtained by the two different orientations. Table 5.31 lists the flexural strength parameters measured during the comparison of different orientations of the specimen.

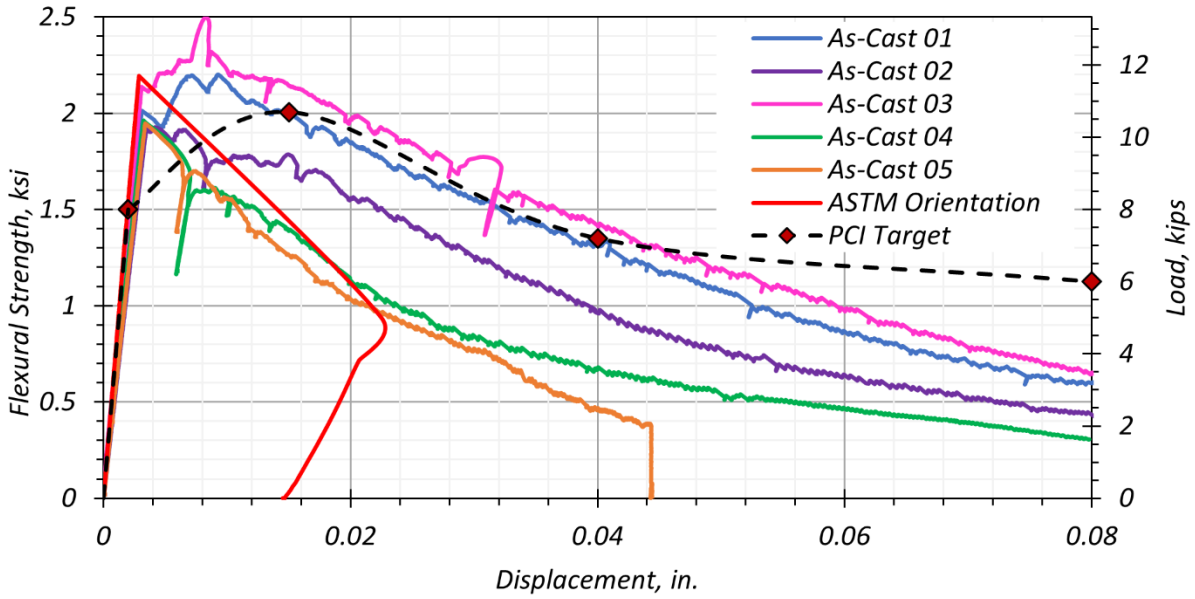

Figure 5.27. Effect of Orientation of Specimens and Fiber Segregation on Flexural Strength.

Table 5.31. Comparison of Different Orientation for Flexural Strength Test.

Specimen ID	First Cracking Strength		Ultimate Flexural Strength		Tough-ness	Equiv. Flexural Strength Ratio	L/300 = 0.04 in.	L/150 = 0.08 in.
	Disp., in.	Stress, ksi	Disp., in.	Stress, ksi	lb.-in.	Percent	Stress, ksi	Stress, ksi
As Cast-01	0.0031	1.92	0.0075	2.10	560	68.0	1.26	0.55
As Cast-02	0.0038	1.82	0.0049	1.84	450	57.5	0.92	0.34
As Cast-03	0.0035	2.01	0.0085	2.38	610	71.0	1.34	0.49
As Cast-04	0.0035	1.87	0.0035	1.87	350	43.5	0.61	0.28
As Cast-05	0.0036	1.86	0.0036	1.86	240	30.0	0.43	0.00
ASTM Orientation	0.0032	2.09	0.0032	2.09	180	20.5	0.00	0.00

Notes: Specimen with "ASTM Orientation" had an abrupt drop in load. The results of this specimen may not be a true representation of the mix because of brittle behavior arising from the orientation of the specimen.

The as-cast orientation shows a ductile behavior as opposed to the brittle behavior observed during the tests conducted when the specimen is oriented as per ASTM C1609 (2019). It is proposed to use the as-cast orientation for those mixes when fiber segregation is suspected or for highly flowable mixes in order to check the load-deflection profile up to a deflection of *L*/150, in which *L* is the span length in inches. However, the results may overestimate the tensile capacity due to a

higher fiber concentration near the bottom face of the prism. Figure 5.28 illustrates how the fibers bridge the crack, and a ductile behavior is exhibited when the specimen is oriented in as-cast specimens; meanwhile, the ASTM orientation shows brittle failure due to fiber segregation at the bottom face under tension.

Specimen 05, tested as a part of the modified orientation test matrix, failed at a midspan deflection of 0.044 in. due to lack of fibers at the top. Almost all the fibers of this specimen settled at the bottom of the prism, leading to brittle failure because the crack propagated above the neutral axis of the beam leading to brittle fracture. Figure 5.28 presents the different faces of the prisms after the inferred tension bending test. The photos highlight that those faces with less fibers undergo brittle fracture; in contrast, the cracks on faces with higher fiber content are bridged, resulting in ductile behavior.

(a) As-cast specimen 01-04: Fibers bridge the crack and result in ductile behavior up to 0.08 in. midspan deflection

(b) As-cast specimen 05: Bottom tensile crack face

(c) As-cast specimen 05: Side face – fibers settled at bottom with no fibers at top

(d) ASTM orientation – left to right: Side face with fibers, bottom tensile face with segregated fibers, Side face with no fibers showing brittle failure

Figure 5.28. Cracks Occurring in Flexure Prisms with Different Orientations.

5.6.2.7 Shrinkage

Shrinkage testing was conducted in accordance with ASTM C157 (2017) and modifications by ASTM C1856 (2017). Two test groups were prepared, with three specimens for each group. One

group was for autogenous shrinkage and the other was for total shrinkage. Total shrinkage is defined as the sum of the drying and autogenous shrinkages. For autogenous shrinkage, three 3 × 3 × 11.25 in. prisms were sealed with aluminum foil to prevent water evaporation from the specimens; the other three specimens for total shrinkage were not sealed (Figure 3.10). Section 3.3.6 discusses the test method in detail.

(a) Length Comparator with a Prism

(b) Total Shrinkage and Autogenous Shrinkage Specimens

Figure 5.29. Shrinkage Test Device and Specimens.

Figure 5.30 shows weight loss of the mixtures. The weight loss of the specimens for autogenous shrinkage is very low compared to the specimens for total shrinkage, which indicates that the shrinkage values measured using the sealed specimens can be considered as autogenous shrinkage.

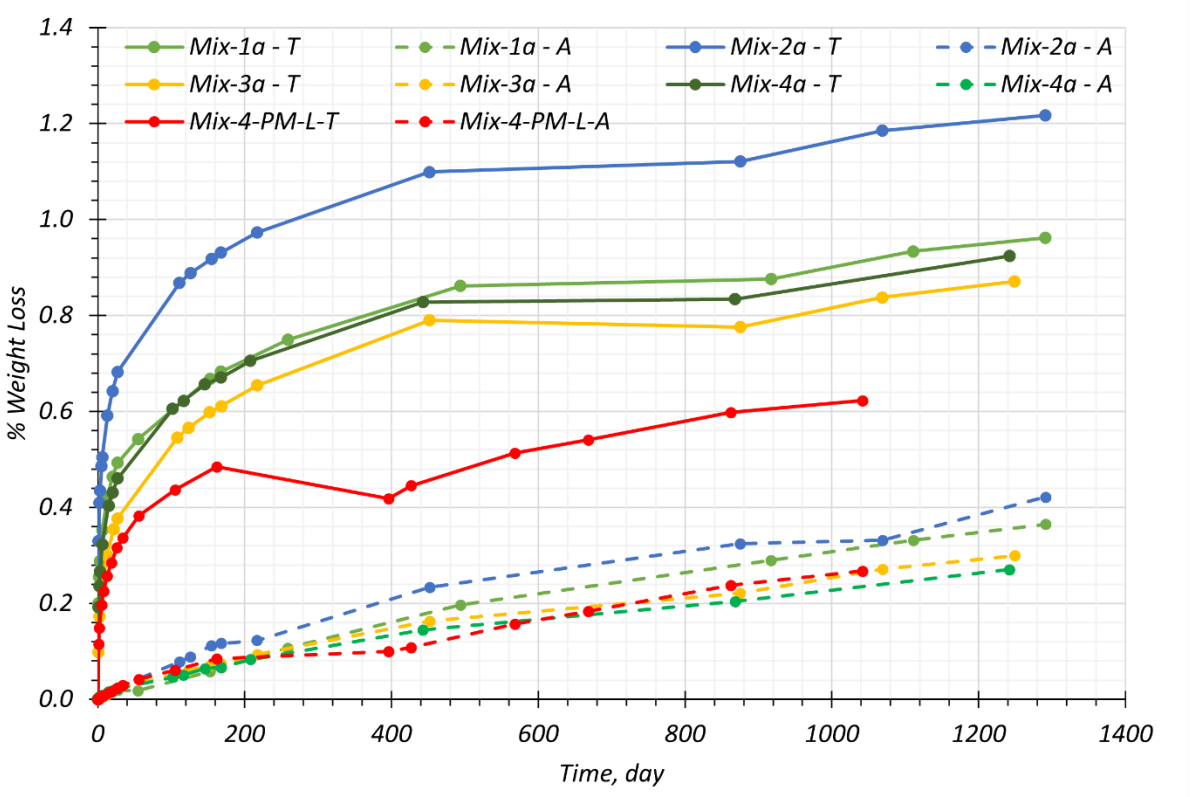

T: Total shrinkage specimens
A: Autogenous shrinkage specimens

Figure 5.30. Weight Loss of UHPC Mixtures.

Shrinkage of Mix-4-PM-L was studied in comparison with Mix-1a, Mix-2a, Mix-3a, and Mix-4a, which were the developed mixtures that were part of Task 4, discussed in Chapter 4. The shrinkage readings for Mix-1a, Mix-2a, Mix-3a, and Mix-4a are documented in more detail by Shah (2021). Figure 5.31 compares the total shrinkage and autogenous shrinkage for these mixtures. Table 5.32 shows the ratio of autogenous shrinkage to total shrinkage.

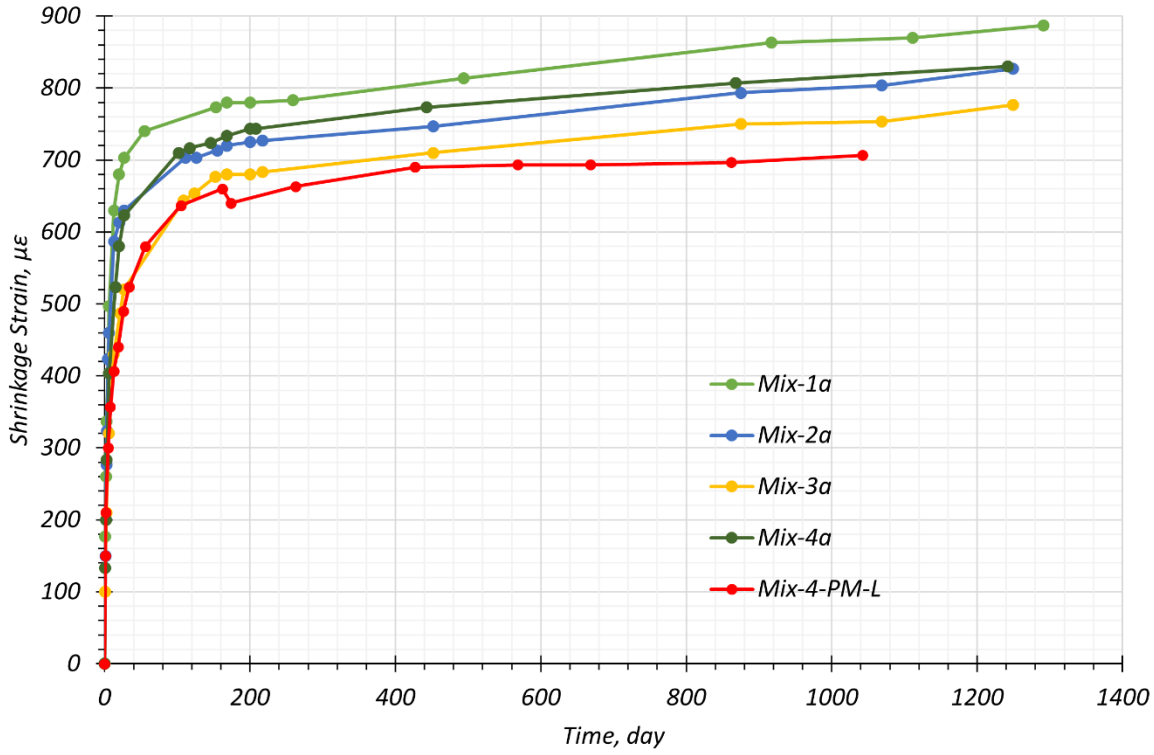

(a) Total Shrinkage

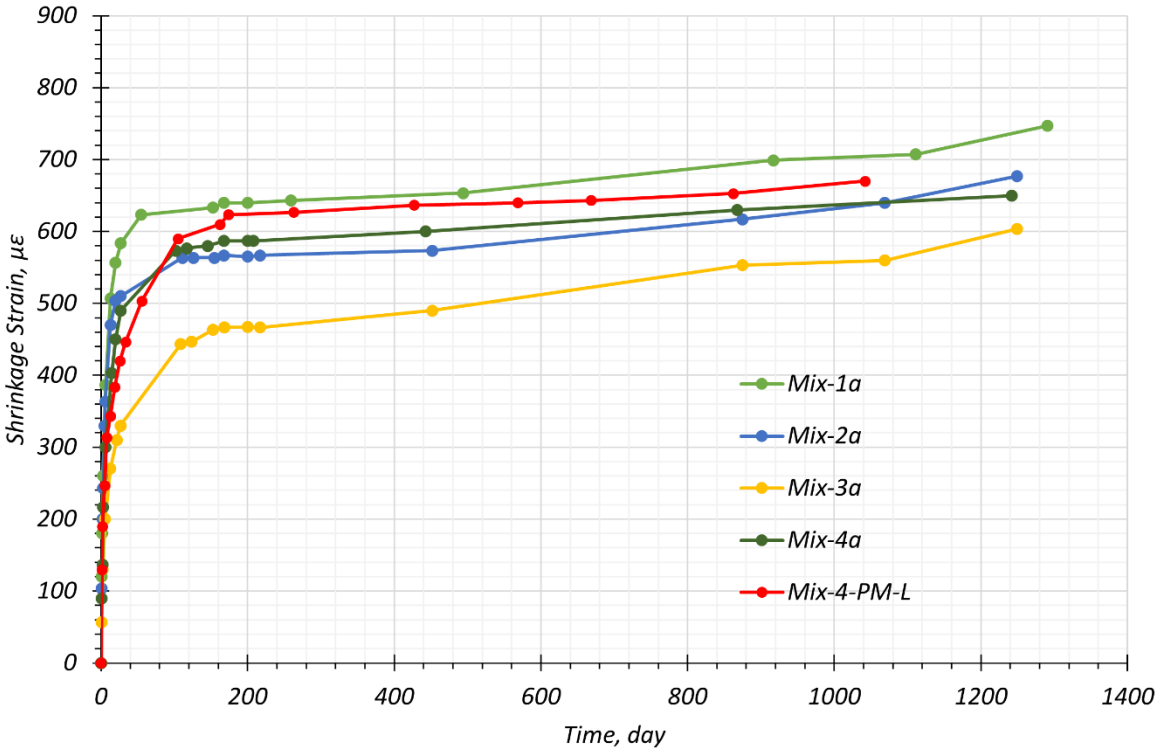

(b) Autogenous Shrinkage

Figure 5.31. Shrinkage Test Results.

Mix-4-PM-L has a relatively low total shrinkage value up to 668 days. The main factors contributing to the lower total shrinkage for this mix might be the larger particle size of the sand and low drying shrinkage. The other mixtures contain sands sieved by #16 (0.05 in.), while Mix-4-PM-L contains sands with #4 (0.19 in.) maximum particle size. The large particle size of sands may form a skeleton to resist length change. In addition, weight loss of Mix-4-PM-L is lower than the other mixtures. The accelerated hydration reaction of Type III cement (C-5) due to abundant C_3S plus C_2S contents (74.9 percent) might facilitate achieving a denser mixture quickly. Consequently, its drying shrinkage value is lower (Table 5.32). As a result, Mix-4-PM-L has a lower total shrinkage value relative to the other mixtures. The ultimate total shrinkage of Mix-4-PM-L is expected to be approximately 700 με.

Table 5.32. Ratio of Autogenous Shrinkage to Total Shrinkage and Silica Fume Content.

Description	Mix-1a	Mix-2a	Mix-3a	Mix-4a	Mix-4-PM-L
AS[1]	699	617	552	630	643
TS[2]	863	793	773	807	693
DS[3]	164	176	221	177	50
AS/TS, %	81	78	71	78	93
SF/C[4], %	21.4	21.4	5.7	10.7	10.7

Notes:
1. AS: Autogenous shrinkage
2. TS: Total shrinkage
3. DS: Drying shrinkage = T-A
4. SF/C: Ratio of silica fume to cement by volume
5. Reading age: Mix-1a, Mix-2a, Mix-3a, Mix-4a, and Mix-4-PM-L at 917, 875, 875, 868, and 668 days, respectively
6. Unit: με

Zhang et al. (2003) reported that autogenous shrinkage increases with silica fume content. In the mix group of Type I/II cement (C-2), which includes Mix-1a, Mix-2a, Mix-3a, and Mix-4a, this phenomenon can be explained. Mix-3a of the lowest silica fume content showed a low autogenous shrinkage value and a low ratio of autogenous shrinkage to total shrinkage (A/T) (see Table 5.32). All other mixes (i.e., Mix-1a, Mix-2a, and Mix-4a) show similar A/T, approximately 80 percent. The autogenous shrinkage value of Mix-4-PM-L is slightly higher than the autogenous shrinkage of Mix-4a although the mixture proportion for both the mixes are the same. However, Mix-4-PM-L shows a high A/T, 93 percent, due to the low drying shrinkage value. In addition, Mix-4-PM-L showed low autogenous shrinkage up to 70 days compared to Mix-4a. The factor might be wet sand. Wet sand in Mix-4-PM-L might have released a certain portion of the absorbed water when the internal RH decreased. Thus, the absorbed water in sand delays the decrease in internal RH.

As a result, the initial development of autogenous shrinkage of Mix-4-PM-L was slower than Mix-4a, which includes oven-dried sands. Haber et al. (2018) reported that four out of six proprietary UHPCs showed 600–800 με of total shrinkage at 168 days and noted that the shrinkage values of the other two UHPCs were extremely low and high, respectively. Overall, the total shrinkage of Mix-4-PM-L is in the common range observed for proprietary UHPCs.

5.6.3 Durability

The durability of the finalized UHPC mixture (Mix-4) was investigated using both lab-made and plant-made UHPCs. Lab-cast test specimens without steel fibers were used for measuring true bulk and surface resistivities, and rapid chloride ion penetration as a significant deviation of the test results due to fiber interference were clearly observed. The specimens cast at the plant were used for freeze-thaw resistance, scaling resistance, and abrasion resistance tests. This section discusses the test results in detail.

5.6.3.1 Bulk and Surface Resistivity

5.6.3.1.1 Overview

The bulk resistivity test measures the conductivity of concrete specimens in accordance with ASTM C1760 (2021). Section 3.4.2 discusses the test method. Conductivity is quantified by passing an electrical charge through the specimens (Figure 3.12). The conductivity depends on PSR, pore sizes, and connectivity of pores of the concrete (Spragg et al. 2016). The resistivity of the specimen is the reciprocal of the conductivity. The bulk resistivity measurement, with proper consideration to PSR, is a measure of concrete transport properties (i.e., permeability), which can effectively be correlated with the durability performance of UHPC. Cooper (2020) documented bulk and surface resistivity testing for Mix-1a, Mix-2a, and Mix-3a in more detail.

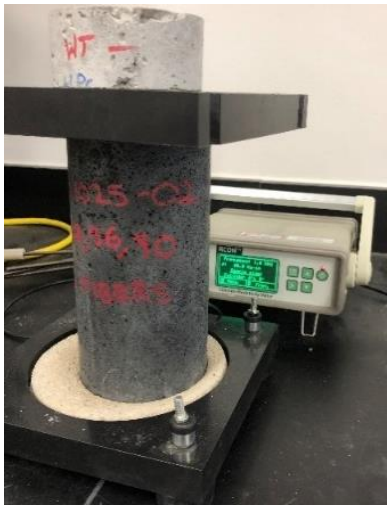

(a) Bulk Resistivity Testing

(b) Surface Resistivity Testing

Figure 5.32. Bulk and Surface Resistivity Testing Equipment and Specimens.

5.6.3.1.2 Bulk Resistivity

Three 4 × 8 in. cylinder specimens without steel fibers were cast for resistivity testing and cured in a room at 68°F and 95 percent RH as per ASTM C192 (2016). Table 5.33 shows the bulk resistivity readings taken at 7, 14, 21, 28, and 56 days and the measured values. The resistivity values for Mix-1a, Mix-2a, and Mix-3a mixtures developed in Task 4 using a Type I/II cement are also included in Table 4.29 for a comparative assessment. Even though the bulk resistivity values of Mix-4-LM-L prior to 56 days are slightly lower than Mix-1a and Mix-2a, the bulk resistivity value at 56 days is comparable to Mix-1a and Mix-2a. Both Mix-1a and Mix-2a contain 15 percent silica fume proportion by cement weight, whereas Mix-3a and Mix-4 series contain 4 percent and 8 percent silica fume proportion by cement weight. At 28 days, it is clear that the higher the silica fume content, the higher the resistivity. However, at 56 days, the resistivity values for Mix-1a, Mix-2a, and Mix-4-LM-L are in a similar range (202–208 kΩ-cm), although the silica fume content of Mix-4 (i.e., 8 percent) is lower than the other two mixes (i.e., 15 percent). However, Mix-3a shows a distinctly lower resistivity value (i.e., 105 kΩ-cm) than those values in all the other mixes, which is in alignment with the silica fume content. Interestingly, the predicted service lives based on the bulk resistivity values at 28 days for Mix-1a, Mix-2a, and Mix-4-LM-L (i.e., 314, 317, and 233 years, respectively) are also higher than for Mix-3a (174 years, discussed in Section 4.6.3). Therefore, a valid trend in general is the higher the resistivity, the higher the predicted service life. As a result, the durability performance of Mix-4-LM-L is expected to be

similar to the performance of Mix-1a and Mix-2a after 56 days. The bulk resistivity value for Mix-4-PM-L is slightly higher than Mix-4-LM-L. This result might be because the gradation of sand from the precaster is better than the sand used for Mix-4-LM-L and improves packing density, as discussed in Section 5.3.3. Therefore, high durability and a long service life span of Mix-4-LM-L and Mix-4PM-L are expected.

Table 5.33. Bulk Resistivity Test Results.

Mixture	7 days	14 days	21 days	28 days	56 days
Mix-4-PM-L	22.0	40.6	60.3	86.5	210.0
Mix-4-LM-L	25.3	37.5	55.9	78.8	201.5
Mix-1a	23.4	46.6	-	105.9	206.9
Mix-2a	23.6	47.2	-	106.9	207.8
Mix-3a	17.7	30.6	-	58.7	105.2

Note:
Unit: kΩ-cm
- : Not available

5.6.3.1.3 Surface Resistivity

The surface resistivity test also measures conductivity like the bulk resistivity in accordance with AASHTO T 358 (2017). Section 3.4.2 discusses the test method. The same specimens for the bulk resistivity test were used for the surface resistivity test. The surface resistivity readings were taken at 7, 14, 21, 28, and 56 days, which are the same ages used for the bulk resistivity test. Table 5.34 shows the measured values.

Table 5.34. Surface Resistivity Test Results.

Mixture	Surface Resistivity (kΩ-cm)				
	7 days	14 days	21 days	28 days	56 days
Mix-4-PM-L	21.7	41.3	61.8	87.3	213.8
Mix-4-LM-L	20.4	35.7	54.8	74.4	194.7
Mix-1a	23.7	44.7	-	106.4	211.3
Mix-2a	26.3	45.6	-	105.5	213.8
Mix-3a	16.6	28.8	-	56.5	100.5

- : Not available

Similar to the results of the bulk resistivity test, the surface resistivity results of Mix-4-PM-L and Mix-4-LM-L are slightly lower than Mix-1a and Mix-2a prior to 56 days but are similar at 56 days. The results of Mix-4-PM-L are similar to Mix-4-LM-L, as noted for the bulk resistivity test. AASHTO T 358 (2017) provides classifications for chloride ion penetration depending on surface resistivity values, as shown in Table 3.1 in Section 3.4.1. Figure 5.33 shows the chloride ion

penetration categories of the mixtures. All UHPC mixtures are in the *Very Low* category for chloride ion penetration at 56 days, whereas the category of a conventional HPC, which was developed as part of TxDOT 0-6958, *Developing Performance Specifications for High Performance Concrete*, is in the *Low* category at 56 days. The category for Mix-1a and Mix-2a at 90 days is *Negligible*. Although the 90-day data for Mix-4-PM-L are not available, the projected trend based on the 56-day data indicates this mix will be in the *Negligible* category as well. Therefore, high durability and a long service life span for both Mix-4-LM-L and Mix-4-PM-L are also expected based on surface resistivity results.

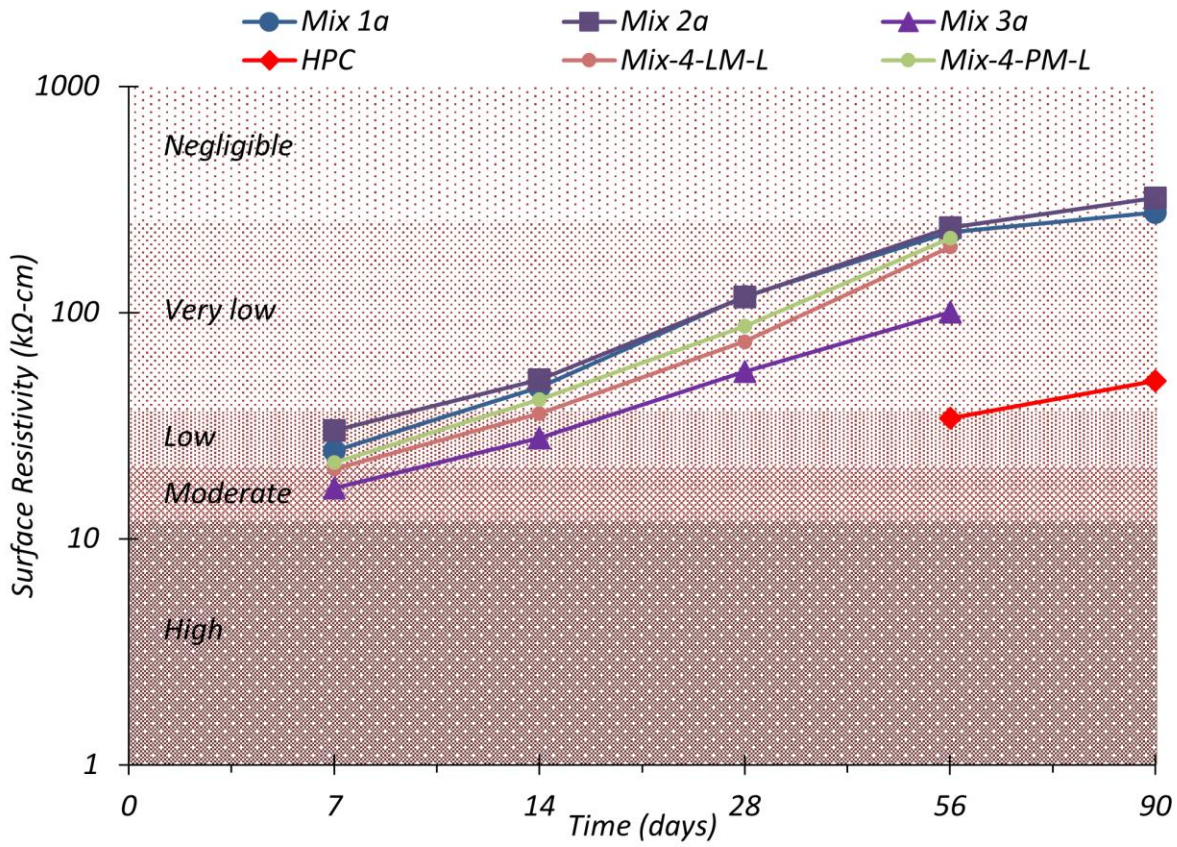

Figure 5.33. Surface Resistivity Results with Category as per ASTM C1202 (2017).

5.6.3.2 Rapid Chloride Ion Penetration

The RCPT was conducted to investigate the resistance of the developed UHPC mixtures to chloride ion penetration in accordance with ASTM C1202 (2017). Section 3.4.1 discusses the test method. The test measures a passing electrical charge through a specimen. Two specimens of 2 in. thickness with a 4 in. diameter were made by cutting a cylinder specimen used for the bulk and

surface resistivity tests at the age of 56 days. The top and bottom end surfaces were exposed to sodium hydroxide and sodium chloride, respectively. A 60 V direct current passed through the specimens for 6 hours. Figure 3.11 shows the cut specimens and RCPT test setup.

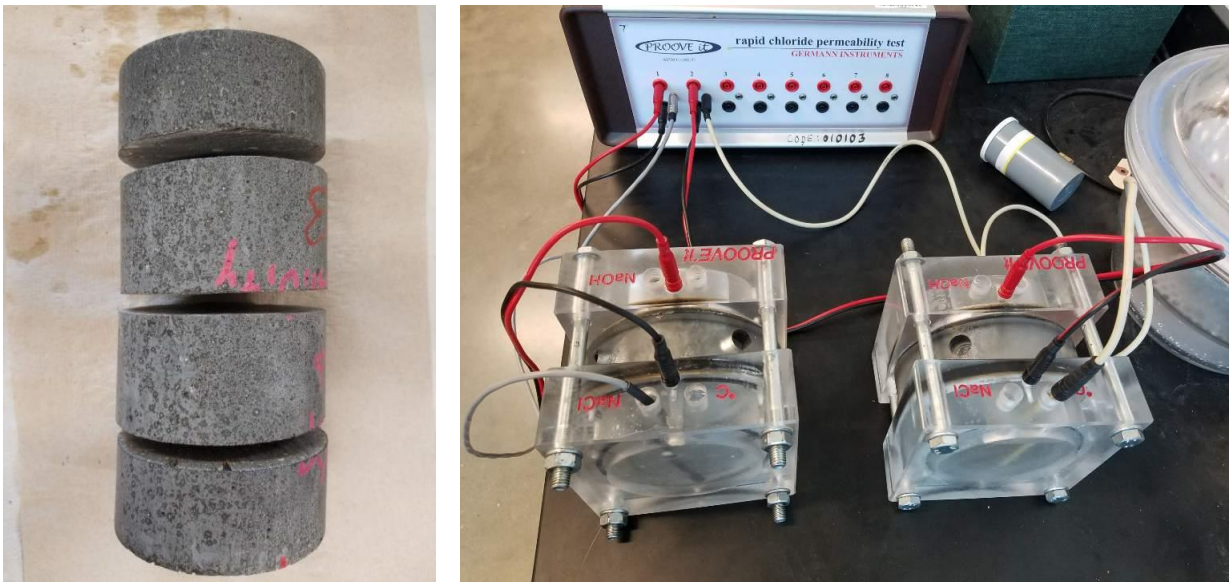

(a) Cut specimens *(b) Test setup*

Figure 5.34. Specimen Preparation and Test Setup for RCPT.

After the 6-hour test, the charge passed was measured. Table 5.35 reveals that Mix-4-PM-L is classified as *Negligible* as per ASTM C1202 (2017). Mix-4-PM-L has a lower charge passed value than Mix-1a and Mix-2a. The results indicate that the three UHPC mixtures have comparable durability in terms of chloride ion penetration. Based on the resistivity and RCPT based durability testing, Mix-4-PM-L can be considered a highly durable mix with a significantly long service life. The RCPT testing for Mix-1a and Mix-2a is further documented by Cooper (2020).

Table 5.35. RCPT Test Results.

Mixture	Charge Passed, Coulombs	Classification
Mix-1a	65.7	Negligible
Mix-2a	74.2	Negligible
Mix-4-PM-L	53.9	Negligible

Note: Charge passed less than 100 Coulombs is classified *Negligible* in accordance with ASTM C1202 (2017).

5.6.3.3 Freeze-Thaw Resistance

The freeze-thaw resistance test was used to determine the resistance of the UHPC mixture in the laboratory in accordance with ASTM C666 (2015) and modifications for UHPC by ASTM C1856

(2017). Section 3.4.3 discusses the test method. Three 3 × 3 × 11.25 in. prisms were cast at the plant with Mix-4-PM-P. The specimens were cured in 70°F at 95 percent RH for 14 days. A total of 300 freeze-thaw cycles with a 4-hour duration for each cycle were applied, which consisted of a freezing environment at 0°F for 3 hours and a thawing environment at 40°F for 1 hour. Prior to the test, the fundamental transverse frequency and weight were measured as per ASTM C215 (2019). Readings of fundamental transverse frequency and mass were performed every 30 cycles (Figure 3.13).

Figure 5.35. Fundamental Transverse Frequency Test Setup.

ASTM C666 (2015) recommends repeating the test until 300 cycles or until its RDM reaches 90 percent of the initial modulus, whichever is achieved first. Table 5.36 shows the freeze-thaw resistance test results.

Table 5.36. Freeze-Thaw Resistance Test Results.

Reading Cycle	Specimen No.	Weight, lb	Transverse Frequency, Hz	RDM	Weight Change, %
Initial Readings	1	8.9433	3462	N/A	N/A
	2	9.0319	3462	N/A	N/A
	3	8.9089	3417	N/A	N/A
Readings at 300 cycles	1	8.9477	3462	100	+0.049
	2	9.0337	3462	100	+0.020
	3	8.9128	3417	100	+0.045

N/A: Not applicable

The three UHPC specimens cast from Mix-4-PM-P showed no change in transverse frequency and little increase in mass. These test results show that Mix-4-PM-P has a high resistance to a freezing and thawing environment. Other researchers have reported the same conclusion—that no degradation was observed in the freeze-thaw test (Acker and Behloul 2004; Ahlborn et al. 2008; Graybeal 2006a).

5.6.3.4 Scaling Resistance

The scaling resistance test is used to evaluate scaling resistance of a concrete qualitatively in accordance with ASTM C672 (2012). Section 3.4.4 discusses the test method. The surface of the concrete is exposed to a deicing chemical (calcium chloride solution) in a freezing-thawing environment. Two specimens with an 81 $in.^2$ top surface area and a 1 in. high dike around the perimeter of the top surface were cast at the precast plant using Mix-4-PM-P. The specimens were exposed to a total of 50 freezing and thawing cycles. Each cycle consists of exposure to a freezing temperature (0°F) for 18 hours and a thawing temperature (73°F) for 6 hours. The calcium chloride solution was replaced at the end of every five cycles. The specimens were evaluated visually according to the rating criteria outlined in ASTM C672 (2012) (Table 3.2).

Figure 5.36 shows the surface conditions of the specimens before and after the test. The surfaces of the specimens were damaged slightly while demolding the specimens. The concrete surface of the initially damaged area was more degraded after the test. The damaged area can be categorized as Rating 1 as per Table 3.2. The scaled depth of the surface is less than 1/8 in. However, the undamaged area was affected insignificantly by the freezing and thawing temperature with the deicing chemical solution. The area on the surface of the specimens that was not damaged from demolding is evaluated as having no surface scaling (Rating 0). This result matches with the results of Graybeal (2006a), which indicated no surface scaling of proprietary UHPC after 215 cycles. Overall, Mix-4-PM-P shows high resistance to a freezing-thawing environment with or without the deicing chemical based on the results of freeze-thaw and scaling resistance tests.

(a) Specimen prior to Testing *(b) Specimen at End of Testing Program*

Figure 5.36. Scaling Resistance Test Results.

5.6.3.5 Abrasion Resistance

The surface abrasion resistance of Mix-4-PM-P was evaluated using rotating cutters in accordance with ASTM C944 (2012) and modifications for UHPC based on ASTM C1856 (2017). Section 3.4.5 discusses the test method. Three 4 × 8 in. cylinders were cast at the plant and cured in a room at 70°F and 95 percent RH for 28 days. The top and bottom surfaces from a 4 × 8 in. cylinder were prepared by cutting the cylinder specimens to the appropriate height of the specimen. The applied loading was 44-lb, as per ASTM C1856 (2017). The size of the cutter was modified to 2.375 in. diameter even though a 1.5 in. diameter is recommended by ASTM C944 (2012) because the device in the lab cannot accommodate 1.5 in. diameter cutters. The increase in the diameter will likely provide a more severe abrasion to the concrete surface. Figure 3.14 shows the test setup.

The top and bottom surfaces of the three specimens were abraded for 2 minutes each, and then debris on the surface was cleaned by blowing with air. This 2-minute abrasion was repeated five times for a total of 10 minutes for each surface. Mass loss was measured at the end of each 2-minute abrasion period. Figure 5.37 shows the abraded bottom surface for one of the specimens.

(a) Before Abrasion Test *(b) After Abrasion Test*

Figure 5.37. Abraded Bottom Surface of Mix-4-PM-P.

Figure 5.38 shows the test results of Mix-1a, Mix-2a, Mix-3a, and Mix-4-PM-P. Note that Mix-1a, Mix-2a, and Mix-3a were part of the first group of UHPC mixtures developed in the lab using Type I/II cement, and abrasion resistance testing for Mix-1a, Mix-2a, and Mix-3a was also documented by Cooper (2020). Generally, the mass loss of the top surface is greater than the bottom surface due to the uneven surface condition of the top surface of a cast cylinder. Mix-4-PM-P shows the lowest mass loss of both the top and the bottom surfaces for the considered mixtures.

Graybeal (2006a) reported that the average mass loss of the bottom surface of proprietary UHPC was 1.0 g, which is greater than the 0.65 g loss observed for Mix-4-PM-P. Graybeal used the same load, but the diameter of the specimen was 6 in. The larger diameter of the specimen may explain the greater mass loss. In addition, inclusion of relatively coarser sand particle size in Mix-4-PM-P might be a factor in the higher abrasion resistance in comparison to Graybeal's results. Even though there is a slight difference in results, a high abrasion resistance property of Mix-4-PM-P is clear.

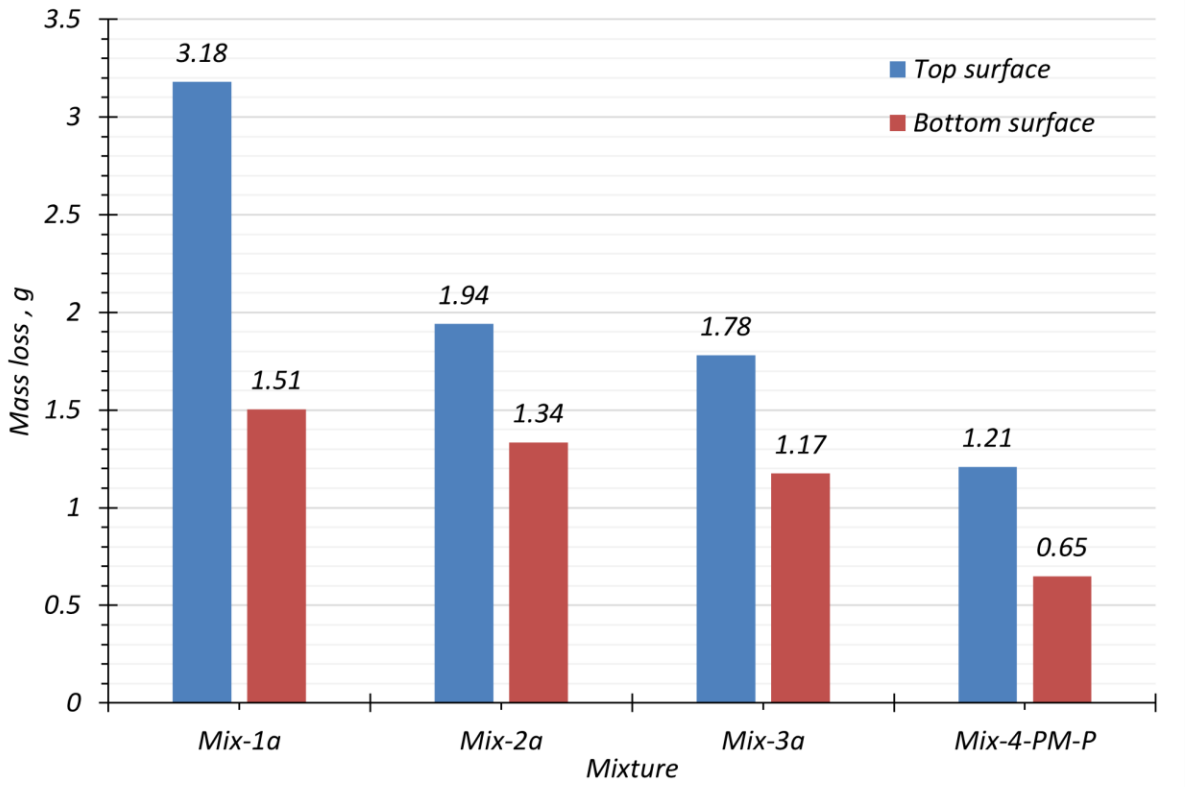

Figure 5.38. Average Mass Loss after Five 2-Minute Abrasion Periods.

5.6.3.6 Alkali Silica Reaction Resistance

The alkali silica reaction resistance of the UHPC was investigated using the ACCT method developed by Mukhopadhyay et al. (2018). Section 3.4.6 discusses the test method. The test used two types of UHPC samples for comparison purposes: (1) UHPC with a reactive sand, and (2) UHPC with the sand sourced from the precast plant in Texas. The results from the two types of the UHPC samples were compared with CC containing reactive sand to identify the level of the alkali silica reaction resistance of the UHPC. In addition, the reactivity of the two considered sands were tested in accordance with ASTM C1260 (2014), and Table 5.37 shows the test results.

Table 5.37. Sand Reactivity in Accordance with ASTM C1260 (2014).

Sand	Expansion Results, %
Reactive sand	0.381
Nonreactive sand	0.082

Notes:
1. Nonreactive sand is sourced from the precast plant in Texas.
2. Expansion of less than 0.1 percent is indicative of innocuous behavior (ASTM C1260 2014).
3. Expansion greater than 0.2 percent is indicative of potentially deleterious behavior (ASTM C1260 2014).

Figure 5.39 shows the ACCT results of the UHPC samples and the comparison of ASR resistance of UHPC and CC. The UHPC with reactive sand shows slightly higher expansion than the UHPC with nonreactive sand (see Figure 5.39[a]). However, the expansion values of the two UHPCs are extremely low (well below the 0.04 percent expansion limit) in comparison to the expansion of CC with reactive sand (Figure 5.39[b]). The possible reason for the extremely low expansion due to ASR in the UHPC is that there is no available free water in the system. Free water is needed for ASR to occur. High alkali content and sufficient water along with an adequate ionic migration are the necessary criteria to initiate ASR and make it expansive. Because cement content in UHPC is very high, it satisfies the high alkali content requirement. However, lack of free water is a characteristic of UHPC since *w*/*cm* in UHPC is very low (0.181 *w*/*cm*). The extremely dense microstructure of UHPC also minimizes ionic migration. In the ACCT method, the 3 × 6 in. UHPC specimen was immersed into a soak solution with chemistry equal to the pore solution chemistry of the tested specimen. Although the specimen remained immersed in alkaline solution during the entire testing duration, the dense microstructure did not allow penetration of water from the soak solution into the specimen. As a result, the measured ASR expansion over time by the ACCT method was found to be negligible compared to the CC with the same highly reactive fine aggregate. Since the actual mix design was tested by the ACCT method, the reliability of ACCT-based ASR evaluation is high.

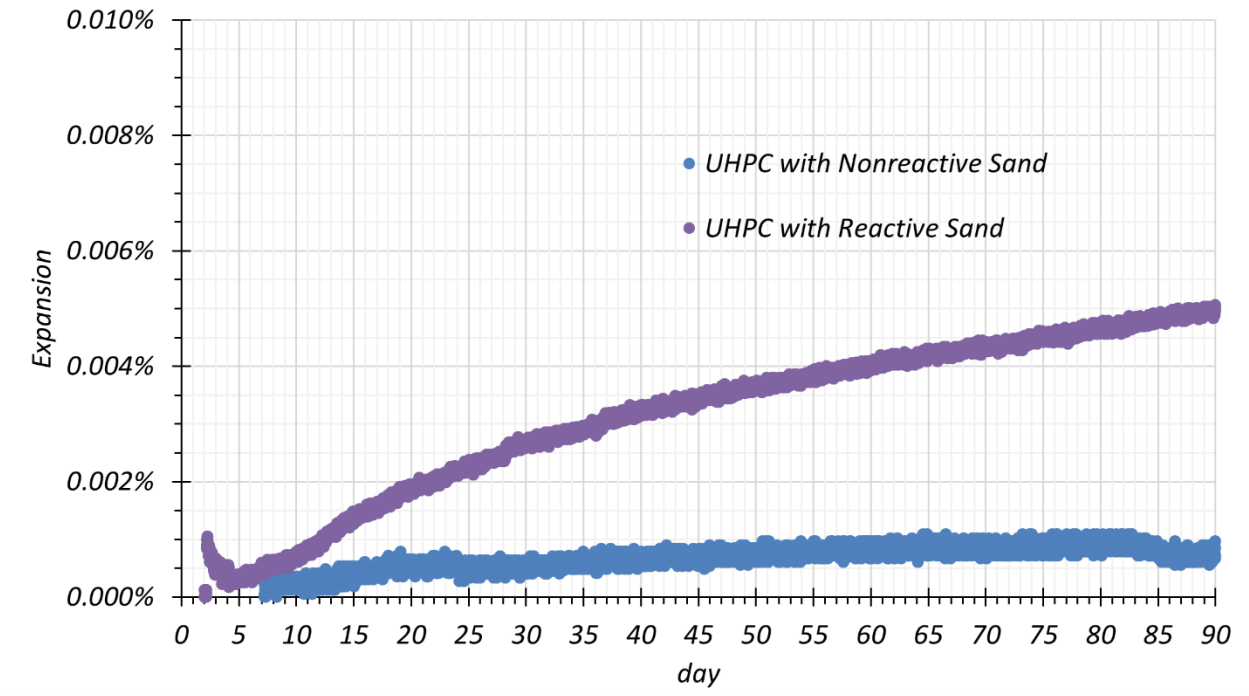

(a) UHPC

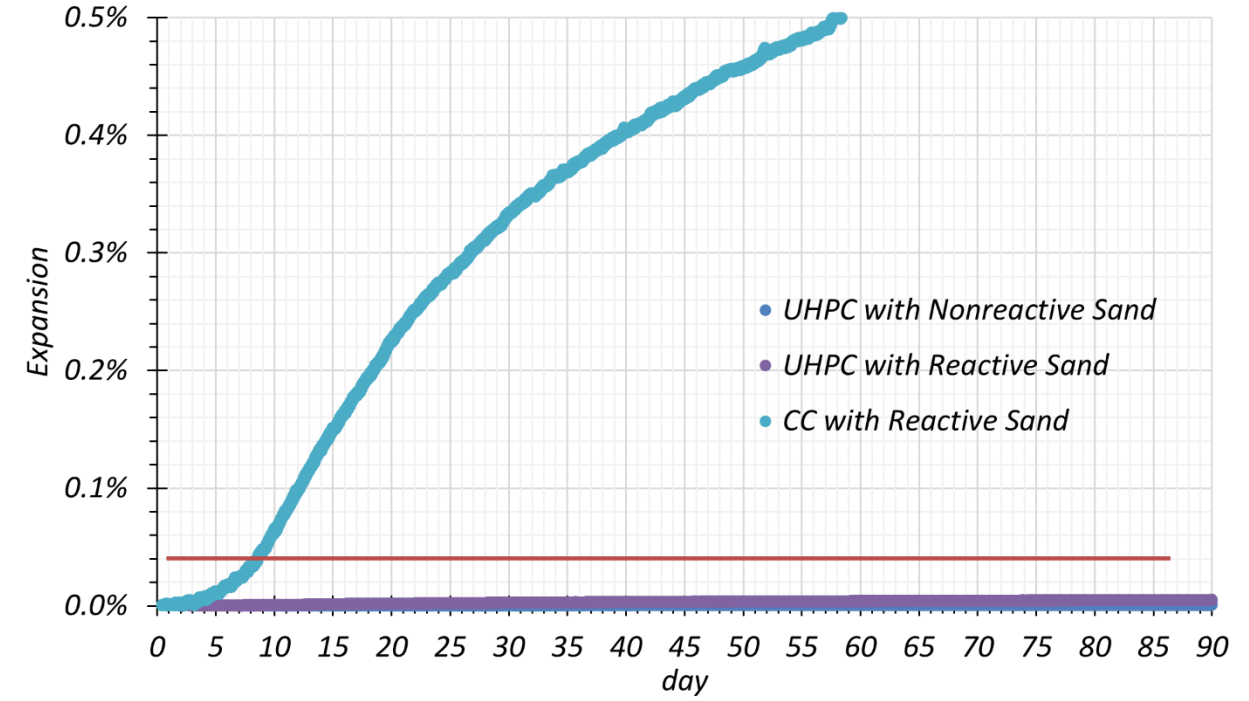

Red line: 0.04% expansion limit

(b) UHPC and CC

Figure 5.39. ACCT Results for UHPC Compared to CC.

5.6.4 Microstructure

Petrographic examination according to ASTM C856 (2020), *Standard Practice for Petrographic Examination of Hardened Concrete*, was performed to understand the microstructure of the selected UHPC mixtures. Two thin sections of Mix-4-PM-L (2 × 3 in. and 20–25 µm thickness) were prepared for 3 days and 28 days. The thin sections were investigated under a transmitted light optical microscope. Figure 5.40 shows the magnified 3-day old specimen. The blue-colored circles indicated by the red arrow are small air voids. The black-colored ellipses indicated by green arrows are a cross-sectional view of steel fibers. It shows that the fibers are randomly oriented. The shape of sand particles is subangular, which might not be beneficial for workability, whereas the perfect spherical shape of fly ash shown in Figure 5.41 gives better rheological characteristics. Figure 5.41 also shows a strong steel fiber and cement paste matrix bond.

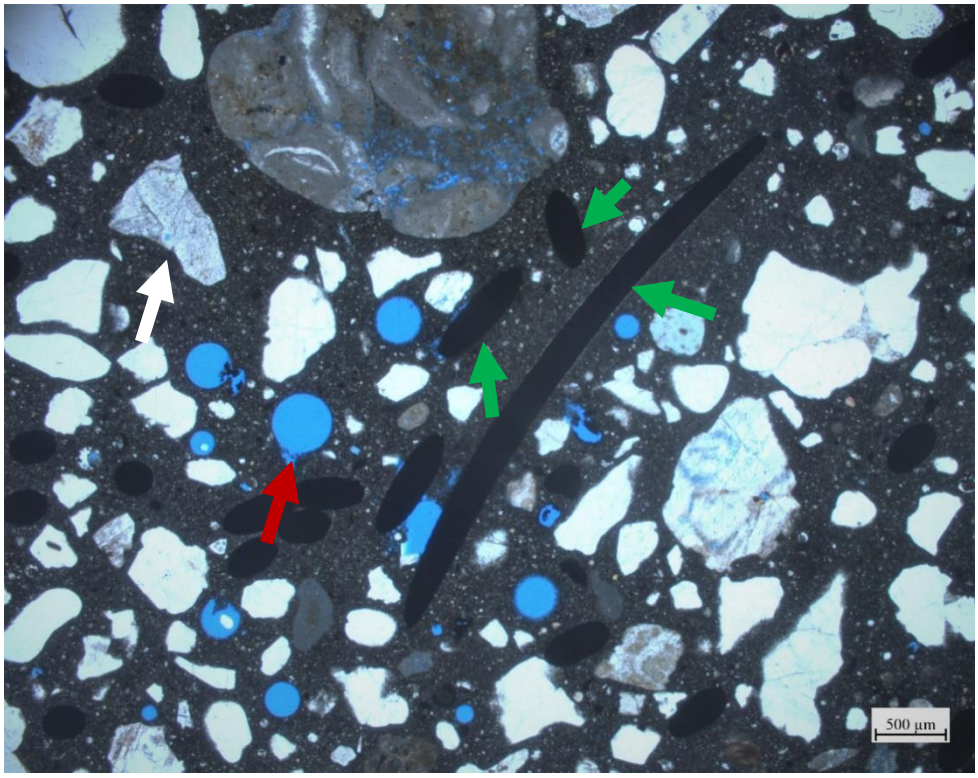

(Red arrow: air voids, Green arrow: steel fibers, White arrow: sand particles)

Figure 5.40. Microstructure of 3-Day Specimen.

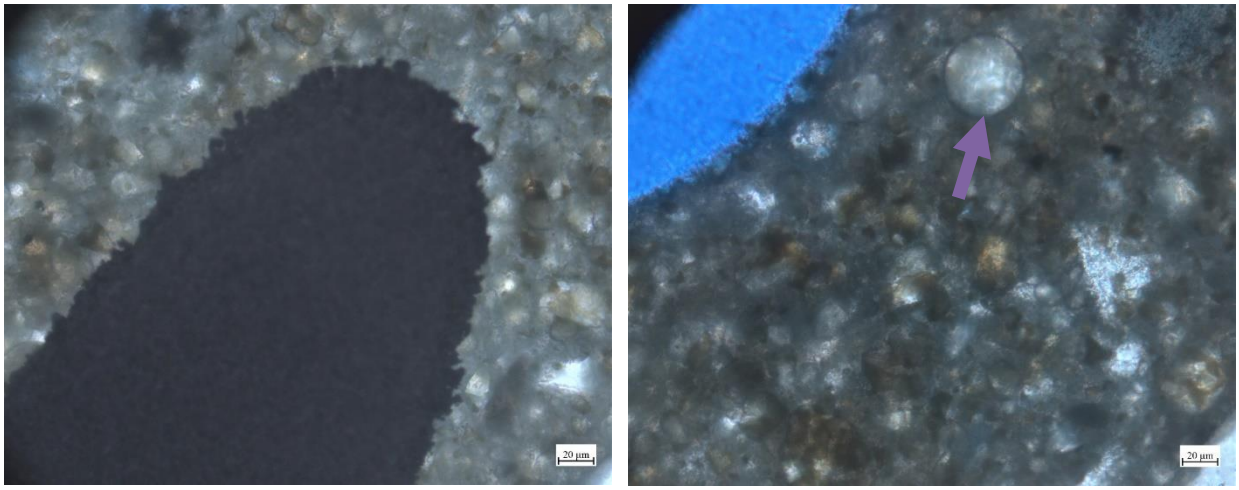

(a) Bond between Steel Fiber and Matrix *(b) Spherical Shape of Fly Ash*

(Purple arrow: fly ash)

Figure 5.41. Bond between Fiber and Matrix and Shape of Fly Ash at 3 Days.

Figure 5.42 shows the presence of unhydrated cement particles indicated by yellow arrows. Acker (2004) reported that UHPC with 0.2 *w*/*c* has 53 percent unreacted clinker. This finding can be shown visually in Figure 5.42. Unhydrated cement particles represent the remaining unhydrated portions of the cement particles (i.e., preferably the core of the cement particles) after hydration reaction from the surface. As a result, a strong bond between hydrated and unhydrated parts is expected. Unhydrated cores of cement particles act as hard inclusions strongly bonded with hydrates (Aïtcin 2016). Practically no blue dye impregnation in the cement paste matrix and along the interfacial transition zones between fiber-cement paste matrix and aggregate- cement paste matrix (Figure 5.42) indicates a highly dense microstructure of the cement paste matrix.

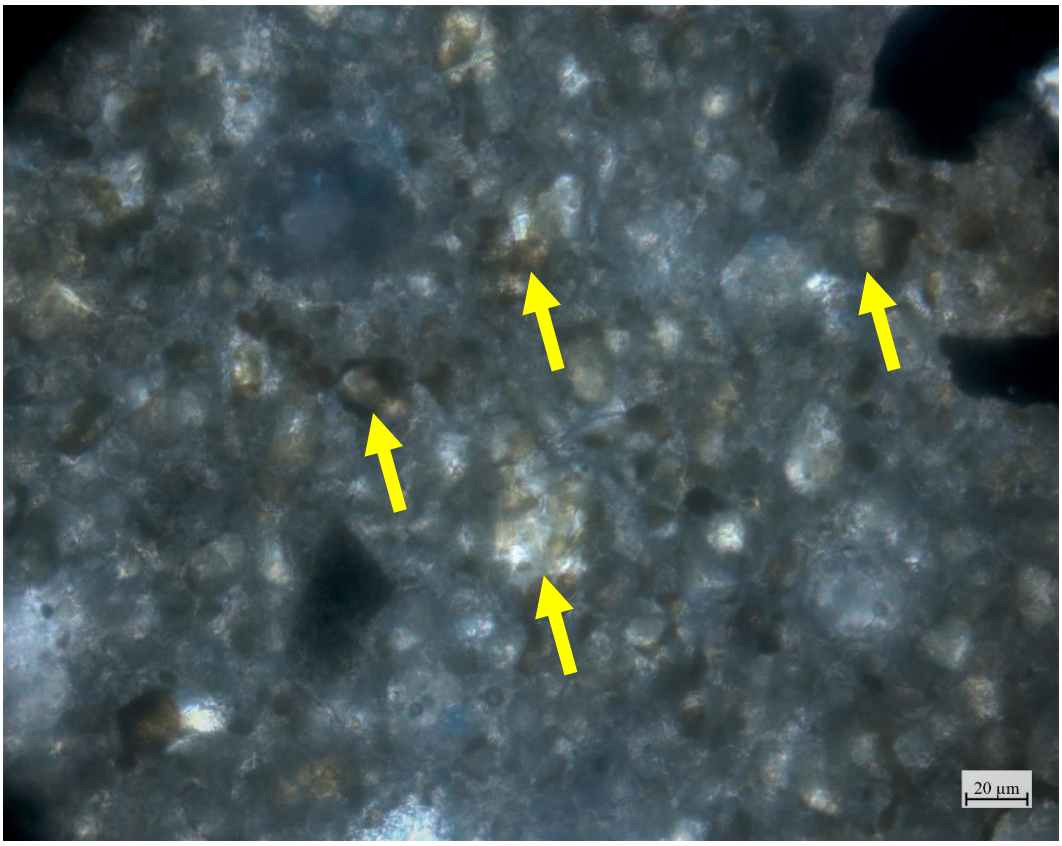

(Yellow arrow: unhydrated cement particles)

Figure 5.42. Unhydrated Cement Particles at 3 Days.

The reaction of silica fume with calcium hydroxide is expected to begin within 3 days after contacting water (Aïtcin 2016). However, agglomerates of unreacted silica fumes were observed from the 28-day aged specimen (Figure 5.43). This observation suggests that a part of the silica fume content (7.5 percent by cement weight) acts as a filler. The cost of silica fume is expensive compared to other cementitious materials. In addition, silica fume increases water demand due to its fine particle size. Therefore, the replacement of silica fume with cheaper cementitious materials might be an option to reduce the material cost and water demand. However, the replacement ratio should be determined carefully because it can cause lower durability and a shorter service life span. Finding an appropriate substitution material and ratio can be a future research topic.

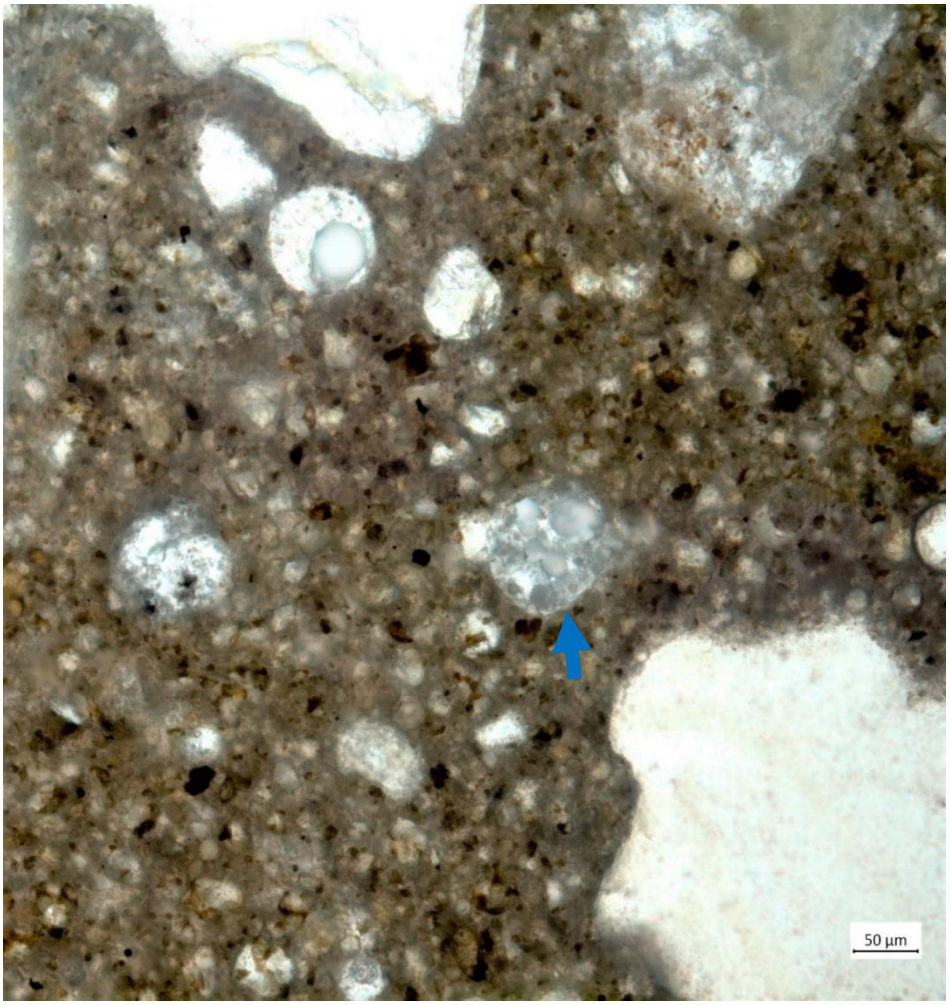

(Blue arrow: agglomerates of silica fume)

Figure 5.43. Agglomerates of Silica Fume at 28 Days.

5.7 DISCUSSION AND FINDINGS

The selected mixture, Mix-4, was optimized with the materials used at the selected precast plant in Texas.

- The HRWR, sand, and the replacement of cement have an insignificant impact on the flowability and compressive strength at 1 day and 28 days when adjusting water and HRWR contents and paste volume fraction. However, the mixing procedure was changed to accommodate the wet sand (stockpile) condition.

- The reduced water content due to moisture content in sand causes an insufficient *w*/*c* for paste mixing before the addition of sand. As a result, splitting the cement addition was adopted to keep a constant *w*/*c* during mixing.

A 2 cyd trial batch was developed at the precast plant. The following observations and adjustments were considered:

- Adjustment of water content is needed to avoid excess water addition due to the residual water in the mixer. Holding 10 percent of the water at the water addition step is considered.
- Long steel fiber addition time for the large volume extended the total mixing time. Fabrication of a screen with a vibrator was considered to shorten the time of steel fiber addition.

The fresh and hardened properties were investigated using the cast specimens at the precast plant during the trial batch:

- The flow spread at the precast plant was higher (11.5 in.) than at the lab (10.6 in.) due to the remaining water in the mixer.
- The results of unit weight and air contents were similar from both the plant and the lab.
- The highest core temperature of the UHPC block (2.0 ft × 1.6 ft × 6.0 ft) was 214°F at 13 hours after casting.
- The 1-day compressive strength (14.1 ksi at the lab, 14.3 ksi at the plant) and 28-day compressive strength (18.7 ksi at the lab and 17.9 ksi at the plant) were comparable.
- The compressive strength of the cored sample from the UHPC block was 9.5 percent higher than the cast cylinder at 65 days.
- The MOE of the specimens tested in this study was in the range of 5000–7000 ksi.
- The Poisson's ratio was in the range of 0.22–0.28.
- The behavior of specimens from all the lab mixtures and the precast plant trial batch under uniaxial tension were quite similar. Mix-4-PM-P, which is the selected mixture optimized with materials used at the precast plant and prepared in the precast plant mixer, exhibited slightly higher tensile strength than Mix-4-LM-L and Mix-4-PM-L. The average peak strength of the specimens cast from the three trials was 1.14 ksi at a strain of 581 με.

- The flexure strength for the specimens cast using precast plant materials at the lab and the plant was very similar in the post-crack region. The peak strengths varied from 1.51 ksi to 2.17 ksi.
- The results of total and autogenous shrinkages of Mix-4-PM-L are 693 με and 643 με at 668 days, respectively. The shrinkage results are slightly lower than the results of the lab mixtures (Mix-1a, Mix-2a, Mix-3a, and Mix-4a) because the larger maximum sand particle size mitigates shrinkage.

The durability test results indicate superior durability performance:

- Both bulk and surface resistivity test results of Mix-4-PM-L are in the *Very Low* category at 56 days and the RCPT results are in the *Negligible* category.
- There was no degradation from the freeze-thaw test after 300 cycles. Scaling resistance tests showed very slight scaling (*Rating 1*) after 50 cycles.
- Mix-4-PM-L has high abrasion resistance (0.65 g mass loss from the bottom).
- Alkali silica reaction of Mix-4-PM-L was not found. Alkali silica reactivity was negligible.

The microstructure of Mix-4-PM-L was studied using the transmitted light optical microscope. The photos showed unreacted cement particles that act as a hard inclusion connected fully to hydrates at the surface of the cement particles as well as to well-distributed steel fibers and agglomerates of silica fume.

6 FABRICATION OF PRECAST, PRETENSIONED UHPC BRIDGE GIRDERS AND MATERIAL-LEVEL EXPERIMENTS

6.1 INTRODUCTION

Two 50 ft long Tx34 girder specimens and a 70 ft long Tx54 girder specimen were fabricated with the developed nonproprietary UHPC mixture at the selected precast plant in Texas. The details for each girder specimen are documented in Volume 2 of this report. While casting the girders for full-scale structural testing, companion small-scale specimens were prepared to investigate material properties. This chapter describes the production of the precast, pretensioned UHPC bridge girder specimens and material-level experiments using the companion specimens. Section 6.2 discusses mixing the UHPC, transporting fresh UHPC to the casting bed, placing multiple UHPC batches, and curing for the three girders. Water content adjustment and the steel fiber addition method were updated based on the observations from the 2 cyd trial batch at the plant. Section 6.3 presents the fresh properties measured at the precast plant while fabricating the girders. Section 6.4 describes the short-term hardened properties, such as compressive strength, MOE, Poisson's ratio, uniaxial tensile strength, and flexure strength. Section 6.5 discusses the long-term hardened properties, including creep and shrinkage.

6.2 PRODUCTION OF UHPC GIRDER

6.2.1 Lessons Learned from Trial Batch at Precast Plant

The issues that were identified from the trial batch are (1) the presence of residual water after cleaning the mixer drum before starting UHPC mixing, and (2) a long duration for steel fiber addition for the large volume batch of more than 2 cyd. The residual water caused an increase in the water content of the UHPC trial batch mix, which resulted in a higher flow spread value (11.5 in.) than the target range of 10–10.5 in. and segregation of steel fibers. To avoid these issues, holding 10 percent of the water was considered. The addition of this remaining 10 percent of water was determined based on the turnover time (when paste consistency looks adequate) and/or the flow spread value. The laboratory experience showed no segregation of steel fibers when the flow spread value is lower than 11.0 in.

The second observation was the extended time for steel fiber addition. The addition of steel fibers was conducted manually during the trial batch due to the lack of an automated system for adding

the steel fibers at the plant. To reduce fiber addition time, a screen that fits with the opening size of the mixer (1 ft × 5 ft) was fabricated with a vibrator (Figure 6.1). These two key lessons learned from the trial batch led to a successful girder fabrication with multiple batches. However, some issues were experienced with the vibrator used; therefore, further adjustments were made, as described below.

Figure 6.1. Fabricated Vibrator-Equipped Screen for Steel Fiber Addition.

6.2.2 Tx34-1 Girder Fabrication

The first precast, pretensioned UHPC bridge girder with the standard Tx34 shape, labeled Tx34-1, was cast on June 11, 2021, at a precast plant in San Marcos, Texas. The girder specimen was 50 ft long with 30 straight strands. The weather conditions at the time of casting (2–4 p.m.) were 94 °F and partly cloudy. The gaged R-bars and thermocouples were installed on June 10, 2021 (Figure 6.2). The Volume 2 report provides detailed information on the girder reinforcement and instrumentation.

Figure 6.2. Tx34-1 Prestressing and Reinforcement on the Casting Bed.

6.2.2.1 Mixing and Placement

Three batches (3 cyd per batch) of UHPC (Mix-4-PM-P) were planned for the 50 ft long Tx34-1 girder. The plant twin-shaft mixer with 6 cyd capacity was used; thus, only 50 percent of the mixer capacity was used for mixing UHPC to ensure sufficient power (El-Tawil et al. 2018; Haber et al. 2018). The total moisture content of the sand (the same natural sand that the plant was using for making conventional SCC) was 6.0 percent (0.8 percent absorption capacity and 5.2 percent free water). The mixture design was adjusted according to the sand moisture content (Table 5.15). Prior to mixing, the bags of silica fume and steel fibers were loaded on the mixer platform (Figure 6.3). In addition, the residual water in the mixer drum after cleaning was removed manually, as much as practical, to avoid the issue of increased water content in the first UHPC batch.

Table 6.1. Adjusted UHPC Mixture Design for Tx34-1.

Description	Mixture Design (Oven-Dried Condition Sand)	Adjusted Mixture Design
Cement	1522	1522
Silica fume	114	114
Fly ash	158	158
Sand	1706	1815
Water	326	223
HRWR	36.6	36.6
Steel fibers	200	200
w/cm	0.181	0.181

Unit: lb/yd^3

Figure 6.3. Loading Bags of Silica Fume and Steel Fibers on the Mixer Platform.

The mixing sequence followed the targeted mixing procedure (Figure 6.5), as discussed Section 5.4.2. First, silica fume was added to the mixer manually (Figure 6.4). The main cement (69 percent of the total cement content) and fly ash were then added using the automated system in the plant. After adding dried cementitious materials, the mixer was run for 3 minutes. Table 6.2 describes the mixing sequence and time duration. For Batch 1, 90 percent of water was added, with 10 percent water held at the water addition step. Prior to adding sand, checking the time to achieve

adequate paste consistency (turnover) was added as a mandatory step. The turnover time is a key indicator for the adequacy of water added at the beginning (90 percent of the total water for the mixture design). If water content is sufficient, a turnover time should be shorter than 5.5 minutes after adding an HRWR. If not, the turnover time increases. For Batch 1, the turnover time was within 5 minutes after adding the HRWR. Therefore, the addition of tail water (10 percent of the total water for the mixture design that is held back) was not needed. The manual procedure was not adequate to completely remove the residual water inside the mixing drum. The sand and the tail cement (i.e., the remaining cement) were then added through the automated system. After adding the tail cement, the door of the mixer was opened, and the screen was installed. The vibrator attached on the screen did not give adequate assistance to vibrate the fibers into the mixer. A standard concrete vibrator was then identified as an alternative to apply vibration directly on the screen while adding the fibers from the bags. This alternative technique was found to be successful in adding steel fibers within 9 minutes. Due to the time taken to identify an alternative vibrator and conduct some trials to check its effectiveness, the steel fiber addition time increased to 18.5 minutes. As a result, the total mixing time was 38 minutes for Batch 1. The flow spread value for Batch 1 was 10.4 in. The fresh UHPC was discharged into a Tuckerbuilt (Figure 6.6) with a temperature of 91°F at discharge.

Figure 6.4. Manual Addition of Silica Fume.

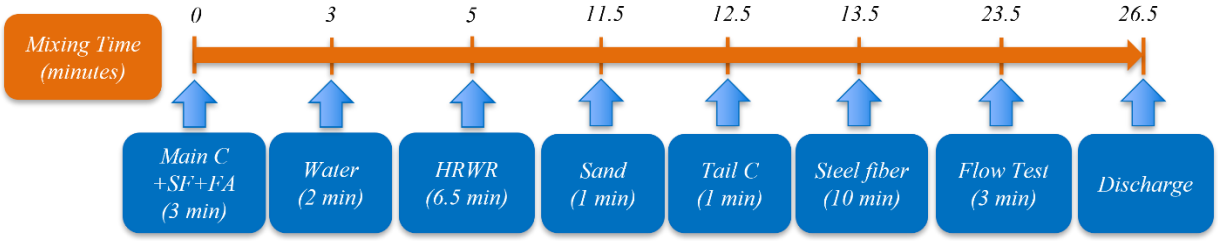

Figure 6.5. Targeted Mixing Procedure.

Figure 6.6. Fresh UHPC Discharged into a Tuckerbuilt Concrete Transporter.

Table 6.2. Targeted and Actual Mixing Sequence for Tx34-1.

Description	Targeted Mixing Sequence		Batch 1 Mixing Sequence		Batch 2 & 3 Mixing Sequence	
	Step Duration, min.	Elapsed Time, min.	Step Duration, min.	Elapsed Time, min.	Step Duration, min.	Elapsed Time, min.
SF add. (M)	0[1]	0	0[1]	0	0[1]	0
Main C add. (A)	0[1]	0	0[1]	0	0[1]	0
FA add. (A)	0[1]	0	0[1]	0	0[1]	0
Dry mixing	3	3	3	3	3	3
Water add. (A)	1	4	1	4	1	4
Mixing	1	5	1	5	1	5
HRWR add. (M)	1	6	1	6	1	6
Mixing	5.5	11.5	5.5	11.5	3	9
Sand add. (A)	1	12.5	1	12.5	1	10
Tail C add. (A)	1	13.5	1	13.5	1	11
Steel fiber add. (M)	10	23.5	18.5[2]	32	9	20
Flow test	3	26.5	3	35	3	23
Discharge	3	29.5	3	38	3	26

Notes:
1. Silica fume, main cement, and fly ash were added prior to running a mixer.
2. The vibrator did not work. Replacement of the vibrator took time.

SF: silica fume
C: cement
FA: fly ash
Add.: addition
M: manual addition
A: Automated addition

The mixing sequence of Batch 2 and 3 was the same as Batch 1 except for the turnover time and the fiber addition time. Because residual water inside the mixing drum after discharging Batch 1 and before mixing Batch 2 did not exist, 100 percent water was added for both Batch 2 and Batch 3 at the water addition step. As a result, the turnover time of Batch 2 and Batch 3 was reduced to 3 minutes after addition of the HRWR. The steel fiber addition took 9 minutes for both Batch 2 and Batch 3. As a result, the total mixing time was 26 minutes for both batches. This result was faster than the target total mixing time primarily due to the shorter fiber addition time and the maximum utilization of high-power mixing of the plant mixer with 100 percent water addition at the beginning.

Fresh UHPC was placed into a casting bed using a Tuckerbuilt concrete transporter (Figure 6.7). To prevent cold joints between the placements, the casting bed was covered between the placements (Figure 6.8). In addition, water was sprinkled on the burlap to minimize moisture loss from the placed UHPC surfaces and to avoid creating dried surfaces (referred to as “elephant skin”). The total time from the mixing to the placement and finishing of the entire girder took 1 hour and 40 minutes.

Figure 6.7. Placement of Fresh UHPC Using a Tuckerbuilt.

Figure 6.8. UHPC Covered between Placements.

6.2.2.2 Prestress Transfer

The next day, before demolding the girder, a compression test was conducted at 16 hours of the girder age using 4 in. cube specimens at the plant. The average strength was 10.5 ksi. Because the design strength is 18 ksi, a minimum of 12 ksi ($0.65f_c'$) at release was specified to minimize creep of premature concrete. Thus, a compression test was conducted once again at 21 hours, and the average strength was 12.5 ksi. Immediately after the test, prestress releasing was conducted at 21 hours (Figure 6.9). Note that the strength of the Surecure 4 × 8 in. cylinders, which were cured at the matched temperature with the girder, was greater than 15 ksi at 16 hours. The compression test machine of the precast plant was not able to break the Surecure samples due to the limited machine capacity. The Tx34-1 girder specimen was transported to the lab 13 days after casting.

Figure 6.9. Prestress Releasing (Flame Cutting Strands).

6.2.2.3 Tx34-1 Girder Surface Evaluation

Following removal of the girder forms, the surface of the Tx34-1 girder was reviewed and documented. The girder surface had observable transition lines that appeared to follow the flow between the first and second batches and between the second and third batches of the UHPC pour.

Figure 6.10 presents the surface condition of the Tx34-1 girder specimen with transition lines and surface texture. The flowability of the first batch was slightly less (10.4 in.) than the following two batches (11.3 in.), and the transition line between the first and second batch was distinctly visible. This line was purely an indicator of the transition between batches but did not cause any cold joint or interface slip between batches. Micro texture was observed at some parts of the girder along the top flange and the web. This occurrence was attributed to the minor texture of the forms at some locations or residual dust or sand in the forms prior to the placement of fresh UHPC.

Figure 6.11 presents the top surface of the girder with grooves formed using a sharp, pointed tool after casting while the UHPC was still in a plastic state. The grooves were added to increase the coefficient of friction and roughness of the surface to improve the bond between the UHPC and the cast-in-place CC deck slab. However, the grooves did not retain the intended width and depth of the ridges to create friction between the interface surface because of the self-consolidating

nature of UHPC. This surface preparation only led to increased chipping of the top surface when removing the laitance later at the laboratory. Therefore, no surface preparation was implemented on the remaining two girder specimens.

Hairline cracks were seen along the transition lines between batches, branching from the transition lines along the stirrup (R-bar) locations. The cracks may have been due to differential temperature at the stirrups and shrinkage. The density of the cracks emerging from the flow line reduced drastically in the half span without any stirrups. Figure 6.12 presents the transition lines and hairline cracks observed and mapped in the field. No noticeable defects were found from the impact of the release of strands at the girder ends. The condition of the girder end with mild steel reinforcement to mitigate splitting cracks appeared to be the same as the end without the splitting resistance reinforcement. Note that the presence of steel fibers appeared to mitigate cracking at the girder end without mild steel reinforcement.

(a) Transition Lines between Batches

(b) Surface Microtexture

Figure 6.10. Tx34-1 Surface Condition.

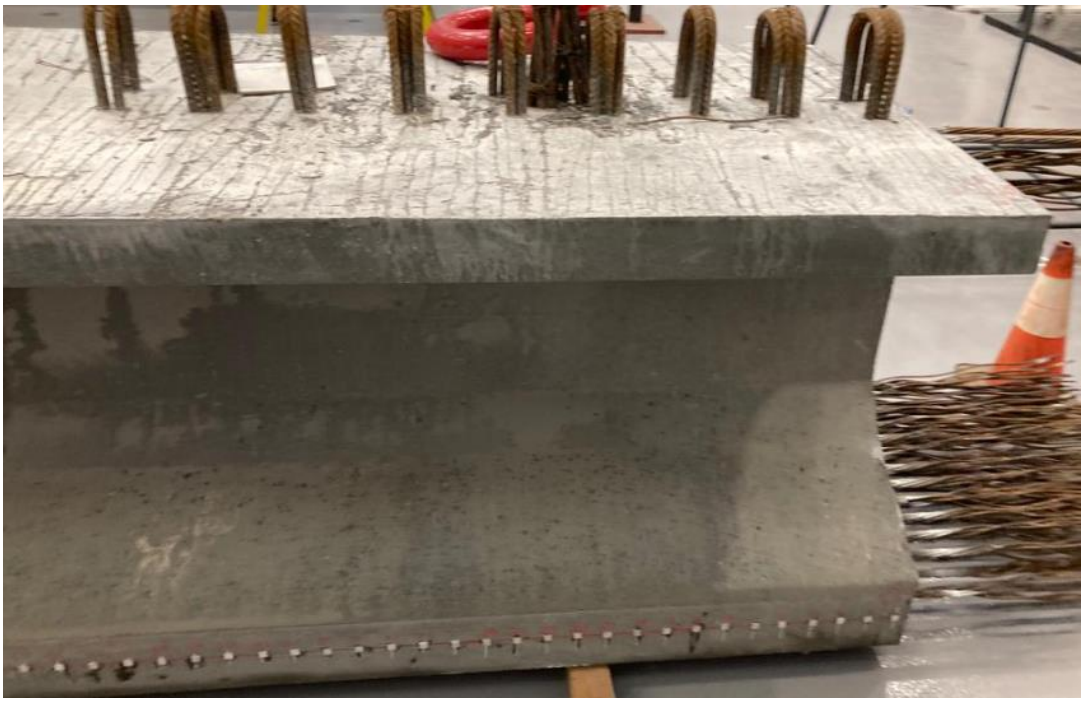

Figure 6.11. Tx34-1 Top Girder Surface Grooved for Roughness.

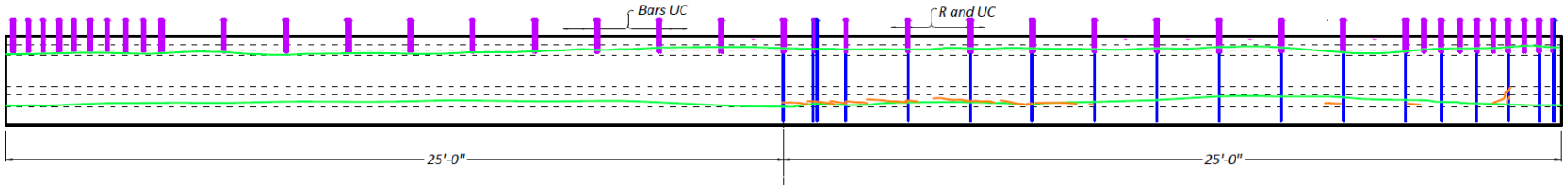

(a) North Elevation

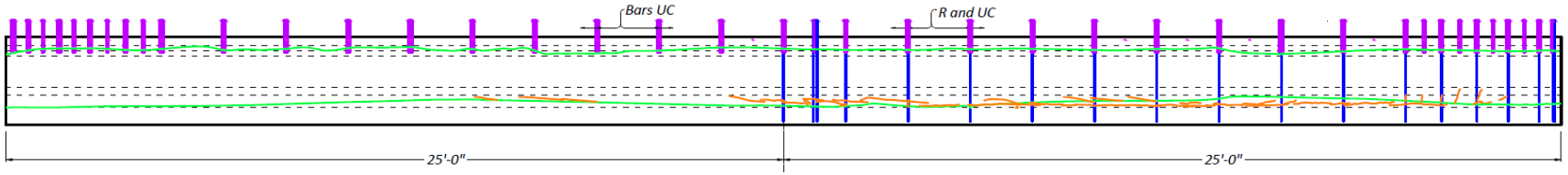

(b) South Elevation

Transition Lines between Batches Hairline Temperature and Shrinkage Cracks

Figure 6.12. Tx34-1 Transition Lines and Cracks Observed after Form Removal.

6.2.3 Tx34-2 Girder Fabrication

The second girder specimen with the standard Tx34 shape, labeled Tx34-2, was cast on August 20, 2021, at the same precast plant. The weather conditions at the time of casting were 94°F and partly cloudy. Tx34-2 has a harped strand profile (a total of 38 strands, including 6 harped strands) whereas Tx34-1 has straight strands profile. The gaged R-bars and thermocouples were installed on August 19, 2021 (Figure 6.13). The Volume 2 report provides detailed information on the girder reinforcement and instrumentation.

Figure 6.13. Tx34-2 Prestressing and Reinforcement on the Casting Bed.

6.2.3.1 Mixing and Placement

Three batches (3 cyd per batch) of UHPC (Mix-4-PM-P) were also planned for the 50 ft long Tx34-2 girder. The same 6 cyd twin-shaft mixer was used at the precast plant (50 percent of the mixer capacity was used for UHPC mixing). The total sand moisture content was 4.5 percent (0.8 percent absorption capacity and 3.7 percent free water). Table 6.3 shows the adjusted mixture design according to the sand moisture content. The mixing preparation and sequence were the same as for

Tx34-1. The bags of silica fume and steel fibers were loaded on the mixer platform prior to mixing, and the residual water in the mixer was removed manually, as much as was practical.

Table 6.3. Adjusted Mixture Design for Tx34-2.

Description	Mixture Design (Oven-Dried Condition Sand)	Adjusted Mixture Design
Cement	1522	1522
Silica fume	114	114
Fly ash	158	158
Sand	1706	1787
Water	326	249
HRWR	36.6	36.6
Steel fibers	200	200
w/cm	0.181	0.181

Unit: lb/yd^3

Table 6.4 describes the mixing sequence and the time duration. For Batch 1, 90 percent water was added, and 10 percent water was held at the water addition step. The turnover time for Batch 1 was observed to be 3.5 minutes after adding the HRWR. The sand and the tail cement (24 percent of the total cement) were added as per the planned mixing sequence. After adding the tail cement, the screen was installed over the mixer opening, and the fibers were added (Figure 6.14). The screen with a typical concrete vibrator worked well. As a result, the steel fiber addition time was 11 minutes for Batch 1. The flow spread value was 9.5 in., which is 1 in. lower than the target value (10.5 in.). Thus, the remaining 9 percent water was added and mixed for an additional 2 minutes, followed by the conducting of a second flow table test. Since an adequate flow (10.4 in.) was achieved from the second flow test, the fresh UHPC mix was allowed to discharge. Because of the additional time needed to adjust the mix for adequate flow, the total mixing time was 33.5 minutes for Batch 1. The temperature of the fresh UHPC at discharge was 96°F.

Table 6.4. Targeted and Actual Mixing Sequence for Tx34-2.

Description	Targeted Mixing Sequence		Batch 1 Mixing Sequence		Batch 2 and 3 Mixing Sequence	
	Step Duration, min.	Elapsed Time, min.	Step Duration, min.	Elapsed Time, min.	Step Duration, min.	Elapsed Time, min.
SF add. (M)	0[1]	0	0[1]	0	0[1]	0
Main C add. (A)	0[1]	0	0[1]	0	0[1]	0
FA add. (A)	0[1]	0	0[1]	0	0[1]	0
Dry mixing	3	3	3	3	3	3
Water add. (A)	1	4	1	4	1	4
Mixing	1	5	1	5	1	5
HRWR add. (M)	1	6	1	6	1	6
Mixing	5.5	11.5	3.5	9.5	3	9
Sand add. (A)	1	12.5	1	10.5	1	10
Tail C add. (A)	1	13.5	1	11.5	1	11
Steel fiber add. (M)	10	23.5	11	22.5	8 for B2 7.5 for B3	19 for B2 18.5 for B3
Flow test	3	26.5	3	25.5	3	22 for B2 21.5 for B3
Tail W add. (A)	N/A	N/A	2	27.5	N/A	N/A
2nd Flow test	N/A	N/A	3	30.5	N/A	N/A
Discharge	3	29.5	3	33.5	3	25 for B2 24.5 for B3

Notes:
1. Silica fume, main cement, and fly ash were added prior to running the mixer.
SF: silica fume
C: cement
FA: fly ash
Add.: addition
M: manual addition
A: Automated addition
N/A: Not applicable
B2: Batch 2
B3: Batch 3

Figure 6.14. Manual Addition of Steel Fibers Using Screen and Concrete Vibrator.

For Batch 2, 100 percent water was added at the water addition step, and the turnover time was 3 minutes after addition of the HRWR. The steel fiber addition took 8 minutes. The total mixing time was 25 minutes, with 10.3 in flow spread and a temperature of 103°F for the fresh UHPC at discharge. Even though Batch 2 had a relatively short turnover time (3 minutes), its flow spread value was 10.3 in., with 100 percent water at the water addition step. This outcome might have been due to the high temperature of the fresh UHPC. The temperature of the materials, such as cement, fly ash, and stockpile sand, may have increased from Batch 1 to Batch 2 because of increasing ambient temperature. Note that the water chilling system was unavailable due to maintenance at the plant. For Batch 3, 102 percent water was added at the water addition step to compensate for the high temperature of the fresh UHPC and achieve adequate flowability. The turnover time, the fiber addition time, and the total mixing time were 3.0, 7.5, and 24.5 minutes, respectively. The flow spread was improved to 10.5 in. and the temperature at discharge was 102°F.

The same practices used with the first girder were used for the placement of Tx34-2. A Tuckerbuilt truck was used to transport and place fresh UHPC into the casting bed, the casting bed was covered with burlap cloth between the placements, and the burlap was sprinkled with water (Figure 6.15). The total time from initiating mixing to the final placement took 1 hour and 35 minutes.

6.2.3.2 Prestressing Transfer

A compression test was conducted at 19 hours using 4 in. cube specimens at the plant. The compression test device was not able to break the 4 in. cube due to its limited capacity. However, the compressive strength at the maximum loading of the test was determined to be greater than 12 ksi. Because the strength was greater than 12 ksi ($0.65f_c'$), prestressing transfer was conducted by flame-cutting at 19 hours. Ten days after casting, the Tx34-2 girder specimen was transported to the laboratory.

Figure 6.15. UHPC Covered after Casting.

6.2.3.3 Tx34-2 Girder Surface Evaluation

Following removal of the girder forms, the surface of the Tx34-2 girder was reviewed and documented. Similar to Tx34-1, transition lines could be identified between the first and second batches and between the second and third batches of the UHPC pour. The transition lines were less distinct than the transition lines observed between the batches for Tx34-1. The transition from one batch to another could be felt when touching the girder surface of Tx34-1; however, for Tx34-2, this transition was not observed. The flow spread value for the Tx34-2 batches were more consistent throughout the girder batches (10.4, 10.3, and 10.5 in. for Batch 1, 2, and 3, respectively). The time interval between the batches was also shorter. These two reasons may have

also resulted in smoother transition lines. No cracks were visible along the transition lines for the second specimen before and after prestressing release.

Figure 6.16 presents the surface condition of the Tx34-2 girder specimen and shows the transition lines between batches. The uneven surface texture of the girder, particularly in the top surface of the bottom flange, can also be observed.

Figure 6.17 shows the top surface of Tx34-2 without any surface treatment. This approach did lead to some roughness so that the surface was not completely smooth. Figure 6.18 documents the transition lines between batches for Tx34-2.

Counterweights were placed at the hold-down locations prior to the release of prestressing strands. A few hairline cracks were observed at the top flange of the Tx34-2 girder specimen, near the hold-down points. These cracks were noted to have closed shut after the release of prestressing strands. The girder ends were checked for any defects due to the impact from the release of strands, and the ends with and without splitting resistance reinforcement were intact and without any defects.

(a) Transition Lines between Batches

(b) Surface Microtexture

Figure 6.16. Tx34-2 Surface Condition.

Figure 6.17. Tx34-2 Top Girder Surface without Any Surface Preparation.

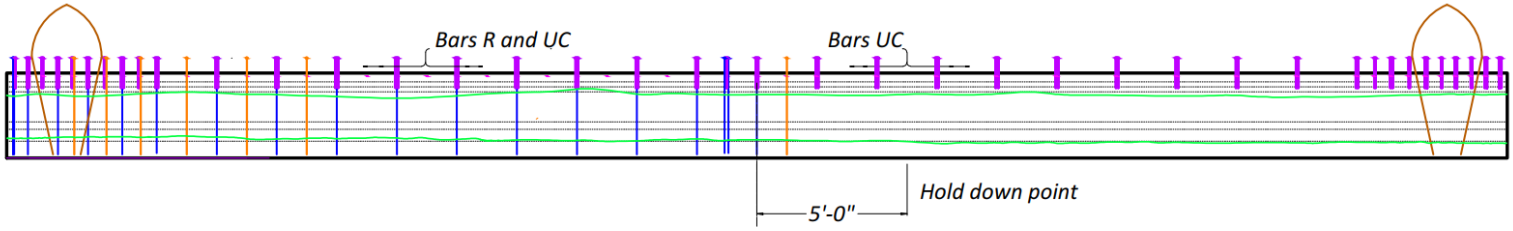

(a) North Elevation

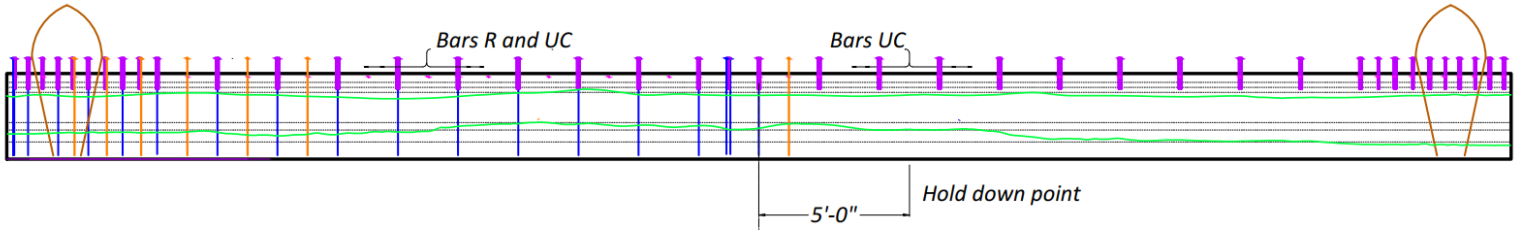

(b) South Elevation

Transition Line between Batches

Figure 6.18. Tx34-2 Transition Lines Observed after Form Removal.

6.2.4 Tx54 Girder Fabrication

The third girder, made in the standard Tx54 shape and labeled Tx54, was cast on April 8, 2022, at the same precast plant. The weather conditions were sunny and windy with a temperature of 80°F. Because Tx34-2, with a harped strand profile, showed improved structural behavior during the full-scale testing at the lab (see Volume 2 report), the harped strand profile (a total of 48 strands, including eight harped strands) was also applied to the Tx54 girder specimen. The reinforcement, gaged R-bars (hoops), and thermocouples were installed a day before casting (Figure 6.19).

Figure 6.19. Tx54 Prestressing and Reinforcement on the Casting Bed.

6.2.4.1 Mixing and Placement

Five batches (3.1 cyd per batch) of UHPC (Mix-4-PM-P) were planned for the 70 ft long Tx54 girder. The same twin-shaft plant mixer, with utilization of 52 percent of the total mixer capacity of 6 cyd, was used for UHPC mixing. The total sand moisture content was 5.1 percent (0.8 percent absorption capacity and 4.3 percent free water). Table 6.5 shows the adjusted mixture design

according to the moisture content. The mixing preparation and sequence were the same as for the previous two girders. The bags of silica fume and steel fibers were loaded on the mixer platform prior to mixing. The residual water inside the mixing drum was removed manually (Figure 6.20).

Table 6.5. Adjusted Mixture Design for Tx54.

Description	Mixture Design (Oven-Dried Condition Sand)	Adjusted Mixture Design
Cement	1522	1522
Silica fume	114	114
Fly ash	158	158
Sand	1706	1798
Water	326	239
HRWR	36.6	36.6
Steel fibers	200	200
w/cm	0.181	0.181

Unit: lb/yd^3

Figure 6.20. Removal of Residual Water Using Dry Sand inside the Mixing Drum.

Table 6.6 presents the mixing sequence and time of mixing for all the batches. Table 6.7 presents the amount and sequence of water (main and tail) addition, turnover times, and flow spread values for all the batches. For Batch 1, 90 percent water added at the water addition step with 10 percent

water held (Table 6.7). The turnover time of Batch 1 was observed to be 3.5 minutes after adding the HRWR. The manual addition of steel fibers took 9.5 minutes (Figure 6.21). All mixing sequences were smooth and fast in comparison to the previous two girders. However, the flow spread value for Batch 1 was 9.8 in. This lower spread value might be due to additional drying of the sampled fresh UHPC for the flow test caused by the high wind speed (12 miles per hour) on the day of casting. Even though the flow spread value was slightly low, Batch 1 was discharged because the turnover time was short (3.5 minutes). The temperature of the fresh UHPC at discharge was 86°F.

Figure 6.21. Manual Addition of Steel Fibers for Tx54.

For Batch 2, 93.5 percent water was added at the water addition step to increase flow relative to Batch 1. However, the flow spread value was the same (9.8 in.). Thus, an additional 2.2 percent tail water was added and mixed for 2 minutes. The second flow spread value was increased to 10.3 in. For Batch 3, 103.3 percent water was added at the water addition step to improve flowability in consideration of the weather conditions (windy). However, the flow spread value was 9.3 in.

Thus, 3.2 percent additional water was added as tail water and mixed for an additional 2 minutes. The second flow spread value was 9.8 in. For Batch 4 and Batch 5, 106.5 percent water was added at the water addition step. The flow test results were 10.1 in. and 10.0 in. for Batch 4 and Batch 5, respectively. The time for steel fiber addition was 7.5 minutes for all the Batches except Batch 1. The temperatures at discharge were 89°F, 84°F, 92°F, and 92°F for Batches 2, 3, 4, and 5, respectively.

Table 6.6. Targeted and Actual Mixing Sequence with Time of Mixing for Tx54.

Description	Targeted Mixing Sequence and Time		Actual Mixing Sequence and Time	
	Step Duration, min.	Elapsed Time, min.	Step Duration, min.	Elapsed Time, min.
Manual addition of silica fume	0[1]	0	0[1]	0
Add main cement	0[1]	0	0[1]	0
Add fly ash	0[1]	0	0[1]	0
Dry mixing	3.0	3.0	3.0	3.0
Add total designed water or main water	1.0	4.0	1.0	4.0
Mixing	1.0	5.0	1.0	5.0
Manual addition of HRWR	1.0	6.0	1.0	6.0
Mixing	5.5	11.5	3.5 (B1), 2.5 (B2), 2.0 (B3, B4, B5)	9.5 (B1), 8.5 (B2), 8.0 (B3, B4, B5)
Add sand	1.0	12.5	1.0	10.5 (B1), 9.5 (B2), 9.0 (B3, B4, B5)
Add tail cement	1.0	13.5	1.0	11.5 (B1), 10.5 (B2), 10.0 (B3, B4, B5)
Manual addition of steel fiber	10.0	23.5	9.5 (B1), 7.5 (B2), 7.5 (B3, B4, B5)	21.0 (B1), 18.0 (B2), 17.5 (B3, B4, B5)
Flow test (first time)	3.0	26.5	3.0	24.0 (B1), 21.0 (B2), 20.5 (B3, B4, B5)
Add tail water (whenever needed)	N/A	N/A	2.0 (B2, B3)	23.0 (B2), 22.5 (B3)
Flow test (second time, whenever needed)	N/A	N/A	3.0 (B2, B3)	26.0 (B2), 25.5 (B3)
Discharge	3.0	29.5	3.0	27.0 (B1), 29.0 (B2), 28.5 (B3), 23.5 (B4, B5)

Notes:

1. Silica fume, main cement, and fly ash were added prior to running the mixer.
2. N/A: Not applicable
3. Batch number in parentheses

Table 6.7. Turnover Time and Flow Spread as a Function of Amount and Sequence of Water (Main and Tail) Addition for Tx54 Batches.

Batch ID	Total Water Content (Main Water + Tail Water), %	Water Addition	Turnover Time after Adding HRWR, min.	Flow Spread, in. (First/Second Flow), in.
B1	90.0	Main water	3.5	9.8
B2	95.7 (93.5 + 2.2)	Main and tail water	2.5	9.8 / 10.3
B3	106.5 (103.3 + 3.2)	Main and tail water	2.0	9.3 / 9.8
B4	106.5	Main water	2.0	10.1
B5	106.5	Main water	2.0	10.0

The same transportation (i.e., use of Tuckerbuilt), placement, and after-placement (i.e., applying a burlap cover between placements with sprinkling water) practices used with Tx34 girders were used for the Tx54 girder. The total time for mixing five UHPC batches and placement to construct the Tx54 girder was 2 hours and 45 minutes.

6.2.4.2 Prestressing Transfer

A compression test was conducted using the Surecure samples at 16 hours. The average strength was 14.8 ksi. Thus, the prestressing transfer was conducted at 19 hours. The Tx54 girder specimen was transported to the laboratory at the age of 10 days.

6.2.4.3 Tx54 Girder Surface Evaluation

Following removal of the girder forms, the surface of the Tx54 girder was reviewed and documented. The girder surface was found to be similar to that of Tx34-2. A few hairline cracks observed at the top flange near the hold-down points were noted to close after the release of the prestressing strands. The transition lines between the batches were visible, but less noticeable when the surface was touched than with the Tx34-1 specimen and more similar to the Tx34-2 specimen. This result is possibly due to the revised placement practice used for Tx54, which was to pour the fresh UHPC on top of the previous placement from one location rather than moving along the girder form. This increased the energy of the flow and led to breaking away any elephant skin that formed on the surface between batches.

Figure 6.22 shows the transition lines and the counterweights loaded on the beam during the release of strands. The surface texture of Tx54 was more pronounced than any of the other girder

specimens. This effect was attributed to the residual concrete on the forms and differences in the form preparation. Figure 6.23(a) and (b) present transition lines at the east end and diagonal cracks at the east end in the top flange. Figure 6.24 presents the surface texture of Tx54.

Figure 6.22. Transition Lines of Tx54.

(a) Lower Transition Line at East End

(b) Diagonal Cracks at Junction of Top Flange and Web (3.5 ft to 6.5 ft from East End)

Figure 6.23. Transition Line and Diagonal Cracks of Tx54.

Due to a shortage of UHPC in the final batch, likely attributable to the lower flow that led to more sticking of the UHPC to the mixer and Tuckerbuilts, a small volume of SCC was placed primarily on the half span without any transverse stirrups to ensure the form was completely full. This SCC layer in the top flange is also observable in Figure 6.24. This unintended topping of the top flange

with SCC formed a rough surface that may provide a better interface for composite action between the UHPC girder and the CIP deck slab. The Volume 2 report provides more information about the composite action.

Figure 6.24. Surface Texture of Tx54.

Figure 6.25(a) highlights slight peeling of some of the UHPC at the top flange. Figure 6.25(b) shows the surface texture on the web, and a 0.0015 in. crack was observed in the patch.

(a) Peeling of UHPC after Removal of Forms at Top Flange

(b) Surface Texture in the Web

Figure 6.25. Tx54 Surface Condition Photos.

Figure 6.26(a) and (b) present the SCC topping of the UHPC top flange and the surface texture of the UHPC at the ends.

(a) SCC Topping at Top Flange at End without Stirrups

(b) SCC Topping in Top Flange and Surface Texture of UHPC Girder

Figure 6.26. Tx54 Surface Condition Photos.

The other surface textures were more carefully examined in the lab for crack widths. Figure 6.27 shows a crack opening of 0.10 in. observed at the south end of the girder at the transition line in the top flange. Figure 6.28 presents the transition lines on the Tx54 girder.

Figure 6.27. Crack Opening at Transition Line Tx54.

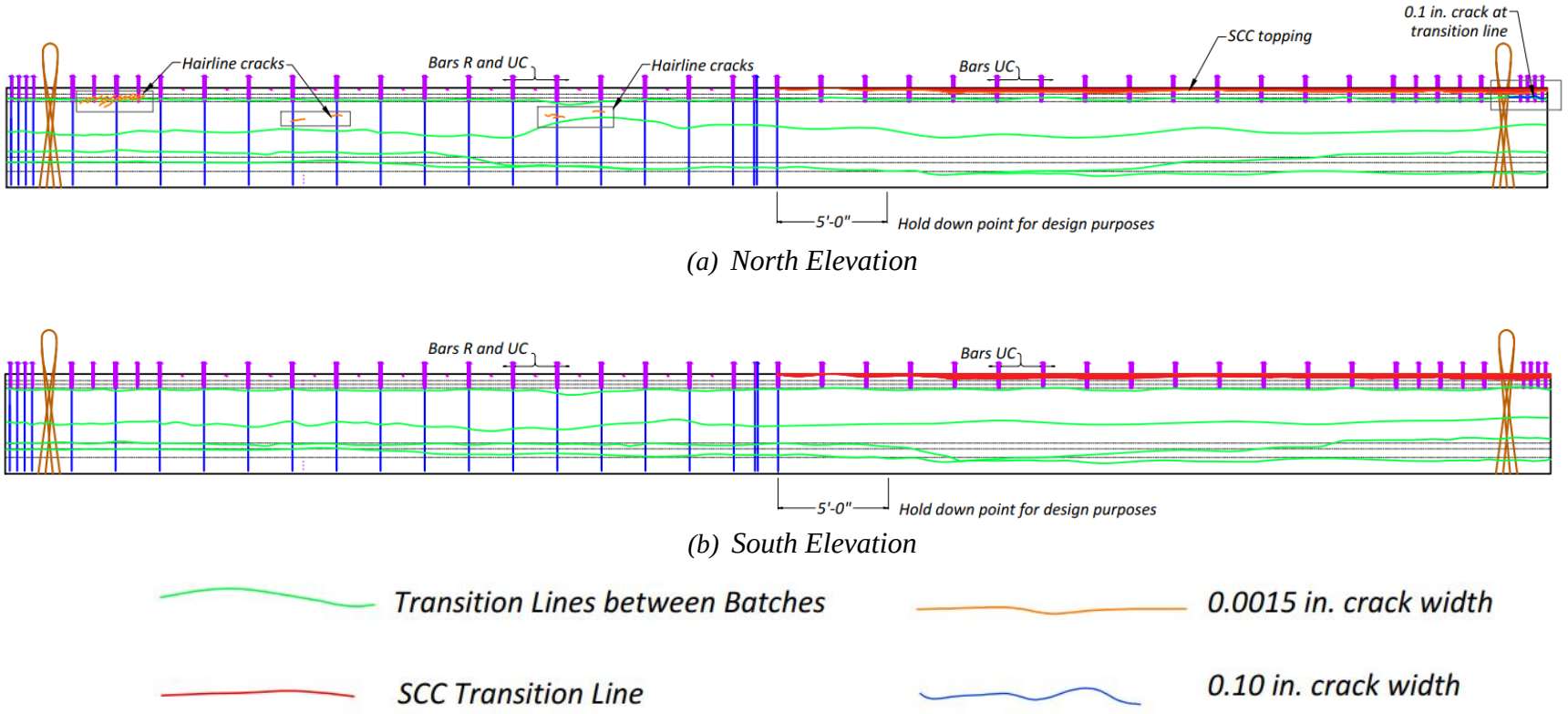

Figure 6.28. Tx54 Transition Lines and Cracks Observed after Form Removal.

6.3 FRESH PROPERTIES

This section describes fresh properties of the UHPC mixture produced at the precast plant for the girder specimen fabrication and provides a comparison with laboratory test results. Section 6.3.1 discusses flow spread values and temperatures at the discharge of each batch. Section 6.3.2 describes density and air content of the fresh UHPC. Thermocouples were installed at different depths over the girder height. Section 6.3.3 describes the temperature development at different depths of the girders at early ages.

6.3.1 Flow Spread and Temperature at Discharge

The targeted flow spread value of the selected mixture is 9–11 in. in the laboratory. For girder fabrication at the plant, however, the preferred range of 10.0–10.5 in. flow spread is more ideal when considering outside windy conditions, multiple batches, an extended time to placement when specifying the minimum value (10.0 in.), and less segregation of steel fibers for specifying the maximum value (10.5 in.). Even though the ideal range of flow spread is 10.0–10.5 in., an acceptable flow spread range for UHPC production at a precast plant can be 9.5–11.0 in. because there are no performance and workability issues from UHPC within this range. However, lower than 9.5 in. or greater than 11.0 in. may increase the risk of forming elephant skin (when a flow is lower than 9.5 in.) or of fiber segregation (when a flow is higher than 11.0 in.), respectively. As per the observations, Table 6.8 shows the recommendation for flow spread with a color code system. Section 8.4.2 discusses the impact of flow spread value on fiber segregation. The flow table test in accordance with ASTM C1437 (2015) was conducted on the mixer platform at the precast plant. Table 6.9 and Figure 6.29 show the flow spread results of each batch for the three girders.

Table 6.8. Recommended Flow Spread Range.

Flow Spread Range, in.	Color Code	Description	Comments
Flow < 9.5	Red	Unacceptable	• Poor workability • Higher risk of elephant skin formation
9.5 ≤ Flow < 10.0	Orange	Acceptable	• Relatively low workability • Some risk of elephant skin formation
10.0 ≤ Flow < 10.5	Green	Desirable	• Good workability • Lower risk of fiber segregation
10.5 ≤ Flow ≤ 11.0	Yellow	Acceptable	• Some risk of fiber segregation • More acceptable than flows below 10.0 in.
Flow > 11.0	Red	Unacceptable	• Higher risk of fiber segregation

Table 6.9. Flow Spread at Discharge.

Batch No.	Tx34-1, in.	Tx34-2, in.	Tx54, in.
B1	10.4	10.4	9.8
B2	11.3	10.3	10.3
B3	11.3	10.5	9.8
B4	-	-	10.1
B5	-	-	10.0

- : Not available

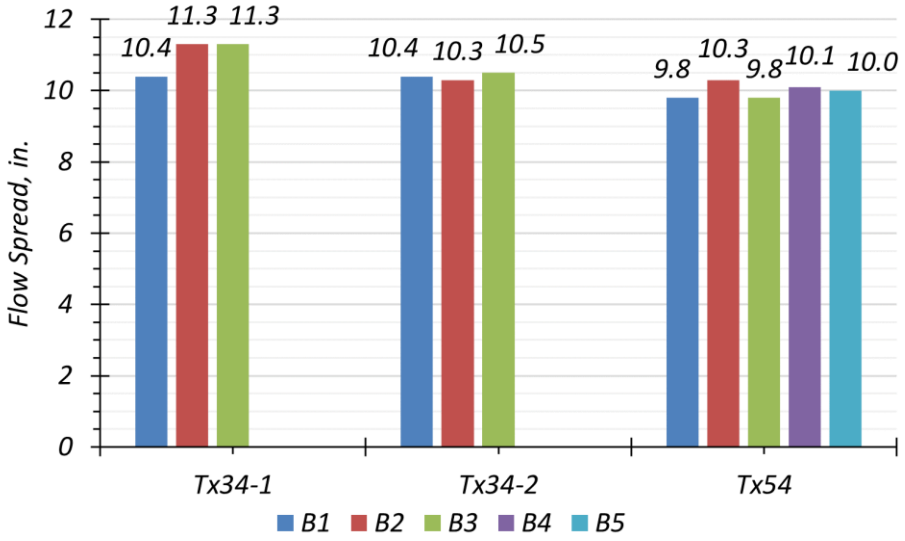

Figure 6.29. Flow Spread at Discharge.

The range of flow spread values at discharge is 10.4–11.3, 10.3–10.5, and 9.8–10.3 in. for Tx34-1, Tx34-2, and Tx54, respectively. Batch 2 and Batch 3 of Tx34-1 showed relatively high flow spread values (11.3 in.). A flow spread value greater than 11.0 in. may cause segregation of steel

fibers. As a result, the tensile strength of Tx34-1 from the companion specimens for uniaxial tensile testing showed a lower peak tensile strength (0.45 ksi) than Tx34-2 (0.67 ksi) and Tx54 (0.92 ksi), as shown in Table 6.23, and a relatively lower shear capacity was observed during the full-scale testing of Tx34-1 when compared to the other two girders (see Volume 2 report). The flow spread values of Tx34-2 batches showed good consistency. The spread of 10.3–10.5 in. was found to be an ideal spread range to ensure good flow during placement as well as avoid steel fiber segregation. Tx54 batches showed relatively low flow spread values compared to the batches for the Tx34 girders. The possible reasons that may have caused the low spread values are (1) windy and low RH ambient conditions during flow measurements, and (2) variability of sand moisture content. If the moisture content in sand is overestimated, the adjusted water content is not sufficient. For example, if the actual moisture content in sand is 1.0 percent lower than the measured moisture content in sand (5.1 percent for Tx54), an additional 10.4 percent of the adjusted water content is needed to ensure the designed water content. In other words, 10.4 percent of the adjusted water content is short for the designed water content. This water shortage in the UHPC may have occurred in B3 to B5. The fresh UHPC with 9.8 in. flow spread was not adequate (viscous in nature) for easy casting of the companion specimens for material-level experiments. Therefore, it is expected that 10.0–10.5 in. flow is an ideal range for placement.

Table 6.10 and Figure 6.30 show the temperatures at discharge for Tx34-1 and Tx34-2 were high due to the high ambient temperature during mixing in hot summer conditions in Texas. In addition, chilled water was not available at the plant. Even though the high temperature at discharge may affect workability, it did not cause any issue during placement, and flow spread (e.g., 10.5 in.) was adequate. The higher temperature at discharge was expected to accelerate cement hydration, shorten setting time, and increase early strength gain. As a result, Tx34-2 showed high early strength gain (discussed in Section 6.3.3). Therefore, the effect of high discharge temperatures during summer mixing can be beneficially used to achieve high early strength gain in UHPC without any heat treatment, and the use of ice or chilled water can be eliminated.

Table 6.10. Temperature at Discharge.

Batch No.	Tx34-1, °F	Tx34-2, °F	Tx54, °F
Ambient Temperature	94	94	80
B1	91	96	86
B2	96	103	89
B3	98	102	84
B4	-	-	92
B5	-	-	92

Notes:
1. Cast in June 2021, August 2021, and April 2022 for Tx34-1, Tx34-2, and Tx54, respectively.
2. No chilled water used.
3. - : Not available

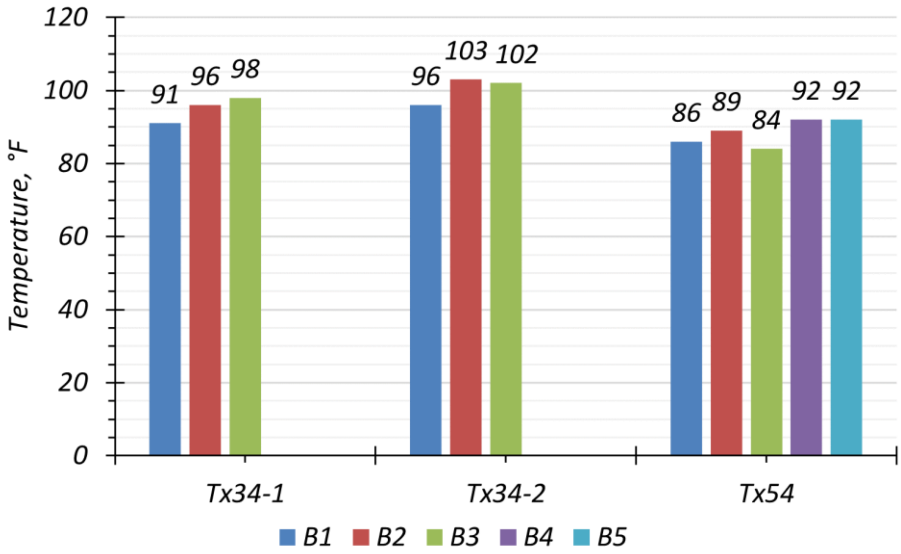

Figure 6.30. Temperature at Discharge.

6.3.2 Unit Weight and Air Content

The testing for unit weight and air content was conducted on the mixer platform at the precast plant in accordance with ASTM C138 (2015). Table 6.11 and Figure 6.31 show the results of the three girders. The results for unit weight showed good consistency and ranged from 150.6–152.4 lb/ft^3. The gravimetric air content values were from 1.8 to 2.9 percent. The results of unit weight and air content of Mix-4-PM-L were 151.3 lb/ft^3 and 2.5 percent, respectively. Thus, the results from the laboratory and the precast plant are consistent.

Table 6.11. Unit Weight and Air Content.

Girder, Batch No.	Unit Weight, lb/ft^3	Air Content, %	Flow Spread, in.
Tx34-1, B1	152.4	1.8	10.4
Tx34-2, B1	150.6	2.9	10.4
Tx54, B2	151.0	2.7	10.3

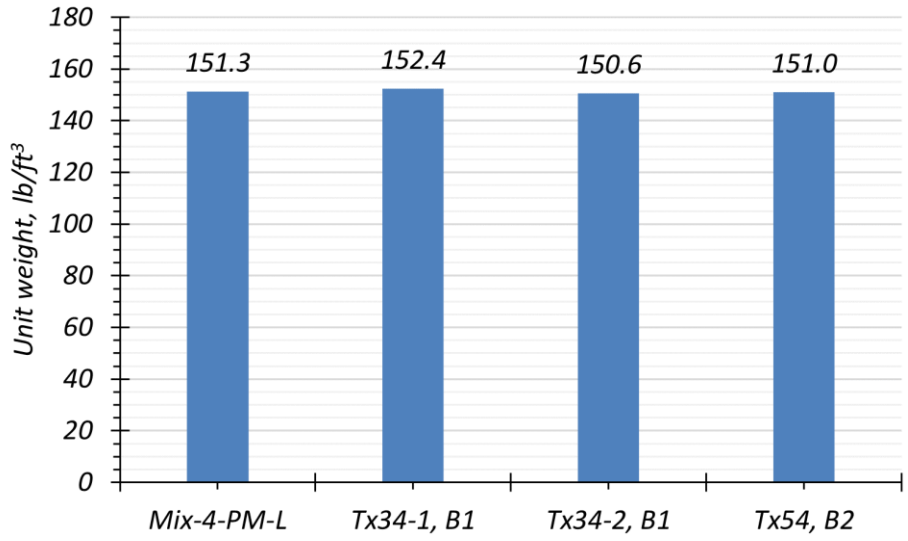

(a) Comparison of Unit Weight Results

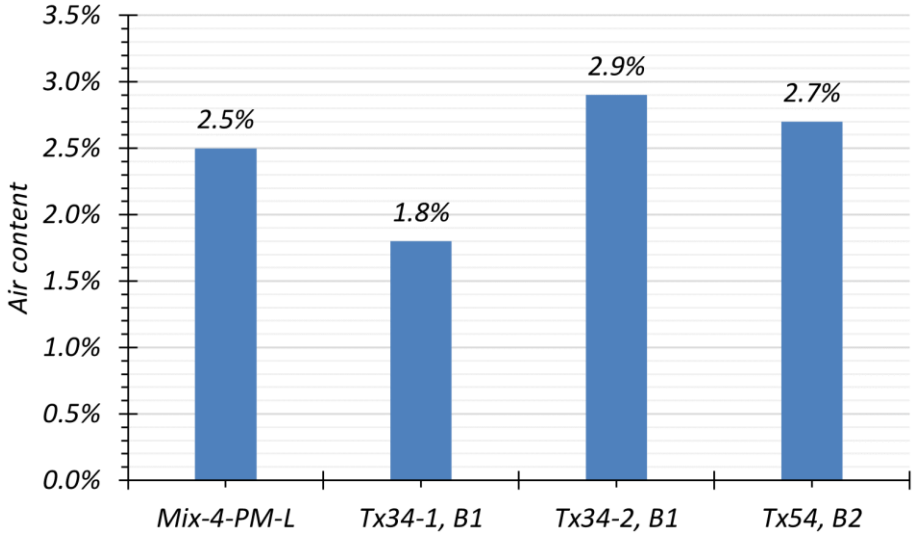

(b) Comparison of Air Content Results

Figure 6.31. Unit Weight and Air Content.

6.3.3 Temperature of Girder

The temperature development of the girder at early age (up to 16–18 hours from casting) was recorded using thermocouples located at the midspan of the girder (Figure 6.32). The temperature

in the bottom flange was higher than the other locations in the web and top flange. The maximum temperature was 212°F at 11 hours, 204°F at 9 hours, and 192°F at 12 hours for Tx34-1, Tx34-2, and Tx54, respectively (Figure 6.33). The temperature rise of Tx34-2 began 3 hours after casting, and Tx34-2 reached its peak temperature earlier than the other two girders. This result might be due to Tx34-2 mixes having the highest discharge temperature as a result of the high ambient temperature and high temperature of the materials in August. The high temperature at discharge may accelerate the formation of nucleates of CSH after a relatively short dormant period. The nucleates accelerate themselves because they provide additional places for nucleation (Thomas et al. 2011). As a result, the Tx34-2 UHPC achieved the highest temperature at a relatively earlier age than the others, whereas the Tx54 UHPC had a slow temperature gain and a lower maximum temperature due to the lower discharge temperature and ambient temperature (46°F) during the night. This occurrence gives insight into how the heat from the hydration reaction can be used for early strength gain. During the winter season, covering a girder with an insulating material may help retain the heat from hydration. As a result, the heat may act as a heat treatment-like effect.

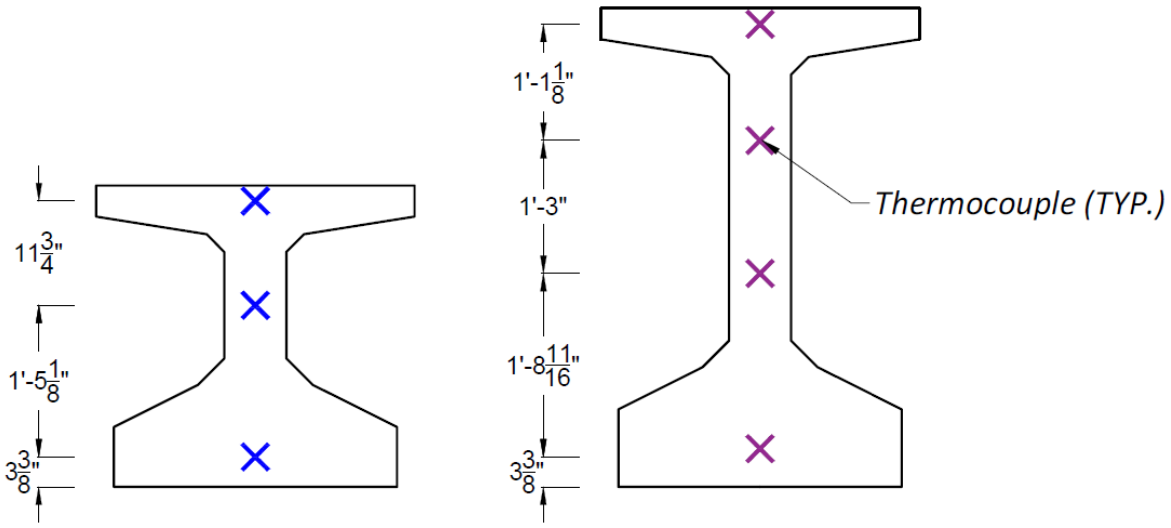

(a) Tx34-1 and Tx34-2 *(b) Tx54*

Figure 6.32. Locations of Thermocouples.

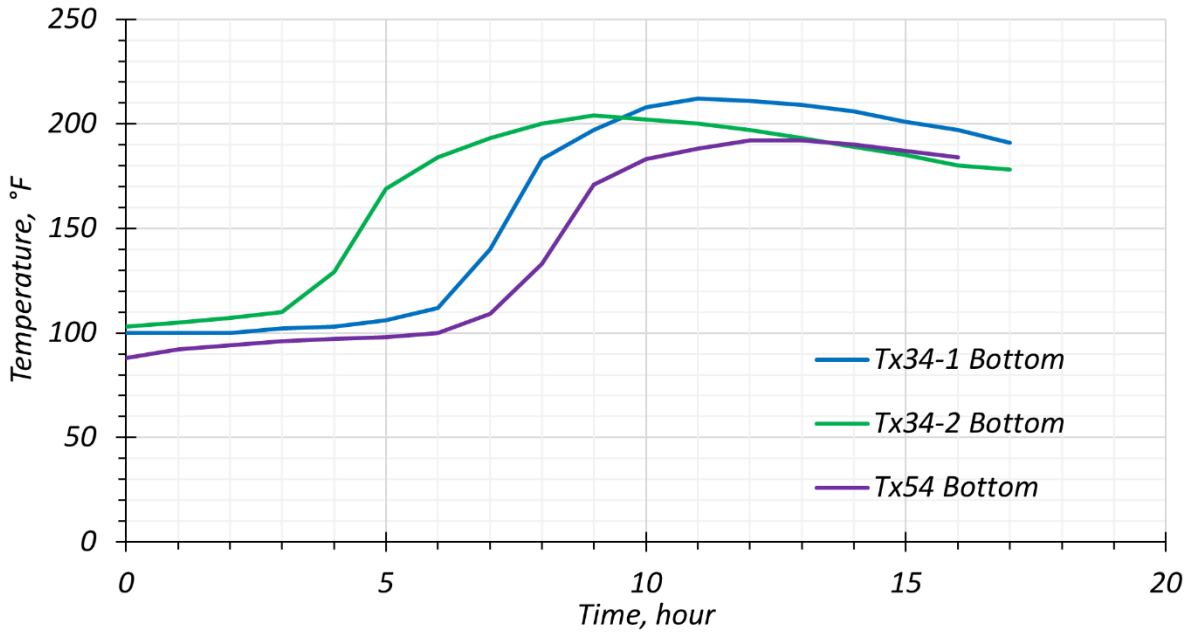

Figure 6.33. Temperature Development of Girders at Bottom Flange.

The occurrence of a temperature gradient was observed in both the Tx34-1 and Tx54 girders. A large temperature difference between the top and bottom flanges (i.e., 75°F at 8 hours for Tx34-1 and 86°F at 10 hours for Tx54) is depicted in Figure 6.34 and Figure 6.36. Interestingly, Tx34-2 had a small temperature difference (20°F at 6 hours) between the top and bottom flanges (Figure 6.35). The difference of temperatures at the top and bottom flanges existed only at the very early age (i.e., 6–10 hours after placement when concrete was still in its plastic state) and did not last long (i.e., a minimum difference occurred within 16 hours). Thus, the temperature change does not appear to have caused cracking.

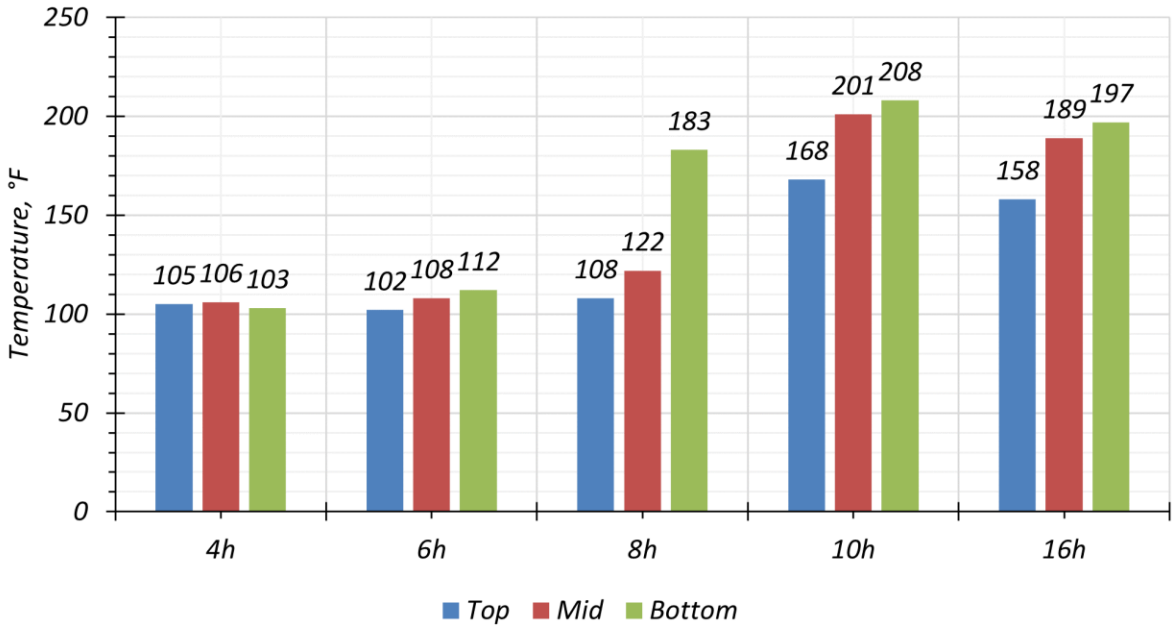

Figure 6.34. Tx34-1 Temperature Gradient.

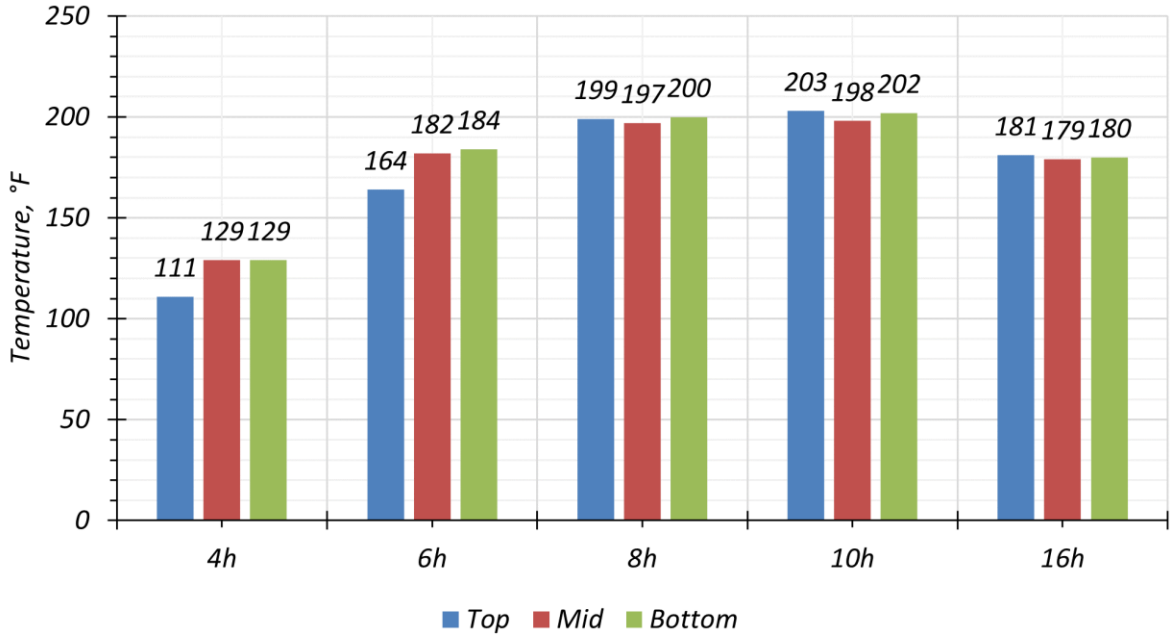

Figure 6.35. Tx34-2 Temperature Gradient.

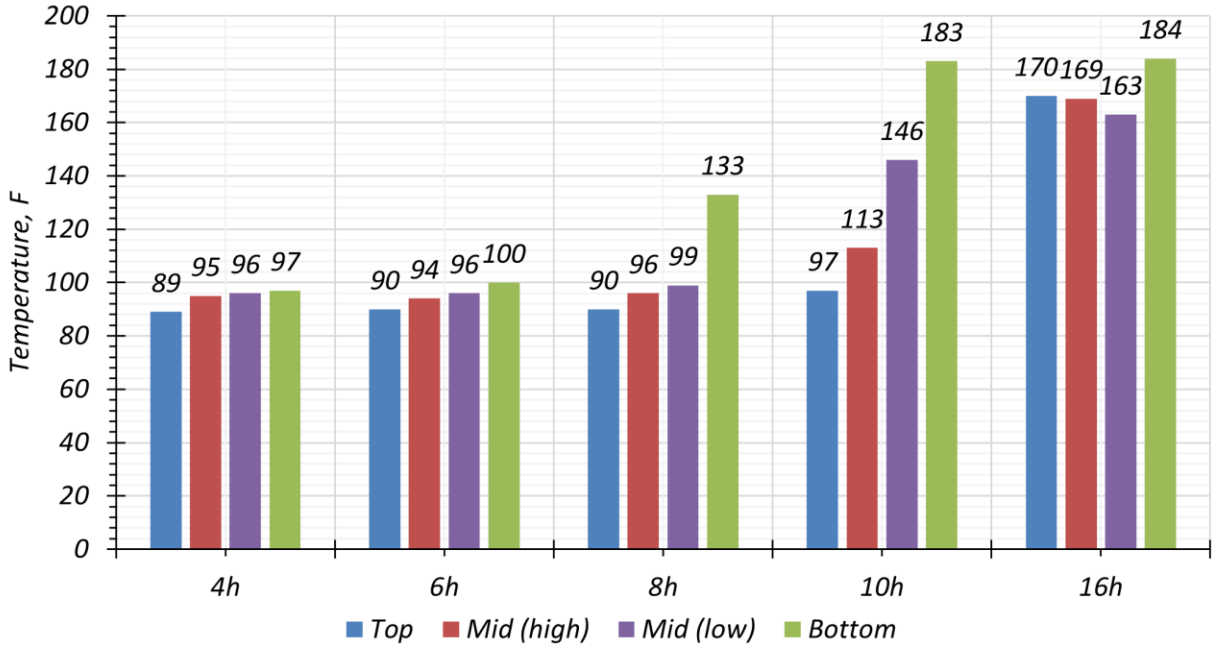

Figure 6.36. Tx54 Temperature Gradient.

6.4 SHORT-TERM HARDENED PROPERTIES

Hardened properties of the UHPC for the three girders were investigated using the companion specimens cast at the plant. This section discusses compressive strength, MOE, Poisson's ratio, uniaxial tensile strength, and flexural tensile strength. Table 6.12, Table 6.13, and Table 6.14 summarize the overall test matrix for Tx34-1, Tx34-2, and Tx54, respectively.

Table 6.12. Tx34-1 Companion Sample Collection from Batches and Test Matrix.

Property	Sample	B1	B2	B3	Test Matrix
Compression	3 × 6 in. cylinder	12	24	12	B1: 1d, 7d, 28d, and 1 coring set B2: 1d, 3d, 7d, 28d, 56d, and 2 sets for girder test days B3: 1d, 7d, 28d, and 1 extra set
Compression	4 in. cube	9	-	-	16h and 21h at the plant 1 extra set at the lab
MOE	3 × 6 in. cylinder	12	-	-	3d, 28d, 1 set for girder test day, and 1 extra set
Flexural tension	4 × 4 × 14 in. prism	-	6	3	B2: 3d and 28d B3: 1 set for girder test day
Uniaxial tension	2 × 2 × 17 in. prism	-	20	-	7d, 28d, 1 set for girder test day, and 1 extra set
Shrinkage	3 × 3 × 11.25 in. prism	-	-	6	3 for autogenous shrinkage, 3 for total shrinkage
Creep	3 × 6 in. cylinder	-	-	7	2 for creep, 2 for shrinkage, and 3 extra

Notes:
1. B1, B2, and B3 are Batch 1, Batch 2, and Batch 3, respectively.
2. Each set consists of 3 samples.
3. - : Not available

Table 6.13. Tx34-2 Companion Sample Collection from Batches and Test Matrix.

Property	Sample	B1	B2	B3	Test Matrix
Compression	3 × 6 in. cylinder	9	21	9	B1: 1d, 28d, and 1 coring set B2: 1d, 3d, 7d, 28d, 56d, and 2 sets for girder test days B3: 1d, 28d, and 1 extra set
Compression	4 in. cube	9	-	-	19h at the plant 2 extra set at the lab
MOE	3 × 6 in. cylinder	12	-	-	3d, 28d, 1 set for girder test day, and 1 extra set
Flexural tension	4 × 4 × 14 in. prism	6	-	3	B1: 3d and 28d B3: 1 set for girder test day
Uniaxial tension	2 × 2 × 17 in. prism	-	20	-	7d, 28d, 1 set for girder test day, and 1 extra set
Shrinkage	3 × 3 × 11.25 in. prism	-	-	6	3 for autogenous shrinkage, 3 for total shrinkage
Creep	3 × 6 in. cylinder	-	-	7	2 for creep, 2 for shrinkage, and 3 extra

Notes:
1. B1, B2, and B3 are Batch 1, Batch 2, and Batch 3, respectively.
2. Each set consists of 3 samples.
3. - : Not available

Table 6.14. Tx54 Companion Sample Collection from Batches and Test Matrix.

Property	Sample	B1	B2	B3	B4	B5	Test Matrix
Compression	3 × 6 in. cylinder	9	21	15	9	9	B1: 1d, 28d, and 1 extra set B2: 1d, 3d, 7d, 28d, 56d, and 2 sets for girder test days B3: 1d, 28d, 1 coring set, and 2 extra set B4: 1d, 28d, and 1 extra set B5: 1d, 28d, and 1 extra set
Compression	4 in. cube	-	-	-	9	-	18h at the plant 2 extra sets at the lab
MOE	3 × 6 in. cylinder	-	12	-	-	-	3d, 28d, 1 set for girder test day, and 1 extra set
Flexural tension	4 × 4 × 14 in. prism	8	-	1	-	-	B1: 3d, 28d, 2 specimens for girder test day, and 1 extra set B3: 1 specimen for girder test day
Uniaxial tension	2 × 2 × 17 in. prism	-	-	10	10	-	7d, 28d, 1set for girder test day, and 1 extra set
Shrinkage	3 × 3 × 11.25 in. prism	-	-	-	-	6	3 for autogenous shrinkage, 3 for total shrinkage
Creep	3 × 6 in. cylinder	-	-	14	-	-	2 for creep, 2 for shrinkage, and 3 extra

Notes:
1. B1, B2, B3, B4, and B5 are Batch 1, Batch 2, Batch 3, Batch 4, and Batch 5, respectively.
2. Each set consists of 3 samples.
3. - : Not available

6.4.1 Compressive Strength

The compressive strength of the UHPC produced for the three girders was measured using 3 × 6 in. cylindrical specimens. The strength at the very early age (19–21 hours) was tested at the plant using 4 in. cubes due to the unavailability of an end grinder. Table 6.15 shows the test results. Tx34-1 and Tx34-2 achieved the targeted strength for transfer (12 ksi) within 21 hours. The compressive strength of the Surecure samples from Tx54 was 14.8 ksi at 16 hours. Even though the cast companion samples did not achieve the targeted strength due to the low overnight temperature, the Tx54 girder achieved sufficient strength due to heat of hydration.

Table 6.15. Early Age Strength at the Plant Using 4 in. Cubes.

Description	Tx34-1		Tx34-2	Tx54
Individual Compressive strength, ksi	at 16 h	at 21 h	at 19 h	at 18 h
	10.8	12.5	>12[1,3]	3.5
	9.8	13.3		3.2
	10.9	11.8		3.4
Average, ksi	10.5	12.5	-	3.4[2]

Notes:
1. The cubes were not tested to full strength due to the load limit of the testing device.
2. Surecure samples from Tx54 gave a strength of 14.8 ksi at 16 hours.
3. One 4 in. cube was tested for each age.
4. - : Not available

After transporting the companion specimens to the lab, the compressive strength at 1, 7, 28, and 56 days was determined (Table 6.16). Note that CoV test results are for three individual specimens. The specimens for the compression test were cast from Batch 2 for all three girders. Figure 6.37 shows the compressive strength gain of the three girders. Some key observations are the following:

- The average 1-day compressive strengths of the three girders fall within the 15.2–16.1 ksi range. This measurement is higher than the compressive strength for Mix-4-PM-L (mixed at the laboratory), which is 14.1 ksi.
- The 28-day average compressive strengths of Tx34-1 (18.9 ksi) and Tx34-2 (18.0 ksi) are also comparable to the laboratory strength results for Mix-4-PM-L (18.7 ksi).
- Generally, the compressive strength results of the companion specimens of the three girders are consistent with Mix-4-PM-L. However, the strengths at 7 and 28 days of Tx54 are low. This result might be due to errors from the sample preparation process, such as casting and end surface preparation. In the case of sample preparation, the lower flow for Tx54 did cause more difficulty in casting the smaller samples. To verify the strength of Tx54, UHPC cylinders using the same materials as Tx54 were cast at the lab. Table 6.17 shows the results. The strength results at 11 and 28 days were 17.3 and 19.2 ksi, respectively, which match with the strengths of the other girders.

Table 6.16. Compressive Strength of Girder UHPC.

Description		1-day	7-day	28-day	56-day
Tx34-1	S1	15.8[2]	19.5	18.0	20.5
	S2	15.1[2]	17.2	19.1	18.3
	S3	14.4[2]	20.3	19.7	18.0
	Average	15.5	19.1	18.9	18.9
	CoV	2.2%	7.3%	3.7%	5.8%
Tx34-2	S1	15.1	16.4	17.9	18.0
	S2	14.7	15.8	17.6	19.4
	S3	15.7	17.0	18.3	19.3
	Average	15.2	16.4	18.0	18.9
	CoV	2.7%	3.0%	1.6%	3.4%
Tx54	S1	15.7	15.6	15.5	19.0
	S2	16.4	14.9	17.8	18.3
	S3	16.3	16.2	16.2	19.2
	Average	16.1	15.6	16.5	18.8
	CoV	2.0%	3.5%	5.9%	2.0%

Note:
1. All the compressive strength specimens are from Batch 2.
2. Tested with neoprene pads and steel caps due to unavailability of an end grinder.
3. Unit: ksi

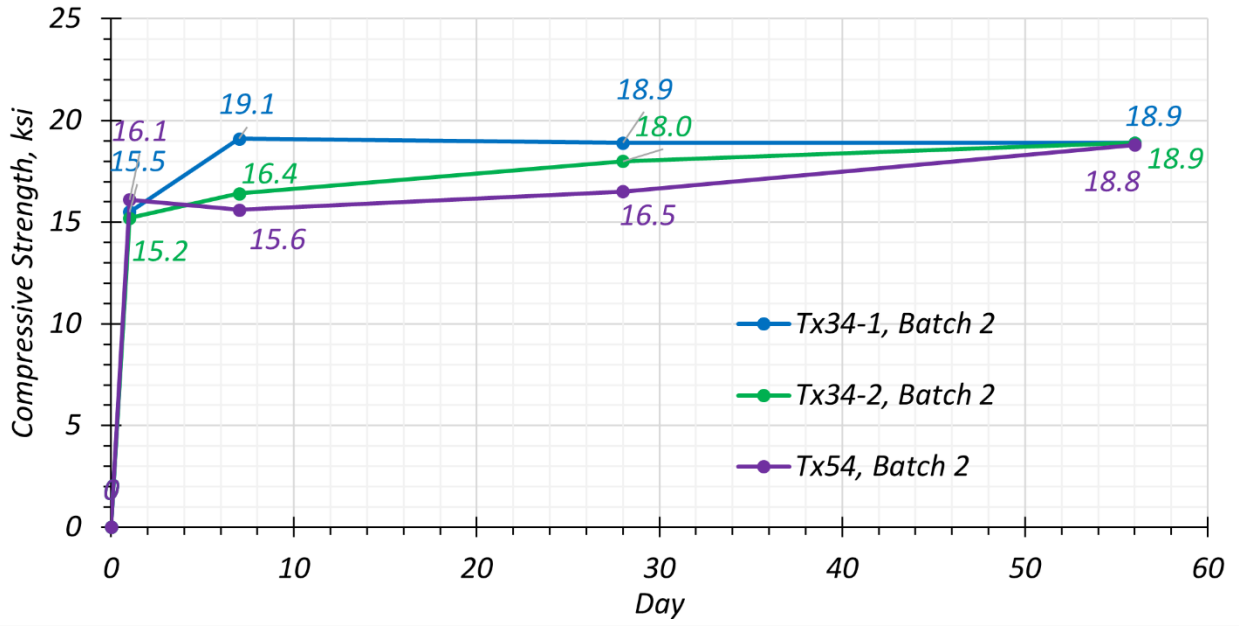

Figure 6.37. Tx54 Compressive Strength Gain of the Girders.

Table 6.17. Tx54 Compressive Strength Verification Results.

Description		1-day	11-day	28-day
Tx54 mixed at the lab	S1	14.9	16.3	19.3
	S2	15.2	18.2	19.9
	S3	15.3	17.3	18.4
	Average	15.1	17.3	19.2
	CoV	1.2%	4.4%	3.3%

Unit: ksi

6.4.2 Modulus of Elasticity and Poisson's Ratio

The MOE was measured as per the procedure explained in Section 3.3.2. The companion specimens cast with the three girders were tested at key ages. Table 6.18 presents the test matrix with the number of specimens cast for different testing ages. The companion specimens for Tx34-1 were cast for more testing ages than the other two girder specimens. The workability of the mix was fast-reducing due to the high temperature in the field, which made it difficult to cast a large number of cylinders without losing the appropriate flowability. Over the passage of time, the research team also observed that the steel fibers in the mix were settling to the bottom of the wheelbarrows. Based on this experience with the first girder, fewer testing ages were decided to be included to improve sample fabrication quality.

Table 6.18. Test Matrix for MOE and Poisson's Ratio.

Girder Specimen	3 days	7 days	28 days	56 days	Full-Scale Test Day
Tx34-1 (Batch 2)	3	3	3	3	3 (184 days)
Tx34-2 (Batch 1)	3	0	3	0	3 (166 days)
Tx54 (Batch 2)	3	3	3	0	3 (45 days)

Note: The full-scale test day refers to the period of the full-scale girder tests.
The age of specimens on the full-scale companion specimen testing day is given in parentheses.

Table 6.19 presents the MOE results for the girder companion specimens tested at different ages. The data are represented graphically in Figure 5.15, wherein the MOE of the companion specimens is plotted against the age of testing and against the compressive strength measured on that day. Table 5.24 and Figure 6.39 present the data for Poisson's ratio for the companion specimens. The MOE and Poisson's ratio values for the three girders were quite similar.

The MOE ranged from 6000 ksi to 7500 ksi for the samples cast during the UHPC girder fabrication. The Poisson's ratio ranged from 0.20–0.33. Both the MOE and Poisson's ratio values were consistent with less than 10 percent CoV. The MOE of Tx54 companion cylinders at later

ages were consistently higher than Tx34-1 and Tx34-2. The results are also similar to the MOE and Poisson's ratio measured for the laboratory mixes and the precast plant trial batch. The equation used to compute the predicted or theoretical MOE is explained in Section 5.6.2.3. The prediction was derived based on the data collected during the previous laboratory and precast plant material-level trials. The girder companion cylinders showed a slightly higher MOE than the prediction. The prediction serves as a lower bound for the observed data.

Table 6.19. Modulus of Elasticity of Girder UHPC.

Description		3 days	7 days	28 days	56 days	Test day[1]
Tx34-1	S1	6988	6009	6378	Note 5	Note 5
	S2	6654	6106	6613	6452	6802 (184)
	S3	6343	6019	5999	6459	6455 (184)
	Average	6662	6044	6330	6455	6628 (184)
	CoV	4.0%	0.7%	4.0%	0.1%	2.6% (184)
Tx34-2	S1	6446	-	7163	-	6498 (166)
	S2	6311	-	7019	-	6802 (166)
	S3	Note 4	-	6470	-	Note 4
	Average	6379	-	7091	-	6498 (166)
	CoV	1.1%	-	4.3%	-	2.3% (166)
Tx54	S1	6717	6924	7096	-	7526 (45)
	S2	6727	7631	7985	-	7285 (45)
	S3	6782	6766	7188	-	7527 (45)
	Average	6742	7107	7423	-	7446 (45)
	CoV	0.4%	5.3%	5.4%	-	1.5% (45)

Notes:
1. Testing age in parentheses
2. - : Not available
3. The measured value is not included as per the precision recommendations of ASTM C469 (2014). Imperfections in the specimen may have caused the deviation in behavior.
4. Unit: ksi

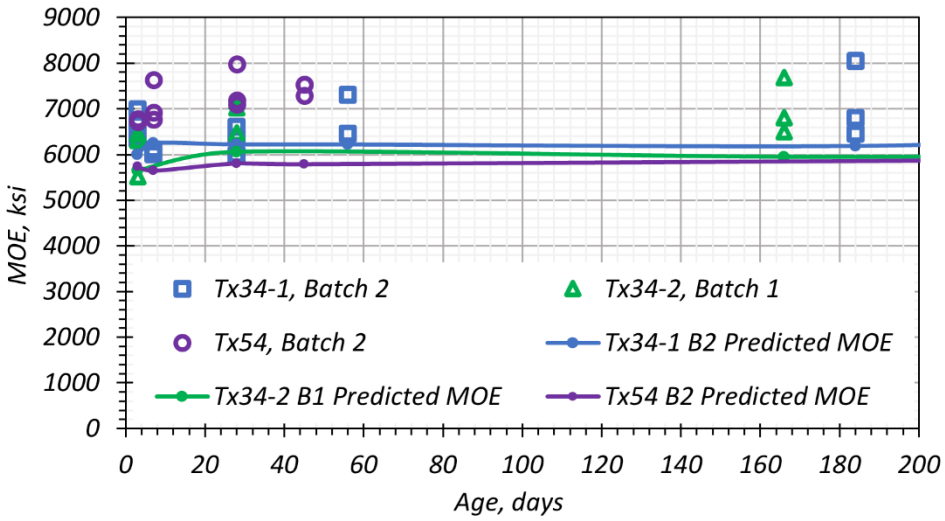

(a) MOE versus Age

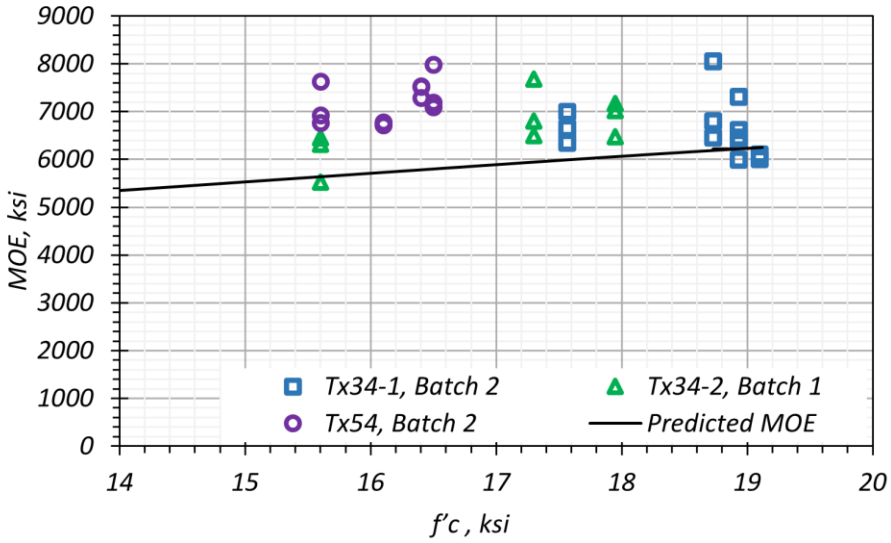

(b) MOE versus Compressive Strength

Figure 6.38. MOE for Companion Specimens Cast with Girders.

Table 6.20. Poisson's Ratio of Girder UHPC.

Description		3 days	7 days	28 days	56 days	Test Day[1]
Tx34-1	S1	0.26	0.23	0.25	Note 3	Note 3
	S2	0.23	0.28	0.23	0.28	0.33 (184)
	S3	0.26	0.26	0.23	0.25	0.30 (184)
	Average	0.25	0.27	0.23	0.26	0.31 (184)
	CoV	5.3%	3.8%	3.4%	6.4%	4.3%
Tx34-2	S1	0.25	-	0.28	-	0.27 (166)
	S2	0.27	-	0.27	-	0.30 (166)
	S3	Note 3	-	0.26	-	Note 3
	Average	0.26	-	0.27	-	0.29 (166)
	CoV	3.8%	-	3.4%	-	4.7%
Tx54	S1	0.22	0.25	0.24	-	0.23 (45)
	S2	0.18	0.30	0.27	-	0.26 (45)
	S3	0.23	0.31	0.26	-	0.29 (45)
	Average	0.23	0.31	0.26	-	0.26 (45)
	CoV	1.9%	2.3%	4.2%	-	9.9%

Notes:
1. Testing age in parentheses
2. - : Not available
3. The measured value is not included as per the precision recommendations of ASTM C469 (2014). Imperfections in the specimen may have caused the deviation in behavior.

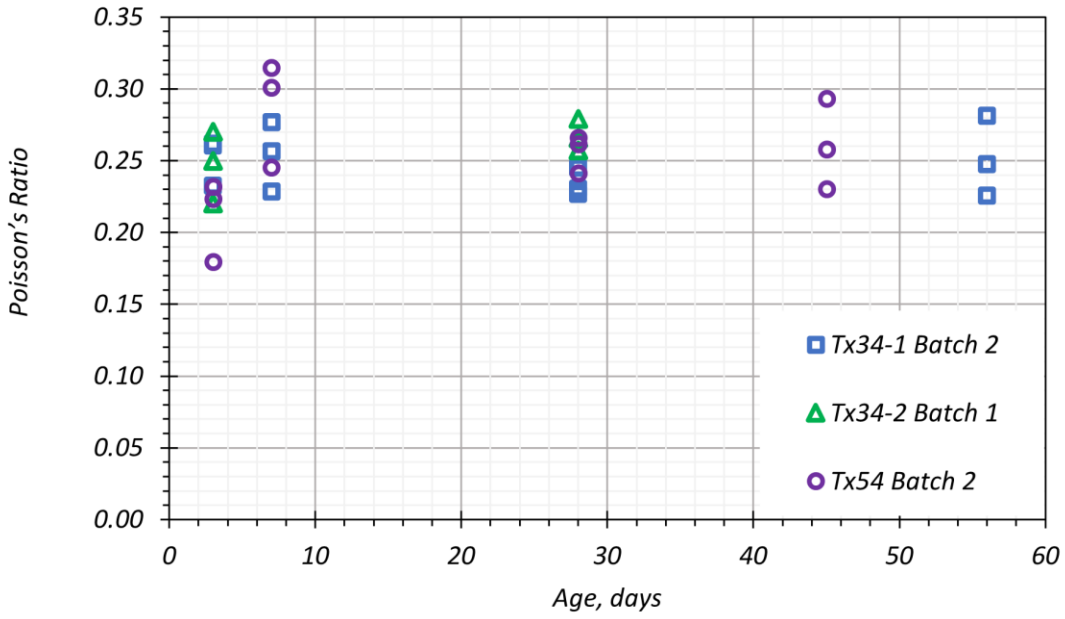

Figure 6.39. Poisson's Ratio for Companion Specimens Cast with Girders.

6.4.3 Direct Uniaxial Tension Test

The direct uniaxial tension test specimens were tested at 7 days, 28 days, and—during the period of the full-scale girder testing—at the time of the flexure or shear tests. Section 3.3.3 documents the method of conducting the uniaxial tension strength test. The tensile strength of UHPC directly impacts the shear capacity of the structural element; therefore, the volume of UHPC poured into the web of the girder was of interest for monitoring the uniaxial tension strength. For Tx34-1 and Tx-34-2, the specimens were cast from Batch 2, which corresponds to the volume of UHPC poured into the web. For Tx54, where the web is deeper by 20 in., Batch 3 and Batch 4 corresponded to the web region. Table 6.21 presents the testing ages and the number of specimens tested.

The number of specimens shown in Table 6.21 includes specimens that were deemed valid specimens during testing, along with an additional number of specimens tested without a successful result given in parentheses. Many of the specimens, especially from Tx34-1 and Tx34-2, either cracked during gripping or developed sudden cracks within the grip region (outside the gage length), rendering the LVDT data unsuitable for inferring the tensile behavior of the specimen due to the absence of post-cracking data. Figure 6.40 presents the specimens from Tx34-1 tested at 28 days. Most of the specimens cracked outside the gage length, and the photo illustrates the various crack locations that led to unreliable data. Specimens that were crushed at the grips were considered invalid specimens.

Table 6.21. Test Matrix for Direct Uniaxial Tension Test.

	Number of Samples		
Girder Specimen	**7 days**	**28 days**	**Full-Scale Test Day**
Tx34-1 Batch 2	4 (3)	3 (3)	3 (4) [184 days]
Tx34-2 Batch 2	5 (2)	5 (2)	4 (2) [166 days]
Tx54 Batch 3	3 (0)	4 (0)	3 (0) [45 days]
Tx54 Batch 4	3 (1)	3 (0)	3 (0) [45 days]

Notes:
1. The full-scale test day refers to testing during the period of the full-scale tests, including flexure and shear tests.
2. The number of specimens that could not be tested successfully is within parentheses.
3. The age of specimens on the full-scale companion specimen test day is within brackets.

(a) Cracked outside gage length

(b) Cracked at the grips

(c) Crushed at the grips

(d) Cracked outside gage length

(e) Cracked outside gage length

(f) Cracked within gage length

Figure 6.40. Tx34-1 28-Day Direct Uniaxial Tension Specimens.

Table 6.22, Table 6.23, and Table 6.24 summarize the test data from the key test ages for the companion specimens of the three full-scale girders.

- The first cracking stress is computed per the recommendation of AASHTO T 397 Draft (AASHTO 2022); it is that stress in the stress-strain curve corresponding to the point of the intersection of a line passing through the 0.02 percent strain with a slope of the MOE in the elastic tensile region of the stress-strain curve.
- The tensile MOE is the slope of the stress-strain curve when the stress transitions from −1 ksi (compression) to 0 ksi under tension.
- The peak stress is the maximum stress recorded for a particular sample.

The test data are graphically compared for the three girders on the respective test ages in Figure 6.41, Figure 6.42, and Figure 6.43. Specimen 5 data at 7 days and Specimen 4 data at 28 days for Tx34-2 are based on digital image correlation analysis of the tension test video due to lack of data from LVDT because the cracks formed outside the gage length. The PCI limit (eConstruct 2020) for the direct tension test, based on an inverse analysis, is set to 0.75 ksi until a strain of 0.004. At the early age of 7 days, Tx34-1 and Tx34-2 were observed to have average tensile strength lower

than 0.70 ksi. Tx54 specimens were observed to have an average tensile strength higher than 0.70 ksi, which is closer to the performance of the specimens tested from the lab mix and precast plant trial batch. This trend is similar for the 28-day and full-scale test day strength. The lower tensile strength of the Tx34-1 and Tx34-2 may be more pronounced at the material test level because of the lower concentration of fibers in the tension test specimens due to fiber settlement during their fabrication. However, the strength in the girder may be slightly higher than that of the individual specimens due to a higher volume of UHPC in the larger girder cross sections.

Table 6.22. Direct Uniaxial Tension Test Data at 7 Days.

Description		First Cracking		Peak Stress		MOE, ksi
		Strain, με	Stress, ksi	Strain, με	Stress, ksi	
Tx34-1	S1	300	0.54	113	0.74	6266
	S2	63	0.38	63	0.38	6686
	S3	350	0.76	154	0.84	5938
	S4	288	0.54	148	0.59	6133
	Average	250	0.55	120	0.64	6256
	CoV	N/A	25%	N/A	27%	4%
Tx34-2	S1	192	0.62	197	0.63	6173
	S2	130	0.78	131	0.79	6194
	S3	84	0.50	87	0.52	6201
	S4	85	0.51	95	0.58	6122
	S5[1]	409	0.44	1360	0.63	6186
	Average	177	0.56	419	0.63	6176
	CoV	N/A	21%	N/A	14%	0.46%
Tx54	S1-B3	148	0.98	148	0.98	6659
	S2-B3	127	0.73	659	0.88	6472
	S3-B3	157	0.85	157	0.88	6385
	S4-B4	186	0.44	1037	0.69	4904
	S5-B4	86	0.56	86	0.57	6235
	S6-B4	218	1.40	218	1.40	6570
	Average	162	0.81	374	0.88	6024
	CoV	N/A	38%	N/A	30%	10%

Note: Test data of Specimen 5 of Tx34-2 were obtained by digital image correlation analysis of testing video due to issues with specimens cracking outside of the gage length.
N/A: Not applicable

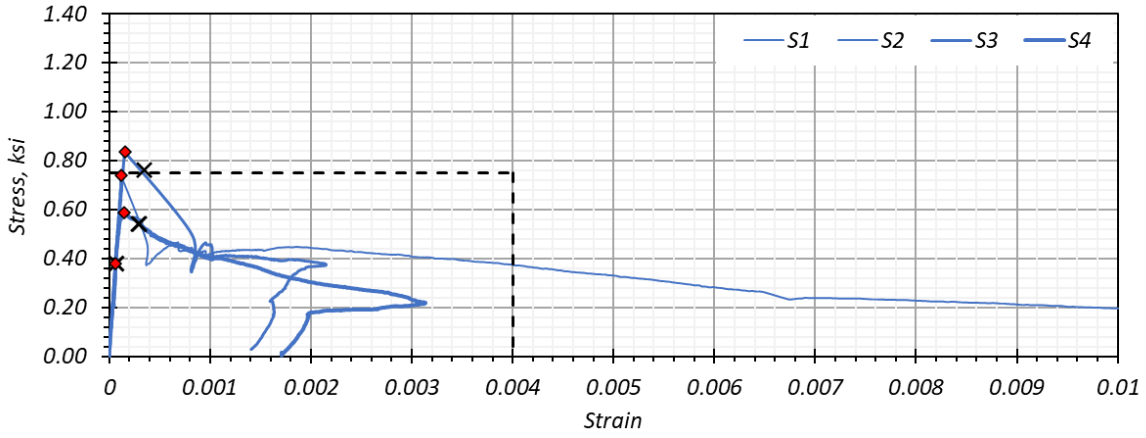

(a) Tx34-1

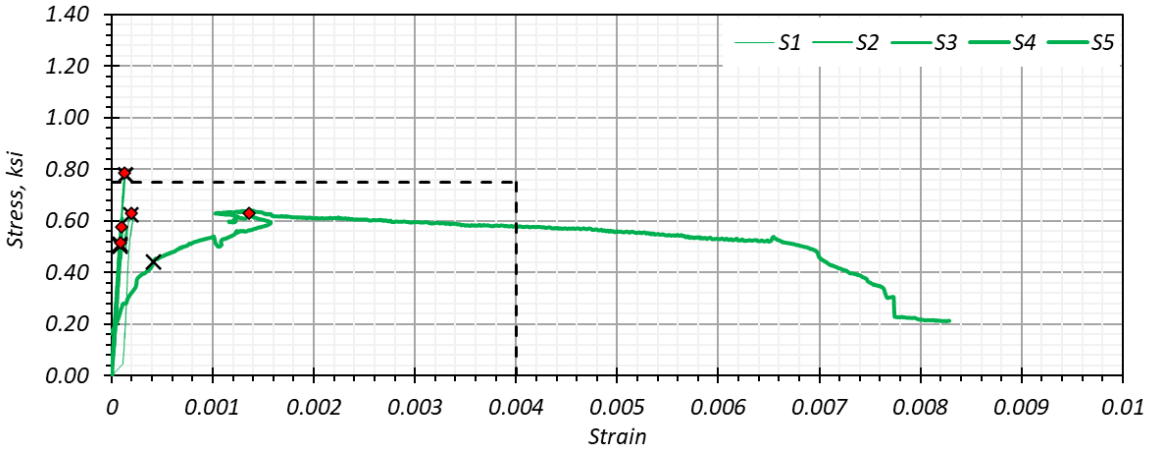

(b) Tx34-2

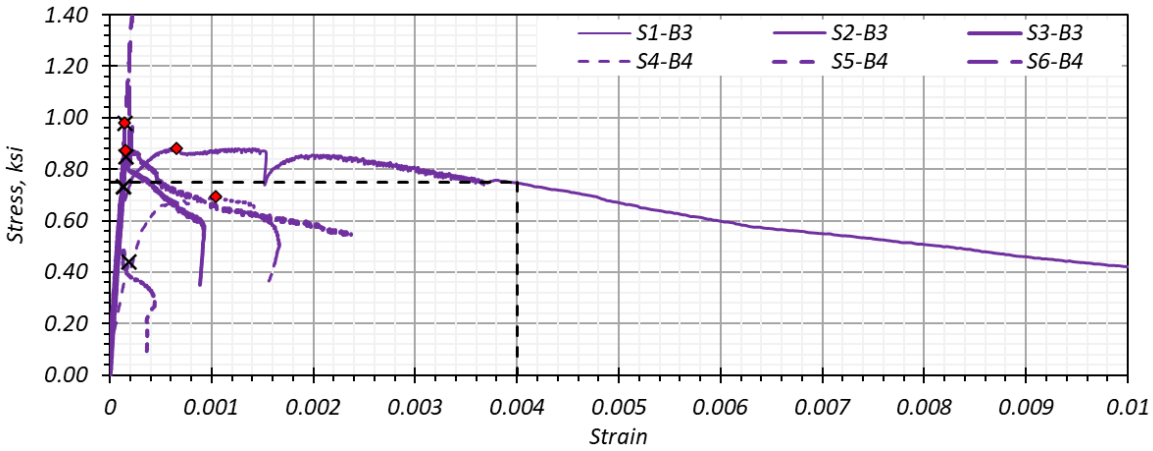

(c) Tx54

× *First Cracking Stress* ◆ *Peak Stress* - - - *PCI Limit*

Figure 6.41. Direct Uniaxial Tension Test Results at 7 Days.

Table 6.23. Direct Uniaxial Tension Test Data at 28 Days.

Description		First Cracking		Peak Stress		MOE, ksi
		Strain, με	Stress, ksi	Strain, με	Stress, ksi	
Tx34-1	S1	130	0.16	1316	0.49	1468
	S2[1]	0	-0.01	0	See Note 1	1694
	S3	44	0.35	58	0.43	7154
	S4	86	0.41	85	0.42	6076
	S5[1]	See Note 1	0.03	See Note 1	0.00	6566
	Average	87	0.31	486	0.45	4899
	COV	N/A	35%	N/A	7%	50%
Tx34-2	S1	96	0.66	115	0.69	6738
	S2	100	0.65	99	0.65	6383
	S3	83	0.49	94	0.55	6213
	S4[2]	407	0.62	407	0.62	5706
	S5	101	0.70	121	0.86	6623
	Average	157	0.62	168	0.67	6332
	COV	N/A	11%	N/A	15%	6%
Tx54-2	S1-B3	125	0.79	125	0.79	6892
	S2-B3	130	0.97	158	0.98	6926
	S3-B3	164	1.02	166	1.04	6675
	S4-B3	94	0.89	145	1.10	7077
	S5-B4	422	0.58	1883	0.96	4157
	S6-B4	152	0.71	152	0.71	6746
	S7-B4	551	0.86	973	0.87	5145
	Average	234	0.83	515	0.92	6231
	COV	N/A	17%	N/A	14%	17%

Notes:
1. Specimen cracked during the compression phase and is not considered in the average.
2. Specimen 4 test data were obtained by digital image correlation analysis of testing video due to lack of data from LVDT because the crack formed outside the gage length.
3. The full-scale test day refers testing during the period of the full-scale tests including flexure and shear tests.
4. The age of specimens on the full-scale companion specimen test day is within parentheses.
5. N/A: Not applicable

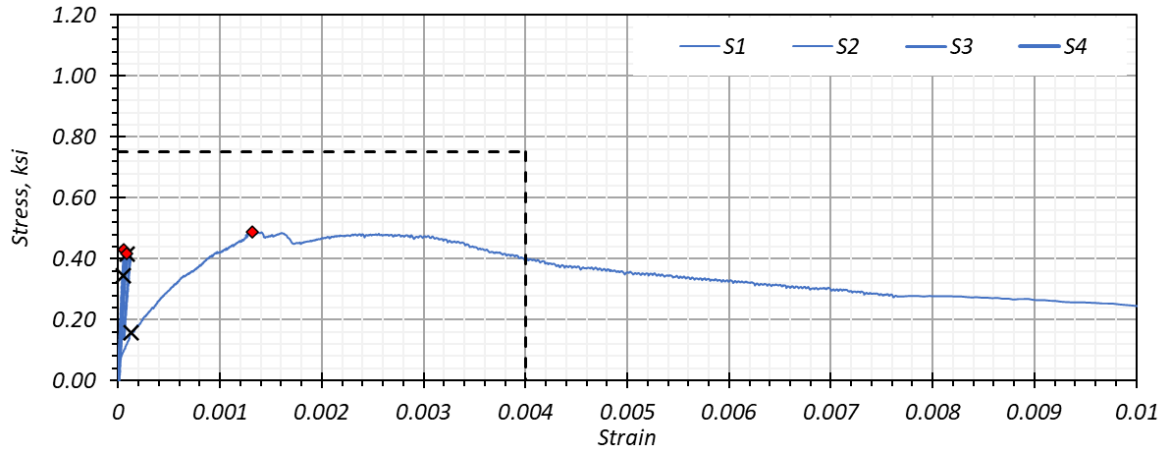

(a) Tx34-1

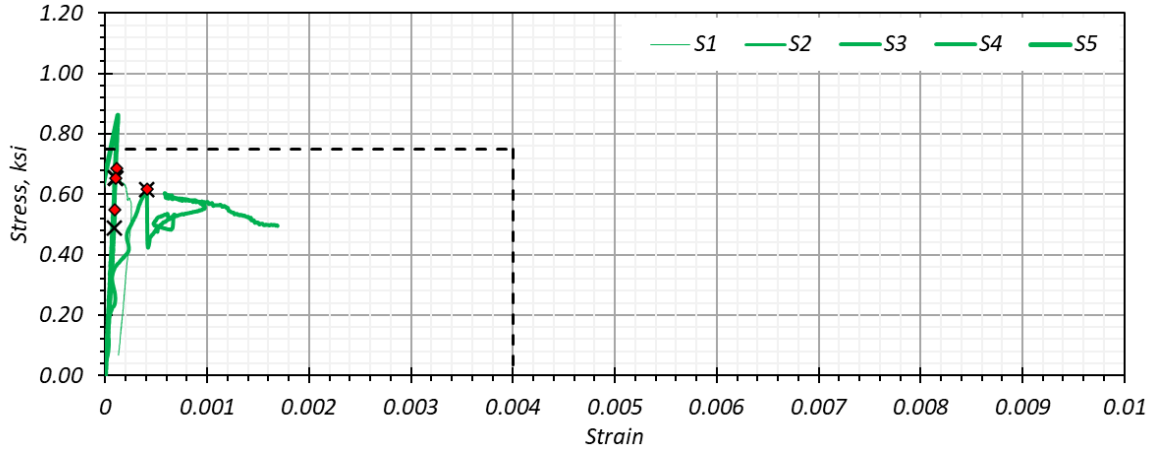

(b) Tx34-2

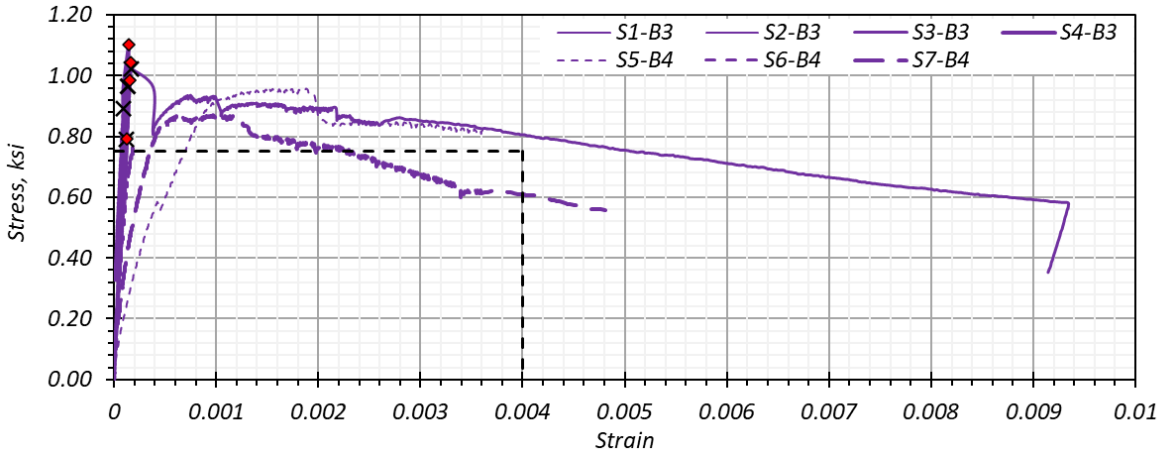

(c) Tx54

Figure 6.42. Direct Uniaxial Tension Test Results at 28 Days.

Table 6.24. Direct Uniaxial Tension Test Data Corresponding to Full-Scale Test Day.

Description		First Cracking		Peak Stress		MOE, ksi
		Strain, με	Stress, ksi	Strain, με	Stress, ksi	
Tx34-1 (184 days)	S1	254	0.33	1234	0.55	6753
	S2	**338**	**0.45**	**870**	**0.49**	**3078**
	S3	**300**	**0.61**	**111**	**0.70**	**6664**
	Average	319	0.53	491	0.60	4871
	CoV	N/A	37%	N/A	18%	37%
Tx34-2 (166 days)	**S1**	**544**	**0.62**	**779**	**0.70**	**7036**
	S2	171	0.52	317	0.55	4567
	S3	423	0.42	1214	0.52	1872
	Average	544	0.62	779	0.70	7036
	CoV	N/A	N/A	N/A	N/A	N/A
Tx54 (45 days)	**S1-B3**	**340**	**0.65**	**110**	**0.77**	**6889**
	S2-B3	**326**	**0.85**	**584**	**0.98**	**7071**
	S3-B3	**455**	**1.22**	**188**	**1.24**	**6906**
	S4-B4	**324**	**0.83**	**223**	**1.32**	**6866**
	S5-B4	**500**	**1.22**	**219**	**1.52**	**7265**
	Average	389	0.95	265	1.16	7000
	CoV	N/A	24%	N/A	23%	2%

Notes:
1. Specimens that are not shown in bold font cracked during the compression phase and are not considered in the average.
2. N/A: Not Applicable

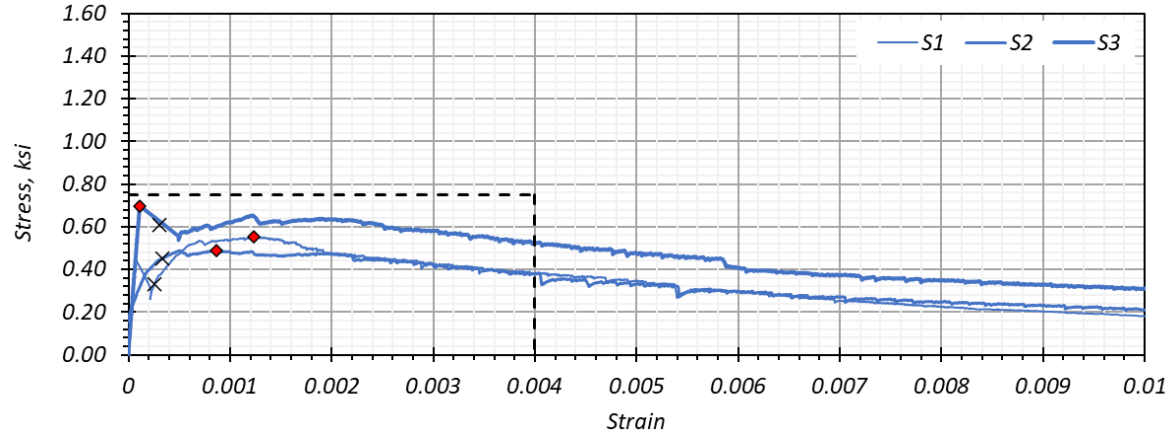

(a) Tx34-1 (188 days)

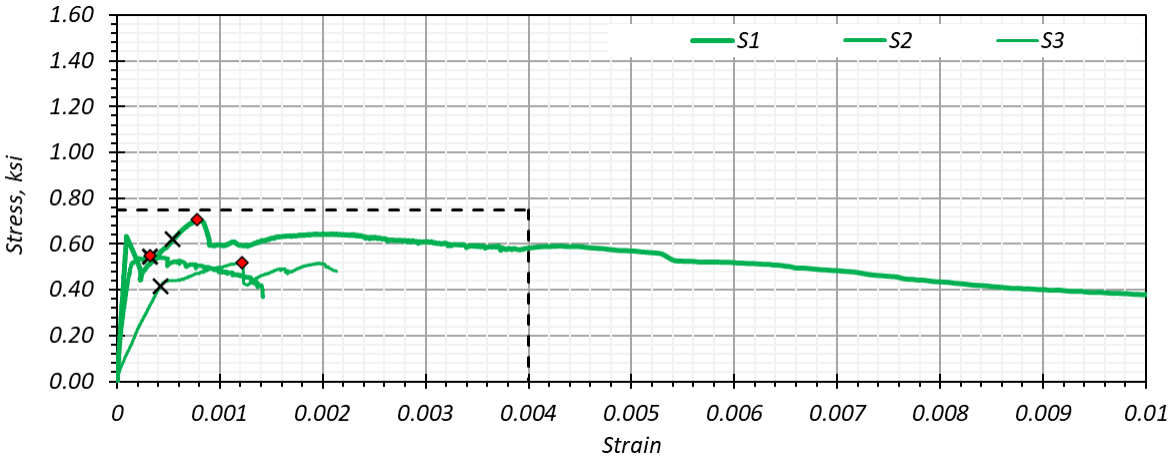

(b) Tx34-2 (166 days)

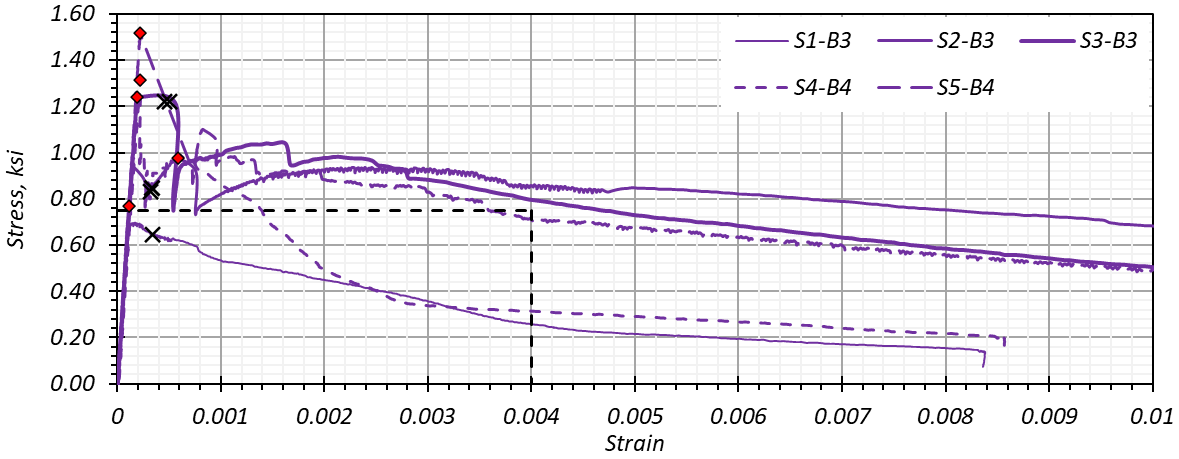

(c) Tx54 (45 days)

× *First Cracking Stress* ◆ *Peak Stress* - - - *PCI Limit*

Figure 6.43. Direct Uniaxial Tension Test Results Corresponding to Full-Scale Test Day.

The following observations were drawn from the uniaxial tension strength tests:

- The behavior of the specimens from the Tx34-1 girder casting under uniaxial tensile strength was poor when compared to that of Tx54. There was marked improvement in the tensile capacity and post-cracking load-carrying capacity of the specimen under tension for the specimens of Tx54.
- The specimens from Tx34-2 were similar to Tx34-1, with a slight improvement in the overall strength. The Tx34-1 and Tx34-2 specimens showed lower tensile strength and very low ductility, which may be due to high fiber settlement observed in the companion specimens of the first two girders.
- The post-cracking behavior of the Tx34-1 and Tx34-2 specimens was quite brittle in nature, and therefore most of the tests did not show the desired post-cracking capacity of UHPC for the first two girder companion specimens.
- Tx34-1 companion specimens showed a tensile strength lower than the PCI (eConstruct 2020) suggested minimum limit of 0.75 ksi, while Tx34-2 was either less than or equal to the suggested limit. Tx54 specimens met and exceeded this limit under the direct uniaxial tension test.

6.4.4 Inferred Tension Bending Test

The flexural performance of the companion specimens was studied by conducting four point bending tests in accordance with ASTM C1609 (2019). Section 3.3.4 elaborates on the test method. Three specimens were tested at 3 days, 27 days, and during the period of full-scale testing, including during flexure and shear tests. The early age tensile strength was one of the key parameters to be observed, and therefore this age was included for this test matrix. The uniaxial tension test did not yield good results in terms of being able to conduct the test at an early age of 3 days. Therefore, it was conducted at 7 days instead based on previous testing experience. Table 6.25 presents the testing ages and the number of specimens tested. The first specimen of the Tx34-1 was conducted in the orientation recommended by the ASTM standard; however, there was fiber settlement in the prism, and the lack of fibers on one side of the cross section led to brittle failure of the prism. Therefore, all other specimens in this test were tested in as-cast orientation. Section 5.6.2.6 mentions a detailed reasoning behind the orientation. The Tx34-2 specimens were planned

to be cast from Batch 2 to accommodate the large number specimens being cast across all batches. Because there was settlement of fibers observed in the first set of prisms, which implied higher tensile strength at the bottom flange of the girder, the subsequent girder companion specimens were planned to be cast from Batch 1 to be more representative of the bottom flange flexure strength of the girder. In cases where the UHPC from a certain batch was not adequate in quantity to cast the prism, the prisms were cast from the subsequent batch. This process is indicated as notes for the data when applicable.

Table 6.25. Test Matrix for Inferred Tension Bending Test.

Girder Specimen	3 Days	28 Days	Full-Scale Test Day
Tx34-1 Batch 2	3	3	3 (187 days)[1]
Tx34-2 Batch 1	3	3	3 (165 days)[2]
Tx54 Batch 1	3	3	3 (46 days)[3]

Notes:
1. Full-scale test day specimens of Tx34-1 were from Batch 3 due to limited volume available from Batch 2.
2. Full-scale test day specimens of Tx34-2 were from Batch 3 due to limited volume available from Batch 1.
3. Specimen 3 of full-scale test day specimens of Tx54 was from Batch 3 due to limited volume available from Batch 1.

Table 5.26, Table 5.27, and Table 5.28 summarize the test data from the key test ages for the companion specimens of the three full-scale girders. The test data are graphically compared for the three girders on the respective test ages in Figure 6.44, Figure 6.45, and Figure 6.46. The settlement of fibers to the bottom of the prisms was more pronounced for Tx34-1, followed by Tx34-2. The distribution of fibers was more uniform for the Tx54 companion prisms, and this observation was consistent with the superior tensile performance of the companion tension specimens and the girder itself.

Table 6.26. Inferred Tension Bending Test Data at 3 Days.

Specimen ID		First Cracking Strength		Ultimate Flexural Strength		Tough-ness	Equiv. Flexural Strength Ratio	*L*/300 = 0.04 in.	*L*/150 = 0.08 in.
		Stress, ksi	Disp., in.	Stress, ksi	Disp., in..	lb.-in.	Percent	Stress, ksi	Stress, ksi
Tx34-1	S1[1]	1.80	0.003	1.80	0.003	610	79.0	1.36	0.93
	S2	1.86	0.003	2.35	0.009	720	90.5	1.63	0.89
	S3[2]	1.76	0.003	1.76	0.003	220	29.5	0.42	0.16
	Avg.	1.83	0.003	2.08	0.006	670	85.0	1.50	0.91
	CoV	2%	N/A	13%	N/A	8%	7%	9%	2%
Tx34-2	S1	1.76	0.003	1.76	0.003	400	54.0	0.86	0.54
	S2	1.94	0.003	1.94	0.003	510	61.5	1.15	0.67
	S3	2.00	0.003	2.00	0.003	480	56.0	1.02	0.55
	Avg.	1.90	0.003	1.90	0.003	460	57.0	1.01	0.59
	CoV	5%	N/A	5%	N/A	10%	6%	14%	11%
Tx54	S1	2.05	0.003	2.06	0.003	600	69.0	1.28	0.77
	S2	2.07	0.003	2.13	0.012	690	78.0	1.54	1.00
	S3	2.18	0.003	2.18	0.003	590	63.5	1.32	0.76
	Avg.	2.10	0.00	2.13	0.01	630	70.0	1.38	0.84
	CoV	3%	N/A	2%	N/A	7%	9%	9%	13%

Notes:

1. Tx34-1 Specimen 1 showed brittle response because it was oriented by rotating the specimen on its side (such that the bottom of the specimen is oriented to one of the sides), as per ASTM C1609 (2019), while all the remaining specimens were oriented as-cast such that the bottom of the specimen remains at the bottom.
2. Tx34-1 Specimen 3 is not considered for the average due to high disparity.
3. N/A: Not applicable

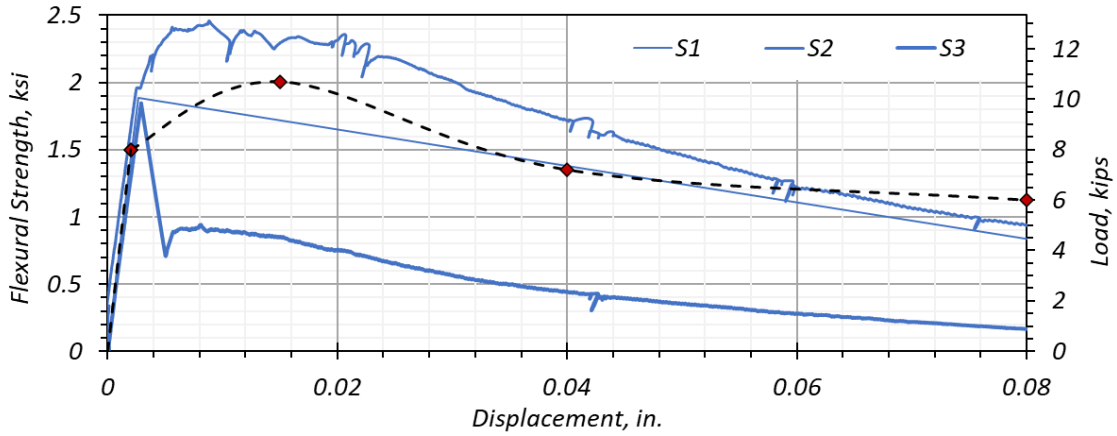

(a) Tx34-1

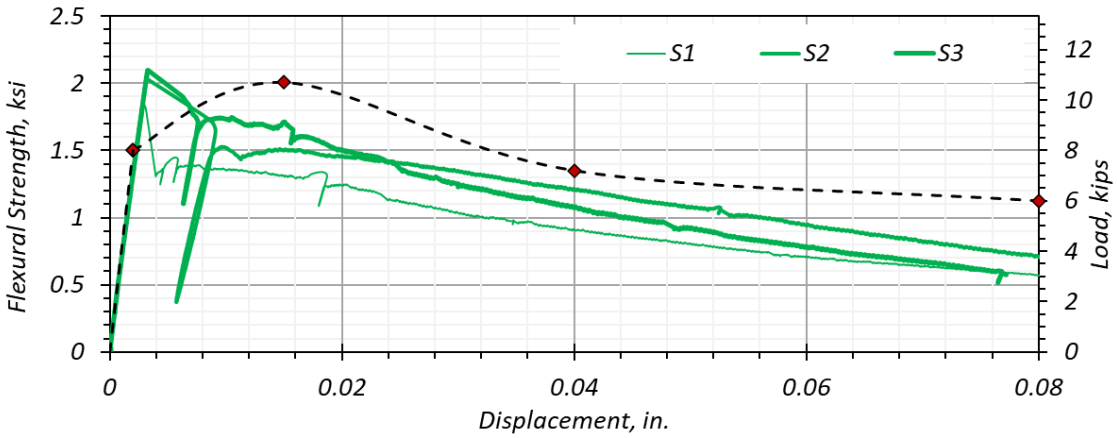

(b) Tx34-2

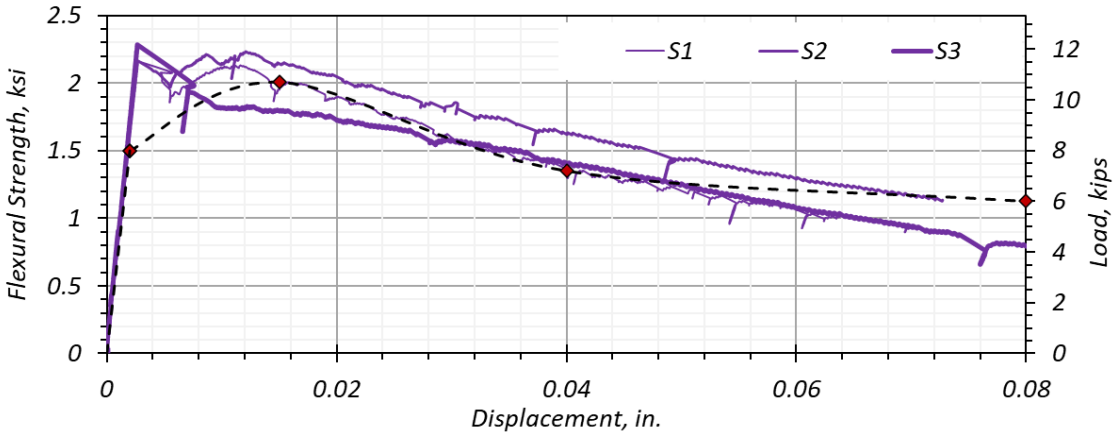

(c) Tx54

Figure 6.44. Inferred Tension Bending Test Results at 3 Days.

Table 6.27. Inferred Tension Bending Test Data at 27 Days.

Specimen ID		First Cracking Strength		Ultimate Flexural Strength		Tough-ness	Equiv. Flexural Strength Ratio	*L*/300 = 0.04 in.	*L*/150 = 0.08 in.
		Stress, ksi	Disp., in.	Stress, ksi	Disp., in..	lb.-in.	Percent	Stress, ksi	Stress, ksi
Tx34-1	S1	1.95	0.003	1.95	0.003	430	52.0	0.90	0.43
	S2	1.85	0.003	1.85	0.003	290	37.0	0.56	0.24
	S3	1.76	0.003	1.76	0.003	350	47.0	0.42	0.16
	Avg.	1.85	0.003	1.85	0.003	360	45.5	0.63	0.28
	CoV	4%	N/A	4%	N/A	16%	14%	32%	41%
Tx34-2	S1	2.16	0.003	2.16	0.003	510	55.5	1.05	0.56
	S2	1.10	0.003	1.10	0.005	350	74.5	0.74	0.46
	S3	2.09	0.003	2.09	0.003	440	49.0	1.02	0.55
	Avg.	1.78	0.003	1.78	0.004	430	59.5	0.94	0.52
	CoV	27%	N/A	27%	N/A	15%	18%	17%	10%
Tx54	S1	1.80	0.002	1.85	0.020	660	86.5	1.52	1.02
	S2	1.81	0.003	1.81	0.003	500	65.0	1.11	0.65
	S3	2.06	0.003	2.06	0.003	420	48.0	0.84	0.44
	Avg.	1.89	0.003	1.91	0.01	530	66.5	1.16	0.71
	CoV	6%	N/A	6%	N/A	19%	24%	16%	22%

N/A: Not applicable

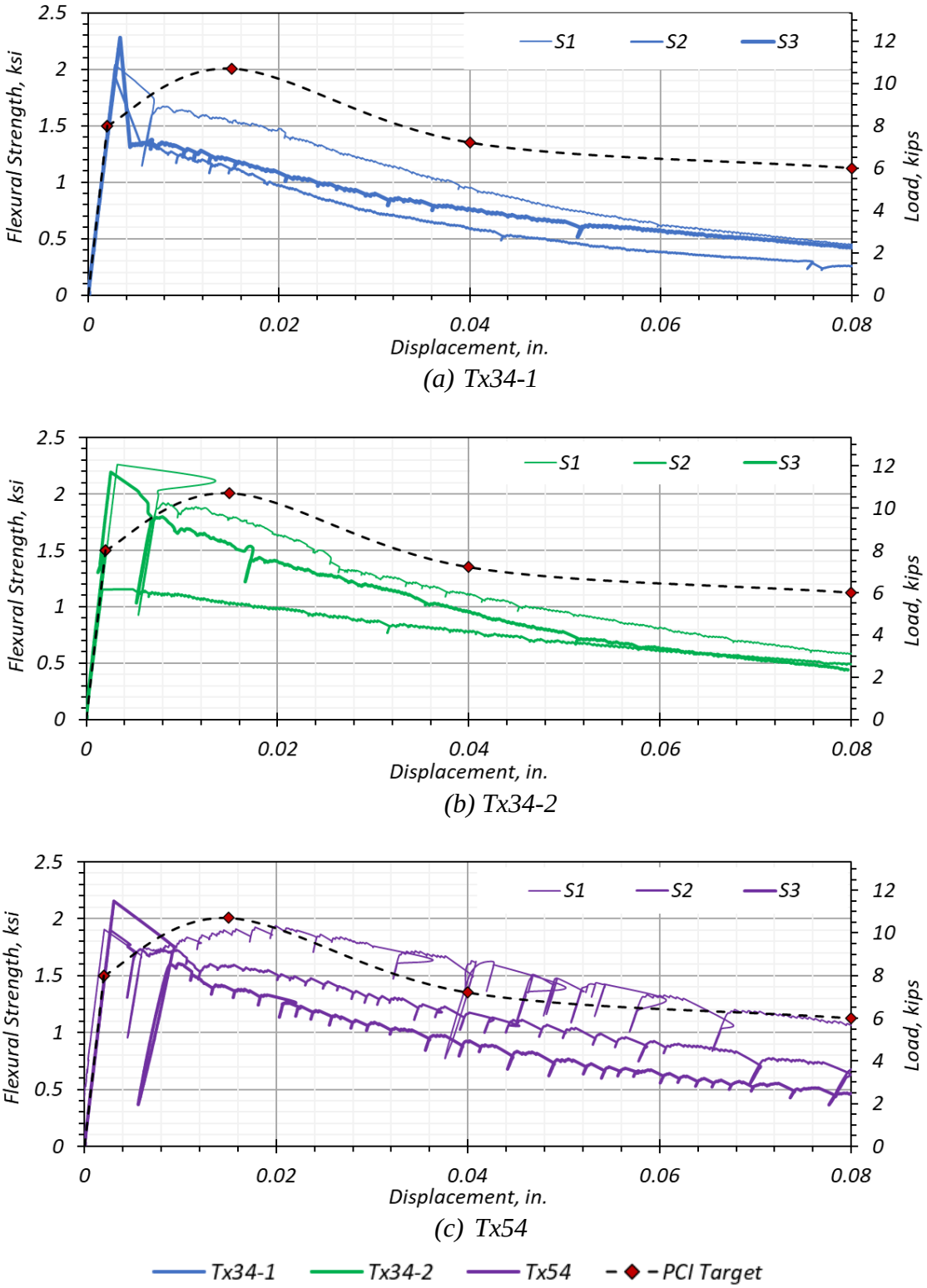

(a) Tx34-1

(b) Tx34-2

(c) Tx54

Figure 6.45. Inferred Tension Bending Test Results at 27 Days.

Table 6.28. Inferred Tension Bending Test Data at Full-Scale Test Day.

Specimen ID		First Cracking Strength		Ultimate Flexural Strength		Tough-ness	Equivalent Flexural Strength Ratio	*L*/300 = 0.04 in.	*L*/150 = 0.08 in.
		Stress, ksi	Disp., in.	Stress, ksi	Disp., in.	lb.-in.	Percent	Stress, ksi	Stress, ksi
Tx34-1	S1[1]	2.03	0.003	2.03	0.003	590	68.0	1.30	0.79
	S2[1]	2.13	0.003	2.30	0.010	600	66.0	1.28	0.61
	S3[1]	1.84	0.016	2.04	0.016	690	87.5	1.68	0.93
	Avg.	2.00	0.007	2.12	0.010	630	74.0	1.42	0.77
	CoV	6%	N/A	6%	N/A	7%	13%	13%	17%
Tx34-2	S1[2]	1.84	0.003	1.84	0.003	420	53.5	0.89	0.43
	S2[2]	1.19	0.004	1.19	0.004	310	62.0	0.67	0.37
	S3[2]	1.34	0.004	1.36	0.004	300	52.5	0.61	0.33
	Avg.	1.46	0.004	1.46	0.004	340	56%	0.72	0.38
	CoV	19%	N/A	19%	N/A	16%	8%	14%	8%
Tx54	S1	2.21	0.003	2.21	0.003	570	60.0	1.20	0.67
	S2	2.17	0.003	2.27	0.007	680	73.5	1.46	0.75
	S3[3]	2.01	0.003	2.18	0.005	620	73.0	1.28	0.94
	Avg.	2.13	0.003	2.22	0.010	620	69	1.31	0.79
	CoV	4%	N/A	2%	N/A	7%	9%	10%	6%

Notes:
1. Full-scale test day specimens of Tx34-1 were from Batch 3 due to limited volume available from Batch 2.
2. Full-scale test day specimens of Tx34-2 were from Batch 3 due to limited volume available from Batch 1.
3. Specimen 3 of full-scale test day specimens of Tx54 was from Batch 3 due to limited volume available from Batch 1.
4. N/A: Not applicable

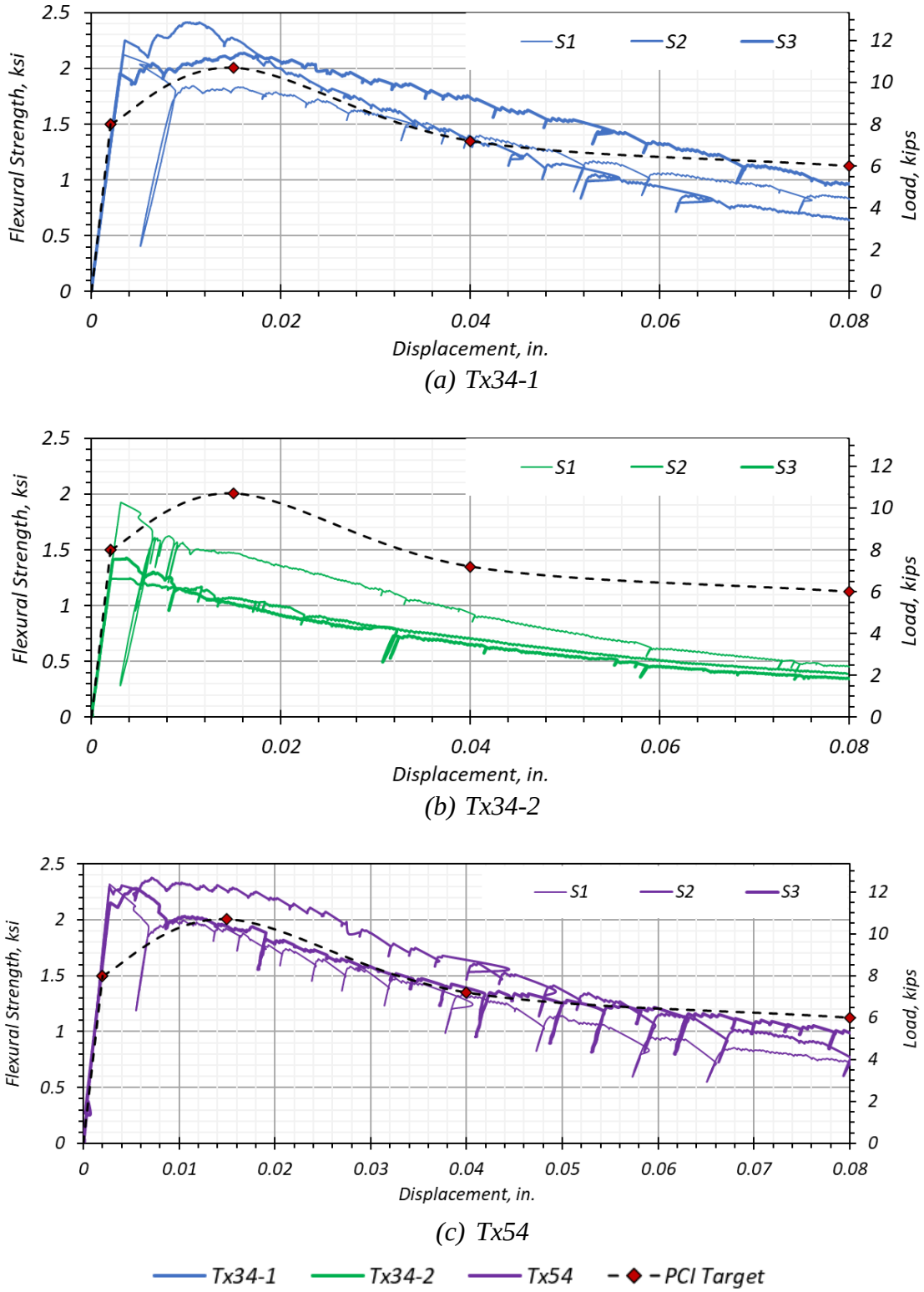

Note: Full-Scale Test Days: Tx34-1 = 187 days; Tx34-2 = 165 days; Tx54 = 46 days after casting

Figure 6.46. Inferred Tension Bending Test Results at Full-Scale Test Day.

The fiber settlement observed from the uniaxial tension test and flexure test prism is illustrated in the photographs of the cross section shown in Figure 6.47, Figure 6.48, and Figure 6.49. The fiber settlement observed in the tension and flexure prisms was quite similar. The following are the observations of fiber settlement:

- Figure 6.47(a) and (b) present the flexure and tension specimen cross sections at the plane of failure, thereby exposing the fiber density of Tx34-1 companion specimens, respectively. The images illustrate that most of the fibers were settled to the bottom third of the prisms, with almost no fibers present at the top of the Tx34-1 companion specimens.
- Figure 6.48(a) and (b) present the flexure and uniaxial tension companion specimens of Tx34-2 after failure, respectively. Fibers are distributed more uniformly compared to Tx34-1 specimens with more concentration of fibers at the bottom. However, the overall concentration of fibers is quite low. This effect is potentially due to the settlement of the fibers within the wheelbarrow from which the specimens were cast.
- Figure 6.49(a) and (b) show the cross section of the flexure and tension specimens of Tx54 companion prisms, respectively, after breaking the prisms open upon completion of the test. The fiber distribution and concentration of these specimens were much superior to Tx34-1 and Tx34-2 specimens. The Tx54 companion specimens had a more uniform distribution of fibers across the full depth of the cross section, from top to bottom.

The impact of fiber settlement and segregation is directly reflected in the tension test results and in the shear performance of the girders. However, when compared to the tension test, the flexural performance test results do not reflect this impact as clearly because the test was conducted in as-cast orientation, with fibers at the bottom face subjected tension. Since the prescribed test is for FRC, it was necessary to conduct the test in as-cast orientation because any other orientation would lead to a sudden brittle failure of the prisms, thus causing the test to abort abruptly.

(a) As-Cast Orientation with Fibers Settled to the Bottom

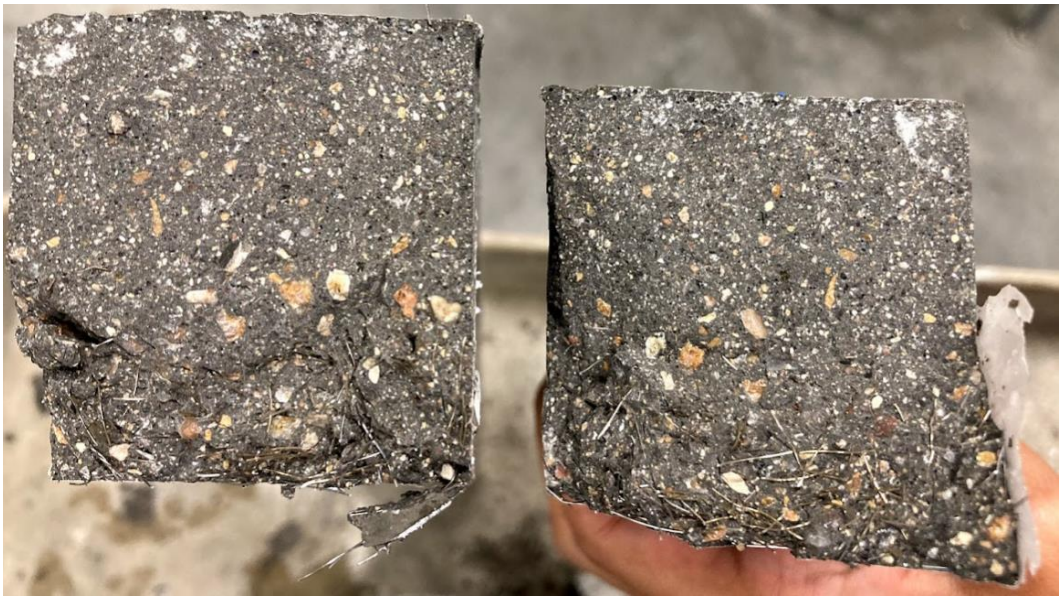

(b) As-Cast Orientation with Most Fibers Settled to the Bottom

Figure 6.47. Tx34-1 Specimen Cross Section at the Plane of Failure.

(a) Tx34-2 Flexure Specimen—As-Cast Orientation with Improved Fiber Distribution

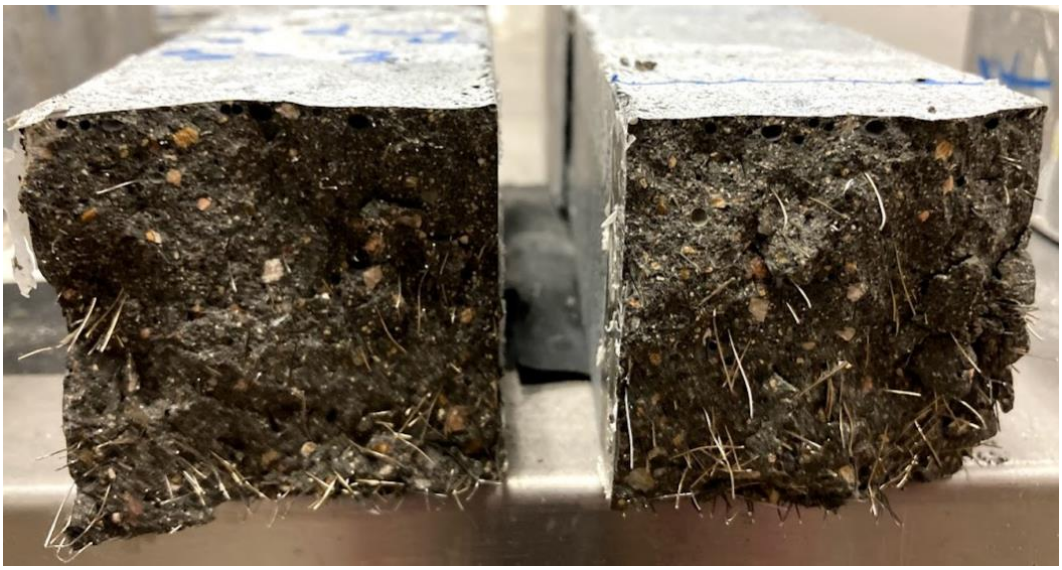

(b) Tx34-2 Tension Specimen—As-Cast Orientation with Improved Fiber Distribution

Figure 6.48. Tx34-2 Specimen Cross Section at the Plane of Failure.

(a) As-Cast Orientation with Improved Fiber Distribution

(b) As-Cast Orientation with Improved Fiber Distribution

Figure 6.49. Tx54 Specimen Cross Section at the Plane of Failure.

PCI (eConstruct 2020) recommended the ACI Committee 318 (2019) steel FRC ductility requirements for UHPC, which require a 90 percent first peak crack strength at 0.04 in. midspan displacement and a 75 percent first peak crack strength at 0.08 in. midspan displacement. Based on an inverse analysis of flexural performance test, ACI Committee 318 (2019) recommended a first peak crack strength of 1.5 ksi and ultimate flexure strength of 2 ksi for the minimum required tensile strength (eConstruct 2020).

The flexural performance test results for Tx34-1 and Tx34-2 show higher CoV at 3 days and 27 days than Tx54. This result is often due to one specimen showing low post-cracking strength, which may be because of lower fiber concentration in that specimen. The flexure strength of Tx54 is consistent for all specimens at 3 and 27 days. At early age, Tx34-1 and Tx34-2 have an average first peak crack strength and average ultimate flexural strength slightly lower than 2 ksi but higher than 1.5 ksi, while Tx54 had both these values slightly higher than 2 ksi.

The full-scale test day first peak crack strength of all three girder companion specimens is consistent and greater than or equal to 2 ksi on an average. With an average of 1.46 ksi, Tx34-2 showed lower ultimate flexural strength at the full-scale test day, whereas the other two companion specimens showed an ultimate flexural strength higher than 2 ksi. This result may indicate further lower concentration of fibers in the volume of Batch 3 used to cast these specimens.

Though the ACI Committee 318 (2019) limits of ductility are not fully met by many of the companion specimens at 0.04 in. and 0.08 in. displacement, the flexural capacity of the corresponding girders was sufficiently high to withstand service and factored load conditions. Therefore, the ductility requirements may need to be lowered for the UHPC with a lower volume of fibers that was considered for this project. The direct tension test was found to be a more representative indicator of the tensile performance of the girders, wherein the tension test results indicated a clear increase in tensile strength, from Tx34-1 to Tx34-2 to Tx54. This result seems to correlate well with the fiber distribution observed in the specimens. The trend was not as distinct for the flexural performance test results.

6.5 LONG-TERM HARDENED PROPERTIES

Creep and shrinkage were studied using the companion specimens of the three girders. This section describes the results of creep and shrinkage testing with the prediction models for the developed UHPC.

6.5.1 Creep

6.5.1.1 Creep Testing

The creep of the developed UHPC was investigated. The creep test was conducted with the targeted loading of $0.4f_c'$ at 28 days in accordance with ASTM C512 (2015) for Tx34-1 and Tx34-2 using the companion specimens. For Tx54, two creep tests with two different loading levels were performed: one for $0.65f_c'$ at 10 days and the other for $0.4f_c'$ at 28 days. High level loading at an early age ($0.65f_c'$ at 10 days) was conducted to identify the creep behavior of prestressed UHPC. Note that $0.65f_c'$ is the compressive stress limit at prestress transfer, according to AASHTO LRFD Bridge Design Specifications 9th edition (AASHTO 2020). The creep frames were loaded to the targeted loading using the MTS machine in the laboratory (Figure 6.50). For creep testing of Tx34-1 and Tx34-2, two cylinders for creep, two loading blocks created from half cylinders, two cylinders for associated shrinkage, and a dummy cylinder were used. A dummy cylinder was used for the height adjustment for the creep frame. However, a dummy cylinder was not used for the two creep tests for the Tx54 UHPC.

The creep frames were loaded to the targeted loading of $0.4f_c'$ or $0.65f_c'$. The strains prior to loading, at targeted loading, and immediately after unloading were measured using a data acquisition system. Immediately after unloading, elastic recovery occurred due to the elastic strain of the steel rods. As a result, the actual loading by the springs in the creep frame was lower than the targeted loading (Table 6.29). The ratio of the actual loading to f_c' was 28 to 39 percent. The elastic strains of the four creep tests are listed and range from 844 to 1026 με. Tx54 showed the high elastic strain due to the highest loading rate (39 percent). Immediately after unloading, the creep frame with the data acquisition system was stored in the humidity-controlled room at 68°F and 50 percent RH (Figure 6.51). The strains of the creep and the associated shrinkage specimens were continuously collected using the data acquisition system.

Figure 6.50. Loading a Creep Frame.

Table 6.29. Creep Loading Information.

Description	Tx34-1	Tx34-2	Tx54 Early Age Loading	Tx54
f_c'	18.9	18.0	15.9	16.9
Loading, ksi	7.6	7.2	9.9	7.8
Elastic recovery[1], ksi	2.3	2.0	4.5	1.2
Actual loading, ksi	5.3	5.2	5.4	6.6
Actual loading / f_c'	28%	29%	34%	39%
Elastic strain, με	913	844	974	1026

Note: Elastic recovery was calculated based on the difference of the strains between loading and unloading.

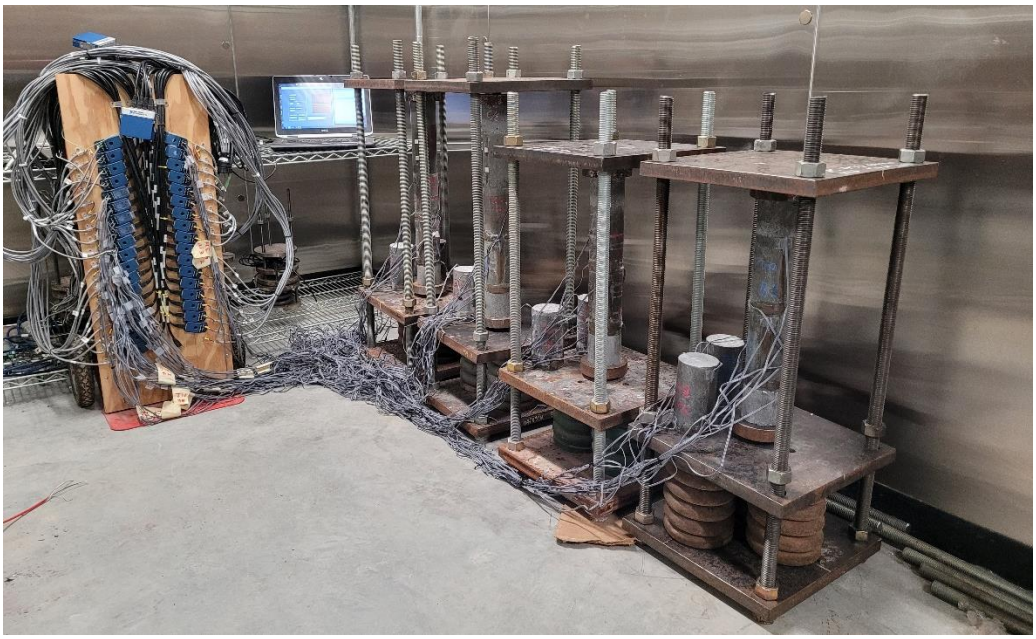

Figure 6.51. Four Creep Frames with Data Acquisition System.

6.5.1.2 Test Results

The creep strain was calculated by subtracting the strains of the associated shrinkage specimens from the strains of the creep specimens. The creep coefficient is a ratio of the creep strain to the elastic strain. Figure 6.52 and Figure 6.53 show the recorded creep strains and creep coefficients as a function of time, respectively. Appendix B shows the creep testing results of individual specimens.

The creep coefficients of Tx34-1 and Tx34-2 are 0.55 at 690 days and 0.68 at 619 days, respectively. The creep coefficients of Tx54 at early age loading at 421 days and Tx54 at 404 days are 0.56 and 0.48, respectively. The range of creep coefficient is expected to be 0.7 to 0.9 based on the proposed prediction model (discussed in Section 6.5.1.3). This creep coefficient of the developed UHPC (0.7–0.9) is smaller than 1.9 for the current AASHTO LRFD 9th edition equation in AASHTO (2020) and smaller than for matured CC, which ranges from 1.5–3.0 (Haber et al. 2018).

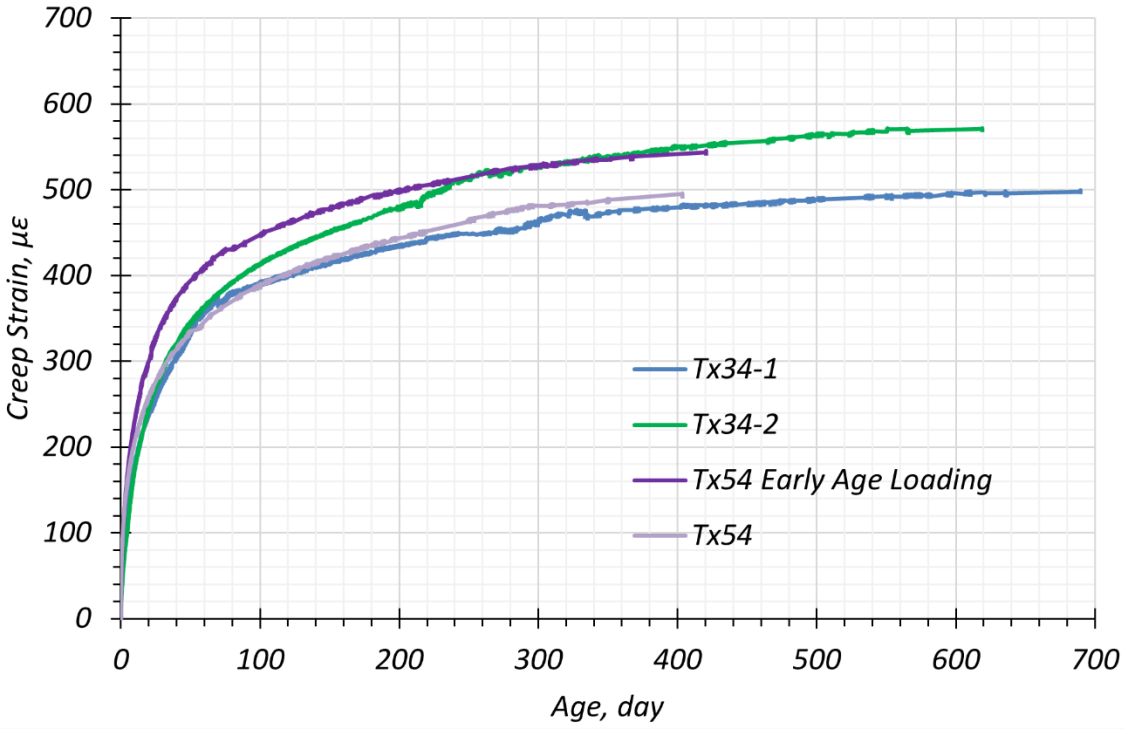

Figure 6.52. Creep Strains Results.

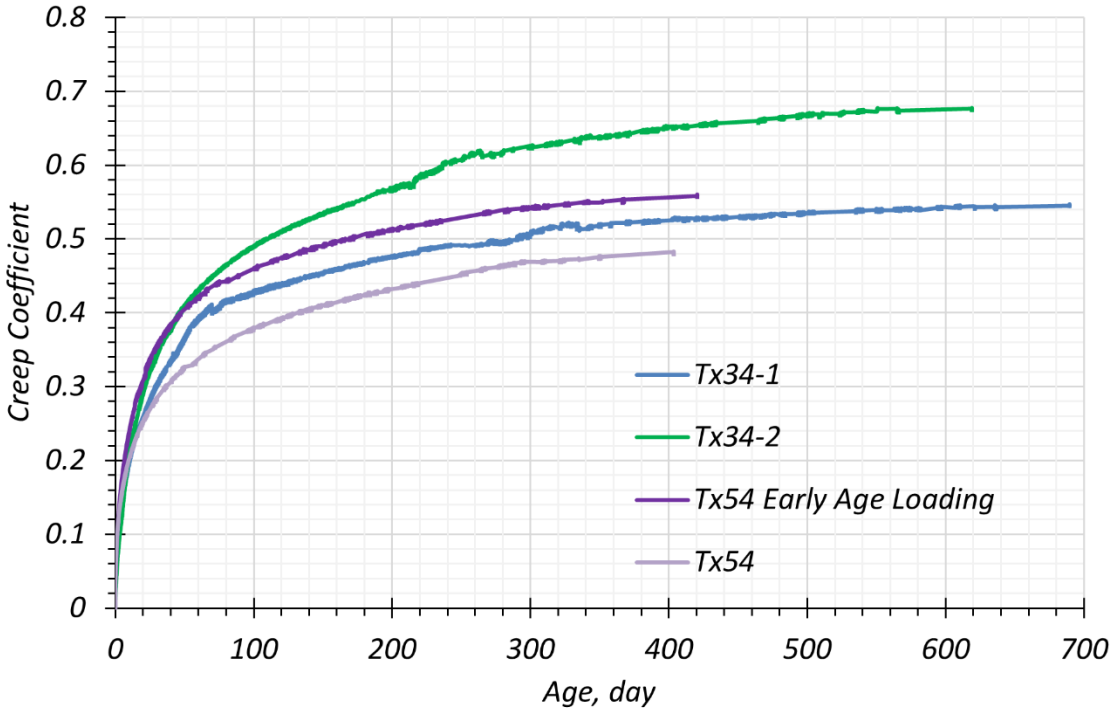

Figure 6.53. Creep Coefficient Results.

6.5.1.3 Proposed Creep Prediction Model

6.5.1.3.1 Proposed Expression and Ultimate Creep Coefficient

Based on the test results of creep and shrinkage of the developed mixture, a proposed creep model was established. This model was developed by modifying the parameters of the current AASHTO LRFD creep coefficient equation while keeping the basic framework of the LRFD equation. The current AASHTO LRFD equation is for CC to predict prestress loss, as described in AASHTO LRFD 9th edition Section 5.4.2.3 (AASHTO 2020). Note that the equations of AASHTO LRFD (2020) are limited to concrete with f'_{ci} greater than 12 ksi or f'_c greater than 15 ksi. Table 6.30 shows the proposed creep coefficient equation and correction factors that are compared to the current AASHTO LRFD equation and correction factors.

Table 6.30. Comparison of Parameters for Creep Prediction Equation.

Factor	AASHTO LRFD	Proposed Creep Model
Creep coefficient equation, $\psi_{(t,ti)}$	$\psi_{(t,ti)} = \psi_{ult} K_{hc} K_f K_s K_{td} t_i^{-0.118}$	$\psi_{(t,ti)} = \psi_{ult} K_{hc} K_f K_s K_{td}$
Ultimate creep coefficient, ψ_{ult}	$\psi_{ult} = 1.9$	$\psi_{ult} = 0.8$
Humidity correction factor, K_{hc}	$K_{hc} = 1.56 - 0.008H$	$K_{hc} = 1.0$ or $1.12 - 0.0024H$
Strength correction factor, K_f	$K_f = \frac{5}{(1 + f'_{ci})}$	$K_f = \frac{19}{(7 + f'_{ci})}$
Size correction factor, K_s	$K_s = 1.45 - 0.13\left(\frac{V}{S}\right) \geq 1.0$	$K_s = 1.0$
Time development factor, K_{td}	$K_{td} = \frac{t}{12(\frac{100 - 4f'_{ci}}{f'_{ci} + 20}) + t}$	$K_{td} = \frac{t^{0.6}}{(8 + t^{0.6})}$
Loading age correction factor, K_L	$K_L = t_i^{-0.118}$	$K_L = 1.0$

Notes:

H = Average annual ambient RH, percent
$\frac{V}{S}$ = Volume to surface area ratio, in.
t = Time between the time of loading and the considered time for creep effect, days
t_i = The age of concrete at the loading, days
f'_{ci} = Compressive strength at loading, ksi

The ultimate creep coefficient of the developed mixture ranged from 0.7–0.9. It is lower than the ultimate creep coefficient of the current AASHTO LRFD 9th edition expression, which is 1.9. Mohebbi et al. (2022) showed the ultimate creep coefficient of eight proprietary UHPCs ranged from 0.68–1.17 when loaded at a mature age.

6.5.1.3.2 Humidity Correction Factor

All creep testing was conducted at 50 percent RH in the same humidity-controlled room for consistency. Therefore, development of a humidity correction factor was not done in this project. PCI recommended the use of 1.0 conservatively as a humidity correction factor for UHPC (eConstruct 2020). From this research, the durability testing such as RCPT, bulk and surface resistivities, and freeze-thaw resistance showed that the developed UHPC has significantly low permeability as described in Section 5.6.3. In addition, the drying shrinkage of the selected UHPC mixture accounts for less than 20 percent of total shrinkage as shown in Table 5.32. The results of the durability testing and the drying shrinkage support that it is difficult for the moisture in the air to penetrate the developed UHPC. This means that the UHPC is not significantly affected by the humidity condition.

Mohebbi and Graybeal (2022) proposed a humidity correction factor for UHPC, which is $k_{hc} = 1.12 - 0.0024H$. Figure 6.54 shows the impacts of application for this humidity correction factor on the developed creep model from this study. The practical humidity range from 30 to 80 RH was used (Al-Omaishi et al. 2009). The creep coefficients are 0.79 from the selected humidity correction factor of 1.0, 0.73 from 80 RH, and 0.83 from 30 RH at 54,750 days (150 years). The difference in the creep coefficient is -7.6 percent and +5.1 percent for 80 RH and 30 RH compared to a humidity correction factor of 1.0. Because the impact of the humidity correction factor is not significant, 1.0 was considered for the humidity correction factor in this project, consistent with the recommendation by PCI for UHPC (eConstruct 2020). However, the expression $k_{hc} = 1.12 - 0.0024H$, which is the humidity correction factor suggested by Mohebbi and Graybeal (2022), can be considered as a refinement.

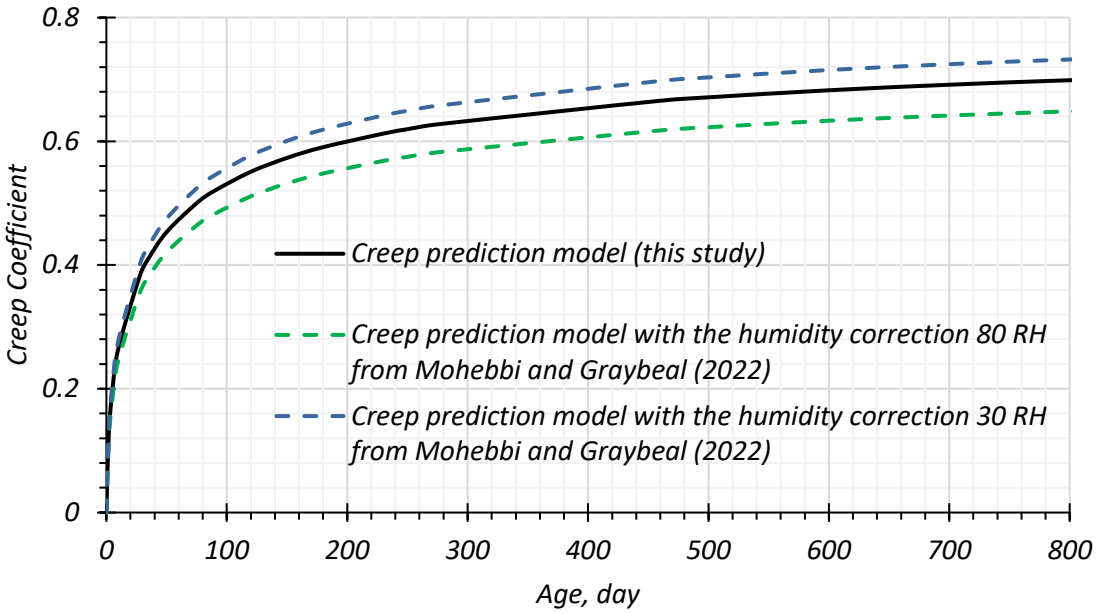

Figure 6.54. Humidity Correction Factor Impacts.

6.5.1.3.3 Size Correction Factor

Size correction factor considers the effects of humidity on the creep and shrinkage of different member thickness. Creep and shrinkage of CC tend to be lower in a thicker member than a thinner member because a thicker member has less impact from humidity conditions due to a relatively higher volume-to-surface ratio (Tadros et al. 2003). A higher volume-to-surface ratio means a lower drying impact. In this study, the creep effect of different volume-to-surface ratios of specimens was not investigated. However, the dense matrix of UHPC makes UHPC less affected by humid environments. In other words, it is difficult for water in the air to penetrate into UHPC; moreover, water evaporation from UHPC is low. Therefore, the humidity impact of the size correction factor is considered to be 1.0 conservatively. Mohebbi and Graybeal (2022) and eConstruct (2020) also recommend 1.0 for the size correction factor for UHPC.

6.5.1.3.4 Strength Correction Factor

The strength correction factor of AASHTO LRFD 9th edition is based on 4 ksi at release and 5 ksi at service. The developed UHPC mixture has 12 ksi at release and 19 ksi at service. Thus, the strength correction factor was updated in the same way. The time development correction factor is established according to ACI 209R-92 (1997) and Haber et al. (2018), as shown in

Equation (6.1). For the developed UHPC mixture, 0.6 and 8 provide the best fit for parameters ψ and a, respectively.

$$K_{td} = \frac{t^{\psi}}{a+t^{\psi}} \quad (6.1)$$

where:

K_{td} = Time development correction factor

t = Time after loading, days

ψ, a = Fitting parameters

6.5.1.3.5 Loading Age Correction Factor

The loading age correction factor is applied to correct the maturity of concrete when loading is applied. For CC, loading at early age of concrete (premature concrete) causes a higher creep coefficient due to the relatively less developed strength and MOE of the concrete. However, the developed UHPC achieves high early strength gain, generally 60–70 percent of the strength of the matured UHPC within 24 hours. Thus, the loading age impact is less than CC. Figure 6.53 shows that the creep coefficient of the Tx54 UHPC specimens with early age loading (loaded at 10 days) is not higher than the creep coefficient of the other three mixtures that were loaded at 28 days. Thus, the loading age correction factor for the developed UHPC mixture is 1.0.

6.5.1.3.6 Evaluation of Creep Prediction Model

The creep coefficients from the creep testing were compared with those coefficients from the proposed prediction model in Figure 6.55. The selected creep coefficients for Tx34-1, Tx34-2, Tx54 early age loading, and Tx54 with the prediction model are 0.8, 0.9, 0.75, and 0.7, respectively (Table 6.31). The predictions match well with the results of the creep tests. For the prediction, 50 percent and 0.6 were used for H and V/S, respectively. An RH of 50 percent was used in the room in which the creep frames were stored. The ratio of volume to surface area of the 3 × 6 in. cylinder is 0.6. Table 6.29 provides the compressive strength at loading, f'_{ci}.

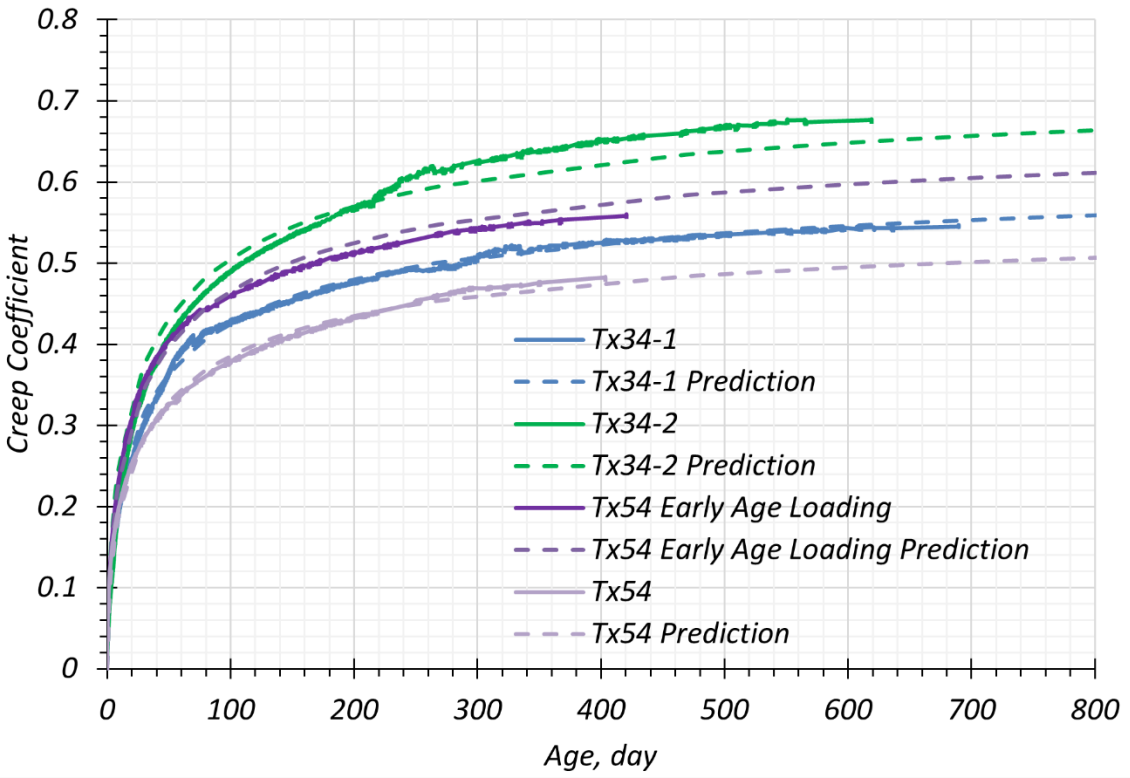

Figure 6.55. Comparison of Creep Coefficients and Prediction Model Values.

Table 6.31. Expected Creep Coefficients.

Description	Tx34-1	Tx34-2	Tx54 Early Age Loading	Tx54
Expected creep coefficient	0.8	0.9	0.75	0.7

Note: Expected creep coefficient is based on providing the best fit with the proposed prediction model.

Even though the proposed creep model for the developed UHPC mixture has limitations, the prediction of the creep coefficient matched well with the test results for the developed nonproprietary UHPC mixtures. This model can be further refined by conducting additional validation testing to further quantify the effects of humidity and loading age. In addition, data from other creep studies for UHPC can be reviewed to assess the prediction for other mixtures to provide a more general expression for UHPC.

6.5.2 Shrinkage

6.5.2.1 Shrinkage Testing

Shrinkage testing was conducted using the collected companion specimens cast at the precast plant. Two test groups were prepared with three specimens for each group. One group was for autogenous shrinkage, and the other group was for total shrinkage. Total shrinkage is defined as the sum of the drying and autogenous shrinkages. For autogenous shrinkage, three 3 × 3 × 11.25 in. prisms were sealed with aluminum foil to prevent water evaporation from the specimens; conversely, the other three specimens for total shrinkage were not sealed, as described in Section 3.3.6. The shrinkage specimens of the three girders were demolded after transporting the specimens to the lab from the precast plant. Immediately after demolding, zero readings were conducted and then stored in the humidity-controlled room with 68°F and 50 percent RH. Length change measurements of the specimens was taken every 2 days for the first week, once a week for the first month, and once a month for later ages. Table 6.32 provides the number of shrinkage samples.

Table 6.32. Experimental Plan for Shrinkage Testing.

Companion Sample	Number of Total Shrinkage Samples	Number of Autogenous Shrinkage Samples
Tx34-1	3	3
Tx34-2	3	3
Tx54	3	3

6.5.2.2 Test Results

Figure 6.56 shows the total shrinkage values of the three girders and Mix-4-PM-L. Appendix B shows the shrinkage testing results of individual specimens. The total shrinkage values of the specimens cast at the precast plant show a similar trend to the shrinkage values of the laboratory-made specimens (Mix-4-PM-L) except for Tx34-2, which is slightly lower for approximately the first 8 months. Figure 6.56(b) shows the autogenous shrinkage results. The difference between the total and autogenous shrinkage at the last readings ranges from 70–111 με.

Figure 6.57 shows the weight loss of the shrinkage specimens. The total shrinkage group has an approximately 0.45–0.62 percent weight loss, whereas the autogenous shrinkage group has 0.10–

0.42 percent weight loss. The weight loss results of all the specimens are similar, except Tx34-2 shows some differences similar to the total and autogenous shrinkage measurements.

The ultimate shrinkage value is expected to be approximately 700 με as per the test results. Mix-4-PM-L shows that the total shrinkage has negligible increase after 400 days. The expected ultimate shrinkage value (700 με) is greater than 480 με of the current AASHTO LRFD 9th edition equation according to AASHTO (2020) because there is a large amount of fine materials, such as silica fume, in the UHPC mixture in comparison to CC, as discussed in Section 4.5.1.1.1, 4.5.2.1.4, and 5.6.2.7.

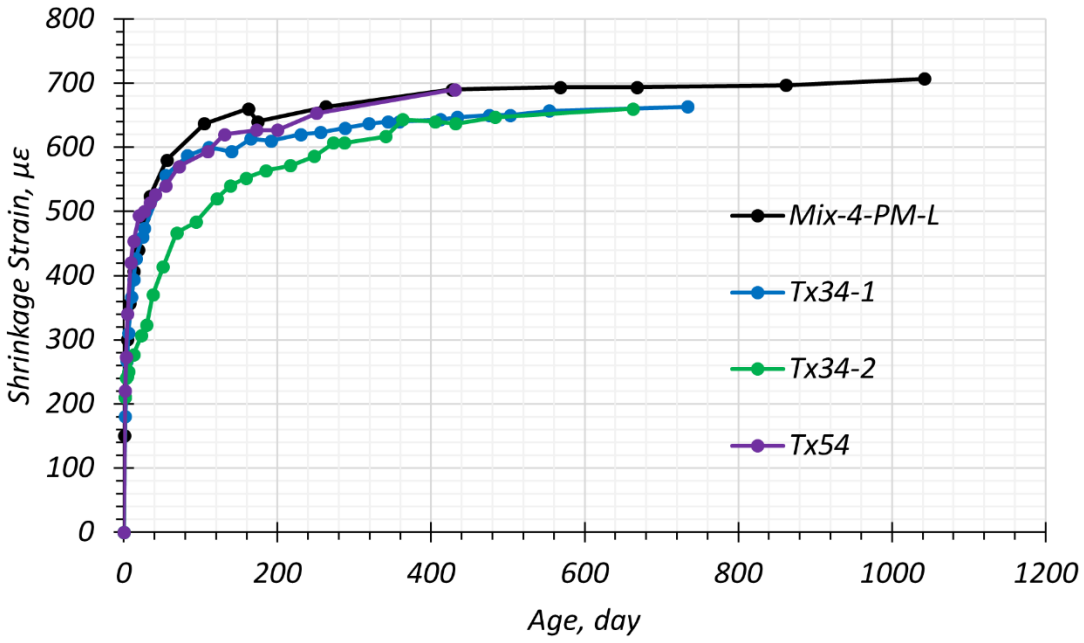

(a) Total Shrinkage

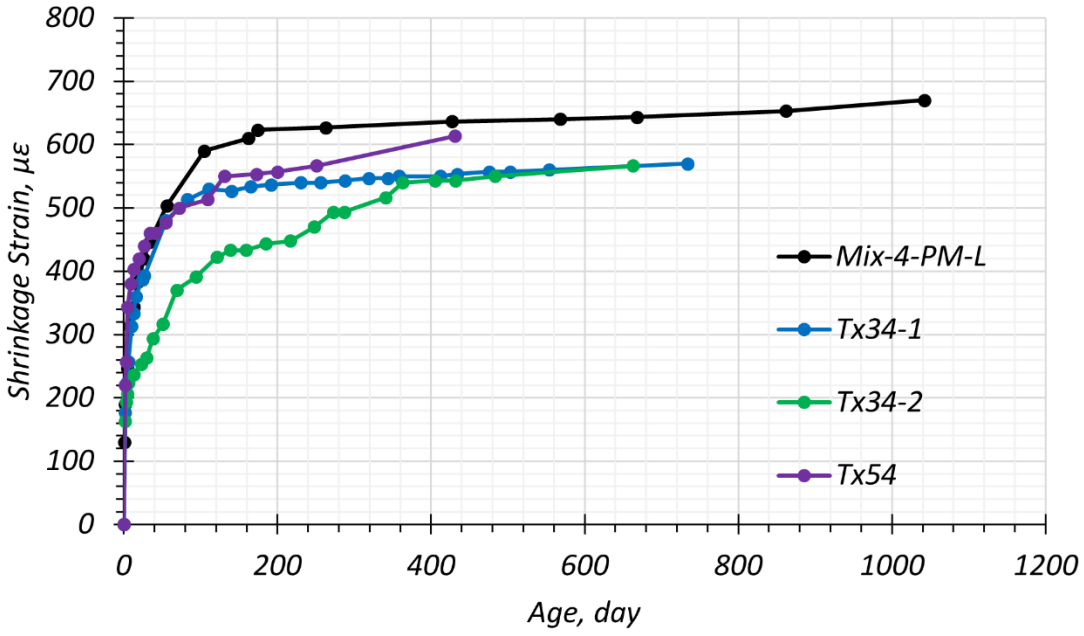

(b) Autogenous Shrinkage

Figure 6.56. Shrinkage of Companion Specimens.

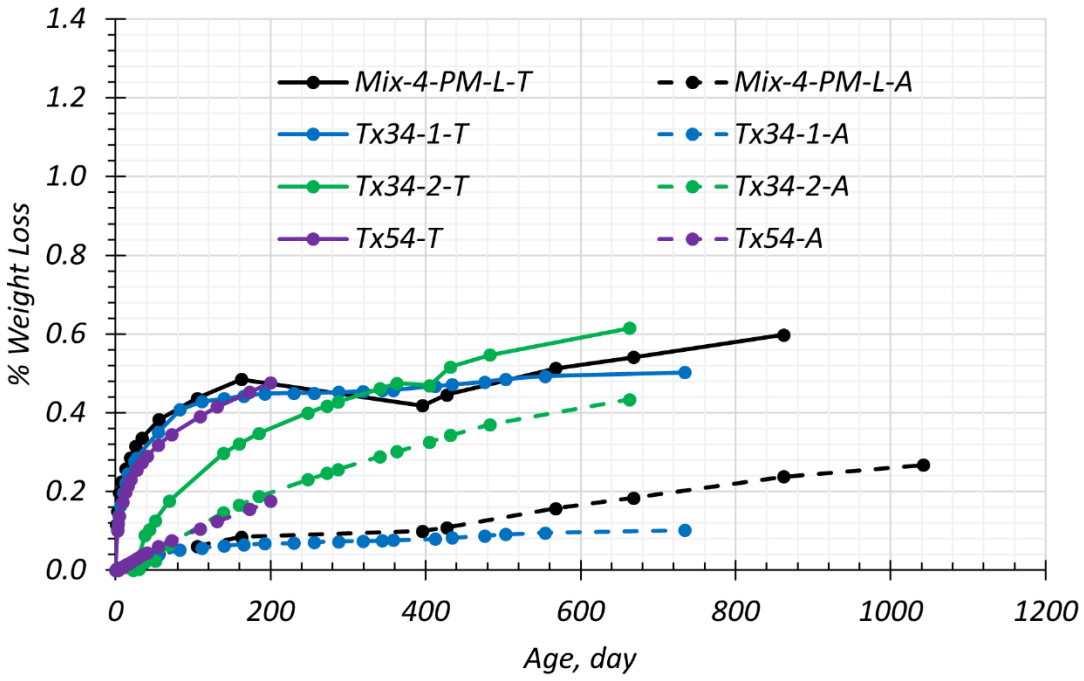

T: total shrinkage
A: autogenous shrinkage

Figure 6.57. Weight Loss of Companion Specimens.

6.5.2.3 Proposed Shrinkage Prediction Model

A proposed shrinkage model was developed based on the shrinkage test results of the plant-made UHPC. This model was developed using the existing framework of the current AASHTO LRFD shrinkage strain equation described in AASHTO LRFD 9th edition Section 5.4.2.3 (AASHTO 2020) and modifications for the UHPC application. Table 6.33 shows the proposed shrinkage equation and correction factors compared to the current AASHTO LRFD 9th edition equation and factors. Like creep prediction, the equations of AASHTO LRFD (2020) are not applicable for concrete with f'_{ci} and f'_c greater than 12 and 15 ksi, respectively. The proposed correction factors, which are humidity, strength, size, and time development correction factors, are the same as the correction factors for the proposed creep model. A value of 700 με is considered as the ultimate shrinkage strain in the prediction equation for the developed UHPC, whereas the AASHTO LRFD 9th edition equation has 480 με as the ultimate shrinkage strain.

Table 6.33. Comparison of Parameters for Shrinkage Prediction Equation.

Factor	AASHTO LRFD	Proposed Shrinkage Model
Shrinkage strain, ε_{sh}	$\varepsilon_{sh} = 480 \times 10^{-6} K_{hs} K_f K_s K_{td}$	$\varepsilon_{sh} = 700 \times 10^{-6} K_{hs} K_f K_s K_{td}$
Humidity correction factor, K_{hs}	$K_{hs} = 2 - 0.014H$	$K_{hs} = 1 + 0.2(1 - 0.014H)$
Strength correction factor, K_f	$K_f = \frac{5}{(1 + f'_{ci})}$	$K_f = \frac{19}{(7 + f'_{ci})}$
Size correction factor, K_s	$K_s = 1.45 - 0.13\left(\frac{V}{S}\right) \geq 1.0$	$K_s = 1.0$
Time development factor, K_{td}	$K_{td} = \frac{t}{12(\frac{100 - 4f'_{ci}}{f'_{ci} + 20}) + t}$	$K_{td} = \frac{t^{0.6}}{(4 + t^{0.6})}$

Notes:

H = Average annual ambient RH, percent
$\frac{V}{S}$ = Volume to surface area ratio, in.
t = The age of concrete, days
f'_{ci} = Compressive strength at loading, ksi

6.5.2.3.1 Humidity Correction Factor for Shrinkage

To better understand the impact of humidity on shrinkage of the nonproprietary UHPC mixture, the drying shrinkage results from the laboratory testing of several developed UHPC mixtures were reviewed (see also Section 5.6.2.7). Drying shrinkage is calculated by subtracting the autogenous shrinkage from the total shrinkage. Figure 6.58 shows the proportions of drying shrinkage of Mix-1a, Mix-2a, Mix-3a, and Mix-4a.

The shrinkage test results of Mix-1a, Mix-2, and Mix-4a showed that 19–22 percent of the total shrinkage value is related to drying shrinkage, which matches the findings from Mohebbi et al. (2022). The drying shrinkage of Mix-3a is 30 percent of the total shrinkage because Mix-3a has a relatively low dense matrix due to the lower silica fume content. As a result, it has proportionately less autogenous shrinkage and more drying shrinkage. Overall, the drying shrinkage accounts for approximately 20 percent except in Mix-3a. These results indicate implicitly that UHPC mixtures are less affected by external humidity conditions due to low permeability than CC. When considering that shrinkage of CC is primarily due to drying shrinkage, the humidity impact on the UHPC mixtures was assumed to be approximately 20 percent of the impact on the CC based on the drying shrinkage proportions of the developed UHPC mixtures. Therefore, the humidity impact of the humidity correction factor is reduced by applying a factor of 0.2. This assumption needs to be validated by investigating the impact of humidity on the UHPC mixture with different humidity

environments. However, that is out of the scope for this research project and can be considered for future study.

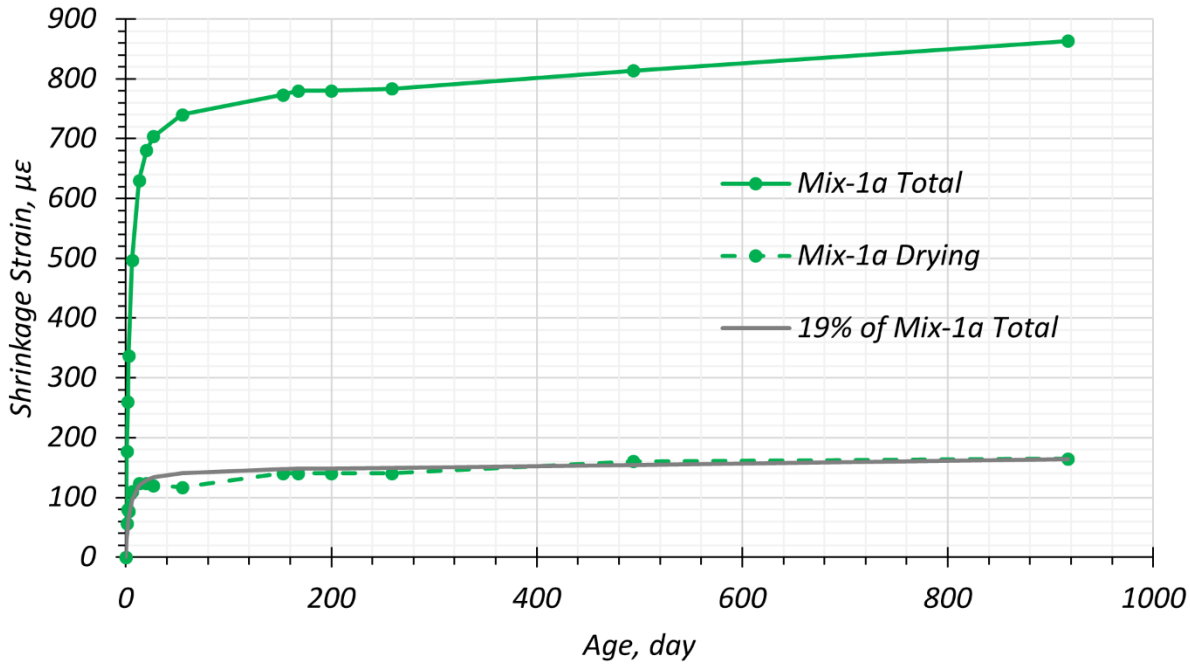

(a) Proportion of Drying Shrinkage of Mix-1a

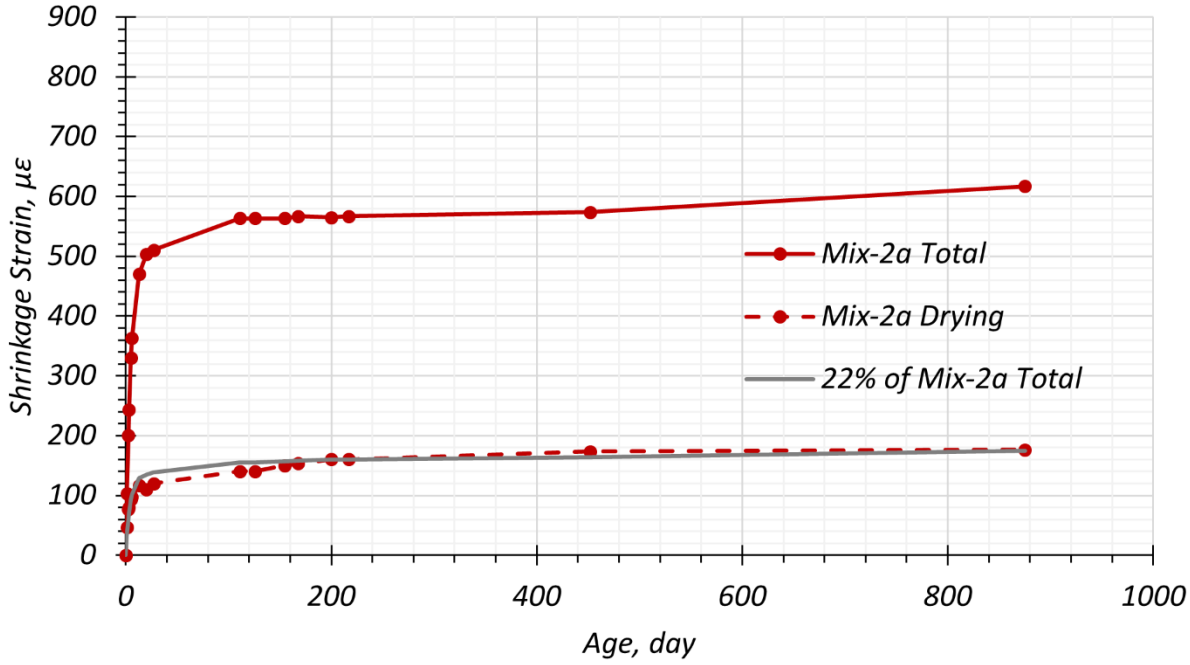

(b) Proportion of Drying Shrinkage of Mix-2a

Figure 6.58. Proportion of Drying Shrinkage of Four Developed Mixtures.

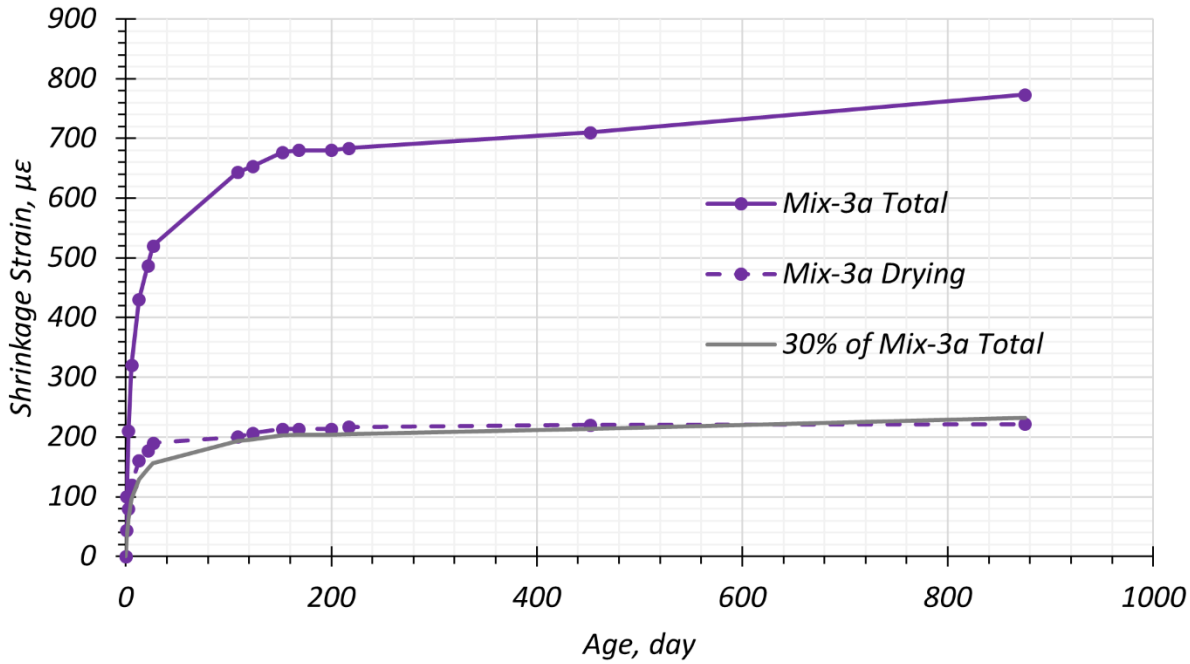

(c) Proportion of Drying Shrinkage of Mix-3a

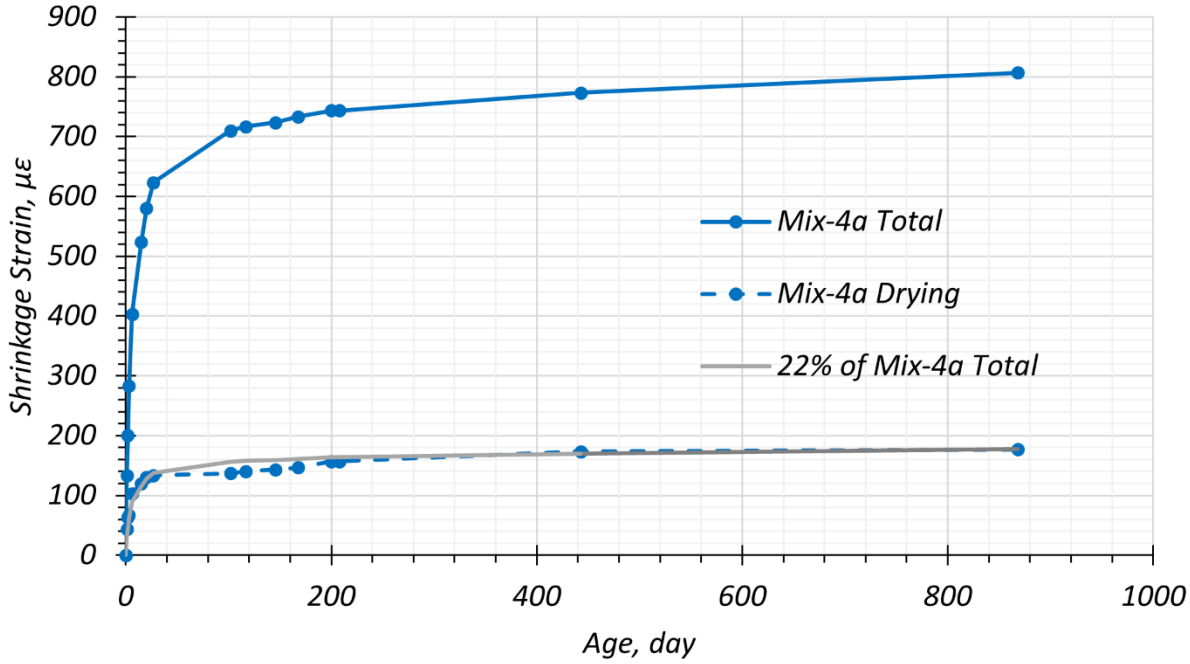

(d) Proportion of Drying Shrinkage of Mix-4a

Figure 6.57. Proportion of Drying Shrinkage of Four Developed Mixtures (Continued).

6.5.2.3.2 Time Development Correction Factor

The time development correction factor for shrinkage is established according to ACI 209R-92 (1997) and Haber et al. (2018), as shown in Equation (6.2). For the developed UHPC mixture, 0.6 and 4.0 provide the best fit for parameters α and f, respectively.

$$K_{td,s} = \frac{t^{\alpha}}{f + t^{\alpha}} \tag{6.2}$$

where:

$K_{td,s}$ = Time development correction factor for shrinkage

t = Time after loading, days

α, f = Fitting parameters

6.5.2.3.3 Evaluation of Shrinkage Prediction Model

Figure 6.59 shows a comparison between the shrinkage test results and the prediction model. The proposed model shows a good prediction of shrinkage of the developed UHPC. For the prediction, 50 percent, 0.66, and 12.5 ksi were used for H, V/S, and f'_{ci}, respectively. An RH of 50 percent was used in the curing room for the shrinkage specimens. The ratio of volume to surface area of the shrinkage specimen is 0.66. The strength at release is 12.5 ksi based on the compressive strength at release of Tx34-1 and Tx34-2.

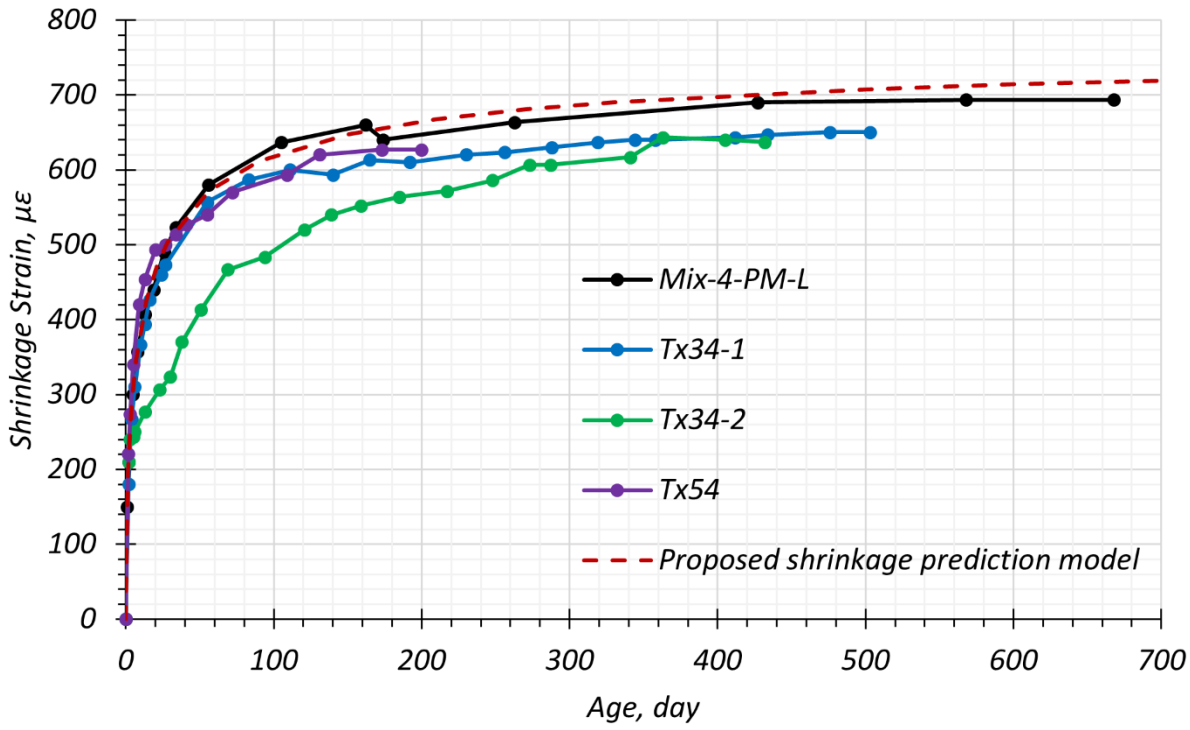

Figure 6.59. Shrinkage Results with Proposed Shrinkage Prediction Model.

6.6 SUMMARY

The fabrication of the three precast, pretensioned UHPC girders at the precast plant was successfully conducted. The twin-shaft mixer of the plant provided sufficient power. As a result, turnover time was shorter than in the laboratory. The quality of the fresh UHPC produced at the plant and at the laboratory was comparable. Multiple batches with separate placements were successfully performed without a cold joint issue. However, the formation of elephant skin on the UHPC surface can occur quickly, making it critical to cast batches as closely as possible. This practice provides lessons learned on how to mix UHPC using the existing facilities. The following factors were observed from the surface evaluation of the three girder specimens:

- The transition lines observed were reflective of the low flowability of the first batch of Tx34-1. Hairline cracks were more concentrated in the half with the minimum reinforcement and less dense in the half without any shear reinforcement. There was no cold joint formation between batches.

- The Tx34-2 girder had a smooth surface with some microtexture. The transition lines were not as distinct as Tx34-1 along the sides, and any cracks observed due to the force in the hold-down points closed after the prestress release.
- Tx54 showed smooth transition lines between batches and more pronounced surface texture along the side faces of the girder. Some cracks with widths ranging from 0.01 in to 0.1 in. were observed in these patches of surface texture. These cracks were observed to be superficial and were most likely due to the presence of residual concrete on the forms and the temperature difference between the UHPC and the forms.

With respect to the hardened properties, the following conclusions were drawn:

- The design compressive strength was achieved for release and service. The UHPC for the Tx34-1 and Tx34-2 girders showed comparable strength values. The compressive strength of the Tx54 UHPC showed slightly lower strength, but it may be due to errors from the sample preparation and the relatively low flow spread values. Verification of the Tx54 compressive strength was conducted at the laboratory using the same materials as at the plant. The strength results were comparable to Tx34-1 and Tx34-2.
- Both the MOE and Poisson's ratio were comparable to the results of the lab mixes and were similar across all three girders. The predictions for the MOE served as a lower bound for the measured results. The MOE of the developed UHPC ranged from 6000–7500 ksi and was higher than that of CC, which ranged from 2000–6000 ksi. Poisson's ratio measured (0.20–0.33) and was higher than for CC (0.11–0.21).
- The uniaxial tensile strength of Tx34-1 and Tx34-2 was quite low (0.31–0.62 ksi), with a nonuniform fiber distribution in the samples. These values were lower than the previously tested laboratory mixes and trial mix. The uniaxial tensile strength of Tx54 was quite high (0.8–1.2 ksi) and comparable to the lab mixes. The influence of the tensile strength on the shear performance of the girder was observed during the full-scale testing, and the details are reported in the Volume 2 report. The measured tensile strength of the developed mix met the PCI (eConstruct 2020) requirements for the Tx54 girder.
- Both the first peak crack strength and ultimate flexure strength of the companion specimens was higher than or equal (1.8–2.1 ksi) to the PCI (eConstruct 2020) requirements for most of the specimens. The ductility requirements set by PCI (eConstruct 2020) and ACI

Committee 318 (2019) are not met for the post-cracking phase of the stress-strain plot, which may be due to the lower volume of fibers used in the developed mix. There was consistent ductile behavior exhibited by Tx54 specimens, while there were variations in the post-cracking strength of companion specimens of Tx34-1 and Tx34-2 girders.

The long-term hardened properties such as creep and shrinkage were studied using the companion specimens of the three girders. The following key findings are noted:

- Creep coefficient (0.7–0.9) of the developed UHPC was lower than the creep coefficient of CC (1.5–3.0).
- The shrinkage value (700 με) was higher than that of CC (480 με).

Based on the test results, prediction models for creep and shrinkage were proposed for prestress loss estimation of the developed nonproprietary UHPC mixture.

7 NONDESTRUCTIVE EVALUATION OF GIRDERS

7.1 INTRODUCTION

This chapter documents nondestructive techniques performed on the Tx34-1, Tx34-2, and Tx54 girder specimens to determine the material properties of UHPC and identify potential discontinuities in the girders. To this end, the technical inspection began with the collection of infrared thermography images followed by a GPR survey. Ultrasonic testing, including UPV and ultrasonic tomography, was conducted at the final stage of this evaluation. After an analysis of the collected data, the findings of this investigation are summarized and reported on in detail at the end of this chapter.

7.2 DESCRIPTION OF THE TESTING EQUIPMENT

This section will briefly describe nondestructive techniques conducted in this study. The testing equipment required for the technical inspection is also documented.

7.2.1 Passive Infrared Thermography

Infrared thermography is a unique and reliable approach to determine surface defects, including fine cracks on concrete structures. This technique is also referred to as passive infrared thermography in contrast to the active approach, which requires an external heat source to raise the sample's temperature before the beginning of the thermal imaging measurements. The equipment needed for the passive infrared thermography are an infrared (IR) camera and a computer to visualize the recorded images. Figure 7.1 shows a simplified diagram that describes how the IR camera produces thermal images based on heat radiation emitted from the concrete surface. As shown in the figure, a germanium lens provided in the camera absorbs the visible light but transmits the infrared light. Then, an IR detector (either thermopile, bolometer, or pyroelectric) converts the thermal energy to a relative electronic signal that can be projected onto a thermogram. The results are then transferred to a display screen, upon which the final image will be color coded according to the emissivity of the object material.

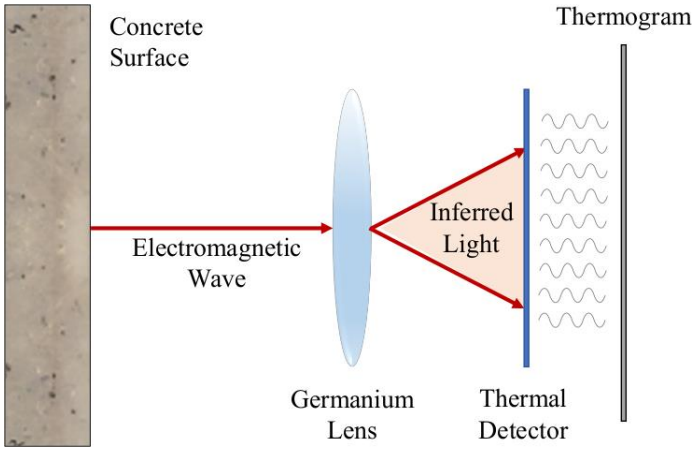

Figure 7.1. Schematic View of Thermal Imaging with IR Camera.

7.2.2 Ground Penetrating Radar

Ground penetrating radar is commonly used to obtain the location of rebars and even air gaps and large voids in concrete. Although GPR is not an effective approach to obtain defects in post-tensioned systems where strands are embedded in the metallic ducts, it is a promising technique to detect voids, particularly those surrounding strands in plastic ducts. The radar-based evaluation technique is also capable of detecting steel bundles and air gaps in pretensioned systems (Hurlebaus et al. 2016). Figure 7.2 represents a schematic view of a GPR system during operation in which electromagnetic waves have been emitted by a transmitting antenna and propagated through the material; then, the reflection signal received from an object with a different dielectric constant in contrast to the medium has been integrated. After recording the travel time of the signal, the results are converted to distance to estimate the depth of the radar penetration. The equipment needed for GPR include an antenna and a computer for visualizing the signals.

7.2.3 Ultrasonic Pulse Velocity

Ultrasonic pulse velocity is a powerful nondestructive technique used to assess the quality of concrete structures that can be performed both in the laboratory and in the field. During performance of UPV, an operator records the travel time of sound waves in the concrete specimen and consequently determines the velocity of the signals for all points of interest. The equipment required for UPV include a pulse generator capable of producing high-frequency signals (typically between 0.1 MHz to 15 MHz), a transmitter and receiver transducers, an oscilloscope to visualize the sound waves, and a couplant (ultrasonic gel) to reduce the air gap between transducers and the

concrete surface. Please note, it is common to send longitudinal sound waves (transmission technique) in the concrete bulk to evaluate the quality of the concrete; however, the operator may also decide to use shear waves (reflection technique) if there is difficulty accessing the other side of the concrete structure. Figure 7.3 designates the principle of UPV, wherein a longitudinal wave is sent from the transmitter transducer and is collected by the receiver.

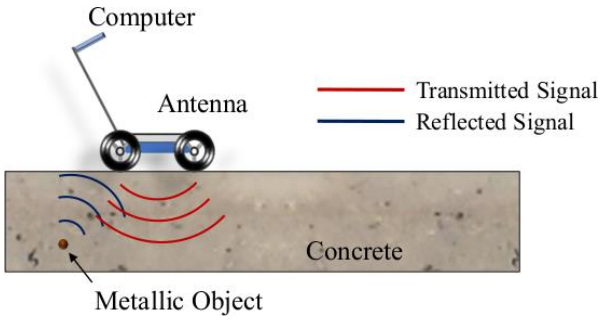

Figure 7.2. Schematic View of GPR in Progress.

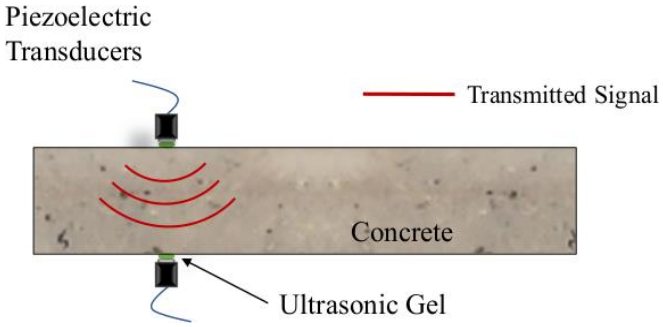

Figure 7.3. UPV—Transmitting Longitudinal Signals in Concrete.

7.2.4 Ultrasonic Tomography

In general, ultrasonic testing is a powerful technique to identify defects in concrete structures. While UPV allows only point measurements (A-Scan), ultrasonic tomography provides scanning of a large area of the concrete surface (B-Scan—two-dimensional data parallel set of A-Scan, C-Scan—two-dimensional data perpendicular set of A-Scan, and S-Scan—two-dimensional data sector set of A-Scan). An ultrasonic tomographer works based on the impact echo technique in which multiple transducers send waveguide-phased arrays into the concrete specimen. The instrument receives the reflected signals simultaneously and converts them into two-dimensional tomography images. Figure 7.4 demonstrates a tomographer in which compression waves are introduced in the concrete specimen. In addition to longitudinal waves, a tomographer can also launch shear waves when each sensor sends the signals into the sample with a delay compared

with the onset activation of the neighboring transducer. Ultrasonic tomography aids in detecting a variety of defects, including cracks, air gaps and voids, and even concrete delamination. It is also capable of obtaining the location of reinforcement and determining the thickness of unsound concrete.

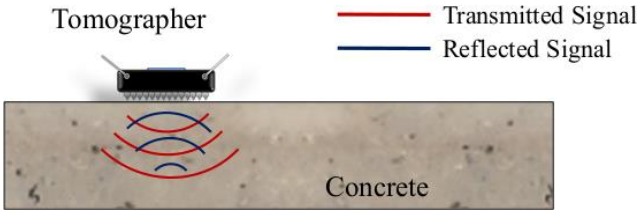

Figure 7.4. Ultrasonic Tomographer—Sending and Receiving Signals.

7.3 EXPERIMENTAL PROGRAM

This section describes the procedure used to conduct nondestructive testing on all three UHPC girders. The examinations of the Tx34-1, Tx34-2, and Tx54 girder specimens began with passive infrared thermography and GPR prior to ultrasonic testing. This work arrangement was made to remove the reflection of the ultrasonic gel in thermal images; moreover, both passive infrared thermography and GPR were performed in a shorter time period than the ultrasonic evaluation of the concrete girders. Since small scanning increments are needed during the ultrasonic tomography, it was decided that the nondestructive technique would be performed following the completion of UPV. Figure 7.5(a) and Figure 7.5(b) show the Tx34-1 girder specimen placed in the High-Bay Structural and Material Laboratory at Texas A&M University before the conducting of nondestructive evaluations, while recording of time travel measurements during the performance of ultrasonic testing are depicted in Figure 7.5(c) and Figure 7.5(d).

(a) South View

(b) East View

(c) UPV in Progress

(d) Ultrasonic Tomography in Progress

Figure 7.5. Nondestructive Evaluation on the UHPC Girders.

7.3.1 Passive Infrared Thermography

Thermography imaging was completed on the south elevation of Tx34-1, Tx34-2, and Tx54 and continued on the other face of the girders (north) before construction of the deck began. During the nondestructive evaluation, an operator positioned an FLIR T640 thermal imaging camera 6 ft from the surface of the concrete web. The constant emissivity set on the IR camera was limited to 0.95. The reflected temperature was recorded at 70°F within a range of 65°F to 75°F. The RH and atmospheric temperature registered by the camera was on average 50 percent and 70°F. Thermal images were taken every 26 in., starting from the west and continuing to the east of the UHPC girders. Figure 7.6 shows the Tx54 girder specimen after completing the thermal imaging recording.

Figure 7.6. Tx54 after Completion of Thermal Imaging Recording.

7.3.2 Ground Penetrating Radar

The technical inspection began with developing a grid pattern on the web, the inclined planes of the top flange, and the bottom flange of all UHPC girders. These grids were used during the collection of GPR profiles and during thermal imaging and ultrasonic tomography scanning. The horizontal grid lines were 2 in. center-to-center (13 grid lines in total) and were marked on both the south and the north of the UHPC girders. Some areas on the south elevation of the UHPC girders were left unmarked for the installation of strain gauge sensors, LVDTs, and other instrumentation equipment. The total length of the Tx34-1 and Tx34-2 girder was divided into a 4-ft grid system (lengthwise), which was used during GPR scanning of the concrete surface. Meanwhile, because the depth of Tx54 was greater, the horizontal grid lines increased to 27 over the girder height.

The grid system was updated on both sides of the Tx54 girder where the whole length was divided into two halves. After marking the grids, a GSSI StructureScan Mini HR was used to develop GPR profiles. The procedure was completed in a series of concrete surface scanning along the marks in both the longitudinal and transverse directions. The depth of the penetrating radar in UHPC differs from normal concrete because the velocity of the radar waves in UHPC was estimated to be slightly less than 3.0 in./ns. The frequency of the antenna was 2.6 GHz. The radar evaluation of Tx34-1, Tx34-2, and Tx54 was performed on the top and bottom flanges and the webs of the girders.

7.3.3 Ultrasonic Pulse Velocity

The purposes of UPV are to identify the quality of the UHPC girders, such as uniformity of concrete, and, if possible, to determine material properties of the concrete structure. Therefore, it was decided to select three locations, including near the ends and midspan (middle) of Tx34-1 and Tx34-2. In this report, these locations are referred to W (representing the west), M (the middle), and E (the east side) of the UHPC girders. Additionally, the south and the north side of the girders are denoted by S and N, respectively. Note that the girders spanned from east to west in the laboratory.

Figure 7.7 designates locations where UPV was performed on all three UHPC girders. Because the length of the Tx54 girder was greater than the other two girder specimens, UPV was also conducted at an additional two locations, which were at the quarters (QW and QE) of the girder span (in addition to the east, the middle, and the west). It was also decided to increase the locations of UPV measurements during the ultrasonic cross scanning of Tx54 because the height of the girder web was 20 in. higher than Tx34-1 and Tx34-2. Pulser/Receiver Panametrics 5072PR was employed in transmission mode to transmit and receive signals. The damping resistor used during UPV was 200 Ω, and the pulse repetition frequency was set at 500 Hz. The cutoff points for low and high pass filters were adjusted to 10 MHz and 1 MHz, respectively. Digital storage oscilloscope Tektronix-TDS 3034 was used to visualize time-variant signals.

In contrast to the compelling results from the probes placed on the sides of each concrete web (cross scanning), no signal was detected from the top flange due to the possible attenuation of sound propagating as a result of the existence of R-bars and strands. The inclined plane and surface roughness of the concrete may also cause the failure of UPV to track down the transmitted signal. Similarly, no signal was observed from the probes positioned across the girder at the bottom flange because of the signal attenuation. However, a strong signal was recorded from the bottom flange, where one probe was placed at the side and the other positioned at the inclined plane (Figure 7.8(b) and Figure 7.9(b)). UPV was repeated three times at all target points to ensure the consistency and the precision of the recordings.

Ultrasonic surface scanning was also performed on all three girders at the same locations that cross scanning was performed to estimate the steel fiber distribution in UHPC both in the horizontal and

vertical directions. Figure 7.8 and Figure 7.9 show the location of transducers during ultrasonic surface measurement on Tx34-1, Tx34-2, and Tx54. The probes were placed within 12 in. horizontally and 10 in. vertically along the girder webs, and this procedure was followed on both the south and the north elevations of the girders.

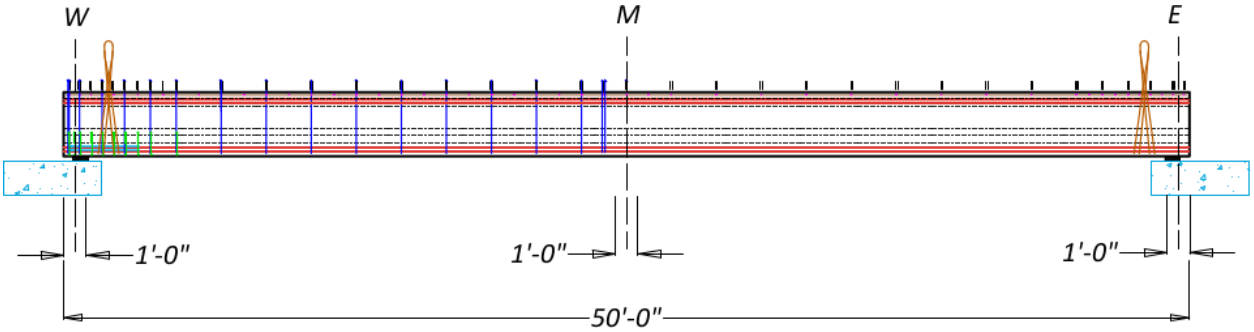

(a) Tx34-1

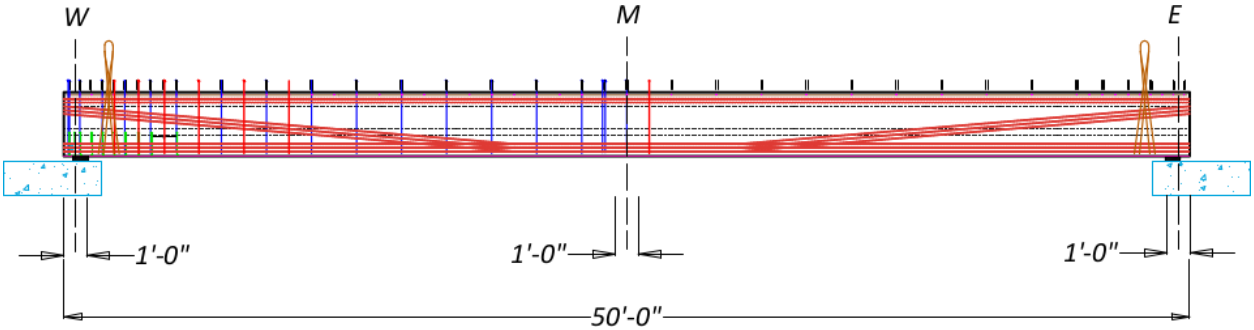

(b) Tx34-2

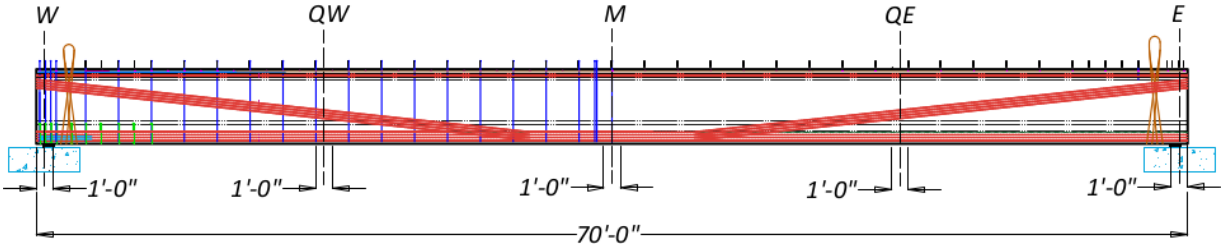

(c) Tx54

Figure 7.7. Position of Transducers during Performance of UPV.

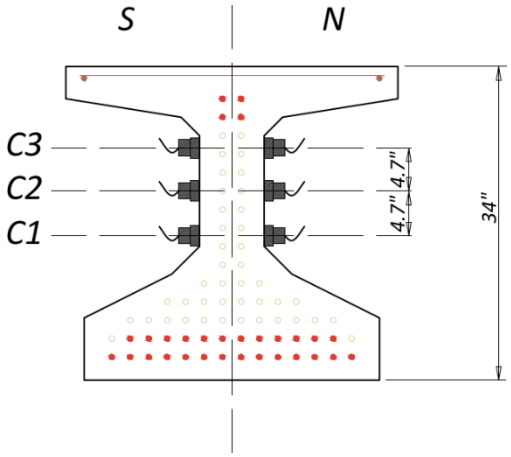

(a) Cross Scanning on Girder Web

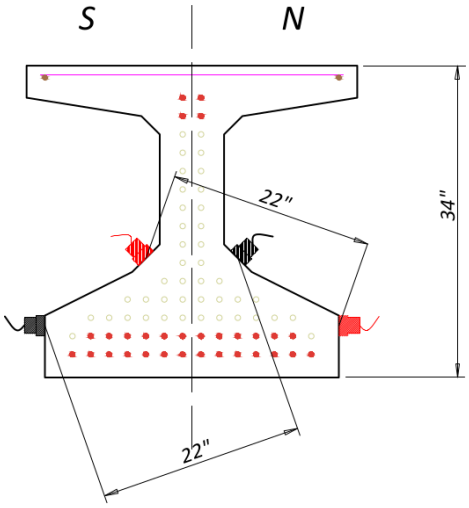

(b) Cross Scanning on Bottom Flange

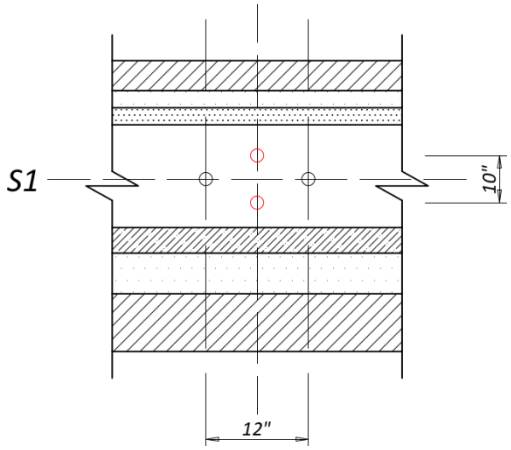

(c) Surface Measurements on Web—Elevation View

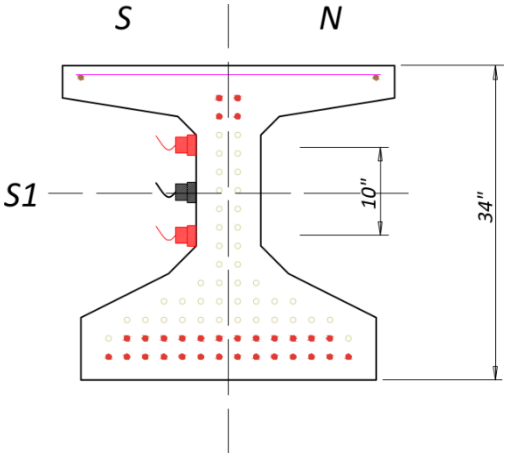

(d) Surface Measurements on Web—Section View

Figure 7.8. Schematic View of Transducer Positions on Tx34-1 and Tx34-2.

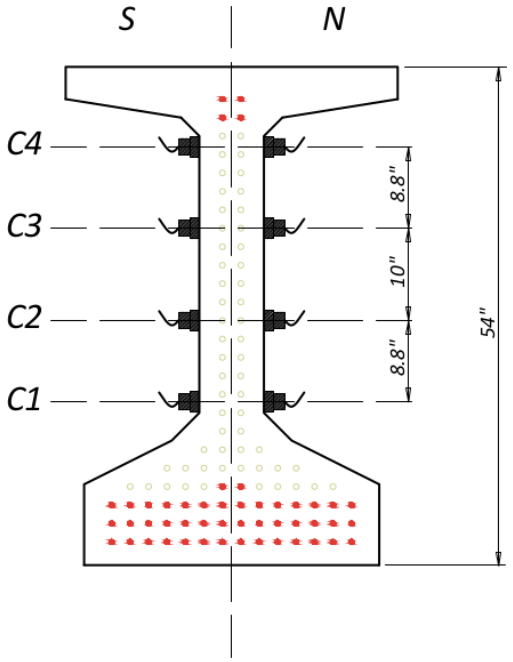

(a) Cross Scanning on Girder Web

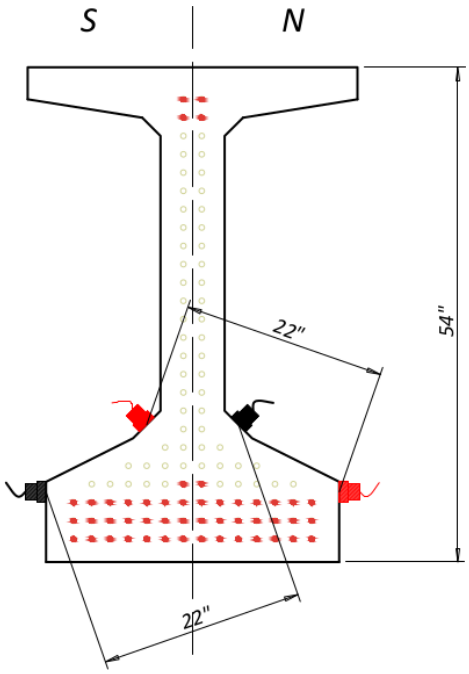

(b) Cross Scanning on Bottom Flange

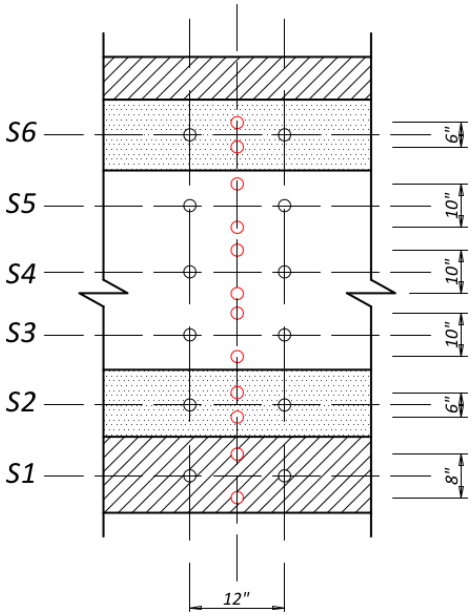

(c) Surface Measurements on Web—Elevation View

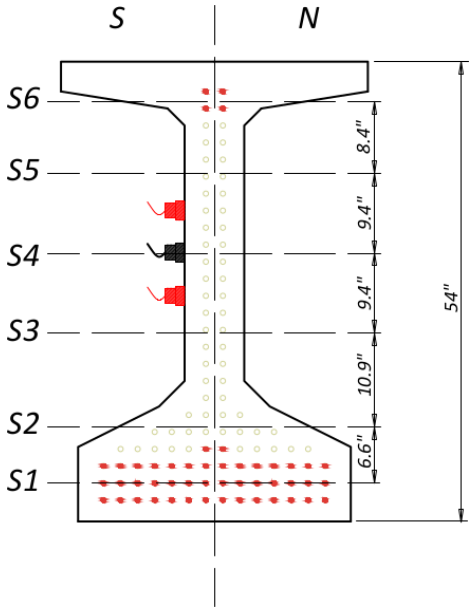

(d) Surface Measurements on Web—Section View

Figure 7.9. Schematic View of Transducer Positions on Tx54.

7.3.4 Ultrasound Tomography

The final step of nondestructive evaluation conducted on Tx34-1, Tx34-2, and Tx54 was ultrasonic tomography imaging. The grid pattern for the ultrasonic testing was similar to that used for GPR. The reader is referred to Section 7.3.2 for the detailing of the grid patterns used in this research

study for all three girders. A1040 MIRA portable handheld tomographer was used to develop the tomography images; the depth of the measurements was set at 19 in. and the frequency of sound waves was fixed at 50 kHz. Please note, the selected depth and the frequency of acoustic waves were sufficient for ultrasonic scanning of the UHPC girders.

An operator began the ultrasonic measurements from the east end of the girders and continued the procedure to scan the entire web and the top and bottom flanges. The scanning images were made every 2 in. along the length of the girders (the length of each segment was 2 in., as discussed in Section 7.3.2). After finishing one side of the structure, the operator repeated the same procedure to complete ultrasonic tomography imaging on the other side of the UHPC girders.

7.4 EVALUATION

This section describes the results of the analysis that was completed on collected data, including ultrasonic measurements, tomography imaging, radar scanning, and thermal imaging, of the Tx34-1, Tx34-2, and Tx54 girder specimens.

7.4.1 Infrared Thermography

The thermal images collected from passive infrared thermography do not show any visible discernible defect on Tx34-1, Tx34-2, and Tx54 except a longitudinal transition line between batches at the top corner of the web that was detected on the west side of Tx54. Figure 7.10 shows both the digital and the thermal images recorded by the FLIR T640 thermal imaging camera for the mentioned defect on Tx54. The infrared images revealed that the crack not only developed on the web of the UHPC girders but also grew on the concrete profile (transverse direction), which was not easily observed in the digital images. Rough surfaces were occasionally detected at a few locations on all three UHPC girders. The surface damage was not considered as severe and may have occurred during removal of the formwork. The surface evaluation of the three girder specimens at the precast plant immediately after demolding is discussed in Section 6.2.2.3, 6.2.3.3, and 6.2.4.3 for Tx34-1, Tx34-2, and Tx54, respectively. It is expected that they will not affect the structural and material durability of the UHPC girder. Figure 7.11 shows some of the surface roughness detected on Tx54.

Spalling of the concrete cover was detected in thermal images recorded at the bottom corner of the web of Tx34-1 (Figure 7.11(e)). Another location where this type of concrete damage was observed was at the east end of the Tx54 on the top flange (Figure 7.11(f)). These defects were observed during formwork removal. The damage was not significant, and no other spalling of the UHPC was found after studying the results of passive infrared thermography for all three girders.

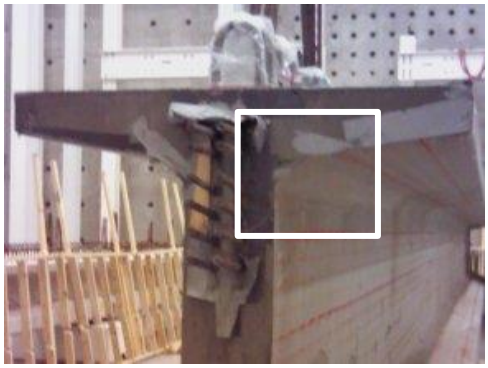

(a) FLIR Digital Image

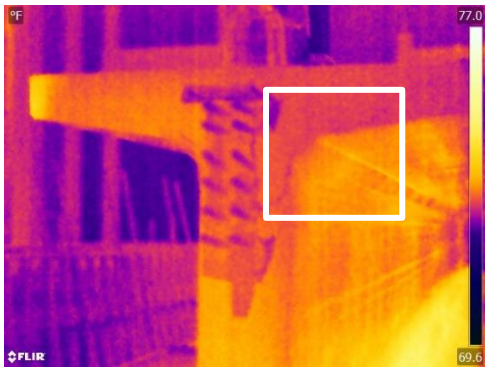

(b) FLIR Infrared Image

(c) FLIR Digital Image—South-west

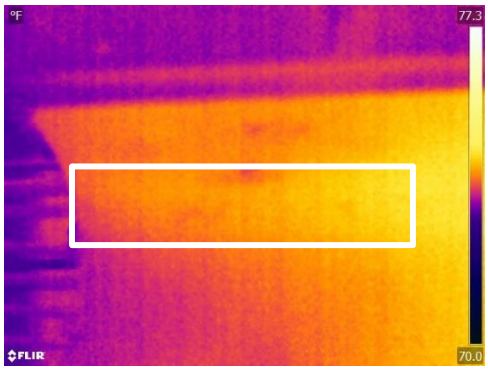

(d) FLIR Infrared Image—South-west

Figure 7.10. Thermal Image of a Longitudinal Batch Transition Line at the West End of Tx54.

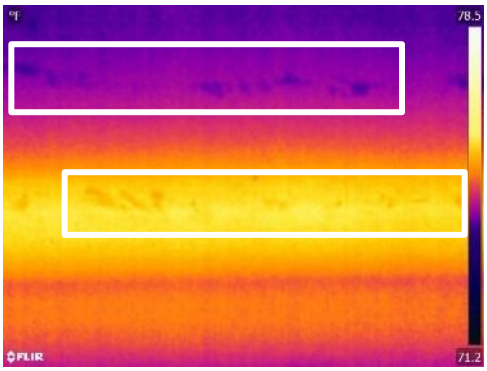

(a) Rough Surface on Web of Tx54

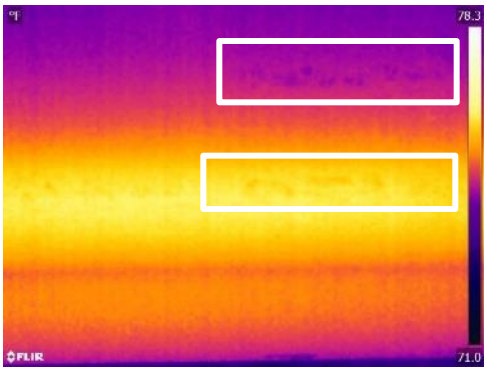

(b) Rough Surface on Web of Tx54

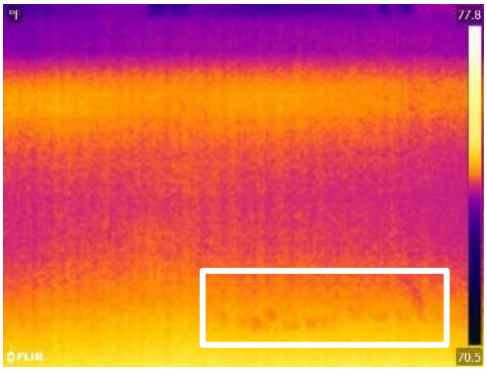

(c) Rough Surface on Bottom Flange of Tx34-2

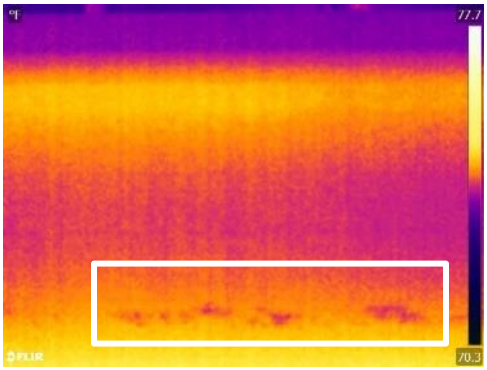

(d) Rough Surface on Bottom Flange of Tx34-2

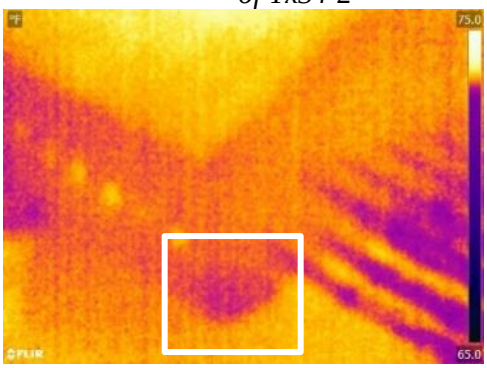

(e) Concrete Spalling Tx34-2

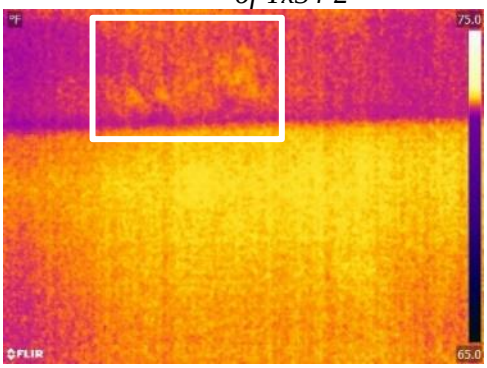

(f) Concrete Spalling Tx54

Figure 7.11. Mild Surface Defects Detected on UHPC Girders.

In addition to these cases, a longitudinal crack was captured on the FLIR digital images (Figure 7.12), but it was not visible in the thermal images, perhaps due to lighting reflection and shadow of the top flange of the UHPC girder. The crack developed on the left side of the web of Tx34-2, 10 ft from the east end of the girder. See Section 7.3.2 for more detail. Based on a review of the thermal images documented in this work, no signs of deterioration on the UHPC surfaces were observed in the infrared pictures except those cases discussed above. Figure 7.13 shows a few

examples of many FLIR digital and thermal images that were taken from Tx34-1, Tx34-2, and Tx54. These photos indicate that there was no sign of significant surface defects on UHPC.

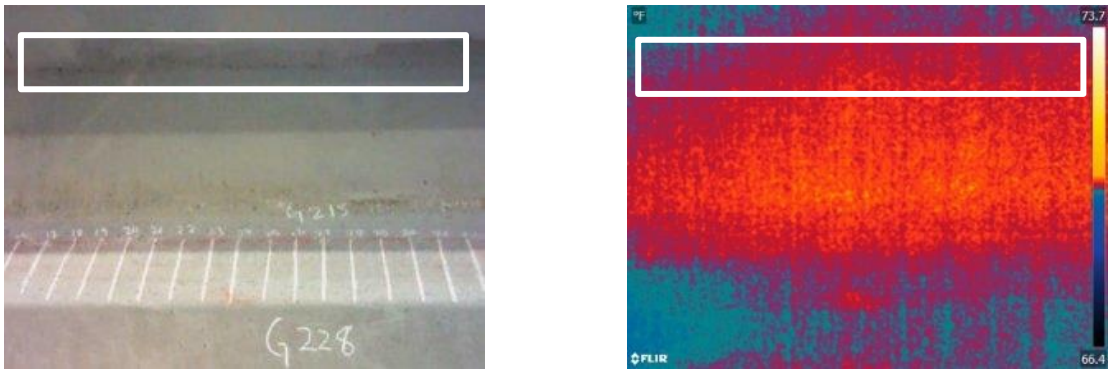

(a) FLIR Digital Image *(b) FLIR Infrared Image*

Figure 7.12. Thermal Image of a Longitudinal Crack Detected on the Web of Tx34-2.

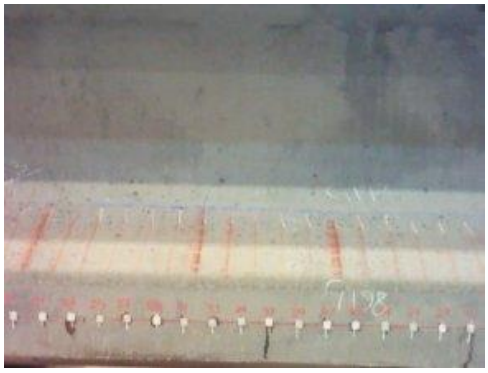

(a) FLIR Digital Image—Tx34-1

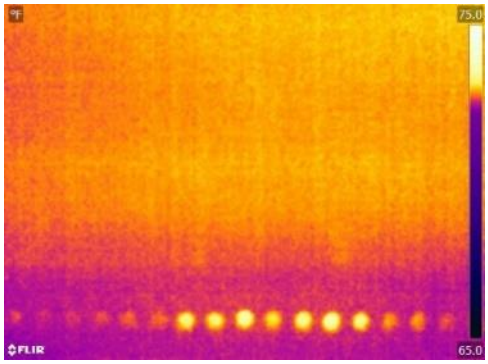

(b) FLIR Infrared Image—Tx34-1

(c) FLIR Digital Image—Tx34-2

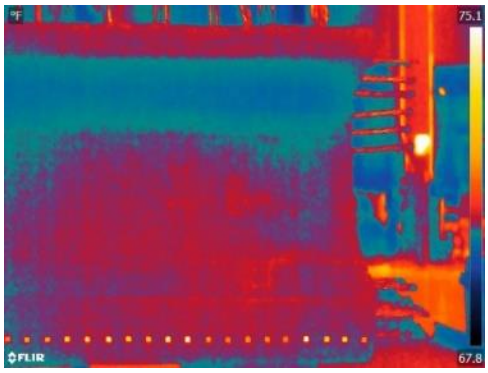

(d) FLIR Infrared Image —Tx34-2

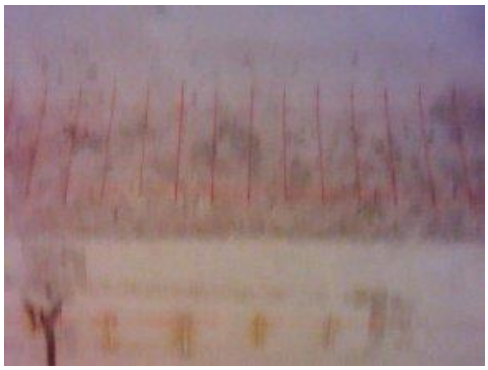

(e) FLIR Digital Image—Tx54

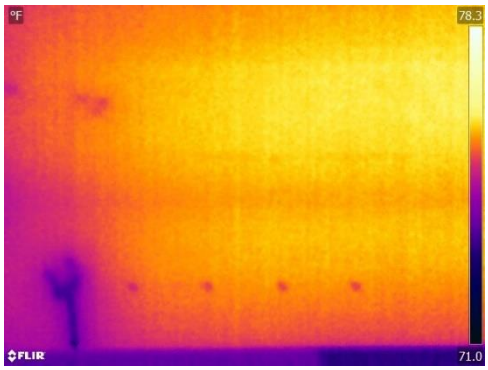

(f) FLIR Infrared Image—Tx54

Figure 7.13. FLIR Images Recorded from the UHPC Girders.

7.4.2 Ground Penetrating Radar

Studying B-Scan GPR profiles collected from the girders revealed no sign of voids or considerable defects in the UHPC girders. It was decided to not use C-Scan on Tx34-1 and Tx34-2 due to dimension limitations, while B-Scan profiles were recorded along four grid lines—the top flange, the web, and the bottom flange, in addition to one on the side of the bottom flange of the UHPC

girders. Similarly, only B-Scan results were collected from Tx54 because some locations on the girder were not accessible for GPR scanning.

At first glance, the contrast between metals and UHPC was not obvious in the GPR recordings. Silica fume is not electrically conductive under normal circumstances, and adding this to concrete should make the mix even less resistant to electromagnetic wave penetration. The low *w*/*c* of the selected UHPC causes reduction in the electrical conductivity of the concrete in general (El-Enein et al. 1995). Therefore, a meaningful observation was expected from the radar-based system examination.

The GPR energy reflected from the objects in UHPC was not as obvious as expected, but it was still possible to detect the location of metals in UHPC to some extent. For example, a strong signal was recorded from GPR surveying on the top flange of Tx34-1, Tx34-2, and Tx54 because the thickness of the concrete is relatively small. The white dashed lines in Figure 7.15 to Figure 7.17 represent the opposite face of UHPC at GPR grid lines—X-Marks in Figure 7.14. Concrete depth was 4.8 in. for the top flange of Tx34-1 and Tx34-2 and 7 in. for the web of all three girders. The depth was 10.5 in. for the bottom flange of Tx34-1 and Tx34-2, and 12.7 in. for the bottom flange of Tx54 at the GPR grid lines marked in Figure 7.14.

A-bars were visible in GPR results reported for top flanges. Some of the hyperbolas representing the reinforcement are marked in Figure 7.15(a), Figure 7.16(a), and Figure 7.17(a). Longitudinal T-bars were also detected on the top flange of Tx34-1, as shown in Figure 7.15(a). Lifting loops were detected in the results from the web of all three girders where hyperbolas with a wider asymptotes guide were recorded because the GPR grid lines and the backend of liftings were not perpendicular; thus, the GPR system crossed the lifting tails with some angle. The location of lifting loops is surrounded with a white-solid box in Figure 7.15 to Figure 7.17. Although it was not a bright signal, the longitudinal strands were also detected in the results from the web of Tx34-2 and Tx54—enclosed in a dashed box in Figure 7.16 and Figure 7.17. Additionally, the location of sensor instrumentation and hold-down points for the harped strands in the web of all three girders are also surrounded with a dotted/dashed box. C-bars and some U-bars were visible in the radar recordings documented from the bottom flange of all girders marked in Figure 7.15 to Figure 7.17 with a yellow box (white arrows for U-bars). Also marked were longitudinal strands

found in 7 in. and 9 in. of concrete depth of the bottom flange of Tx34-1 and Tx34-2 (indicated by dotted/dashed lines). The signals were relatively weak, but it was still possible to see the metallic components in the GPR results from the bottom flange of Tx54.

It was not easy to identify metallic components and distinguish them from steel fibers in GPR results. A possible explanation for weak reflected signals observed in GPR data is the moisture content of the fresh concrete. Electrical conductivity of new concrete is higher than in an aged specimen, and it absorbs most of the radar energy. GPR signal attenuation becomes less significant over time. As shown in Figure 7.15 to Figure 7.17, more information can be accessed from GPR profiles collected for the bottom flange of Tx34-1 and Tx34-2 than from the profile registered for Tx54. The examination was conducted on Tx34-1 and Tx34-2 UHPC specimens approximately 1 month after casting the concrete, whereas it was done a week after the concrete casting of Tx54.

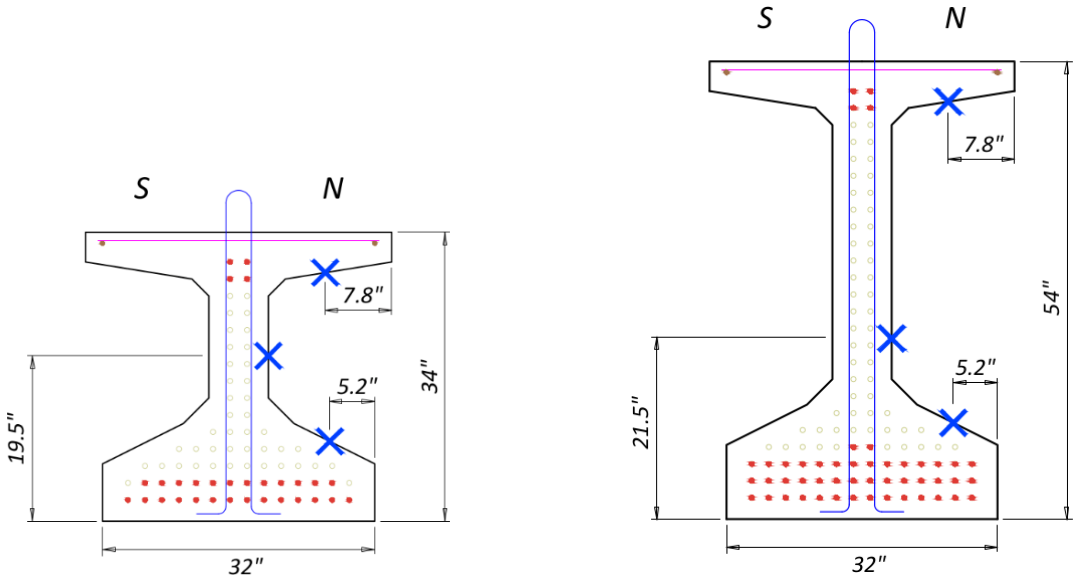

(a) Tx34-1 and Tx34-2 *(b) Tx54*

Figure 7.14. GPR Survey Lines.

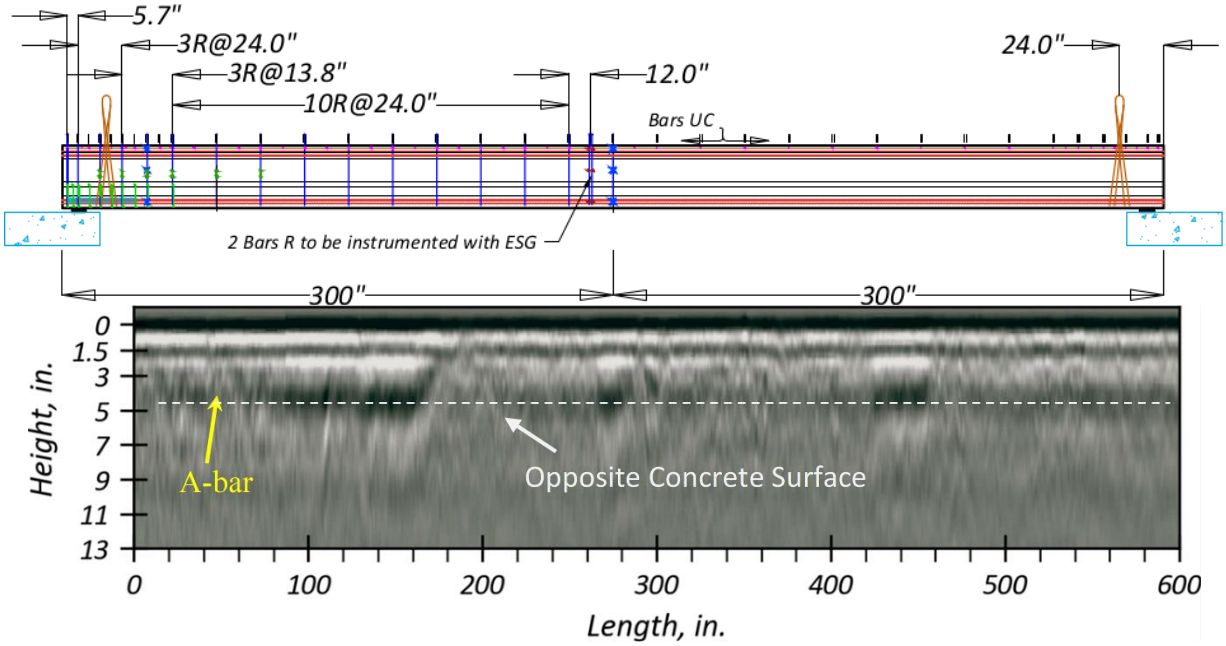

(a) Top Flange

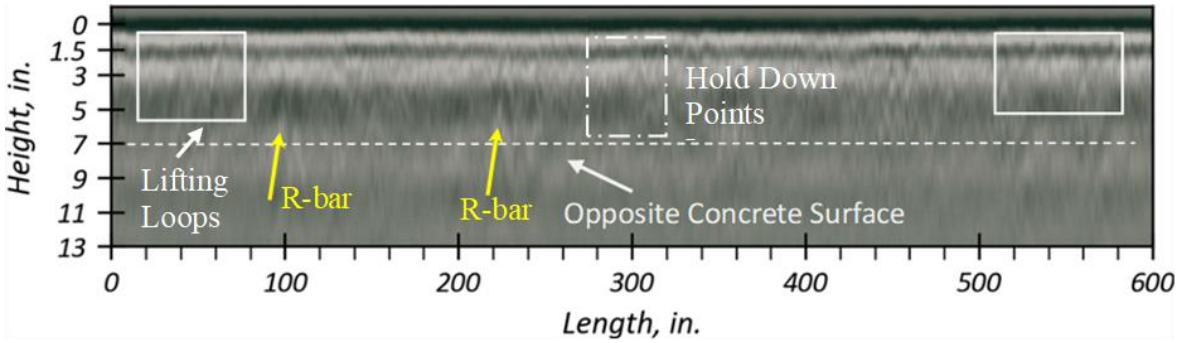

(b) Web

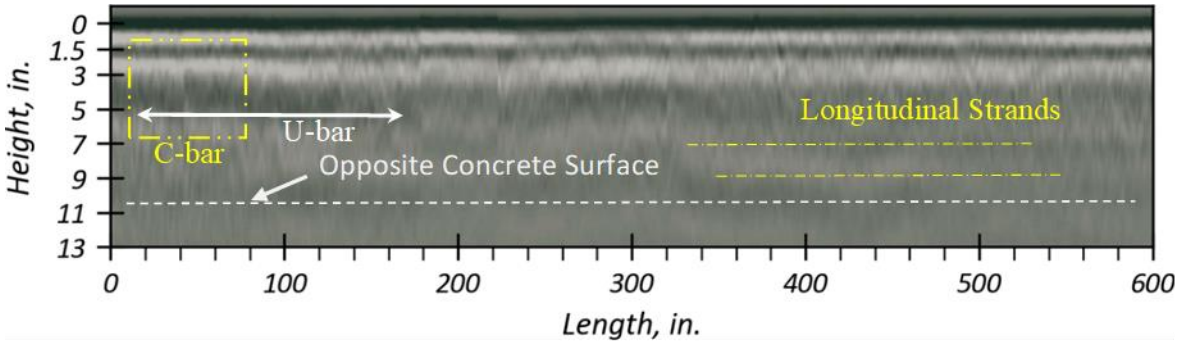

(c) Bottom Flange

Figure 7.15. B-Scan GPR Profiles Collected from Tx34-1.

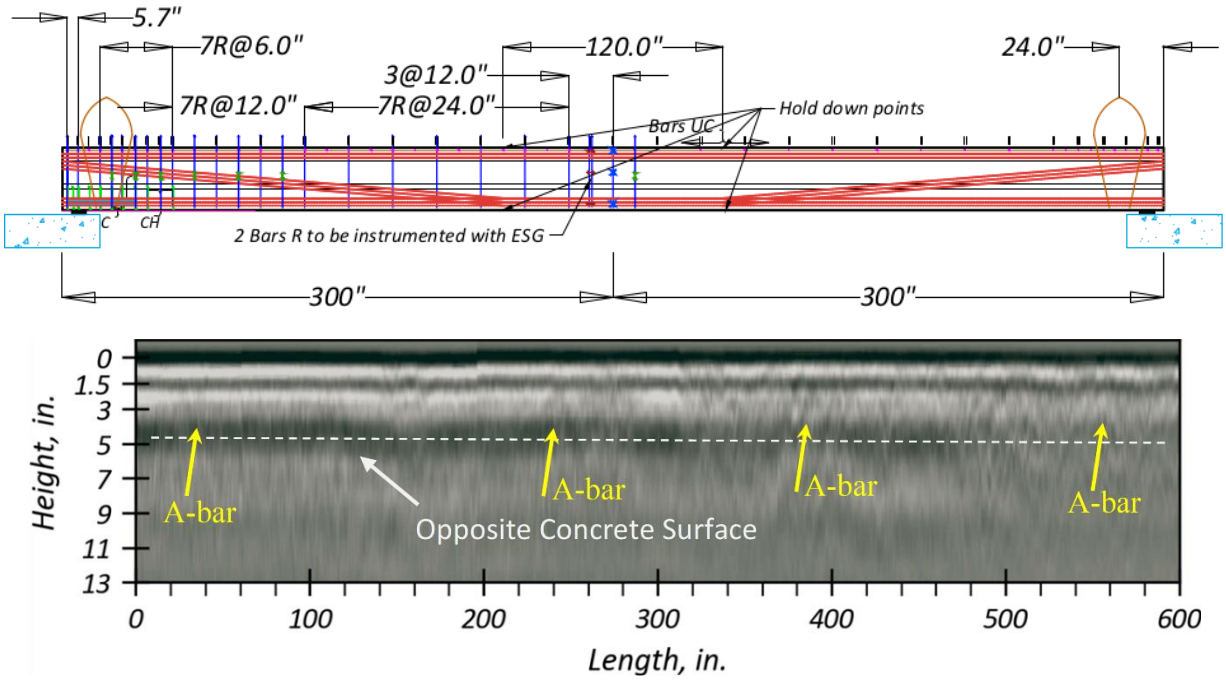

(a) Top Flange

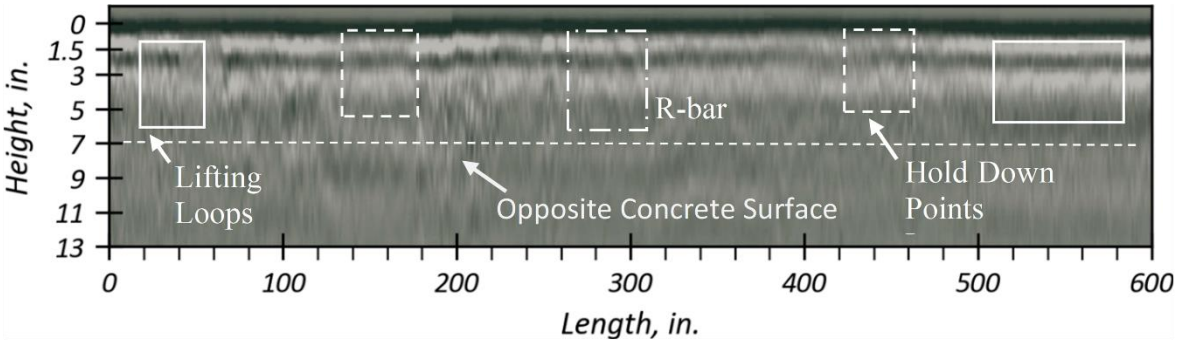

(b) Web

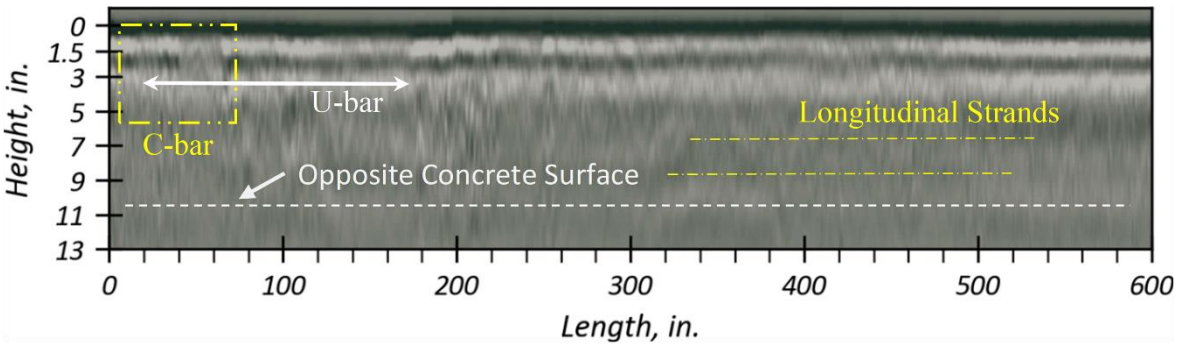

(c) Bottom Flange

Figure 7.16. B-Scan GPR Profiles Collected from Tx34-2.

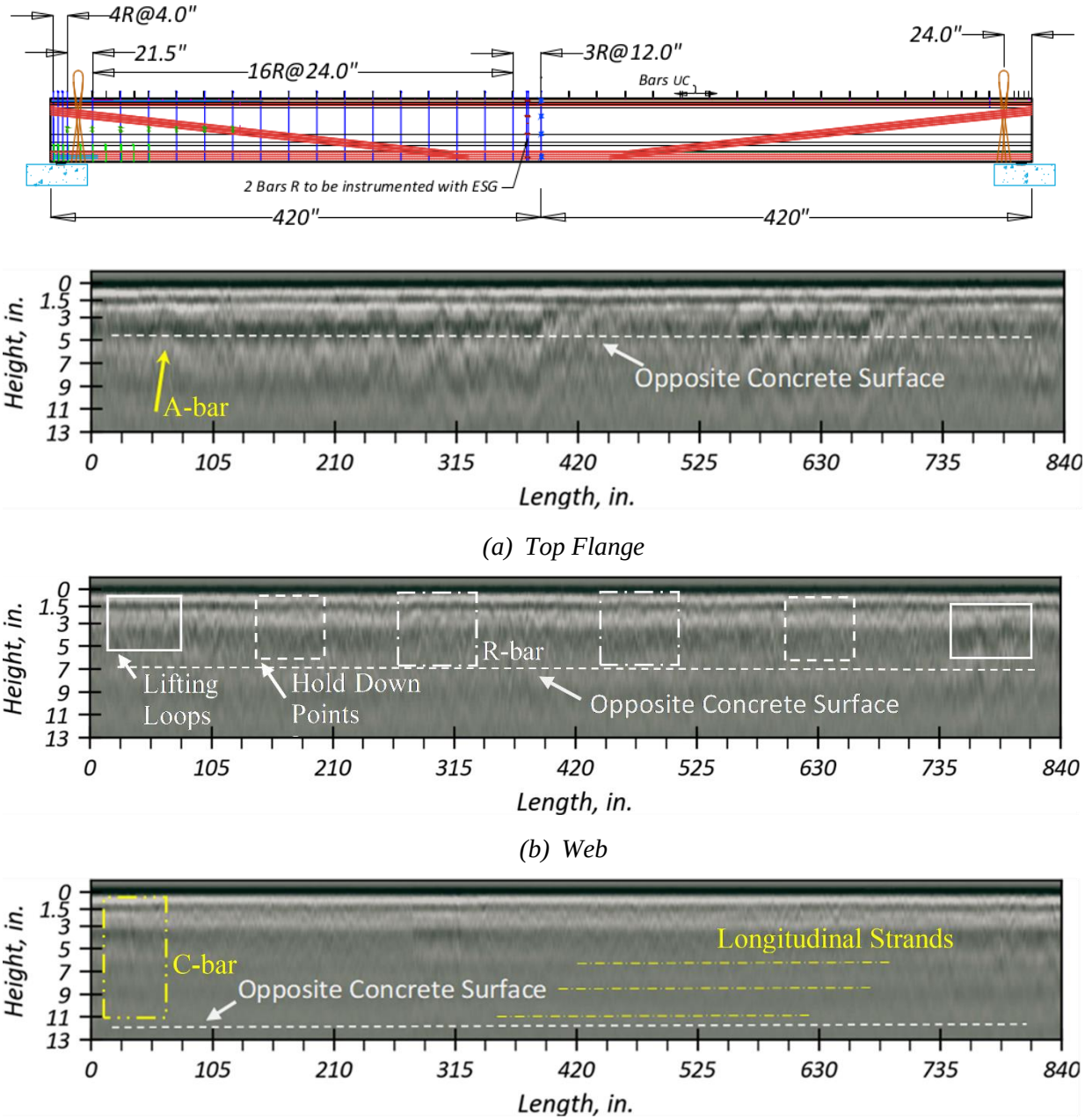

Figure 7.17. B-Scan GPR Profiles Collected from Tx54.

7.4.3 Ultrasonic Pulse Velocity

The average speed of sound waves in the concrete bulk was computed from the UPV time measurements to qualitatively classify the UHPC used in Tx34-1, Tx34-2, and Tx54. Two sets of time measurements completed during UPV included cross-scanning and single-side measurements. In this report, *cross-scanning* refers to the measurements when the transmitter and

the receiver transducers were positioned on either side of the concrete. The concrete depth was 7 in. for the web and 22 in. for the bottom flange of the UHPC girders (Figure 7.8 and Figure 7.9). The single-side measurement refers to the fact that the recordings were collected from only one side of the concrete surface. Because the mechanical properties of a medium influence the propagation of the acoustic waves, they can be used to identify the material properties of the concrete structures. This effect can be mathematically stated in accordance with ASTM C597 (2016) by writing Young's modulus E in terms of the medium density ρ, Poisson's ratio μ, and the square of the average velocity of sound propagated signal v, as follows:

$$E = \frac{(1+\mu)(1-2\mu)}{1-\mu}\,\rho\,v^2 \tag{7.1}$$

Table 7.1 gives the average unit weight used to calculate Young's modulus for Tx34-1, Tx34-2, and Tx54. The unit weight values provided in this table were measured according to ASTM C138 (2015) for the UHPC specimens.

Table 7.1. Unit Weight of UHPC in Girders.

UHPC Girder	ρ, lb/ft^3
Tx34-1	152.4
Tx34-2	150.6
Tx54	151.0

Saint-Pierre et al. (2016) reported a criterion recommended by the National Research Council of Canada so that the quality of the concrete can be identified from the average speed of sound waves in the concrete bulk. This specification was developed based on laboratory testing on the core samples taken from the Frontenac Dam located in Quebec. In this current study, a comparison between the experimental data from UPV recordings and the specifications reported by Saint-Pierre et al. (2016) was made to determine the material properties and quality of the UHPC girders in different locations. Therefore, if the recorded sound waves were higher than 14.8×10^3 ft/s, then the quality of concrete was assumed perfect. If the values were higher than 11.8×10^3 ft/s, the quality of concrete was recognized as good. If the velocity of acoustic waves were higher than 9.8×10^3 ft/s, the quality of concrete was considered fair. Otherwise, a poor-quality concrete was designated (Feldman 1977; Saint-Pierre et al. 2016).

In this project, the velocity of sound waves was measured on the UHPC specimens with and without steel fibers. The velocity of sound waves in a 4 × 8 in. cylinder sample of the UHPC without steel fibers was overall 16×10^3 ft/s in saturated conditions and 15.2×10^3 ft/s in dry conditions. This information was drawn from the ultrasonic testing that was performed on 2-year-old specimens.

Figure 7.18 shows the quality of UHPC (with steel fibers) used in the web of Tx34-1 at the W end, at the M, and at the E end of the girders. As shown, the quality of the concrete is either perfect or almost perfect for the locations where UPV was performed. The quality of UHPC used in the bottom flange is also depicted in Figure 7.19 and indicates a relatively good quality (almost perfect) concrete. Figure 7.20 and Figure 7.21 represent the quality of UHPC in the web and the bottom flange of Tx-34-2, respectively. Similar to UHPC used in Tx34-1, the quality of the concrete is predicted to be perfect in general. The concrete quality used at the east and the west ends of the UHPC girders was found to be slightly better than the middle of both girders.

As shown in Figure 7.22 and Figure 7.23, the quality of UHPC used in the web of Tx54 was predicted to be perfect (or almost perfect) for most locations where UPV was conducted; however, it slightly dropped in the middle of the girder at C3 (5 in. above the mid-height of the web). In addition, the quality of the UHPC was relatively low at the top corners of the web, C1, both at the east and at the west of Tx54 (Figure 7.9(a)). It is believed that signals were disturbed and diverted at these locations because of the helical shape of high-strength steel strands, and the concrete used in the web was in good condition. Finally, the UHPC used in the bottom flange of Tx54 was of perfect quality in contrast to the other girders (Figure 7.24).

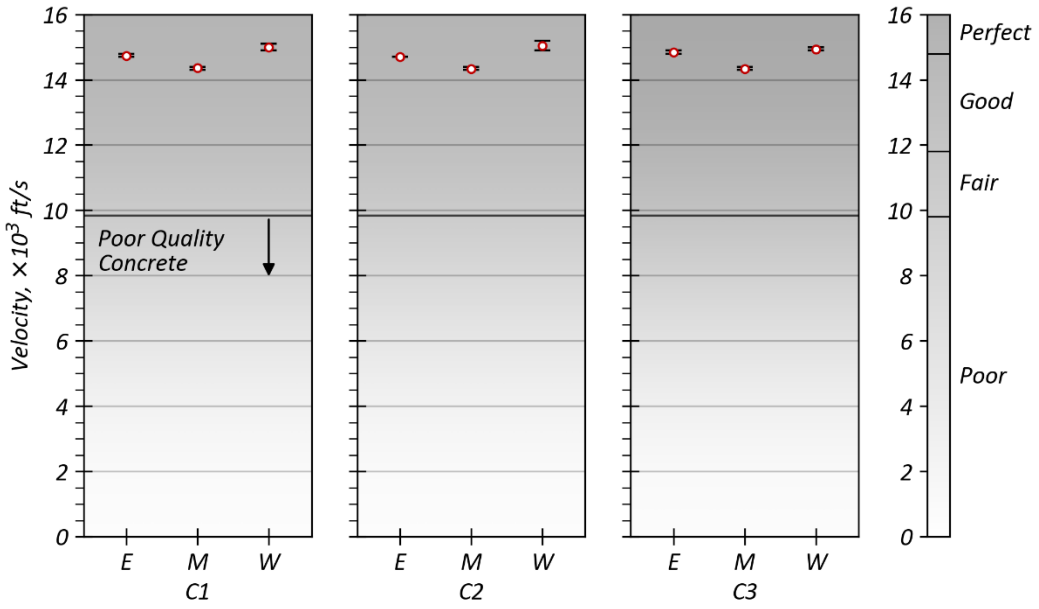

Poor = v < 9.8×10³ ft/s; Fair = 9.8×10³ < v < 11.8×10³ ft/s; Good = 11.8×10³ < v < 14.8×10³ ft/s; Perfect = v > 14.8×10³ ft/s

Figure 7.18. UHPC Quality Based on the Average Traveled Acoustic Waves—Web of Tx34-1.

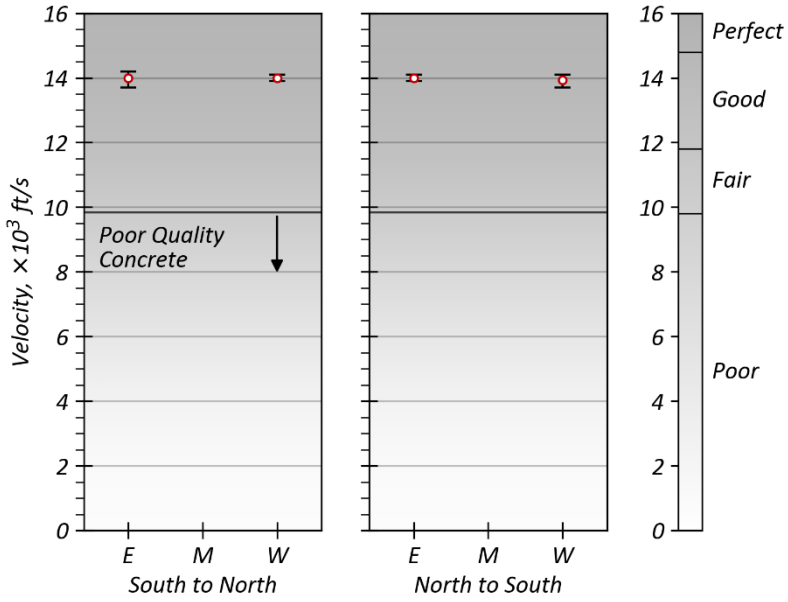

Figure 7.19. UHPC Quality Based on the Average Traveled Acoustic Waves—Bottom Flange of Tx34-1.

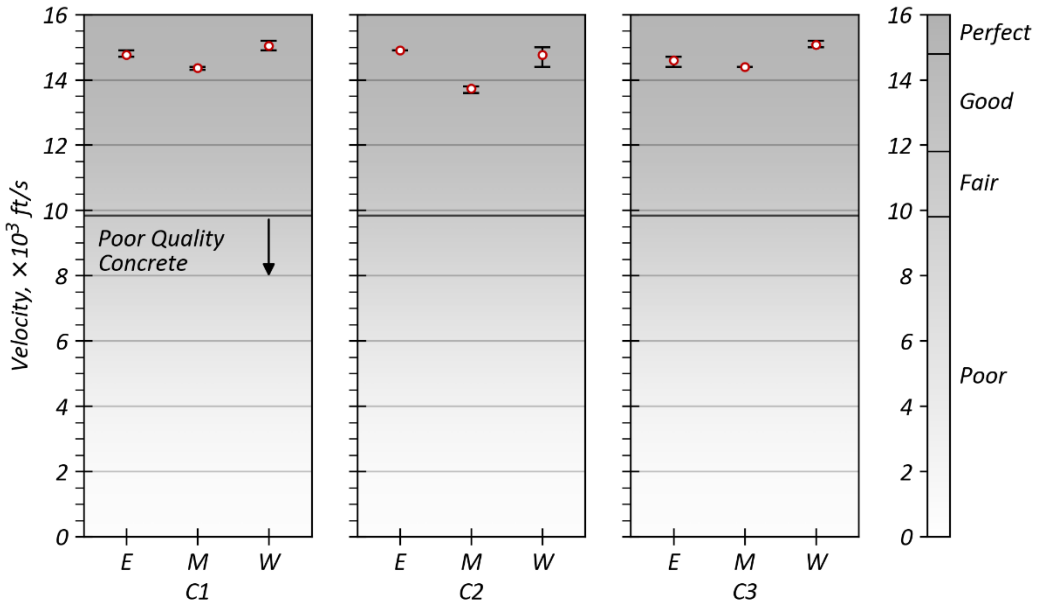

Figure 7.20. UHPC Quality Based on the Average Traveled Acoustic Waves—Web of Tx34-2.

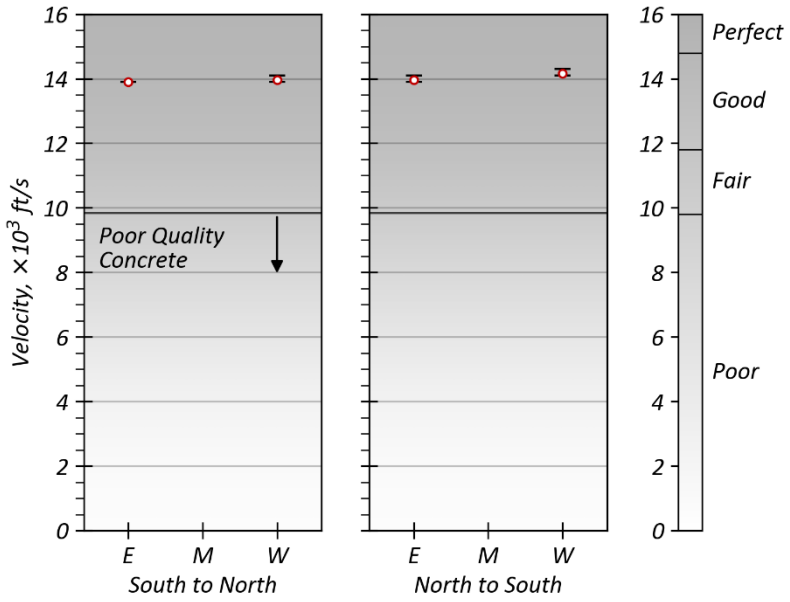

Figure 7.21. UHPC Quality Based on the Average Traveled Acoustic Waves—Bottom Flange of Tx34-2.

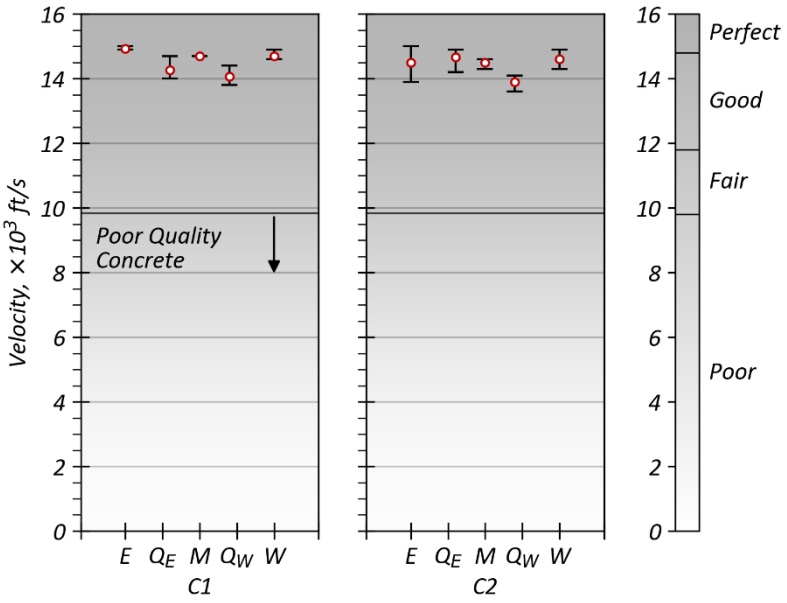

Figure 7.22. UHPC Quality Based on the Average Traveled Acoustic Waves—Web of Tx54—Below the Mid-height of the Web.

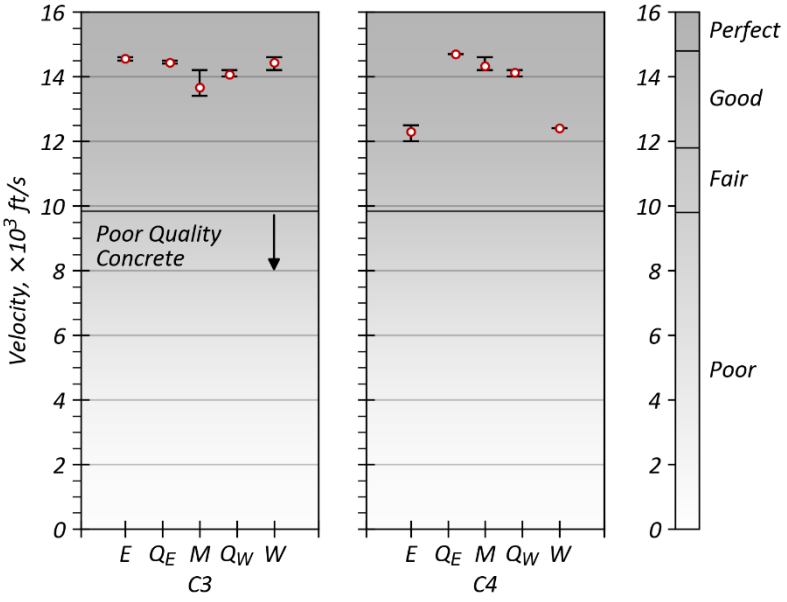

Figure 7.23. UHPC Quality Based on the Average Traveled Acoustic Waves—Web of Tx54—above the Mid-height of the Web.

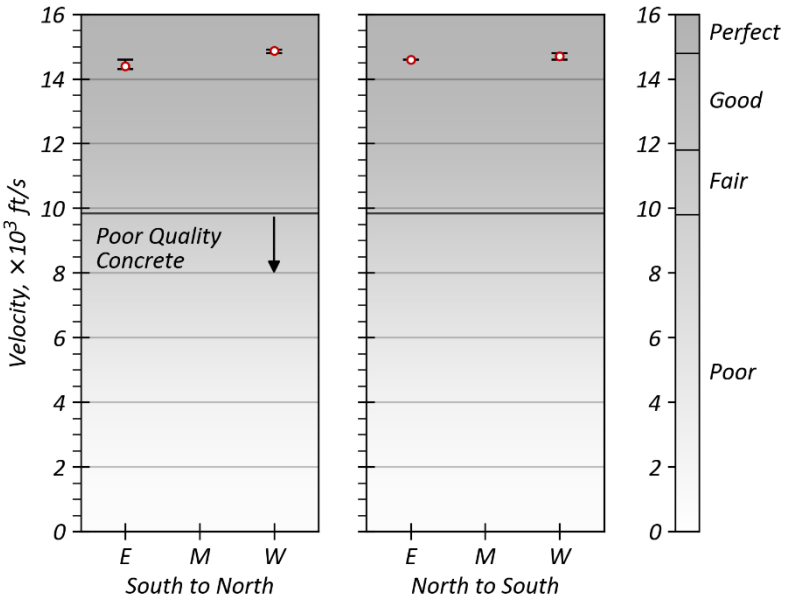

Figure 7.24. UHPC Quality Based on the Average Traveled Acoustic Waves—Bottom Flange of Tx54.

As discussed, surface wave measurements were also conducted separately in horizontal and vertical directions both at the south and the north faces of the web of Tx34-1 and Tx34-2 (Figure 7.8(c) and Figure 7.8(d)). It was decided to finish the ultrasonic surface scanning in more locations on the web as well as both top and bottom flanges of Tx54 (Figure 7.9(c) and Figure 7.9(d)). After recording the traveling time of the signals, the speed of sound waves was calculated based on the transducers' distance. The results were used to determine the distribution ratio (DR), which is defined as a ratio of the horizontal to the vertical sound wave propagation. Figure 7.25 shows the DR calculated for the web of Tx34-1, while Figure 7.26 gives this ratio computed for the web of Tx34-2. Figure 7.27 gives DR values for the web and the top and bottom flanges of Tx54. More recordings are provided for Tx54 because the height of the girder was higher. Note that the DR based on the measured UPV represents the fiber distribution at the concrete surface.

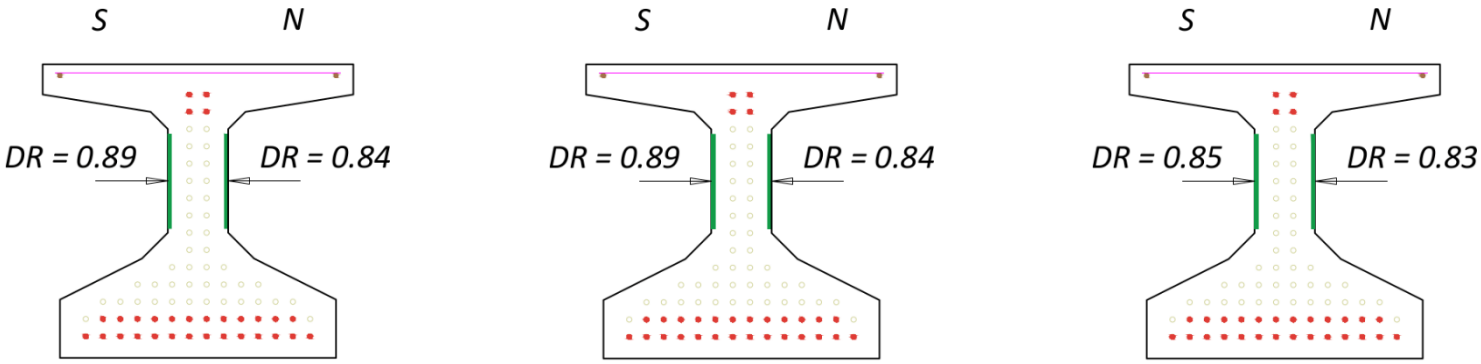

(a) West *(b) Middle* *(c) East*

Figure 7.25. DR Calculated from Surface Wave Measurements on Tx34-1.

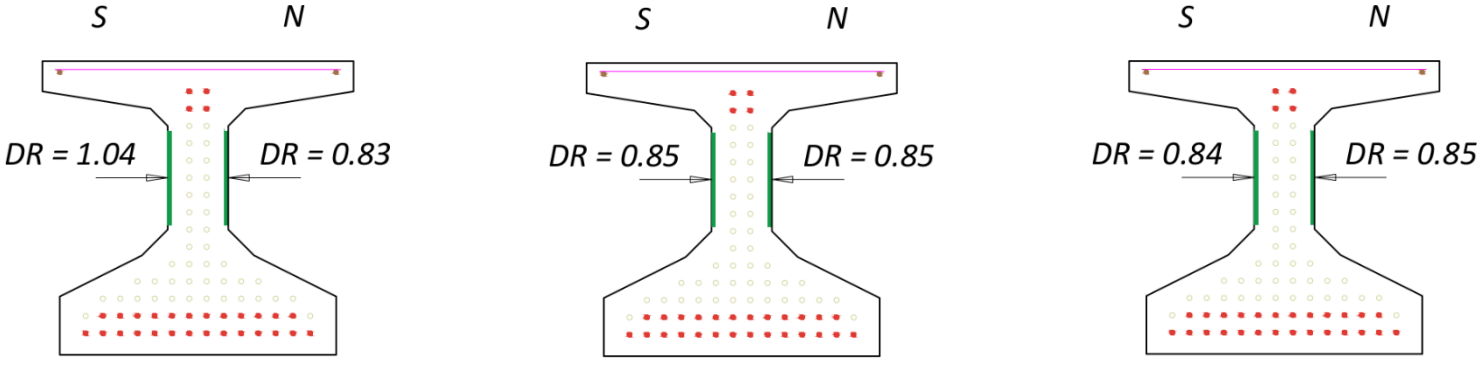

(a) West *(b) Middle* *(c) East*

Figure 7.26. DR Calculated from Surface Wave Measurements on Tx34-2.

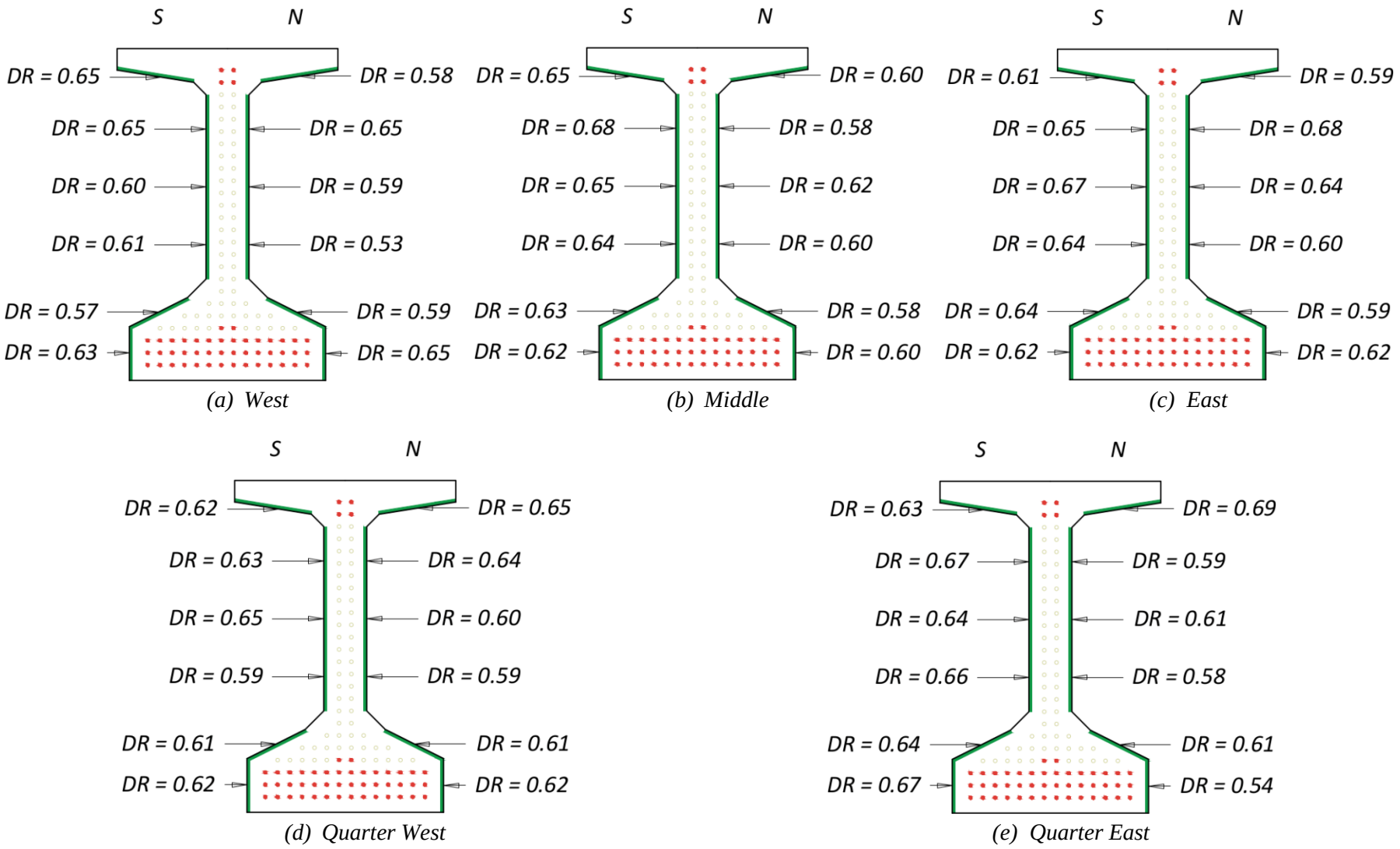

Figure 7.27. DR Calculated from Surface Wave Measurements on Tx54.

Sound waves travel faster in steel fibers than in concrete. Because the average of the DR is less than 1, it can be concluded that steel fibers are aligned more in the horizontal direction on the surface of the UHPC girders. The DR reported in this document was almost consistent for each UHPC girder and was on average 0.85 for Tx34-1 and 0.87 for Tx34-2. The DR was only slightly higher when the examinations were completed at the southwest face of the UHPC girders, which are almost 0.9 for Tx34-1 and 1.04 for Tx34-2. The ratio dropped to on average 0.62 for Tx54, which was lower than what was obtained for the two other girders and implies that more steel fibers were distributed in the horizontal direction in the plane of the web than in the other two girders.

Two longitudinal transition lines between batches were observed during the inspection of the UHPC girders. One was a transition line at the southeast of Tx34-2 (Figure 7.28(a)). Then, no signal was detected during ultrasonic surface scanning where transducers were positioned in a vertical direction at this location because the defect caused distribution of the signal energy across the web surface. Please note, the transition line advanced in a longitudinal direction for 27.8 in. from the west end to the east end, from which it diverted for more than 3 in. at 45 degrees from the center of the web to the top. Another longitudinal transition line (18 in. long) was observed on the web of Tx54, right at the bottom of the top flange at the southwest of the concrete girder (Figure 7.28(b)).

(a) Tx34-2 *(b) Tx54*

Figure 7.28. Longitudinal Transition Line Detected on the Web.

Figure 7.29 to Figure 7.31 represent the average MOE calculated from Equation (7.1) for the three UHPC girders. The results highlight the MOE for the UHPC used in the web and the bottom flange of the girders. The average MOE estimated for the web of Tx34-1 was about 5900 ksi; however, the MOE was reduced to 5350 ksi at the bottom flange. The average Young's modulus computed for Tx34-2 was similar to the results obtained for Tx34-1: 5800 ksi on average for the east and the west ends of the girder web and 5600 ksi on average for the UHPC used in the middle. The MOE was slightly lower for the bottom flange; it was an estimated 5300 ksi on average. Young's modulus was lower for the web of the Tx54. In fact, the average MOE slightly dropped from the bottom flange to the web, where it was predicted as 5800 ksi for the bottom flange and 5450 ksi for the web. Because the average Young's modulus of UHPC is predicted, it becomes possible to estimate the compressive strength (f_c') of the concrete using the following developed equation discussed in Section 6.4.2:

$$E = 1430\sqrt{f_c'} \text{ in ksi} \tag{7.2}$$

Figure 7.32 to Figure 7.34 show the average predictions of compressive strength for all the UHPC girders. The compressive strength of UHPC used in Tx34-1 was predicted as slightly higher than 17 ksi for the web, while it was an estimated 14 ksi on average for the bottom flange. The average compressive strength was found to be the same range for the concrete used in Tx34-2. The compressive strength for the web of Tx54 was on average higher than 16.4 ksi for the bottom flange and 15.4 ksi for the web.

The average compressive strength obtained from UPV was on average 15 percent lower than the values reported from destructive testing reported in Section 8.3. Compression testing was performed on core samples taken from the UHPC girders after finishing the full-scale tests. In addition, properties of UHPC in actual structures differ from the core specimens because of dissimilar curing and compaction conditions. Feldman (1977) reported that up to ±20% deviation is expected in the results from destructive testing on core specimens and UPV conducted on the actual concrete structures. Note that it is not appropriate to make a comparison between the results obtained from UPV conducted in this study and the results reported in Section 8.3 because these examinations were not performed on the same samples, and the age of the specimens and the curing conditions are different.

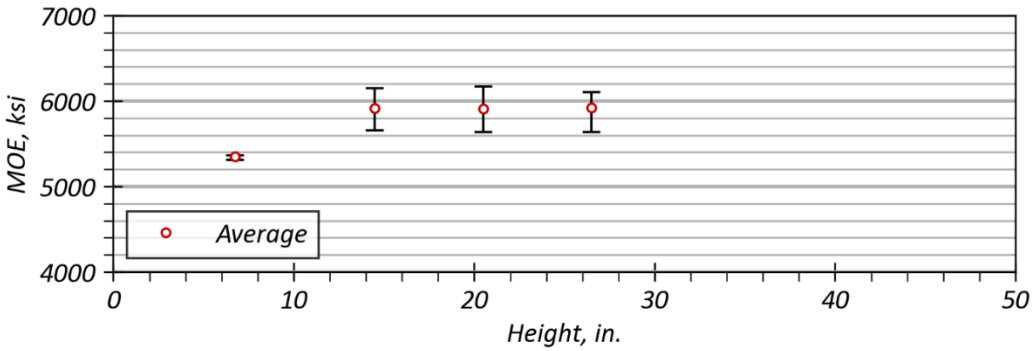

Figure 7.29. Modulus of Elasticity Predicted from UPV for Tx34-1.

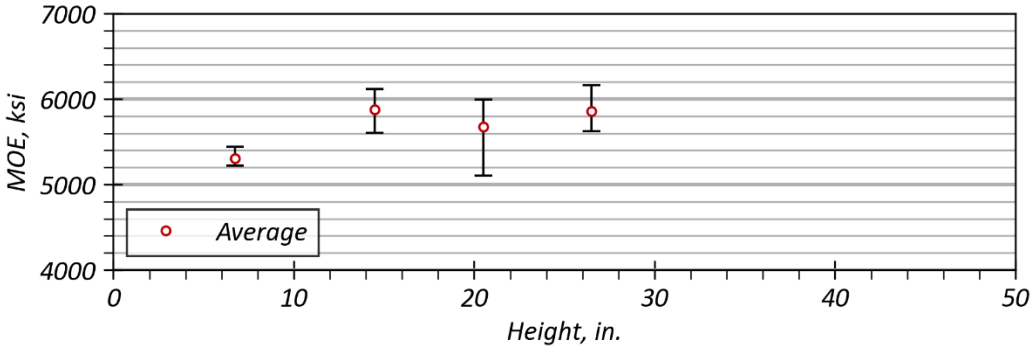

Figure 7.30. Modulus of Elasticity Predicted from UPV for Tx34-2.

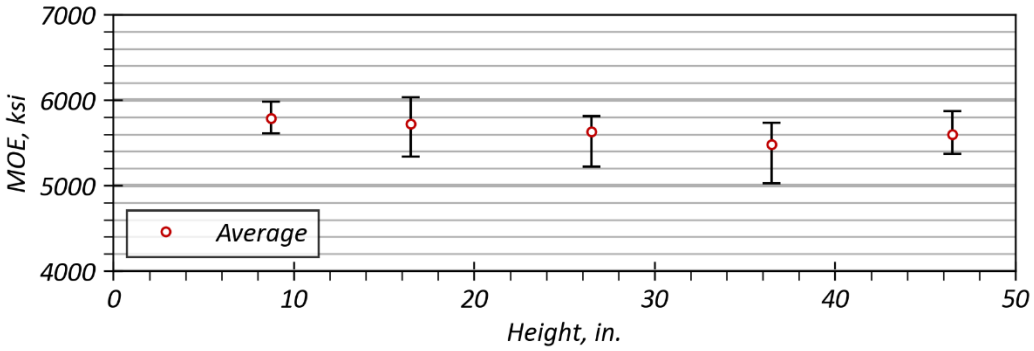

Figure 7.31. Modulus of Elasticity Predicted from UPV for Tx54.

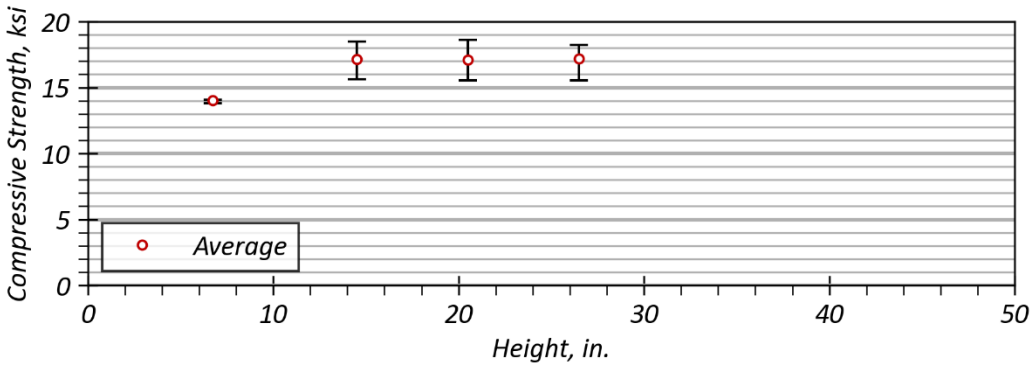

Figure 7.32. Compressive Strength Predicted from UPV for Tx34-1.

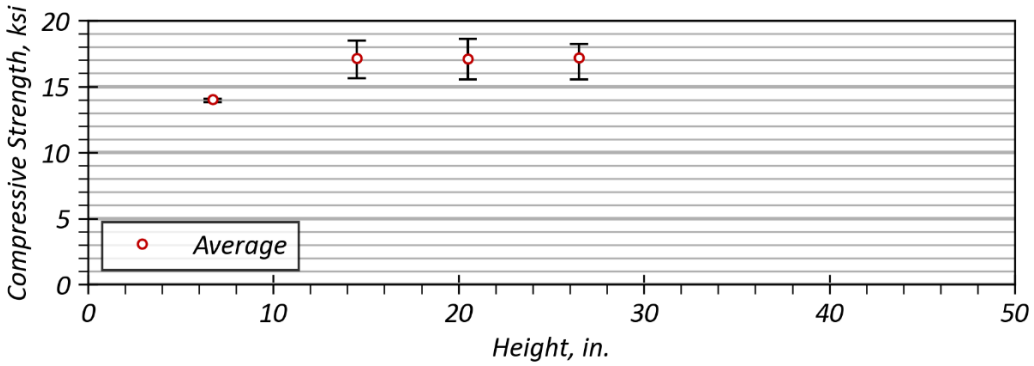

Figure 7.33. Compressive Strength Predicted from UPV for Tx34-2.

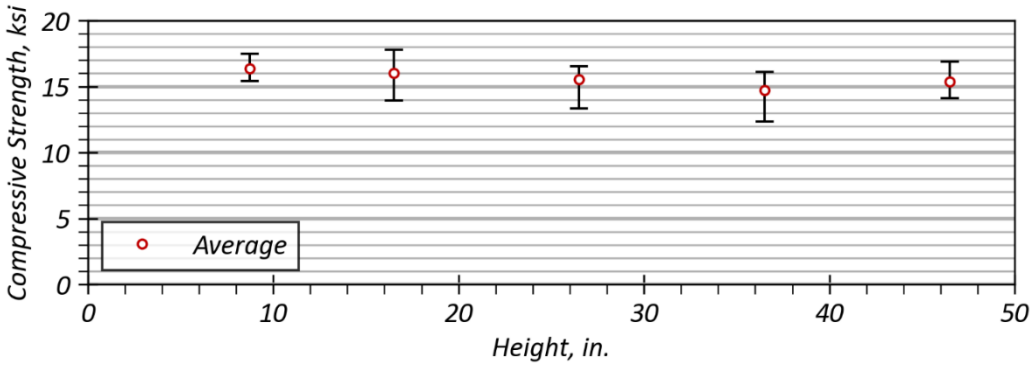

Figure 7.34. Compressive Strength Predicted from UPV for Tx54.

7.4.4 Ultrasonic Tomography

Ultrasonic measurement was completed on the web and the top and bottom flanges of the UHPC girders. Figure 7.35 shows the locations where ultrasonic tomography mapping was conducted. The length of ultrasonic scanning was similar for Tx34-1 and Tx34-2, which was 4 in. for both the web and the bottom flange of the girders and was decreased to 2 in. for the top flange. Ultrasonic

tomography was performed at more locations on Tx54. The length of scanning was 22 in. on the web and 6 in. on the top and bottom flanges.

Figure 7.36 to Figure 7.38 show the final imaging of ultrasonic testing, including the tomography mapping of the UHPC girders. Computed tomography scanning of Tx34-1, Tx34-2, and Tx54 generally showed good results. Because ultrasound is a mechanical wave, it can readily propagate in a nonconductive medium such as UHPC. Thus, it was possible for the tomographer to locate the steel components in all three girders. However, some wave disturbance was observed during the study of ultrasonic mappings from the bottom flange of Tx34-1.

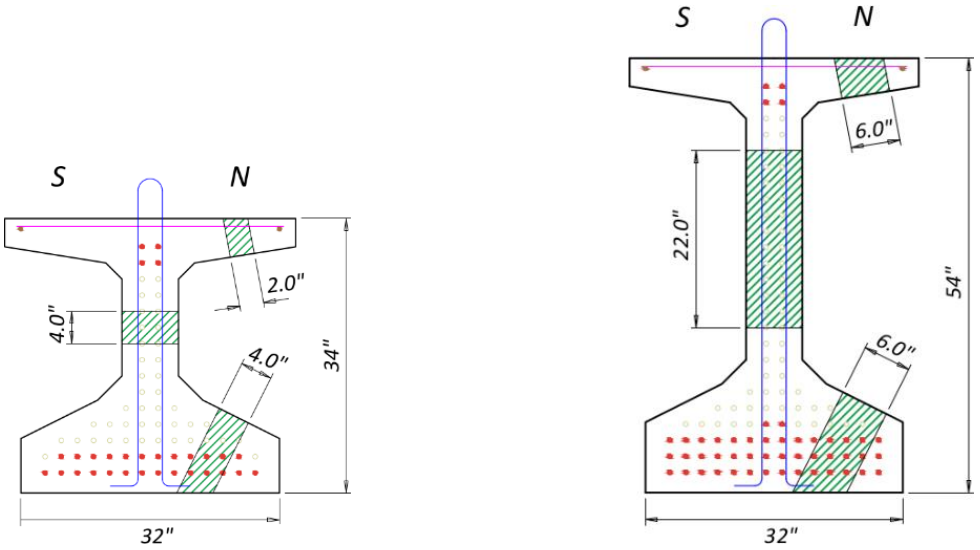

(a) Tx34-1 and Tx34-2 *(b) Tx54*

Figure 7.35. Schematic View of the Transducers' Position during Ultrasonic Tomography Mapping.

After studying the results of the ultrasonic inspection, no delamination or major defect was found in the UHPC girders. It was also possible to detect in tomography images most of the steel components used in the concrete girders. A-bars (transverse reinforcement in top flange) were detectable in tomography imaging computed for the top flanges of all three girders. Some of these transverse rebars are enclosed in white-solid boxes, as shown in Figure 7.36(a), Figure 7.37(a), and Figure 7.38(a). The results given in Figure 7.38(a) show a better presentation of these steel components because the ultrasonic scanning was performed in a greater area for the top flange of Tx54. Nothing unusual was seen in the ultrasonic testing results of the top flanges.

R-bars were visible on the ultrasonic mapping developed for the web of the UHPC girders (Figure 7.36(b), Figure 7.37(b), and Figure 7.38(b)). In addition to R-bars, the receiving signals showed the location of hold-down points for the harped strands in the web of Tx 34-2 that were located 60 in. from the middle of the web. The hold-down points were also recognizable in ultrasonic mapping of Tx54, wherein a curved steel bundle was observed in the middle of the UHPC girder. In addition to the hold-down points, high-strength steel strands were visualized in the tomographic imaging of the web of Tx54. It was also possible to find the location of the lifting loops in the web of all three girders. The lifts were located at 34 in. from the supports of the structures. C-bars located at the west of the UHPC girders were visible in the bottom flange of all three girders (Figure 7.36(c), Figure 7.37(c), and Figure 7.38(c)).

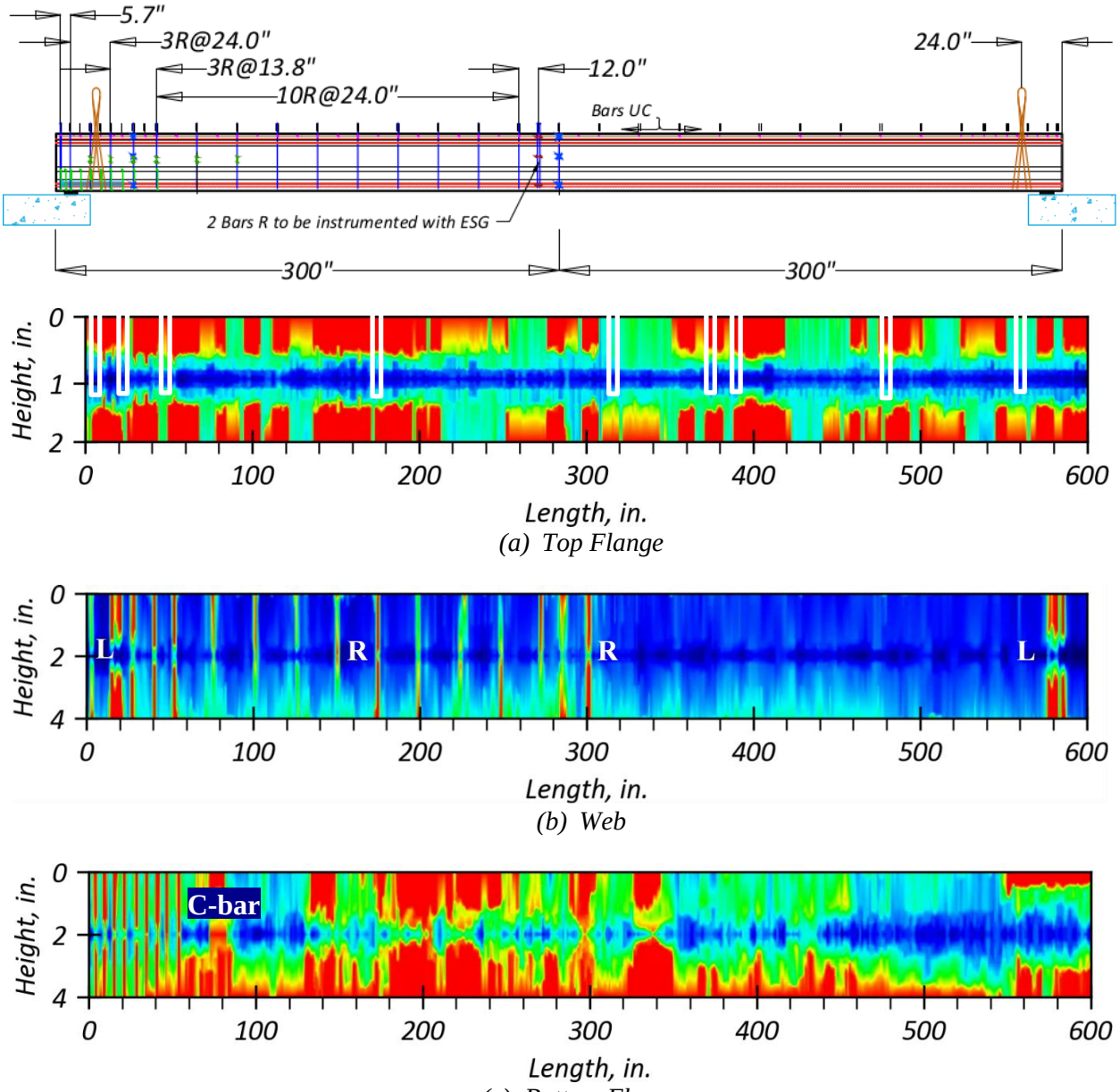

Note: L = Lifting Loops; H = Hold-Down Points; R = R-bars; White-Solid Box = A-bars (transverse reinforcement in the top flange)

Figure 7.36. C-Scan Ultrasonic Tomography Mapping Collected from Tx34-1.

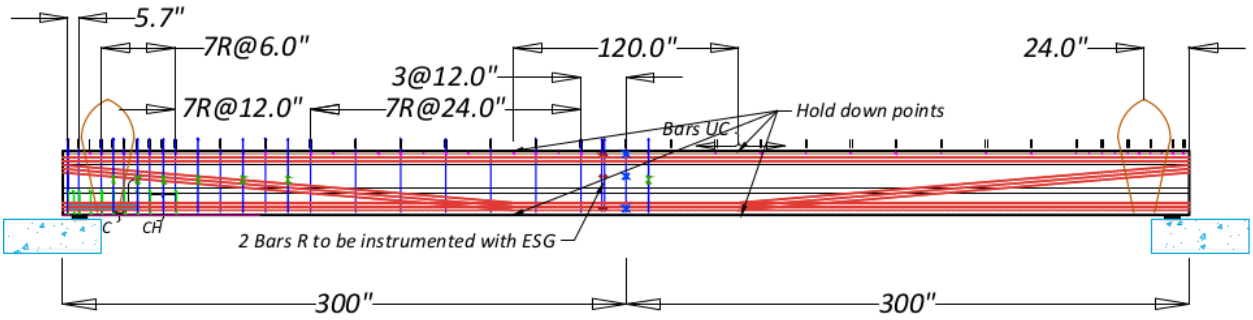

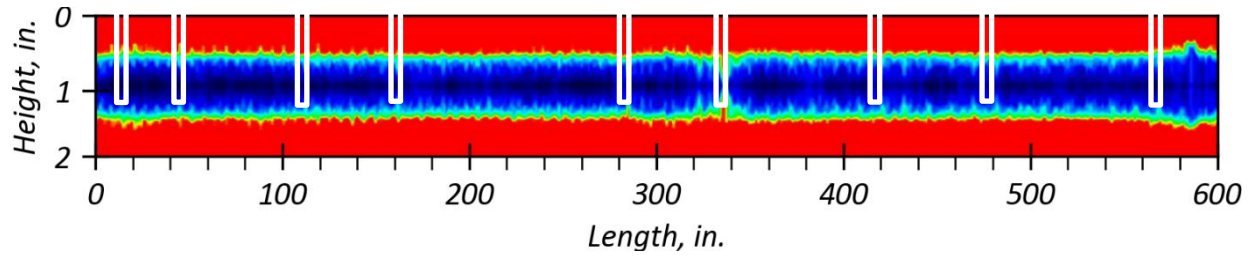

(a) Top Flange

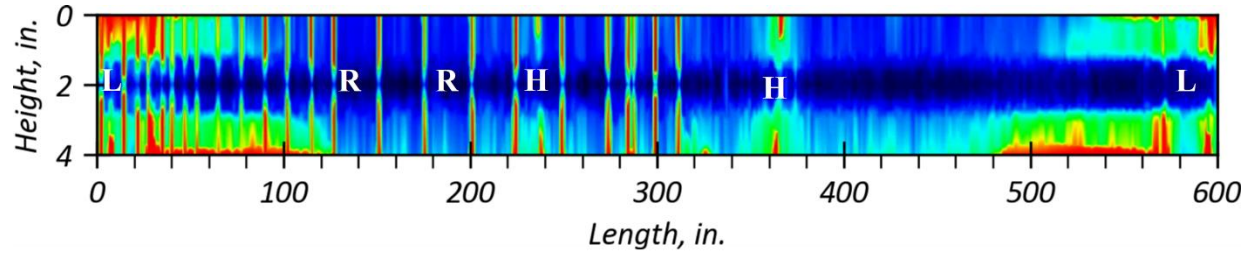

(b) Web

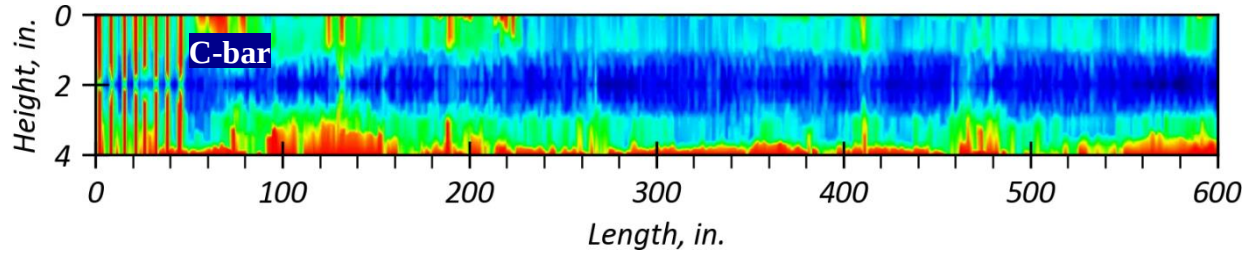

(c) Bottom Flange

Note: L = Lifting Loops; H = Hold-Down Points; R = R-bars; White-Solid Box = A-bars (transverse reinforcement in the top flange)

Figure 7.37. C-Scan Ultrasonic Tomography Mapping Collected from Tx34-2.

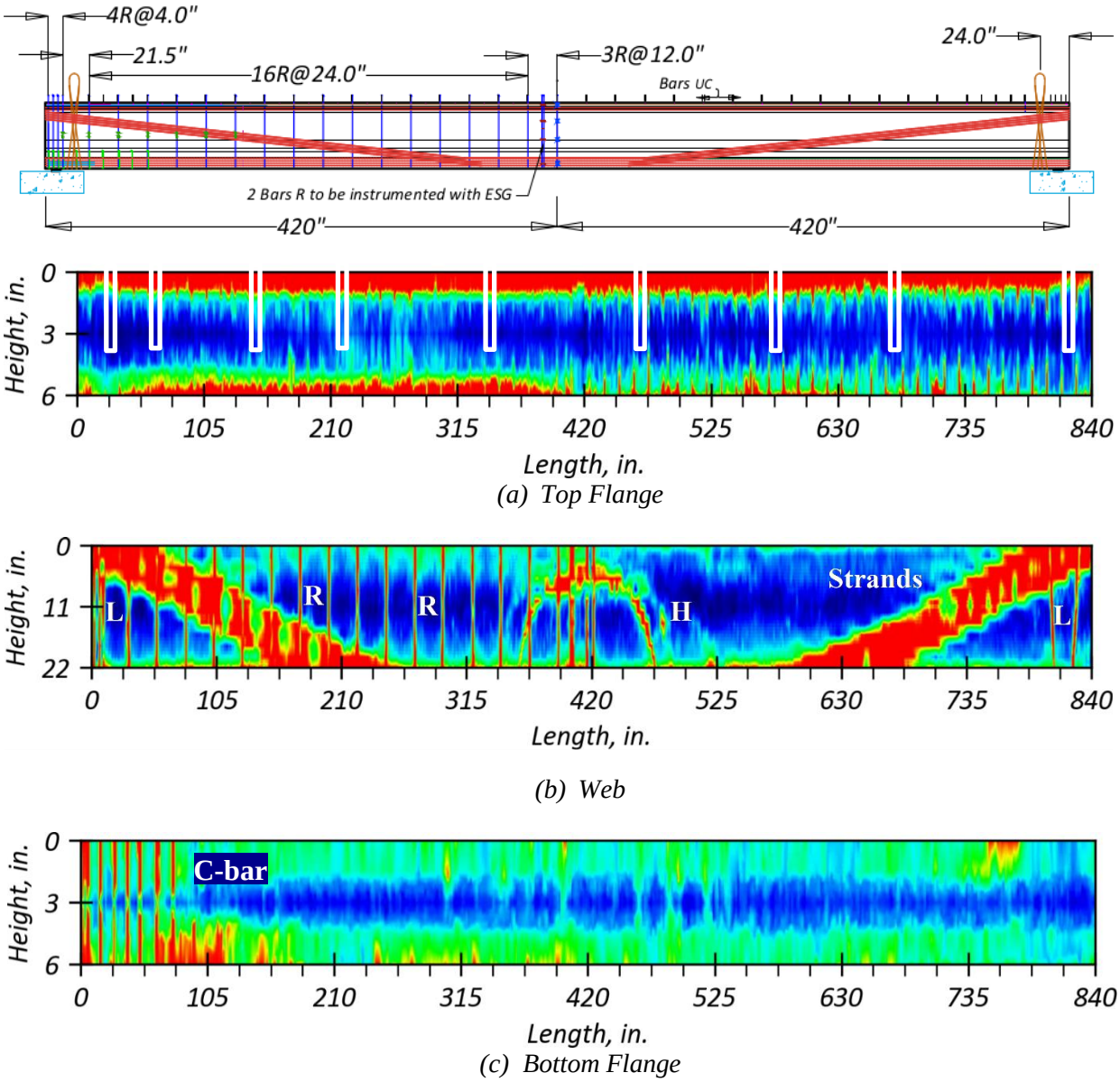

Note: L = Lifting Loops; H = Hold-Down Points; R = R-bars; White-Solid Box = Transverse reinforcement in the top flange

Figure 7.38. C-Scan Ultrasonic Tomography Mapping Collected from Tx54.

7.5 SUMMARY

The quality of UHPC used to build Tx34-1, Tx34-2, and Tx54 was consistent with criteria established by Feldman (1977). This finding is based on UPV recordings from the web and bottom flange of the UHPC girders because signals were barely received by transducers where UPV was conducted at the top flange. This result might be due to the concrete roughness at the top surface and attenuation of sound propagating as a result of the existence of R-bars and high-strength steel strands. The compressive strength of UHPC used in Tx34-1 and Tx34-2 was a predicted 17 ksi on

average for the web and 14 ksi for the bottom flange. Similarly, the compressive strength of UHPC in Tx54 was estimated on average to be 15.6 ksi. Surface wave measurements conducted in horizontal and vertical directions revealed that steel fibers were uniformly distributed with a tendency to be slightly more inclined to the horizontal directions. Moreover, fiber distribution in Tx54 was more significantly inclined to the horizontal directions than in the two other girders. Note that this interpretation is applicable to the steel fibers on the surface of the UHPC girder where it was in contact with concrete formwork.

No delamination or large defect was detected from ultrasonic tomography conducted on Tx34-1, Tx34-2, and Tx54. Steel components were readily recognizable in the tomographic imaging computed for the UHPC girders. Although the contrast between the metallic components and the concrete was not as clear as desired, and the difference between steel reinforcement (or prestressing strands) and steel fibers was not obvious, the radar-based testing system (GPR) was still capable of locating steel reinforcement and prestressing strands in UHPC. Note that silica fume is not electrically conductive and does not attenuate the reflection signal; thus, the use of the GPR system—as long as it is not performed on fresh concrete—is also suitable to determine the location of steel components and to identify defects such as large voids in UHPC.

8 ANALYSIS OF FIBER DISTRIBUTION, VOIDS, AND STRENGTH USING CORED SAMPLES

8.1 INTRODUCTION

Cored samples with a 3 in. diameter were collected from the three girders after full-scale testing at the lab to study the fiber distribution and orientation, look for presence of voids (air voids and other larger voids due to consolidation issues), and determine the compressive strength. The cored samples were thoroughly documented with photo images, rolled-out surface photo images, X-ray CT scanned images, and infrared photo images. Section 8.2 presents the documented images from conventional photo images and the rolled-out surface photo images. Section 8.3 investigates the compressive strength of the cored samples. For qualitative evaluation of fiber distribution and orientation, X-ray CT scanning of selective cores was employed. To get three-dimensional (3D) disposition of fibers, the scanned 2D image slices were stacked through image processing (i.e., 3D reconstruction). The 3D reconstructed images of the cores from different sample locations show fiber distribution and orientation horizontally (i.e., along the girder length) and vertically (i.e., depth-wise along the girder height). The 3D reconstructed images also show voids (air voids and other larger voids that may form due to consolidation issues) in the UHPC cores. In addition to X-ray CT scanning, additional image analysis techniques, including infrared imaging, were conducted to support X-ray CT results. Section 8.4 discusses the results of X-ray CT scan.

8.2 CORED SAMPLES FROM THE GIRDERS

Coring was conducted after full-scale testing using a Hilti DD-250 core drill (Figure 8.1). Figure 8.2 shows the core locations in the three girders. Two, three, and four locations were selected for coring in Tx34-1, Tx34-2, and Tx54, respectively. The core locations (e.g., C1 and C2 for Tx34-1; C1, C2 and C3 for Tx34-2; and C1, C2, C3, and C4 for Tx54, all shown in Figure 8.2) were identified at the midspan and the girder ends, while considering avoiding mild steel reinforcement and large cracks from the full-scale flexure and shear testing. Coring the conventional deck concrete and UHPC girder concrete was performed smoothly. However, the core bits were damaged while cutting through the prestressing strands. As a result, some of the cored samples were damaged. Note that Tx34-2 C3 has a 14 in. height because it was broken while coring due to the intersection of the core bit with harped strands and a large shear crack. The cored samples were

used for compression testing and fiber distribution analysis using an X-ray CT scanner and infrared camera.

Figure 8.1. Coring UHPC Girder Using Hilti DD-250 Coring Machine.

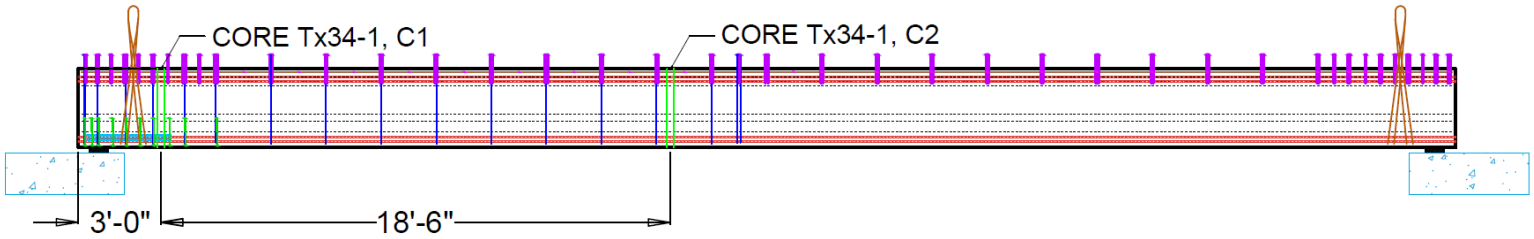

(a) Tx34-1 Core Locations

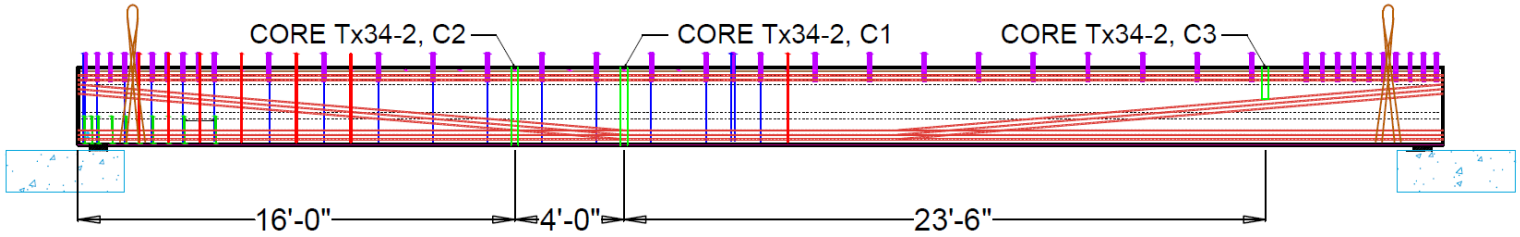

(b) Tx34-2 Core Locations

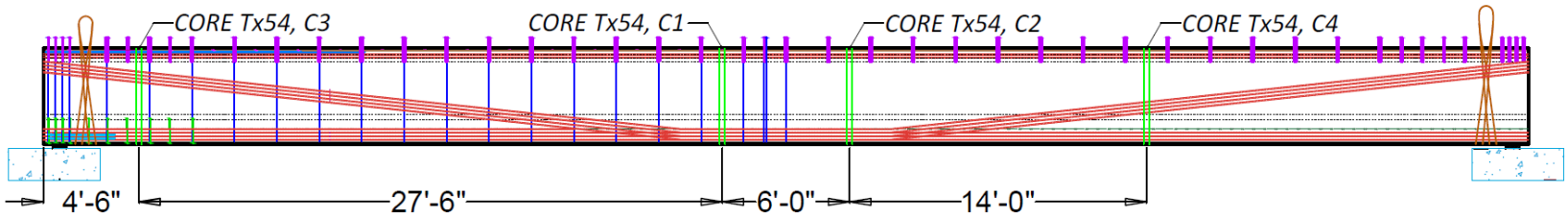

(c) Tx54 Core Locations

Figure 8.2. Core Locations for Girder Specimens.

Figure 8.3, Figure 8.4, and Figure 8.5 show the conventional photo images at 90 degrees and rolled-out surface photo images of the cores for Tx34-1, Tx34-2, and Tx54, respectively. The small brighter spots on the surface are steel fibers. Based on review of the surface images, the steel fibers appear to be well distributed for all cored samples. The distribution of steel fibers is further investigated using the X-ray CT scanned images in Section 8.4.1.

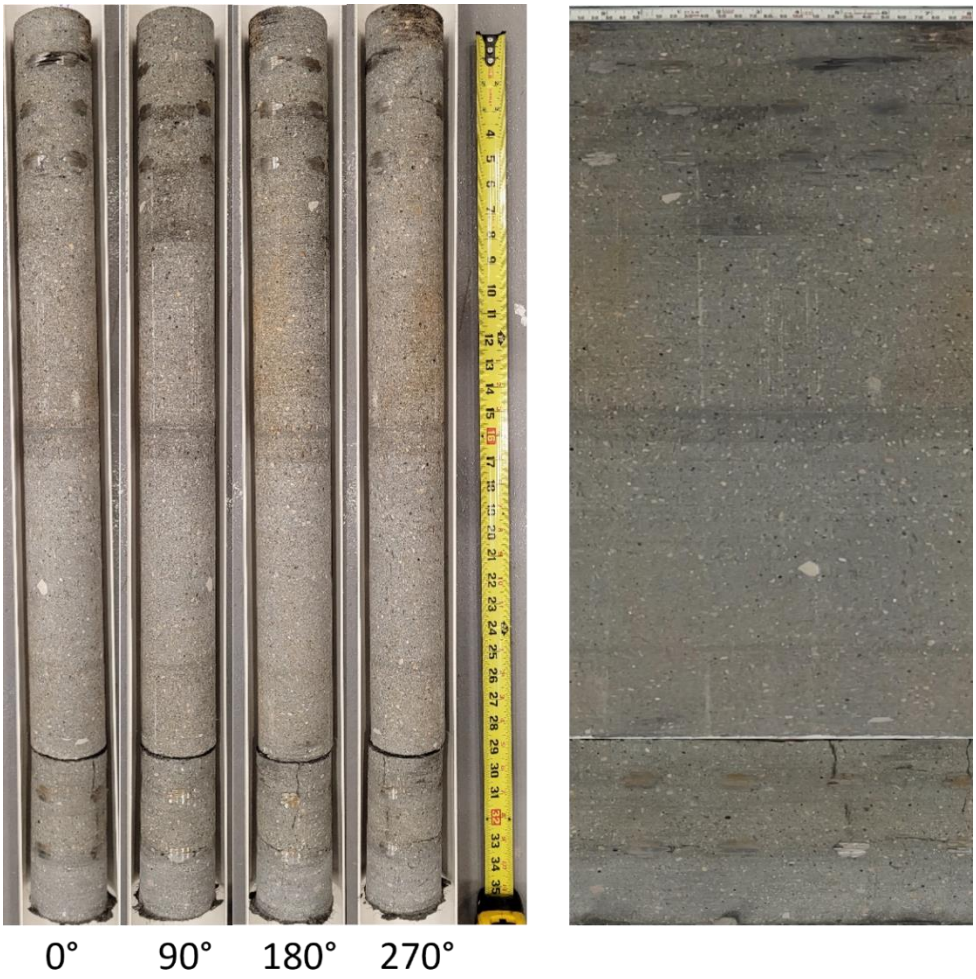

(i) Surface Image of the Core

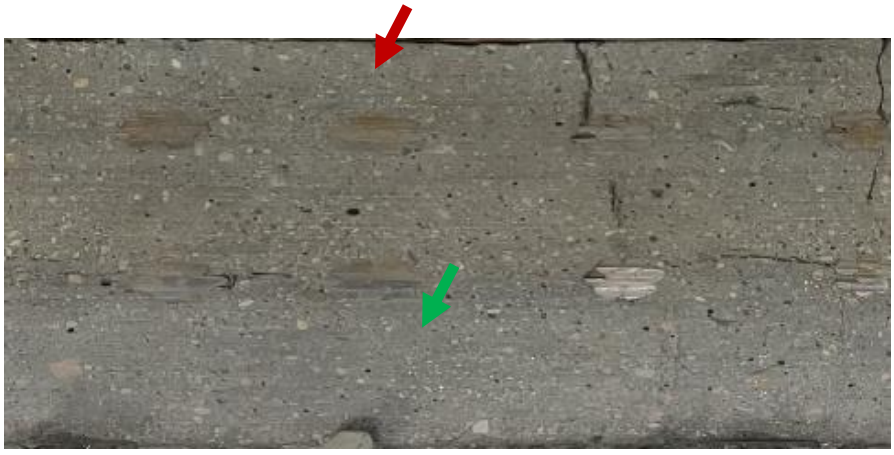

(ii) Enlarged Surface Image

Red arrow: prestressing strand; Green arrow: steel fibers

(a) Core C1

Figure 8.3. Tx34-1 Core Photos.

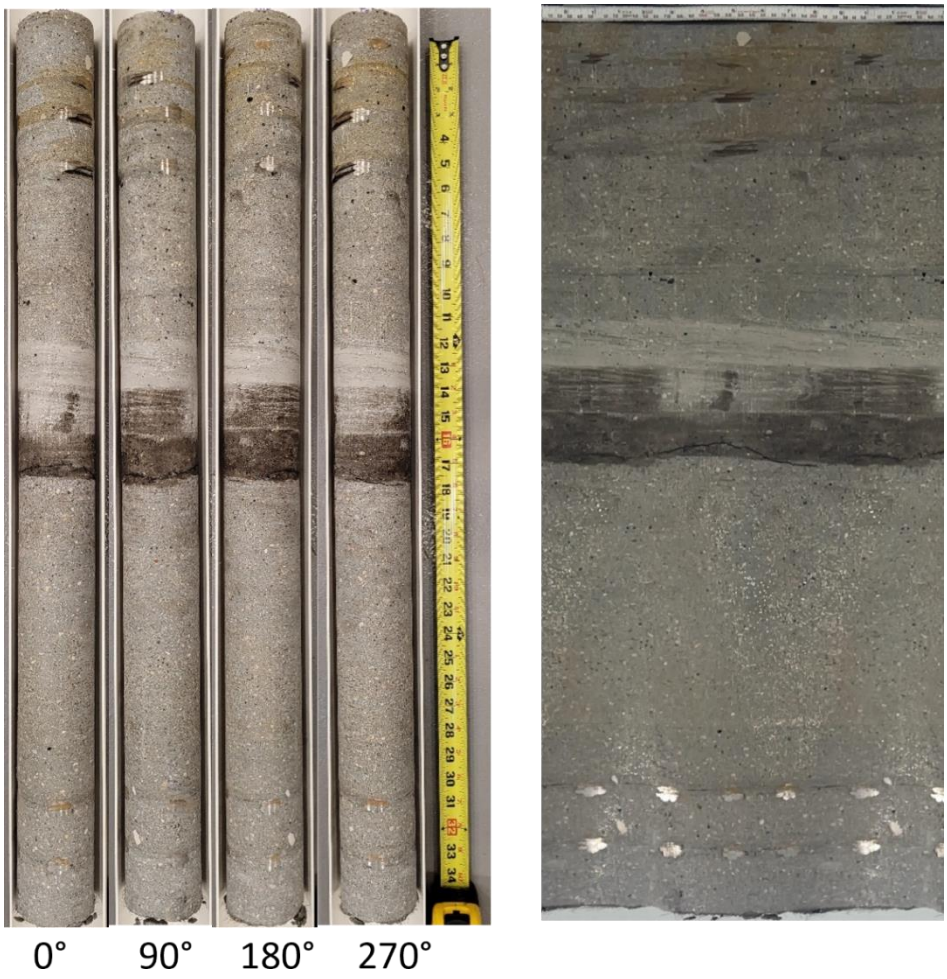

(i) Surface Image of the Core

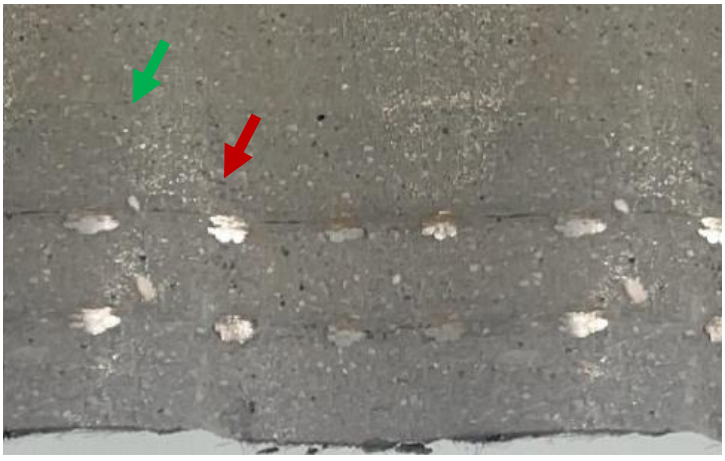

(ii) Enlarged Surface Image

(b) Core C2

Figure 8.3. Tx34-1 Core Photos (Continued).

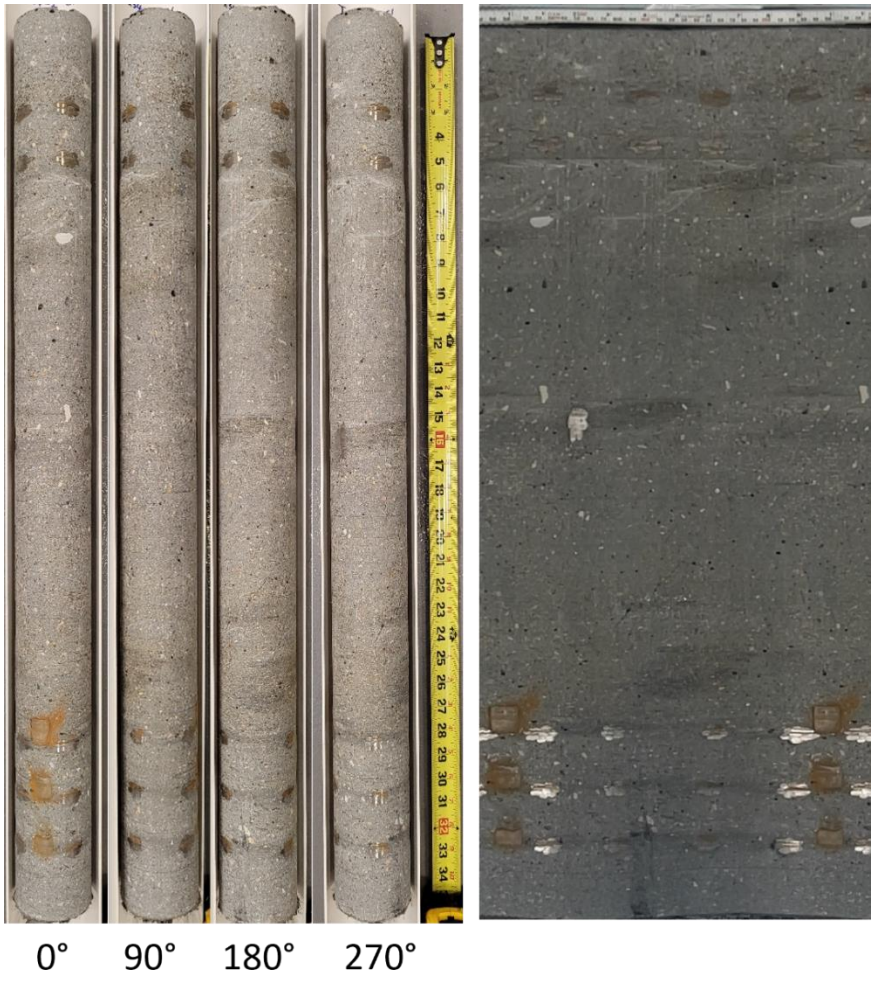

(i) Surface Image of the Core

(ii) Enlarged Surface Image

(a) Core C1

Figure 8.4. Tx34-2 Core Photos.

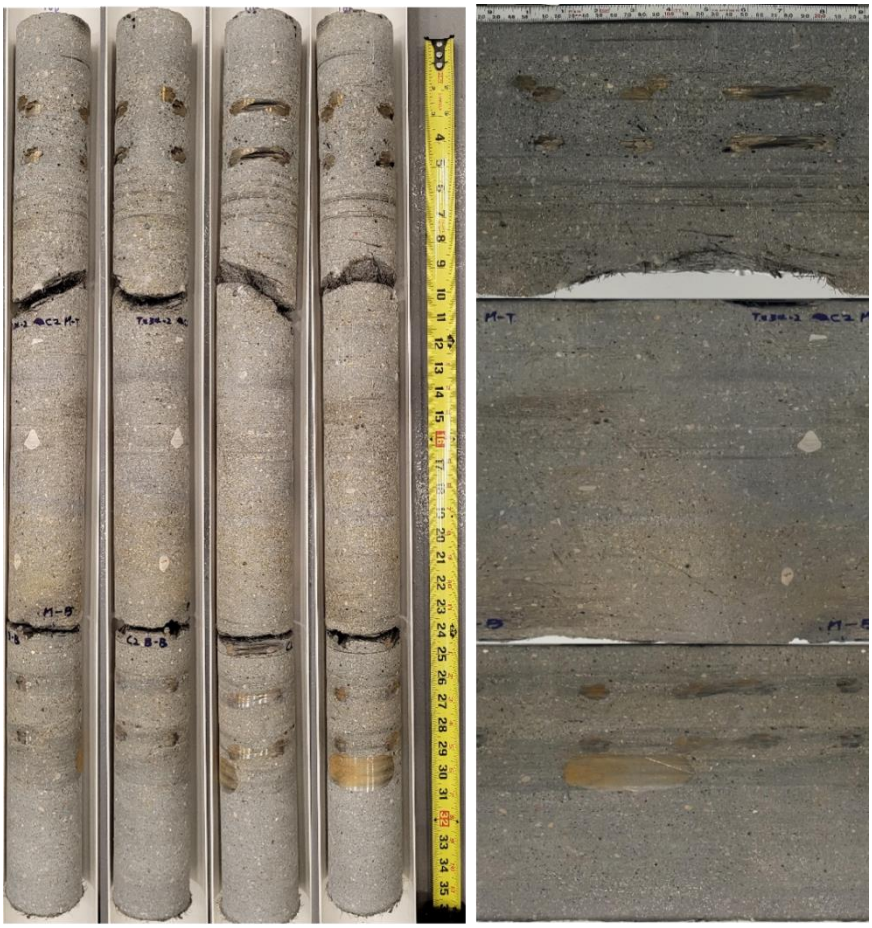

(i) Surface Image of the Core

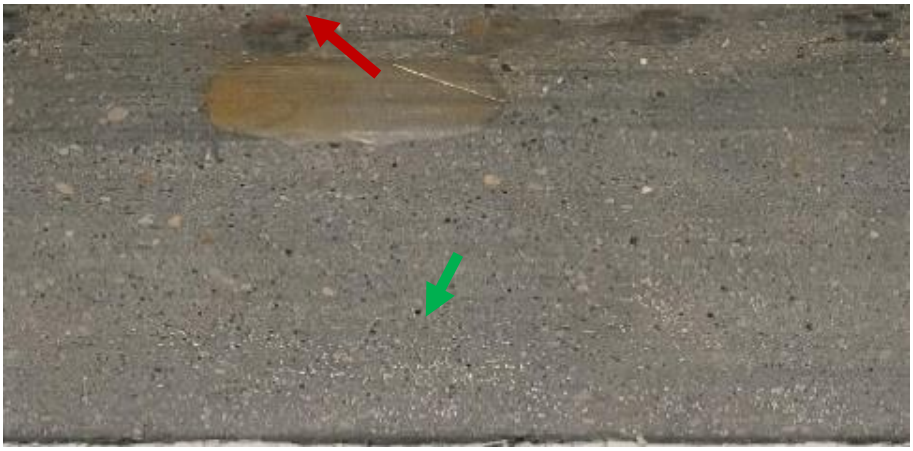

(ii) Enlarged Surface Image

(b) Core C2

Figure 8.4. Tx34-2 Core Photos (Continued).

(i) Surface Image of the Core

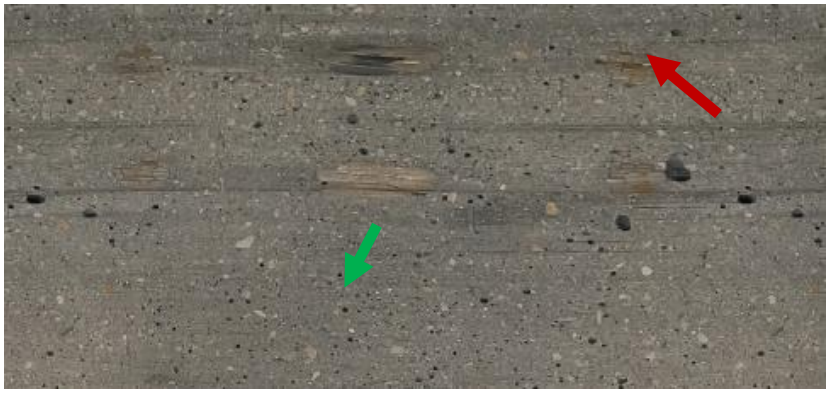

(ii) Enlarged Surface Image

(c) Core C3

Figure 8.4. Tx34-2 Core Photos (Continued).

(i) Surface Image of the Core

Figure 8.5. Tx54 Core Photos.

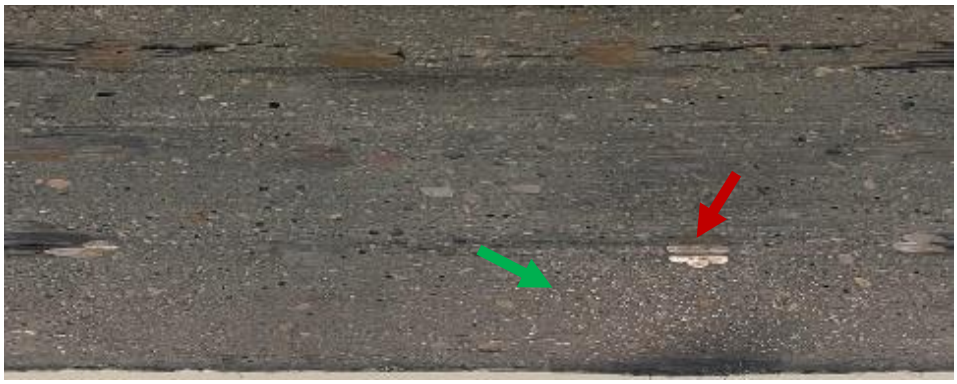

(ii) Enlarged Surface Image

(a) Core C1

Figure 8.5. Tx54 Core Photos (Continued).

(i) Surface Image of the Core

Figure 8.5. Tx54 Core Photos (Continued).

(ii) Enlarged Surface Image

(b) Core C2

Figure 8.5. Tx54 Core Photos (Continued).

(i) Surface Image of the Core

Figure 8.5. Tx54 Core Photos (Continued).

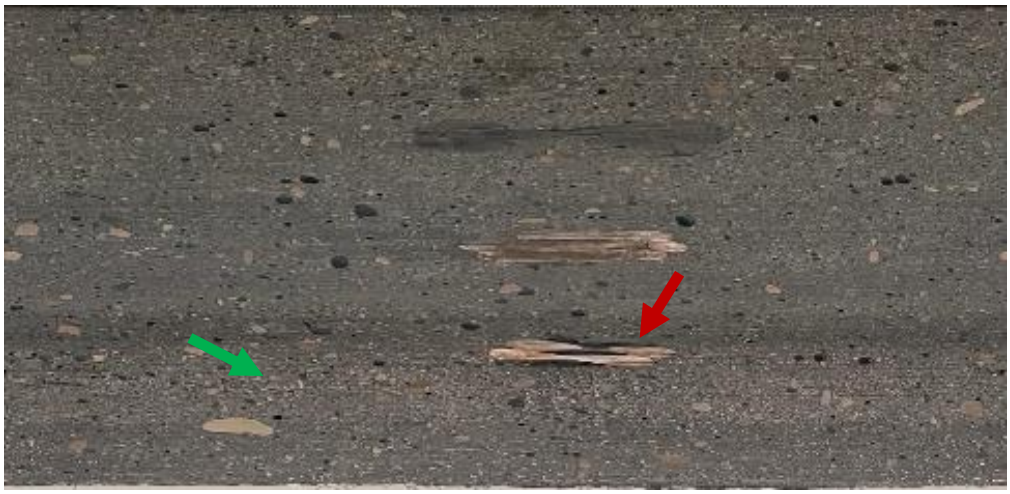

(ii) Enlarged Surface Image

(c) Core C3

Figure 8.5. Tx54 Core Photos (Continued).

(i) Surface Image of the Core

Figure 8.5. Tx54 Core Photos (Continued).

(ii) Enlarged Surface Image

(d) Core C4

Figure 8.5. Tx54 Core Photos.

8.3 COMPRESSIVE STRENGTH OF CORED SAMPLES

The compressive strengths were measured using cores from the three girder specimens. The compressive strength values of the cored samples were compared with the strength measurements using cylinders. Figure 8.6, Figure 8.7, and Figure 8.8 show the locations of the samples for compressive strength testing from girder specimens Tx34-1, Tx34-2, and Tx54, respectively. The compressive strength samples are 6 in. long and are cut from the 3 in. diameter cores, yielding 3 × 6 in. cylinders. Table 8.1, Table 8.2, and Table 8.3 show the compressive strength test results of both the cored samples and the cast cylinders for Tx34-1, Tx34-2, and Tx54, respectively. Figure 8.9 presents the notation for the core identifiers.

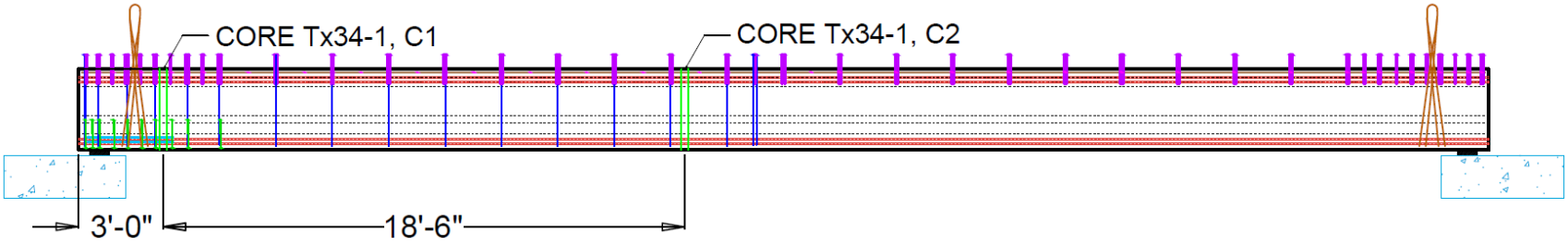

a) Tx34-1 Core Location

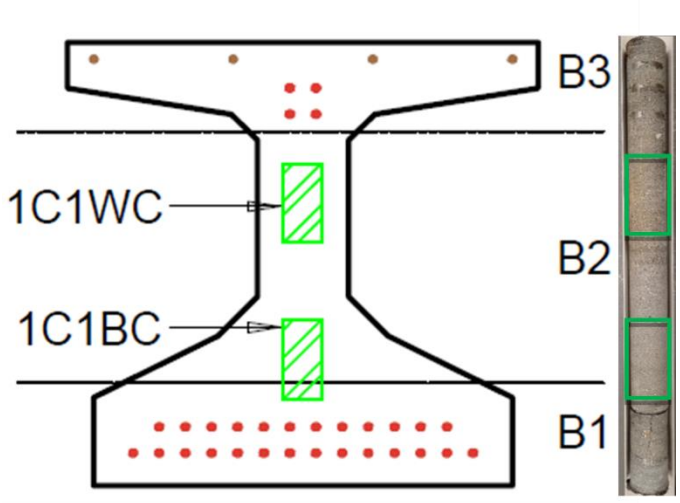

(b) Sample Locations of C1

1C1WC: 19.6 ksi
1C1BC: 18.4 ksi

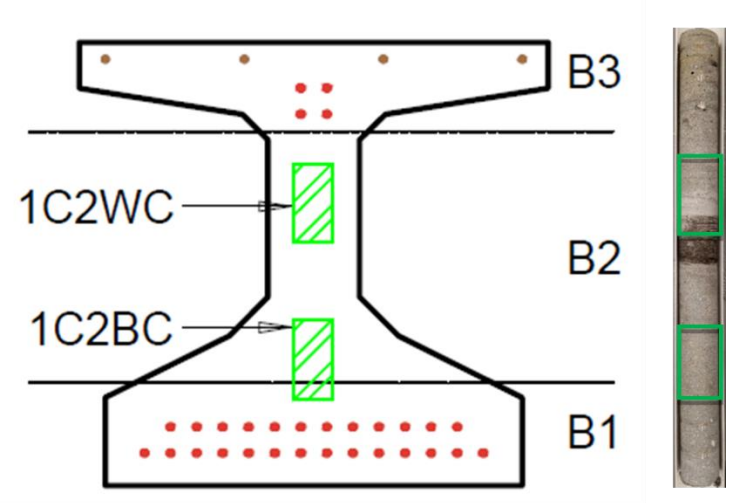

(c) Sample Locations of C2

1C2WC: 20.4 ksi
1C2BC: 19.8 ksi

Figure 8.6. Tx34-1 Sample Locations for Compressive Strength.

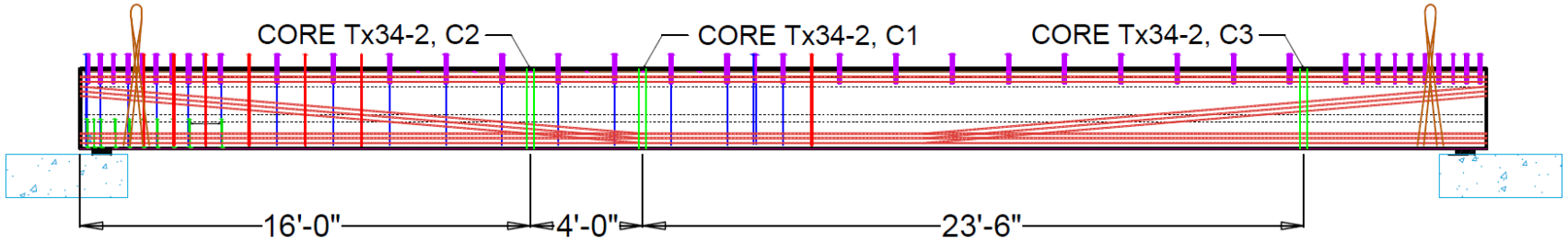

(a) Tx34-2 Core Location

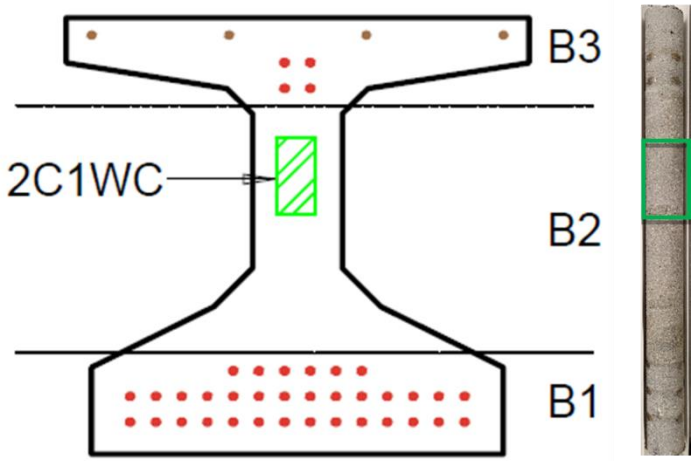

(b) Sample Location of C1

2C1WC: 19.9 ksi

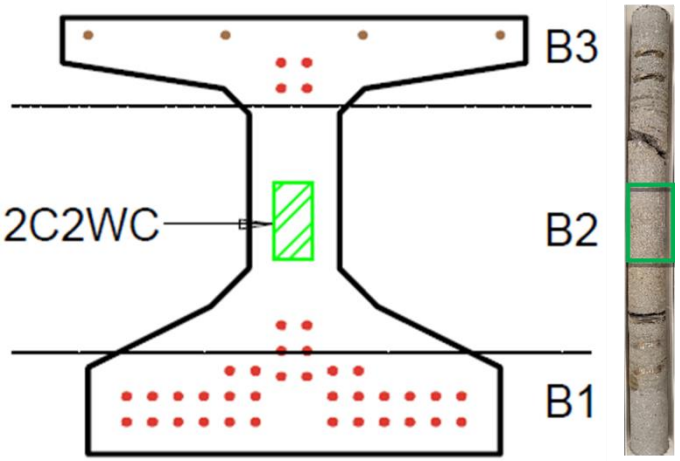

(c) Sample Location of C2

2C2WC: 20.2 ksi

Figure 8.7. Tx34-2 Sample Locations for Compressive Strength.

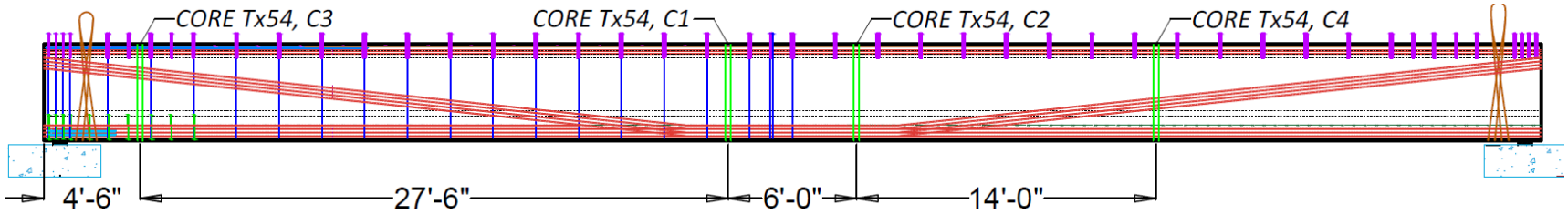

(a) Tx54 Core Location

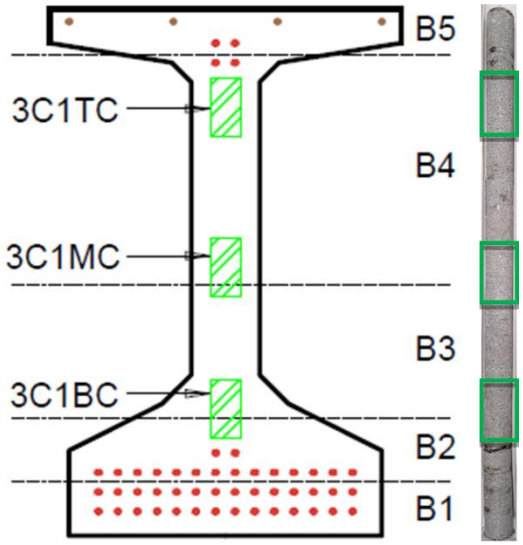

(b) Sample Locations of C1

3C1TC: 13.0 ksi
3C1MC: 19.6 ksi
3C1BC: 16.9 ksi

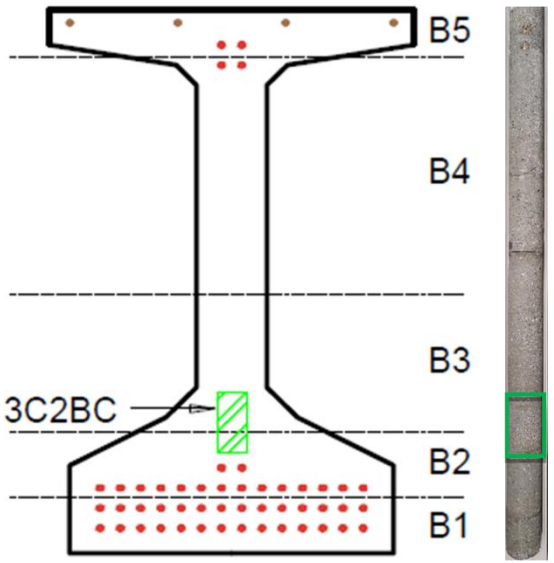

(c) Sample Locations of C2

3C2BC: 19.1 ksi

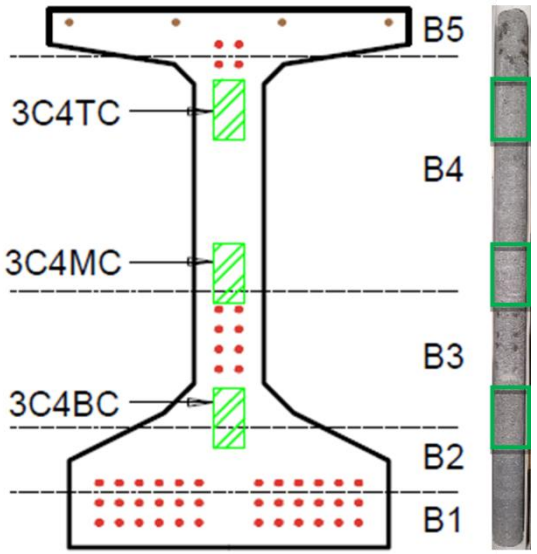

(d) Sample Locations of C4

3C4TC: 20.2 ksi
3C4MC: 21.8 ksi
3C4BC: 18.1 ksi

Figure 8.8. Tx54 Samples Location for Compressive Strength.

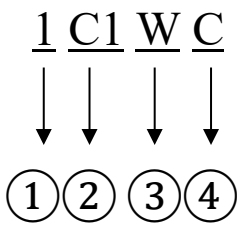

① = Girder number: 1, 2, and 3 are for Tx34-1, Tx34-2, and Tx54, respectively.

② = Core number

③ = Sample location for compression test: W, B, T, and M are for web, bottom, top, and middle, respectively.

④ = C for compression

Figure 8.9. Core ID Notation.

Table 8.1. Tx34-1 Compressive Strength of Cored Samples.

Cores		**Cast Cylinders**	
Core ID	Strength, ksi	Cylinder No.	Strength, ksi
1C1WC	19.6	1	19.3
1C1BC	18.4	2	17.9
1C2WC	20.4	3	-
1C2BC	19.8	-	-
Average	19.6	Average	18.6
CoV	3.7%	CoV	3.1%

Note:
1. Tested at the age of 391 days.
2. - : Not available.

Table 8.2. Tx34-2 Compressive Strength of Cored Samples.

Cores		**Cast Cylinders**	
Core ID	Strength, ksi	Cylinder No.	Strength, ksi
2C1WC	19.9	1	19.5
2C2WC	20.2	2	16.7
-	-	3	18.5
Average	20.0	Average	18.2
CoV	0.8%	CoV	6.3%

Note:
1. Tested at the age of 321 days.
2. - : Not available.

Table 8.3. Tx54 Compressive Strength of Cored Samples.

Cores		Cast Cylinders	
Core ID	Strength, ksi	Cylinder No.	Strength, ksi
3C1TC	13.0[1]	1	16.2
3C1MC	19.6	2	17.6
3C1BC	16.9	3	17.7
3C2BC	19.1	-	-
3C4TC	20.2	-	-
3C4MC	21.8	-	-
3C4BC	18.1	-	-
Average	19.3	Average	17.2
CoV	8.1%	CoV	3.9%

Note:
1. Outlier—this value is excluded from the average and CoV. CoV is 14.5 percent with this value.
2. Tested at the age of 90 days.
3. - : Not available.

The average strengths of the cored samples from the three girders are 19.6, 20.0, and 19.3 ksi for Tx34-1, Tx34-2, and Tx54, respectively. The strength values are 5.4 percent, 9.9 percent, and 12.2 percent higher than the strength values from the cast cylinders for Tx34-1, Tx34-2, and Tx54, respectively. These findings may be because high heat of hydration at a very early age acts as a heat treatment. As a result, improved microstructure can be formed versus the cast cylinders. In addition, steel fibers are located half a fiber length inward from the side surface of the mold (Wille et al. 2014b). As a result, the surface of the cylinder is smooth. However, the cored sample has the same fiber content at the side surface and the center of the sample. Therefore, the fibers of the cored sample provide a better bonding effect of the UHPC at the surface than the cast cylinder.

8.4 FIBER DISTRIBUTION AND VOID ANALYSIS

8.4.1 Fiber Distribution and Orientation Analysis Using X-Ray CT Images

The distribution and orientation of steel fibers were studied by employing X-ray CT using a Toshiba Aquillon RXL CT scanner at the TAMU Chevron Petrophysical Imaging Laboratory. The cores were scanned by X-ray CT with a 0.02 in. spacing between slices. The resolution of the scanned images was 170–180 micron per pixel. The X-ray CT scanned slice images were then reconstructed in 3D, providing an image for qualitative evaluation of fiber distribution. There were limitations for quantitative analysis due to low resolution, large interval spacing, and relatively low power to penetrate the dense UHPC matrix. The 3D reconstructed images show the fiber distribution and orientation in a depth of 0.4 in. of the cored cylinder (Figure 8.10). The brightness

and contrast of the images were adjusted to see the steel fibers clearly. The black and white colors in the image indicate UHPC and steel fibers, respectively.

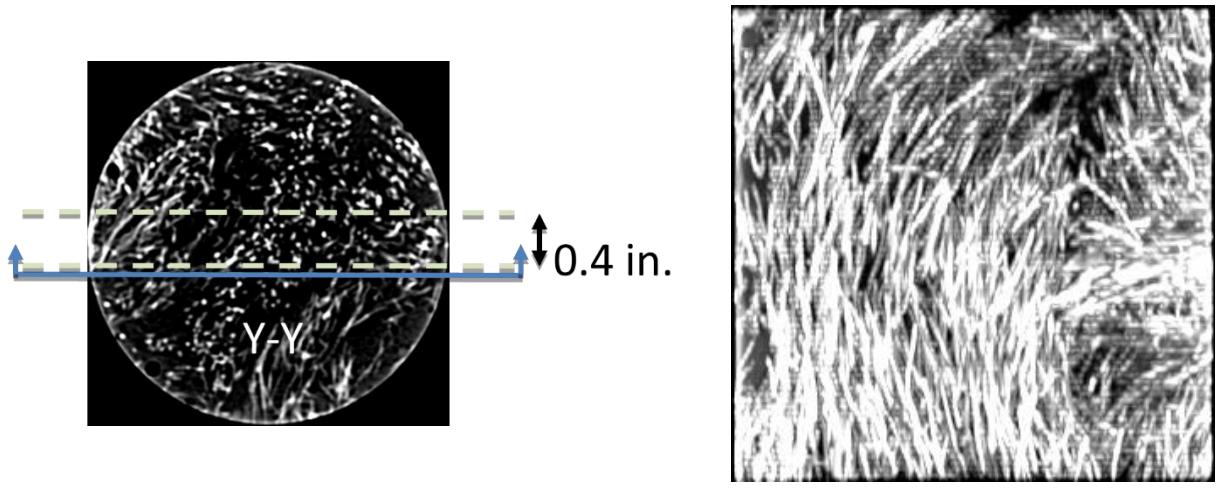

(a) Plan View of a Cored Cylinder

(b) Y-Y Section View with 0.4 in. Depth of Fiber Information

Figure 8.10. Fiber Information of 3D Reconstructed Images.

8.4.1.1 Tx34-1 Girder

Figure 8.11 shows the X-ray CT scanned locations of the Tx34-1 cores. The horizontal dashed lines on the cross sections indicate the theoretical location of each batch (B1, B2, B3). The 3D reconstructed images showing the fiber distribution of Tx34-1 C1 and C2 cored samples are provided in Figure 8.12 and Figure 8.13, respectively.

Figure 8.14 shows the fiber distribution along the girder length in comparison with the fiber distribution of C1 and C2. Core sections 1C1T and 1C2T, located near the top flange, show randomly distributed steel fibers. The fibers of 1C1W located at the web are aligned vertically. The X-X section (plan) view shows several white dots, and the Y-Y section (elevation) view shows vertically aligned steel fibers. This feature may be because the fiber distribution at the location close to the UHPC pour points from the Tuckerbuilt tends to be aligned vertically at the web due to the narrow width. This occurrence is called the wall effect (Wille et al. 2014b). In contrast, the fibers of core section 1C2W located at the web are somewhat aligned along the girder length, which can be seen clearly from the X-X plan view. A possible reason is that the UHPC flows toward the ends of the girder from the pour point. While flowing, fibers are aligned longitudinally

(flow direction) (Yoo and Banthia 2016). Based on these findings from the literature, UHPC from Batch 2 may have been poured to the left or right side of C2 and then flowed toward C2. As a result, the fibers tend to be aligned more horizontally than vertically.

Core sections 1C1B and 1C2B in Figure 8.14 show the fiber distribution at the bottom flange. The fibers of both 1C1B and 1C2B are aligned along the girder length (horizontally). The UHPC likely flowed both in the longitudinal and transverse directions in the bottom flange because the bottom flange has a wide width. In addition to the flow effect, the wall effect by the strands at the bottom flange may influence the alignment at the bottom flange. The same alignment trend at the bottom flange was observed for Tx34-2 (C2) and Tx54 (C1 and C3), which is discussed in the following section.

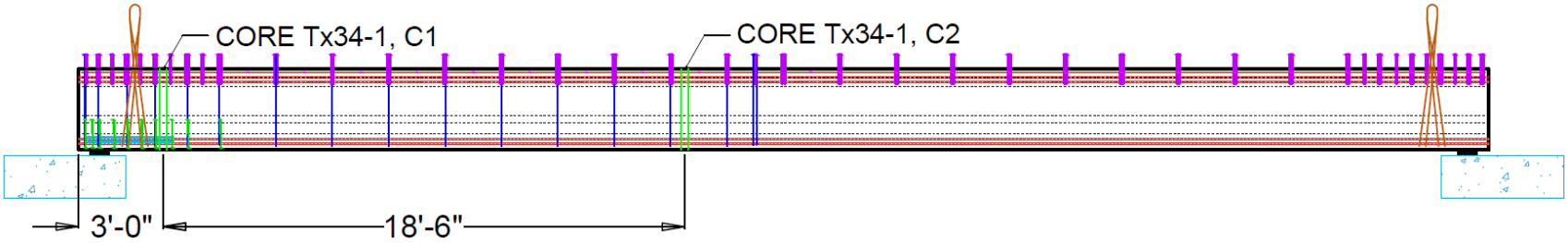

(a) Tx34-1 Core Location

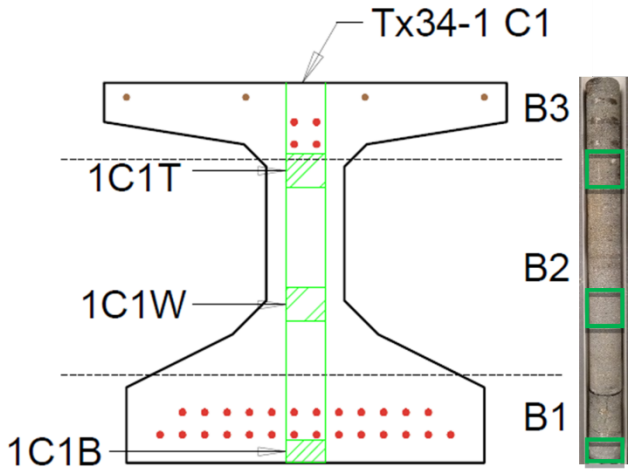

(b) X-ray CT Scan Locations of C1

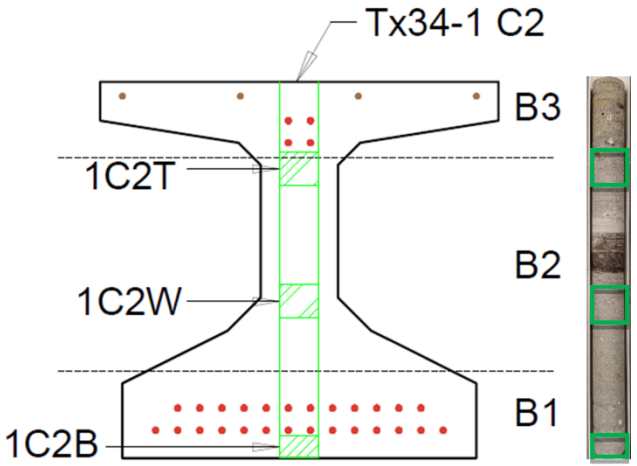

(c) X-ray CT Scan Locations of C2

B1, B2, and B3: Batch 1, Batch 2, and Batch 3, respectively
Diameter of the cored sample: 3 in.

Figure 8.11. Tx34-1 Sample Locations for X-Ray CT Scans.

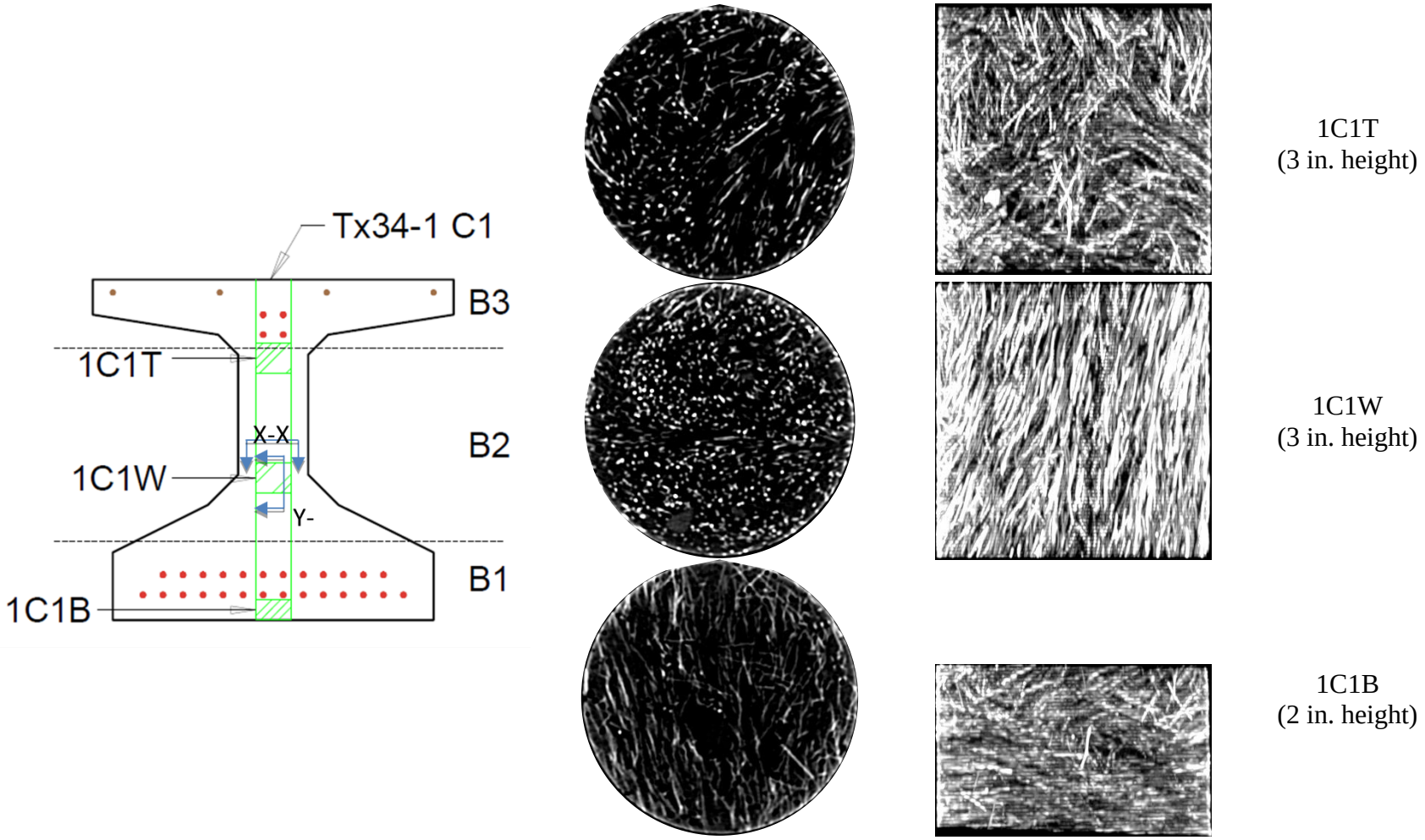

(a) X-ray CT Sample Location *(b) X-X* *(c) Y-Y*

Flow spread: 10.4 in., 11.3 in., and 11.3 in. for B1, B2, and B3, respectively
Black color: UHPC
White color: steel fibers

Figure 8.12. Tx34-1 C1 Fiber Distribution over the Girder Height.

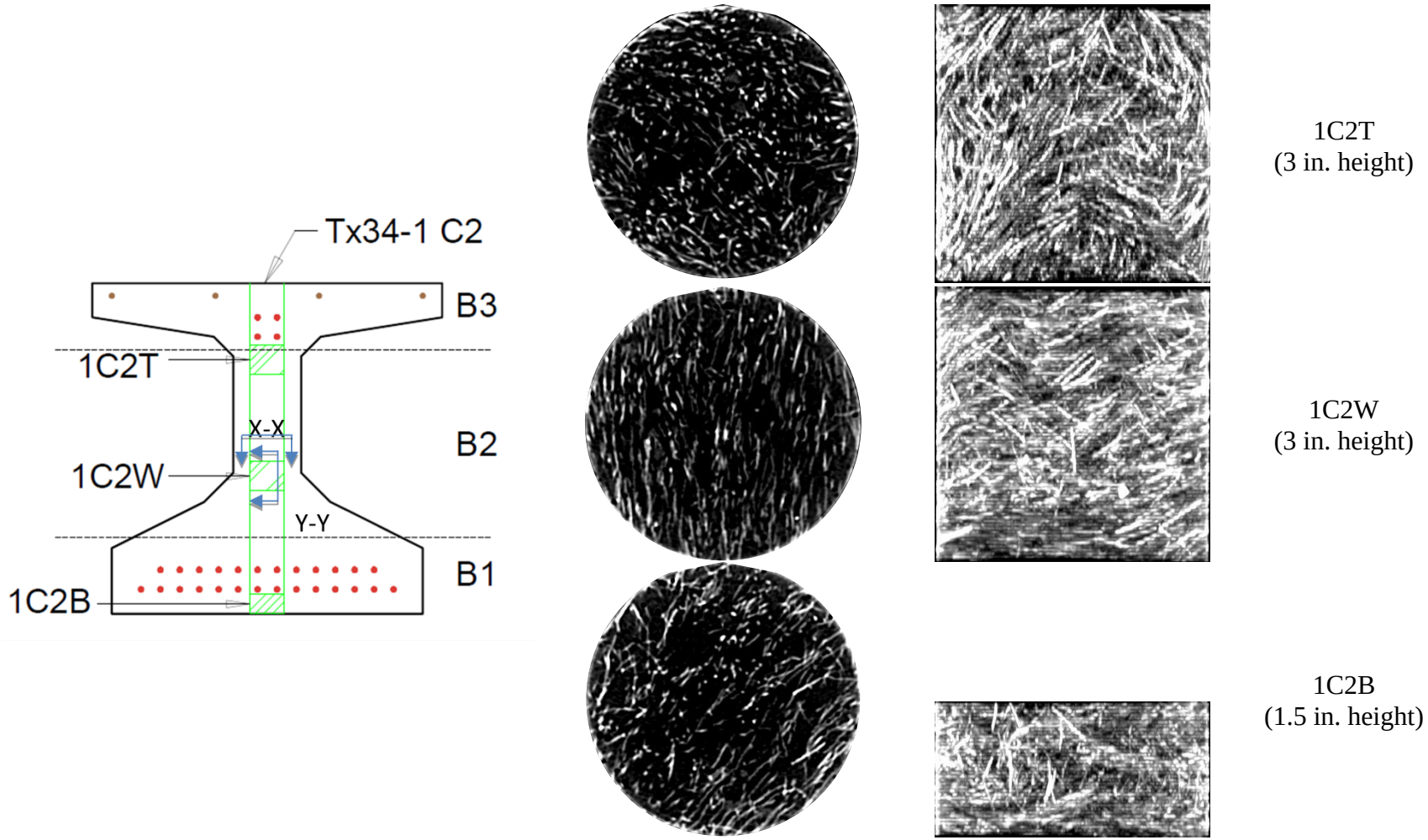

(a) X-ray CT Sample Location *(b) X-X* *(c) Y-Y*

Flow spread: 10.4 in., 11.3 in., and 11.3 in. for B1, B2, and B3, respectively
Black color: UHPC
White color: steel fibers

Figure 8.13. Tx34-1 C2 Fiber Distribution over the Girder Height.

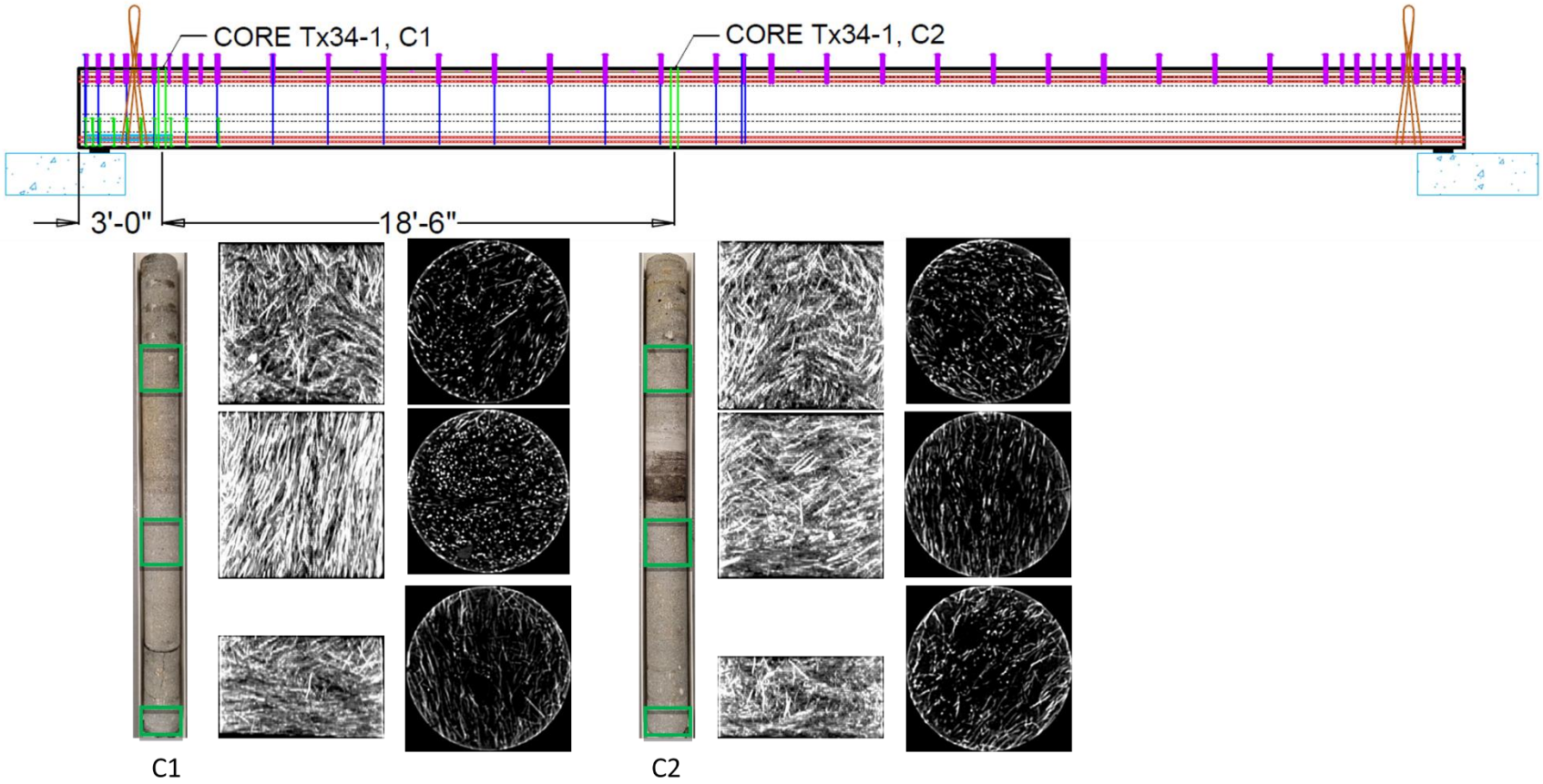

Figure 8.14. Tx34-1 Fiber Distribution along Girder Length.

8.4.1.2 Tx34-2 Girder

Figure 8.15 shows the X-ray CT scanned locations of the Tx34-2 cores. The horizontal dashed lines on the cross sections indicate the theoretical location of each batch (B1, B2, B3). Figure 8.16, Figure 8.17, and Figure 8.18 show the fiber distribution and orientation of steel fibers for C1, C2, and C3, respectively. Figure 8.19 shows the comparison of the fiber distribution along the girder length of C1, C2, and C3 of Tx34-2.

The Tx34-2 C1 core contains the steel rods that were used to hold down the strands for harping. Thus, it could not be used for X-ray CT scanning except for the top flange area. The Tx34-2 C2 and C3 cores were damaged from both coring and full-scale testing. As a result, C2 was cored in three pieces, and only the top portion of the girder was cored for C3.

The fiber distribution of Tx34-2 cores shows a similar trend as seen in the Tx34-1 cores. In general, core sections 2C1T, 2C2T, and 2C2T show random fiber distribution without any segregation of fibers. However, 2C1T and 2C2T show dominant vertical orientation of fibers compared to 2C3T. Core section 2C2W indicates the fiber distribution at the web and shows well-distributed fibers. Core section 2C2B is located at the bottom of the girder, where the fiber orientation is somewhat aligned horizontally, similar to the results from Tx34-1 regarding the bottom flange.

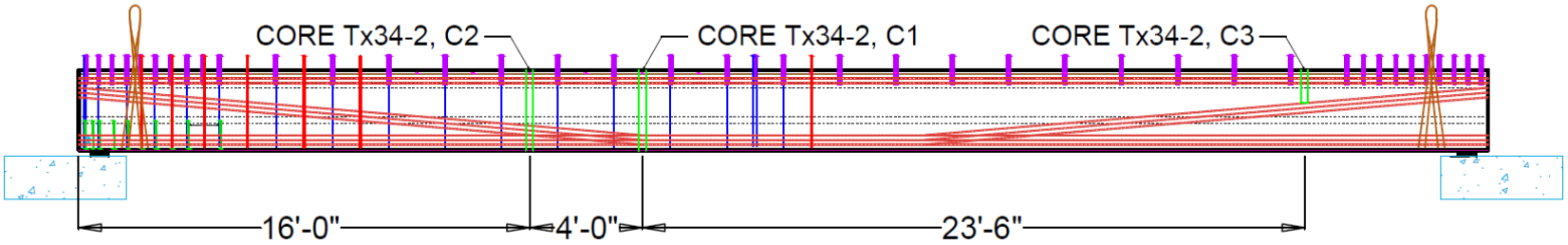

(a) Tx34-2 Core Location

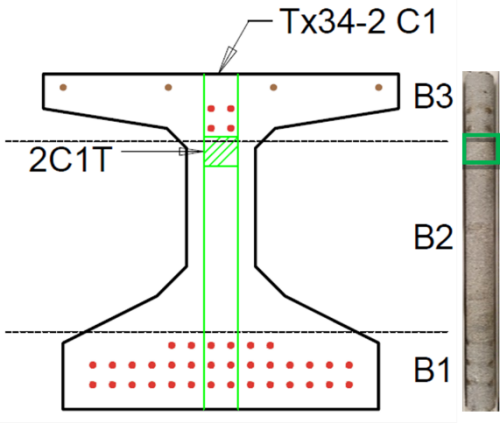

(b) X-ray CT Scan Location of C1

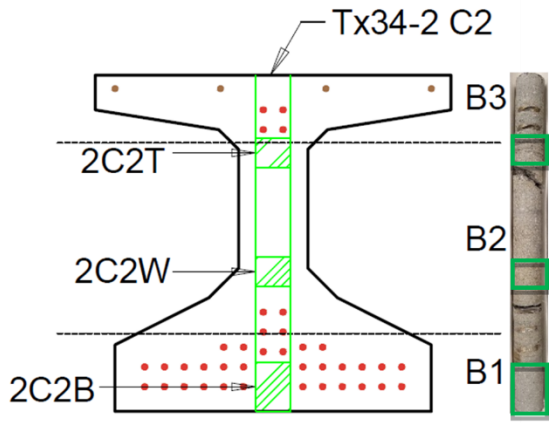

(c) X-ray CT Scan Locations of C2

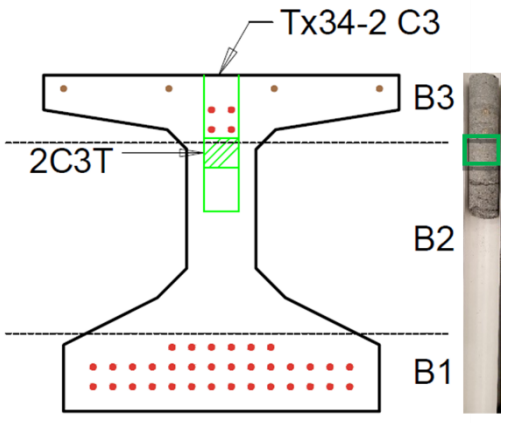

(d) X-ray CT Scan Location of C3

B1: Batch 1
B2: Batch 2
B3: Batch 3
Diameter of the cored sample: 3 in.

Figure 8.15. Tx34-2 Sample Location for X-Ray CT Scans.

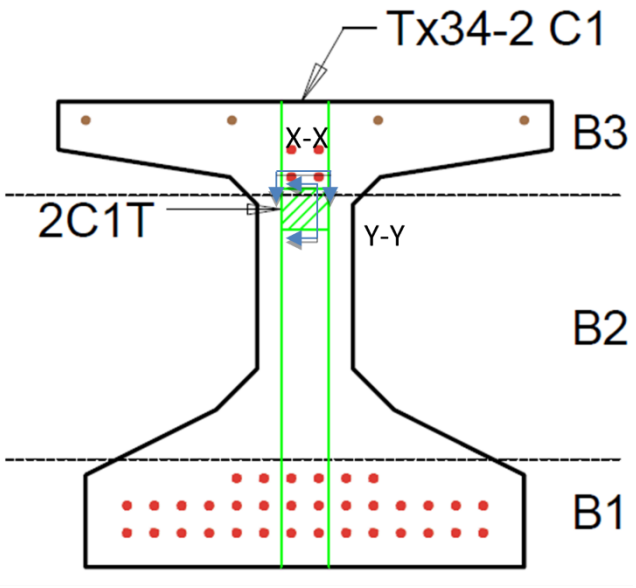

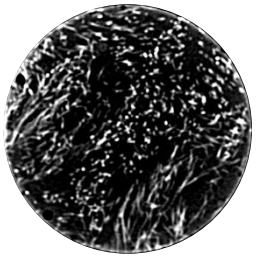

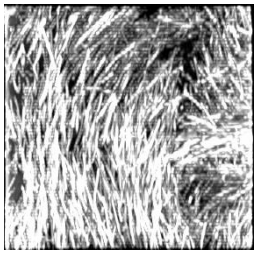

2C1T
(3 in. height)

(a) X-ray CT Scan Location of C1 *(b) X-X* *(c) Y-Y*

Flow spread: 10.4 in., 10.3 in., and 10.5 in. for B1, B2, and B3, respectively
Black color: UHPC
White color: steel fibers

Figure 8.16. Tx34-2 C1 Fiber Distribution over the Girder Height.

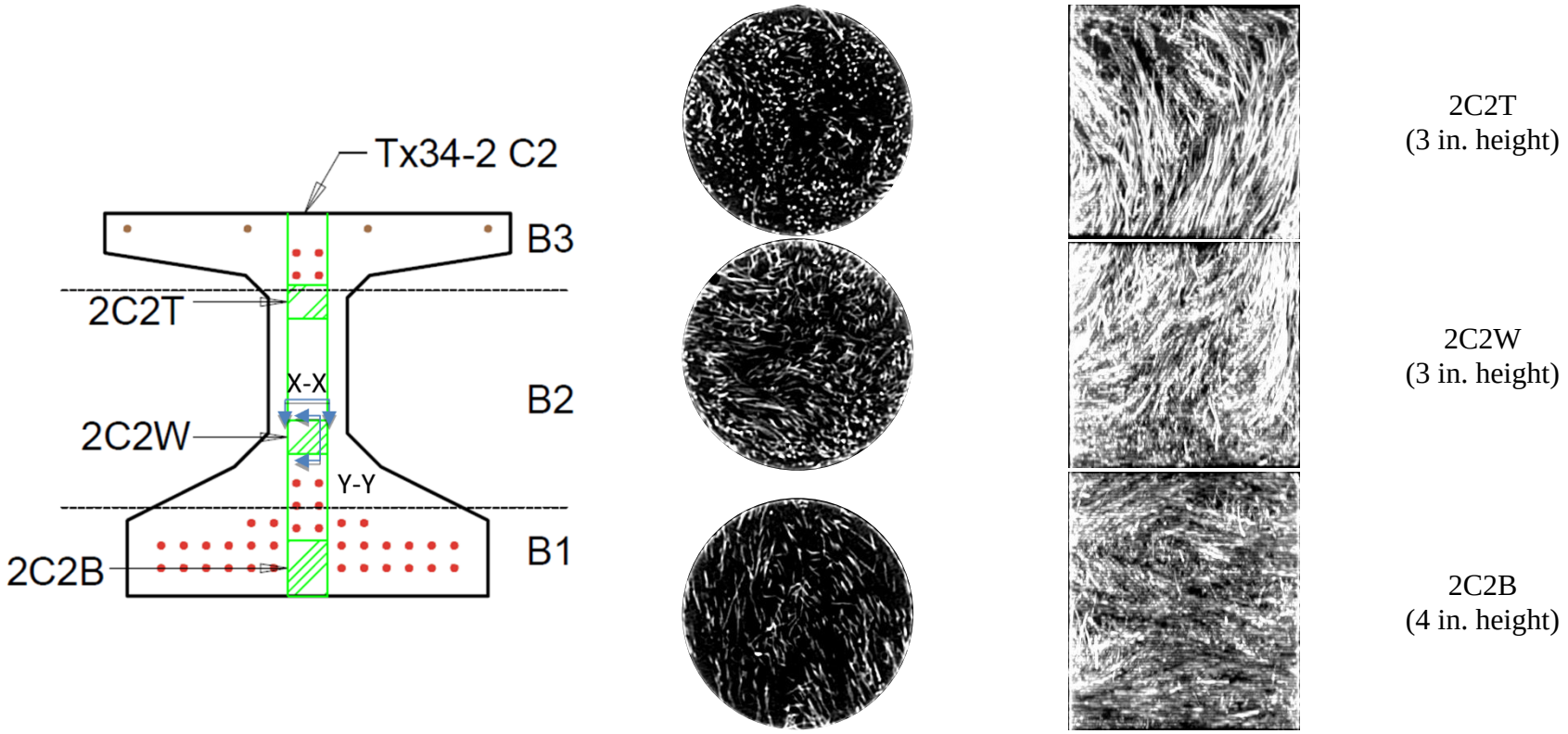

(a) X-ray CT Scan Location of C2 *(b) X-X* *(c) Y-Y*

Flow spread: 10.4, 10.3, and 10.5 in. for B1, B2, and B3, respectively
Black color: UHPC
White color: steel fibers

Figure 8.17. Tx34-2 C2 Fiber Distribution over the Girder Height.

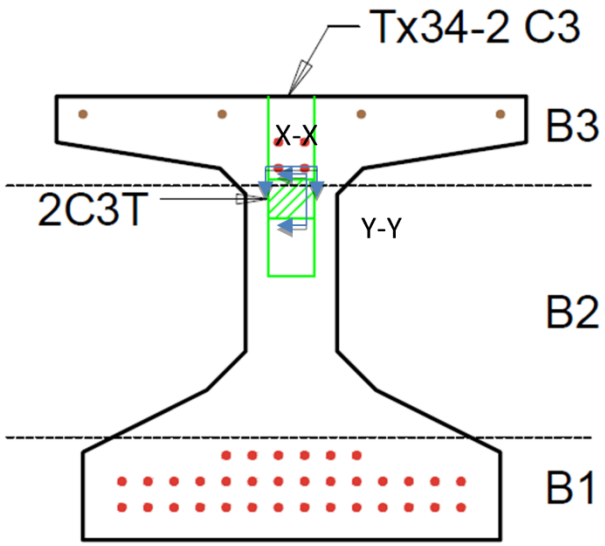

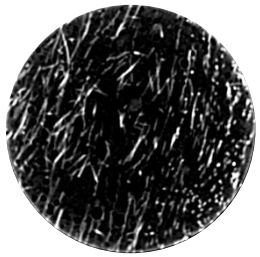

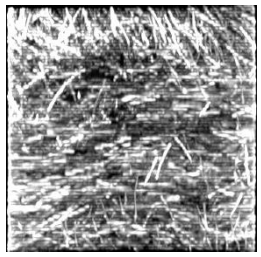

2C3T
(3 in. height)

(a) X-ray CT Scan Locations for C3 *(b) X-X* *(c) Y-Y*

Flow spread: 10.4 in., 10.3 in., and 10.5 in. for B1, B2, and B3, respectively
Black color: UHPC
White color: steel fibers

Figure 8.18. Tx34-2 C3 Fiber Distribution over the Girder Height.

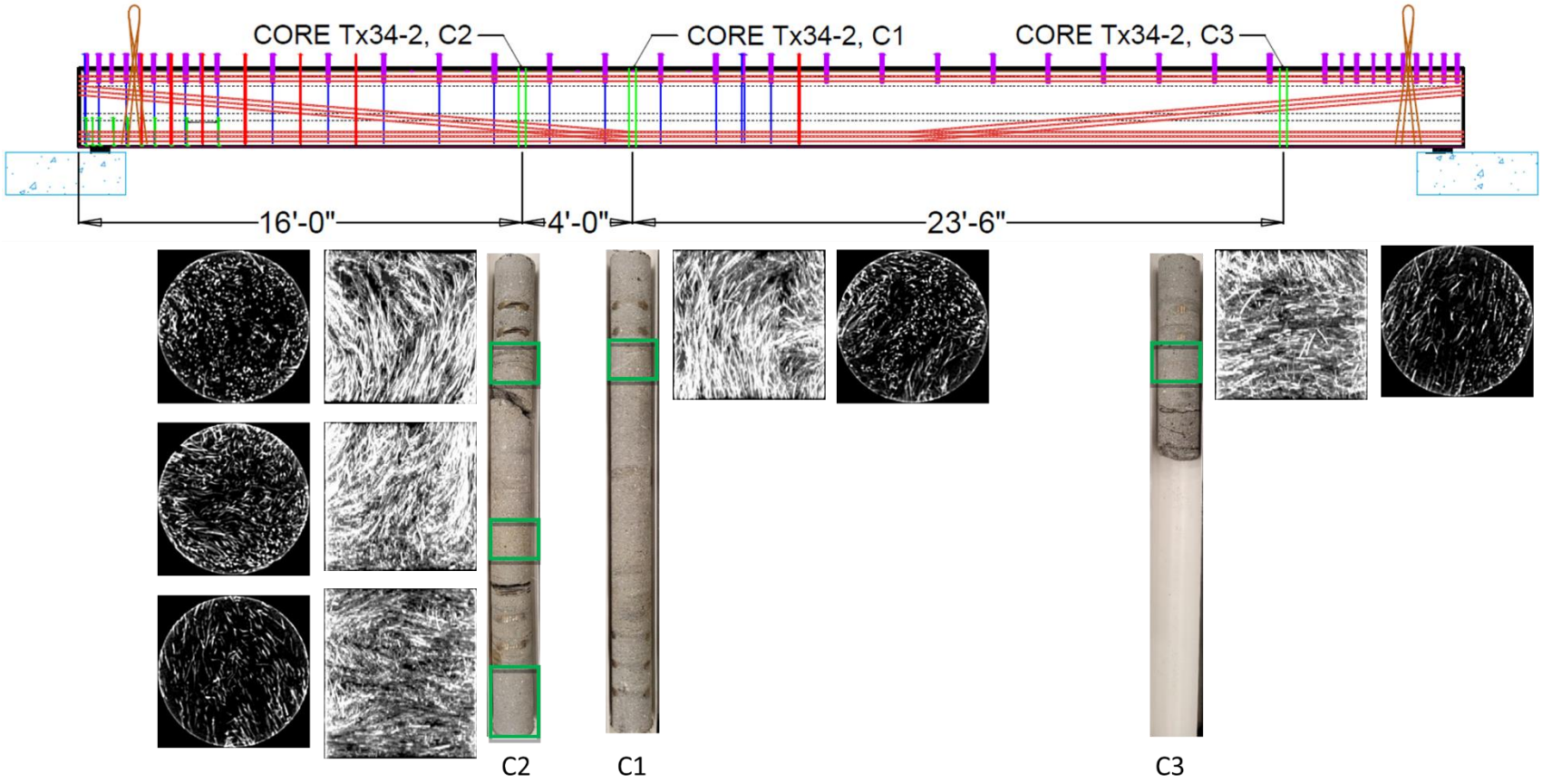

Figure 8.19. Tx34-2 Fiber Distribution along Girder Length.

8.4.1.3 Tx54 Girder

Tx54 has four cored samples. Cores C1 and C2 are from the midspan region, C3 is taken near one girder end, and C4 is from the quarter span at the other girder end (Figure 8.20). The horizontal dashed lines on the cross sections indicate the theoretical location of each batch (B1, B2, B3, B4, B5). For the Tx54 girder X-ray CT scanning, longer sample lengths were considered for the X-ray CT to see the fiber distribution and orientation along the girder height. The X-ray CT samples of Tx34-1 and Tx34-2 have a 3–4 in. height. The tallest sample height from the Tx54 is 23 in. (core section 3C4T). Even though the tall samples are useful to see the fiber distribution vertically, the X-ray scanned image of the taller samples has a relatively lower resolution than the shorter samples. Thus, the X-X section (plan) views of the tall samples have blurred fiber images (Figure 8.21).

Figure 8.21 through Figure 8.24 present fiber distribution and orientation by the 3D reconstructed scanned images of the C1 to C4 cored samples. Overall, the fibers are distributed randomly along the girder height. Cores C2 and C4, which have 20 in. and 23 in. long samples, show the fiber distribution along the girder height clearly. Figure 8.25 shows the fiber distribution along the girder length by presenting the fiber distribution of the four cored samples. These images show that the fibers are randomly distributed along the girder length and along the girder height.

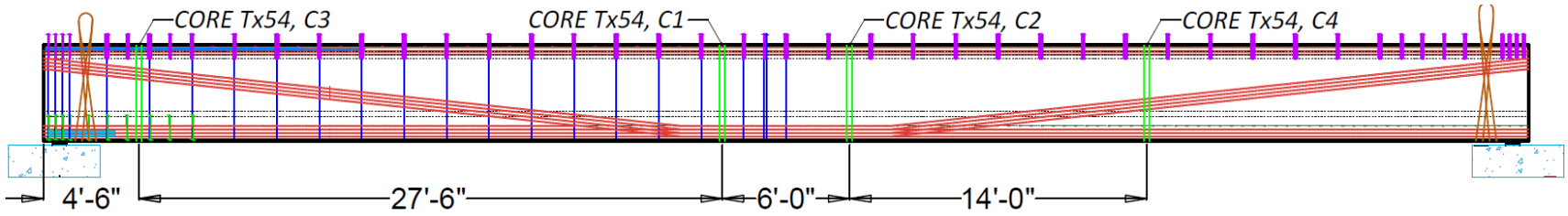

(a) Tx54 Core Location

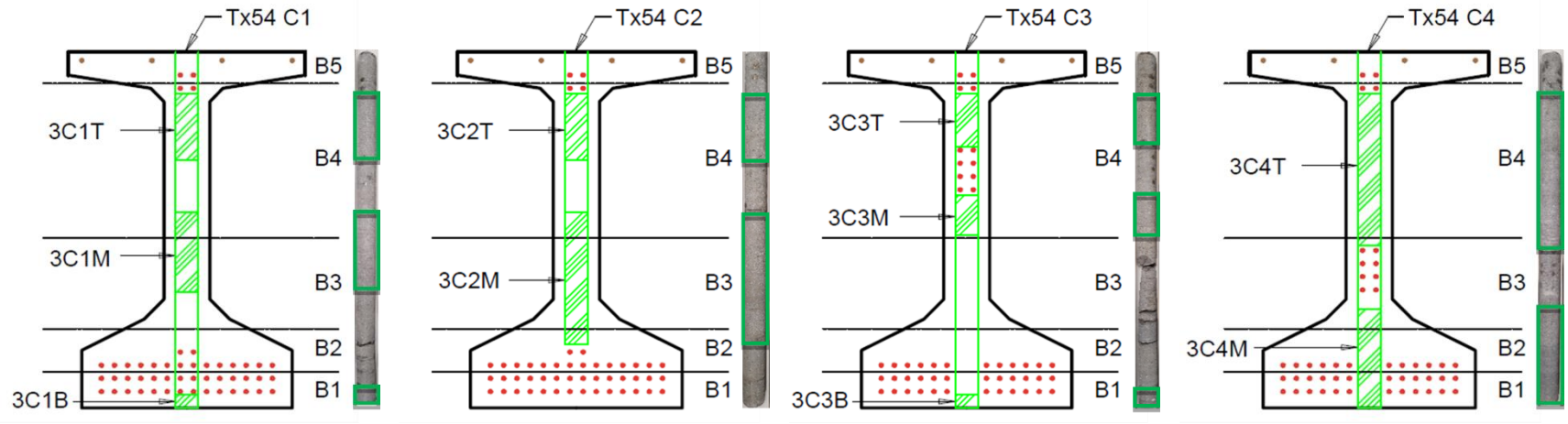

(b) X-ray CT Scan Location of C1

(c) X-ray CT Scan Location of C2

(d) X-ray CT Scan Location of C3

(e) X-ray CT Scan Location of C4

B1, B2, B3, B4, and B5: Batch 1, 2, 3, 4, and 5, respectively
Diameter of the cored sample: 3 in.

Figure 8.20. Tx54 Sample Locations for X-Ray CT Scans.

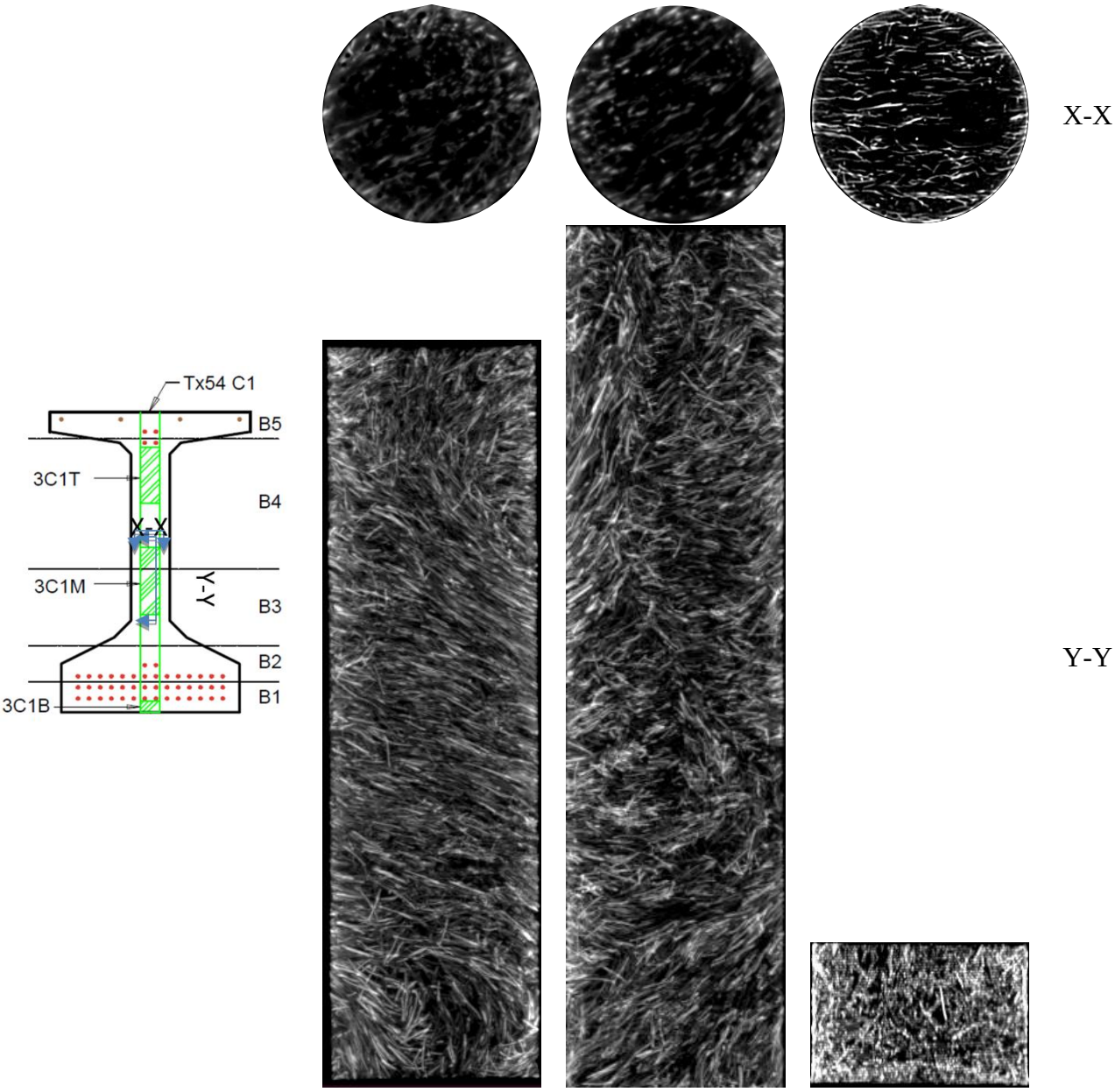

(a) X-ray CT Sample Locations

(b) 3C1T (10 in. height)

(c) 3C1M (12 in. height)

(d) 3C1B (2 in. height)

Flow spread: 9.8 in., 10.3 in., 9.8 in., 10.1 in., and 10.0 in. for B1, B2, B3, B4, and B5, respectively
Black color: UHPC
White color: steel fibers

Figure 8.21. Tx54 C1 X-Ray CT Scanned Images.

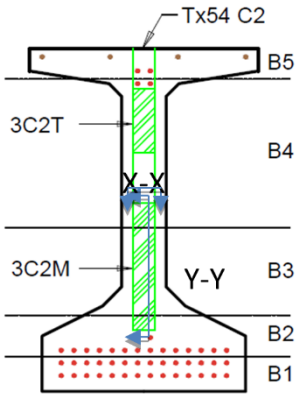

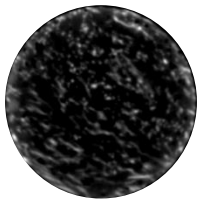

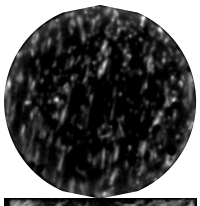

X-X

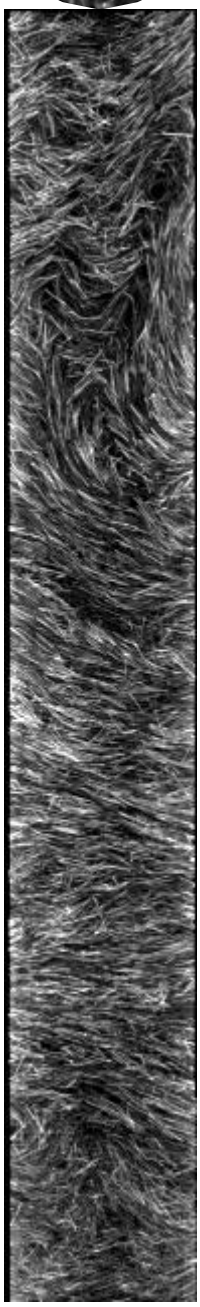

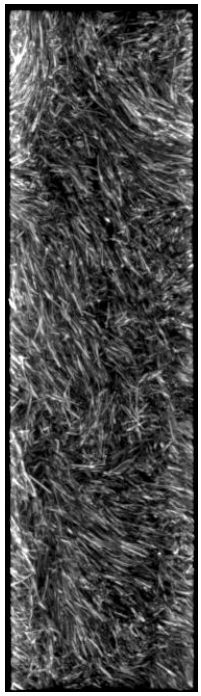

Y-Y

(a) X-ray CT Sample Locations

(b) 3C2T (10 in. height)

(c) 3C2M (20 in. height)

Flow spread: 9.8 in., 10.3 in., 9.8 in., 10.1 in., and 10.0 in. for B1, B2, B3, B4, and B5, respectively

Figure 8.22. Tx54 C2 X-Ray CT Scanned Images.

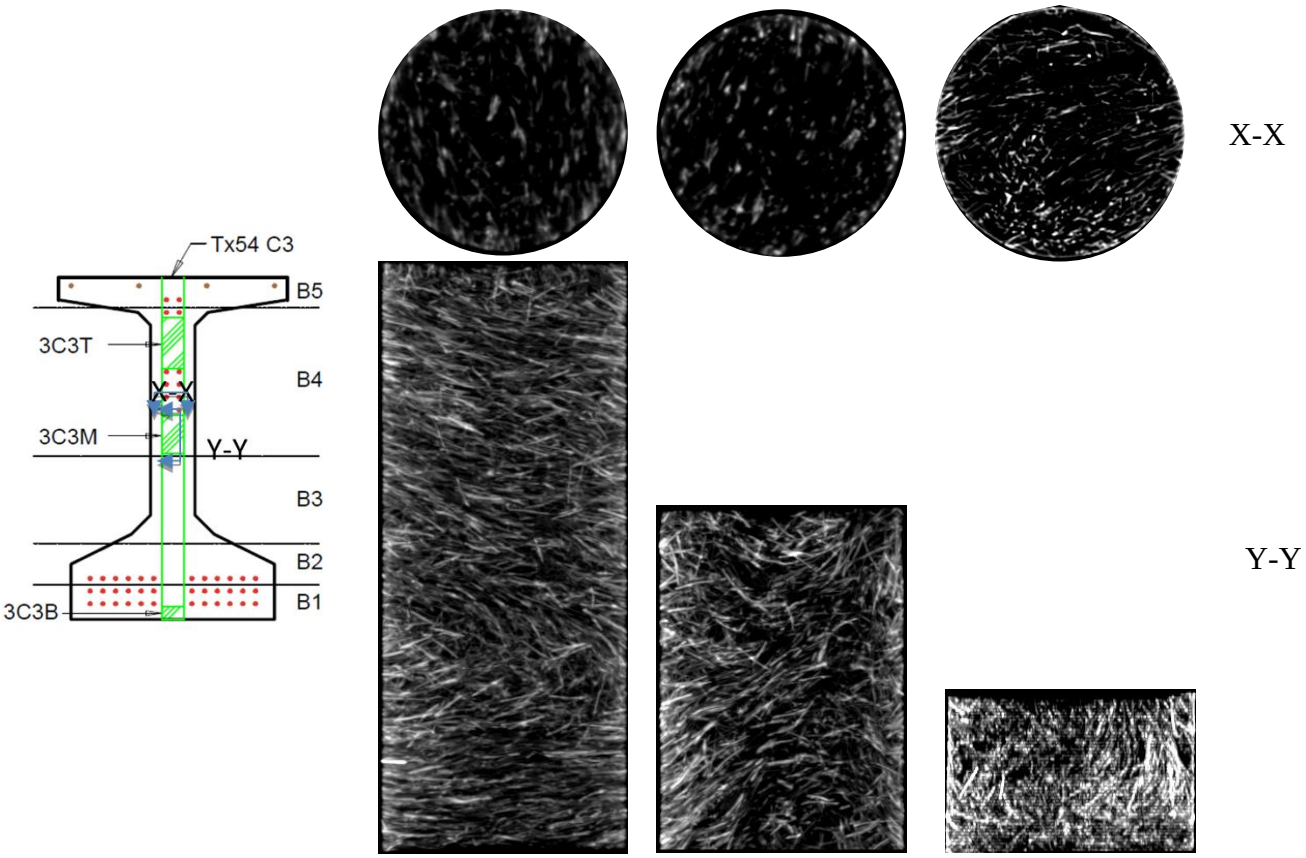

(a) X-ray CT Sample Locations

(b) 3C3T (7 in. height)

(c) 3C3M (5 in. height)

(d) 3C3B (2 in. height)

Flow spread: 9.8 in., 10.3 in., 9.8 in., 10.1 in., and 10.0 in. for B1, B2, B3, B4, and B5, respectively
Black color: UHPC
White color: steel fibers

Figure 8.23. Tx54 C3 X-Ray CT Scanned Images.

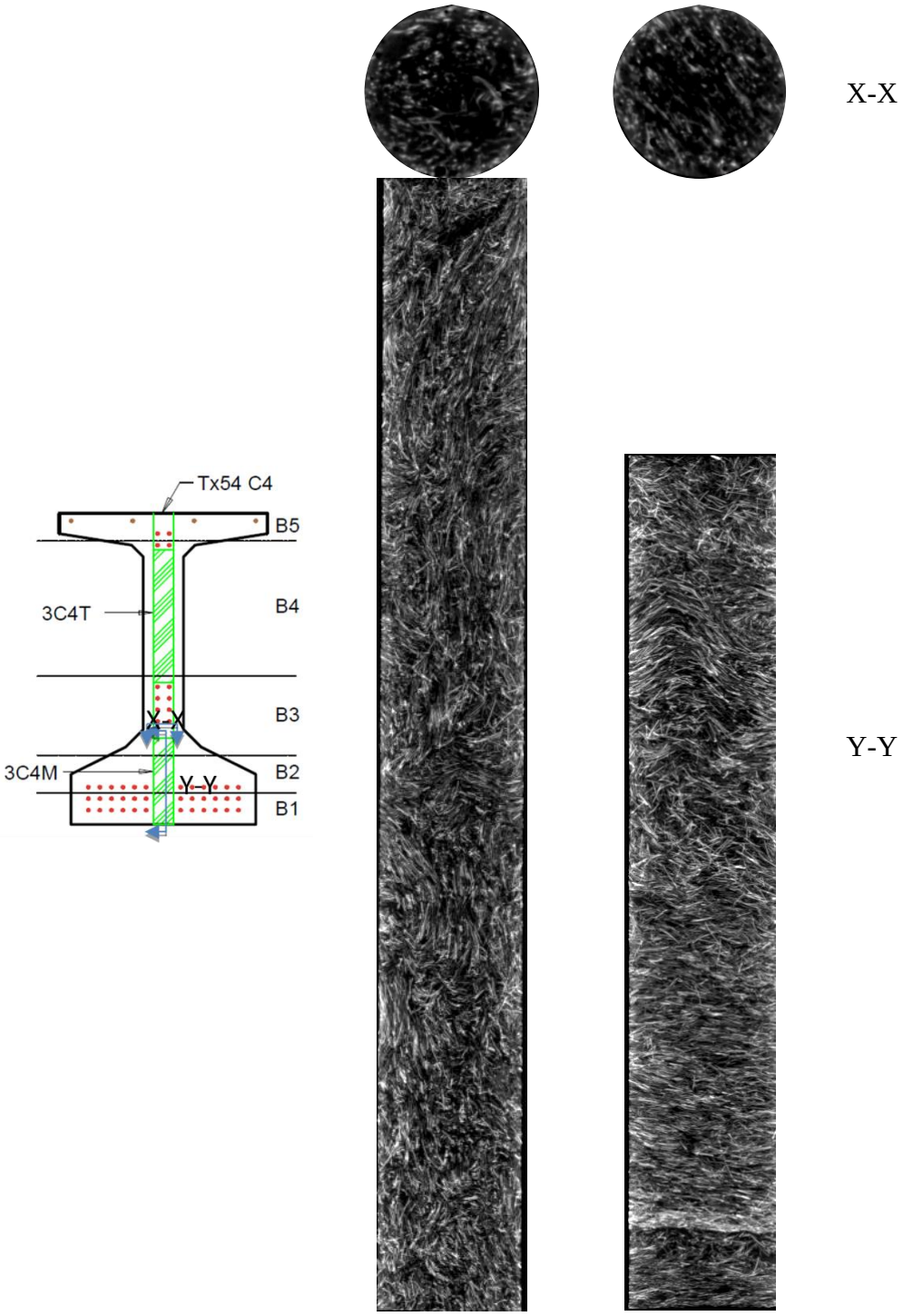

(a) X-ray CT Sample Locations

(b) 3C4T (23 in. height)

(c) 3C4M (17 in. height)

Flow spread: 9.8 in., 10.3 in., 9.8 in., 10.1 in., and 10.0 in. for B1, B2, B3, B4, and B5, respectively
Black color: UHPC
White color: steel fibers

Figure 8.24. Tx54 C4 X-Ray CT Scanned Images.

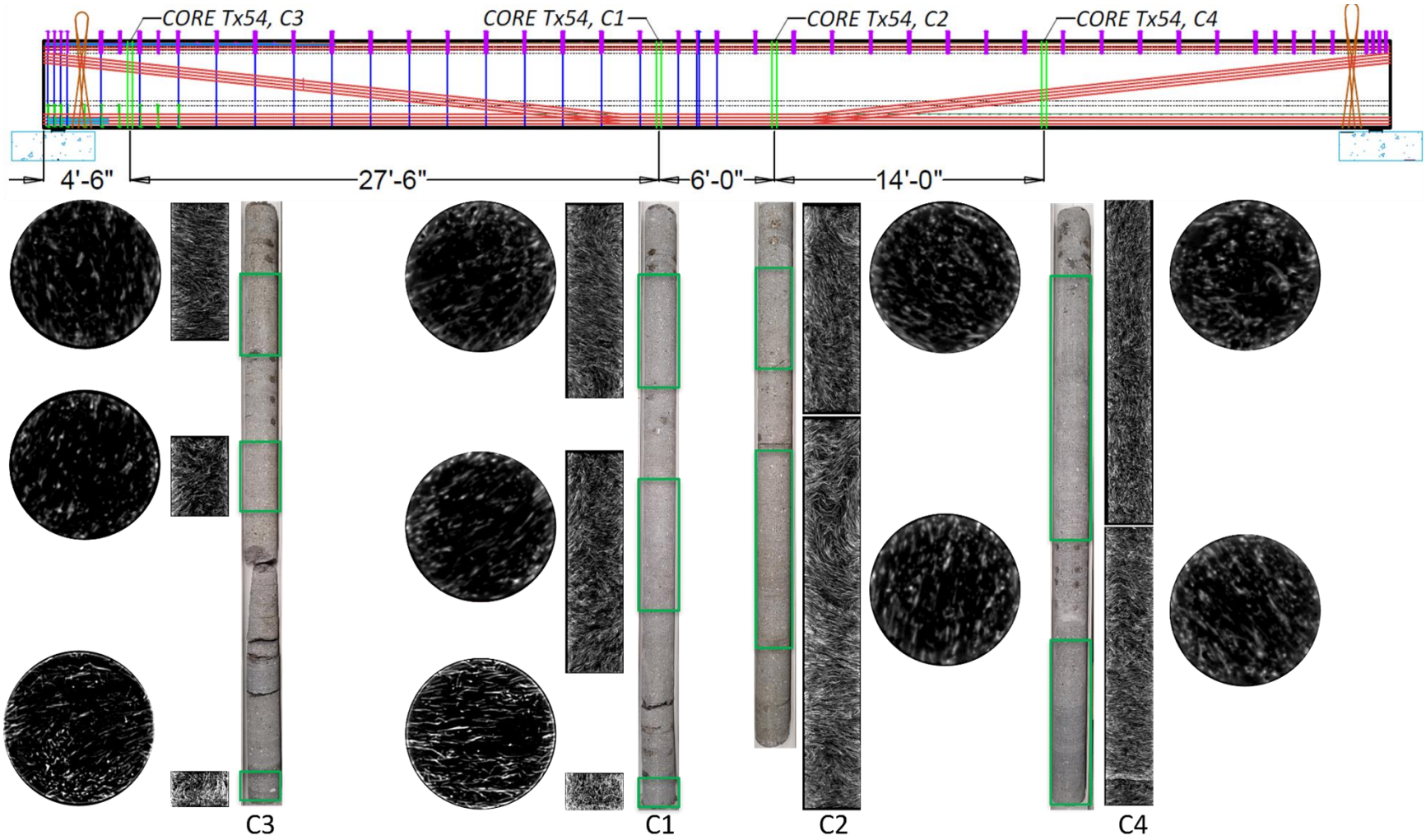

Figure 8.25. Tx54 Fiber Distribution along Girder Length.

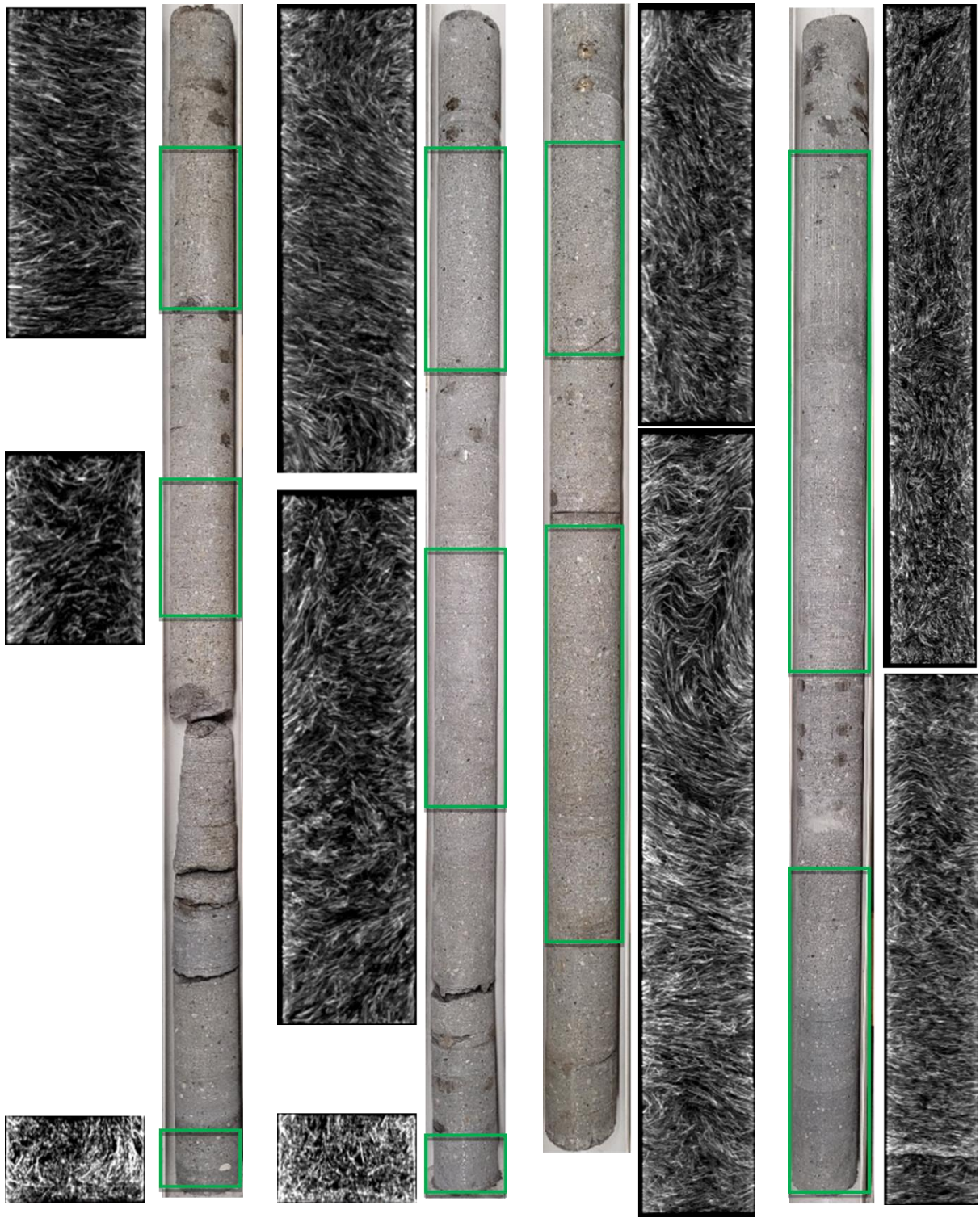

(a) C3 *(b) C1* *(c) C2* *(d) C4*

Figure 8.26. Comparison of Fiber Distribution of Tx54 Cores.

The advantage of a longer sample scan is to detect any fiber segregation issues. If there is segregation of steel fibers, fiber concentration will appear different along the sample height due to settlement. There is no observable difference in the concentration of fibers along the height from the core sample sections taller than 10 in. (3C1T, 3C1M, 3C2T, 3C2M, 3C4T, and 3C4M). The only location of high fiber concentration is observed near the bottom of 3C4M, which is close to the transition line between Batch 1 and Batch 2 (Figure 8.27). This concentration might be formation of elephant skin between Batch 1 and Batch 2 because the mixing time for Batch 2 (29 minutes) was 5 minutes longer than the common mixing time (24 minutes) of the other batches. The longer mixing time was due to a second water addition and additional mixing and a second flow table test (10.3 in.) because of a low flow spread value from the first flow table test (9.8 in.). It is a suggestion of fiber segregation for Batch 2, which has a 10.3 in. flow spread. However, besides this location, there is no other observation of a high concentration of steel fibers. Overall, the lower flow spread of Tx54 batches (9.8–10.3 in.) did not cause any significant fiber segregation based on the X-ray CT images. However, the lower flow spread of the Tx54 UHPC made it more difficult to discharge the UHPC from the Tuckerbuilt due to its relatively high viscosity. As a result, more residual UHPC adhered to the inside of the Tuckerbuilt.

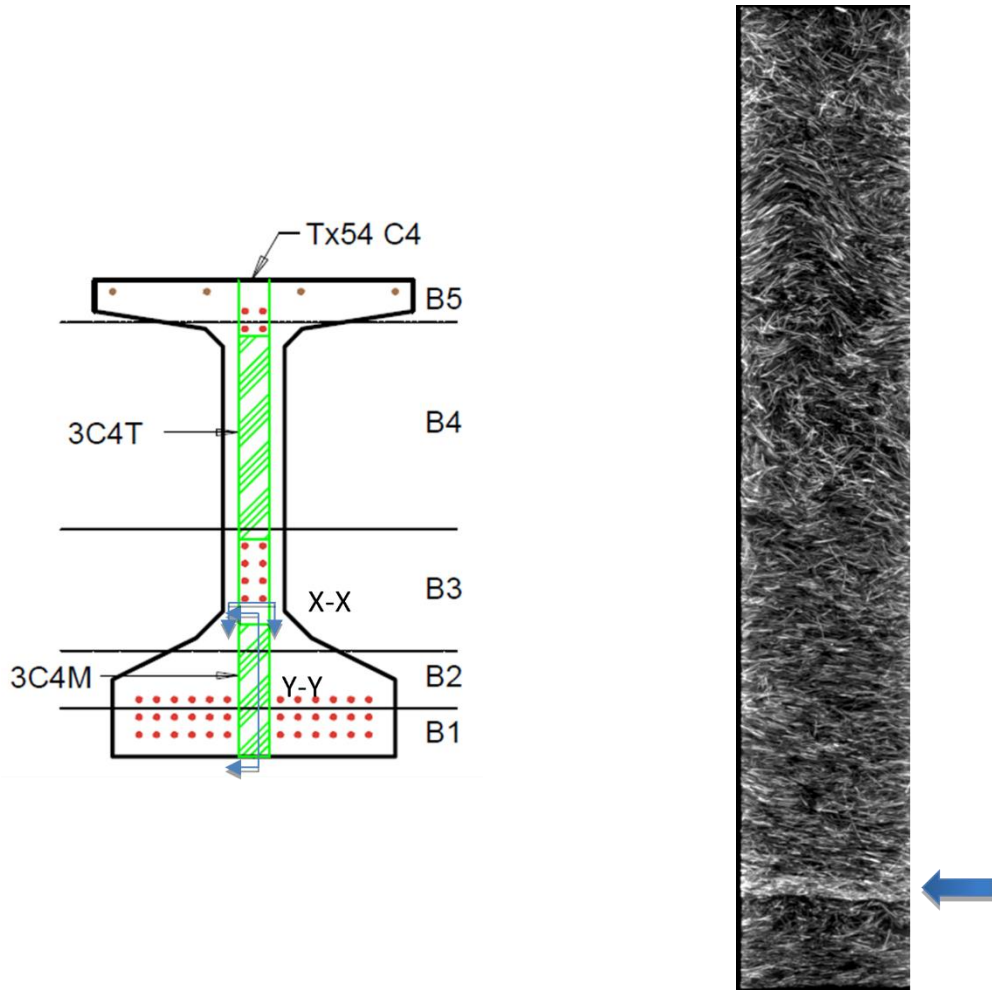

(a) X-ray CT Sample Location *(b) Fiber Concentration Location of 3C4M*

Figure 8.27. Tx54 Fiber Concentration at the Bottom of 3C4M.

8.4.2 Flow Impact on Fiber Distribution

8.4.2.1 X-Ray CT Image Analysis

The flow spread value is an indicator of the quality of fresh UHPC, including the probability of steel fiber segregation. Even though flow spread value does not fully represent the fundamental fresh properties of UHPC (such as viscosity) related to fiber segregation, it does indicate the probability of fiber segregation. Fiber distribution can significantly influence the structural performance. For example, shear behavior of a girder is affected by the fiber distribution in the web. Therefore, the flow spread value can be considered an indicator of the expected structural performance of a UHPC element.

The comparison of fiber distribution between the cores that have different flow spread values at a similar height in the girders provides a better understanding of the impact of flow on fiber segregation probability. Figure 8.28 shows X-ray CT scanned images for the fiber distribution of Tx34-1 C2 and Tx34-2 C2 that are located near the midspan of the girders. The bottom cored samples have a similar fiber distribution because the flow values are the same. However, the mid-height of the cored samples shows a different distribution of the fibers. Tx34-2 C2 has 10.3 in. flow spreads at the mid-height, whereas Tx34-1 C2 has 11.3 in. flow spread at the mid-height. The plan image of Tx34-2 C2 at the mid-height shows higher fiber concentrations than the plan image of Tx34-1 C2 at the mid-height. The lower flow values correspond to higher viscosity. Therefore, Tx34-2 C2 has higher viscosity and a relatively high concentration of fibers. Tx34-1 might have a slight segregation of steel fibers. However, because Tx34-1 was cast with three multiple batches, the segregation of steel fibers may not cause all fibers to settle to the bottom of the girder. Instead, they may settle more at the transition line between the different batches (Figure 8.27). A low flow spread may increase the risk of elephant skin forming between batches because elephant skin forms more quickly on the surface of a batch with a low flow spread. This phenomenon might lead to issues with batches integrating together to avoid a joint.

Along with the X-ray CT scanned images, the uniaxial tensile strength results of Tx34-1 and Tx34-2 samples cast from B2 (the batch for mid-height of the girders) provide the impact of flow spread. Table 6.23 shows peak tensile strength of 0.45 ksi and 0.67 ksi for Tx34-1 and Tx34-2, respectively. Tx34-2 B2 (10.3 in. flow) has a higher peak tensile strength (0.67 ksi) than the 0.45 ksi of Tx34-1 B2 (11.3 in. flow). These test data with the X-ray scanned images shown in Figure 8.28 reveal that the high flow spread caused segregation of steel fibers and resulted in low tensile strength. The Volume 2 report discusses the impact of tensile strength to shear capacity of a girder.

Casting full-scale girders and studying the fiber distribution provides insight into the optimum flow spread value range at a full-scale level point of view. Note that the optimum flow spread value to avoid fiber segregation was lower than 11.0 in. for lab-scale samples for material-level testing. However, Figure 8.27 shows a possibility of fiber settling on the top of the transition surface that occurs for a 10.3 in. flow at full-scale level. This effect might not be caused only by the lower flow since elephant skin formation may have occurred due to an extended mixing and

delivery time. Except for this location, there was no observation of fiber segregation over the girder height in Figure 8.24. Therefore, the optimum flow spread range in terms of fiber segregation may be lower than 10.3 in. Note that a flow spread greater than 10.0 in. is recommended when considering workability.

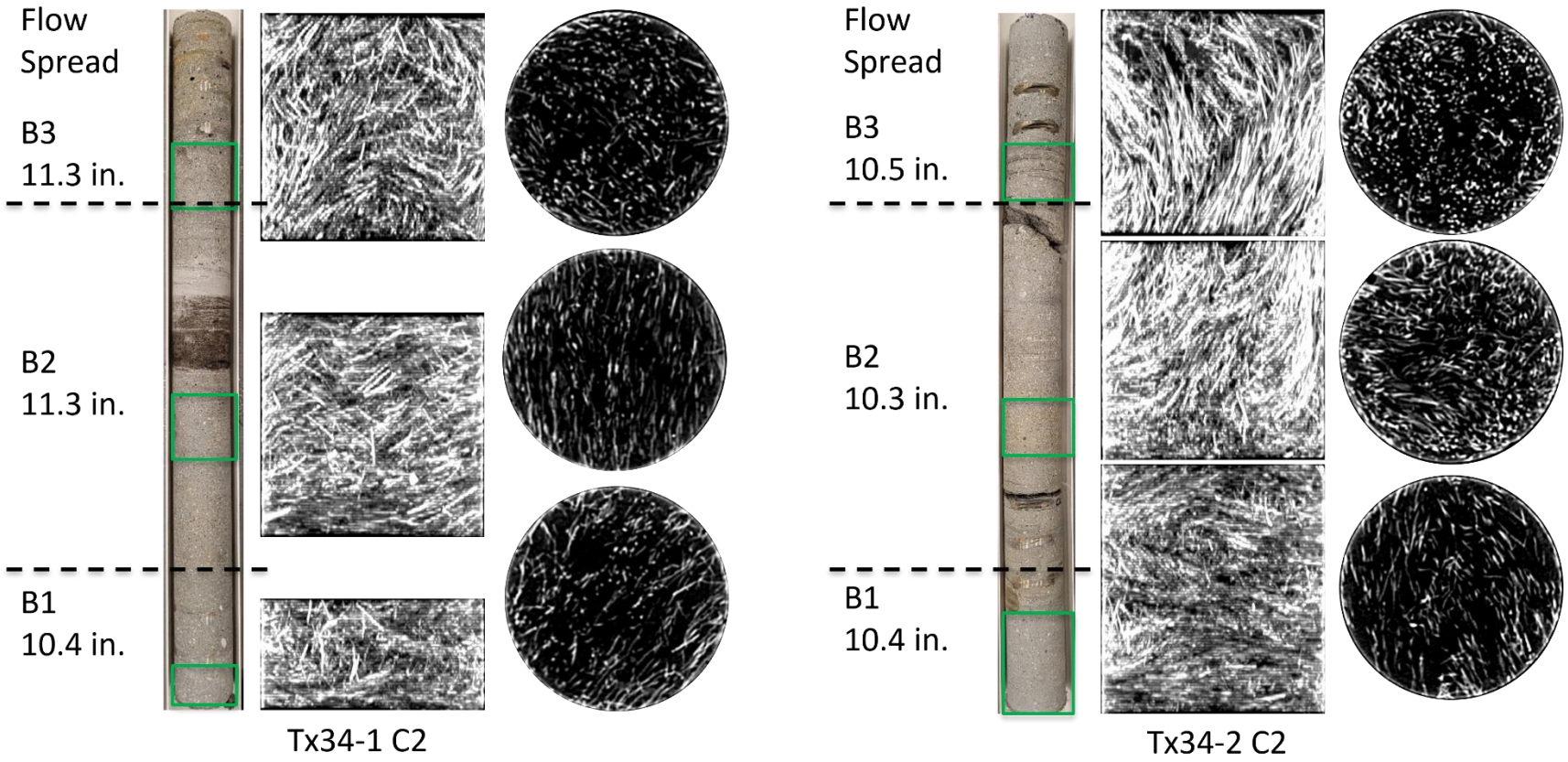

Figure 8.28. Flow Impact on Fiber Distribution.

8.4.2.2 Additional Image Analysis

Another imaging technique was employed to identify the segregation of steel fibers to compare the fiber distribution of Tx34-1 C2 and Tx34-2 C2. Figure 8.29 shows the sample locations that were used for the image processing technique. The samples were half cut vertically to see the fiber distribution along the height.

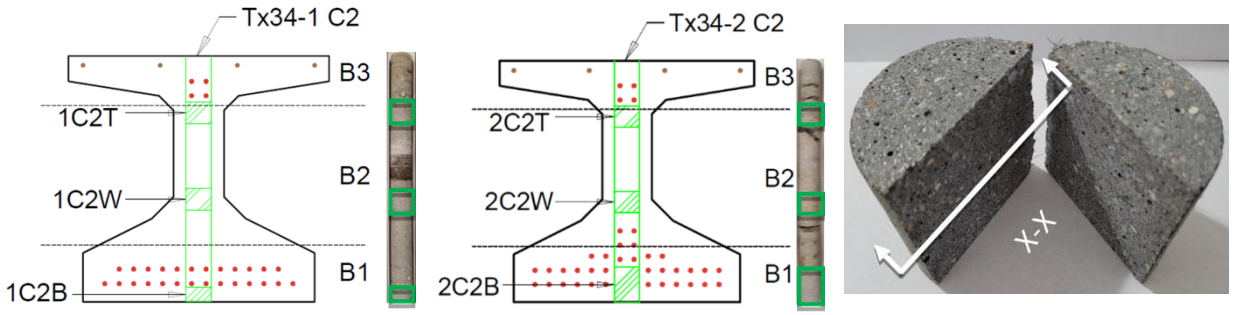

(a) Tx34-1 C2 Sample Location for Image Analysis

(b) Tx34-2 C2 Sample Location for Image Analysis

(c) Cut Section for Image Analysis

Figure 8.29. Sample Location for Image Analysis.

The photos of the half-cut sections from Tx34-1 C2 and Tx34-2 C2 were processed as follows:

1. Convert a photo to 8-bit gray scale.
2. Binarize the image.
3. Remove the noise (objects) smaller than the section area of a fiber.
4. Remove the noise (objects) greater than the longitudinal area of a fiber.

Figure 8.30 and Figure 8.31 show the image process sequence for Tx34-1 C2 and Tx34-2 C2, respectively. Figure 8.32 shows the comparison of the fiber concentrations at the same location. At the web, the flow spreads for Tx34-1 and Tx34-2 are 11.3 in. and 10.3 in., respectively. It is visually observed that Tx34-2 (2C2W) has a slightly higher fiber concentration in the web than Tx34-1 (1C2W). At the top flange, the fiber concentration of Tx34-2 is also higher than Tx34-1, similar to the web. This comparison of fiber distribution is consistent with the results of the uniaxial tension test and X-ray image analysis mentioned in the previous section.

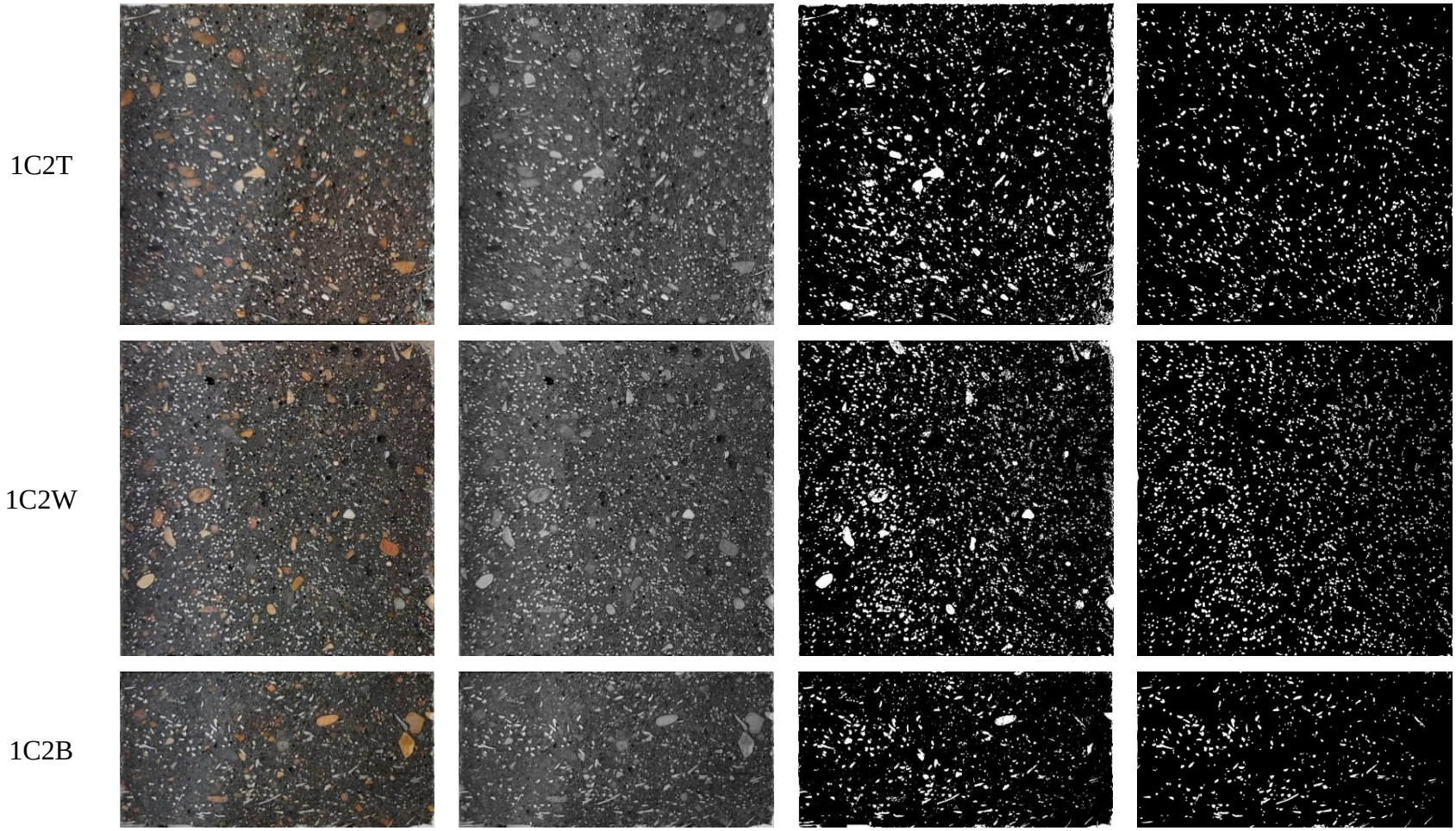

Figure 8.30. Tx34-1 C2 Image Processing for Fiber Distribution.

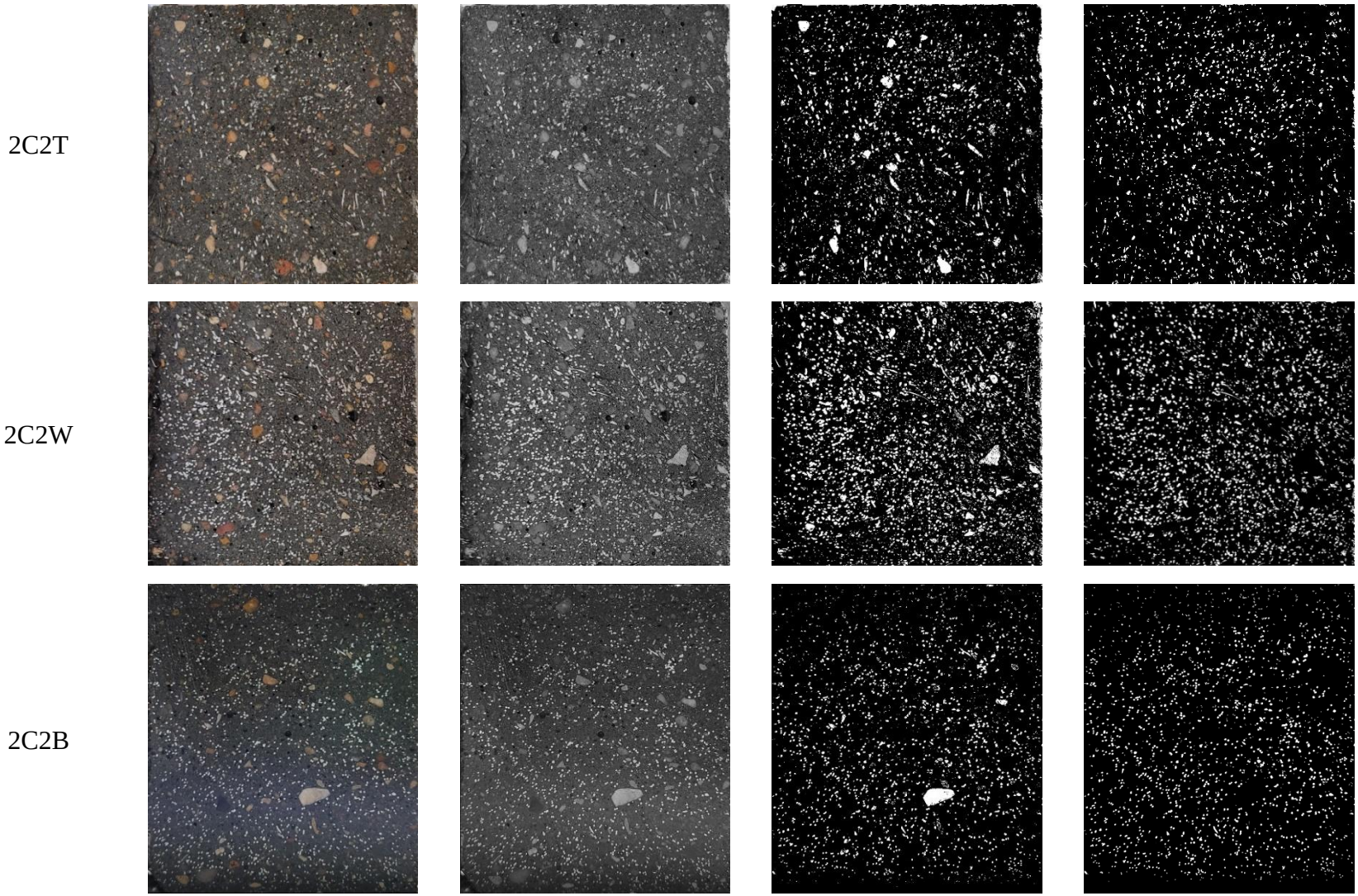

Figure 8.31. Tx34-2 C2 Image Processing for Fiber Distribution.

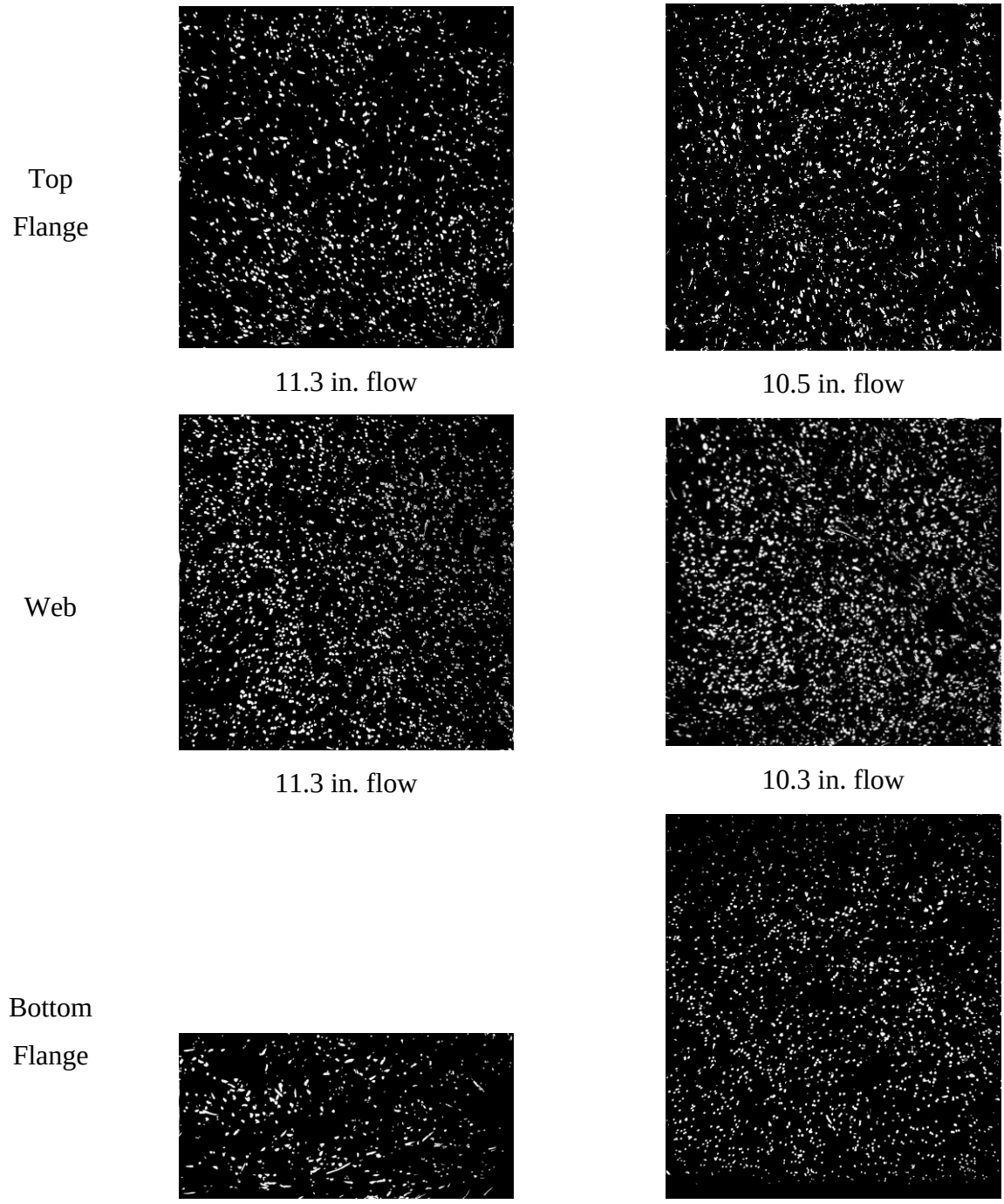

Figure 8.32. Fiber Concentration Comparison between Tx34-1 and Tx34-2.

The peak tensile strength of Tx54 is 0.92 ksi (Table 6.23), which is the highest among the three girders due to its relatively low flow spread values (9.8 in. and 10.1 in. for B3 and B4,

respectively). These results suggest that an approximately 10.0 in. flow is beneficial in avoiding segregation of steel fibers and in creating a high tensile strength. However, the workability of Tx54 was relatively lower than Tx34-2 due to its low flow spread value range (9.8–10.3 in.). Therefore, the ideal flow spread value range for the girder fabrication—when considering both fiber distribution and workability—is a 10.0–10.5 in. flow. However, from a practical point of view, with consideration of an extended mixing time for a large volume production at a precast plant and a delivery time for placement, a 9.5–11.0 in. flow spread is acceptable (see Section 6.3.1).

8.4.3 Fiber Distribution Analysis Using Infrared Images

Fiber distribution using infrared images was studied using the samples (Figure 8.29). The samples were placed in the temperature-controlled room at 140°F for 5 minutes. Due to the difference in heat conductivity between the UHPC paste and the steel fibers, the fiber distribution was clearly identified using the infrared camera. Figure 8.33 and Figure 8.34 show the infrared images of Tx34-1 C2 and Tx34-2 C2, respectively. The infrared images also show the same observations with respect to fiber distribution as discussed for the previous image processing technique. The Tx34-2 2C2W sample has a higher fiber concentration than the Tx34-1 C2 1C2W due to the low flow spread value. Figure 8.35 for the Tx54 Core C4 shows the same fiber concentration location shown in Figure 8.27 (using the X-ray CT scanned image). This infrared image supports the observation that there is a slight segregation of steel fibers from Batch 2 of Tx54 at the transition line between Batch 1 and Batch 2.

(a) Tx34-1, 1C2T Photo Image

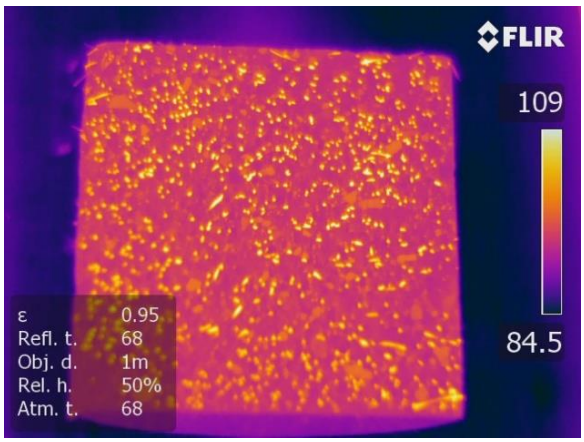

(b) Tx34-1, 1C2T Infrared Image

(c) Tx34-1, 1C2W Photo Image

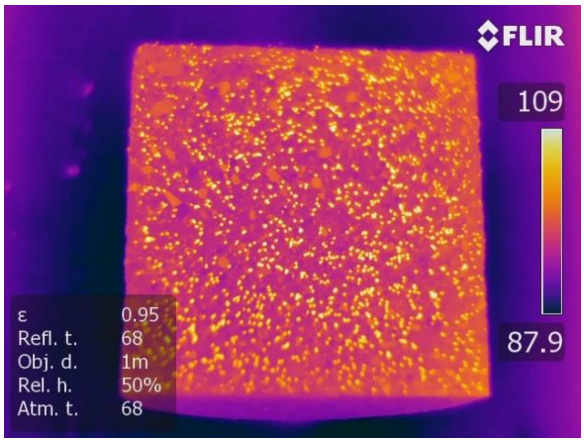

(d) Tx34-1, 1C2W Infrared Image

(e) Tx34-1, 1C2B Photo Image

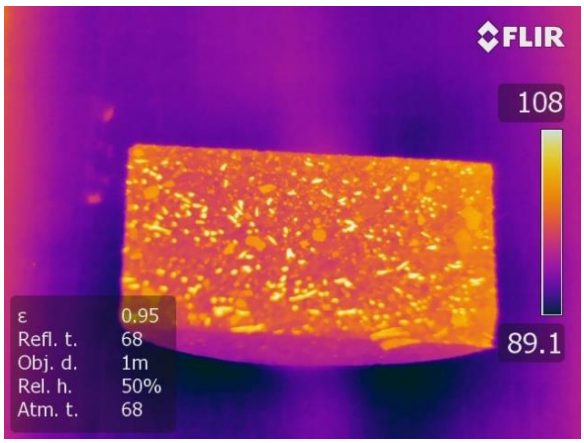

(f) Tx34-1, 1C2B Infrared Image

Figure 8.33. Infrared Images for Fiber Distribution of Tx34-1 C2 Samples.

(a) Tx34-2, 2C2T Photo Image

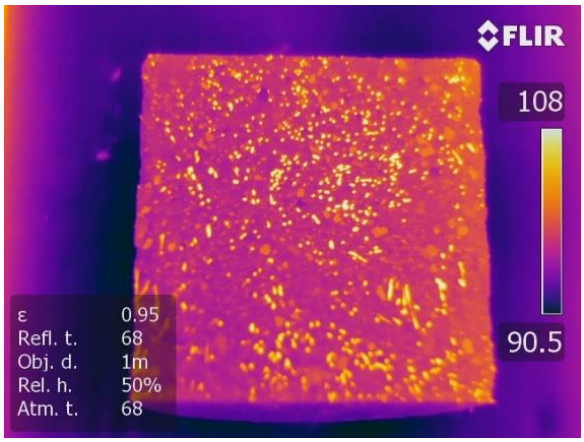

(b) Tx34-2, 2C2T Infrared Image

(c) Tx34-2, 2C2W Photo Image

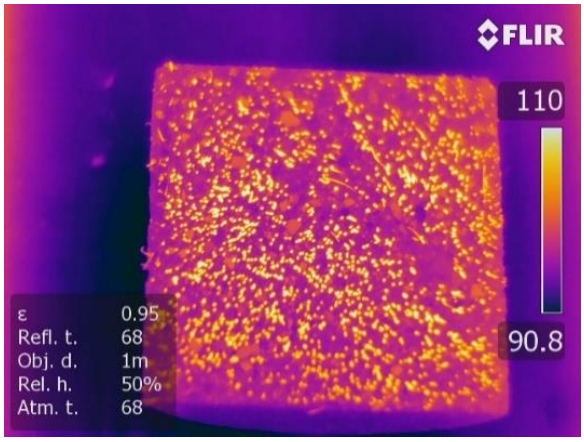

(d) Tx34-2, 2C2W Infrared Image

(e) Tx34-2, 2C2B Photo Image

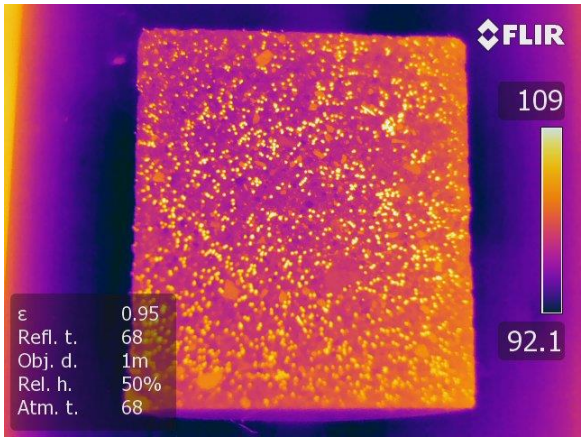

(f) Tx34-2, 2C2B Infrared Image

Figure 8.34. Infrared Images for Fiber Distribution of Tx34-2 C2 Samples.

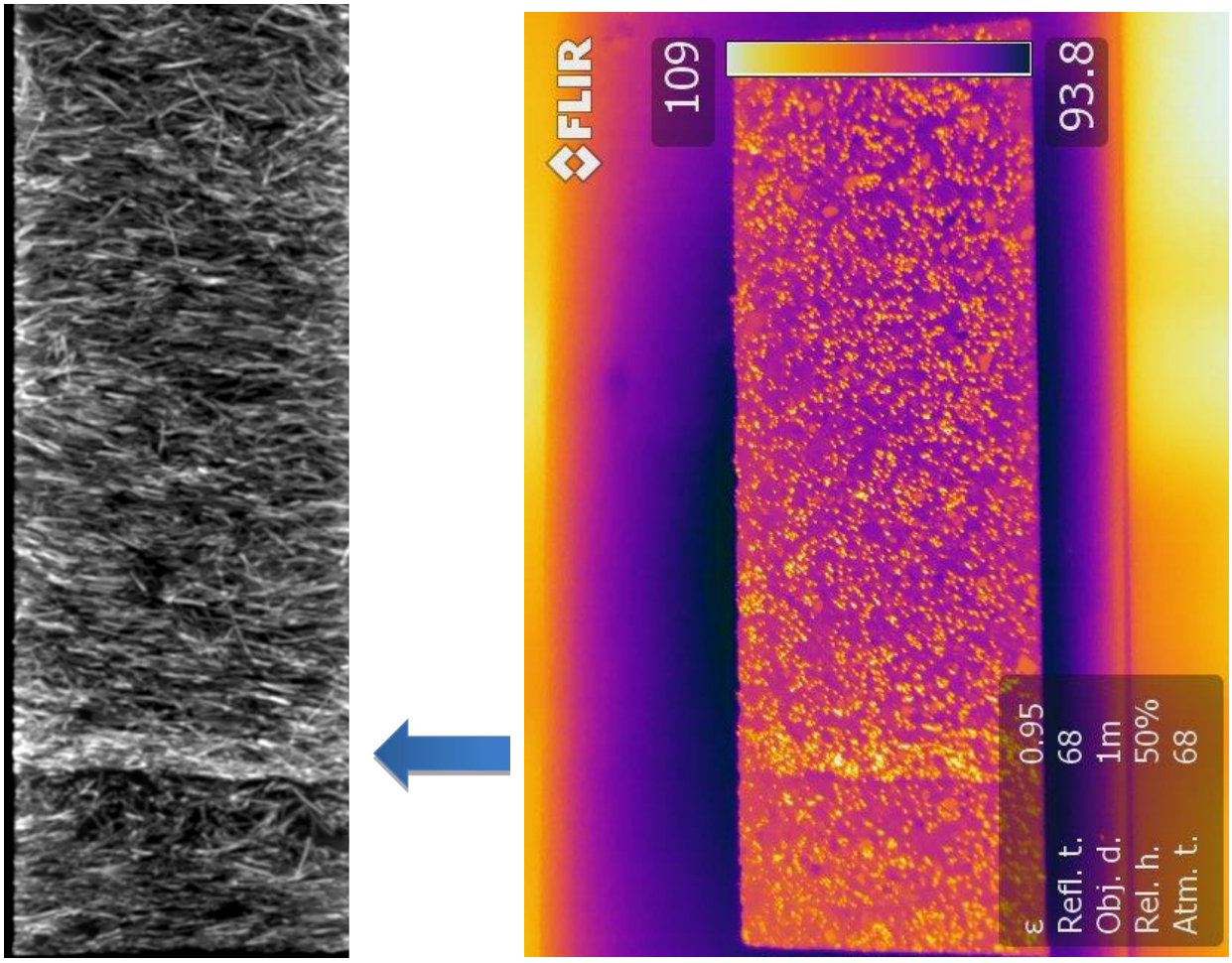

(a) Fiber Concentration Location of 3C4M from X-ray CT Image

(b) Fiber Concentration Location of 3C4M from Infrared Image

Figure 8.35. Fiber Concentration of 3C4M from Infrared Image.

8.4.4 Void Analysis Using X-Ray CT Images

Voids in the cored samples were detected by X-ray CT scanning using the same samples used to analyze the fiber distribution. Figure 8.36, Figure 8.37, and Figure 8.38 show the voids of the scanned samples from Tx34-1, Tx34-2, and Tx54, respectively. Although the flow spread values ranged from 9.8 in. to 11.3 in. from bottom to top of the three girders, the observed voids are not largely different over the girder height. The flow spread of Tx54 ranged from 9.8 in. to 10.3 in.

and did not cause a large void in the girder. Figure 8.39 shows a comparison of voids at the top and bottom of all three girders. The small voids (approximately 0.01–0.1 in. diameter) are distributed regardless of flow spread values of the cores. Therefore, UHPC with at least 9.8 in. flow spread (the lowest flow value from the batches of the three girders) did not exhibit a large void in the sections examined from the cored samples of the girder specimens Note that there was no use of internal or external vibration during UHPC placement.

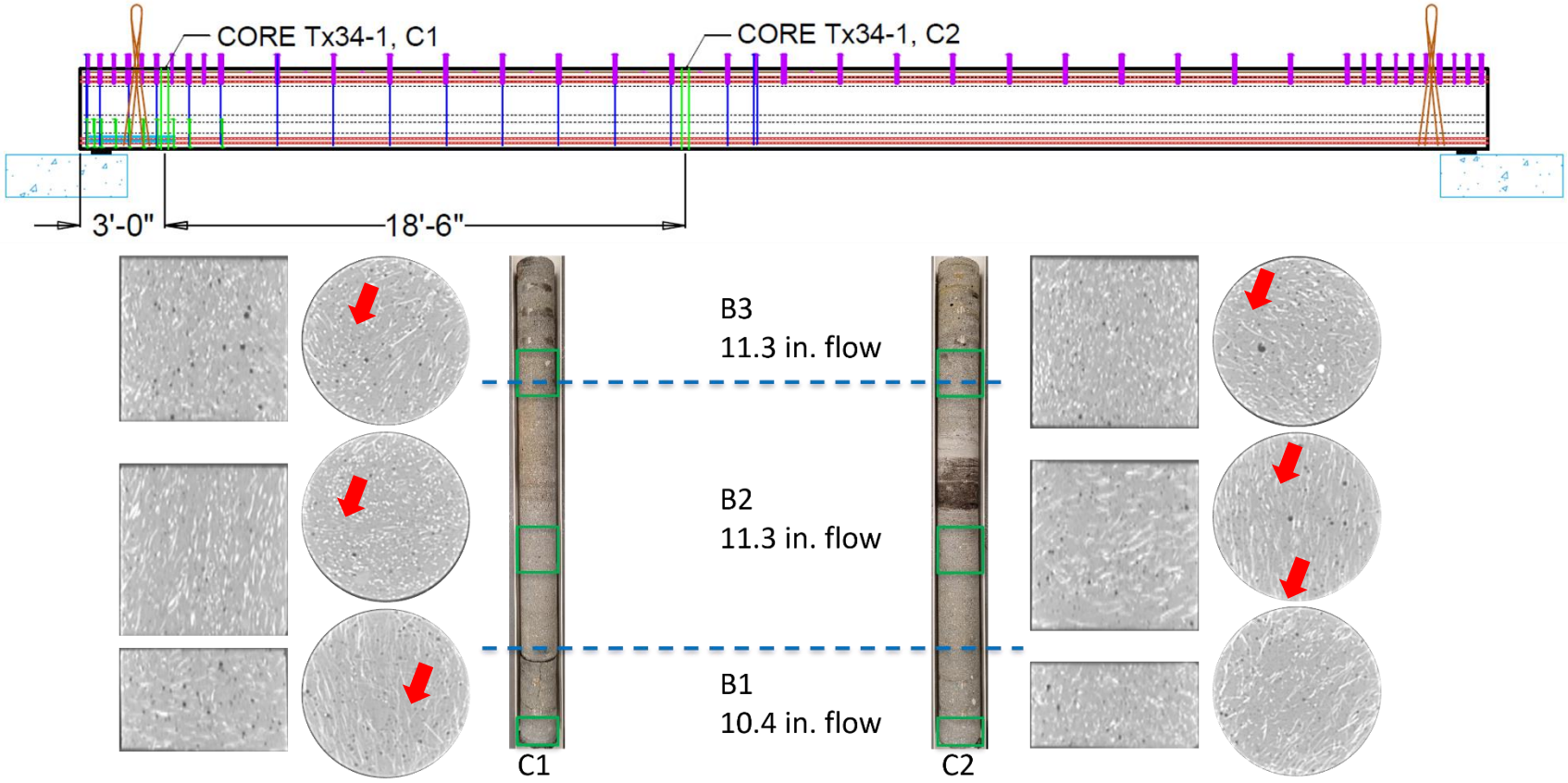

Legend:
Gray = UHPC
White = steel fibers
Black = voids (the red arrows indicate voids)

Figure 8.36. Voids of Tx34-1.

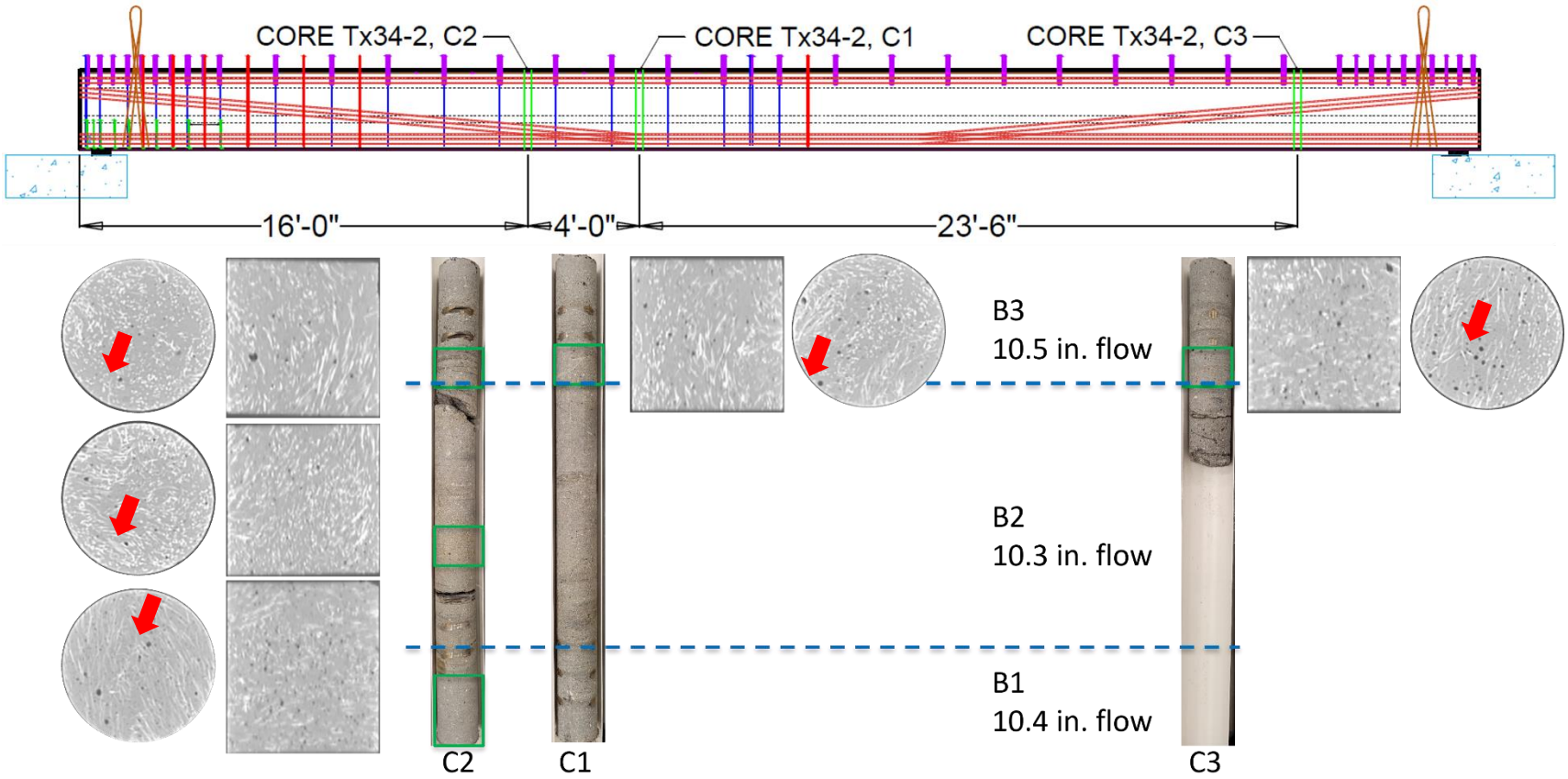

Legend:
Gray = UHPC
White = steel fibers
Black = voids (the red arrows indicate voids)

Figure 8.37. Voids of Tx34-2.

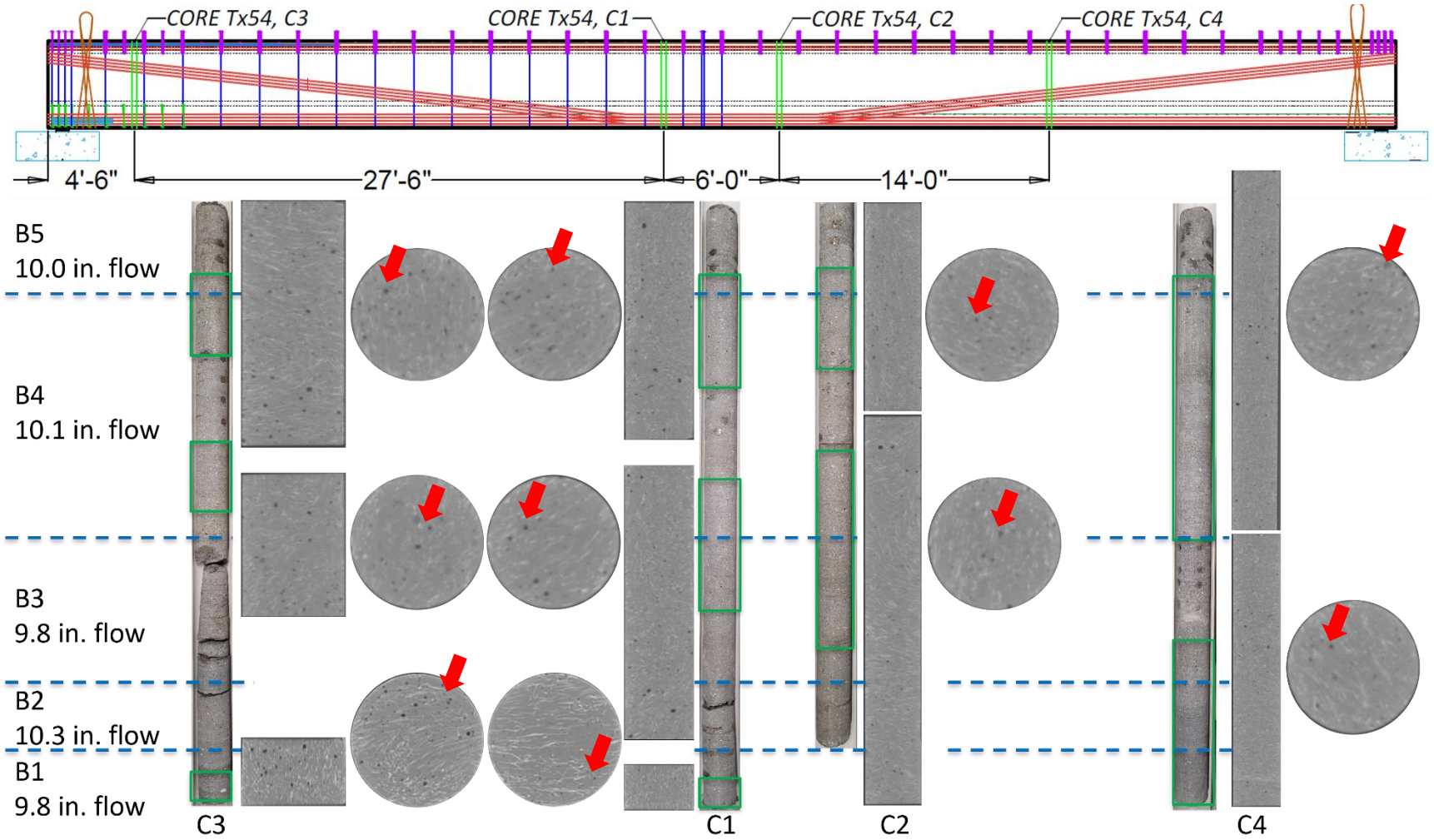

Legend:
Gray = UHPC
White = steel fibers
Black = voids (the red arrows indicate voids)

Figure 8.38. Voids of Tx54.

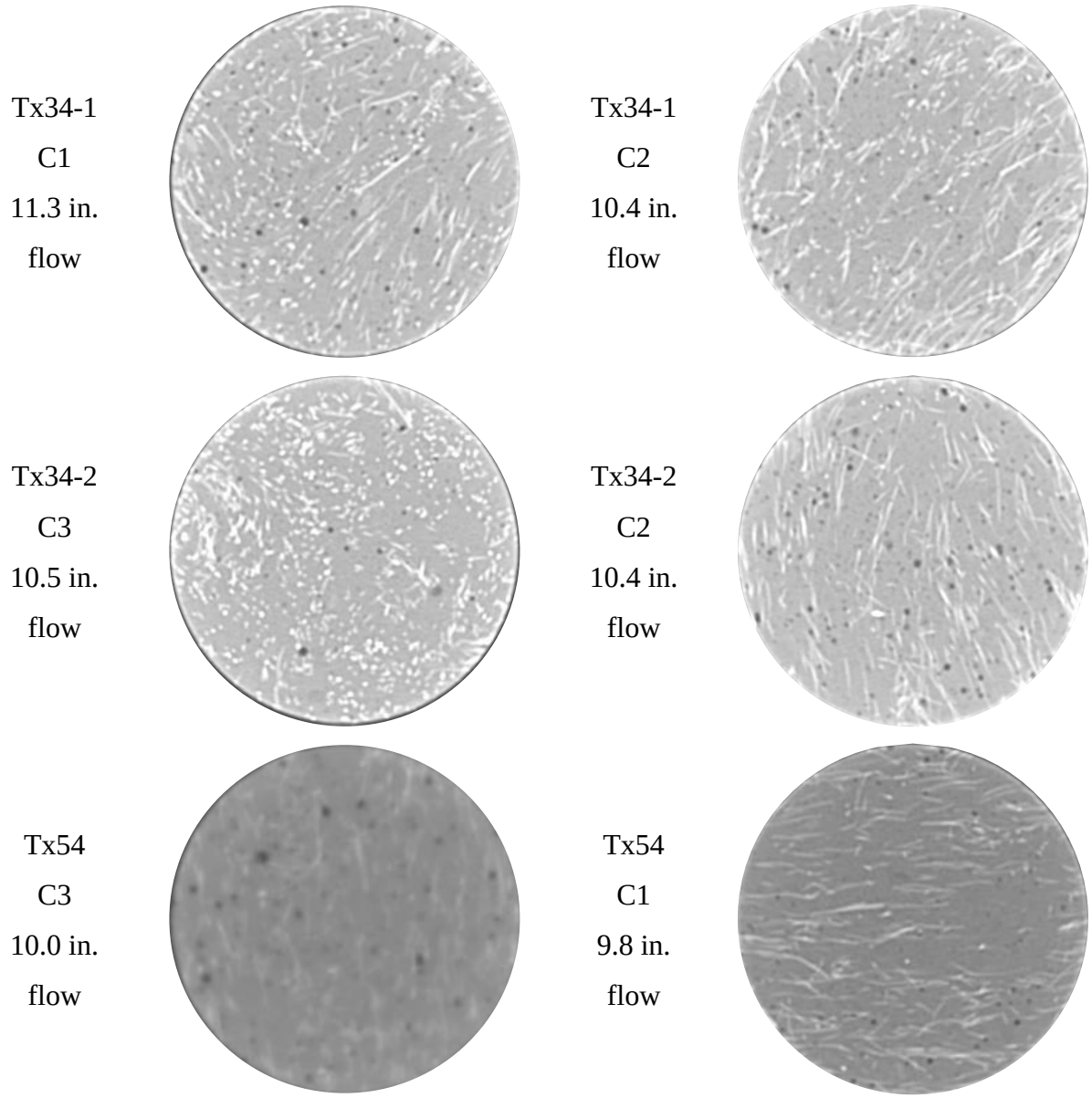

(a) Voids at Top *(b) Voids at Bottom*

Note: Tx54 C3 at top image has relatively low resolution due to long length of the sample.
Legend:
Gray = UHPC
White = steel fibers
Black = voids

Figure 8.39. Comparison of Voids at Top and Bottom.

8.5 SUMMARY

This chapter documents the surface images and compressive strength of the cores and describes the fiber distribution and voids of the cores using X-ray CT and other image analysis techniques. The following observations were made:

- The average compressive strength of the cores was 19.6 ksi, 20.0 ksi, and 19.3 ksi for Tx34-1, Tx34-2, and Tx54, respectively. This is 5.4 percent, 9.9 percent, and 12.2 percent higher than the cast cylinders for Tx34-1, Tx34-2, and Tx54, respectively. The possible reason for the high strength of the cored samples is the high heat of hydration, which is greater than the 192°F temperature of the girders. The high heat may improve microstructure and accelerate strength gain (Kang et al. 2017). As a result, the cores have higher compressive strength than the cast cylinder.
- X-ray CT scanned image slices were used for 3D reconstruction to identify the fiber distribution and orientation. All the cores from the three girders show randomly distributed fibers without significant segregation of the steel fibers. However, slight fiber segregation in the web of Tx34-1 was observed from X-ray CT images and other image techniques, which is due to the high flow spread value of Tx34-1 for Batch 2 and Batch 3. The lower uniaxial tension test results (Section 6.4.3) and full-scale testing results (Volume 2 report) also support this fiber segregation in the web of Tx34-1.
- There were no significant large voids in the cores from the three girders regardless of flow spread values. The maximum size of the observed voids was approximately 0.1 in. diameter. Therefore, a 10.0–10.5 in. flow is recommended to avoid any fiber segregation and voids and for sufficient workability for girder fabrication.
- Fiber distribution and orientation were studied using the various imaging techniques, including X-ray CT scanned images, binarized conventional photo images, and infrared images. Even though all the techniques were effective in identifying fiber distribution and segregation, only 3D reconstructed X-ray CT scanned images explicitly showed fiber orientation.

9 SUMMARY AND CONCLUSIONS

This Volume 1 report primarily discusses the development, implementation, and evaluation of nonproprietary UHPC mixtures for precast, pretensioned girder applications using locally available Texas materials. This process includes the development of nonproprietary UHPC mixtures, including the optimization of the selected nonproprietary mixture for precast plant application; production of precast, pretensioned UHPC girders; development of the material properties of the selected UHPC mixture and comparison between lab-made and plant-made UHPC; nondestructive evaluation of the girders; and observations related to fiber distribution and orientation. The following sections provide a brief summary and key findings for each of the research tasks.

9.1 DEVELOPMENT OF NONPROPRIETARY UHPC MIXTURES

Nonproprietary UHPC mixtures were developed using locally available materials found in Texas. The developed mixtures were designed to achieve the targeted properties identified from the analytical feasibility study (see Volume 2). The target properties are the following:

- A sufficient flow spread value (9–11 in.)
- A 1-day compressive strength of 10–14 ksi without any special treatment
- A 28-day compressive strength of 18–20 ksi without any special treatment
- 4–8 hours for initial set and 7–10 hours for final set

These properties were used to evaluate the developed mixtures for screening purposes at the laboratory. In addition to the targeted properties, bulk and surface resistivities, shrinkage, abrasion resistance, and material cost were considered in the evaluation of the developed mixtures. The following are the key findings identified from the development of nonproprietary UHPC mixtures for precast plant applications, with a specific focus on precast, pretensioned bridge girders:

- *Eight UHPC mixtures successfully developed using locally available materials.* Four mixture proportions were developed, and each proportion was optimized with Type I/II and Type III cements. Each mixture has a specific 1-day and 28-day compressive strength range of 10–14 ksi and 16–21 ksi, respectively. The following is the procedure for mixture development:

- Proportioning the paste by volume (cement, silica fume, fly ash, water, and a HRWR).
- Reducing *w*/*c* while increasing *HRWR*/*c* until achieving the highest compressive strength within the targeted flow spread value.
- Selection of the promising paste proportion.
- Evaluation of UHPC with different ratios of paste volume to sand volume by flow spread value and compressive strength.
- Selection of the ratio of paste volume to sand volume.

- *High early strength gain strategies*. High early strength gain is a critical for UHPC mixtures for precast, pretensioned bridge girder applications to meet both aspects of structural design and practical production at the precast plant:
  - **Silica fume content**. Large silica fume content reduces the early strength gain due to the diluting proximity of cement particles. A UHPC mixture with 4 percent silica fume by cement weight showed the highest 1-day compressive strength. However, the low silica fume content decreased durability. A UHPC mixture with silica fume of 8 percent by cement weight provides sufficient early strength gain without significantly compromising durability compared to the UHPC mixture containing 15 percent silica fume by cement weight.
  - **HRWR content**. The HRWR is a key constituent material in terms of early strength gain and workability. A high-charged HRWR provides high efficiency of rapid particle dispersion with a relatively quick setting time (6–8 hours) while maintaining sufficient workable time. Even though a large dose of the HRWR is needed to reduce water content for highly packed UHPC that has superior mechanical properties and durability, an overdose of the HRWR causes retardation of hydration. Thus, the recommended HRWR dosage is lower than the saturated dosage to avoid retardation but requires a sufficient amount for particle dispersion.
- *Optimum fiber volume.* An optimal fiber volume for the selected Mix-4 was chosen by testing the behavior of the mix under uniaxial tension and compression for different fiber contents by volume, including 1 percent, 1.5 percent, and 2 percent. Based on the workability, compressive strength, and tensile strength of the 1.5 percent fiber volume mix and its advantage of being more economical, this percentage was used for next steps.

- *Key properties of the selected mixture.* The optimized selected UHPC with the Type III cement widely used by precasters in Texas achieved 13.1 ksi and 20.4 ksi compressive strength at 1 day and 28 days, respectively, with a 11.0 in flow spread at the laboratory.
- *Material cost.* The material cost of the selected UHPC is approximately $600 per cyd, including steel fibers. It is significantly less expensive than the cost of proprietary UHPC mixture (approximately $2000).
- *Service life prediction of the selected mixture.* Service life prediction shows high durability of the developed UHPC mixtures. The formation factors were computed based on the bulk resistivity test results and used for the service life prediction. The predicted service life span of the selected mixture is greater than 200 years.

9.2 OPTIMIZATION OF UHPC MIXTURE FOR PRECAST PLANT APPLICATIONS

The selected mixture and mixing procedure were optimized using the materials at a precast plant in Texas with consideration of the precast plant processes, such as material addition methods and batch volume. The properties of the plant-made UHPC from a 2 cyd trial batch at the precast plant were systematically investigated. The key findings are as follows:

- *Optimization of the selected mixture with precaster materials.* The selected mixture was optimized with the materials used at the selected precast plant in Texas:
  - The replacement of cement, the HRWR, and sand has an insignificant impact on the flowability and compressive strength at 1 day and 28 days when adjusting water and HRWR contents and paste volume fraction. However, the mixing procedure was changed to accommodate the wet sand (stockpile) condition.
  - The reduced water content due to moisture content in sand causes an insufficient *w*/*c* for paste mixing before addition of sand. As a result, splitting the cement addition was adopted to keep a constant *w*/*c* during mixing.
- *Trial batch at the precast plant.* A 2 cyd trial batch was conducted at the precast plant. The following observations and adjustments were considered:
  - Adjustment of water content is needed to avoid excess water addition due to the residual water in the mixer. Holding 10 percent of the water at the water addition step may sometimes be necessary.

- The manual steel fiber addition time for the large volume extended the total mixing time. Fabrication of a vibrating screen was considered to shorten the time for steel fiber addition.

- *Fresh and hardened properties of plant-made UHPC.* The fresh and hardened properties were investigated using the cast specimens at the precast plant during the trial batch:
  - The flow spread at the precast plant was higher (11.5 in.) than at the lab (10.6 in.) due to the remaining water in the mixer.
  - The results of unit weight and air contents were similar from both the plant and the lab.
  - The highest core temperature of a UHPC block cast during the trial batch (2.0 ft × 1.6 ft × 6.0 ft) was 214°F at 13 hours after casting.
  - The 1-day compressive strength (14.1 ksi at the lab, 14.3 ksi at the plant) and 28-day compressive strength (18.7 ksi at the lab and 17.9 ksi at the plant) were comparable.
  - The compressive strength of the cored sample from the UHPC block was 9.5 percent higher than the cast cylinder at 65 days.
  - The MOE of the specimens tested in this study was in the range of 5000–7000 ksi.
  - The Poisson's ratio was in the range of 0.22–0.28.
  - The behavior of specimens from all the lab mixtures and the precast plant trial batch under uniaxial tension were quite similar to the Mix-4-PM-P, which is the selected mixture optimized with materials used at the precast plant and which exhibits slightly higher tensile strength than the other two mixtures. The average peak strength of the specimens cast from the three trials was 1.14 ksi at a strain of 581 με.
  - The flexure strength for the specimens cast using precast plant materials at the lab and the plant was very similar in the post-crack region. The peak strengths varied from 1.51 ksi to 2.17 ksi.
  - The results of total and autogenous shrinkages of Mix-4-PM-L are 693 με and 643 με at 668 days, respectively. The shrinkage results are slightly lower than the results of the lab mixtures (Mix-1a, Mix-2a, Mix-3a, and Mix-4a) because the larger maximum sand particle size mitigates shrinkage.
- *Durability.* The durability test results of plant-made UHPC indicate superior durability performance:

- Both bulk and surface resistivity test results of Mix-4-PM-L are in the *Very Low* category at 56 days.
- The RCPT results are *Negligible*.
- There was no degradation from a freeze-thaw test after 300 cycles.
- A scaling resistance test showed a very slight scaling (*Rating 1*) after 50 cycles.
- Mix-4-PM-L has high abrasion resistance (0.65 g mass loss from the bottom).
- Alkali silica reaction of Mix-4-PM-L was not found. Alkali silica reactivity was negligible.

- *Microstructure.* The microstructure of Mix-4-PM-L was studied using the transmitted light optical microscope and using thin sections (20–25 μm thickness) made of UHPC specimens at the age of 3 days and 28 days.
  - The sand particles are mostly subangular in shape with few angular particles, whereas fly ash particles are mostly spherical in shape.
  - The presence of a greater number of unhydrated cement particles was observed due to lack of water. Unhydrated cement particles represent the remaining unhydrated portions of the cement particles (i.e., preferably the core of the cement particles) after hydration reaction from the surface. As a result, a strong bond between hydrated and unhydrated parts is expected. Unhydrated cores of cement particles act as hard inclusions strongly bonded with hydrates.
  - The presence of an almost nonporous interfacial transition zone without any presence of aligned calcium hydroxide suggests a relatively stronger bond between fiber and cement paste matrix.
  - The presence of agglomerated silica fume particles was observed in some locations.

9.3 FABRICATION OF UHPC GIRDERS AND MATERIAL-LEVEL EXPERIMENTS

The fabrication of the three precast, pretensioned UHPC girders at the precast plant was successfully conducted. The twin-shaft mixer of the plant provided sufficient power. As a result, turnover time was shorter than at the laboratory. The quality of the fresh UHPC produced at the plant and at the laboratory was comparable. Multiple batches with separate placements were successfully performed without a cold joint issue. However, the formation of the elephant skin on the UHPC surface can occur quickly, making it critical to cast batches as closely as possible to one

another. This practice provides lessons learned on how to mix UHPC using the existing facilities. The following describes the casting process:

1. Discharge fresh UHPC from the mixer into the transport truck.
2. Place the fresh UHPC into a girder form.
3. Cover the mold with burlap (or similar cloth) and sprinkle water on top of the burlap to avoid elephant skin.
4. Mix the next batch while transporting and placing previous batch.
5. Place the next batch on the top surface of the previously placed UHPC to break up any elephant skin formed from the previous UHPC batch. Placing from one location helps create a velocity of flow that helps to disturb the elephant skin. The last girder (Tx54) was placed by pouring at alternate ends for each subsequent batch.
6. Prior to the release of prestressing strands, the vertical surfaces of the girders were evaluated. There were lines along the flow of different batches, but no cold joint formation was observed. For Tx34-1, some temperature and shrinkage cracks were noticed along the flow lines of different batches. These cracks were not as pronounced for Tx34-2 and were negligible for Tx54. After the release of strands, some of these hairline cracks were observed to have closed under the prestressing force.
7. The top surface of Tx34-1 girder was scratched on the surface with a pointed object to create surface roughness; however, due to the self-consolidating nature of UHPC, the ridges created made the top surface chip more. Therefore, this practice was not continued for Tx34-2 and Tx54. There was no interface slip failure between the composite cast-in-place deck and the girder for all three specimens.

With respect to the hardened properties, the following conclusions were drawn:

- *Compressive strength*. The design compressive strength was achieved for release and service. The UHPC for the Tx34-1 and Tx34-2 girders showed comparable strength values. Even though the compressive strength of the Tx54 UHPC showed slightly lower strength, it may be due to issues during the sample preparation due to the relatively low flow spread values. Verification of the Tx54 compressive strength was conducted at the laboratory

using the same materials as at the plant. The strength results were comparable to Tx34-1 and Tx34-2.

- *Modulus of elasticity and Poisson's ratio.* Both the MOE and Poisson's ratio values were comparable to the results of the lab mixes and were similar across all three girders. The predictions for the MOE served as a lower bound for the measured results. The MOE of the developed UHPC ranged from 6000–7500 ksi and is higher than that of CC (from 2000–6000 ksi). Poisson's ratio (0.20–0.33) was higher than CC (0.11–0.21) (Ahlborn et al. (2008).
- *Uniaxial tensile strength.* The uniaxial tensile strength of Tx34-1 and Tx34-2 was quite low (0.31–0.62 ksi), with a nonuniform fiber distribution in the samples. These values were lower than the previously tested laboratory mixes and trial mix. The uniaxial tensile strength of Tx54 was higher (0.8–1.2 ksi) and comparable to the lab mixes. The influence of the tensile strength on the shear performance of the girder was observed during the full-scale testing, and the details are reported in Volume 2 of the report. The measured tensile strength of the developed mix met the PCI (eConstruct 2020) recommendations of 0.75 ksi minimum tensile strength for the Tx54 girder, whereas for Tx34-1, the tensile strength was lower than limit recommended by PCI, and for Tx34-2, it was less than or equal to this limit. The testing was conducted in accordance with the method proposed by the FHWA in AASHTO T 397 Draft (AASHTO 2022). This method is also in accordance with the recommended test for studying behavior under tension by FHWA (2022)
- *Flexure strength.* Both the first peak crack strength and ultimate flexure strength of the companion specimens was higher than or equal (1.8–2.1 ksi) to the PCI (eConstruct 2020) recommendations for most of the specimens. The ductility recommendations by PCI (eConstruct 2020) and ACI Committee 318 (2019), developed for fiber-reinforced concrete, are not met for the post-cracking phase of the stress-strain plot. This effect may be due to the lower volume of fibers used in the developed mix. There was consistent ductile behavior exhibited by Tx54 specimens, while variations were observed in the post-cracking strength of the companion girder specimens of Tx34-1 and Tx34-2.
- *Creep and shrinkage.* The long-term hardened properties *creep* and *shrinkage* were studied using the companion specimens of the three girders. The key findings are:

- The creep coefficient (0.7–0.9) of the developed UHPC is lower than that of CC (1.5–3.0).
- The shrinkage value (700 με) is higher than that of CC (480 με).
- Based on the test results, prediction models for creep and shrinkage were proposed for prestress loss estimation of the developed nonproprietary UHPC mixture.

9.4 NONDESTRUCTIVE EVALUATION OF THE GIRDERS

A technical investigation was performed to identify material properties and detect any defects, such as large voids, delamination, and cracks. An in-depth study and evaluation were conducted on the UHPC used in Tx34-1, Tx34-2 and Tx54 by employing passive infrared thermography, ground penetration radar, UPV, and ultrasonic tomography.

- *Quality of UHPC evaluated by UPV.* Studying the data collected from the three UHPC girder specimens revealed that the quality of the UHPC used to build these girders was consistent, as per the criteria established by Feldman (1977). The velocity of sound waves was estimated to be 15.2×10^3 ft/s in UHPC core samples, and the average velocity of sound waves in Tx34-1, Tx34-2, and Tx54 was on average more than 14×10^3 ft/s. These results indicate that the quality of the concrete used for the construction of the UHPC girders was in fact high. The compressive strength of Tx34-1 and Tx34-2 obtained by UPV was an estimated 17 ksi and 14 ksi at the web and the bottom flange, respectively. Similarly, the compressive strength of Tx54 was estimated to be on average 15.6 ksi. Note that the compressive strength at 28 days using 3 × 6 in. cylinders is 18.9, 18.0, and 16.5 ksi for Tx34-1, Tx34-2, and Tx54, respectively. The results of UPV are slightly lower than the strength from the standard compression tests.
- *Steel fiber distribution and orientation.* Another conclusion drawn from UPV measurements was that steel fibers were uniformly distributed in the UHPC girders. Fibers in general were inclined to the horizontal plane close to the surface of the concrete. This observation was even more apparent for fibers used in Tx54.
- *Defects.* No delamination or large defect was detected from ultrasonic tomography conducted on Tx34-1, Tx34-2, and Tx54. Steel components were readily recognizable in the tomographic imaging computed for the UHPC girders. Although the contrast between the metallic components and the concrete was not as clear as desired and the difference

between steel strands and steel fibers was not obvious, the radar-based testing system was still capable of locating reinforcement in UHPC. Note that silica fume is not electrically conductive and does not attenuate the reflection signal; thus, the use of a GPR system—as long as it is not performed on fresh concrete—is also suitable to determine the location of steel reinforcement and to identify defects such as large voids in UHPC.

9.5 FIBER DISTRIBUTION AND ORIENTATION

The samples from the three girders were collected by coring after full-scale testing. Two, three, and four cored samples were used for fiber distribution analysis and strength of the cores. Fiber distribution and orientation and voids were studied by employing X-ray CT and other image analysis techniques.

- *Strength of the cores.* The average compressive strength of the cores was 19.6 ksi, 20.0 ksi, and 19.3 ksi for Tx34-1, Tx34-2, and Tx54, respectively. These strengths are 5.4 percent, 9.9 percent, 12.2 percent higher than the cast cylinders for Tx34-1, Tx34-2, and Tx54, respectively. The possible reason for the high strength of the cored samples is the high heat of hydration of the girders, which is greater than 192°F. The high heat may improve microstructure and accelerate strength gain (Kang et al. 2017). As a result, the cores have higher compressive strength than the cast cylinder.
- *Fiber distribution and orientation.* X-ray CT scanned image slices were used for 3D reconstruction to identify the fiber distribution and orientation. All the cores from the three girders show randomly distributed fibers without significant segregation of the steel fibers. However, slight fiber segregation in the web of Tx34-1 was observed from X-ray CT images and other image techniques due to the high flow spread value of Tx34-1 for Batch 2 and Batch 3. The lower uniaxial tension test results and full-scale testing results also support this fiber segregation in the web of Tx34-1.
- *Voids Analysis.* There were no significant large voids in the cores from the three girders regardless of flow spread values (9.8–11.3 in.). The maximum size of the observed voids was approximately 0.1 in. diameter.
- *Effectiveness of image techniques.* Fiber distribution and orientation were studied using the various imaging techniques, including X-ray CT scanned image, binarized conventional photo image, and infrared image. Even though all the techniques were effective in

identifying fiber distribution and segregation, only 3D reconstructed X-ray CT scanned images explicitly showed fiber orientation.

9.6 RECOMMENDATIONS FOR UHPC PRODUCTION

After considering the nonproprietary UHPC mixtures developed for this research, the following highlights several key recommendations for UHPC production. More detailed guidelines are provided in the Volume 3 report.

- *Removal of water in the mixer drum.* Prior to mixing, any water in the mixer drum should be removed completely. Normally, water and sand are used to clean the remaining concrete in the mixer from the previous batch. A small amount of sand and water used for cleaning may remain in the mixer and affect flowability. The more water, the higher the flowability, and it leads segregation of steel fibers. Thus, the remaining water should be removed.
- *Water addition.* The quality of UHPC is significantly affected by the amount of added water. When additional water is added beyond that required by design, it will increase flowability, reduce strength and durability, and cause segregation of steel fibers. Therefore, water content control is essential for a successful UHPC batch. Starting with a lower amount of water in the UHPC mixture initially while mixing allows for easy adjustment by adding water later if needed. However, having too much water in the UHPC mixture is irreversible. To prevent extra water from being mixed with the UHPC, it is recommended that only 90 percent of the targeted water should be added at the water addition step for the first batch. The addition of the 10 percent tail water should be determined depending on the flowability level of the paste right before adding the sand. If the turnover time is longer than the targeted time, adding the remaining water is the solution. This approach can be used to adjust water content because the moisture content in sand may vary.
- *Flow spread.* Based on the workability experience at the plant (discussed in Section 6.3.1), flow impact on fiber distribution (discussed in Section 8.4.2), and void analysis (discussed in Section 8.4.4), a flow range of 10.0–10.5 in. is ideal to avoid fiber segregation and voids and for sufficient workability for girder fabrication. Based on the experience gained in this project, the acceptable range for flow spread is 9.5–11.0 in. A flow spread less than 9.5 in. or greater than 11.0 in. is not considered acceptable. Potential performance considerations within that range are discussed in this volume and in the guidelines provided in Volume 3

of this report. Note that a change in the viscosity of a UHPC mixture may impact the acceptable flow range with respect to fiber segregation. The viscosity of UHPC is influenced by the use of a viscosity modifying agent or an HRWR containing a viscosity modifying agent, along with the chemical composition of cement.

- *Temperature control.* The temperature of UHPC at discharge is an important indicator for the resulting target flow spread value and quality of the fresh concrete. A high temperature of the fresh UHPC greater than 80°F can decrease the flow spread and thus the workability. The recommended fresh UHPC temperature at discharge from literature is 50–80°F from eConstruct (2020), less than 80°F from Graybeal (2019), and less than 85°F from El-Tawil et al. (2018). Therefore, the use of chilled water or ice is an option for obtaining a desired temperature range during hot weather. If those are not available, adjustment of the amount of water or HRWR based on the flow spread value at discharge is another option. However, water or HRWR content should be adjusted carefully because this affects hardened properties and durability. Otherwise, a low temperature of fresh UHPC below 50°F tends to decrease strength gain (eConstruct 2020) and increase the flow spread and thus increases the risk of fiber segregation, which can impact the tensile properties. Therefore, it is recommended to adjust water content based on the temperature at discharge to achieve a target flow spread from a trial batch. Note that a high discharge temperature can be utilized for high early strength gain with an appropriate placement plan to avoid elephant skin.
- *Placement.* In case of multiple batches placed individually in the girder form, the time between batches should be minimized to avoid the formation of elephant skin on top of the UHPC surface. In addition, the girder form should be covered between batches to prevent surface drying. Pouring the fresh UHPC directly on top of the previous UHPC placement can break the surface of elephant skin, particularly when filling the form at one end for a given batch and then moving to the other end for the next batch to help balance the surface level along the length of the girder.
- *Compressive strength*. Compressive strength at release greater than 65 percent of compressive strength at service is recommended to avoid increased creep effects (Graybeal 2014). A minimum 18 ksi compressive strength at service is recommended for the applications considered in this study. Even though cast cylinders may not achieve the desired strength at release in a low temperature environment, the strength of the UHPC

girder can increase more quickly due to a high internal heat from cement hydration reaction. Compression testing using at least three cylinder samples matched-cured at the girder temperature is recommended to determine the compressive strength of the UHPC girder at release, especially during cooler temperatures (below 40°F). If matched-temperature cylinders are not available at the precast plant, casting a UHPC block that is representative of the girder size could be an option. Cores taken from the UHPC block should provide a more representative strength of the UHPC.

REFERENCES

Aaleti, S., Petersen, B., and Sritharan, S. (2013). "Design Guide for Precast UHPC Waffle Deck Panel System, Including Connections." Federal Highway Administration, Springfield, VA.

Aarup, B. (2004). "CRC - A Special Fibre Reinforced High Performance Concrete." *Proc., International Symposium on Advances in Concrete through Science and Engineering*, Northwestern University.

AASHTO (2020). "AASHTO LRFD Bridge Design Specifications, Ninth Edition." American Association of State Highway and Transportation Officials, Washington, DC.

AASHTO T358 (2017). "Standard Method of Test for Surface Resistivity Indication of Concrete's Ability to Resist Chloride Ion Penetration." American Association of State Highway and Transportation Officials, Washington, DC.

AASHTO T 132-87 (2009). "Standard Method of Test for Tensile Strength of Hydraulic Cement Mortars." American Association of State Highway and Transportation Officials, Washington, DC.

AASHTO T 197 (2015). "Standard Method of Test for Time of Setting of Concrete Mixtures by Penetration Resistance." American Association of State Highway and Transportation Officials, Washington, DC.

AASHTO T 259 (2002). "Standard Method of Test for Resistance of Concrete to Chloride Ion Penetration." American Association of State Highway and Transportation Officials, Washington, DC.

AASHTO T 260 (2009). "Standard Method of Test for Sampling and Testing for Chloride Ion in Concrete and Concrete Raw Materials." American Association of State Highway and Transportation Officials, Washington, DC.

AASHTO T 336 (2019). "Standard Test Method for the Coefficient of Thermal Expansion of Hydraulic Cement Concrete." American Association of State Highway and Transportation Officials, Washington, DC.

AASHTO T 358 (2017). "Standard Method of Test for Surface Resistivity Indication of Concrete's Ability to Resist Chloride Ion Penetration." American Association of State Highway and Transportation Officials, Washington, DC.

AASHTO T 397 (2022). "Standard Method of Test for Uniaxial Tensile Response of Ultra-High Performance Concrete." American Association of State Highway and Transportation Officials, Washington, DC.

AASHTO T 397 Draft (2022). "Standard Method of Test for Uniaxial Tensile Response of Ultra-High Performance Concrete." American Association of State Highway and Transportation Officials, Washington, DC.

AASHTO TP142 (2021). "Standard Specification for Accelerated Determination of Potentially Deleterious Expansion of Concrete Cylinder Due to Alkali–Silica Reaction (Accelerated Concrete Cylinder Test, ACCT)." American Association of State Highway and Transportation Officials, Washington, DC.

Abbas, S., Nehdi, M., and Saleem, M. (2016). "Ultra-High Performance Concrete: Mechanical Performance, Durability, Sustainability and Implementation Challenges." *International Journal of Concrete Structures and Materials*, 10(3), 271-295.

Abbas, S., Soliman, A. M., and Nehdi, M. L. (2015). "Exploring Mechanical and Durability Properties of Ultra-High Performance Concrete Incorporating Various Steel Fiber Lengths and Dosages." *Construction and Building Materials*, 75, 429-441.

ACI 209R-92 (1997). "Prediction of Creep, Shrinkage, and Temperature Effects in Concrete Structures." American Concrete Institute, Farmington Hills, MI.

ACI 211.1-91 (1991). "Standard Practice for Selecting Proportions for Normal, Heavyweight, and Mass Concrete." American Concrete Institute, Farmington Hills, MI.

ACI 232.3R-14 (2014). "Report on High-Volume Fly Ash Concrete for Structural Applications." American Concrete Institute, Farmington Hills, MI.

ACI 239R-18 (2018). "Ultra-High-Performance Concrete: An Emerging Technology Report." *Emerging Technology Series*, American Concrete Institute, Farmington Hills, MI.

ACI 363R-10 (2010). "Report on High-Strength Concrete." American Concrete Institute, Farmington Hills, MI.

ACI 544.1R-96 (2002). "Report on Fiber Reinforced Concrete." American Concrete Institute, Farmington Hills, MI.

ACI 544.4R-18 (2018). "Guide to Design with Fiber-Reinforced Concrete." American Concrete Institute, Farmington Hills, MI.

ACI Committee 318 (2019). "Building Code Requirements for Structural Concrete and Commentary." American Concrete Institute, Farmington Hills, MI.

Acker, P. (2004). "Swelling, Shrinkage and Creep: A Mechanical Approach to Cement Hydration." *Materials and Structures*, 37(4), 237-243.

Acker, P., and Behloul, M. (2004). "Ductal® Technology: A Large Spectrum of Properties, a Wide Range of Applications." *Proc., The International Symposium on UHPC*, Kassel University Press, 11-23.

AFGC (2013). "Ultra High Performance Fibre-Reinforced Concretes (Bétons Fibrés à Ultra-Hautes Performances)." AFGC-SETRA, Bagneux, France.

Ahlborn, T. M., Misson, D. L., Peuse, E. J., and Gilbertson, C. G. (2008). "Durability and Strength Characterization of Ultra-High Performance Concrete Under Variable Curing Regimes." *Proc., 2nd Int. Symp. on Ultra High Performance Concrete*, Kassel University Press, 197-204.

Ahlborn, T. M., Peuse, E. J., and Misson, D. L. (2008). "Ultra-High Performance Concrete for Michigan Bridges Material Performance–Phase I." Michigan Department of Transportation, Lansing, MI.

Ahmad, S. H., and Shah, S. P. (1985). "Structural Properties of High Strength Concrete and its Implications for Precast Prestressed Concrete." *PCI Journal*, 30(6), 92-119.

Aitcin, P.-C. (1993). "High-Performance Concrete Demystified." *Concrete International*, 15(1), 21-26.

Aïtcin, P.-C. (1998). *High Performance Concrete*, CRC press, Boca Raton, FL.

Aïtcin, P.-C. (2016). "The Importance of The Water–Cement and Water–Binder Ratios." *Science and Technology of Concrete Admixtures*, Elsevier, 3-13.

Aïtcin, P.-C. (2016). "Phenomenology of Cement Hydration." *Science and Technology of Concrete Admixtures*, Elsevier, 15-25.

Aïtcin, P.-C. (2016). "Portland Cement." *Science and Technology of Concrete Admixtures*, Elsevier, 27-51.

Aïtcin, P.-C. (2016). "Supplementary Cementitious Materials and Blended Cements." *Science and Technology of Concrete Admixtures*, Elsevier, 53-73.

Al-Omaishi, N., Tadros, M. K., and Seguirant, S. J. (2009). "Elasticity Modulus, Shrinkage, and Creep on High-Strength Concrete as adopted by AASHTO." *PCI Journal*, 54(3).

Alaee, F. J., and Karihaloo, B. L. (2003). "Retrofitting of Reinforced Concrete Beams with CARDIFRC." *Journal of Composites for Construction*, 7(3), 174-186.

Alford, N. M., and Birchall, J. D. (1985). "The Properties and Potential Applications of Macro-Defect- Free Cement." *Proc., Symposium on Very High Strength Cement-Based Materials*, Materials Research Society Symposia Proceedings, Pittsburgh, PA, 265- 276.

Alkaysi, M. (2016). "Strength and Durability of Ultra-High Performance Concrete Materials and Structures." Doctor of Philosophy Dissertation, University of Michigan, Ann Arbor, MI.

Alkaysi, M., and El-Tawil, S. (2016). "Effects of Variations in the Mix Constituents of Ultra High Performance Concrete (UHPC) on Cost and Performance." *Materials and Structures*, 49(10), 4185-4200.

Alkaysi, M., El-Tawil, S., Liu, Z., and Hansen, W. (2016). "Effects of Silica Powder and Cement Type on Durability of Ultra High Performance Concrete (UHPC)." *Cement Concrete Composites*, 66, 47-56.

Alsalman, A., Dang, C. N., and Micah Hale, W. (2017). "Development of Ultra-High Performance Concrete with Locally Available Materials." *Construction and Building Materials*, 133, 135-145.

Amen, D. K. (2011). "Degree of Hydration and Strength Development of Low Water-to-Cement Ratios in Silica Fume Cement System." *International Journal of Civil and Environment Engineering*, 11(5), 10-16.

Andrade, M., Frias, M., and Aarup, B. (1996). "Durability of Ultra-High Strength Concrete: Compact Reinforced Composite." *Proc., BHP96 Fourth International Symposium on Utilization of High-Strength/High-Performance Concrete*, 29-31.

Andreasen, A. (1930). "Über die Beziehung zwischen Kornabstufung und Zwischenraum in Produkten aus losen Körnern (mit einigen Experimenten)." *Kolloid-Zeitschrift*, 50(3), 217-228.

Archie, G. E. (1942). "The Electrical Resistivity Log as an Aid in Determining Some Reservoir Characteristics." *Transactions of the AIME*, 146(01), 54-62.

Arezoumandi, M., Ezzell, M., and Volz, J. S. (2014). "A Comparative Study of the Mechanical Properties, Fracture Behavior, Creep, and Shrinkage of Chemically Based Self-Consolidating Concrete." *Frontiers of Structural and Civil Engineering*, 8(1), 36-45.

Arora, A., Aguayo, M., Hansen, H., Castro, C., Federspiel, E., Mobasher, B., and Neithalath, N. (2018). "Microstructural Packing-and Rheology-Based Binder Selection and Characterization for Ultra-High Performance Concrete (UHPC)." *Cement and Concrete Research*, 103, 179-190.

Arora, A., Yao, Y., Mobasher, B., and Neithalath, N. (2019). "Fundamental Insights into the Compressive and Flexural Response of Binder-and Aggregate-Optimized Ultra-High Performance Concrete (UHPC)." *Cement and Concrete Composites*, 98, 1-13.

ASTM 512 (2015). "Standard Test Method for Creep of Concrete in Compression." ASTM International, West Conshohocken, PA.

ASTM C39 (2016). "Standard Test Method for Compressive Strength of Cylindrical Concrete Specimens." ASTM International, West Conshohocken, PA.

ASTM C39 (2020). "Standard Test Method for Compressive Strength of Cylindrical Concrete Specimens." ASTM International, West Conshohocken, PA.

ASTM C78 (2009). "Standard Test Method for Flexural Strength of Concrete (Using Simple Beam with Third-Point Loading)." ASTM International, West Conshohocken, PA.

ASTM C109 (2016). "Standard Test Method for Compressive Strength of Hydraulic Cement Mortars (Using 2-in. or [50-mm] Cube Specimens)." ASTM International, West Conshohocken, PA.

ASTM C138 (2015). "Standard Test Method for Density (Unit Weight), Yield, and Air Content (Gravimetric) of Concrete." ASTM International, West Conshohocken, PA.

ASTM C143 (2012). "Standard Test Method for Slump of Hydraulic-Cement Concrete." ASTM International, West Conshohocken, PA.

ASTM C144 (2018). "Standard Specification for Aggregate for Masonry Mortar." ASTM International, West Conshohocken, PA.

ASTM C157 (2008). "Standard Test Method for Length Change of Hardened Hydraulic-Cement Mortar and Concrete." ASTM International, West Conshohocken, PA.

ASTM C157 (2017). "Standard Test Method for Length Change of Hardened Hydraulic-Cement Mortar and Concrete." ASTM International, West Conshohocken, PA.

ASTM C190 (1990). "Standard Test Method for Tensile Strength of Hydraulic Cement Mortars." ASTM International, West Conshohocken, PA.

ASTM C191 (2018). "Standard Test Methods for Time of Setting of Hydraulic Cement by Vicat Needle." ASTM International, West Conshohocken, PA.

ASTM C192 (2016). "Standard Practice for Making and Curing Concrete Test Specimens in the Laboratory." ASTM International, West Conshohocken, PA.

ASTM C215 (2019). "Standard Test Method for Fundamental Transverse, Longitudinal, and Torsional Resonant Frequencies of Concrete Specimens." ASTM International, West Conshohocken, PA.

ASTM C230 (2008). "Standard Specification for Flow Table for Use in Tests of Hydraulic Cement." ASTM International, West Conshohocken, PA.

ASTM C230 (2014). "Standard Specification for Flow Table for Use in Tests of Hydraulic Cement." ASTM International, West Conshohocken, PA.

ASTM C293 (2016). "Standard Test Method for Flexural Strength of Concrete (Using Simple Beam With Center-Point Loading)." ASTM International, West Conshohocken, PA.

ASTM C403 (2016). "Standard Test Method for Time of Setting of Concrete Mixtures by Penetration Resistance." ASTM International, West Conshohocken, PA.

ASTM C469 (2014). "Standard Test Method for Static Modulus of Elasticity and Poisson's Ratio of Concrete in Compression." ASTM International, West Conshohocken, PA.

ASTM C496 (1996). "Standard Test Method for Splitting Tensile Strength of Cylindrical Concrete Specimens." ASTM International, West Conshohocken, PA.

ASTM C511 (2019). "Standard Specification for Mixing Rooms, Moist Cabinets, Moist Rooms, and Water Storage Tanks Used in the Testing of Hydraulic Cements and Concretes." ASTM International, West Conshohocken, PA.

ASTM C512 (2015). "Standard Test Method for Creep of Concrete in Compression." ASTM International, West Conshohocken, PA.

ASTM C597 (2016). "Standard Test Method for Pulse Velocity Through Concrete." ASTM International, West Conshohocken, PA.

ASTM C618 (2019). "Standard Specification for Coal Fly Ash and Raw or Calcined Natural Pozzolan for Use in Concrete." ASTM International, West Conshohocken, PA.

ASTM C666 (2015). "Standard Test Method for Resistance of Concrete to Rapid Freezing and Thawing." ASTM International, West Conshohocken, PA.

ASTM C672 (2012). "Standard Test Method for Scaling Resistance of Concrete Surfaces Exposed to Deicing Chemicals." ASTM International, West Conshohocken, PA.

ASTM C856 (2020). "Standard Practice for Petrographic Examination of Hardened Concrete." ASTM International, West Conshohocken, PA.

ASTM C944 (2012). "Standard Test Method for Abrasion Resistance of Concrete or Mortar Surfaces by the Rotating-Cutter Method." ASTM International, West Conshohocken, PA.

ASTM C1018 (1997). "ASTM C1018 - 97 Standard Test Method for Flexural Toughness and First-Crack Strength of Fiber-Reinforced Concrete (Using Beam With Third-Point Loading) (Withdrawn 2006)." ASTM International, West Conshohocken, PA.

ASTM C1064 (2017). "Standard Test Method For Temperature of Freshly Mixed Hydraulic-Cement Concrete." ASTM International, West Conshohocken, PA.

ASTM C1202 (1997). "Standard Test Method for Electrical Indication of Concrete's Ability to Resist Chloride Ion Penetration." ASTM International, West Conshohocken, PA.

ASTM C1202 (2017). "Standard Test Method for Electrical Indication of Concrete's Ability to Resist Chloride Ion Penetration." ASTM International, West Conshohocken, PA.

ASTM C1240 (2015). "Standard Specification for Silica Fume Used in Cementitious Mixtures." ASTM international, West Conshohocken, PA.

ASTM C1260 (2014). "Standard Test Method for Potential Alkali Reactivity of Aggregates (Mortar-Bar Method)." ASTM International, West Conshohocken, PA.

ASTM C1437 (2015). "Standard Test Method for Flow of Hydraulic Cement Mortar." ASTM International, West Conshohocken, PA.

ASTM C1556 (2011). "Standard Test Method for Determining the Apparent Chloride Diffusion Coefficient of Cementitious Mixtures by Bulk Diffusion." ASTM International, West Conshohocken, PA.

ASTM C1609 (2019). "Standard Test Method for Flexural Performance of Fiber-Reinforced Concrete (Using Beam With Third-Point Loading)." ASTM International, West Conshohocken, PA.

ASTM C1609/C1609M (2012). "Standard Test Method for Flexural Performance of Fiber-Reinforced Concrete (Using Beam With Third-Point Loading)." ASTM International, West Conshohocken, PA.

ASTM C1760 (2021). "Standard Test Method for Bulk Electrical Conductivity of Hardened Concrete." ASTM International, West Conshohocken, PA.

ASTM C1856 (2017). "Standard Practice for Fabricating and Testing Specimens of Ultra-High-Performance Concrete." ASTM International, West Conshohocken, PA.

Baby, F., Graybeal, B., Marchand, P., and Toutlemonde, F. (2012). "Proposed Flexural Test Method and Associated Inverse Analysis for Ultra-High-Performance Fiber-Reinforced Concrete." *Materials Journal*, 109(5), 545.

Bache, H. H. (1981). "Densified Cements Ultra-Fine Particle-Based Materials." *International Conference on Superplasticizers in Concrete*, Aalborg Portland Cement, Ottawa, Canada.

Bache, H. H. (1987). "Compact Reinforced Composite Basic Principles." Aalborg Portland Cement, Denmark.

Barcelo, L., Boivin, S., Acker, P., Toupin, J., and Clavaud, B. (2001). "Early Age Shrinkage of Concrete: Back to Physical Mechanisms." *Concrete Science and Engineering*, 3(10), 85-91.

Batoz, J. F., and Behloul, M. (2011). *Designing Building with UHPFRC*, Wiley, Hoboken, NJ.

Behloul, M., Bernier, G., and Cheyrezy, M. (1996). "Tensile Behavior of Reactive Powder Concrete." *Proc., of the 4th International Symposium on Utilization of HSC/HPC, BHP*, 1375-1381.

Behloul, M., Chanvillard, G., Casanova, P., and Orange, G. (2002). "Fire Resistance of Ductal® Ultra High Performance Concrete." *Proc., 1st fib Congress*, 421-430.

Behloul, M., and Lee, K. (2003). "Ductal® Seonyu Footbridge." *Structural Concrete Journal of the fib*, 4(4), 195-201.

Benson, S., and Karihaloo, B. (2005). "CARDIFRC®-Development and Mechanical Properties. Part III: Uniaxial Tensile Response and Other Mechanical Properties." *Magazine of Concrete Research*, 57(8), 433-443.

Bentz, D. P. (2007). "A Virtual Rapid Chloride Permeability Test." *Cement and Concrete Composites*, 29(10), 723-731.

Bentz, D. P., and Aitcin, P.-C. (2008). "The Hidden Meaning of Water-Cement Ratio." *Concrete International*, 30(5), 51-54.

Bernard, E. (2009). "Influence of Test Machine Control Method on Flexural Performance of Fiber Reinforced Concrete Beams." *Journal of ASTM International*, 6(9), 1-16.

Berry, M., Snidarich, R., and Wood, C. (2017). "Development of Non-Proprietary Ultra-High Performance Concrete: Project Summary Report." Montana Department of Transportation, Helena, MT.

Bissonnette, B., and Pigeon, M. (1995). "Tensile Creep at Early Ages of Ordinary, Silica Fume and Fiber Reinforced Concretes." *Cement Concrete Research*, 25(5), 1075-1085.

Blais, P. Y., and Couture, M. (1999). "Precast, Prestressed Pedestrian Bridge-World's First Reactive Powder Concrete Structure." *PCI journal*, 44, 60-71.

Bonneau, O., Lachemi, M., Dallaire, E., Dugat, J., and Aitcin, P.-C. (1997). "Mechanical Properties and Durability of Two Industrial Reactive Powder Concretes." *Materials Journal*, 94(4), 286-290.

Bonneau, O., Vernet, C., Moranville, M., and Aïtcin, P.-C. (2000). "Characterization of the Granular Packing and Percolation Threshold of Reactive Powder Concrete." *Cement and Concrete Research*, 30(12), 1861-1867.

Bornemann, R., Schmidt, M., Fehling, E., and Middendorf, B. (2001). "Ultra High Performance Concrete UHPC Manufacturing, Properties and Applications." *Concrete and Reinforced Concrete Construction*, 96, 458-467.

Boulay, C., Rossi, P., and Tailhan, J.-L. (2004). "Uniaxial Tensile Test on a New Cement Composite Having a Hardening Behaviour." *Proc., 6th International RILEM Symposium on Fibre-Reinforced Concretes (BEFIB'2004), RILEM*, 61-68.

Boulekbache, B., Hamrat, M., Chemrouk, M., and Amziane, S. (2010). "Flowability of Fibre-Reinforced Concrete and its Effect on the Mechanical Properties of the Material." *Construction Building Materials*, 24(9), 1664-1671.

Brouwers, H., and Radix, H. (2005). "Self-Compacting Concrete: the Role of the Particle Size Distribution." *Proc., First International Symposium on Design, Performance and Use of SCC, Hunan, China*, 109-118.

Brühwiler, E., Bastien-Masse, M., Mühlberg, H., Houriet, B., Fleury, B., Cuennet, S., Schär, P., Boudry, F., and Maurer, M. (2015). "Strengthening the Chillon Viaducts Deck Slabs with Reinforced UHPFRC." *Proc., IABSE Symposium Report,* International Association for Bridge and Structural Engineering, 1-8.

Carrasquillo, R. L., Nilson, A. H., and Slate, F. O. (1981). "Properties of High Strength Concrete Subject to Short-Term Loads." *Proc., Journal Proceedings,* 171-178.

CEB FIP Model Code 2010 fib (2010). "Model Code 2010, fib-CEB FIP, Bulletin 65." *International Federation for Structural Concrete (fib),* Volume 1.

Chanvillard, G., and Rigaud, S. (2003). "Complete Characterization of Tensile Properties of Ductal UHPFRC According to the French Recommendations." *Proc., The 4th International RILEM workshop High Performance Fiber Reinforced Cementitious Composites,* 21-34.

Chen, Y., Matalkah, F., Weerasiri, R. R., Balachandra, A. M., and Soroushian, P. (2017). "Dispersion of Fibers in Ultra-High-Performance Concrete." *Concrete International,* 39(12), 45-50.

Cheyrezy, M. (1999). "Structural Applications of RPC." *J. Concrete,* 33(1), 20-23.

Cheyrezy, M., Maret, V., and Frouin, L. (1995). "Microstructural Analysis of RPC (Reactive Powder Concrete)." *Cement and Concrete Research,* 25(7), 1491-1500.

Collepardi, S., Coppola, L., Troli, R., and Collepardi, M. (1997). "Mechanical Properties of Modified Reactive Powder Concrete." *Proc., SP-173: Fifth CANMET/ACI International Conference on Superplasticizers and Other Chemical Admixtures in Concrete,* American Concrete Institute, 1-22.

Cooper, B. A. (2020). "Durability of Non-Proprietary Ultra-High-Performance Concrete for Pretensioned Bridge Girders." Master of Science Thesis, Texas A&M University, College Station, TX.

Coppola, L., Troli, R., Cerulli, T., and Collepardi, M. (1996). "The Influence of Materials on the Performance of Reactive Powder Concrete." *Proc., International Congress on High-Performance Concrete, and Performance and Quality of Concrete Structures,* 502-513.

CSA S6:19 (2019). "Canadian Highway Bridge Design Code." Canadian Standards Association (CSA), Toronto, Canada.

Cwirzen, A. (2007). "The Effect of the Heat-Treatment Regime on the Properties of Reactive Powder Concrete." *Advances in Cement Research,* 19(1), 25-34.

Cwirzen, A., Penttala, V., and Cwirzen, K. (2008). "The Effect of Heat Treatment on the Salt Freeze-Thaw Durability of UHSC." *Proc., The 2nd International Symposium on Ultra High Performance Concrete,* Kassel University Press, 221-230.

de Larrard, F., and Sedran, T. (1994). "Optimization of Ultra-High-Performance Concrete by the Use of a Packing Model." *Cement and Concrete Research*, 24(6), 997-1009.

de Matteis, D., Novarin, M., Marchand, P., Fabry, N., Petel, A., and Chanut, S. (2008). "A Fifth French Bridge Including UHPFRC Components, the Widening of the Pinel Bridge, in Rouen (France)." *Proc., International Symposium on UHPC*, Kassel University Press.

Denarié, E., Bruhwiler, E., and Znidaric, A. (2005). "Full Scale Application of UHPFRC for the Rehabilitation of Bridges-from Lab to the Field." *5th FWP/SAMA-RIS Sustainable and Advance Materials*, Brussels, Belgium.

Dhir, R., Hubbard, F., Munday, J., Jones, M., and Duerden, S. (1988). "Contribution of PFA to Concrete Workability and Strength Development." *Cement and Concrete Research*, 18(2), 277-289.

DIN 4102-2 (1977). "Fire Behaviour of Building Materials and Building Components; Building Components; Definitions, Requirements and Tests." German Institute for Standardisation (Deutsches Institut für Normung), Berlin, Germany.

eConstruct (2020). "Implementation of Ultra-High-Performance Concrete in Long-Span Precast Pretensioned Elements for Concrete Buildings and Bridges." Wiss, Janney, Elstner Associates, University of Nebraska-Lincoln, The NCSU Constructed Facilities Laboratory, Precast/Prestressed Concrete Institute, Chicago, IL.

Ehlen, M. A. (2019). "Life-365 Service Life Prediction Model and Computer Program for Predicting the Service Life and Life-Cycle Cost of Reinforced Concrete Exposed to Chlorides, version 2.2.3.", the Life-365™ Consortium III.

El-Enein, S. A., Kotkata, M., Hanna, G., Saad, M., and Abd El Razek, M. (1995). "Electrical Conductivity of Concrete Containing Silica Fume." *Cement and Concrete Research*, 25(8), 1615-1620.

El-Helou, R. G., Haber, Z. B., and Graybeal, B. A. (2022). "Mechanical Behavior and Design Properties of Ultra-High-Performance Concrete." *ACI Materials Journal*, 119(1).

El-Tawil, S., Alkaysi, M., Naaman, A. E., Hansen, W., and Liu, Z. (2016). "Development, Characterization and Applications of a Non Proprietary Ultra High Performance Concrete for Highway Bridges." Michigan Department of Transportation, Lansing, MI.

El-Tawil, S., Tai, Y.-S., Meng, B., Hansen, W., and Liu, Z. (2018). "Commercial Production of Non-Proprietary Ultra High Performance Concrete." Michigan Department of Transportation, Lansing, MI.

EN 12350-2 (2011). "Testing Fresh Concrete Part 2: Slump Test." German Standardization Body, Beuth Verlag, Berlin, Germany.

EN 12350-5 (2011). "Testing Fresh Concrete Part 5: Flow Table Test." German Standardization Body, Beuth Verlag, Berlin, Germany.

Eurocode 2 (2004). "BS EN 1992, Eurocode 2: Design of Concrete Structures." *Part 1-1: General rules and rules for buildings*Brussels, Belgium, 225.

Feldman, R. (1977). "Non-Destructive Testing of Concrete CBD-187." *Canadian Building Digests*, 187.

Ferrara, L. (2012). "High Performance Fiber Reinforced Self-Compacting Concrete (HPFR. SCC): A Smart Material for High End Engineering Applications." *Proc., HAC 2012 Congreso Iberoamericano Hormigon Autocompactante*, Universidad Politecnica de Madrid, 323-334.

FHWA (2022). "Proposed AASHTO LRFD Guide Specifications for Structural Design with UHPC." *Draft Under Review*, American Association of State Highway and Transportation Officials, Washington, DC.

Foden, A. J., and McDonagh, M. D. (2016). "Benefits of Ultra-High Performance Concrete for the Rehabilitation of the Pulaski Skyway." *Proc., International Interactive Symposium on Ultra-High Performance Concrete*, Iowa State University Digital Press.

Frohlich, S., and Schmidt, M. (2012). "Influences on Repeatability and Reproducibility of Testing Methods for Fresh UHPC." *Proc., Ultra-High Performance Concrete and Nanotechnology in Construction. Proceedings of Hipermat 2012. 3rd International Symposium on UHPC and Nanotechnology for High Performance Construction Materials*, Kassel University Press, 225.

Garas, V., Kurtis, K., and Kahn, L. (2012). "Creep of UHPC in Tension and Compression: Effect of Thermal Treatment." *Cement and Concrete Composites*, 34(4), 493-502.

Garas, V. Y., Kahn, L. F., and Kurtis, K. E. (2010). "Tensile Creep Test of Fiber-Reinforced Ultra-High Performance Concrete." *Journal of Testing and Evaluation*, 38(6), 674-682.

Gelardi, G., and Flatt, R. (2016). "Working Mechanisms of Water Reducers and Superplasticizers." *Science and Technology of Concrete Admixtures*, Elsevier, 257-278.

Giesler, A. J., Applegate, S. B., and Weldon, B. D. (2016). "Implementing Nonproprietary, Ultra-High-Performance Concrete in a Precasting Plant." *PCI Journal*, 61(6), 68 - 80.

Granju, J., and Grandet, J. (1989). "Relation Between the Hydration State and the Compressive Strength of Hardened Portland Cement Pastes." *Cement and Concrete Research*, 19(4), 579-585.

Graybeal, B. (2009). "UHPC in the US Highway Infrastructure." *Proc., Designing Building with UHPFRC*, Marsille, France.

Graybeal, B. (2019). "Design and Construction of Field-Cast UHPC Connections." Federal Highway Administration, McLean, VA.

Graybeal, B., and Davis, M. (2008). "Cylinder or Cube: Strength Testing of 80 to 200 MPa (11.6 to 29 ksi) Ultra-High-Performance Fiber-Reinforced Concrete." *ACI Materials Journal*, 105(6), 603.

Graybeal, B. A. (2006a). "Material Property Characterization of Ultra-High Performance Concrete." Federal Highway Administration, McLean, VA.

Graybeal, B. A. (2006b). "Structural Behavior of Ultra High Performance Concrete Prestressed I-Girders." Federal Highway Administration, McLean, VA.

Graybeal, B. A. (2006c). "Practical Means for Determination of The Tensile Behavior of Ultra-High Performance Concrete." *Journal of ASTM International*, 3(8), 1-9.

Graybeal, B. A. (2007). "Compressive Behavior of Ultra-High-Performance Fiber-Reinforced Concrete." *ACI Materials Journal*, 104(2), 146.

Graybeal, B. A. (2011). "Ultra-high performance concrete."TechNote, FHWA-HRT-11-038, Federal Highway Administration, McLean, VA.

Graybeal, B. A. (2014). "Design and Construction of Field-Cast UHPC Connections." Federal Highway Administration, McLean, VA.

Graybeal, B. A. (2017). "Emerging UHPC-Based Bridge Construction and Preservation Solutions." *AFGC-ACI-fib-RILEM International Symposium on Ultra-High Performance Fibre-Reinforced Concrete*, 965 - 974.

Graybeal, B. A., and Baby, F. (2013). "Development of Direct Tension Test Method for Ultra-High-Performance Fiber-Reinforced Concrete." *ACI Materials Journal*, 110(2).

Graybeal, B. A., and Baby, F. (2019). "Tension Testing of Ultra-High Performance Concrete." Federal Highway Administration, McLean, VA.

Graybeal, B. A., and Stone, B. (2012). "Compression Response of a Rapid-Strengthening Ultra-High Performance Concrete (UHPC) Formulation." US Department of Transportation, Federal Highway Administration, McLean, VA.

Greene, G. G., and Graybeal, B. (2013). "Lightweight Concrete: Mechanical Properties." Federal Highway Administration, McLean, VA.

Grünewald, S., and Walraven, J. (2001). "Parameter-study on the Influence of Steel Fibers and Coarse Aggregate Content on the Fresh Properties of Self-Compacting concrete." *Cement and Concrete Research*, 31(12), 1793-1798.

Gu, C., Ye, G., and Sun, W. (2015). "Ultra High Performance Concrete-Properties, Applications and Perspectives." *Science China Technological Sciences*, 58(4), 587-599.

Haber, Z. B., De la Varga, I., Graybeal, B. A., Nakashoji, B., and El-Helou, R. (2018). "Properties and Behavior of UHPC-class Materials." Federal Highway Administration, McLean, VA.

Haber, Z. B., Munoz, J. F., and Graybeal, B. A. (2017). "Field Testing of an Ultra-High Performance Concrete Overlay." Federal Highway Administration, McLean, VA.

Hannawi, K., Bian, H., Prince-Agbodjan, W., and Raghavan, B. (2016). "Effect of Different Types of Fibers on the Microstructure and the Mechanical Behavior of Ultra-High Performance Fiber-Reinforced Concretes." *Composites Part B: Engineering*, 86, 214-220.

Hassan, A., Jones, S., and Mahmud, G. (2012). "Experimental Test Methods to Determine the Uniaxial Tensile and Compressive Behaviour of Ultra High Performance Fibre Reinforced Concrete (UHPFRC)." *Construction and Building Materials*, 37, 874-882.

Heinz, D., Dehn, F., and Urbonas, L. (2004). "Fire Resistance of Ultra High Performance Concrete (UHPC)-Testing of Laboratory Samples and Columns under Load." *Proc., International Symposium on Ultra High Performance Concrete*, Kassel University Press, 703-715.

Heinz, D., and Ludwig, H.-M. (2004). "Heat Treatment and the Risk of DEF Delayed Ettringite Formation in UHPC." *Proc., International Symposium on Ultra-High Performance Concrete*, Kassel University Press, 717-730.

Hermann, A., Langaro, E., SILVA, S. L. D., and Klein, N. S. (2016). "Particle Packing of Cement and Silica Fume in Pastes Using an Analytical Model." *Revista IBRACON de Estruturas e Materiais*, 9(1), 48-65.

Herold, G., and Müller, H. (2004). "Measurement of Porosity of Ultra High Strength Fibre Reinforced Concrete." *Proc., The International Symposium on Ultra-High Performance Concrete*, Kassel University Press, 685-694.

Hertel, C., Orgass, M., and Dehn, F. (2002). "Brandschutztechnische Aspekte bei Faserbetonen." *König, G., Holschemacher, K., Dehn, F.: Faserbeton-Innovationen im Bauwesen*.

Hirschi, T., and Wombacher, F. (2008). "Influence of Different Superplasticizers on UHPC." *Proc., The Second International Symposium on Ultra High Performance Concrete*, Kassel University Press, 77-84.

Hjorth, L., Alford, M. N., Mangabhai, R., Hirsch, P., Moir, G., Jefferis, S., Blundell, R., Kelly, A., Defosse, C., and Sing, K. (1983). "Development and Application of High-Density Cement-Based Materials." *Philosophical Transactions of the Royal Society A*, 167-173.

Holmen, J. K., Frodal, B. H., Hopperstad, O. S., and Børvik, T. (2017). "Strength Differential Effect in Age Hardened Aluminum Alloys." *International Journal of Plasticity*, 99, 144-161.

Hornain, H. (2007). *GranDuBé: Grandeurs Associées à la Durabilité des Bétons*, Presses des Ponts, France.

Hunger, M. (2010). "An Integral Design Concept for Ecological Self-Compacting Concrete." Technische Universiteit Eindhoven, Eindhoven, The Netherlands.

Hurlebaus, S., Hueste, M., Karthik, M., and Terzioglu, T. (2016). "Condition Assessment of Bridge Post-Tensioning and Stay Cable Systems Using NDE Methods." Texas A&M Transportation Institute, College Station, Texas.

Ibrahim, M. A., Farhat, M., Issa, M. A., and Hasse, J. A. (2017). "Effect of Material Constituents on Mechanical and Fracture Mechanics Properties of Ultra-High-Performance Concrete." *ACI Materials Journal*, 114(3), 453.

ISO 834-11 (2014). "Fire Resistance Tests - Elements of Building Construction - Part 11: Specific Requirements for The Assessment of Fire Protection to Structural Steel Elements." International Orgarnization for Standards.

Jeroen, D., Boel, V., and De Schutter, G. (2015). "Freeze-Thaw Resistance of Ultra-High Performance Concrete in Normal and Severe Conditions." *XIII International Conference on Durability of Building Materials and Components - XIII DBMC*, V. M. J. Marco Quattrone, ed., Rilem, 174-181.

JIS A 1149 (2017). "Method of Test for Static Modulus of Elasticity of Concrete." Japanese Standards Association (JSA), Tokyo, Japan.

Joe, C. D., Moustafa, M., and Ryan, K. L. (2017). "Cost and Ecological Feasibility of using UHPC in Highway Bridges." University of Nevada, Reno. Solaris University Transportation Center.

JSCE-SF7 (1984). "Method of Tests for Fiber Content of Steel Fiber Reinforced Concrete." Japanese Society of Civil Engineers, Yotsuya 1-chome, Shinjuku-ku, Tokyo 160-0004, Japan.

JSCE (2006). "Recommendations for Design and Construction of Ultra High Strength Fiber Reinforced Concrete Structures (Draft)." *JSCE Guidelines for concrete No. 9.*, Tokyo, Japan.

JSCE (2007). "Standard Specifications for Concrete Structures- Materials and Construction." Japan Society of Civil Engineers, Tokyo, Japan.

JSCE (2008). "JSCE Recommendations for Design and Construction of High Performance Fiber Reinforced Cement Composites with Multiple Fine Cracks (HPFRCC)." Japan Society of Civil Engineering, Tokyo, Japan.

JSCE (2008). "Recommendations for Design and Construction of Ultra High-Strength Fiber-Reinforced Concrete Structures." Japan Society of Civil Engineers, Tokyo, Japan.

Jungwirth, J., and Muttoni, A. (2004). "Structural Behavior of Tension Members in UHPC." *Proc., International Symposium on Ultra High Performance Concrete*, Kassel University Press, , 533-544.

Kang, S.-H., Lee, J.-H., Hong, S.-G., and Moon, J. (2017). "Microstructural Investigation of Heat-Treated Ultra-High Performance Concrete for Optimum Production." *ACI Materials*, 10(9), 1106.

Kang, S.-T., Choi, J.-I., Koh, K.-T., Lee, K. S., and Lee, B. Y. (2016). "Hybrid Effects of Steel Fiber and Microfiber on the Tensile Behavior of Ultra-High Performance Concrete." *Composite Structures*, 145, 37-42.

Karim, R., Najimi, M., and Shafei, B. (2019). "Assessment of Transport Properties, Volume Stability, and Frost Resistance of Non-Proprietary Ultra-High Performance Concrete." *Construction and Building Materials*, 227, 11-31.

Keierleber, B., Bierwagen, D., Wipf, T., and Abu-Hawash, A. (2010). "FHWA, Iowa Optimize Pi Girder." Aspire.

Khayat, K. H., and Valipour, M. (2014). "Design of Ultra High Performance Concrete as an Overlay in Pavements and Bridge Decks." Missouri University of Science and Technology. Center for Transportation, Jefferson City, MO.

Khayat, K. H., and Valipour, M. (2018). "Design and Performance of Cost-Effective Ultra High Performance Concrete for Bridge Deck Overlays." Missouri. Dept. of Transportation. Construction and Materials Division, Jefferson City, MO.

Kim, Y. J. (2018). "Development of Cost-Effective Ultra-High Performance Concrete (UHPC) for Colorado's Sustainable Infrastructure." Colorado Department of Transportation, Denver, CO.

Kruppa, J. (1988). "Méthode de Prévision par le Calcul du Comportement au feu des Poteaux Mixtes (Acier+ Béton)." *Construction métallique*(3).

Kusumawardaningsih, Y., Fehling, E., Ismail, M., and Aboubakr, A. A. M. (2015). "Tensile Strength Behavior of UHPC and UHPFRC." *Procedia Engineering*, 125, 1081-1086.

Kwon, S., Nishiwaki, T., Kikuta, T., and Mihashi, H. (2014). "Development of Ultra-High-Performance Hybrid Fiber-Reinforced Cement-Based Composites." *ACI Materials Journal*, 111(3).

LafargeHolcim (2016). "Enrico Navarra Gallery Roof, France." *https://www.ductal.com/en/navarra-house-ductalr-roof* (Accessed Dec. 20, 2018).

Lankard, D. R. (1984). "Slurry Infiltrated Fiber Concrete (SIFCON): Properties and Applications." *MRS Online Proceedings Library Archive*, 42.

Larsen, I. L., and Thorstensen, R. T. (2020). "The Influence of Steel Fibres on Compressive and Tensile Strength of Ultra High Performance Concrete: A Review." *Construction and Building Materials*, 256, 119459.

Lawler, J. S., Zampini, D., and Shah, S. P. (2005). "Microfiber and Macrofiber Hybrid Fiber-Reinforced Concrete." *Journal of Materials in Civil Engineering*, 17(5), 595-604.

Le Hoang, A., and Fehling, E. (2017). "Influence of Steel Fiber Content and Aspect Ratio on the Uniaxial Tensile and Compressive Behavior of Ultra High Performance Concrete." *Construction and Building Materials*, 153, 790-806.

Le Roy, R. (1995). "Déformations Instantanées et Différées des Bétons à Hautes Performances." Doctoral Dissertation, École Nationale des Ponts et Chaussées, France.

Li, L. G., and Kwan, A. K. H. (2011). "Mortar Design Based on Water Film Thickness." *Construction and Building Materials*, 25(5), 2381-2390.

Li, L. G., and Kwan, A. K. H. (2014). "Packing Density of Concrete Mix under Dry and Wet Conditions." *Powder Technology*, 253, 514-521.

Li, V. C., and Wu, H.-C. (1992). "Conditions for Pseudo Strain-Hardening in Fiber Reinforced Brittle Matrix Composites." *Applied Mechanics Reviews*, 45(8), 390-398.

Liu, J., Song, S., and Wang, L. (2009). "Durability and Micro-Structure of Reactive Powder Concrete." *Journal of Wuhan University of Technology-Mater. Sci. Ed.*, 24(3), 506-509.

Ma, J., Orgass, M., Dehn, F., Schmidt, D., and Tue, N. (2004). "Comparative Investigations on Ultra-High Performance Concrete with and without Coarse Aggregates." *Proc., International symposium on ultra high performance concrete*, Kassel University Press, 205-212.

Ma, J., and Schneider, H. (2002). "Properties of Ultra-High-Performance Concrete." *Leipzig Annual Civil Engineering Report*, 7, 25-32.

MacGregor, J. G., Wight, J. K., Teng, S., and Irawan, P. (1997). *Reinforced Concrete: Mechanics and Design*, Prentice Hall Upper Saddle River, NJ.

Maeder, U., Lallemant-Gamboa, I., Chaignon, J., and Lombard, J.-P. (2004). "Ceracem, a New High Performance Concrete: Characterisations and Applications." *Proc., First international symposium on ultra high performance concrete*, Kassel University Press, 59-68.

Magureanu, C., Sosa, I., Negrutiu, C., and Heghes, B. (2012). "Mechanical Properties and Durability of Ultra-High-Performance Concrete." *ACI Materials Journal*, 109(2), 177-184.

Malhotra, V., and Mehta, P. (2012). "High-Performance, High-Volume Fly Ash Concrete for Building Durable and Sustainable Structures." Supplementary Cementing Materials for Sustainable Development, Inc., Ottawa, Canada.

Marchon, D., and Flatt, R. (2016). "Impact of Chemical Admixtures on Cement Hydration." *Science and Technology of Concrete Admixtures*, Elsevier, 279-304.

Mardani-Aghabaglou, A., Tuyan, M., Yılmaz, G., Arıöz, Ö., and Ramyar, K. (2013). "Effect of Different Types of Superplasticizer on Fresh, Rheological and Strength Properties of Self-Consolidating Concrete." *Construction and Building Materials*, 47, 1020-1025.

Martinie, L., Rossi, P., and Roussel, N. (2010). "Rheology of Fiber Reinforced Cementitious Materials: Classification and Prediction." *Cement Concrete Research*, 40(2), 226-234.

Mazanec, O., and Schießl, P. (2008). "Mixing Time Optimisation for UHPC." *Proc., The Second International Symposium on Ultra High Performance Concrete*, Kassel University Press, 401-408.

Mendonca, F., El-Khier, M. A., Morcous, G., and Hu, J. (2020). "Feasibility Study of Development of Ultra-High Performance Concrete (UHPC) for Highway Bridge Applications in Nebraska." Nebraska Department of Transportation, Lincoln, Nebraska.

Meng, W., and Khayat, K. H. (2018). "Effect of Hybrid Fibers on Fresh Properties, Mechanical Properties, and Autogenous Shrinkage of Cost-Effective UHPC." *Journal of Materials in Civil Engineering*, 30(4), 04018030.

Meng, W., Valipour, M., and Khayat, K. H. (2016). "Optimization and Performance of Cost-Effective Ultra-High Performance Concrete." *Materials and structures*, 50(1), 29.

Mindess, S., Young, F., and Darwin, D. (2003). *Concrete 2nd Edition*, Prentice-Hall Englewood Cliffs, NJ.

Mindess, S., Young, J. F., and Darwin, D. (1981). *Concrete*, Prentice-Hall Englewood Cliffs, NJ.

Model Code (1990). "Model Code 1990, CEB FIP, fib." Comite Euro-International Du Beton, Paris, France.

Mohebbi, A., and Graybeal, B. (2022). "Prestress Loss Model for Ultra-High Performance Concrete." *Engineering Structures*, 252, 113645.

Mohebbi, A., Graybeal, B., and Haber, Z. (2022). "Time-Dependent Properties of Ultra High-Performance Concrete: Compressive Creep and Shrinkage." *Journal of Materials in Civil Engineering*, 34(6), 04022096.

Möser, B., Pfeifer, C., and Stark, J. (2008). "Durability and Microstructural Development during Hydration in Ultra-High Performance Concrete." *Concrete Repair, Rehabilitation and Retrofitting II. CRC Press.*, 105-106.

Mukhopadhyay, A., Liu, K.-W., and Jalal, M. (2018). "Further Validation of ASR Testing and Approach for Formulating ASR-Resistant Concrete Mix: Technical Report." TxDOT, Austin, TX.

Mukhopadhyay, A., Liu, K.-W., and Jalal, M. (2019). "An Innovative Approach to Fly Ash Characterization and Evaluation to Prevent Alkali-Silica Reaction." *ACI Materials Journal*, 116(4), 173-181.

Müller, U., Meng, B., Kühne, H.-C., Nemecek, J., Fontana, P., and Fehling, E. (2008). "Micro Texture and Mechanical Properties of Heat Treated and Autoclaved Ultra High Performance Concrete (UHPC)." *Proc., 2nd International Symposium on Ultra High Performance Concrete*, Kassel University Press, 213-220.

Musha, H., Ishida, Y., T, Y., and Yamashita (2007). "Mikaneike Bridge—The First Continuous Girder Bridge Using Ultra-High Strength Fiber Reinforced Concrete." *Journal of Prestressed Concrete Japan*, 49(No. 5), 18-26.

Naaman, A. E., and Homrich, J. R. (1989). "Tensile Stress-Strain Properties of SIFCON." *ACI Materials Journal*, 86(3), 244-251.

Naaman, A. E., and Wille, K. (2012). "The Path to Ultra-High Performance Fiber Reinforced Concrete (UHP-FRC): Five Decades of Progress." *Proceedings of Hipermat 2012 3rd International Symposium on UHPC and Nanotechnology for High Performance Construction Materials*, Kassel University Press, 3-15.

Namman, A., and Reinhardt, H. (2003). "Setting the Stage, toward Performance Based Classification of FRC Composites, High Performance Fiber Reinforced Cement Composties (HPFRCC 4)." *Proc. of the 4th Int. RILEM Workshop*.

NF-P-18-451 (2018). "French Standard Execution of Concrete Structures - Specific Rules for UHPFRC." AFNOR, La Plaine Saint-Denis, France.

NF-P-18-470 (2016). "French Standard Concrete – Ultra-High Performance Fibre-Reinforced Concretes – Specifications, Performance, Production and Conformity." AFNOR, La Plaine Saint-Denis, France.

NF-P-18-710 (2016). "French Standard National Addition to Eurocode 2 – Design of Concrete Structures: Specific Rules for Ultra-High Performance Fibre-Reinforced Concretes (UHPFRC)." AFNOR, La Plaine Saint-Denis, France.

Ngo, T. (2016). "Application of UHPC in Long Span Bridge Design." Master Degree Thesis, Delft University of Technology, Delft, The Netherlands.

NIST (2017). "Estimation of Pore Solution Conductivity." <https://www.nist.gov/el/materials-and-structural-systems-division-73100/inorganic-materials-group-73103/estimation-pore>.

Nkinamubanzi, P.-C., and Aïtcin, P.-C. (2004). "Cement and Superplasticizer Combinations: Compatibility and Robustness." *Cement, Concrete and Aggregates*, 26(2), 1-8.

Nkinamubanzi, P.-C., Mantellato, S., and Flatt, R. (2016). "Superplasticizers in Practice." *Science and Technology of Concrete Admixtures*, Elsevier, 353-377.

Oh, S., Noguchi, T., and Tomosawa, F. (1999). "Toward Mix Design for Rheology of Self-Compacting Concrete." *Proc., First International RILEM Symposium on Self-Compacting Concrete*, RILEM, 361-372.

Orgass, M., and Klug, Y. (2004). "Fibre Reinforced Ultra-High Strength Concretes." *Proc., The International Symposium on Ultra High Performance Concrete*, Kassel University Press, 637-648.

Ozyildirim, C. (2011). "Evaluation of Ultra-High-Performance Fiber-Reinforced Concrete." Virginia Department of Transportation, Richmond, VA.

Park, J.-J., Yoo, D.-Y., Park, G.-J., and Kim, S.-W. (2017). "Feasibility of Reducing the Fiber Content in Ultra-High-Performance Fiber-Reinforced Concrete under Flexure." *ACI Materials Journal*, 10(2), 118.

Park, J.-S., Kim, Y. J., Cho, J.-R., and Jeon, S.-J. (2015). "Early-age Strength of Ultra-High Performance Concrete in Various Curing Conditions." *ACI Materials Journal*, 8(8), 5537-5553.

Park, J. J., Kang, S. T., Koh, K. T., and Kim, S. W. (2008). "Influence of the Ingredients on The Compressive Strength of UHPC as a Fundamental Study to Optimize The Mixing Proportion." *Proc., The Second International Symposium on Ultra High Performance Concrete*, Kassel University Press, 105-112.

Park, S. H., Kim, D. J., Ryu, G. S., and Koh, K. T. (2012). "Tensile Behavior of Ultra High Performance Hybrid Fiber Reinforced Concrete." *Cement Concrete Composites*, 34(2), 172-184.

Passuello, A., Moriconi, G., and Shah, S. P. (2009). "Cracking Behavior of Concrete with Shrinkage Reducing Admixtures and PVA Fibers." *Cement Concrete Composites*, 31(10), 699-704.

Perry, V. H., and Seibert, P. J. (2008). "The Use of UHPFRC (Ductal®) for Bridges in North America: The Technology, Applications and Challenges Facing Commercialization." *Proc., The Second International Symposium on Ultra High Performance Concrete*, Kassel University Press, 815-822.

Piérard, J., Dooms, B., and Cauberg, N. (2012). "Evaluation of Durability Parameters of UHPC using Accelerated Lab Tests." *Proc., The 3rd International Symposium on UHPC and Nanotechnology for High Performance Construction Materials*, Kassel University Press, 371-376.

Pimienta, P., Mindeguia, J.-C., Simon, A., Behloul, M., Felicetti, R., Bamonte, P., and Gambarova, P. G. (2012). "Literature Review on the Behavior of UHPFRC at High Temperature." *Proc., Hipermat 2012 3rd International Symposium on UHPC and Nanotechnology for High Performance Construction Materials*, Kassel University Press, 549-556.

Pistilli, M. F., and Willems, T. (1993). "Evaluation of Cylinder Size and Capping Method in Compression Strength Testing of Concrete." *Cement, Concrete and Aggregates*, 15(1), 59-69.

Planete-tp (2008). "Peace Bridge in Seoul." *http://www.planete-tp.com/en/peace-bridge-in-seoul-a892.html* (Accessed Dec. 19, 2018).

Pyo, S., El-Tawil, S., and Naaman, A. E. (2016). "Direct Tensile Behavior of Ultra High Performance Fiber Reinforced Concrete (UHP-FRC) at High Strain Rates." *Cement Concrete Research*, 88, 144-156.

Pyo, S., Wille, K., El-Tawil, S., and Naaman, A. E. (2015). "Strain Rate Dependent Properties of Ultra High Performance Fiber Reinforced Concrete (UHP-FRC) Under Tension." *Cement and Concrete Composites*, 56, 15-24.

Ran, Q., Somasundaran, P., Miao, C., Liu, J., Wu, S., and Shen, J. (2009). "Effect of the Length of the Side Chains of Comb-Like Copolymer Dispersants on Dispersion and Rheological Properties of Concentrated Cement Suspensions." *Journal of Colloid and Interface Science*, 336(2), 624-633.

Rebentrost, M., Wight, G., and Fehling, E. (2008). "Experience and Applications of Ultra-High Performance Concrete in Asia." *Proc., The 2nd International Symposium on UHPC*, Kassel University Press, 19-30.

Reinhardt, H., and Naaman, A. (1992). "International Workshop—High Performance Fibre Reinforced Cement Composites." *Materials and Structures*, 25(1), 60-62.

Resplendino, J. (2008). "Ultra-High Performance Concretes—Recent Realizations and Research Programs on UHPFRC Bridges in France." *Proc., The 2nd International Symposium on UHPC*, Kassel University Press, 31-43.

Resplendino, J. (2011). "Introduction: What is a UHPFRC?" *Designing and Building with UHPFRC: State of the Art and Development*, F. Toutlemonde, and J. Resplendino, eds., ISTE and John Wiley & Sons, London, UK and Hoboken, NJ.

Resplendino, J., and Toulemonde, F. (2011). *Designing and Building with UHPFRC: State of the Art and Development*, ISTE and John Wiley & Sons, London, UK and Hoboken, NJ.

Resplendino, J., and Toulemonde, F. (2013a). *Designing and Building with UHPFRC*, John Wiley & Sons, Hoboken, NJ.

Resplendino, J., and Toutlemonde, F. (2013b). "The UHPFRC Revolution in Structural Design and Construction." *Proc., The International Symposium on Ultra-High Performance Concrete. UHPFRC 2013*, RILEM.

Richard, P., and Cheyrezy, M. (1995). "Composition of Reactive Powder Concretes." *Cement and Concrete Research*, 25(7), 1501-1511.

Richard, P., and Cheyrezy, M. H. (1994). "Reactive Powder Concretes with High Ductility and 200 - 800 MPa Compressive Strength." *ACI Special Publication*, 144.

Richardson, I. (2004). "Tobermorite/Jennite-and Tobermorite/Calcium Hydroxide-Based Models for the Structure of CSH: Applicability to Hardened Pastes of Tricalcium Silicate, β-Dicalcium Silicate, Portland Cement, and Blends of Portland Cement with Blast-Furnace Slag, Metakaolin, or Silica Fume." *Cement and Concrete Research*, 34(9), 1733-1777.

Riding, K. A., Ferraro, C. C., Hamilton, H., Voss, M. S., and Alrashidi, R. (2019). "Requirements for Use of Field-Cast, Proprietary Ultra-High-Performance Concrete in Florida Structural Applications." Florida Department of Transportation, Tallahassee, FL.

RILEM CPC 7 (1975). "Direct Tension Final Recommendation, E&FN Spon.", *Materials and Structures*, 579–582.

RILEM TC 162-TDF (2002). "Test and Design Methods for Steel Fibre Reinforced Concrete, Recommendations." *Materials and Structures*, 579–582.

Rossi, P. (1997). "High Performance Multimodal Fiber Reinforced Cement Composites (HPMFRCC): The LCPC Experience." *ACI Materials Journal*, 94(6), 478-783.

Rossi, P. (2000). "Ultra-High Performance Fibre Reinforced Concretes (UHPFRC): An Overview." *Fifth RILEM Symposium on Fibre-Reinforced Concretes (FRC)*, 87-100.

Rossi, P. (2001). "Ultra-High Performance - A French Perpective on Approaches used to Produce Highstrength, Ductile Fiber Reinforced Concrete." *Concrete International*, 23(12), 46-52.

Roux, N., Andrade, C., and Sanjuan, M. (1996). "Experimental Study of Durability of Reactive Powder Concretes." *Journal of Materials in Civil Engineering*, 8(1), 1-6.

Roy, D. M., Gouda, G., and Bobrowsky, A. (1972). "Very High Strength Cement Pastes Prepared by Hot Pressing and Other High Pressure Techniques." *Cement Concrete Research*, 2(3), 349-366.

Royce, M. (2016). "Utilization of Ultra High Performance Concrete (UHPC) in New York." *Proc., First International Interactive Symposium on UHPC*, Iowa State University, 1-9.

Russell, H. G., and Graybeal, B. A., (2013). "Ultra-High Performance Concrete: A State-of-the-Art Report for the Bridge Community." Federal Highway Administration, McLean, VA.

Saint-Pierre, F., Philibert, A., Giroux, B., and Rivard, P. (2016). "Concrete Quality Designation Based on Ultrasonic Pulse Velocity." *Construction and Building Materials*, 125, 1022-1027.

Sakai, E., Akinori, N., Daimon, M., Aizawa, K., and Kato, H. (2008). "Influence of Superplasticizers on The Fluidity of Cements With Different Amount of Aluminate Phase." *Proc., Second International Symposium on Ultra High Performance Concrete*, Kassel University Press, 85-92.

Sbia, L. A., Peyvandi, A., Lu, J., Abideen, S., Weerasiri, R. R., Balachandra, A. M., and Soroushian, P. (2017). "Production Methods for Reliable Construction of Ultra-High-Performance Concrete (UHPC) Structures." *Materials and Structures*, 50(1), 7.

Schachinger, I., Hilbig, H., Stengel, T., and Fehling, E. (2008). "Effect of Curing Temperature at An Early Age on The Long-Term Strength Development of UHPC." *Proc., 2nd International Symposium on Ultra High Performance Concrete*, Kassel University Press, 205-213.

Scheffler, B., and Schmidt, M. (2012). "Application of Ultra-High Performance Concrete for Multifunctional Road Pavements." *Proc., The 3rd International Symposium on UHPC and Nanotechnology for High Performance Construction Materials*, Kassel University Press, 913-920.

Scheydt, J. C., and Muller, H. (2012). "Microstructure of Ultra High Performance Concrete (UHPC) and its Impact on Durability." *Proc., The 3rd International Symposium on UHPC and Nanotechnology for High Performance Construction Materials*, Kassel University Press, 349-356.

Schmidt, M. (2012). "Sustainable Building with Ultra-High-Performance Concrete (UHPC)—Coordinated Research Program in Germany." *Proc., Hipermat 2012 3rd International Symposium on UHPC and Nanotechnology for High Performance Construction Materials*, Kassel University Press, 17-25.

Schmidt, M., and Fehling, E. (2005). "Ultra-High-Performance Concrete: Research, Development and Application in Europe." *ACI Special publication*, 228, 51-78.

Schmidt, M., and Fröhlich, S. (2010). "Testing of UHPC." *Proc., The Third International fib Congress and Exhibition Incorporating the PCI Annual Convention and National Bridge Conference,* Washington, DC.

Schmidt, W., Brouwers, H., Kühne, H.-C., and Meng, B. (2011). "Correlation Between Setting, Heat Evolution, and Deformations of Cementitious Binder Systems Depending on Type and Amount of Superplasticizer." *Proc., The 13th International Congress on the Chemistry of Cement*, Madrid, Spain.

SFRC Consortium (2014). "Design Guideline for Structural Applications of Steel Fibre Reinforced Concrete." Danish Technological Institute, Taastrup, Denmark.

Shah, J. H. (2021). "Shrinkage Characteristics and Modeling of Ultra-High-Performance Concrete." Master of Science Thesis, Texas A&M University, College Station, TX.

Shaheen, E., and Shrive, N. G. (2006). "Optimization of Mechanical Properties and Durability of Reactive Powder Concrete." *ACI Materials Journal*, 103(6), 444.

Shi, C., Wu, Z., Xiao, J., Wang, D., Huang, Z., and Fang, Z. (2015). "A Review on Ultra High Performance Concrete: Part I. Raw Materials and Mixture Design." *Construction and Building Materials*, 101, 741-751.

Shutt, C. (2009). "UHPC Joint Provides New Solutions." ASPIRE, Ramsey Construction Inc., Lakeville, N.Y.

Sika (2018). "Sika® ViscoCrete®-4100.", Sika, Lyndhurst, NJ.

Soliman, N. A., and Tagnit-Hamou, A. (2017). "Using Particle Packing and Statistical Approach to Optimize Eco-Efficient Ultra-High-Performance Concrete." *ACI Materials Journal*, 114(6).

Spragg, R., Qiao, C., Barrett, T., and Weiss, J. (2016). "Assessing a Concrete's Resistance to Chloride Ion Ingress Using The Formation Factor." *Corrosion of Steel in Concrete Structures*, Elsevier, 211-238.

Spragg, R. P., De La Varga, I., Montanari, L., and Graybeal, B. A. (2019). "Using Formation Factor to Define the Durability of UHPC." *Proc., International Interactive Symposium on Ultra-High Performance Concrete*, Iowa State University Digital Press.

Stiel, T., Karihaloo, B., and Fehling, E. (2004). "Effect of Casting Direction on the Mechanical Properties of CARDIFRC." *Proc., The International Symposium on Ultra-High Performance Concrete*, Kassel University Press, 481-493.

Stoeux, D., Batoz, J. F., Jacques, L., and Guingot, L. (2011). "UHPFRC–A Material for Perforated Panels and Lattice Work: Controlling Shrinkage in Order to Experiment with Various Shapes." *Designing Building with UHPFRC*, 87-100.

Sujivorakul, C. (2002). "Development of High Performance Fiber-Reinforced Cement Composites using Twisted Polygonal Steel Fibers." University of Michigan, Ann Arbor, MI.

Swiss Society of Engineers and Architects (2013). "Bétons fibrés Ultra-Performant: Matériaux, Dimensionnement et Exécution (UHPC: Materials, Design and Construction)." Swiss Society of Engineers and Architects, Zurich, Switzerland.

Tadros, M. K. (2019). "Ultra-High-Performance Concrete." *Structure*.

Tadros, M. K., Al-Omaishi, N., Seguirant, S. J., and Gallt, J. (2003). "NCHRP Report 496: Prestress losses in pretensioned high-strength concrete bridge girders." Transportation Research Board, Washington DC.

Tadros, M. K., and Morcous, G. (2009). "Application of Ultra-High Performance Concrete to Bridge Girders." Nebraska Department of Roads, Lincoln, Nebraska.

Tanaka, Y., Maekawa, K., Kameyama, Y., Ohtake, A., Musha, H., and Watanabe, N. (2011). "The Innovation and Application of UHPFRC Bridges in Japan." *Designing and Building with UHPFRC: State of the Art and Development*, ISTE and John Wiley & Sons, London, UK and Hoboken, NJ, 149-187.

Tanaka, Y., Musha, H., Tanaka, S., and Ishida, M. (2010). "Durability Performance of UFC Sakata-Mira Footbridge under Sea Environment." *Proc., Framcos*, 1648-1654.

Tanesi, J., Ardani, A., and Montanari, L. (2019). "Formation Factor Demystified and its Relationship to Durability." Federal Highway Administration, McLean, VA.

Tattersall, G. H., and Banfill, P. F. (1983). *The Rheology of Fresh Concrete*, Pitman Advanced Pub. Program, Boston, MA.

Taylor, H. F. (1997). *Cement Chemistry*, Thomas Telford London.

Thibaux, T. (2008). "UHPFRC Prestressed Beams as an Alternative to Composite Steel-Concrete Decks: The Example of Pinel Bridge (France)." *Waleaven & Stoelhorst*, 1077-1083.

Thomas, J. J., Biernacki, J. J., Bullard, J. W., Bishnoi, S., Dolado, J. S., Scherer, G. W., and Luttge, A. (2011). "Modeling and Simulation of Cement Hydration Kinetics and Microstructure Development." *Cement and Concrete Research*, 41(12), 1257-1278.

Thomas, M., Green, B., O'Neal, E., Perry, V., Hayman, S., and Hossack, A. (2012). "Marine Performance of UHPC at Treat Island." *Proc., The 3rd International Symposium on UHPC and Nanotechnology for High Performance Construction Materials*, Kassel University Press, 365-370.

Todd, J. D. (1955). "The Determination of Tensile Stress/Strain Curves for Concrete." *Proceedings of the Institution of Civil Engineers*, 4(2), 201-211.

Toutlemonde, F., and Resplendino, J. (2011). *Designing and Building with UHPFRC: State of the Art and Development*, Wiley, Hoboken, NJ.

Tue, N. V., Ma, J., and Orgass, M. (2008). "Influence of Addition Method of Superplasticizer on the Properties of Fresh UHPC." *Proc., The 2nd International Symposium on Ultra-High Performance Concrete*, Kassel University Press, 93-100.

TxDOT (2008). "DMS-4640, Chemical Admixtures for Concrete." TxDOT, Austin, TX.

TxDOT (2008). "Tex-418-A, Compressive Strength of Cylindrical Concrete Specimens Archives." TxDOT, Austin, TX.

TxDOT (2009). "DMS-4610, Fly Ash." TxDOT, Austin, TX.

TxDOT (2016). "DMS-4630, Silica Fume." TxDOT, Austin, TX.

TxDOT (2018). "Slag Cement: Material Producer List." TxDOT, Austin, TX.

TxDOT (2019). "DMS-4640, Material Producer List - Chemical Admixtures for Concrete." TxDOT, Austin, TX.

TxDOT (2019). "Fibers for Class A and Class B Concrete Applications: Material Producer List." TxDOT, Austin, TX.

TxDOT (2019). "Fly Ash: Material Producer List." TxDOT, Austin, TX.

TxDOT (2019). "Material Producer List." TxDOT, Austin, TX.

TxDOT (2019). "Silica Fume: Material Producer List." TxDOT, Austin, TX.

TxDOT (2023). "Bridge Design Manual - LRFD." TxDOT, Austin, TX.

Van, V., and Ludwig, H. (2012). "Proportioning Optimization of UHPC Containing Rice Husk Ash and Ground Granulated Blast-Furnace Slag." *Proc., The 3rd International Symposium on UHPC and Nanotechnology for High Performance Construction Materials*, Kassel University Press, 197-205.

Vernet, C. P. (2004). "Ultra-Durable Concretes: Structure at the Micro-and Nanoscale." *MRS Bulletin*, 29(5), 324-327.

Voo, Y., Foster, S., and Hassan, M. (2014). "The Current State of Art of Ultra-High Performance Concrete Bridge Construction in Malaysia." *Proc., The 12th International Conference on Concrete Engineering and Technology*, University of Malaysia, 12-14.

Voo, Y., Foster, S., and Pek, L. (2017). "Ultra-High Performance Concrete: Technology for Present and Future. " *Proc., Building Construction Authority Joint Seminar on Concrete for Sustainability, Productivity and The Future*, ACI.

Voo, Y. L., Sittampalam, K., Peng, C. W., and Singh, S. (2014). "Design of Ultra-High Performance Concrete Jetty in Marine Environment." *Proc., The 12th International Conference on Concrete Engineering & Technology-2014*, University of Malaysia, 239-248.

Wang, D., Shi, C., Wu, Z., Xiao, J., Huang, Z., and Fang, Z. (2015). "A Review on Ultra High Performance Concrete: Part II. Hydration, Microstructure and Properties." *Construction and Building Materials*, 96, 368-377.

Wang, R., and Gao, X. (2016). "Relationship between Flowability, Entrapped Air Content and Strength of UHPC Mixtures Containing Different Dosage of Steel Fiber." *Applied Sciences*, 6(8), 216.

Wang, W., Liu, J., Agostini, F., Davy, C. A., Skoczylas, F., and Corvez, D. (2014). "Durability of an Ultra High Performance Fiber Reinforced Concrete (UHPFRC) under Progressive Aging." *Cement Concrete Research*, 55, 1-13.

Way, R., and Wille, K. (2012). "Material Characterization of an Ultra-High Performance Fibre-Reinforced Concrete under Elevated Temperature." *Proc., The 3rd International Symposium on UHPC and Nanotechnology for High Performance Construction Materials*, Kassel University Press, 565-572.

Wee, T.-H., Babu, D. S., Tamilselvan, T., and Lim, H.-S. (2006). "Air-Void System of Foamed Concrete and its Effect on Mechanical Properties." *ACI materials journal*, 103(1), 45.

Weiss, W. J., Barrett, T. J., Qiao, C., and Todak, H. (2016). "Toward a Specification for Transport Properties of Concrete Based on the Formation Factor of a Sealed Specimen." *Advances in Civil Engineering Materials*, 5(1), 179-194.

Weiss, W. J., Spragg, R. P., Isgor, O. B., Ley, M. T., and Van Dam, T. (2018). "Toward Performance Specifications for Concrete: Linking Resistivity, RCPT and Diffusion Predictions Using the Formation Factor for Use in Specifications." *High Tech Concrete: Where Technology and Engineering Meet*, Springer, Cham, 2057-2065.

Weldon, B. D., Jauregui, D. V., Newtson, C. M., Taylor, C. W., Montoya, K. F., and Allena, S. (2010). "Feasibility Analysis of Ultra High Performance Concrete for Prestressed Concrete Bridge Applications."Las Cruces, NM.

Wen-yu, J., Ming-zhe, A., Gui-ping, Y., and Jun-min, W. (2004). "Study on Reactive Powder Concrete used in the Sidewalk System of the Qinghai-Tibet Railway Bridge." *Proc., International Workshop on Sustainable Development and Concrete Technology*, Center for Transportation Research and Education, Iowa State University, 333-338.

Wille, K. (2008). "Entwicklung und Beschreibung des Tragverhaltens neuartiger Verbund-konstruktionen unter Verwendung eines flächigen Bewehrungselementes." PhD Dissertation, University of Leipzig, Leipzig, Germany.

Wille, K., and Boisvert-Cotulio, C. (2013). "Development of Non-Proprietary Ultra-High Performance Concrete for Use in the Highway Bridge Sector." Federal Highway Administration, McLean, VA.

Wille, K., and Boisvert-Cotulio, C. (2015). "Material Efficiency in the Design of Ultra-High Performance Concrete." *Construction and Building Materials*, 86, 33-43.

Wille, K., El-Tawil, S., and Naaman, A. (2014). "Properties of Strain Hardening Ultra High Performance Fiber Reinforced Concrete (UHP-FRC) under Direct Tensile Loading." *Cement and Concrete Composites*, 48, 53-66.

Wille, K., Kim, D. J., and Naaman, A. E. (2011). "Strain-Hardening UHP-FRC with Low Fiber Contents." *Materials and Structures*, 44(3), 583-598.

Wille, K., Naaman, A. E., and El-Tawil, S. (2011). "Optimizing Ultra-High Performance Fiber-Reinforced Concrete." *Concrete International*, 33(9), 35-41.

Wille, K., Naaman, A. E., El-Tawil, S., and Parra-Montesinos, G. J. (2012). "Ultra-High Performance Concrete and Fiber Reinforced Concrete: Achieving Strength and Ductility without Heat Curing." *Materials and Structures/Materiaux et Constructions*, 45(3), 309-324.

Wille, K., Naaman, A. E., and Parra-Montesinos, G. J. (2011). "Ultra-High Performance Concrete with Compressive Strength Exceeding 150 MPa (22 ksi): A Simpler Way." *ACI materials journal*, 108(1).

Wille, K., and Parra-Montesinos, G. J. (2012). "Effect of Beam Size, Casting Method, and Support Conditions on Flexural Behavior of Ultra-High-Performance Fiber-Reinforced Concrete." *ACI Materials Journal*, 109(3), 379-388.

Wille, K., Tue, N. V., and Parra-Montesinos, G. J. (2014b). "Fiber Distribution and Orientation in UHP-FRC Beams and Their Effect on Backward Analysis." *Materials and Structures*, 47(11), 1825-1838.

Williamson, G. R. (1974). "The Effect of Steel Fibers on the Compressive Strength of Concrete." *ACI Special Publication*, 44, 195-208.

Wu, Z., Shi, C., He, W., and Wu, L. (2016). "Effects of Steel Fiber Content and Shape on Mechanical Properties of Ultra High Performance Concrete." *Construction and building materials*, 103, 8-14.

Wuest, J., and Brühwiler, E. (2008). "Model for Predicting the UHPFRC Tensile Hardening." *Proc., Ultra High Performance Concrete (UHPC): Proceedings of the Second International Symposium on Ultra High Performance Concrete*, Kassel University Press, 153.

Yahia, A., Mantellato, S., and Flatt, R. (2016). "Concrete Rheology: A Basis for Understanding Chemical Admixtures." *Science and Technology of Concrete Admixtures*, Elsevier, 97-127.

Yang, I. H., Joh, C., and Kim, B. S. (2010). "Structural Behavior of Ultra High Performance Concrete Beams Subjected to Bending." *Engineering Structures*, 32(11), 3478-3487.

Yazıcı, H., Yiğiter, H., Karabulut, A. Ş., and Baradan, B. (2008). "Utilization of Fly Ash and Ground Granulated Blast Furnace Slag as an Alternative Silica Source in Reactive Powder Concrete." *Fuel*, 87(12), 2401-2407.

Yoo, D.-Y., Lee, J.-H., and Yoon, Y.-S. (2013). "Effect of Fiber Content on Mechanical and Fracture Properties of Ultra High Performance Fiber Reinforced Cementitious Composites." *Composite Structures*, 106, 742-753.

Yoo, D. Y., and Banthia, N. (2016). "Mechanical Properties of Ultra-High-Performance Fiber-Reinforced Concrete: A Review." *Cement and Concrete Composites*, 73, 267-280.

Yoo, D. Y., Lee, J. H., and Yoon, Y. S. (2013). "Effect of Fiber Content on Mechanical and Fracture Properties of Ultra High Performance Fiber Reinforced Cementitious Composites." *Composite Structures*, 106, 742-753.

Yudenfreund, M., Skalny, J., Mikhail, R. S., and Brunauer, S. J. C. (1972). "Hardened Portland Cement Pastes of Low Porosity II. Exploratory Studies. Dimensional Changes." *Cement Concrete Research*, 2(3), 331-348.

Zdeb, T. (2013). "Ultra-High Performance Concrete Properties and Technology." *Bulletin of the Polish Academy of Sciences: Technical Sciences*, 61(1), 183-193.

Zhang, M., Tam, C., and Leow, M. (2003). "Effect of Water-to-Cementitious Materials Ratio and Silica Fume on the Autogenous Shrinkage of Concrete." *Cement and Concrete Research*, 33(10), 1687-1694.

Zhang, Y., Zhang, W., She, W., Ma, L., and Zhu, W. (2012). "Ultrasound Monitoring of Setting and Hardening Process of Ultra-High Performance Cementitious Materials." *NDT and E International*, 47, 177-184.

Zia, P., Ahmad, S., and Leming, M. (1997). "High-Performance Concretes: a State-of-Art Report (1989-1994)." Federal Highway Administration, McLean, VA.

APPENDIX A.
QUESTIONNAIRE TO IDENTIFY LOCALLY AVAILABLE MATERIALS AND CURING PRACTICES

A.1 INTRODUCTION

A questionnaire was developed to identify the locally available materials that can be sourced in Texas and the curing practices and facilities that may be available to Texas precasters for the development and implementation of UHPC mixtures for pretensioned bridge girders. The participants on the questionnaire are the representatives of several industries, including precasters, material suppliers, and ready-mix suppliers, along with the TxDOT Materials Division.

The scope and recipients of the questionnaire were finalized in consultation with the TxDOT Project Monitoring Committee. A web-based questionnaire was developed in the Qualtrics platform by the research team. The research team developed an introductory e-mail for use by the TxDOT Project Monitoring Committee members, who sent invitations to participate to the relevant industry contacts. In addition, the research team promoted the questionnaire to the precast industry during the local Precast Concrete Manufacturers Association (PCMA) meetings in 2019.

A link to the online questionnaire was provided to the participants along with an explanation of how the responses will be used in the project. The web-based questionnaire was developed in such a way that the participants are directed to different questions depending on their industry. The research team followed up with reminders to the project monitoring committee members, as needed, to help increase the response rate.

A total of 12 participants responded to the questionnaire. All participants have been assigned a unique ID number in this summary report to keep their identities anonymous. Table A.1 provides the respondent ID number, and their identified industry (or industries). The location information for the respondents is intentionally not provided in Table A.1 to maintain the anonymity of the respondents.

Table A.1. Participant Information.

Participant ID	Industry
PC-1	Precaster
PC-2	Precaster
PC-3	Precaster
PC-4	Precaster
PC&GC	Precaster and General Contractor
PC&RM	Precaster, Ready-Mix Supplier, and Material Supplier
GC&RM	General Contractor and Ready-Mix Supplier
GC-1	General Contractor
GC-2	General Contractor
GC-3	General Contractor
TxDOT	TxDOT Materials Division
ANOM	Anonymous

Note: PC = precaster, GC = general contractor, RM = ready-mix supplier, TX = TxDOT Material Division, and ANOM = anonymous

The following sections provide the questions and the responses from the various participants of the questionnaire and compile and synthesize the information under relevant categories. The following organization was used for this summary report:

- Section A.1 of the report provides a brief introduction of the document and lists participant IDs and their industries.
- Section A.2 focuses on the availability of UHPC constituent materials and contains names of the suppliers of the different constituent materials that are locally available and identified. The geographic locations of the constituents are also noted when this information is available.
- Section A.3 presents the curing conditions and prestressing release time for the fabrication of precast components from UHPC.
- Section A.4 summarizes information related to the current experience and potential for implementing UHPC for bridge construction in Texas based on the past experience of the participants, the capability and willingness to adapt UHPC, and the concerns or recommendations based on the concrete mixing equipment.

A.2 AVAILABILITY OF UHPC CONSTITUENT MATERIAL IN TEXAS

The first set of questions focused on availability of materials that may be used to develop nonproprietary UHPC mixtures in Texas. The responses are summarized below.

A.2.1 Intermediate Size Aggregate

Some studies have considered the use of intermediate size aggregate (maximum size aggregate = 0.4 in.; passing 3/8 and retaining on 1/8) in UHPC mixtures to improve the economy. Question 1 addresses the availability of intermediate size aggregates that can be used for developing UHPC mixtures. Table A.2 summarizes the responses.

Q1: Please indicate if the following aggregates could be sourced by your organization.

Table A.2. Availability of Intermediate Size Aggregate.

Participant ID	Limestone	Siliceous River Gravel (pea gravel)	Granite	Basalt, Dolomite, and Rhyolite
PC-3	✓			
PC&GC	✓	✓		
PC&RM	✓		✓	
GC&RM	✓	✓		
GC-1	✓			
GC-2	✓	✓		
GC-3	✓	✓		
TxDOT	✓	✓	✓	✓

The responses suggest that limestone, siliceous river gravel (pea gravel), basalt, granite, dolomite, and rhyolite are the intermediate size aggregates available locally in Texas. Based on the geographical locations of the respondents, limestone is available or can be sourced in Austin, Longview, Dallas, Houston, San Marcos, and El Paso; siliceous river gravel (pea gravel) is available or can be sourced in Austin, Longview, Dallas, and Houston; granite is available or can be sourced in El Paso.

A.2.2 Rapid Set Rapid Hardening Cement

High early strength, durability, and beneficial effects of high heat of hydration may be the major advantages of using rapid set rapid hardening (RSRH) cement in UHPC mixtures. However, accommodation of RSRH cement may be a challenge due to its rapid setting property. Question 2 addresses the availability of RSRH cement in Texas and provides additional comments the respondents provided about the challenges due to its rapid setting property. Table A.3 summarizes the responses.

Q2: Please indicate if RSRH cement (calcium sulphoaluminate cement, calcium aluminate cement, geopolymer) could be sourced by your organization. Please also include any concerns you have due to its rapid setting property.

Table A.3. Rapid Set Rapid Hardening (RSRH) Cement.

Participant ID	Availability	Concerns
PC-1	No	-
PC-3	No	-
PC&GC	No	"Cracking, soundness, shrinkage, controlling temperature of the component materials, pot life of mixed batches, and availability of technical assistance from the manufacturers and equipment suppliers."
PC&RM	Yes	"I don't believe Rapid Set cement is the way to go. We should look at admixtures, optimized gradations and conventional Type III cement to achieve higher strength."
GC&RM	Yes	-
GC-1	Yes	-
GC-2	No	-
GC-3	No	"Limited time to deliver, place, consolidate, and finish concrete after water has been introduced to the mix."
TxDOT	Yes	"The durability aspect of Calcium Sulfoalumnate (CSA) and Calcium Aluminate (CAC) cements needs to be vetted prior to implementation."

- : Not available

It can be concluded from the comments that regardless of the possibility of RSRH cement being sourced, the respondents generally do not favor the usage of RSRH cement because of potential problems, such as durability, high heat of hydration, rapid setting, and lack of technical guidance. Based on the geographical locations of the respondents, RSRH cement can be sourced in Austin, Longview, Houston, and El Paso.

A.2.3 Supplementary Cementitious Materials

Questions 3 through 5 request information on availability, prior experience, and suppliers of various SCMs. Table A.4 provides the responses for GGBFS, Table A.5 shows the responses related to silica fume, Table A.6 lists the responses for fly ash, and Table A.7 covers the other supplementary cementitious materials.

Q3: Please indicate if the following SCMs could be sourced by your organization.

Q4: Please indicate the types of SCMs commonly used by your organization to make Portland cement concrete.

Q5: Please provide the name(s) of producers or suppliers for the SCMs used by your organization.

Table A.4. Ground-Granulated Blast-Furnace Slag.

Participant ID	Availability (Q3)	Prior Experience (Q4)	Supplier (Q5)
PC&RM	Maybe	Yes	• Buzzi Unicem
GC-3	Yes	Yes	–
TxDOT	Limited availability (Gr 100)	–	• Caycem LTD • Buzzi Unicem USA • LafargeHolcim (US) • Skyway Cement Company

Notes: GGBFS is available in Cedar Park, El Paso, and Houston.
GGBFS supplier list is taken from TxDOT Materials Division (TxDOT 2018).
- : Not available

Table A.5. Silica Fume.

Participant ID	Availability (Q3)	Prior Experience (Q4)	Supplier (Q5)
PC&RM	Not sure	No	Not sure
TxDOT	Yes	–	• BASF • Cementec Industries. Inc. • Euclid Chemical Corp. • GCP Applied Technologies • Norchem Inc. • R-E-D Industrial Products

Notes: Silica fume supplier list is taken from TxDOT Materials Division (TxDOT 2019).
- : Not available

Table A.6. Fly Ash.

Participant ID	Availability (Q3)	Prior Experience (Q4)	Supplier (Q5)
PC-3	20% Class F	–	• Boral
PC&GC	Class F	–	–
PC&RM	Class C and F	–	• Boral
GC&RM	Class F	–	• Boral, • Martin Lake Plant (Tatum, TX)
TxDOT	All, particularly Class C and Class F	–	**Class C:** • Boral • Charah Inc • CV ASH • FlyAshDirect • Lafarge North America • Salt River Materials Group/Phoenix Cement **Class F:** • ACEMA • Argos Cement LLC • Boral Resources • Charah Inc • CR Minerals Co. LLC • FlyAshDirect • Integrated Materials, Inc. • Millennial Services LLC • Renewable Resources Co. LLC • Salt River Materials Group/Phoenix Cement **Modified Class F Fly Ash:** • rPozz, LLC

Notes:
1. Class C fly ash is commonly available in Cedar Park and El Paso.
2. Class F fly ash is commonly available in Austin, Cedar Park, El Paso, Longview, and San Marcos.
3. Fly ash supplier list is taken from TxDOT Materials Division (TxDOT 2019).
4. - : Not available

Table A.7. Other SCMs.

Participant ID	SCM	Availability (Q3)	Prior Experience (Q4)	Supplier (Q5)
PC&RM	• Silica Flour/Silica Powder • Ground Quartz • Metakaolin • Rice Husk Ash	Not sure	No	Not sure
TxDOT	• Silica Flour/Silica Powder • Ground Quartz • Metakaolin • Rice Husk Ash	Not available	-	-

- : Not answered

There were no responses for colloidal silica and glass powder. The comments suggest that GGBFS, fly ash, and silica fume are readily available, whereas silica four/silica powder, ground quartz, metakaolin, and rice husk ash are not readily available in Texas.

A.2.4 Steel Fibers

Questions 6 through 10 are related to the use of steel fibers in the concrete mix. Table A.8 summarizes the results.

- Q6: Do you have experience in working with UHPC or steel fiber-reinforced concrete (SFRC) mixtures?
- Q7: Please indicate if the following fiber types could be sourced by your organization.
  - Fibers of the diameters: 0.006 in., 0.008 in., 0.0012 in., 0.015 in., and others.
  - Fibers of length: 0.5 in., 0.6 in., 0.8 in., 1.2 in., and others.
  - Fiber types: straight, hooked, twisted, and others.
- Q8: Please indicate the types of fibers commonly used by your organization to make fiber-reinforced concrete.
- Q9: Please provide the name(s) of producers or suppliers for the fibers used by your organization.
- Q10: Would you be able to accommodate the use of 0.5 in. long and 0.008 in. diameter fibers to make UHPC?

Table A.8. Steel Fibers.

Participant ID	Prior Experience (Q6)	Availability (Q7)	Fiber Types Used (Q8)	Supplier (Q9)	Additional Comments (Q10)
PC-2	Yes	–	–	–	–
PC-3	No	–	–	–	–
PC-4	Yes	–	–	–	–
PC&GC	Yes	–	Not Sure	• Dorsett Brothers • Alamo	"Steel fiber needs high energy mixing to break the strands apart and get them separated. Mixes are difficult to finish smooth, and the mixing process is abrasive on the drums and liners, unsure how effectively they could be mixed in small or micro batches like a volumetric mixer."
PC&RM	Yes	–	Not sure	–	"We can find the product; it would be no problem to incorporate the fiber in the concrete mixture."
GC&RM	Yes	–	–	–	–
TxDOT	Yes	–	–	–	–
ANOM	Yes	0.006 in. and 0.012 in. diameter fibers	0.006 in. diameter fibers		–

- : Not answered

A large majority of the respondents expressed that they had prior experience with fibers; however, there was some concern expressed about the usage of steel fibers by one precaster, while a second precaster was willing to use it.

A.3 CURING RELATED TOPICS

A.3.1 Curing Methods

Questions 11 through 13 are related to the curing methods that are prevalent in the local precast industry. Table A.9 lists the responses related to the curing techniques currently being used for precast construction. Table A.9 and Table A.10 list the responses pertaining to the steam and thermal curing capabilities.

Q11: What type of curing methods are currently being used for precast construction?

Air curing, water curing, steam curing, tempered steam curing, dry curing, delayed steam curing.

Others: Please note if any additional methods could be made available if necessary.

Q12: Do you have steam or thermal curing capability in your facility?

Q13: Please provide any additional comments, including any specific reason(s) not to use steam or thermal curing.

Table A.9. Curing Methods Currently in Use for Precast Members (Q11).

Participant ID	Air Curing	Water Curing	Steam Curing	Delayed Steam Curing	Tempered Steam Curing	Dry Curing	Others
PC-3		✓					
PC&GC	✓	✓	✓		✓		Membrane curing
PC&RM	✓	✓					
TxDOT		✓					

Table A.10. Curing Methods Currently in Use for Precast Members.

Participant ID	Steam/Thermal Curing Capability (Q12)	Reason for Not Using Steam/Thermal Curing (Q13)
PC-3	No	–
PC&GC	No	"Cost and safety concerns; current mixes don't need it as much to get strength."
PC&RM	Yes	–

- : Not answered

Water curing and air curing are currently in use for the majority of the precast construction in Texas. There is a reluctance to adapt steam-curing methods owing to the high cost, safety factors, and present lack of a need for this method of curing.

A.3.2 Heat of Hydration

Question 14 explores the possibility of the use of the higher heat of hydration of RSRH cement to provide a thermal curing effect. Table A.11 presents the responses.

Q14: Do you think the relatively higher heat of hydration of RSRH cement compared to ordinary Portland cement can provide a beneficial thermal curing effect?"

Table A.11. Techniques for Higher Heat of Hydration.

Participant ID	Response
PC-3	"Yes."
PC&GC	"I would think that would depend on the element's shape."
PC&RM	"I don't know."

There appears to be a mixed opinion about the beneficial use of the higher heat of hydration of RSRH cement.

A.3.3 Extension of Prestressing Release Time

Question 15 explores whether the prestressing release time can be extended such that a higher early strength gain can be achieved.

Q15: In the precasting process, is there a potential for the prestressing release time to be extended? Can a gain of sufficient concrete strength for release be tolerated up to 2 days?

The response options include:

Yes.

No, sufficient strength gain must take place within 24 hours.

Alternate options such as cost-benefit trade-off in terms of early release time and heat-treatment are open for consideration.

Table A.12 presents the opinion of the respondents on the feasibility of extending the prestressing release time.

Table A.12. Prestressing Release Time Extension.

Participant ID	Response
PC-3	"Too much expansion and contraction in steel forms, causing thermal cracking in beams that sit for 24+hrs."
PC&GC	"No, sufficient strength gain must take place within 24 hours."
PC&RM	"Yes."

Although two of three respondents steered away from the idea of extending the release time, one respondent indicated that there is a possibility of extending the prestressing release time.

A.4 EXPERIENCE AND IMPLEMENTATION WITH UHPC

A.4.1 Experience with SFRC and UHPC

Question 16 is related to the experience of the respondents to using SFRC or UHPC. Table A.13 presents the comments of the respondents.

Q16: Tell us about your experience in utilizing SFRC (steel fiber-reinforced concrete) or UHPC in the precast process or in bridge construction. Have you been involved in any application or use of UHPC—for example, for strong connection joints?

Table A.13. Experience with SFRC and UHPC.

Participant ID	Experience
PC&GC	"I've used steel fiber in Class E for seal slabs in cofferdams placed in a tremie system, where all concrete was pumped and temperature controlled. Mixing was a big concern, and clumping of larger diameter strand was a constant issue with clogging the pump and accelerated wear on the drum liner and pump reducers. Once the cofferdam was dewatered after the seal had cured, fiber sticking out of the slab was a safety concern, and the slab had to be super cleaned and strand bent over or cut off flush to keep people from getting them stuck thru their boots. UHPC variants have been in use on joint replacements in the northeast for several years. These have been mostly pre-packaged mixes that are commercially available. They are super sticky, difficult to finish, and don't have a consistent set rate even when controlling competent temperatures and surface saturation."
PC&RM	"No."
TxDOT	"No UHPC experience in Texas. A few projects have been let with UHPC connections, but not constructed yet. TxDOT allows steel fibers in Class A and B concrete (riprap, sidewalk). Approved list of fibers for these applications list suppliers and fiber products approved."

Note: Pre-qualified fibers for concrete metal by TxDOT lists Bekaert (1.38 in. and 2.36 in. long fibers); Helix (1.00 in. long fiber)s; and Sika Corporation (2.00 in., and 1.5 in. long fibers) as the producers of the fibers for Class A and Class B Concrete Applications (TxDOT 2019).

Safety and maintenance concerns appear to be the biggest deterrents for the use of SRFC. Aversion to the use of UHPC was indicated due to difficulty in working with the mix and due to the inconsistent set rate despite controlled conditions.

A.4.2 Potential for UHPC Implementation

Question 17 is intended to identify the potential for implementation of UHPC for future bridge construction in Texas. Table A.14 presents the comments from the respondents.

Q17: How well placed is your company, or the industry in general, in adapting to the use and implementation of UHPC in bridge construction? What are your perspectives and/or suggestions regarding the methods to facilitate implementation of UHPC in bridge construction?

Table A.14. Ability to Facilitate UHPC Implementation.

Participant ID	Response
PC&GC	"If the department thinks it will improve durability at an acceptable cost, and we are able to work together on the specifications and application, industry will adapt."
PC&RM	"We are glad to look at any alternatives for casting higher strength concrete bridge girders."

Two respondents showed willingness to incorporate UHPC in their facility if it is better for the industry.

A.4.3 Concrete Mixing Equipment

Question 18 is intended to acquire information about the concrete mixing equipment for the development of nonproprietary UHPC. Table A.15 presents the responses.

Q18: If possible, please provide specifications for the standard concrete mixing equipment used in your facility that may assist in establishment of the limiting criteria on aggregate size and workability.

Table A.15. Concrete Mixing Equipment.

Participant ID	Response
PC&GC	"Storage of separate aggregates, sands, or cements that are inconsistent with other general mixes will be a concern, especially if there are low volume. Environmental controls will also be a concern."
PC&RM	"We produce our own aggregate, so we can make about any size specified. We are experimenting right now with smaller aggregate in our precast and prestress operation. We have a BHS 6-yard compulsory mixer."

There is a mixed response about the possibility of incorporating the UHPC mixes in the existing system; it depends on the ability of the facility to source and handle aggregate that is not commonly used or is in lower volumes than those used for the more conventional mixes.

A.5 SUMMARY

The main findings of the questionnaire are summarized as follows:

- **Availability of UHPC Constituent Materials**

Limestone, siliceous river gravel (pea gravel), basalt, granite, dolomite, and rhyolite are the intermediate size aggregates available locally in Texas.

Limestone is available or can be sourced in Austin, Longview, Dallas, Houston, San Marcos, and El Paso.

Siliceous river gravel (pea gravel) is available or can be sourced in Austin, Longview, Dallas, and Houston.

Granite is available or can be sourced in El Paso.

The respondents generally do not favor the use of RSRH cement because of potential problems such as durability, high heat of hydration, and rapid setting leading to potential difficulty in placing the concrete.

With respect to SCMs, the respondents indicated that GGBFS, fly ash, and silica fume are readily available; whereas silica flour/silica powder, ground quartz, metakaolin, and rice husk ash are not readily available in Texas.

Most respondents said they had prior experience with fibers; however, there was some concern expressed about the use of steel fibers by one precaster, while a second precaster was willing to use them.

- **Curing**

Water curing and air curing are currently in use for the majority of the precast construction in Texas.

There is a reluctance to adapt steam-curing methods owing to the high cost, safety factors, and a present lack of a need for this method of curing.

Although two of three precaster respondents preferred to avoid extending the prestressing release time, one precaster indicated that there is a possibility of extending it.

- **Experience and Implementation of UHPC**

Only two respondents indicated they have experience with UHPC.
Both respondents showed willingness to incorporate UHPC in their facility if it is better for the industry.
Safety and maintenance concerns appear to be the biggest deterrents to the use of SFRC. One of the respondents was averse to the use of UHPC due to difficulty in working with the mix and due to the inconsistent set rate despite controlled conditions.

One respondent expressed concern about storage and environmental controls of the UHPC constituent materials that are inconsistent with other general mixes.

APPENDIX B.
CREEP AND SHRINKAGE TEST RESULTS

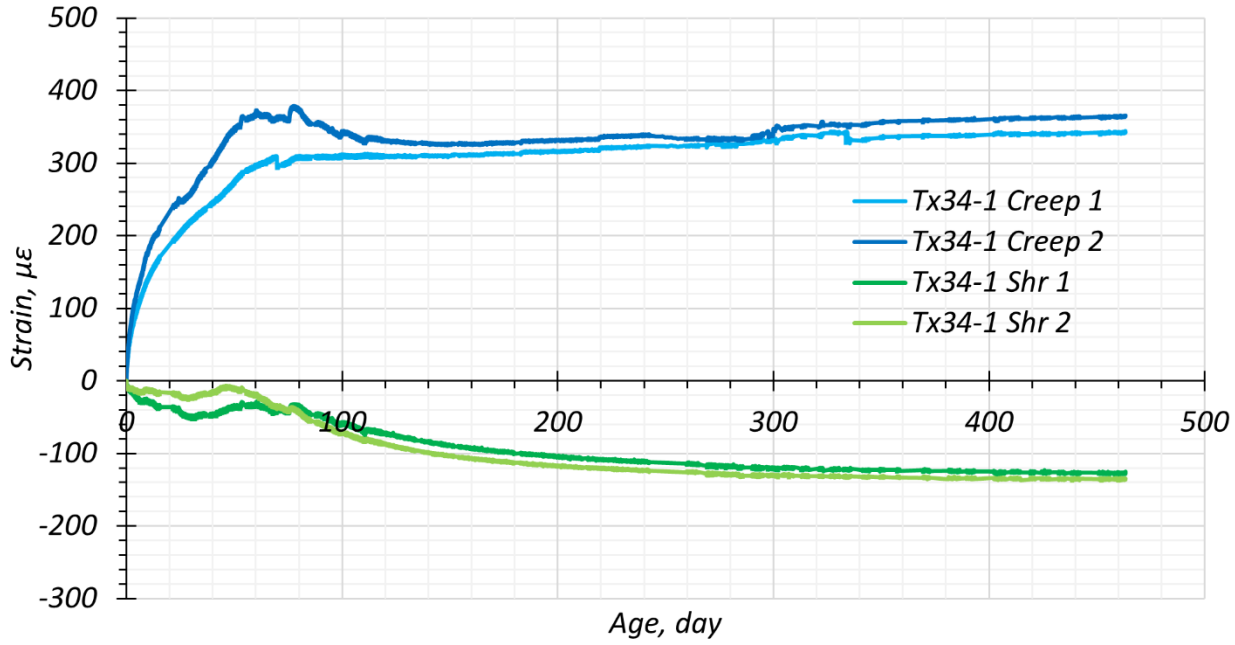

(a) Creep Test Results of Individual Specimens for Tx34-1

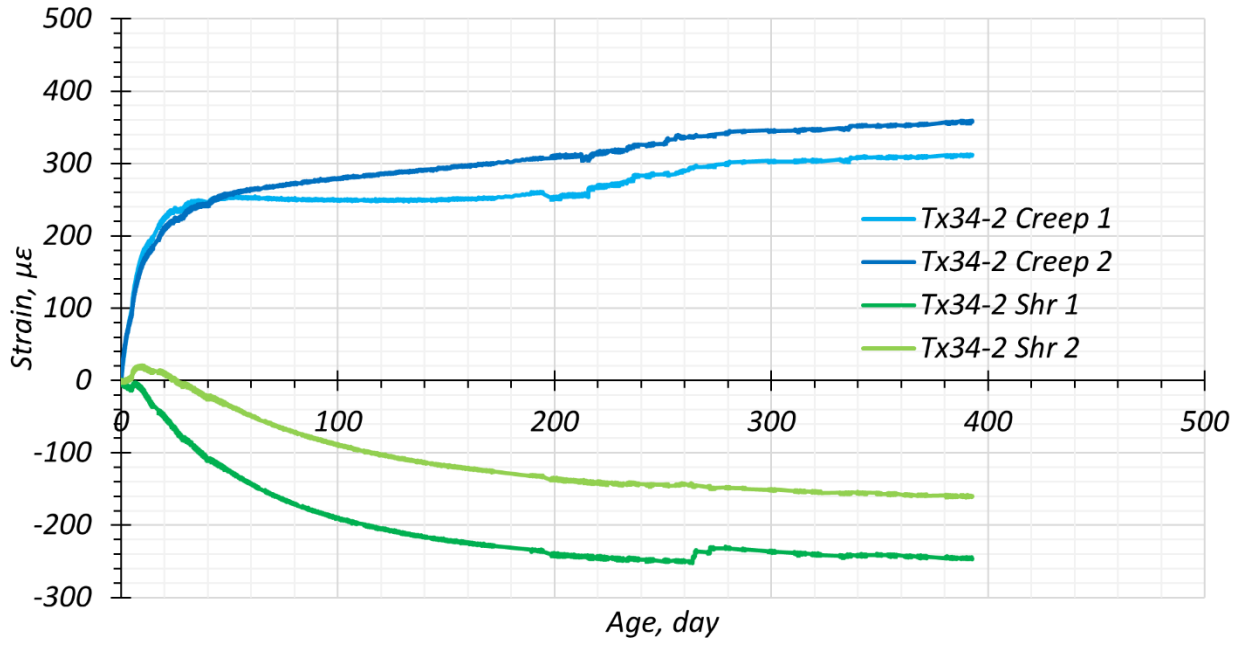

(b) Creep Test Results of Individual Specimens for Tx34-2

Figure B.0.1. Creep Test Results of Individual Specimens.

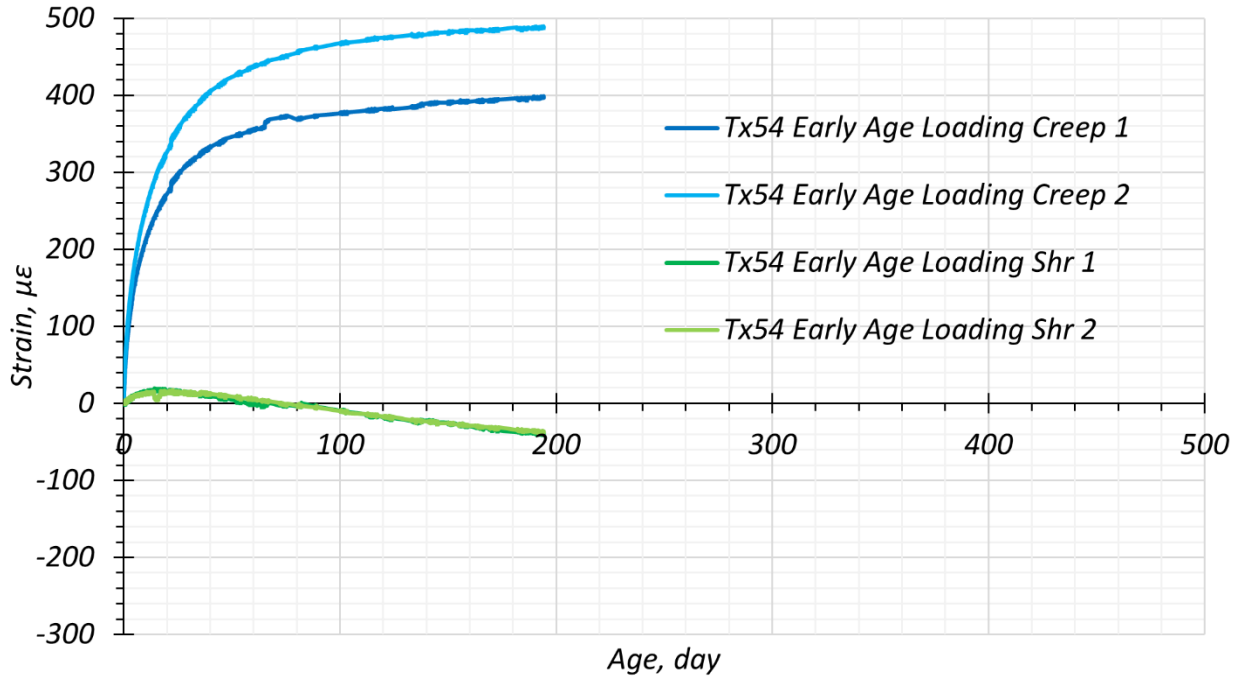

(c) Creep Test Results of Individual Specimens for Tx54 Early Age Loading

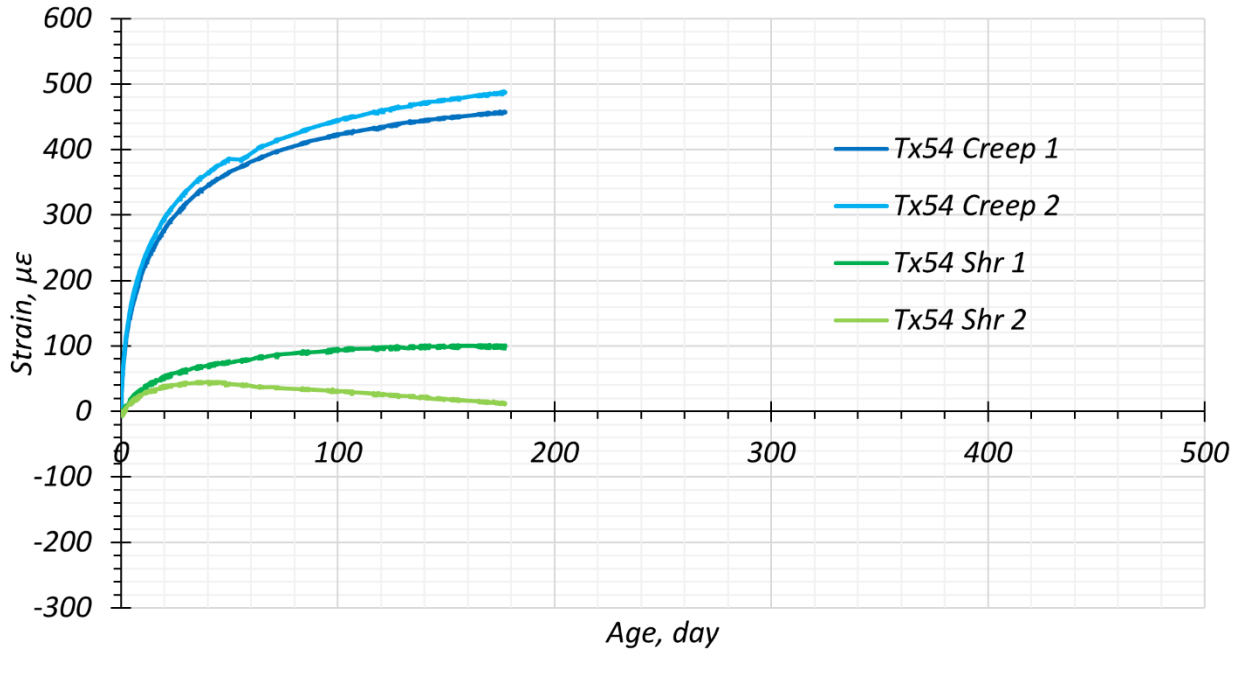

(d) Creep Test Results of Individual Specimens for Tx54

Figure B.1. Creep Test Results of Individual Specimens (Continued).

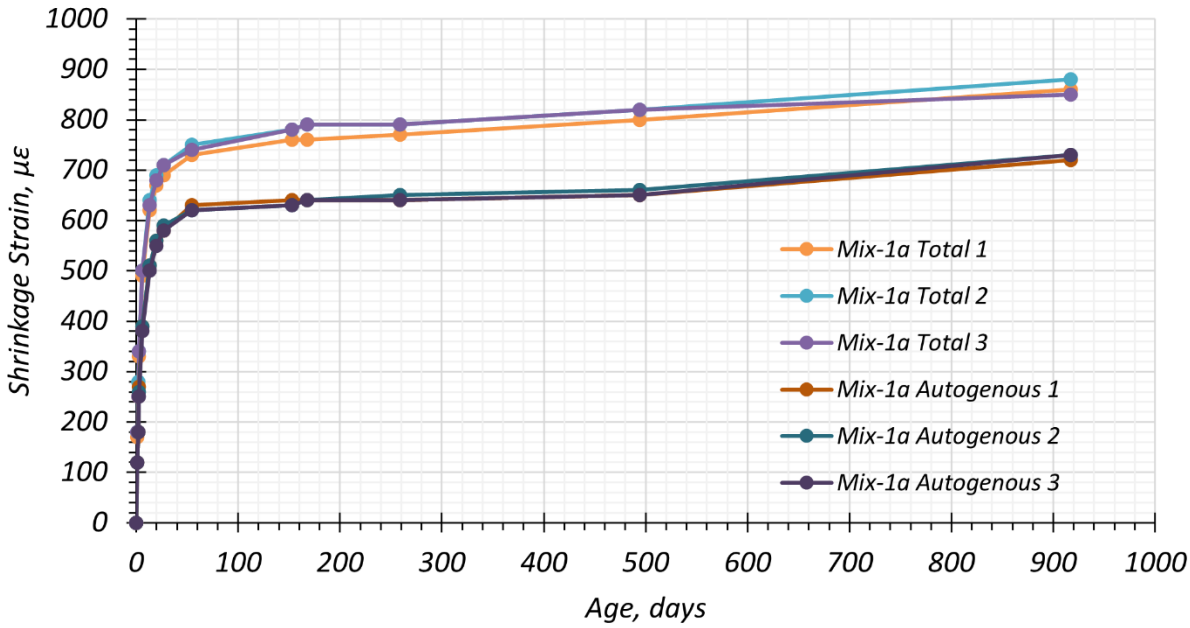

(a) Shrinkage Test Results of Individual Specimens for Mix-1a

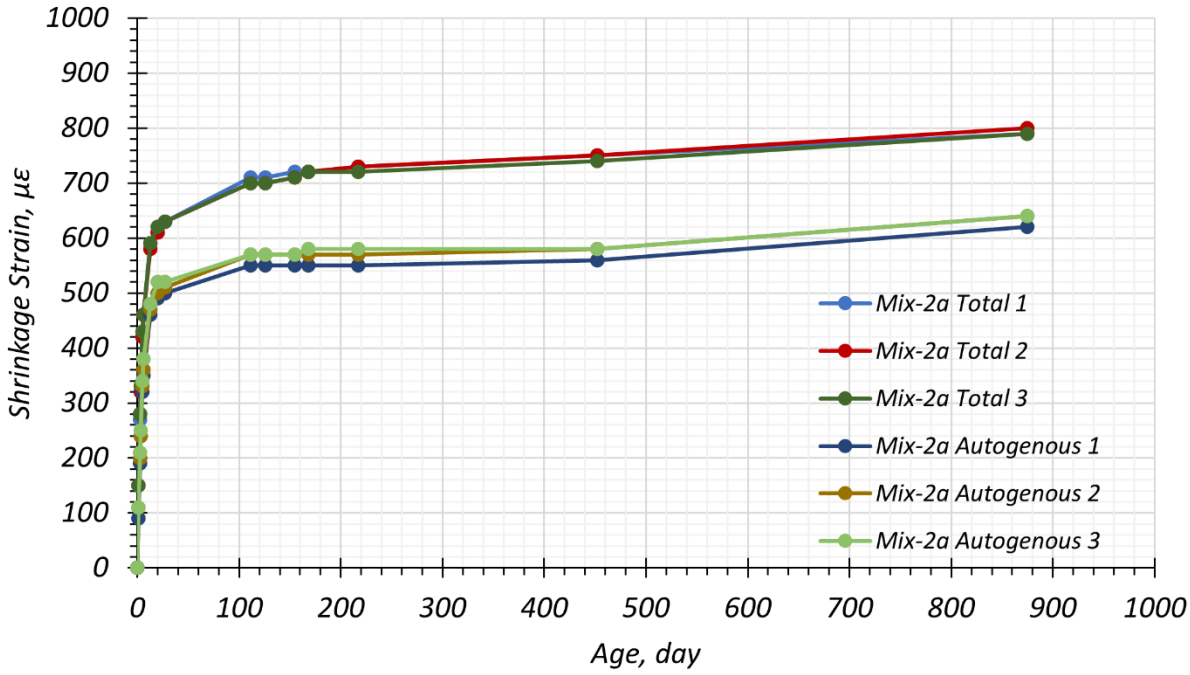

(b) Shrinkage Test Results of Individual Specimens for Mix-2a

Figure B.0.2. Shrinkage Test Results of Individual Specimens.

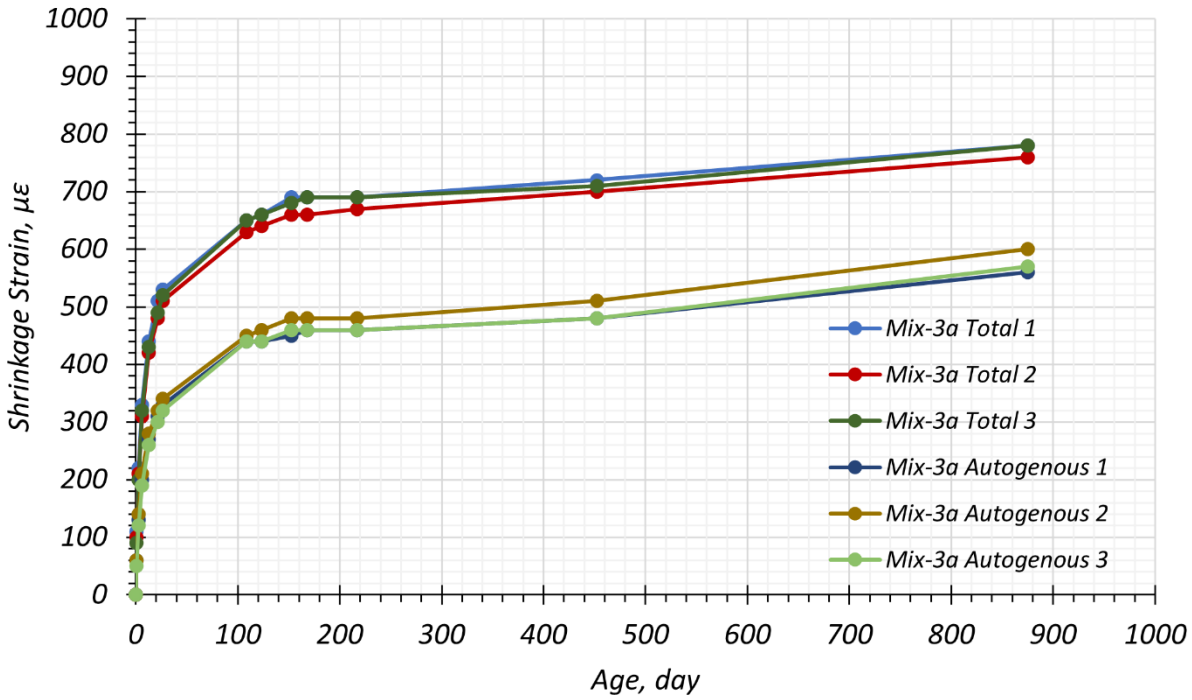

(c) Shrinkage Test Results of Individual Specimens for Mix-3a

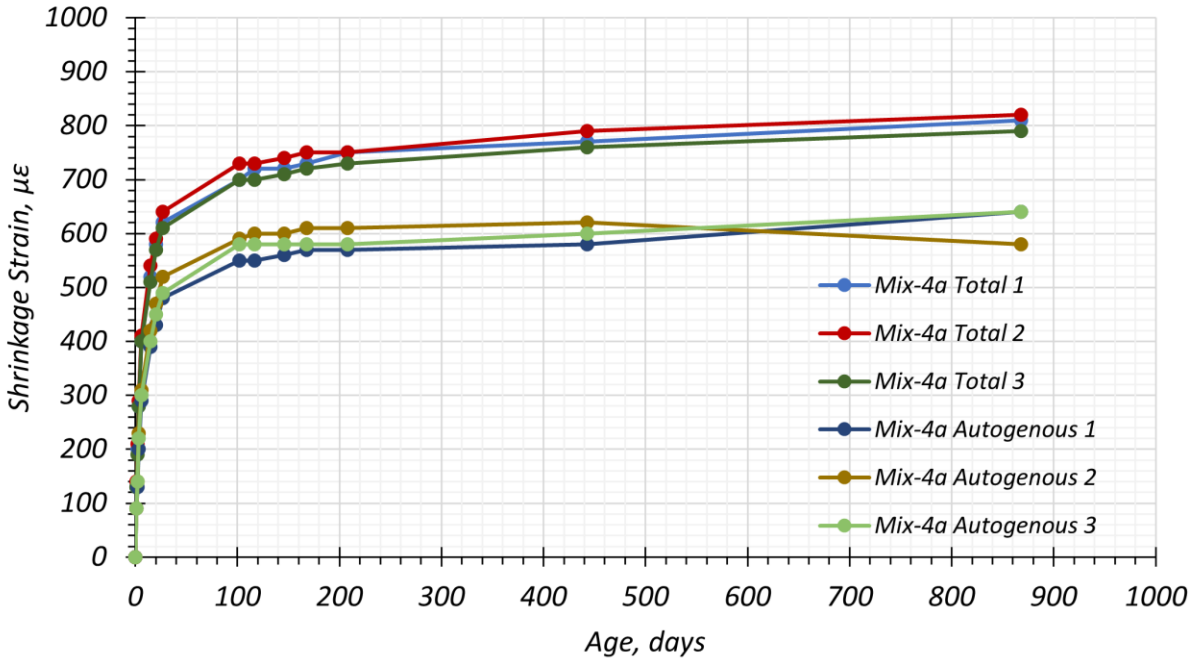

(d) Shrinkage Test Results of Individual Specimens for Mix-4a

Figure B.2. Shrinkage Test Results of Individual Specimens (Continued).

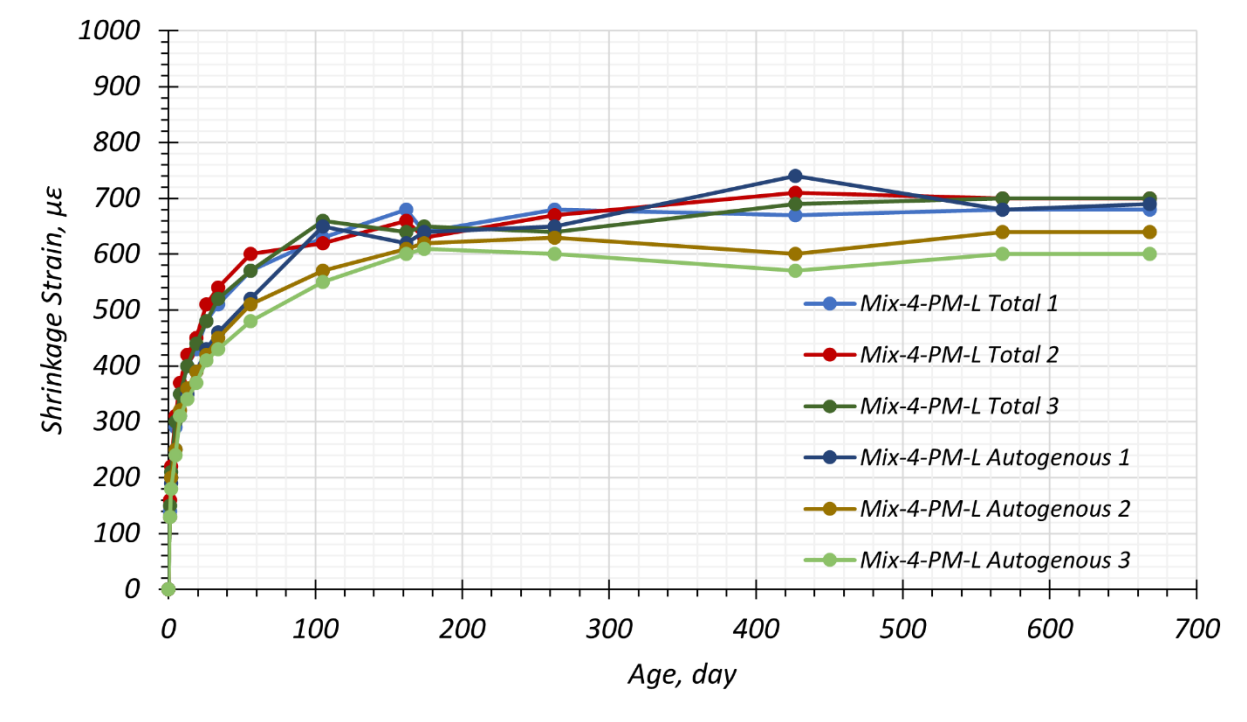

(e) Shrinkage Test Results of Individual Specimens for Mix-4-PM-L

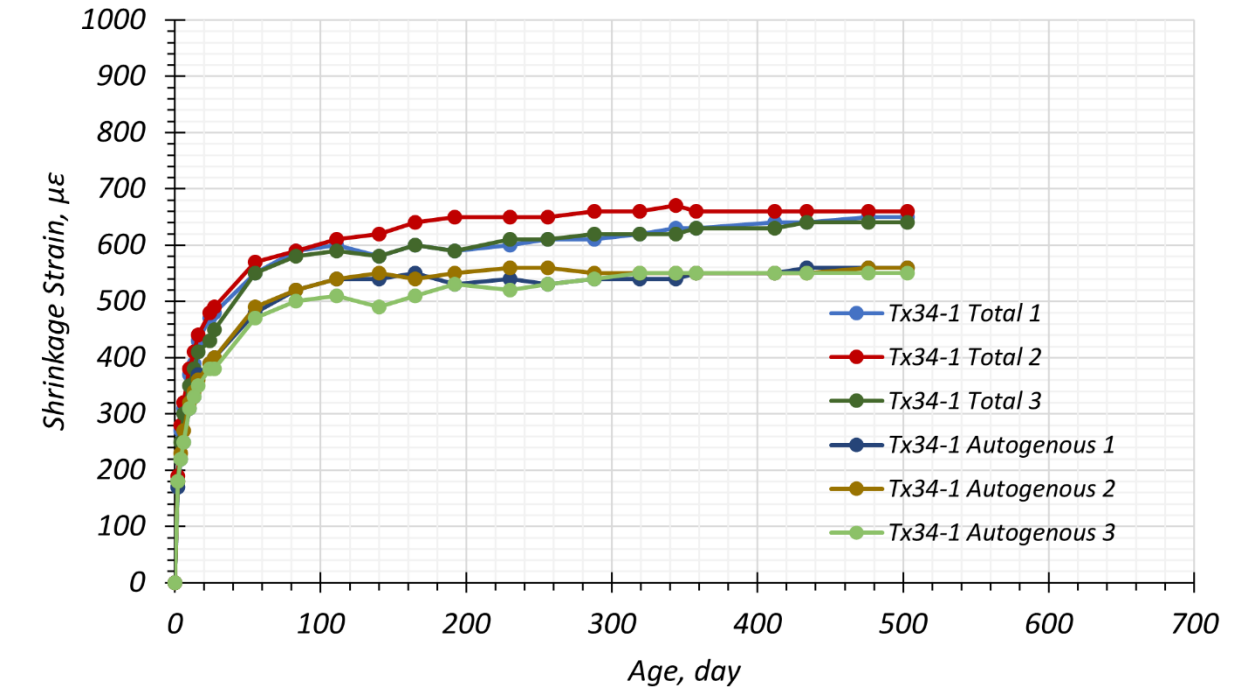

(f) Shrinkage Test Results of Individual Specimens for Tx34-1

Figure B.2. Shrinkage Test Results of Individual Specimens (Continued).

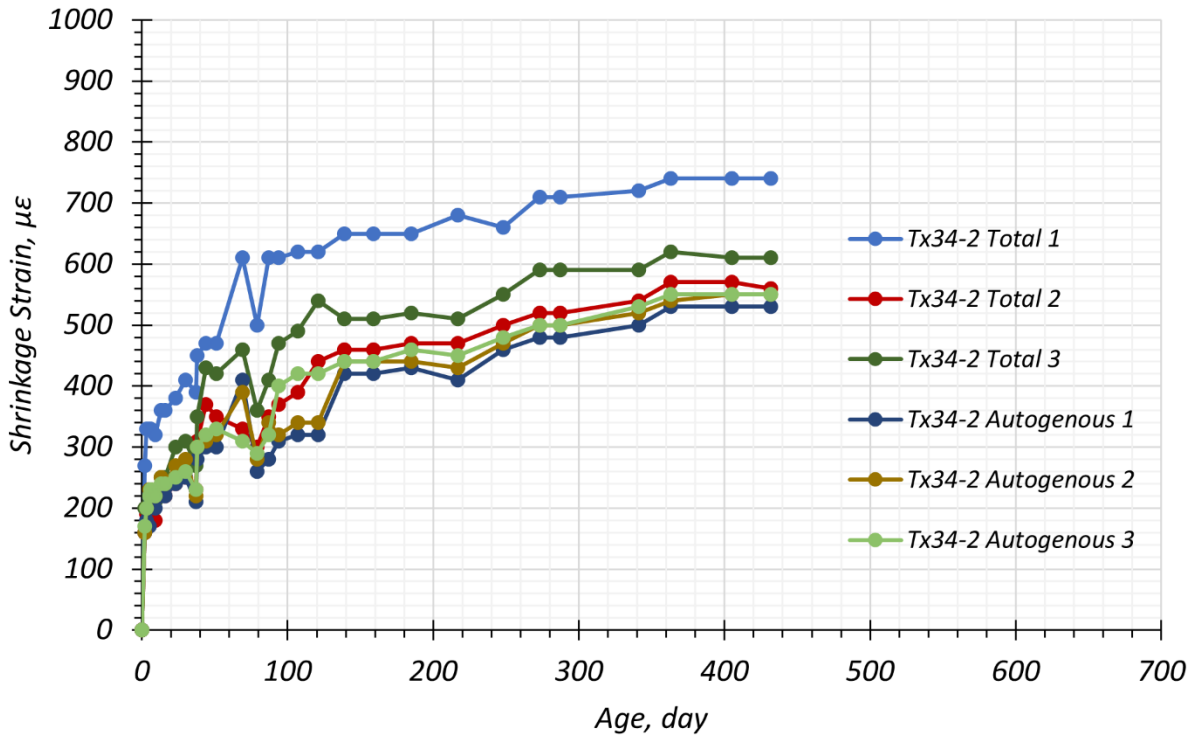

(g) Shrinkage Test Results of Individual Specimens for Tx34-2

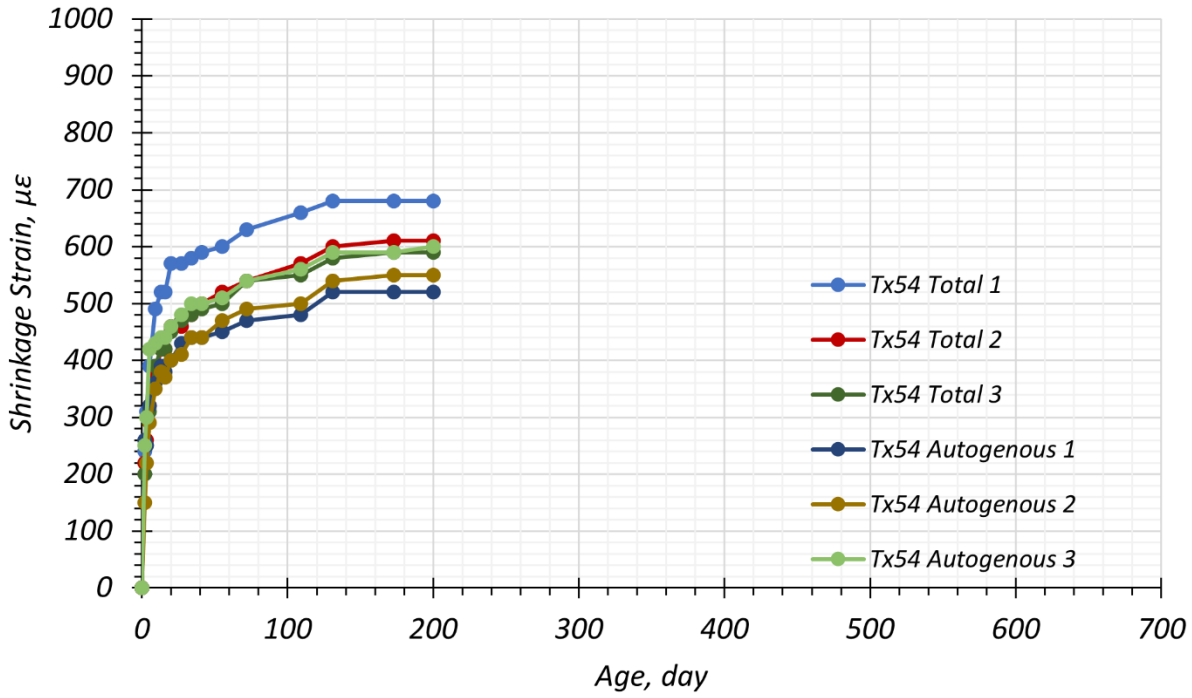

(h) Shrinkage Test Results of Individual Specimens for Tx54

Figure B.2. Shrinkage Test Results of Individual Specimens (Continued).